
CHAPTER 5. RIVER HYDRODYNAMICS CALIBRATION

by

Peter Sucsy, Ph.D.

Ed Carter

David Christian, P.E.

Michael Cullum, P.E.

Kijin Park, Ph.D.

Joseph Stewart, P.E.

Yanfeng Zhang, Ph.D., P.E.

St. Johns River Water Management District
Palatka, Florida

2011

This page intentionally left blank.

TABLE OF CONTENTS

RIVER HYDRODYNAMICS WORKING GROUP.....	VII
LIST OF FIGURES	VIII
LIST OF TABLES	XXIII
ACRONYMS, ABBREVIATIONS, AND CONVERSION FACTORS	XXIX
1 INTRODUCTION.....	1
2 DESCRIPTION OF STUDY AREA	2
2.1 Precipitation and Evaporation	2
2.2 Tributaries.....	3
2.3 Ocean Influence.....	4
2.4 Ocean Tide.....	4
2.5 Salinity.....	5
2.6 River Slope and Lakes	10
2.6.1 Lake Area	10
2.6.2 Lake Volume	11
2.7 Geomorphology and Relict Seawater	12
2.7.1 Spatial Variation of the Hawthorn Formation.....	13
2.7.2 The Offset Course of the St. Johns River.....	13
2.7.3 Springs.....	14
2.7.4 Diffuse Groundwater Discharge.....	16
3 OBSERVED DATA	18
3.1 Water Level	18
3.2 Tidal Harmonics	23
3.3 Discharge	28
3.4 Salinity in the St. Johns River Main Stem.....	40
3.4.1 The Practical Salinity Scale 1978.....	40
3.4.2 Observed Salinity	41
3.4.3 Upstream Extent of Ocean Salinity.....	47
3.4.4 Seasonal Variation of Salinity.....	48

3.5	Springs	49
3.6	Wastewater Treatment Plants	52
3.7	Rainfall	54
3.8	Evaporation.....	58
3.9	Wind	61
3.10	Water Quality	69
3.11	Bathymetry	75
3.11.1	Bathymetric Surveys of the Lower and Middle St. Johns River	75
3.11.2	Check of Middle St. Johns River Bathymetry	76
3.11.3	Digital Elevation Model	77
3.11.4	Final Digital Elevation Model of the Lower and Middle St. Johns River.....	80
4	MODEL FRAMEWORK.....	82
4.1	Ocean Tide.....	83
4.1.1	Effect of Ocean Tide on the St. Johns River	83
4.1.2	Astronomical Tide.....	84
4.1.3	Meteorological Tide	84
4.1.4	Importance of Meteorological Tide.....	87
4.2	Ocean Influence on Middle St. Johns River Stage	89
4.2.1	Introduction	89
4.2.2	Comparison Between River Stage at DeLand and Mayport	90
4.2.3	Comparison Between River Stage and Discharge at DeLand.....	91
4.2.4	Correlation of River Stage and Discharge at DeLand by Q-Limit.....	91
4.2.5	Evidence for Sea Level Rise in the middle St. Johns River	93
4.2.6	Summary	94
4.3	Slope–Discharge Relationships in the Middle St. Johns River	95
4.3.1	Slope–Discharge Relationship in Middle St. Johns River	97
4.3.2	Evidence for Errors in Vertical Levels Between Stations.....	98
4.3.3	Correcting for Leveling Errors Between Stations	98
4.4	Modeling Salinity in the Lower and Middle St. Johns River	104
4.4.1	Introduction	104
4.4.2	Salt Composition of the St. Johns River Main Stem.....	105
4.4.3	Conductivity–Chloride Relationships in the Oligohaline Reaches	109
4.4.4	Dominance of Relict Seawater in the Salt Composition of the Oligohaline Reach of the St. Johns River	111
4.4.5	Classification of Sources of Salt by Salt Composition	116
4.4.6	Discharge–Chloride Relationships.....	120
4.5	Summary.....	126
5	MODEL BOUNDARY CONDITIONS	127
5.1	Model Grids	127
5.2	Ocean Water Level and Salinity	128
5.3	Tributary Discharge and Salinity.....	129
5.3.1	Tributary Discharge.....	129
5.3.2	Tributary Salinity	132

5.4	Spring Discharge and Salinity	138
5.4.1	Methods of Estimating Spring Discharge	139
5.4.2	Summary of Spring Boundary Conditions	142
5.5	Diffuse Groundwater Discharge	143
5.6	Wastewater Treatment Plants	147
5.7	Meteorology: Rainfall, Evaporation, and Wind	149
6	MODEL CALIBRATION.....	149
6.1	Introduction	149
6.2	EFDC Model Grid Development.....	150
6.2.1	Introduction	150
6.2.2	Development of the Base Grid of the Lower St. Johns River	151
6.2.3	Grid Convergence	155
6.2.4	Adding Depths to the Model Grids	165
6.2.5	Final Model Grids	173
6.3	Vertical Grid Resolution.....	177
6.4	Selection of Calibration Period.....	178
6.5	Comparative Statistics	183
6.6	Calibration of Bottom Roughness	184
6.6.1	Calibration of Lower St. Johns River Bottom Roughness	184
6.6.2	Calibration of Middle St. Johns River Bottom Roughness	187
6.6.3	Summary of Bottom Roughness Calibration	221
6.7	Final Calibration	222
6.7.1	Final Calibration of the EFDC-LSJR Hydrodynamic Model.....	222
6.7.2	Final Calibration of Middle St. Johns River Model	242
6.8	Summary.....	251
7	MODEL CONFIRMATION.....	252
7.1	Introduction	252
7.2	Confirmation of the Lower St. Johns River Model	253
7.2.1	Hourly Water Level.....	253
7.2.2	Tidal Discharge	255
7.2.3	Salinity	263
7.3	Confirmation of the Middle St. Johns River Model	269
7.3.1	Daily Water Level	269
7.3.2	Discharge.....	273
7.3.3	Salinity	284
7.4	Confirmation of the Combined St. Johns River Model	298
7.4.1	Water Level	299
7.4.2	Discharge.....	302
7.4.3	Salinity	303

8 CONCLUSIONS 306

BIBLIOGRAPHY 1

RIVER HYDRODYNAMICS WORKING GROUP

Name (Organization)	Role
Peter Sucsy, Ph.D. (SJRWMD)	Working Group Leader, Author
Ed Carter (SJRWMD)	Author
David Christian, P.E. (SJRWMD)	Author
Michael Cullum, P.E. (SJRWMD)	Technical Director
Kijin Park, Ph.D. (SJRWMD)	Author
Joseph Stewart, P.E. (SJRWMD)	Author
Yanfeng Zhang, Ph.D., P.E. (SJRWMD)	Author

LIST OF FIGURES

Figure 2–1.	Monthly total rainfall averaged over 1996 to 2005 and spatially averaged over the EFDC model area.	3
Figure 2–2.	Propagation of astronomical tidal wave between the river mouth and Lake George. Each curve shows the spatial variation of the height of tide at identical times. m = meters.....	5
Figure 2–3.	Salinity ecological zones based on the Venice Salinity Classification for the St. Johns River using observed mean salinity. Salinity ranges by zone are as follows: euhaline (30 to 40), polyhaline (18 to 30), mesohaline (5 to 18), oligohaline (0.5 to 5), and fresh (< 0.5). SR46H = State Road (SR) 46 above Lake Harney.....	7
Figure 2–4.	Five-point plots of observed salinity distributions in the St. Johns River over the first 100 river kilometers.	8
Figure 2–5.	Five-point plots of observed salinity distributions in the St. Johns River for river kilometers 100 to 310, Racy Point to Lake Harney.	8
Figure 2–6.	Division of St. Johns River by extent of (a) astronomical and meteorological tides and (b) source of salinity. RSW = relict seawater.	9
Figure 2–7.	Comparison of surface area (km ²) of lacustrine water bodies in the lower and middle St. Johns River. All water bodies are represented to scale. MSJR = middle St. Johns River. LSJR = lower St. Johns River.....	11
Figure 2–8.	Graphic representation of volume of lacustrine water bodies in the lower and middle St. Johns River. Where one box is nested inside another box, the smaller box is located upstream. LSJR = Lower St. Johns River.....	12
Figure 2–9.	Topography and geology of the St. Johns River Basin between Lake Harney and the Ocklawaha River. The river enters a geologically older valley downstream of Lake Harney as it flows around the Volusia Block Fault.....	14
Figure 2–10.	Comparison of chloride levels and pool elevation for St. Johns River springs.	15
Figure 2–11.	Salt composition of selected springs compared to the Ocean Standard. Springs are sorted by chloride abundance. Springs most similar to ocean water lie below an elevation of 5 ft NGVD29 and have salts dominated by relict seawater.	16

Figure 2–12. Chloride concentration in the Upper Floridan aquifer (UFA) within the St. Johns River Water Management District (SJRWMD). High chloride concentrations occur directly along the path of the SJR between Lake Poinsett and Lake George.....	17
Figure 3–1. Locations of stations with continuously observed water level active for the model simulation period of 1996 to 2005. Map numbers are defined in Table 3–1.....	19
Figure 3–2. Locations of stations with harmonic tidal constituents for water level. Map numbers are defined in Table 3–3.	24
Figure 3–3. Locations of stations with continuously observed discharge. Map numbers are defined in Table 3–6.	29
Figure 3–4. Map showing locations of observed tidal discharge for the northern end of the lower St. Johns River. ADCP = Acoustic Doppler Current Profiler, SJR = St. Johns River.	35
Figure 3–5. Map showing locations of observed tidal discharge for the marine portion of the lower St. Johns River. ICW = Intracoastal Waterway, SJR = St. Johns River.	36
Figure 3–6. Map showing locations of observed tidal discharge for the southern portion of the lower St. Johns River. SJR = St. Johns River, ADCP = Acoustic Doppler Current Profiler.	37
Figure 3–7. Locations of observed salinity stations (#1 to 21) in the lower St. Johns River. Orange circles denote Water Quality Monitoring Network (WQMN) locations and yellow squares denote locations of continuous monitoring. SJR = St. Johns River.	42
Figure 3–8. Locations of observed salinity stations (22 to 37) in the middle St. Johns River. Orange circles denote Water Quality Monitoring Network (WQMN) locations and yellow squares denote locations of continuous monitoring. SJR = St. Johns River.	43
Figure 3–9. Comparison of salinity between Shands Bridge and Buffalo Bluff during the greatest observed upstream extent of salinity in May 2007. SJSR16, SRP, SJM37, and BB22 are salinity stations.....	48
Figure 3–10. Location and magnitude of St. Johns River Water Management District springs with measured discharge.....	50
Figure 3–11. Mean discharge and conductivity of selected SJRWMD springs sorted by discharge.....	51

Figure 3–12. Locations and sizes of wastewater treatment plants discharging directly to the St. Johns River main stem during the year 1995. WWTP = wastewater treatment plant, WWTF = wastewater treatment facility. 53

Figure 3–13. Locations of rain gauge stations near the St. Johns River. 55

Figure 3–14. Annual rainfall averaged over all stations, 1975 to 2006. 56

Figure 3–15. Average monthly total rainfall within the EFDC model area (1995 to 2005)..... 57

Figure 3–16. Monthly averaged potential evaporation (1975 to 2005) estimated by Hargreaves Method for rain gauge stations near the St. Johns River..... 59

Figure 3–17. Average monthly net rainfall (1975 to 2005) for rain gauge stations near the St. Johns River main stem. 60

Figure 3–18. Locations of stations with observed hourly wind. IAP = International Airport, AP = airport. 62

Figure 3–19. Comparison of daily averaged wind speed at Hastings and Apopka for 2004. 64

Figure 3–20. Comparison of east-west wind run at Hastings, Umatilla, and Orlando, 2000 to 2005. 67

Figure 3–21. Comparison of north-south wind run at Hastings, Umatilla, and Orlando, 2000 to 2005. 68

Figure 3–22. Water Quality Monitoring Network (WQMN) stations used for examination of salinity, chloride, and salt composition. 70

Figure 3–23. Comparison of bathymetry from 1939 National Ocean Service (NOS) and 2007 St. Johns River Water Management District SJRWMD surveys (m NAVD88). Left plot is the former river channel entering Lake Monroe that was cut off by the Monroe Canal. Right plot is the river channel between Lake Jesup and Lake Monroe. NAVD = North American Vertical Datum of 1988. 77

Figure 3–24. National Ocean Service (NOS) bathymetric survey of Lake Monroe in the middle St. Johns River..... 79

Figure 3–25. Surveyed transects at approximate 500 m spacing (left) and thalweg-enforced interpolated transects at approximate 25 m spacing (right). The thalweg-enforced transects were used to interpolate bathymetry to the DEM at 10-m horizontal resolution..... 80

Figure 3–26. Final Digital Elevation Model (DEM) of lower and middle St. Johns River used to assign depths and shorelines for the EFDC hydrodynamic model.	81
Figure 4–1. Separation of observed hourly water level at Bar Pilot Dock into astronomical and meteorological tide. For illustration, plots show time series over a 1-month period (May 2000) referenced to MSL. Total water level (top), astronomical tide (middle), and meteorological tide (bottom).	86
Figure 4–2. Meteorological tide over a 1-yr period (2000) at Bar Pilot Dock.	87
Figure 4–3. Monthly averaged water level (1928 to 2008) at Mayport, FL, near the mouth of the St. Johns River.	88
Figure 4–4. Annual averaged sea level anomaly (referenced to the year 2000), Mayport, FL.	89
Figure 4–5. Comparison of daily averaged river stage at Mayport and DeLand, 2000 to 2007.	90
Figure 4–6. Comparison of river stage and discharge at DeLand (USGS 02236000).	91
Figure 4–7. Pearson Correlation and coefficient of determination (r^2) versus discharge limit (Q-Limit) at DeLand.	92
Figure 4–8. Standardized Regression Coefficient (β) versus Q-Limits, Mayport (M) versus DeLand (Q).	93
Figure 4–9. Temporal trends in stage (H) and discharge (Q) at DeLand and stage (M) at Mayport, 1956 to 2007.	94
Figure 4–10. Manual observations of discharge and stage at St. Johns River at Christmas (SR 50), 1933 to 2010. Source: USGS.	96
Figure 4–11. Manual observations of discharge and stage at St. Johns River at Sanford (US 17), 1941 to 2010. Source: USGS.	97
Figure 4–12. Slope–discharge relationship between DeLand (SR 44) and Astor (SR 40), 1994 to 2009. The red line shows a classical Manning’s relationship where discharge (Q) is proportional to the square root of surface slope (Slope ^{1/2}).	98
Figure 4–13. Slope–discharge relationship between Sanford (US 17) and DeLand (SR 44), 1987 to 2009.	99
Figure 4–14. Slope–discharge relationship between DeLand (SR 44) and Astor (SR 40) for the year 2000 and limited to discharge below the long-term median.	100

Figure 4–15. Relationship between discharge at Astor and the difference in stage between DeLand (SR 44) and Astor (SR 40), 1994 to 2009. Stage differences are presented as box plots representing the mean stage difference with 95% confidence limits within 100 mgd bins..... 101

Figure 4–16. Relationship between discharge at DeLand and the difference in stage between Sanford (US 17) and DeLand (SR 44), 1987 to 2009. Stage differences are presented as box plots representing the mean stage difference with 95% confidence limits within 100 mgd bins..... 102

Figure 4–17. Relationship between discharge at Sanford and the difference in stage between Lake Harney (SR 46 near Geneva) and Sanford (US 17), 1987 to 2009. Stage differences are presented as box plots representing the mean stage difference with 95% confidence limits within 100 mgd bins. 103

Figure 4–18. Maucha diagrams comparing relative abundance of eight major ions in ocean water with the oligohaline reach of the St. Johns River (U.S. 192 to SR 40)..... 107

Figure 4–19. Maucha diagrams for the St. Johns River main stem. For each location the Maucha diagrams show, from left to right, relative salt abundance under low-, median-, and high-flow conditions. 108

Figure 4–20. Observed conductivity and chloride,U.S.192 to SR 40, compared with chloride of diluted seawater at the same conductivity (Seawater Line)..... 110

Figure 4–21. Spatial variation of chloride:conductivity ratio along the St. Johns River from U.S.192 to SR 40. The ratio for diluted seawater ranges from 0.21 to 0.30 for the ranges of conductivity considered. 111

Figure 4–22. Ratios of Cl concentration with concentrations of SO₄, Mg, and Ca for springs, surface tributaries, and the middle St. Johns River main stem. The Seawater Line (dashed) is the ratio of diluted seawater..... 113

Figure 4–23. Maucha diagrams for lakes in the St. Johns River valley between SR 50 and SR 46. 115

Figure 4–24. Springs representative of the four categories of salt composition used to classify springs. 116

Figure 4–25. Maucha diagrams for major springs in the study area. 117

Figure 4–26. Tributaries representative of the four categories of salt composition used to classify St. Johns River tributaries under low-flow conditions..... 118

Figure 4–27. Maucha diagrams of selected tributaries to the St. Johns River under low-flow (left) and high-flow (right) conditions.	119
Figure 4–28. Cl (mg L^{-1}) versus flow (cfs) proceeding downstream, (a) U.S.192 (Site LWE), b) SR 520 (Site LPO), (c) SR 50 (Site SRS), (d) SR 46 (Site SRN), (e) U.S.17 (Site 20010003), and (f) SR 40 (Site 20010002).	122
Figure 4–29. Gauge location at SR 46 in the Wekiva River and locations of major springs upstream of the gauge.	124
Figure 4–30. Discharge–chloride relationship for Wekiva River at SR 46 (Site 2235000). Relationship for total flow (top) and relationship without springs (bottom).	125
Figure 5–1. Gauged and ungauged watersheds of the middle and lower St. Johns River. For this study, the entire upper St. Johns River and Ocklawaha River are gauged where they enter the middle and lower St. Johns River, respectively.	131
Figure 5–2. Method of assigning salinity boundary conditions to watersheds.	134
Figure 5–3. Comparison of anthropogenic sources of discharge (OEW and Iron Bridge) and their receiving bodies (St. Johns River and the Econlockhatchee River)	137
Figure 5–4. Continuous, daily observed discharge for Blue Springs (Volusia County), December 2001 to December 2006.	139
Figure 5–5. Comparison of observed discharge with discharge estimated by the Intera Model for Gemini Springs.	140
Figure 5–6. Correlation between well stage and spring discharge (left) and comparison of observed and predicted discharge (right) for Clifton Springs (top) and Croaker Hole (bottom).	141
Figure 5–7. Correlation between Rock and Seminole Spring discharge. (Seminole discharge is adjusted +35 cfs).	142
Figure 5–8. Groundwater segments used for input of diffuse groundwater discharge and associated salinity as model boundary conditions.	145
Figure 6–1. Comparison of EFDC-TMDL hydrodynamic model grid (black) with the expanded base grid (red) established for the EFDC-LSJR hydrodynamic model.	152

Figure 6–2. Effective tidal area ($\times 10^6 \text{ m}^2$) estimated from observed ADCP tidal discharge at mouths of four principle tidal creeks. Numbers in brackets are effective tidal areas for the EFDC-TMDL hydrodynamic model. Cells in red are areas adjusted for the EFDC-LSJR hydrodynamic model to match ADCP tidal discharge. 154

Figure 6–3. Cell divisions used to create successively finer model grids for testing grid convergence..... 155

Figure 6–4. Comparison of horizontal resolution near Jacksonville for the 1X (top, black), 4X (middle, blue), and 16X (bottom, red) grids used for testing grid convergence. 157

Figure 6–5. Cell center locations used for water level output..... 158

Figure 6–6. M_2 amplitude and phase simulated for each of three successively finer grids at Main Street Bridge, Site 10. 162

Figure 6–7. M_2 amplitude and phase simulated for each of three successively finer grids at Shands Bridge, Site 15. 163

Figure 6–8. M_2 amplitude and phase simulated for each of three successively finer grids at Buffalo Bluff, Site 18. 164

Figure 6–9. M_2 amplitude and phase simulated for each of three successively finer grids at Moccasin Landing, Site 20. 165

Figure 6–10. Model cells defining a lateral transect. 167

Figure 6–11. Model cells along a transect overlain on the 10-m DEM. 167

Figure 6–12. Points used to draw a continuous set of line segments across the river transect..... 168

Figure 6–13. Sub-division of each line segment into 10 equal sections. 168

Figure 6–14. A z-value is assigned to each endpoint of the sub-divided sections using the depth of the nearest 10-m DEM cell..... 168

Figure 6–15. Equally spaced z-values plotted along the grid transect by distance. The cross-sectional area of the transect is calculated by numerical integration using Simpson’s Rule..... 169

Figure 6–16. Minimum, average, and maximum bottom elevation of DEM points falling within model cells along the thalweg of the middle St. Johns River..... 170

Figure 6–17. Locations of transects where model cell depths are compared to DEM cell depths.....	171
Figure 6–18. Comparison of model cell depths with DEM cell depths across four representative transects in the lower St. Johns River. Equivalent x- and y-scales are maintained for ease of comparison between plots.	172
Figure 6–19. Comparison of model cell depths with DEM cell depths across four major lakes in the lower and middle St. Johns River. Equivalent x- and y- scales are maintained for ease of comparison between plots.....	173
Figure 6–20. Final grid for the EFDC-LSJR hydrodynamic model with emphasis on the shelf region.	174
Figure 6–21. Final grid for the EFDC-LSJR hydrodynamic model with emphasis on the river region.	175
Figure 6–22. Final grid for the EFDC-MSJR hydrodynamic model.....	176
Figure 6–23. Sensitivity of mean salinity and salinity stratification to number of vertical layers for a 1-yr period (1997).	178
Figure 6–24. Observed daily averaged discharge and salinity at Sanford, U.S.17 (USGS 02236000), for the middle St. Johns River calibration period.	179
Figure 6–25. Low flow duration frequency curves for DeLand with minimum N-day averages over the model confirmation period (1996 to 2005) and middle St. Johns River calibration period (March to September, 2001). Duration frequency curves use the DeLand long-term record of 1957 to 2008.	180
Figure 6–26. High flow duration frequency curves for DeLand with minimum N-day averages over the confirmation period (1996 to 2005) and middle St. Johns River calibration period (March to September, 2001). Duration frequency curves use the DeLand long-term record of 1957 to 2008.	181
Figure 6–27. Observed 30-day averaged discharge and salinity at Main Street Bridge near Jacksonville (USGS) for the lower St. Johns River calibration period.....	182
Figure 6–28. Segments used for Parameter ESTimation (PEST) optimization of bottom roughness.....	186
Figure 6–29. Acoustic Doppler Current Profiler (ADCP) profile of velocity at U.S.17 for a low discharge and high discharge period.....	188

Figure 6–30. Nomograph comparing Manning's n values to bottom roughness z_o and depth for ranges of values within the middle St. Johns River..... 191

Figure 6–31. Initial bottom roughness assigned to precalibrated middle St. Johns River model (EFDC-MSJR)..... 192

Figure 6–32. Calibrated bottom roughness assigned to calibrated model of the middle St. Johns River model (EFDC-MSJR). 195

Figure 6–33. Steady-state discharge tests used for model calibration of the EFDC-MSJR hydrodynamic model..... 196

Figure 6–34. Comparison of observed and simulated discharge-slope relationships between DeLand (SR 44) and Astor (SR 40) for High and Low Roughness models..... 197

Figure 6–35. Comparison of observed and simulated discharge–slope relationships between Sanford (US 17) and DeLand (SR 44) for High and Low Roughness models..... 198

Figure 6–36. Comparison of observed and simulated discharge–slope relationships between Lake Harney (SR 46 at Lake Harney) and Sanford (US 17) for High and Low Roughness models..... 199

Figure 6–37. Simulated versus observed daily water level at DeLand (SR 44) over the calibration period..... 201

Figure 6–38. Scatter plot of paired values of observed and simulated daily water level at DeLand (SR 44) over the calibration period, March to September, 2001..... 201

Figure 6–39. Simulated versus observed daily water level at Sanford (US 17) over the calibration period..... 202

Figure 6–40. Scatter plot of paired values of observed and simulated daily water level at Sanford (US 17) over the calibration period, March to September 2001..... 202

Figure 6–41. Simulated versus observed daily water level at Lake Jesup outlet (SR 46 at Lake Jesup) over the calibration period. 203

Figure 6–42. Scatter plot of paired values of observed and simulated daily water level at Lake Jesup outlet (SR 46 at Lake Jesup) over the calibration period, March to September, 2001. 203

Figure 6–43. Simulated versus observed daily water level above Lake Harney (SR 46 at Lake Harney) over the calibration period..... 204

Figure 6–44. Scatter plot of paired values of observed and simulated daily water level above Lake Harney (SR 46 at Lake Harney) over the calibration period, March to September 2001.	204
Figure 6–45. Simulated versus observed daily discharge at Astor (SR 40) over the calibration period.....	206
Figure 6–46. Scatter plot of paired values of observed and simulated daily discharge at Astor (SR 40) over the calibration period, March to September 2001.....	207
Figure 6–47. Simulated versus observed daily discharge at DeLand (SR 44) over the calibration period.....	208
Figure 6–48. Scatter plot of paired values of observed and simulated daily discharge at DeLand (SR 44) over the calibration period, March to September 2001.....	209
Figure 6–49. Simulated versus observed daily discharge at Sanford (US 17) over the calibration period.....	210
Figure 6–50. Scatter plot of paired values of observed and simulated daily discharge at Sanford (U.S. 17) over the calibration period, March to September 2001.....	211
Figure 6–51. Simulated versus observed daily discharge at Lake Jesup outlet (SR 46 at Lake Jesup) over the calibration period.	212
Figure 6–52. Scatter plot of paired values of observed and simulated daily discharge at Lake Jesup outlet (SR 46 at Lake Jesup) over the calibration period, March to September, 2001.....	213
Figure 6–53. Simulated versus observed hourly discharge at DeLand during April 2001.	216
Figure 6–54. Simulated versus observed hourly discharge at Lake Jesup outlet during 1 to 14 May 2001.....	217
Figure 6–55. Simulated versus observed hourly discharge at Lake Jesup outlet during August 2001.	218
Figure 6–56. Simulated versus observed daily salinity at DeLand (SR 44) over the calibration period.....	220
Figure 6–57. Simulated versus observed daily salinity at Sanford (US 17) over the calibration period.....	221
Figure 6–58. Simulated and observed hourly water level at Main Street Bridge, September 1997.....	222

Figure 6–59. Simulated and observed hourly water level at Buffalo Bluff, September 1997..... 223

Figure 6–60. Simulated and observed M_2 amplitude and phase by river kilometer during the calibration period, August 1997 to April 1999..... 225

Figure 6–61. Comparison of observed and simulated tidal discharge at Marker 22 on 22 September 1997..... 229

Figure 6–62. Comparison of observed and simulated tidal discharge at Shands Bridge on 25 September 1997..... 229

Figure 6–63. Comparison of observed and simulated tidal discharge at Hog Eye Point on 26 September 1997..... 230

Figure 6–64. Simulated and observed daily averaged discharge at Main Street Bridge for 1998. 232

Figure 6–65. Simulated and observed daily averaged discharge at Buffalo Bluff for 1998..... 232

Figure 6–66. Simulated and observed daily averaged discharge at Dunns Creek for 1998..... 233

Figure 6–67. Locations for the NOAA vertical velocity profile measurements. 234

Figure 6–68. Vertical velocity profile comparison at (a) Blount Island East, (b) Dames Point, and (c) Trout River (simulated values left and observed values right). 235

Figure 6–69. Salinity time series comparison at Dames Point station during the calibration period (top, middle, and bottom depths of observation). 238

Figure 6–70. Salinity time series comparison at Acosta Bridge during the calibration period (top, middle, and bottom depths of observation). 239

Figure 6–71. Salinity time series comparison at Buckman Bridge during the calibration period (top, middle, and bottom depths of observation). 240

Figure 6–72. Salinity time series comparison at Shands Bridge during the calibration period (top, middle, and bottom depths of observation). 241

Figure 6–73. Salinity time series comparison at Dancy Point during the calibration period (top and bottom depths of observation). 242

Figure 6–74. Simulated versus observed daily salinity above Lake Harney (SR 46 AT Lake Harney) over the calibration period. Simulated salinity compares the Low Roughness model and SR46H Observed Scenario.	244
Figure 6–75. Simulated versus observed daily salinity upstream of Lake Monroe (station OW-SJR-1) over the calibration period. Simulated salinity compares the Low Roughness model and SR46H Observed Scenario.	245
Figure 6–76. Simulated versus observed daily salinity at Sanford (US 17) over the calibration period. Simulated salinity compares the Low Roughness model and SR46H Observed Scenario.	246
Figure 6–77. Simulated versus observed daily salinity at DeLand (SR 44) over the calibration period. Simulated salinity compares the Low Roughness model and SR46H Observed Scenario.	247
Figure 6–78. Cumulative density function comparing observed and simulated salinity at U.S.17 and DeLand for the calibration period, March to September 2001 using the EFDC-MSJR hydrodynamic model.	249
Figure 6–79. Simulated versus observed daily salinity near the outlet of Lake Jesup (station OW-2) and in the west end of the lake (station OW-6) over the calibration period using the EFDC-MSJR hydrodynamic model.	250
Figure 6–80. Simulated versus observed daily salinity in Lake Woodruff (station LWNWR) over the calibration period using the EFDC-MSJR hydrodynamic model.	251
Figure 7–1. Point comparison of observed and simulated tidal discharge for all locations and times during the confirmation period, 1996 to 2005.	256
Figure 7–2. Comparison of observed and simulated tidal discharge at Fruitland on 29 May 2002.	258
Figure 7–3. Comparison of observed and simulated tidal discharge at Georgetown on 29 May 2002.	258
Figure 7–4. Simulated and observed peak ebb discharge by river kilometer over the confirmation period, 1996 to 2005.	259
Figure 7–5. Simulated and observed daily averaged discharge at Main Street Bridge for a dry year (2000) and wet year (2005).	261
Figure 7–6. Simulated and observed daily averaged discharge at Buffalo Bluff for a dry year (2000) and wet year (2005).	262

Figure 7–7. Simulated and observed daily averaged discharge at Dunns Creek for a dry year (2000) and wet year (2005). 263

Figure 7–8. Simulated and observed salinity at station JAXSJR40 (Christopher Point), 1996 to 2005..... 265

Figure 7–9. Simulated and observed salinity at Shands Bridge during the confirmation period, 1996 to 2005..... 266

Figure 7–10. Longitudinal variation of salinity for observed and simulated salinity distributions in the lower St. Johns River during the confirmation period, 1996 to 2005..... 268

Figure 7–11. Longitudinal variation of daily salinity range for observed and simulated distributions of daily salinity range in the lower St. Johns River during the confirmation period, 1996 to 2005..... 269

Figure 7–12. Simulated versus observed daily water level at DeLand (SR 44) over the model confirmation period, 1996 to 2005..... 270

Figure 7–13. Simulated versus observed daily water level at Sanford (US 17) during the model confirmation period, 1996 to 2005..... 271

Figure 7–14. Simulated versus observed daily water level at Lake Jesup outlet (SR 46 at Lake Jesup) during the model confirmation period, 1996 to 2005. 271

Figure 7–15. Simulated versus observed daily water level above Lake Harney (SR 46 at Lake Harney) during the model confirmation period, 1996 to 2005..... 272

Figure 7–16. Scatter plot of paired values of observed and simulated daily water level above Lake Harney (SR 46 at Lake Harney) during the model confirmation period, 1996 to 2005..... 273

Figure 7–17. Simulated versus observed daily discharge at Astor (SR 40) during the model confirmation period, 1996 to 2005..... 275

Figure 7–18. Simulated versus observed daily discharge at DeLand (SR 44) during the model confirmation period, 1996 to 2005..... 275

Figure 7–19. Simulated versus observed daily discharge at Sanford (US 17) during the model confirmation period, 1996 to 2005..... 276

Figure 7–20. Simulated versus observed daily discharge at SR 415 over the period of gauge record (Feb. to Dec., 2005) contained within the model confirmation period. 276

Figure 7–21. Simulated versus observed daily discharge at Lake Jesup outlet (SR 46 at Lake Jesup) during the model confirmation period, 1996 to 2005.	277
Figure 7–22. Scatter plot of paired values of observed and simulated daily discharge at Lake Jesup outlet (SR 46 at Lake Jesup) during the model confirmation period.....	277
Figure 7–23. Simulated versus observed monthly discharge at DeLand (SR 44) during the model confirmation period, 1996 to 2005.	279
Figure 7–24. Simulated versus observed monthly discharge at Lake Jesup outlet (SR 46 at Lake Jesup) during the model confirmation period, 1996 to 2005.....	279
Figure 7–25. Simulated versus observed hourly discharge at DeLand (SR 44) during May 1999.....	280
Figure 7–26. Simulated versus observed hourly discharge at Lake Jesup outlet (SR 46 at Lake Jesup) during May 1999.	281
Figure 7–27. Cumulative density functions of observed and simulated hourly discharge at DeLand (SR 44) during the model confirmation period, 1996 to 2005.	282
Figure 7–28. Cumulative density functions of observed and simulated hourly discharge at Lake Jesup outlet (SR 46 at Lake Jesup) during the model confirmation period, 1996 to 2005.....	283
Figure 7–29. Simulated versus observed daily salinity at DeLand (SR 44) over the period of gauged record.....	285
Figure 7–30. Simulated versus observed daily salinity at Sanford (U.S. 17) over the period of gauged record.....	286
Figure 7–31. Scatter plot of paired values of observed and simulated daily discharge for all synoptic salinity stations during the model confirmation period, 1996 to 2005.....	288
Figure 7–32. Simulated versus observed salinity at Astor (SR 40) during the model confirmation period, 1996 to 2005.	289
Figure 7–33. Simulated versus observed salinity in Lake Woodruff (station LKWNWR) during the model confirmation period, 1996 to 2005.....	289
Figure 7–34. Simulated versus observed salinity at DeLand (SR 44) during the model confirmation period, 1996 to 2005.	290

Figure 7–35. Simulated versus observed salinity at station SJR-DPP during the model confirmation period, 1996 to 2005. 290

Figure 7–36. Simulated versus observed salinity in Lake Monroe (station LMAC) during the model confirmation period, 1996 to 2005. 291

Figure 7–37. Simulated versus observed salinity at station SJR-415 (SR 415) during the model confirmation period, 1996 to 2005. 291

Figure 7–38. Simulated versus observed salinity at station OW-SJR-2 during the model confirmation period, 1996 to 2005. 292

Figure 7–39. Simulated versus observed salinity at OW-SJR-1 during the model confirmation period, 1996 to 2005. 292

Figure 7–40. Simulated versus observed salinity at station SJR-OLH during the model confirmation period, 1996 to 2005. 293

Figure 7–41. Simulated versus observed salinity in Lake Harney (station CLH) during the model confirmation period, 1996 to 2005. 293

Figure 7–42. Simulated versus observed salinity in Lake Jesup (station OW-2) during the model confirmation period, 1996 to 2005. 294

Figure 7–43. Simulated versus observed salinity in Lake Jesup (station OW-4) during the model confirmation period, 1996 to 2005. 294

Figure 7–44. Simulated versus observed salinity in Lake Jesup (station OW-6) during the model confirmation period, 1996 to 2005. 295

Figure 7–45. Map showing bifurcation of St. Johns River flow between DeLand (SR 44) and Lake Woodruff. A fraction of the flow passes through Lake Woodruff and exits at Tick Island. 296

Figure 7–46. Comparison of observed daily discharge at DeLand and Tick Island for the 2008 and 2009 water years. 297

Figure 7–47. Longitudinal variation of the distribution of water levels for the EFDC-Combined, EFDC-MSJR, and EFDC-LSJR hydrodynamic models, and observations throughout the lower and middle St. Johns River during the confirmation period, 1996 to 2005. 302

Figure 7–48. Longitudinal variation of distribution of salinity for the EFDC-Combined, EFDC-MSJR, and EFDC-LSJR hydrodynamic models, and observations throughout the lower and middle St. Johns River during the confirmation period, 1996 to 2005. 305

LIST OF TABLES

Table 2–1.	Six largest tributaries to the St. Johns River.....	4
Table 2–2.	Comparison of the four largest Florida lakes, by surface area, with the lacustrine segment of the lower St. Johns River (LSJR) by area, volume, and volume:area ratio.	10
Table 3–1.	Water level stations in lower and middle St. Johns River listed in north-to-south order. Map numbers refer to Figure 3–1.....	20
Table 3–2.	Descriptive statistics for observed water level, 1996 to 2005.	22
Table 3–3.	Tide stations in lower St. Johns River listed in north-to-south order. Map numbers refer to Figure 3–2.	25
Table 3–4.	Amplitude and phase of the five largest tidal constituents in the lower St. Johns River. Tidal constituents are defined in Table 3–5. Map numbers refer to Table 3–3 and Figure 3–2.	26
Table 3–5.	Name and period of the five largest tidal constituents in the lower St. Johns River.	27
Table 3–6.	Discharge stations in lower and middle St. Johns River listed in north-to-south order. Map numbers refer to Figure 3–3.....	30
Table 3–7.	Descriptive statistics for selected St. Johns River discharge locations, 1996 to 2005. Map numbers refer to Figure 3–3.....	31
Table 3–8.	Gauged tributaries in the study area over the model simulation period (1995 to 2006).	33
Table 3–9.	Harmonic constants for discharge at continuous USGS gauging sites in the lower St. Johns River for the six largest tidal constituents. Tidal constituents are defined in Table 3–5.....	34
Table 3–10.	Acoustic Doppler Current Profiler (ADCP) tidal discharge monitoring sites.....	38
Table 3–11.	St. Johns River salinity stations arranged in downstream to upstream order. Map numbers refer to Figure 3–7 and Figure 3–8.	44
Table 3–12.	Descriptive statistics for St. Johns River salinity stations. Map numbers refer to Figure 3–7 and Figure 3–8.....	46

Table 3–13. Monthly averaged salinity for all months available within station record. The middle St. Johns River (MSJR) is calculated from pooled observations using stations 2236000, LMAC, and OW-SJR-1.....	49
Table 3–14. Rain gauge stations near the St. Johns River listed in north-to-south order. Map numbers refer to Figure 3–13.....	56
Table 3–15. Mean annual rainfall anomalies (mm) referenced to base period 1975 to 2006. Negative values indicate that mean annual rainfall is lower than the average value.....	57
Table 3–16. Annual net rainfall (mm) for rain gauge stations near the St. Johns River main stem. Negative numbers indicate that annual evaporation exceeded annual rainfall.....	61
Table 3–17. Wind stations near St. Johns River listed in north-to-south order. Map numbers refer to Figure 3–18.....	63
Table 3–18. Percentage of occurrence of wind speed by 3-knot intervals for NOAA stations and the FDEP station. Map numbers refer to Figure 3–18.....	63
Table 3–19. Percentage of occurrence of wind speed by 3-mph intervals for FAWN stations. Map numbers refer to Figure 3–18.....	64
Table 3–20. Monthly averaged wind speed (m s^{-1}) for east-west component of wind, 2000 to 2005. Map numbers refer to Figure 3–18.....	65
Table 3–21. Monthly averaged wind speed (m s^{-1}) for north-south component of wind, 2000 to 2005. Map numbers refer to Figure 3–18.....	66
Table 3–22. Water quality sites along the St. Johns River main stem with summary chloride statistics.....	71
Table 3–23. Water quality stations off the St. Johns River main stem, with summary chloride statistics.....	73
Table 3–24. Precision and accuracy of chemical analytes for SJRWMD data.....	74
Table 3–25. Resolution and accuracy of field data obtained using a data sonde.....	74
Table 3–26. Bathymetric survey data used to create a DEM of the lower and middle St. Johns River.....	76
Table 4–1. Comparison of eight main salt constituents in the ocean standard to average values for the St. Johns River.....	106

Table 5–1.	Five largest harmonic constituents adjusted for astronomical tidal prediction at open ocean boundary. Tidal constituents are defined in Table 3–5.	128
Table 5–2.	Distribution of ocean water level at open ocean boundary.	128
Table 5–3.	Distribution of daily averaged discharge (m^3s^{-1}) from in the upper St. Johns River at SR 46 at Lake Harney (SR46H), middle St. Johns River (SJR) tributaries, and lower St. Johns River tributaries (1996 to 2005).	130
Table 5–4.	Equations relating conductivity to discharge for middle St. Johns River surface tributaries	133
Table 5–5.	Coefficients used to represent conductivity-discharge relationships for low-, medium-, and high-conductivity tributaries. The coefficients (a and b) determine conductivity ($\mu\text{S cm}^{-1}$) from discharge (Q , cfs) according to the equation conductivity = aQ^b	135
Table 5–6.	Summary of salinity boundary conditions used to represent surface water runoff to tributaries in the middle St. Johns River (MSJR) model.....	136
Table 5–7.	Summary of salinity boundary conditions used to represent surface water runoff to tributaries in the lower St. Johns River model.	138
Table 5–8.	Summary of spring boundary conditions for the lower St. Johns River (LSJR) and middle St. Johns River (MSJR) hydrodynamic models.	143
Table 5–9.	Discharge and salinity assigned to 20 EFDC groundwater segments as diffuse groundwater discharge boundary conditions.....	146
Table 5–10.	Average discharge of 36 wastewater treatment plants entering the lower St. Johns River (EFDC-LSJR) model.....	148
Table 6–1.	Observed peak tidal discharge (Q_{peak}), estimated tidal prism (TP), and effective tidal area (A_{eff}) for four principle marsh areas in the lower St. Johns River. (Tidal range is assumed 1.2 m.)	155
Table 6–2.	Grid characteristics for three successively finer grids used for testing grid convergence. IC and JC are dimensions of the computational EFDC hydrodynamic model grid. The number of horizontal cells includes wet cells only.....	156
Table 6–3.	Differences in M_2 amplitudes (cm) between grids. Map # refers to Figure 3–2.	159

Table 6–4.	Differences in M_2 phases (degrees) between grids. Map # refers to Figure 3–2.....	161
Table 6–5.	Comparison of 1-, 7-, and 30-day high salinity events for the confirmation period (1996 to 2005) and calibration period (August 1997 to April 1999) at four locations in the lower St. Johns River (LSJR).....	183
Table 6–6.	Initial and optimized bottom roughness for each segment provided to PEST. Segment numbers refer to Figure 6–28.....	185
Table 6–7.	Observed stage, discharge, and velocity at U.S.17 and at upstream (SR 46) and downstream (SR 44) sites for high flow (9 November 2005) and low flow (7 June 2007) events.	189
Table 6–8.	Geometric parameters for the U.S.17 gauged cross section derived from Acoustic Doppler Current Profiler (ADCP) measurement.....	189
Table 6–9.	Manning’s n , drag coefficient, bottom roughness, and bottom stress estimated from observed Acoustic Doppler Current Profiler (ADCP) data at U.S.17.....	190
Table 6–10.	Statistical comparison of simulated and observed water level for High and Low Roughness models at four locations.....	200
Table 6–11.	Statistical comparison of simulated and observed daily discharge for High and Low Roughness model at four locations.	205
Table 6–12.	Observed (Obs) versus simulated (Sim) (Low Roughness model) monthly averaged discharge over the calibration period, March to September 2001.	214
Table 6–13.	Statistical comparison of simulated and observed hourly discharge for High and Low Roughness models at four locations over the calibration period, March to September 2001.	215
Table 6–14.	Statistical comparison of simulated and observed daily salinity for High and Low Roughness models at DeLand and Sanford over the calibration period, March to September 2001.	219
Table 6–15.	Comparison of observed and simulated M_2 tidal amplitude and phase over the calibration period, August 1997 to April 1999.....	224
Table 6–16.	Observed and simulated form number, $(K_1+O_1)/(M_2+S_2)$ during the calibration period, August 1997 to April 1999.....	226
Table 6–17.	Comparison of observed and simulated hourly water level during the calibration period, August 1997 to April 1999.....	227

Table 6–18.	Observed (Obs) and simulated (Sim) distribution of hourly water level for all paired values during the calibration period, August 1997 to April 1999, in m, NGVD29.	228
Table 6–19.	Comparison of observed (Obs) and simulated (Sim) tidal constituents for discharge at USGS continuous discharge stations during the calibration period, August 1997 to April 1999. Tidal constituents are defined in Table 3–5.	230
Table 6–20.	Comparison of observed and simulated daily discharge over the calibration period, August 1997 to April 1999.	231
Table 6–21.	Comparison of observed and simulated hourly salinity at USGS continuous salinity stations over the calibration period, August 1997 to April 1999.	237
Table 6–22.	Statistical comparison of simulated and observed daily salinity for the Low Roughness model and SR46H Observed Scenario at three locations.	248
Table 7–1.	Comparative statistics for observed and simulated hourly water level during the confirmation period, 1996 to 2005.	254
Table 7–2.	Observed (Obs) and simulated (Sim) distribution of water level for all paired values during the confirmation period, 1996 to 2005. Water level in m NAVD88.	255
Table 7–3.	Comparison of observed (Obs) and simulated (Sim) tidal constituents for discharge at USGS continuous discharge stations during the confirmation period, 1996 to 2005. Tidal constituents are defined in Table 3–5.	257
Table 7–4.	Comparison of observed and simulated daily discharge during the confirmation period, 1996 to 2005.	260
Table 7–5.	Comparison of Observed and Simulated Salinity at Water Quality Monitoring Network (WQMN) Stations, 1996 to 2005.	264
Table 7–6.	Comparison of observed and simulated hourly salinity at USGS continuous salinity stations during the confirmation period, 1996 to 2005.	267
Table 7–7.	Statistical comparison of simulated and observed daily water level during model confirmation period, 1996 to 2005.	270
Table 7–8.	Statistical comparison of simulated and observed daily discharge during the model confirmation period, 1996 to 2005.	274

Table 7–9.	Statistical comparison of simulated and observed monthly discharge during the model confirmation period, 1996 to 2005.....	278
Table 7–10.	Statistical comparison of simulated and observed hourly discharge during the model confirmation period, 1998 to 2001.	280
Table 7–11.	Mean and standard deviation of observed and simulated discharge at three locations during the confirmation period, 1996 to 2005. Mean and standard deviations in m^3s^{-1}	284
Table 7–12.	Statistical comparison of simulated and observed salinity during the model confirmation period, 1996 to 2005.	287
Table 7–13.	Ratio of Tick Island discharge to DeLand discharge (R_{TD}) for observed and simulated values sorted by percentiles of the observed distribution of Tick Island discharge.....	298
Table 7–14.	Comparison of hourly water level between EFDC-MSJR, EFDC-LSJR, and EFDC-Combined hydrodynamic models during the confirmation period, 1996 to 2005.....	300
Table 7–15.	Comparison of observed and simulated (EFDC-Combined hydrodynamic model) hourly water level at Astor during the confirmation period, 1996 to 2005.....	301
Table 7–16.	Comparison of hourly discharge between EFDC-MSJR, EFDC-LSJR, and EFDC-Combined hydrodynamic model during the confirmation period, 1996 to 2005. Units of b , $RMSE$, and $AVAE$ are m^3s^{-1}	303
Table 7–17.	Comparison of vertically averaged salinity between EFDC-MSJR, EFDC-LSJR, and EFDC-Combined hydrodynamic models during the confirmation period, 1996 to 2005.	304

ACRONYMS, ABBREVIATIONS, AND CONVERSION FACTORS

$\mu\text{S cm}^{-1}$	Microsiemens per centimeter
A	Amplitude
ADCP	Acoustic Doppler Current Profiler
AVAE	Average absolute error
AVM	Acoustic velocity meters
AVRE	Average relative error
<i>b</i>	Intercept of linear regression line
BR	Bottom roughness
Ca	Calcium
CaCO ₃	Limestone
CaMg(CO ₃) ₂	Dolomite
CaSO ₄	Gypsum
CDFs	Cumulative density functions
Cl	Chloride
cms	Cubic meters per second
CO ₃	Carbonate
DEM	Digital Elevation Model
EFDC	Environmental Fluid Dynamics Code model
EPA	Environmental Protection Agency
F	Form number (ratio of diurnal to semidiurnal amplitudes)
FAWN	Florida Automated Weather Network
FDEP	Florida Department of Environmental Protection
HCO ₃	Bicarbonate
HQ	Stage discharge
HSPF	Hydrologic Simulation Program–FORTRAN
IAP	International Airport
ID	Identification
K	Potassium
LiDAR	Light detection and ranging
LSJR	Lower St. Johns River
LWNWR	Lake Woodruff National Wildlife Refuge
<i>m</i>	Slope of linear regression line
Mg	Magnesium
Mgd	Million gallons per day
MSJR	middle St. Johns River
MSL	Mean sea level
Na	Sodium
NaCl	Sodium chloride

NAVD88	North American Vertical Datum of 1988
NGVD29	National Geodetic Vertical Datum of 1929
NOAA	National Oceanic and Atmospheric Administration
NOS	National Ocean Service
<i>NRECS</i>	Number of records
<i>NS</i>	Nash-Sutcliffe coefficient
NWR	National Wildlife Refuge
OEW	Orlando Easterly Wetlands
ORTS	Orlando Regional Treatment System
P	Phase
PEST	Parameter ESTimation
ppt	Parts per thousand
PSS78	Practical Salinity Scale 1978
Q	Discharge
r^2	Coefficient of determination
<i>RMSE</i>	Root-mean-square error
S	Salinity
SJRWMD	St. Johns River Water Management District
SO ₄	Sulfate
SR	State Road
<i>STDEV</i>	Standard Deviation
TAPPY	Tidal Analysis Package Python
TMDL	Total Maximum Daily Load
TP	Tidal Prism
UCF	University of Central Florida
USACE	United States Army Corps of Engineers
USGS	United States Geological Survey
WQMN	Water Quality Monitoring Network
WSIS	Water Supply Impact Study
WWTP	Wastewater treatment plant

1 INTRODUCTION

The Water Supply Impact Study (WSIS) requires a methodology for quantifying the effects of water withdrawals on hydrodynamics throughout the St. Johns River. Effects on hydrodynamics include variations in water level, discharge, velocity, salinity, and flushing. How these conditions are affected by water withdrawals needs to be understood over a wide range of time scales, including short-term storm events, seasonal droughts, and the long-term effects of sea level rise. The effects on hydrodynamics need to be assessed over nearly 300 km of river. In addition, the goals of WSIS require an examination of the interaction of proposed water withdrawals with other future alterations to the system, such as urbanization and other structural changes to watersheds (see Chapter 6. River Hydrodynamics Results for WSIS scenarios).

Water withdrawals lower water level and reduce the ability of a river to provide natural flushing and repel salinity intrusion (Fischer, et al. 1979). The understanding of how these physical changes affect the natural river systems is central to the goals of WSIS. Reduction of flushing can adversely affect water quality and lead to undesirable blooms of algae. In the estuarine reaches of the river, increased salinity intrusions can adversely affect submersed grass beds and benthic organisms. Assessing and quantifying possible biological, chemical, and ecological effects of water withdrawals requires, first, a means to quantify the underlying effects on hydrodynamics.

We determined that a three-dimensional, numerical, hydrodynamic model is best suited to the needs of the WSIS within the lower and middle St. Johns River. Many of the issues outlined above require analysis of mixing processes dominated by lateral and vertical velocity shear, and thus require simulation of three-dimensional velocity fields. In addition, the estuarine portion of the St. Johns River is a partially stratified estuary where the nonlinear interactions between mixing and stratification are important factors controlling flow. The need to simulate mixing and stratification for the ultimate purpose of predicting flushing and intrusion of seawater dictated the use of a three-dimensional hydrodynamic model. Use of a three-dimensional hydrodynamic model throughout the non-tidal middle St. Johns River is, in part, justified by an analysis showing that low frequency ocean water levels often dominate river stage as far upstream as Lake Harney. The three-dimensional model selected for the WSIS is the Environmental Fluid Dynamics Code (EFDC) (EPA 2011). The modeled region extends from the adjacent shelf outside the river mouth through Lake Harney, or approximately the lower 300 km of the St. Johns River.

This chapter describes the data and procedures used to calibrate and confirm the hydrodynamic model used for the WSIS. The intent of this chapter is to show how model boundary conditions are developed for the model, the assumptions used in setting up the model for specific application to the St. Johns River, and how well the model simulates observed variables. This chapter is highly technical and focuses on the unique dynamics of the river needed for model calibration and validation tasks, such as creation of digital elevation models (DEMs), building and testing of model grids, adjustment of bottom roughness parameters, and comparison of observed with simulated data for different time scales. This chapter does not assess or show results for the effects of water withdrawals. Hydrodynamic model results are presented in Chapter 6. River Hydrodynamics Results.

The hydrodynamic modeling of the river relied on the HSPF hydrologic model and MODFLOW groundwater models for quantification of inflows to the river needed for boundary conditions for the EFDC hydrodynamic model. The hydrologic models are documented in Chapter 3.

Watershed Hydrology and the groundwater models are documented in Chapter 4. Groundwater Hydrology

Application of the EFDC hydrodynamic model to the lower and middle St. Johns River provides a tool for assessing the impacts of water withdrawals on river hydrodynamics. The calibrated model is tested and confirmed for a 10-yr period from 1996 to 2005. This period contains a wide range of meteorological conditions including an extensive drought period (late 1999 through 2001), an extremely wet winter (1997 to 1998), and a season of active tropical storms (autumn 2004). The model is shown to realistically hindcast water level, discharge, salinity, and water age throughout the model domain over a range of time scales and conditions. The model responds realistically to the forces of tide, wind, tributary discharge, rainfall, and evaporation to predict hydrodynamics throughout the lower 300 km of river. Because the EFDC hydrodynamic model is a mechanistic model based on physical equations of fluid motion, it is robust in predicting alterations to the system, such as those required to assess water withdrawals, without altering its underlying parameters. Although all models can be improved at additional time and expense, the present application of the EFDC hydrodynamic model to the St. Johns River is the best available tool for assessing the effects of water withdrawals and other future alterations to river hydrodynamics.

2 DESCRIPTION OF STUDY AREA

The St. Johns River headwaters lie in broad marshes in Indian River County, northwest of the City of Vero Beach at latitude 27.68°N, and flows north for 500 km to exit into the Atlantic Ocean east of the City of Jacksonville at latitude 30.41°N. The St. Johns River drains a large portion of northeast Florida; its basin encompasses nearly 23,000 km². Annual discharge at the mouth is about 5,330 mgd (235 m³s⁻¹). The modeled region extends from the adjacent shelf outside the river mouth through Lake Harney, or approximately the lower 300 km of the St. Johns River.

2.1 PRECIPITATION AND EVAPORATION

The St. Johns River lies within a humid, subtropical climate zone. Average rainfall is about 135 cm yr⁻¹. About half the annual rainfall occurs in the summer and early autumn, from June to September (Figure 2-1). Evaporation rates are also high and on average nearly balance the annual precipitation. Over the study period (1996 to 2005), average annual rainfall was 136.9 cm yr⁻¹, while average annual evaporation was 133.1 cm yr⁻¹.

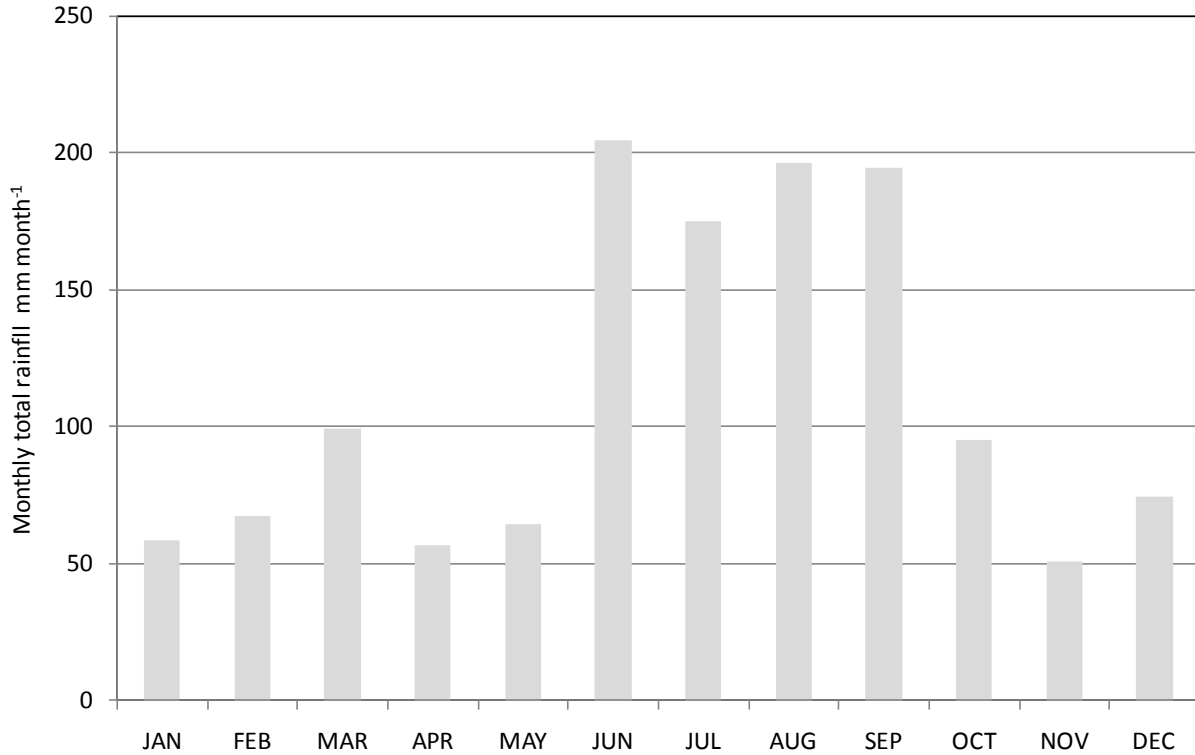


Figure 2–1. Monthly total rainfall averaged over 1996 to 2005 and spatially averaged over the EFDC model area.

2.2 TRIBUTARIES

The Ocklawaha River is the major tributary to the St. Johns River, containing 24.3% of the total St. Johns River basin area and accounting for 15.7% of the mean discharge of the St. Johns River. The Ocklawaha River enters the lower St. Johns River just downstream of Lake George. The lower St. Johns River also contains the second and third largest tributaries. These are Dunns Creek and Black Creek. The six largest tributaries by flow volume are shown in Table 2–1. Chapter 3. Watershed Hydrology provides a complete description of all tributaries to the St. Johns River.

Table 2–1. Six largest tributaries to the St. Johns River.

Tributary	Area (km²)	Average Discharge (mgd)
Ocklawaha River	5,440	838
Dunns Creek	1,543	357
Black Creek	1,317	313
Wekiva River	975	252
Econlockhatchee River	706	179
Rice Creek	925	118

2.3 OCEAN INFLUENCE

The St. Johns River's physical characteristics are greatly affected by its connection to the ocean. Low vertical relief presently allows ocean tide to propagate hundreds of kilometers upstream. The river substrate and aquifers (formed during past ocean inundations) are made of sedimentary rock. Seawater penetrated the Floridan aquifer underlying the middle St. Johns River during high sea level stands of interglacial Pleistocene periods. Flushing of trapped Pleistocene seawater, called relict seawater, into the river continues to allow marine species to thrive far upstream of the influence of modern ocean waters.

2.4 OCEAN TIDE

Ocean tide that propagates into the St. Johns River is dominated by astronomical tides, although meteorological tides are also present. (The term ocean tide is used here to mean deviations of the ocean surface from mean sea level excluding wind waves.) Astronomical tides result from the gravitational attraction of the moon and sun on the rotating earth. Meteorological tides are produced primarily by winds, atmospheric pressure changes, and shifts in large-scale ocean circulation. Both astronomical and meteorological tides are important to the hydrodynamics of the St. Johns River.

Astronomical tide propagates from the ocean to Lake George, which is nearly 200 km from the mouth of the river (Figure 2–2). Tidal range drops quickly from 1.5 m at the mouth (Bar Pilot Dock) to 25 cm at Buckman Bridge, a distance of 55 km. Tidal range then increases upstream of Racy Point before diminishing to about 2 cm in Lake George. The tide is slow to cover the distance to Lake George, and some portion of the river is always at high tide while another is at low tide.

Ocean water level also varies due to meteorological conditions, primarily winds and shifts in atmospheric pressure. Although this ocean water level variability, called meteorological tide, has a smaller range than astronomical tide, it has characteristically longer periods and can propagate farther upstream than astronomical tide. Meteorological tide effects water levels throughout the lower and middle St. Johns River through Lake Harney, more than 300 km upstream. Although

winds and atmospheric pressure shifts also affect the St. Johns River directly, the indirect effects of meteorological tide have the greater effect on river water levels. Remote wind forcing, then, is more important than local wind forcing on river hydrodynamics.

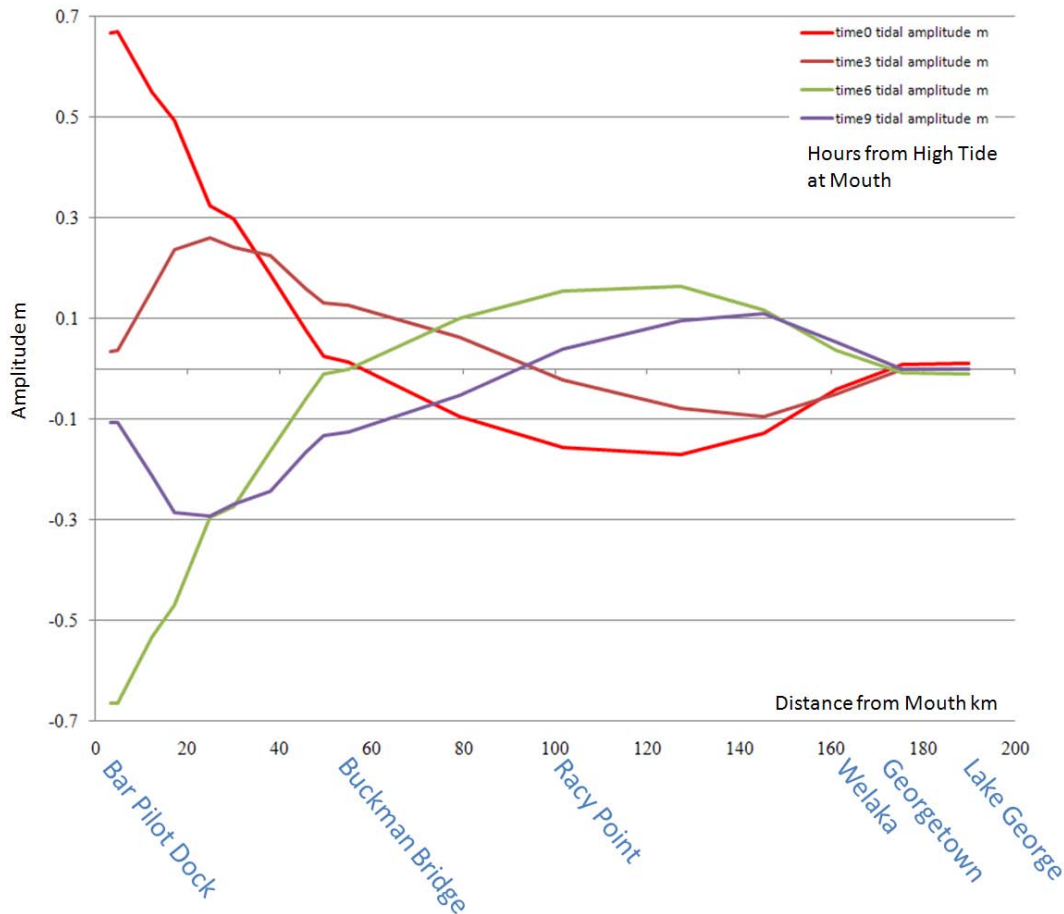


Figure 2–2. Propagation of astronomical tidal wave between the river mouth and Lake George. Each curve shows the spatial variation of the height of tide at identical times. m = meters.

Meteorological tide is quasiperiodic with 2 to 12-day periods and characteristic amplitudes of 10 to 20 cm. Because of the low slope of the St. Johns River, the meteorological tide causes a gradual filling and draining of the river over a large area. Filling events bring large volumes of seawater into the river mouth. During dry conditions, when freshwater discharges are low, the filling by meteorological tide can reverse daily averaged river flow far upstream of the mouth. These reverse flow events can transport ocean salinity into the river, as distinct intrusions of seawater, as far as Shands Bridge, 80 km from the mouth.

2.5 SALINITY

All salinity observations used for the WSIS are derived from conductivity measurements (APHA 1995). Salinity derived from conductivity measurements is defined by a unitless scale called the Practical Salinity Scale (PSS78) (Lewis and Perkin, *Salinity: Its definition and calculation* 1978). Because salinity is a unitless value, a salinity value should not be followed by units (e.g., S =

35.032). In this Chapter, however, we often follow the value with the PSS78 acronym to avoid confusion (e.g., $S = 35.032$ PSS78).

Salinity in the St. Johns River varies from fresh ($S < 0.5$) to marine ($S > 30$). Salinity ecological zones, derived by classifying observed mean salinity according to the Venice Salinity Classification (Venice Symposium 1958), show polyhaline (salinity between 18 and 30) conditions to Dames Point and mesohaline (salinity between 5 and 18) conditions to Buckman Bridge (Figure 2–3). Salinity in these areas results from mixing of fresher river waters with seawater. Upstream areas have broad expanses of oligohaline (salinity between 0.5 and 5) conditions.

Salinity in the St. Johns River varies with river flow and meteorological tide. In the polyhaline zone, large river discharge can lower salinity to 10 (Figure 2–4). The downstream oligohaline zone, between Buckman Bridge and Racy Point, is due to mixing with seawater. Intrusions of seawater can raise salinity to 10 at Buckman Bridge. Upstream of the areas of ocean-influenced salinity, salinity is regularly above 0.5 (Figure 2–5). Salinity in upstream oligohaline zones result from the inflow of relict seawater from underlying groundwater. These waters have chloride levels distinctly greater than typical freshwaters so that all these areas are functionally oligohaline.

A comparison of tidal and salinity characteristics is shown in Figure 2–6. Astronomical tide extends to Lake George, where there is an overlap of ocean salinity and relict seawater. The overlap defines a lower tidal estuarine zone and a tidal freshwater zone. Astronomical tide is absent upstream of Lake George, but meteorological tide extends through Lake Harney. The salinity throughout this reach (Lake George to Lake Harney) is dominated by relict seawater. The areas upstream of Lake Harney are not affected by ocean tide. These areas are divided by relict seawater-dominated waters downstream of Lake Washington and fresh, low-chloride waters upstream of Lake Washington.

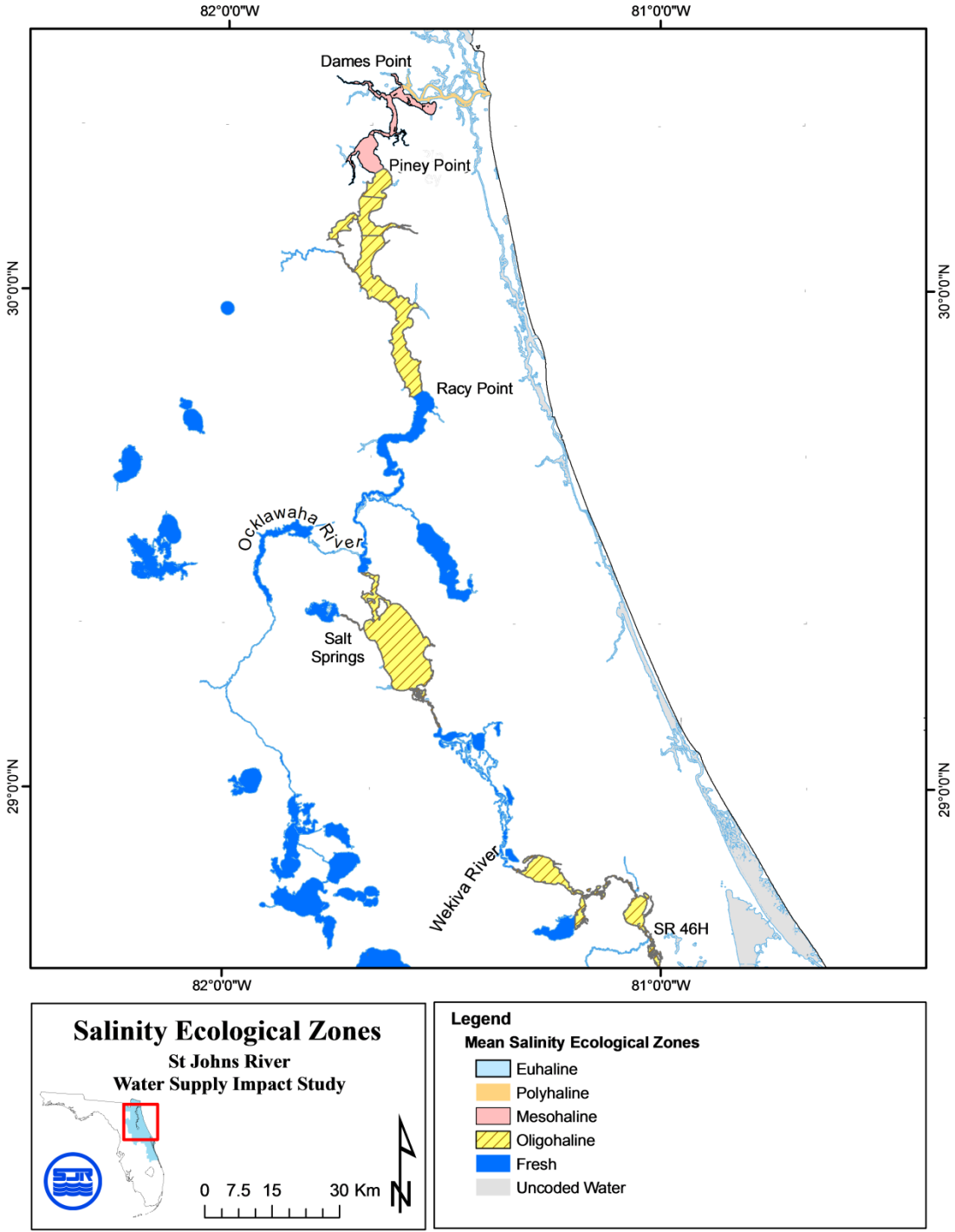


Figure 2–3. Salinity ecological zones based on the Venice Salinity Classification for the St. Johns River using observed mean salinity. Salinity ranges by zone are as follows: euhaline (30 to 40), polyhaline (18 to 30), mesohaline (5 to 18), oligohaline (0.5 to 5), and fresh (< 0.5). SR46H = State Road (SR) 46 above Lake Harney.

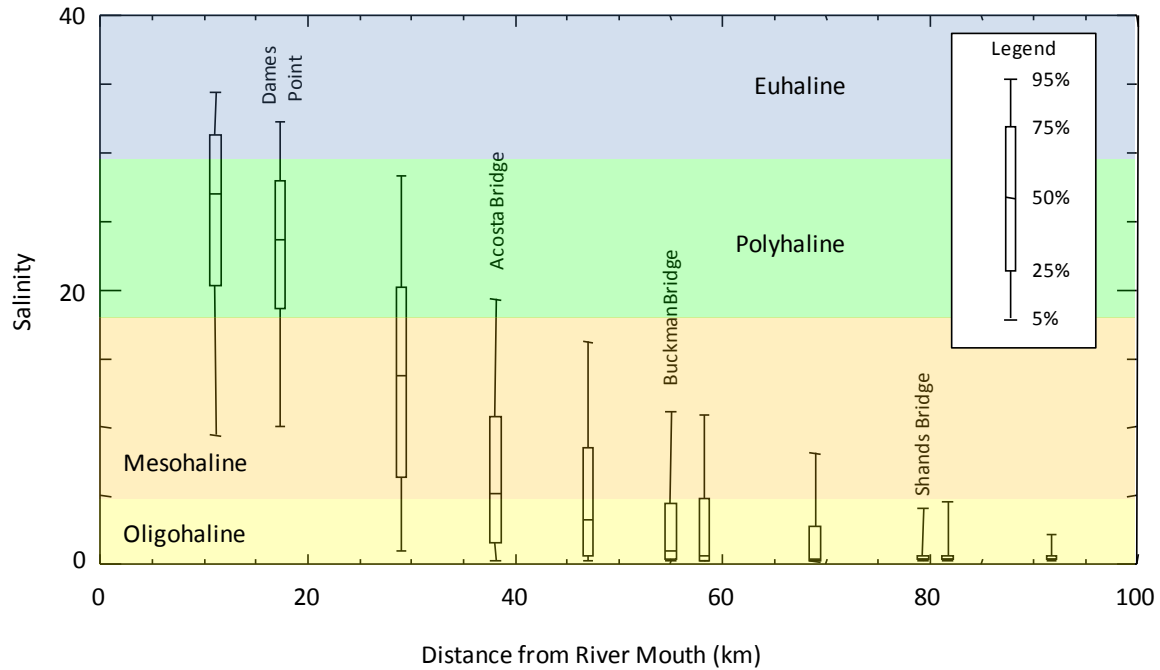


Figure 2-4. Five-point plots of observed salinity distributions in the St. Johns River over the first 100 river kilometers.

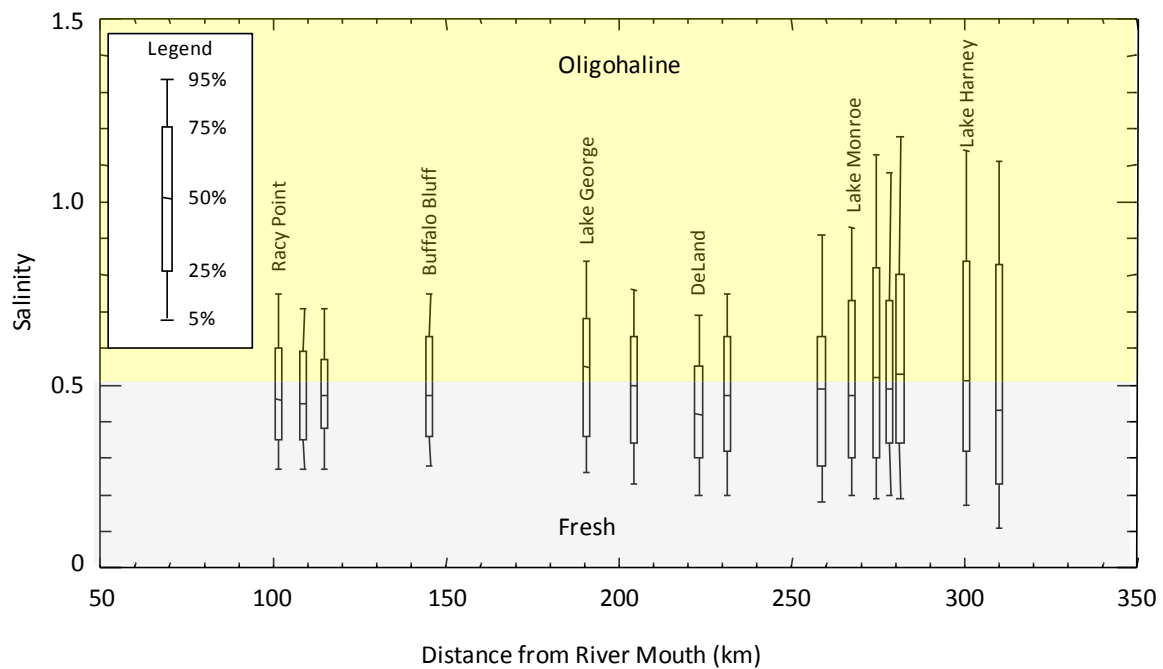


Figure 2-5. Five-point plots of observed salinity distributions in the St. Johns River for river kilometers 100 to 310, Racy Point to Lake Harney.

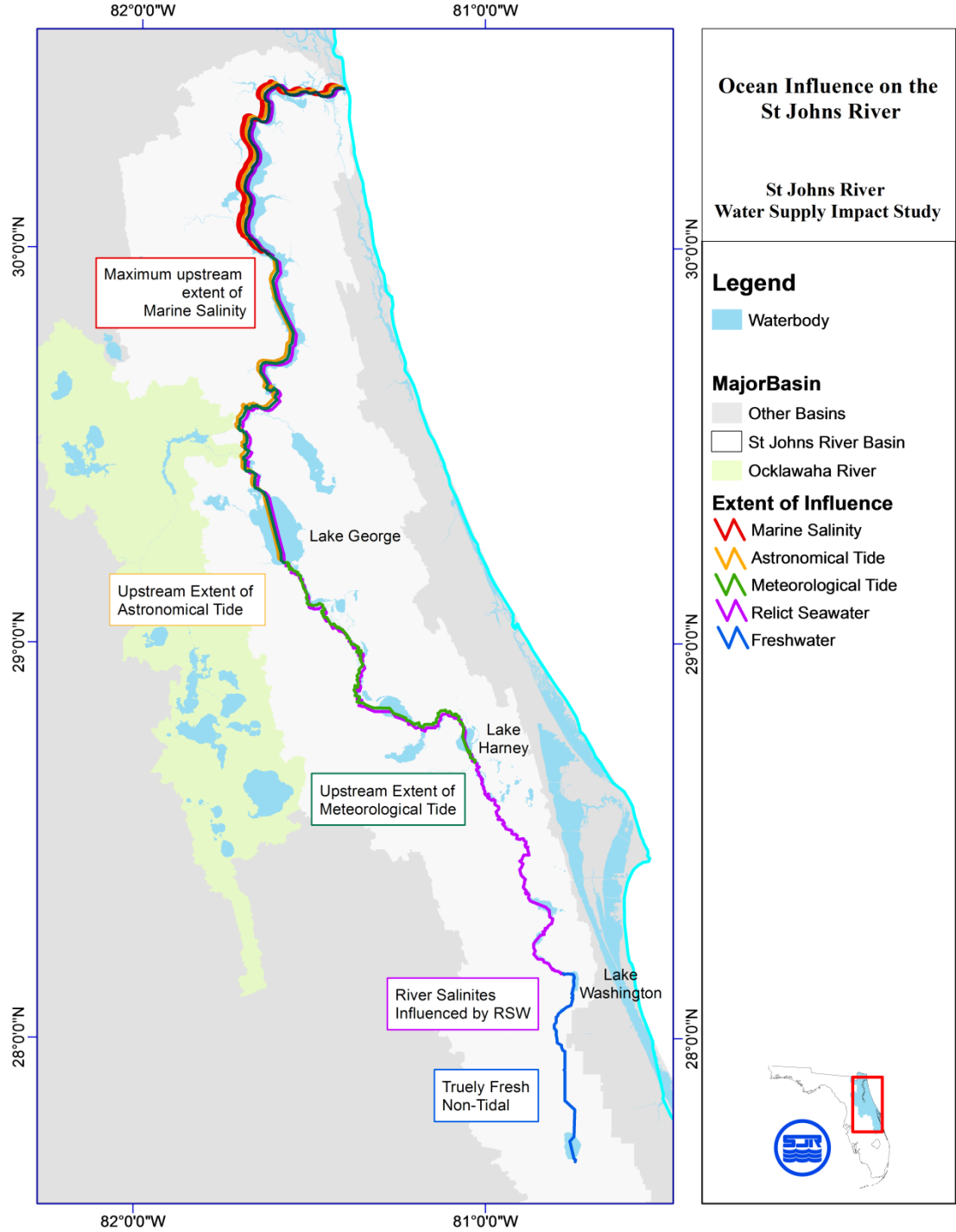


Figure 2-6. Division of St. Johns River by extent of (a) astronomical and meteorological tides and (b) source of salinity. RSW = relict seawater.

2.6 RIVER SLOPE AND LAKES

The St. Johns River has low slope. It drops 7.7 m over its 500 km course, an average slope of 1.5 cm km^{-1} . Most of this drop occurs over the upstream 200 km. Over the lower 300 km (i.e., the lower and middle St. Johns River), the slope is only 3 mm km^{-1} . The low slope results in a more lacustrine than riverine characteristic for much of the river. The middle St. Johns River passes through several lakes and even the broad expanse of the lower St. Johns River has a notable lacustrine character. The Timucuan Indians perceptibly named the river Welaka, meaning River of Lakes.

2.6.1 LAKE AREA

If considered a lake, the lacustrine segment of the lower St. Johns River, between Acosta Bridge and Palatka, is only surpassed in size among Florida lakes by Lake Okeechobee (Table 2–1). Lake George is the second largest lake in Florida and lies just upstream of the lacustrine segment of the lower St. Johns River.

Table 2–2. Comparison of the four largest Florida lakes, by surface area, with the lacustrine segment of the lower St. Johns River (LSJR) by area, volume, and volume:area ratio.

Lake	Area (A, km^2)	Volume (V, km^3)	V:A (m)
Lake Okeechobee	1,280	5.43	2.98
LJSR lacustrine segment (Acosta Bridge to Palatka)	294	0.88	2.99
Lake George	189.1	0.477	2.52
Lake Kissimmee	141.4	0.418	2.96
Lake Apopka	124.1	0.199	1.6

There are 12 lakes in the lower and middle St. Johns River that exceed 1 km^2 of surface area. For ease of visual comparison, the 12 lakes, along with the lacustrine lower St. Johns River, are displayed together in Figure 2–7. The combined area of these waters is 685 km^2 , while the total open water area of the middle and lower St. Johns River is 832 km^2 . More than 82% of this river reach is lacustrine.

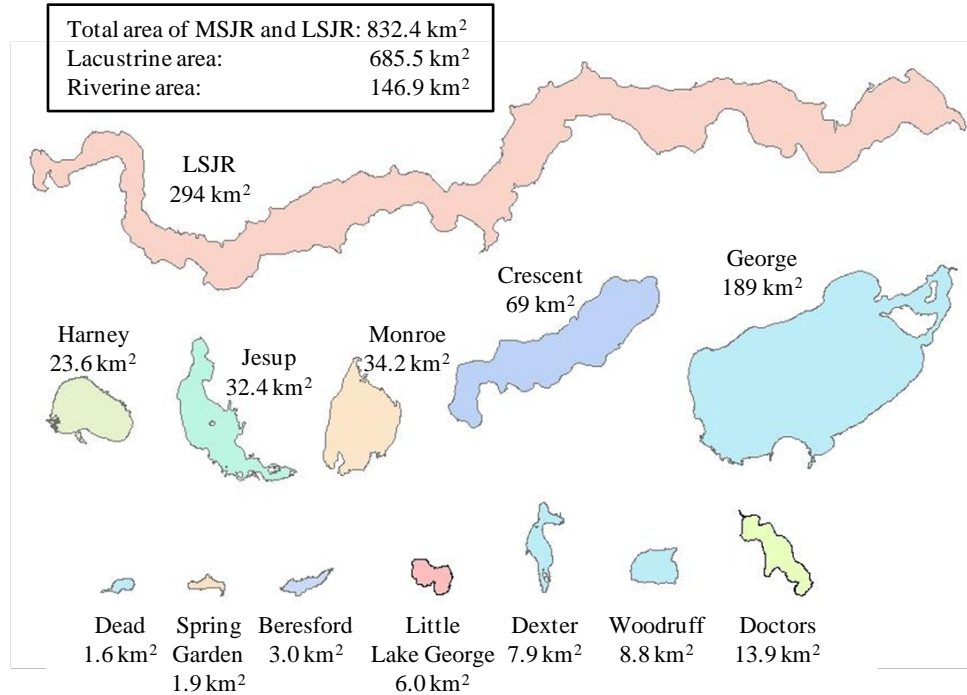


Figure 2–7. Comparison of surface area (km²) of lacustrine water bodies in the lower and middle St. Johns River. All water bodies are represented to scale. MSJR = middle St. Johns River. LSJR = lower St. Johns River.

2.6.2 LAKE VOLUME

Waters of upstream lakes flush through downstream lakes and the relative volumes of interconnected lakes influence water quality. In general, successive downstream volumes are larger than upstream volumes. This relationship is represented graphically using a conceptual box diagram (Figure 2–8). Each rectangle represents a lake volume, and can be thought of as a box of 1 km depth. Where one box is nested inside another box, the smaller box is located upstream. One exception to this rule for nesting is lakes Monroe and Harney. Although Lake Harney is upstream of Lake Monroe, and would nest inside Lake Monroe, these two lakes are shown separately for clarity. Due to the small volume Dead Lake is included with Crescent Lake and Doctors Lake is included with the lacustrine lower St. Johns River. The nesting readily shows that the combined volume of all middle St. Johns River lakes fits within Lake George, while the entire volume of both Lake George and Crescent Lake fit into the lacustrine lower St. Johns River.

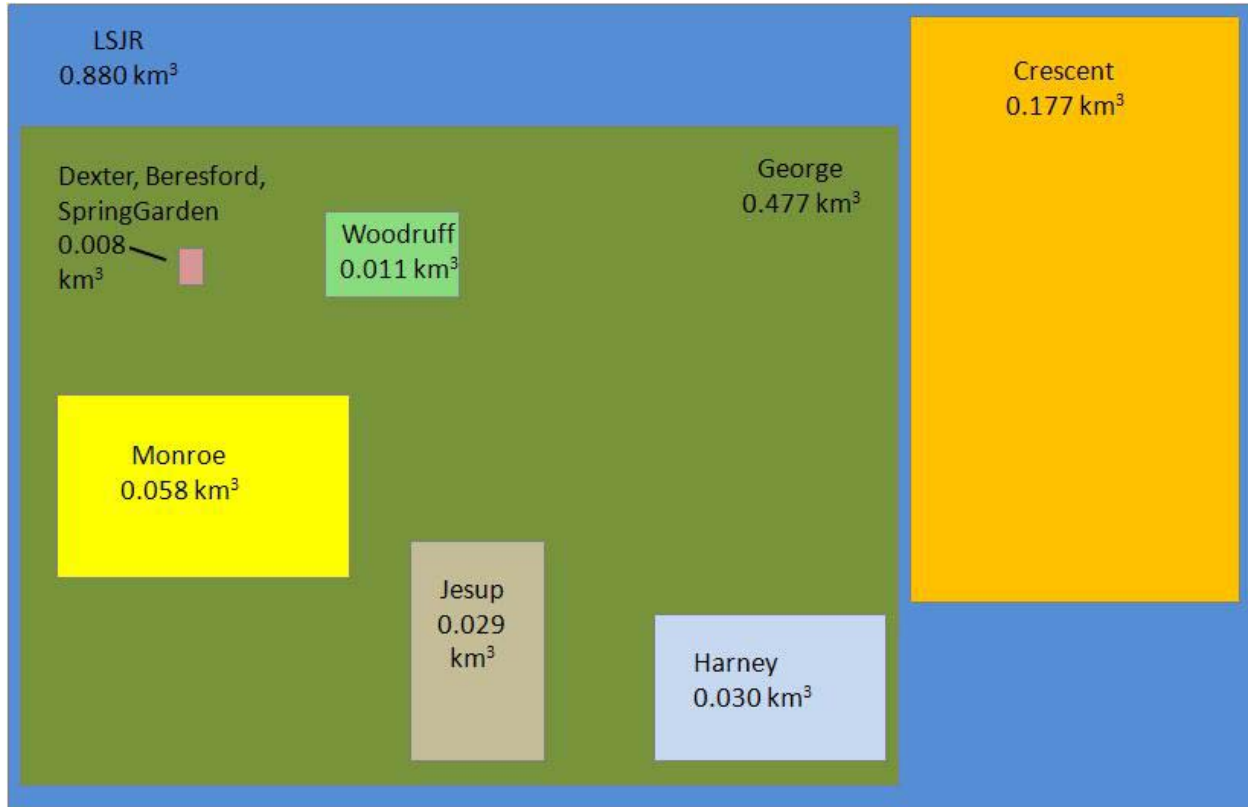


Figure 2–8. Graphic representation of volume of lacustrine water bodies in the lower and middle St. Johns River. Where one box is nested inside another box, the smaller box is located upstream. LSJR = Lower St. Johns River.

2.7 GEOMORPHOLOGY AND RELICT SEAWATER

A broad expanse of the St. Johns River maintains oligohaline conditions because of the influence of relict seawater. Most relict seawater enters the river between Lake George and Lake Pointsett through either springs or diffuse groundwater discharge. Both the presence and flushing of relict seawater in this river reach is related to its geomorphologic features.

During the Eocene and Oligocene Epochs of the Tertiary Period, the Florida Platform was a shallow sea. Reefs grew over millions of years and were then covered in sand as Florida emerged from the water (White, 1970). These reefs now form the limestone substrates that contain the Floridan aquifer (Johnson, 1982). Limestone in the Floridan aquifer is overlain by the less permeable sediments of the Hawthorn Formation. These sediments were deposited in the Miocene and are the Floridan aquifer's principal confining unit (Hoenstine, 1984). Younger deposits that form surficial aquifers covered the Hawthorn Formation to varying depths in the Pliocene and Pleistocene age (Johnson, 1982). The St. Johns River now rests in erosional Hawthorn Formation and younger deposits (White, 1970). For more information on the hydrogeology of the St. Johns River, see Chapter 4, Groundwater Hydrology.

2.7.1 SPATIAL VARIATION OF THE HAWTHORN FORMATION

Variations in thickness of the Hawthorn Formation largely determine the extent of interaction between groundwater and surface waters. Groundwater interactions are least where the Hawthorn Formation is thickest, in the lower St. Johns River and upper portions of the upper St. Johns River. In the lower St. Johns River, the Hawthorn Formation thickens to a maximum of 500 ft downstream of State Road (SR) 40 (Scott 1983). In the upper St. Johns River, the Hawthorn Formation thickens to 400 ft upstream of State Road (SR) 520. Most of the lower St. Johns River and upper St. Johns River occupy a surface feature known as the Eastern Valley (White 1970). In the area now occupied by the lower St. Johns River, episodes of faulting and warping resulted in a downward flexure that deepened this portion of the Eastern Valley (Scott 1983). The deepening resulted in a thick Hawthorn Formation that contributes to the general lack of springs and overall lack of diffuse groundwater discharge (Spechler 1994).

The Hawthorn Formation is thin or absent in the middle St. Johns River and lower portion of the upper St. Johns River, ranging in thickness from 0 to 50 ft (Johnson 1982). In these areas the river receives groundwater inflows from numerous springs and diffuse groundwater discharge. These groundwater inflows flush relict seawater from the underlying Floridan aquifer to the river. The thinning of the Hawthorn Formation in this area primarily resulted from geological uplift followed by erosion of the uplifted Hawthorn Formation sediments. Uplifted features are generally associated with minimal overburden where the Floridan aquifer is closest to the surface (Opdyke 1984).

2.7.2 THE OFFSET COURSE OF THE ST. JOHNS RIVER

The present course of the middle St. Johns River, from Lake Harney to Palatka, flows through a valley older than the Eastern Valley. The offset course of the St. Johns River has distinct hydrogeologic features that cause this reach of the river to be strongly influenced by the Upper Floridan aquifer. Because the Upper Floridan aquifer in this reach of the river contains relict seawater, the middle St. Johns River has high chloride levels and a distinct oligohaline salinity regime.

The path of the river is diverted west around the Volusia Block Fault (Wyrick 1960). The Volusia Block Fault underlies western Volusia County and emerged in the late Tertiary or early Pleistocene period (White 1970) and was likely influenced by the glacial eustatic fluctuations of sea level during the Pleistocene (Alt and Brooks 1965). It now forms the DeLand Ridge, an important recharge area for springs that lie along its base (Figure 2–9). There is evidence for a relict path of the St. Johns River to the east of the Volusia Block Fault that extends directly from Lake Harney to Crescent Lake through the Eastern Valley (Pirkle 1971). The offset course of the St. Johns River may have originated as a spring-fed river starting near the headwaters of the present Wekiva River. The presence of substantial artesian inputs through springs and diffuse groundwater discharge has helped maintain the present course of the middle St. Johns River through this ancestral valley (Pirkle 1971).

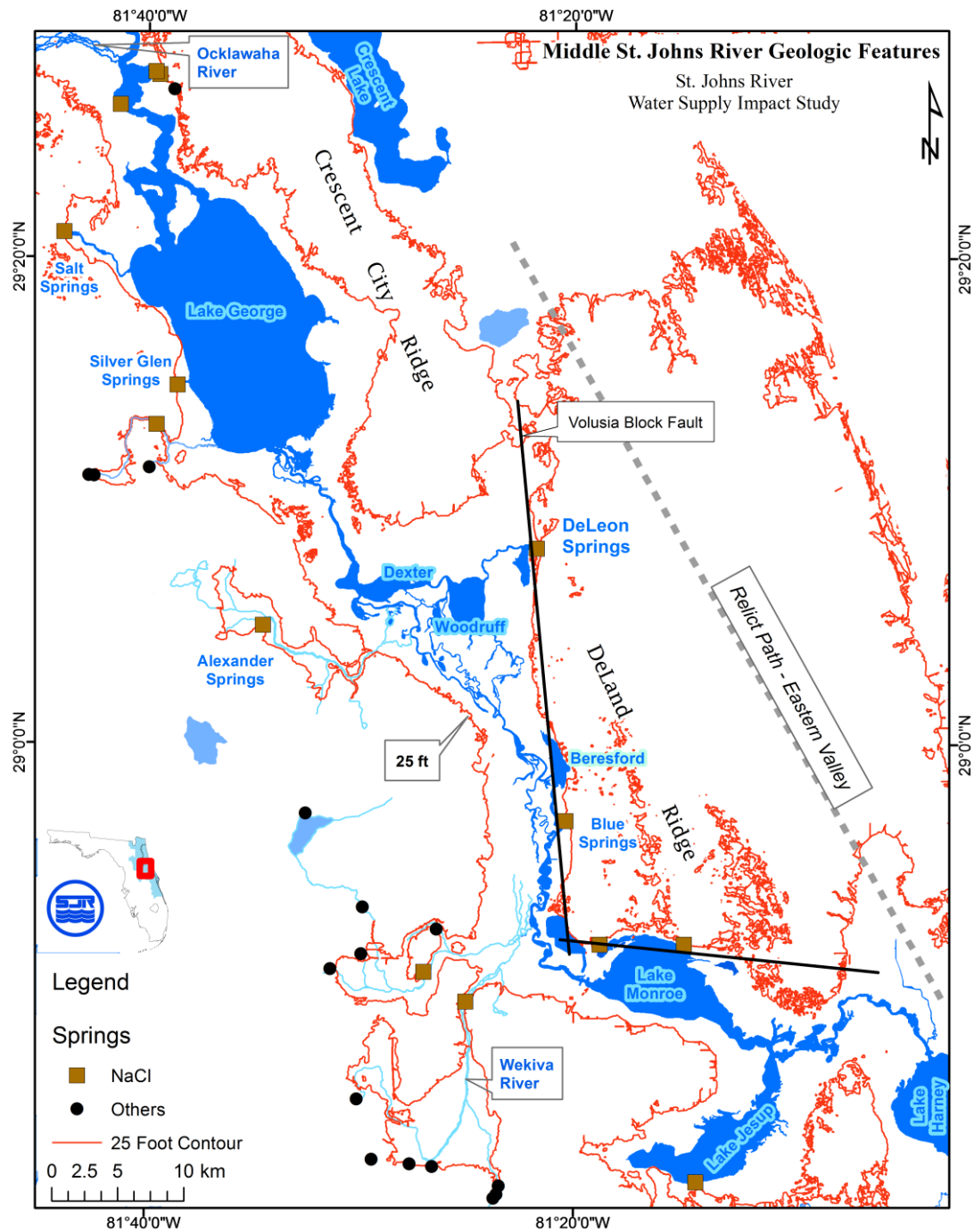


Figure 2–9. Topography and geology of the St. Johns River Basin between Lake Harney and the Ocklawaha River. The river enters a geologically older valley downstream of Lake Harney as it flows around the Volusia Block Fault.

2.7.3 SPRINGS

The many springs found throughout the middle St. Johns River and Lake George are shown in Figure 2–9. Springs that contribute relict seawater to the river are identifiable by a high chloride

level ($> 250 \text{ mg L}^{-1}$ chloride) and a salt composition similar to seawater. These springs occur at lower elevations near the river and are symbolized as sodium chloride (NaCl) springs in Figure 2–9. Springs with pool elevations above 25 ft NGVD29 (National Geodetic Vertical Datum of 1929) have low levels of chloride, while springs below 5 ft have consistently high levels of chloride (Figure 2–10). Salt composition of springs with pool elevations below 5 ft NGVD29 is similar to ocean water and dominated by NaCl, while springs with pool elevations above 25 ft NGVD29 are dominated by bicarbonate, HCO_3 , (Figure 2–11).

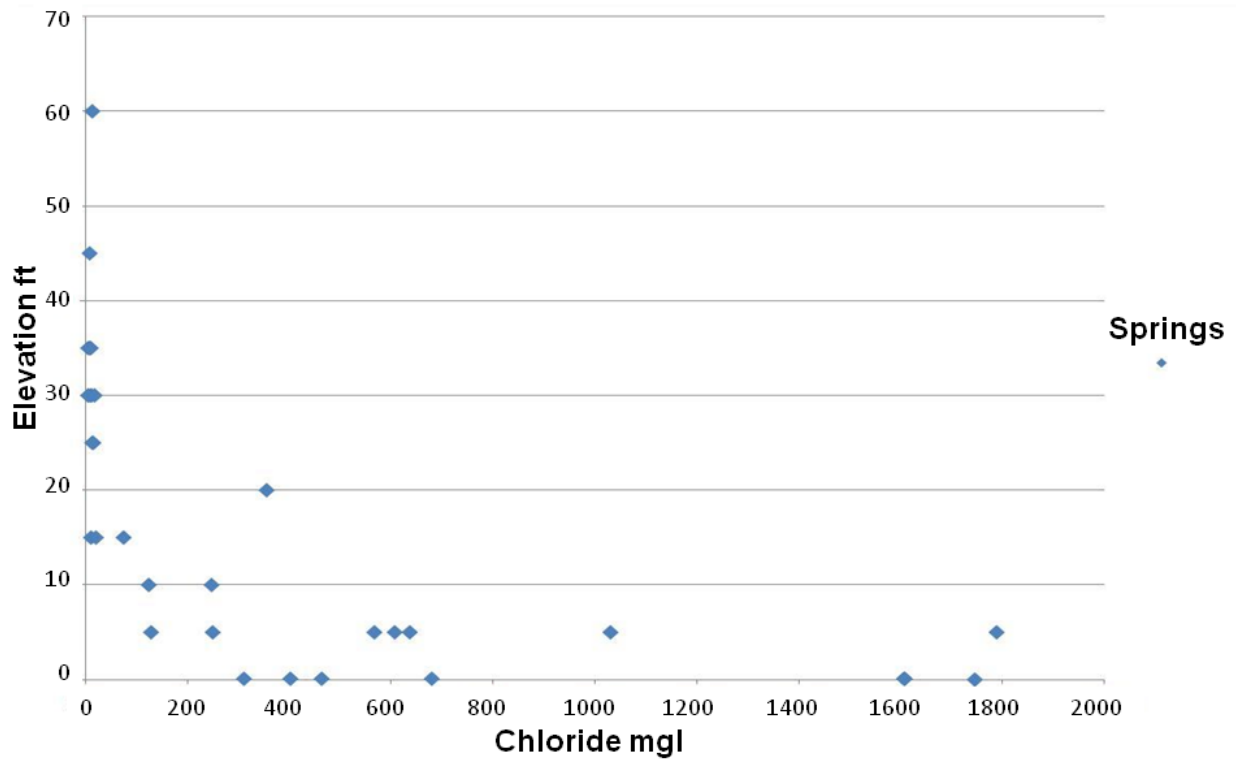


Figure 2–10. Comparison of chloride levels and pool elevation for St. Johns River springs.

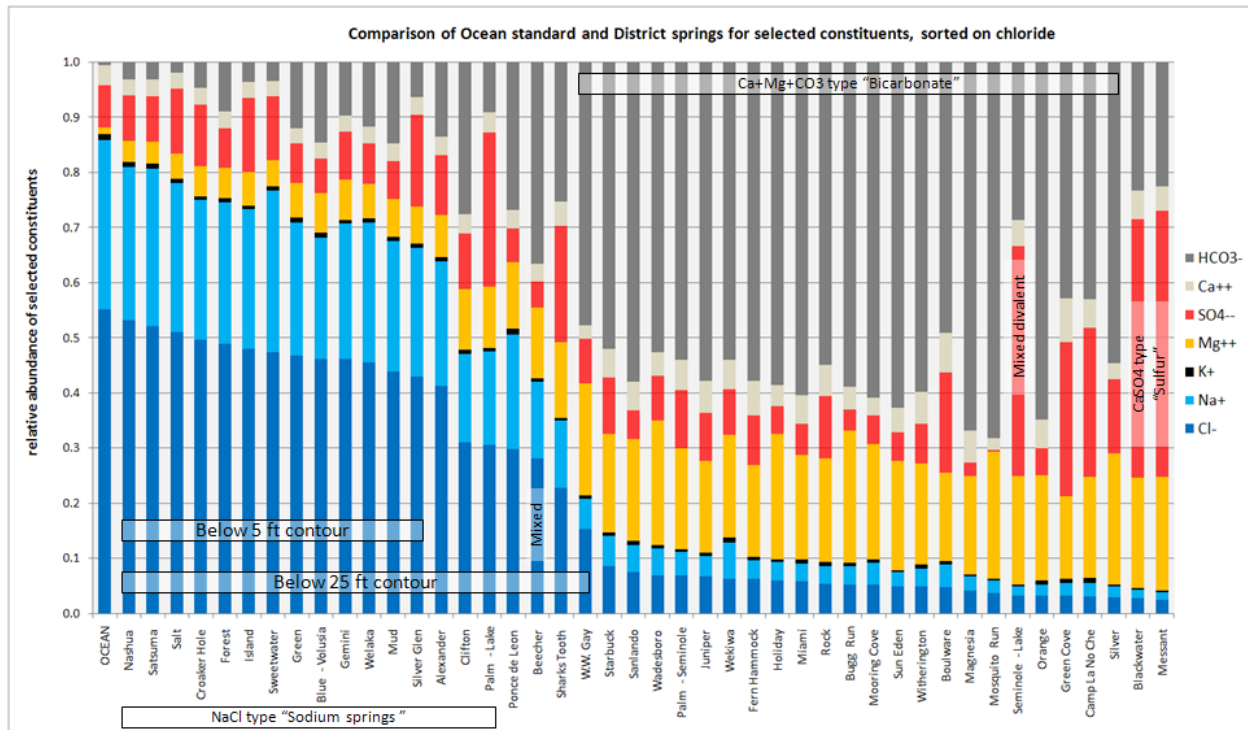


Figure 2–11. Salt composition of selected springs compared to the Ocean Standard. Springs are sorted by chloride abundance. Springs most similar to ocean water lie below an elevation of 5 ft NGVD29 and have salts dominated by relict seawater.

2.7.4 DIFFUSE GROUNDWATER DISCHARGE

In addition to spring discharge, diffuse groundwater discharge is an important source of relict seawater to the river (see Chapter 4. Groundwater Hydrology). The middle St. Johns River, because of its thin Hawthorn Formation, has high diffuse groundwater discharge that contains appreciable quantities of relict seawater. Groundwater chloride concentrations are highest directly beneath the middle St. Johns River channel (Figure 2–12). High diffuse groundwater discharge and chloride coincide because the same factors that now allow groundwater exchange to the river also allowed seawater to inundate the underlying aquifers during past periods of higher sea level stand. The factors allowing groundwater exchange include a thin or absent Hawthorn Formation, faulting along the Volusia Block Fault, and previous channel incision at lower sea level stands (see Chapter 4. Groundwater Hydrology). Finally, because the upper limit of Pleistocene sea level inundations were near the present 25 ft NGVD29 contour, relict seawater is only found below that elevation.

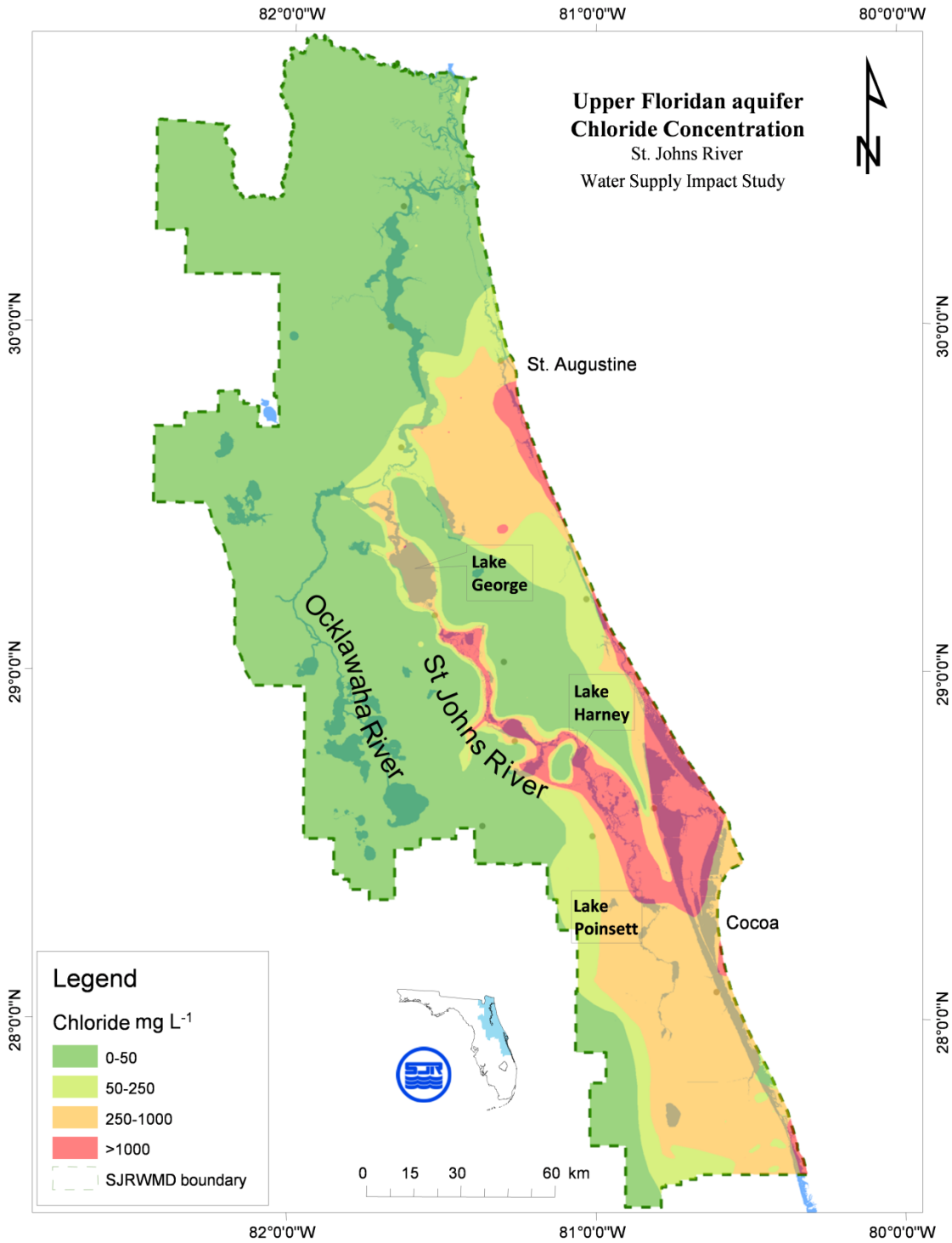


Figure 2–12. Chloride concentration in the Upper Floridan aquifer (UFA) within the St. Johns River Water Management District (SJRWMD). High chloride concentrations occur directly along the path of the SJR between Lake Poinsett and Lake George.

3 OBSERVED DATA

Observed data are required for setting model boundary conditions. Model boundary conditions are the factors applied to the model to predict water motions within the model study area. Model boundary conditions include ocean tide along the open ocean boundary, lateral inflows from tributaries, springs, and wastewater treatment plants, vertical inflows from groundwater (along the bottom) and rainfall (along the surface), loss from evaporation, wind stress on the model surface, and specification of model depths. All inflows to the model, including those from ocean tide, are assigned a salinity. The model simulates the dynamic response of water motions in the model interior to the boundary conditions through time. Because the model simulation period is 1996 to 2005, model boundary conditions must be complete over this period.

Observed data are also required for comparison with simulated results for model calibration and confirmation. The model simulates water level, velocity, discharge, and salinity throughout the horizontal model domain as well as variations with depth. Ideally, observed data used to calibrate the model spans the entire simulation period, but observations over shorter periods can still provide useful insight into the model's dynamic response to boundary conditions.

This section outlines the primary observed data sources used for model boundary conditions and model calibration. For each data type, we show gauge locations, periods of record, and provide a brief summary of the data. The data summaries provide an overview of system characteristics.

3.1 WATER LEVEL

Water levels are the time-varying changes in the elevation of the river's surface. Water levels show how the river surface responds to the combined effects of tide, wind, discharge, and bottom friction at various points along the river. Eighteen water level gauges were active during the simulation period (Figure 3–1). Hourly water levels are available for the tidal portion of the St. Johns River and daily averaged water levels are available in the non-tidal portion of the river. USGS station 02232500 (St. Johns River near Christmas) is outside the study area, but is included here for subsequent discussion regarding development of the upstream model boundary conditions.

Table 3–1 identifies each station shown on Figure 3–1 and provides the collecting agency, station identification (ID), station name, period of record, latitude, longitude, and river kilometer for each water level station. Three stations with notably long periods of record are St. Johns River near DeLand, St. Johns River above Lake Harney, and St. Johns River near Christmas with records extending back to 1934, 1941, and 1933, respectively.

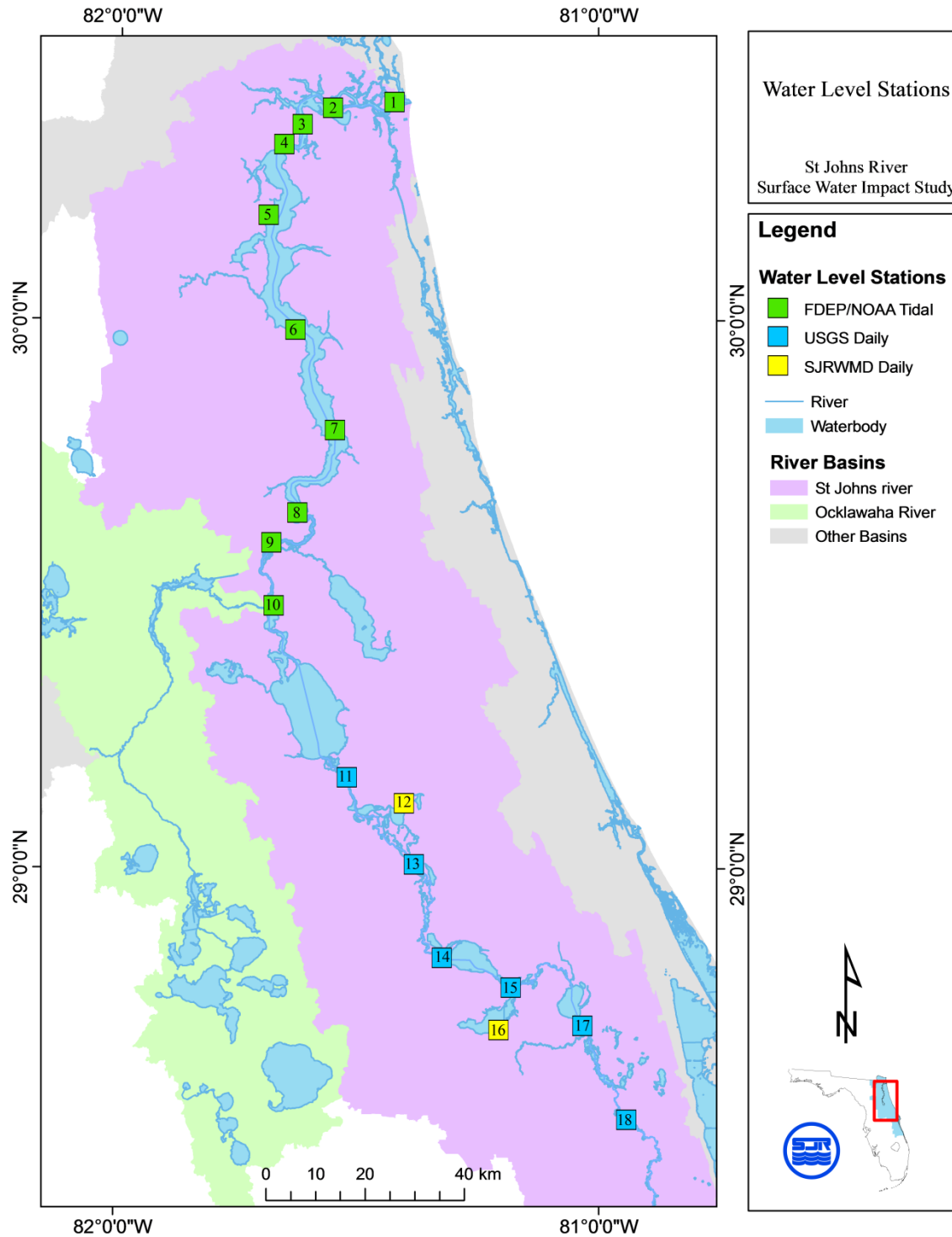


Figure 3–1. Locations of stations with continuously observed water level active for the model simulation period of 1996 to 2005. Map numbers are defined in Table 3–1.

Table 3–1. Water level stations in lower and middle St. Johns River listed in north-to-south order. Map numbers refer to Figure 3–1.

Map #	Station ID	Agency	Station Name	Period of Record	Lat	Long	River km
1	872-0218	NOAA	Bar Pilot Dock	1995–Present	30 23.8	81 25.8	3.4
2	872-0219	FDEP	Dames Point	1995–2007	30 23.2	81 33.5	17.3
3	872-0242	FDEP	Long Branch	1996–2005	30 21.4	81 37.2	30.0
4	872-0226	FDEP	Main Street Bridge	1995–2007	30 19.2	81 39.5	38.1
5	872-0357	FDEP	Buckman Bridge	1995–Present	30 11.5	81 41.4	55.0
6	872-0503	FDEP	Shands Bridge	1995–Present	29 59.0	81 38.0	79.3
7	872-0625	FDEP	Racy Point	1995–Present	29 48.0	81 33.0	101.6
8	872-0774	FDEP	Palatka	1995–2005	29 38.9	81 37.6	127.3
9	872-0767	FDEP	Buffalo Bluff	1995–Present	29 35.6	81 40.9	145.3
10	872-0832	FDEP	Welaka	1996–Present	29 28.6	81 40.5	161.1
11	02236125	USGS	St. Johns River at Astor	1994–Present	29 10.0	81 31.3	204.4
12	15493167	SJRWMD	Lake Woodruff NWR ¹	2004–2005	29 7.2	81 24.2	223.11
13	02236000	USGS	St. Johns River near DeLand	1934–Present	29 0.5	81 23.0	231.4
14	02234500	USGS	St. Johns River near Sanford	1987–Present	28 50.3	81 19.5	262.0
15	02234435	USGS	Lake Jesup outlet	1991–Present	28 47.0	81 10.9	279.7
16	01410650	SJRWMD	Lake Jesup at Oviedo ¹	1996–2006	28 42.4	81 12.4	288.61
17	02234000	USGS	St. Johns River above Lake Harney	1941–Present	28 42.8	81 2.1	310.1
18	02232500	USGS	St. Johns River near Christmas	1933–Present	28 32.6	80 56.6	343.2

¹Distance includes estimated distance off main channel.

Descriptive statistics for the 18 stations are provided in Table 3–2 for the model simulation period of 1996 to 2005. The first three columns of the table provide the map number, station name, and river kilometer for convenience in cross-referencing with Table 3–1. The remaining columns show mean water level for model confirmation period, mean sea level reported by the

National Oceanic and Atmospheric Administration (NOAA) (NOAA 2010), the 90–10 percentile range (defined as the range of water levels between the 90th and 10th percentile of the distribution), the mean tidal range reported by NOAA (NOAA 2010), and the extreme high water level represented by the 99th percentile of the distribution. The p th percentile of the distribution is the value such that p percent of the observations fall at or below it (Moore and McCabe 1989).

Mean water level ranged from -0.13 m at the mouth to 1.62 m near Christmas. NOAA mean sea level (MSL) agrees well with the 10-yr mean water levels for the tidal stations. Mean water level at Astor is below Welaka—a physically unrealistic condition. This indicates an inconsistency in absolute datum between these stations and perhaps between the NOAA and USGS networks in general. This question is examined further in section 4.3. The apparent high mean water level for Lake Woodruff National Wildlife Refuge is an artifact of the short period of record at that location and should not be used for direct comparison with the other gauges.

Mean tidal range from NOAA clearly shows that the tidal portion of the river extends over 160 km from the mouth to Welaka. The USGS stations upstream of Lake George are considered to have an insignificant range of tide.

The 90–10 percentile range is similar to the mean tidal range from the mouth to Main Street Bridge where the water level is tidally dominated. Upstream of Main Street Bridge to Welaka tidal range decreases as short period tidal amplitudes are attenuated. The 90–10 percentile range becomes larger than the tidal range because low frequency ocean forcing is not attenuated and its relative contribution to total water level variability increases. In the tideless reach, from Astor to Christmas, the 90–10 percentile range is increased by high water level driven by stormwater discharge.

Extreme high water is represented by the 99th percentile of the distribution of water levels, that level that exceeds 99% of all values. In the tidal portion of the river, extreme high water is greatest at the mouth and declines rapidly to Main Street Bridge, following the general pattern for tidal range. Throughout most of the lower St. Johns River, from Main Street Bridge to Astor, the river is relatively buffered from extreme high water. This buffering from flood events is likely because (a) large ocean storm surges have periods similar to astronomical tides (hrs) and are attenuated over the first 50 km of the river similarly to astronomical tide, and (b) the river here has a large hydraulic capacity to discharge storm flow volumes, so that storm discharge has only a minor effect on water level. Upstream of Astor, extreme high water events increase because of hydraulic restriction of storm discharges. The maximum deviation of extreme high water from mean water level occurs in Lake Harney. Christmas has a higher absolute extreme high water than Lake Harney because Christmas is located up-slope.

Table 3–2. Descriptive statistics for observed water level, 1996 to 2005.

Map #	Station Name	River km	Mean Water Level	MSL (NOAA)	90–10 Percentile Range	Mean Tidal Range (NOAA)	99% Values Lower Than
1	Bar Pilot Dock	3.4	-0.13	-0.15	1.41	1.39	0.86
2	Dames Point	17.3	-0.12	n/a	1.12	1.05	0.67
3	Long Branch	30.0	-0.07	-0.09	0.84	0.77	0.58
4	Main Street Bridge	38.1	-0.07	-0.09	0.68	0.56	0.49
5	Buckman Bridge	55.0	-0.03	-0.06	0.49	0.28	0.47
6	Shands Bridge	79.3	-0.02	-0.04	0.49	0.27	0.49
7	Racy Point	101.6	-0.01	-0.06	0.50	0.35	0.47
8	Palatka	127.3	-0.02	-0.04	0.54	0.39	0.45
9	Buffalo Bluff	145.3	0.01	-0.02	0.51	0.32	0.48
10	Welaka	161.1	0.05	0.05	0.44	0.13	0.47
11	St. Johns River at Astor	204.4	-0.01	n/a	0.58	insig.	0.60
12	Lake Woodruff NWR*	223.1	(0.25)	n/a	0.79	insig.	0.96
13	St. Johns River near DeLand	231.4	0.06	n/a	0.83	insig.	0.96
14	St. Johns River near Sanford	262.0	0.33	n/a	1.17	insig.	1.65
15	Lake Jesup outlet	279.7	0.40	n/a	1.27	insig.	1.67
16	Lake Jesup at Oviedo	288.6	0.42	n/a	1.38	insig.	1.81
17	St. Johns River above Lake Harney	310.1	0.70	n/a	1.96	insig.	2.52
18	St. Johns River near Christmas	343.2	1.62	n/a	1.66	Insig.	2.91

* Period of record 2004 to 2005.

Units of columns 4 through 8 are meters

Columns 4, 5, and 8 are referenced to NAVD88

NAVD88 = North American Vertical Datum of 1988 (Zilkoski D. B. 1992)

MSL = Mean sea level

n/a = MSL not available from NOAA

insig. = insignificant range of tide

3.2 TIDAL HARMONICS

Tidal harmonics are site-specific constants that describe tidal motions as a sum of simple cosine terms of known periods. The individual cosine terms are called tidal constituents. The period of each tidal constituent is known from astronomical relationships derived from motions of the earth–moon–sun system. The site-specific amplitude and phase of a tidal constituent are called harmonic constants; a set of harmonic constants constitute the tidal harmonics for a given location.

Tidal harmonic constants are calculated from hourly water level observations by the method of harmonic analysis (Schureman 1988). Tidal harmonics are usually very stable over time, so that harmonic constants can be obtained from observations taken from different time periods. Nonstationary tidal harmonics can occur in some rivers (Flinchem and Jay 2000), but this phenomenon is not known for the St. Johns River where peak discharges are likely too small to alter harmonic constants. In the St. Johns River, harmonic constants calculated from observed water levels from the 1970s are nearly identical to present day tidal harmonics. For this reason, there are many more locations for tidal harmonics used for the WSIS than for water level because the latter is restricted to stations active only during the model simulation period. Tidal harmonics are available at 23 locations between the river mouth and Lake George (Figure 3–2). Table 3–3 identifies each station shown on Figure 3–2 and provides the station ID, collecting agency, station name, period of record, latitude and longitude, and river kilometer.

The amplitude and phase of the five largest tidal constituents are shown in Table 3–4. The map number, river kilometer, and station name are repeated for ease of cross referencing with Table 3–3. The full name and period of the three semidiurnal tidal constituents (M_2 , S_2 , and N_2) and two diurnal constituents (K_1 and O_1) are shown in Table 3–5. M_2 has the largest amplitude of all tidal constituents in the St. Johns River, and its predominance causes the familiar pattern of two high and low tides each day.

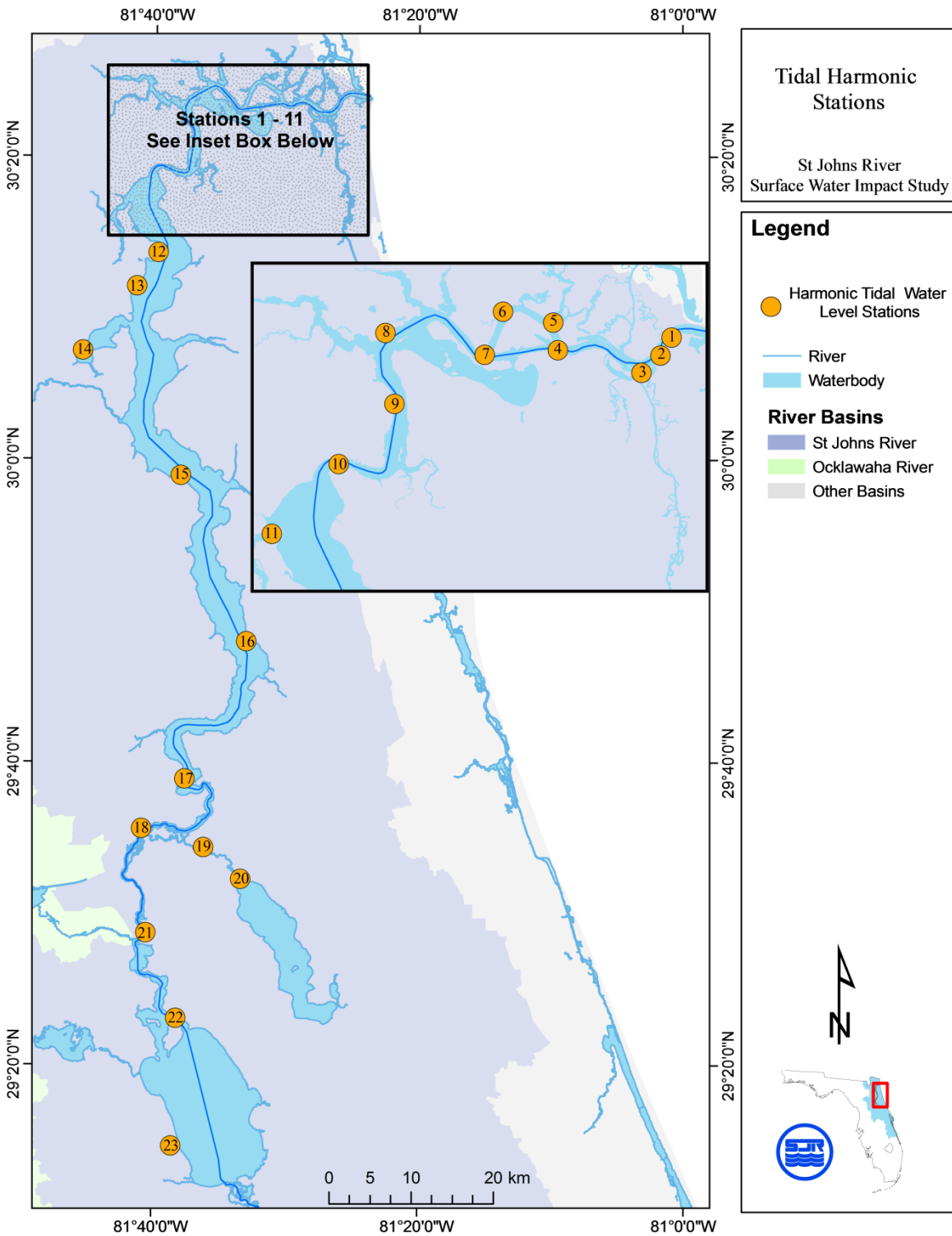


Figure 3–2. Locations of stations with harmonic tidal constituents for water level. Map numbers are defined in Table 3–3.

Table 3–3. Tide stations in lower St. Johns River listed in north-to-south order. Map numbers refer to Figure 3–2.

Map #	Station ID	Agency	Station Name	Period of Record	Lat	Long	River km
1	872-0218	FDEP/NOAA	Bar Pilot Dock	1995–Present	30 23.8	81 25.8	3.4
2	872-0220	NOAA	Mayport	1928–1995	30 23.6	81 25.9	4.9
3	872-0232	NOAA	Pablo Creek Entrance	1977–1978	30 22.6	81 26.9	6.3*
4	872-0221	NOAA	Fulton	1977–1978	30 23.4	81 30.4	12.3
5	872-0198	NOAA	Clapboard Creek	1977–1978	30 24.4	81 30.6	14.0
6	872-0203	NOAA	Blount Island	1977–1978	30 24.8	81 32.7	17.7
7	872-0219	FDEP/NOAA	Dames Point	1995–2007	30 23.2	81 33.5	17.3
8	872-0215	NOAA	Navy Fuel Depot	1977–1978	30 24.0	81 37.6	25.0
9	872-0242	FDEP/NOAA	Long Branch	1996–Present	30 21.4	81 37.2	30.0
10	872-0226	FDEP/NOAA	Main Street Bridge	1995–Present	30 19.2	81 39.5	38.1
11	872-0296	NOAA	Ortega River Entrance	1978–1979	30 16.7	81 42.3	45.7
12	872-0333	NOAA	Piney Point	1978–1979	30 13.7	81 39.8	49.7
13	872-0357	FDEP/NOAA	Buckman Bridge	1995–Present	30 11.5	81 41.4	55.0
14	872-0406	NOAA	Doctors Lake	1978	30 0.2	81 45.5	67.5
15	872-0503	FDEP/NOAA	Shands Bridge	1995–Present	29 59.0	81 38.0	79.3
16	872-0625	FDEP/NOAA	Racy Point	1995–Present	29 48.0	81 33.0	101.6
17	872-0774	FDEP/NOAA	Palatka	1995–Present	29 38.9	81 37.6	127.3
18	872-0767	FDEP/NOAA	Buffalo Bluff	1995–Present	29 35.6	81 40.9	145.3
19	872-0782	NOAA	Sutherland Still	1993–1994	29 34.3	81 36.4	143.9
20	872-0805	NOAA	Moccasin Landing	1993–1994	29 32.3	81 33.4	151.0
21	872-0832	FDEP/NOAA	Welaka	1996–Present	29 28.6	81 40.5	161.1
22	872-0877	NOAA	Georgetown	1973–1978	29 23.1	81 38.2	175.6
23	02236160	USGS	Silver Glen	2003–Present	29 14.7	81 38.6	190.0

* Stations are off the main channel.

Table 3–4. Amplitude and phase of the five largest tidal constituents in the lower St. Johns River. Tidal constituents are defined in Table 3–5. Map numbers refer to Table 3–3 and Figure 3–2.

Map #	River km	Station Name	M ₂		S ₂		N ₂		K ₁		O ₁	
			A	P	A	P	A	P	A	P	A	P
1	3.4	Bar Pilot Dock	0.668	241	0.094	260	0.151	224	0.030	235	0.059	141
2	4.9	Mayport	0.670	241	0.107	262	0.145	223	0.026	232	0.058	142
3	6.3	Pablo Creek Entrance	0.514	254	0.071	272	0.103	245	0.091	152	0.059	142
4	12.3	Fulton	0.565	254	0.095	276	0.104	244	0.060	147	0.041	165
5	14.0	Clapboard Creek	0.546	261	0.068	277	0.096	253	0.080	156	0.053	144
6	17.7	Blount Island	0.533	262	0.066	280	0.093	253	0.082	157	0.052	143
7	17.3	Dames Point	0.537	264	0.067	286	0.116	255	0.063	141	0.044	154
8	25.0	Navy Fuel Depot	0.405	278	0.050	288	0.072	268	0.060	171	0.041	157
9	30.0	Long Branch	0.374	278	0.053	310	0.075	264	0.042	148	0.029	169
10	38.1	Main Street Bridge	0.287	290	0.034	313	0.058	282	0.032	168	0.023	184
11	45.7	Ortega River Entrance	0.174	305	0.026	328	0.034	289	0.024	183	0.017	193
12	49.7	Piney Point	0.133	320	0.017	343	0.021	304	0.006	217	0.011	202
13	55.0	Buckman Bridge	0.127	325	0.014	345	0.024	310	0.019	206	0.015	215
14	67.5	Doctors Lake	0.121	334	0.011	335	0.024	332	0.019	192	0.018	212
15	79.3	Shands Bridge	0.117	25	0.011	55	0.020	6	0.019	225	0.015	239
16	101.6	Racy Point	0.157	66	0.019	100	0.027	48	0.017	246	0.017	247
17	127.3	Palatka	0.185	83	0.021	118	0.033	66	0.017	252	0.015	252
18	145.3	Buffalo Bluff	0.156	96	0.015	136	0.024	76	0.015	260	0.010	267
19	143.9	Sutherland Still	0.139	95	0.016	128	0.034	89	0.014	237	0.010	264
20	151.0	Moccasin Landing	0.009	189	0.002	196	0.003	194	0.004	346	Insig.	—

21	161.1	Welaka	0.063	110	0.008	133	0.011	90	0.005	281	0.004	296
22	175.6	Georgetown	0.009	232	0.004	306	Insig.	—	0.002	81	0.003	4
23	190.0	Silver Glen	0.010	232	0.002	231	Insig.	—	0.003	91	0.001	316

Note:

- A = amplitude of tidal constituent in meters
P = local phase of tidal constituent in degrees
Insig. = amplitude was less than 0.001 m
— = phase was unanalyzable

Table 3–5. Name and period of the five largest tidal constituents in the lower St. Johns River.

Symbol	Name	Period (hrs)
M ₂	Principle lunar semidiurnal	12.42
S ₂	Principle solar semidiurnal	12.00
N ₂	Larger lunar elliptic semidiurnal	12.66
K ₁	Luni-solar diurnal	23.93
O ₁	Principle lunar diurnal	25.82

Amplitudes of the semidiurnal constituents decrease rapidly over the first 50 km from the mouth (see Table 3–4). The rate of decrease is nearly constant, so that the resultant tidal range decreases 2.6 cm km⁻¹ from Bar Pilot Dock to Piney Point. Semidiurnal amplitudes continue to decrease from Piney Point to Shands Bridge, but more slowly; decreasing at a rate of 0.14 cm km⁻¹ in this reach. Semidiurnal amplitudes increase between Shands Bridge and Palatka, and then slowly decrease to Georgetown.

The ratio of diurnal to semidiurnal harmonic amplitudes is called Form Number (F) and ranges from 0.12 at Bar Pilot Dock to 0.27 at Shands Bridge (Morris 1995). The small values of F indicate dominance of semidiurnal constituents. The increase in F at Shands Bridge results in an increase of diurnal inequality of the semidiurnal tide. As semidiurnal harmonic amplitudes increase upstream of Shands Bridge, F declines and ranges from 0.13 to 0.16 from Palatka to Georgetown, again indicating strong semidiurnal tidal variability.

The spatial variation of M₂ phase can be used to estimate the time lag of high and low water between stations (ignoring shallow water effects). For example, the M₂ phase difference between Buckman Bridge and Bar Pilot Dock is 84° (325° to 241°). Because the M₂ constituent has a period of 12.42 hrs, the time lag between these stations can be estimated as (84°/360°) x 12.42 = 2.9 hrs. This means that when high tide occurs at the mouth, mid-tide occurs at Buckman Bridge. The phase difference between the mouth and upstream locations exceeds 180° upstream of Racy Point, so that high and low water occurs simultaneously over the lower 100 km of river.

3.3 DISCHARGE

Sources of discharge to the St. Johns River come from tributaries, springs, diffuse groundwater, direct precipitation, and flows from both industrial and domestic wastewater treatment plants. These sources are either observed or estimated for specification of model boundary conditions. Discharge is also observed at various points along the St. Johns River main stem and these data are used for model calibration and confirmation.

St. Johns River Discharge

Continuous daily discharge was observed at 10 locations along or very near the St. Johns River main stem (Figure 3–3). All these stations are maintained by USGS and published as daily averaged values. The published values are processed and quality-assured by USGS.

All stations, with the exception of Tick Island, span the model simulation period (1996 to 2005). St. Johns River near Christmas lies outside of the study area but is included for subsequent discussion. Three stations (Dunns Creek, Tick Island, and Christmas) do not measure St. Johns River main stem discharge, but are internal to the model. Tick Island is included here because it was established for the WSIS to assess the bifurcation of river flow through Lake Woodruff. Lake Jesup outlet measures flow between the lake and St. Johns River main stem. Dunns Creek similarly measures flow between Crescent Lake and the river.

Table 3–6 identifies each station shown in Figure 3–3 and provides the USGS station ID, station name, period of record, latitude, longitude, and river kilometer. Two stations, St. Johns River near DeLand and St. Johns River near Christmas, have long periods of record for discharge extending back to 1933 and 1934, respectively.

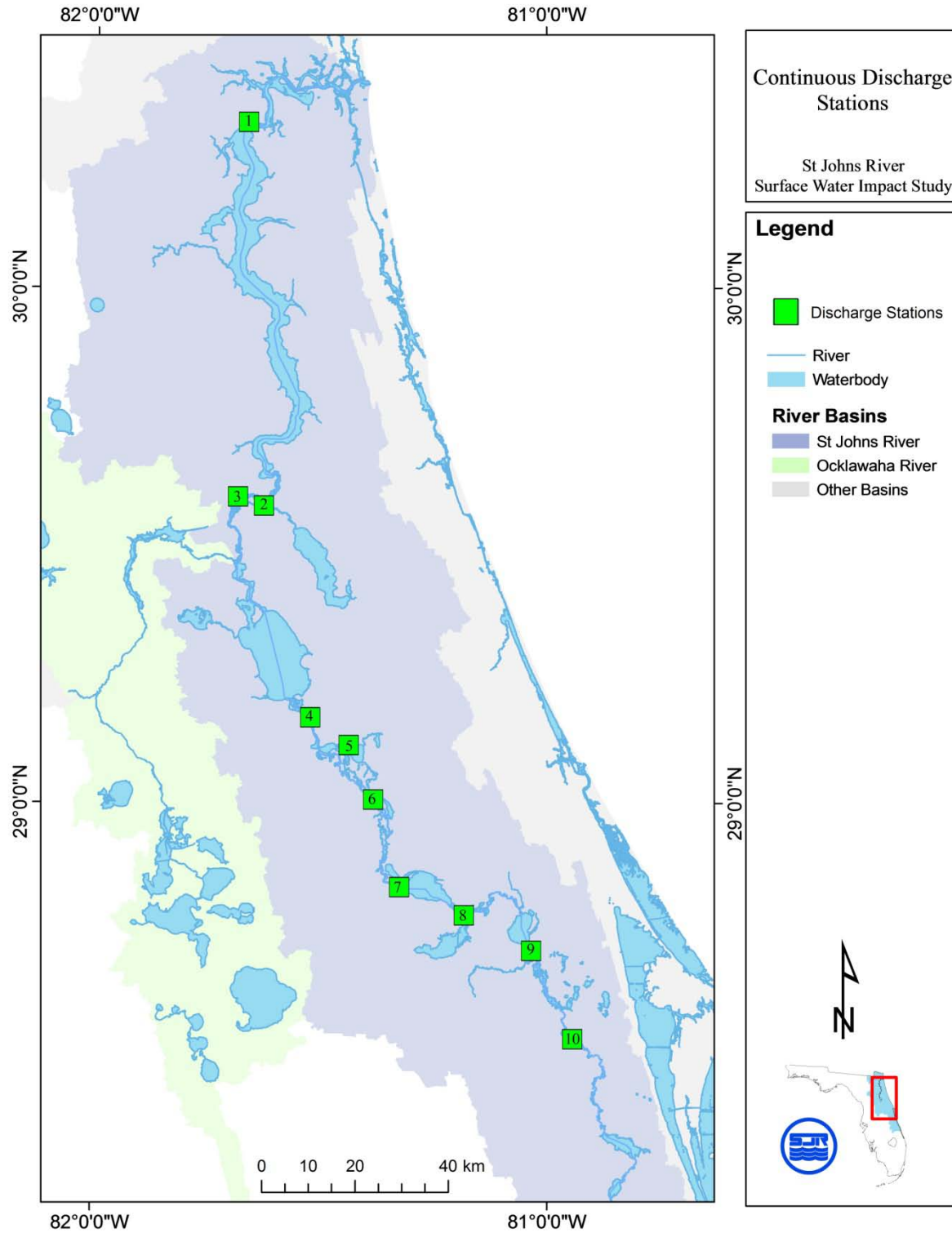


Figure 3–3. Locations of stations with continuously observed discharge. Map numbers are defined in Table 3–6.

Table 3–6. Discharge stations in lower and middle St. Johns River listed in north-to-south order. Map numbers refer to Figure 3–3.

Map #	Station ID	Station Name	Period of Record	Lat	Long	River km
1	02246500	St. Johns River at Jacksonville	1996–Present	30 19.3	81 39.9	38.0
2*	02244440	Dunns Creek	1993–Present	29 34.7	81 37.6	139.2
3	02244040	St. Johns River at Buffalo Bluff near Satsuma	1992–Present	29 35.6	81 40.9	145.3
4	02236125	St. Johns River at Astor	1994–Present	29 10.0	81 31.3	204.4
5**†	02236122	Tick Island Creek near Astor	2007–Present	29 6.8	81 26.2	217.2
6	02236000	St. Johns River near DeLand	1934–Present	29 0.5	81 23.0	231.4
7	02234500	St. Johns River near Sanford	1987–Present	28 50.3	81 19.5	262.0
8*	02234435	Lake Jesup outlet	1993–Present	28 47.0	81 10.9	279.7
9	02234000	St. Johns River above Lake Harney	1981–Present	28 42.8	81 2.1	310.1
10	02232500	St. Johns River near Christmas	1933–Present	28 32.6	80 56.6	343.2

* These stations do not measure St. Johns River mainstem discharge.

† Tick Island period of record is 9/21/2007 to 9/30/2009.

Descriptive statistics for the St. Johns River mainstem discharge stations are shown in Table 3–7. The calculated statistics, with the exception of Tick Island, used the same period of record (1996 to 2005) to make comparison of statistics between stations free of meteorological variability. *NRECS* is the number of records for each time series and differs because of incomplete data records. Mean *Q* is the mean discharge. The remaining columns describe the distribution of discharge; the percentile values indicate the percentage of observations less than the given level of discharge. The final column is the percentage of days for which discharge was negative, that is, the percentage of time of reverse flow events.

Mean discharge for the St. Johns River mainstem stations ranges from 920 to 5512 mgd (40.3 to 241.5 m³s⁻¹). The increase in mean discharge over the model domain, between Lake Harney and Jacksonville, is 4184 mgd (183.3 m³s⁻¹). Seventy-seven percent of this increase occurs within the lower St. Johns River and Lake George, downstream of Astor.

Maximum daily discharge increases dramatically in the downstream direction, for example, from 8397 mgd (367.9 m³s⁻¹) at DeLand to 77,512 mgd (3396.0 m³s⁻¹) at Jacksonville. The large peak daily discharge at Jacksonville is not primarily caused by stormwater runoff, however, but rather is a result of the draining and filling of the estuary caused by meteorological tides.

Meteorological tide also causes reverse flows throughout the lower and middle St. Johns River, from the mouth to at least the outlet of Lake Jesup at river km 262. Reverse flow is defined as a net upstream daily averaged discharge. The percentage of days of reverse flow along the St. Johns River main stem is greatest at Jacksonville (25% of days), the farthest downstream station. Along the St. Johns River main stem this statistic decreases to 13.1% at Buffalo Bluff and ranges from 5.5 to 10.5% between Astor and Sanford. The frequency of occurrence of reverse flows into the three side-channel lakes (Dunns Creek, Tick Island, and Lake Jesup outlet) is as large as the frequency of reverse flow at Jacksonville. Reverse flow days are infrequent at the most upstream locations, Lake Harney and Christmas. Reverse flow conditions at these locations is likely caused by local wind forcing during periods of extreme low discharge rather than meteorological tides.

Reverse flow events in the St. Johns River main stem cause the 7Q10 discharge (7-day, 10-yr low flow) statistic to be negative downstream of Lake Harney. Kroening (2004) reported 7Q10 values of 7.1 mgd ($0.20 \text{ m}^3 \text{ s}^{-1}$) at Christmas, 42.7 mgd ($1.2 \text{ m}^3 \text{ s}^{-1}$) at Lake Harney, -917.7 mgd ($-26.0 \text{ m}^3 \text{ s}^{-1}$) at Sanford (#7), and -769.7 mgd ($-33.7 \text{ m}^3 \text{ s}^{-1}$) at DeLand.

Table 3–7. Descriptive statistics for selected St. Johns River discharge locations, 1996 to 2005. Map numbers refer to Figure 3–3.

Map #	River Km	NRECS	Mean	Min	10%	25%	50%	75%	90%	Max	% < 0.0
1	38.0	3,193	241.5	-1958.4	-251.5	0.5	248.5	475.4	713.2	3396.0	25.0
2*	139.2	3,653	17.4	-236.0	-26.2	-5.8	15.0	37.4	64.2	300.0	30.3
3	145.3	3,653	146.1	-631.1	-24.1	58.0	137.0	236.6	333.9	744.3	13.1
4	204.4	3,475	100.6	-174.9	13.5	44.1	82.4	147.7	219.9	413.2	6.6
5*†	217.2	741	16.6	-78.4	-3.7	0.9	6.7	21.0	56.3	130.7	21.5
6	231.4	3,653	90.6	-92.3	13.1	35.4	73.0	131.3	202.3	367.9	5.5
7	262.0	3,653	72.2	-61.1	-1.2	20.2	51.8	109.0	178.9	322.6	10.5
8 ^b	279.7	3,491	3.8	-83.2	-6.3	-0.5	4.6	9.2	13.1	30.6	26.6
9	310.1	3,653	58.2	-2.2	5.3	14.1	35.4	85.5	142.9	410.4	0.7
10	343.2	3,653	40.3	-3.9	2.5	7.9	23.7	55.8	110.9	213.7	1.8

* These stations do not measure St. Johns River mainstem discharge.

† Tick Island period of record is 9/21/2007 to 9/30/2009.

NRECS = number of records

All discharge values have units of $\text{m}^3 \text{ s}^{-1}$.

Tributary Discharge

Observed tributary discharge is used for model boundary conditions. A considerable fraction of the basin was gauged during the model simulation period (Table 3–8). Discharge from ungauged areas was obtained from hydrologic modeling (see Chapter 3. Watershed Hydrology). Because the upstream discharge boundary condition is coincident with a USGS gauge upstream of Lake Harney (see Table 3–6), the entire 4504 km² of the upper St. Johns River Basin and Econlockhatchee watershed are gauged from the perspective of the EFDC hydrodynamic model. The gauged area within the study area ranged from 11,078 to 12,164 km² over the model simulation period, which is 57% to 63% of the total basin area.

Tributaries that contain no upstream springs or anthropogenic sources typically cease to flow during drought periods and have a minimum discharge of zero. Despite large upstream spring flow, minimum discharge exiting the Ocklawaha River also drops to zero because its outlet is dam controlled. The positive minimum discharge for Etonia Creek is due to the addition of discharge from wastewater treatment plants. Wekiva River and Blackwater Creek have upstream springs. The negative minimum discharge for Deep Creek and Cedar River are reverse flow events caused by meteorological tide.

Table 3–8. Gauged tributaries in the study area over the model simulation period (1995 to 2006).

Tributary	USGS ID	Area (km ²)	Discharge (m ³ s ⁻¹)			Period of Record
			Min	Mean	Max	
Upper St. Johns River	02234000	4,504	-2.2	58.7	410.4	1995–2006
Ocklawaha River	02243960	4,119	0.0	37.1	264.0	1995–2006
Wekiva River	02235000	490	3.9	8.9	39.9	1995–2006
N Black Creek	02246000	458	0.08	5.2	283.0	1995–1997, 2000–2006
Etonia Creek	02245050	376*	0.40	2.0	50.4	1996–2004
S Black Creek	02245500	347	0.23	4.0	192.4	1995–2006
Blackwater Creek	02235200	326	0.06	2.0	22.9	1995–2006
Little Haw Creek	02244420	272	0.0	2.3	51.1	1995–2002
Middle Haw Creek	02244320	203	0.0	2.0	96.0	1996–2002
Deep Creek	02245260	158	-1.8	1.8	70.2	1995–2006
Howell Creek	02234344	135	0.08	2.0	24.8	1999–2006
Sixmile Creek	02245315	123	0.0	1.0	18.1	2002–2006
Simms Creek	02245140	123	0.13	1.5	63.7	1995–2004
Ortega River	02246318	118	0.0	1.6	30.8	2002–2006
Rice Creek	02244473	112	0.06	1.2	49.8	1995–2004
Little Black Creek	02246030	81	0.0	1.8	28.3	2002–2006
Cedar River	02246459	59	-26.8	1.4	45.6	1995–2006
Soldier Creek	02234384	57	0.0	0.4	7.6	1995–2006
Moccasin Branch	02245280	37	0.0	0.8	19.8	2002–2006
Gee Creek	02234400	33	0.0	0.5	9.0	1995–2006
Big Davis Creek	02246150	35	0.0	0.3	13.4	1995–2006

* Area is reduced for Period of Record to reflect noncontributing area (see Chapter 3. Watershed Hydrology).

Tidal Discharge

Tidal discharges are available from two types of observations: (a) continuous observation at 15-minute intervals from Acoustic Velocity Meters (AVM), and (b) manual measurements made over a single tidal cycle using a boat-towed Acoustic Doppler Current Profiler (ADCP).

Continuous tidal discharge, at 15-minute intervals, were obtained from three USGS stations (Main Street Bridge, Buffalo Bluff, and Dunns Creek) and resampled to hourly values (see Table 3–7). The raw data, on 15-minute intervals, are not quality-assured by USGS. Harmonic constants for tidal discharge were derived from the resampled hourly values (Table 3–9). Tidal discharge throughout the lower St. Johns River is dominated by the M_2 tidal constituent.

Table 3–9. Harmonic constants for discharge at continuous USGS gauging sites in the lower St. Johns River for the six largest tidal constituents. Tidal constituents are defined in Table 3–5.

Station	M_2		N_2		S_2		O_1		K_1		M_4	
	A	P	A	P	A	P	A	P	A	P	A	P
Main Street Bridge	4,118	114	742	97	454	132	337	320	453	330	207	5
Buffalo Bluff	273	287	48	270	32	321	30	61	37	76	15	350
Dunns Creek	111	284	19	264	12	311	10	59	12	77	10	4

Note:

A = Amplitude in $m^3 s^{-1}$

P = phase in degrees.

Comparison of Table 3–7 with Table 3–9 shows that the M_2 amplitude for discharge is 2 to 40 times larger than the mean river discharge at these locations. Except during periods of exceptionally high river discharge, tidal discharge dominates hourly variability of discharge, and hourly discharge reverses twice per day.

Discharges observed over a single tidal cycle are available at many locations within the lower St. Johns River (Figure 3–4, Figure 3–5, and Figure 3–6). These measurements were made using a boat-towed Acoustic Doppler Current Profiler (ADCP). For reference, the three continuous monitoring sites are also shown in these figures. ADCP measurements were made by USGS during 1995 to 1997 and by SJRWMD during 2002 to 2006 (Table 3–10).

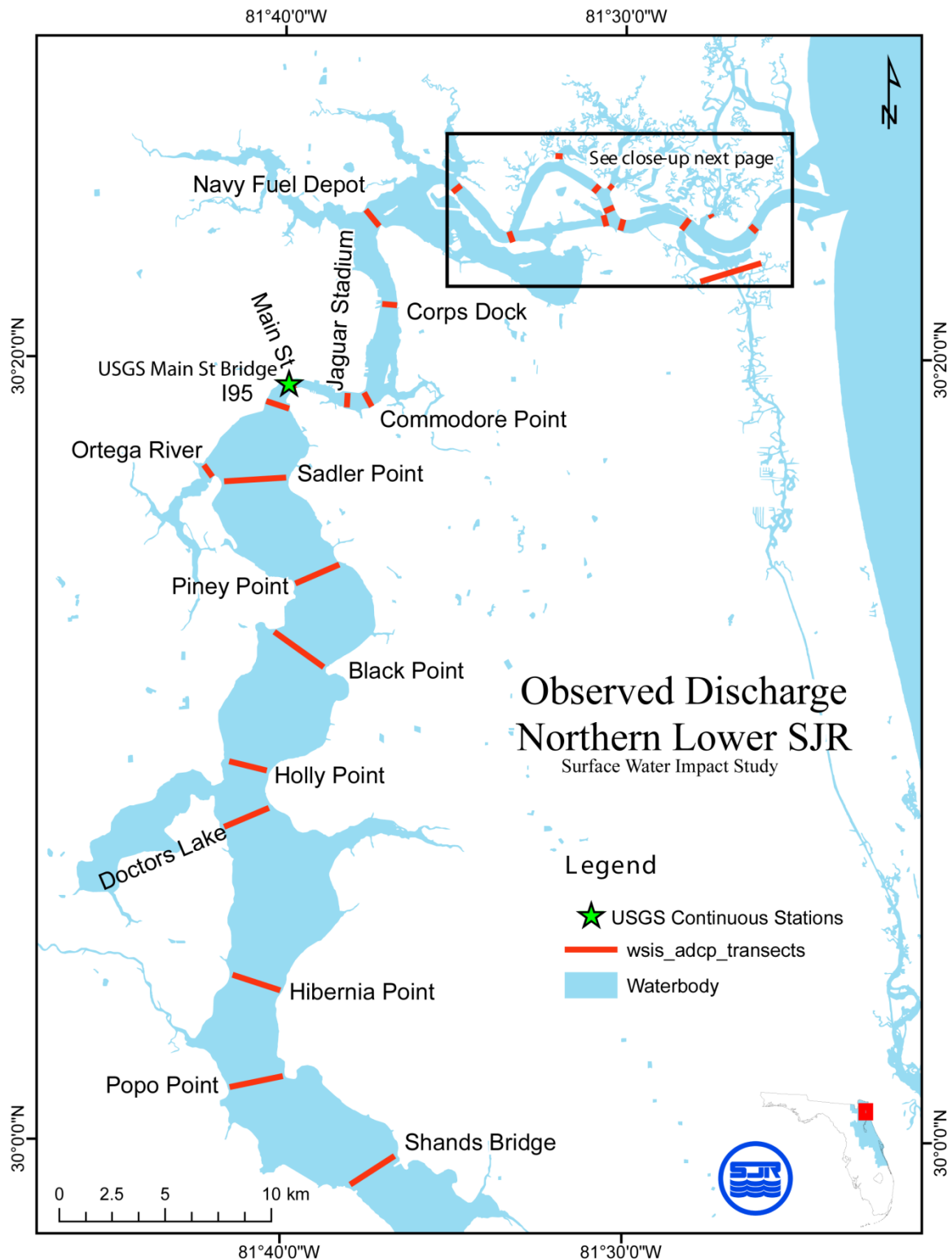


Figure 3-4. Map showing locations of observed tidal discharge for the northern end of the lower St. Johns River. ADCP = Acoustic Doppler Current Profiler, SJR = St. Johns River.

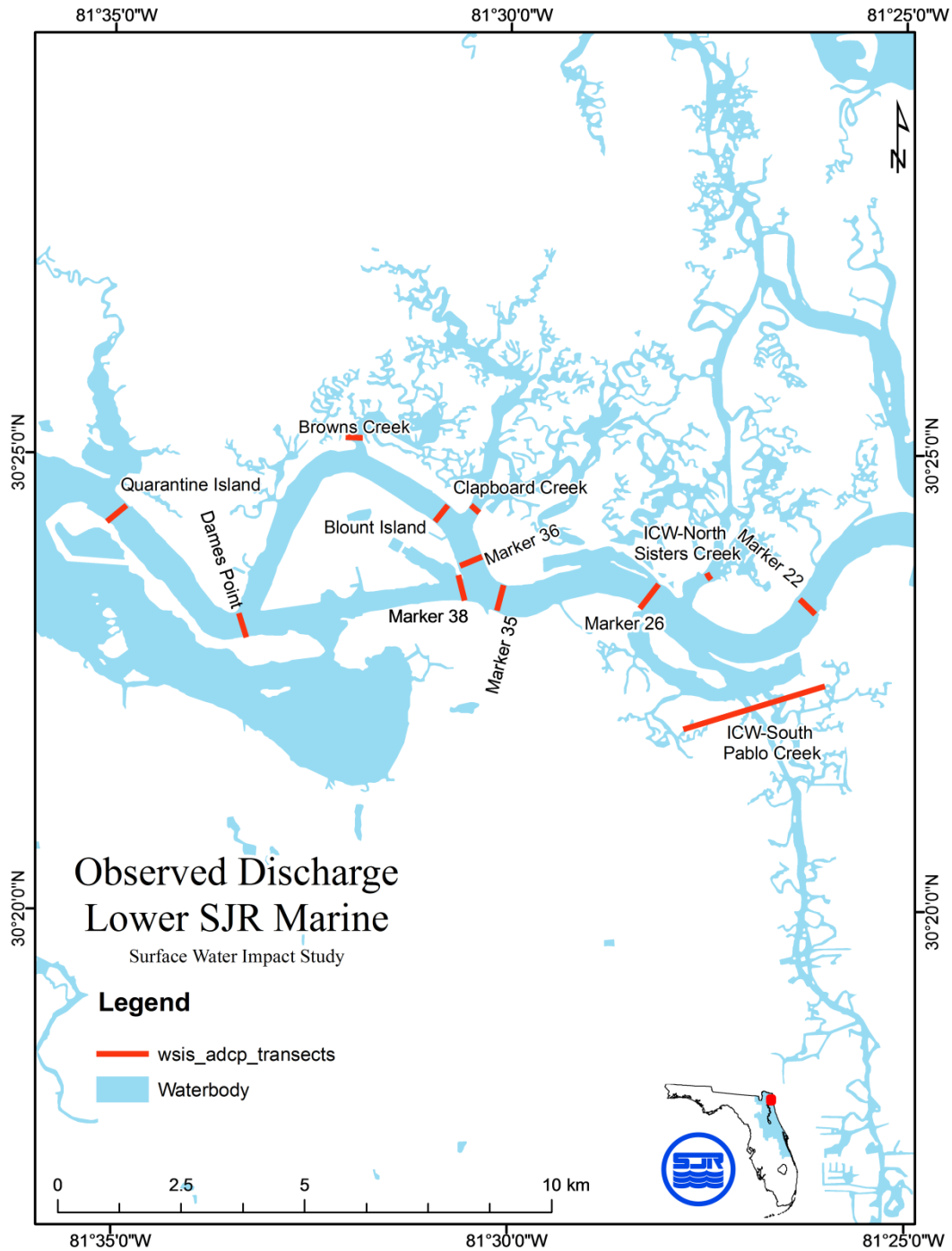


Figure 3–5. Map showing locations of observed tidal discharge for the marine portion of the lower St. Johns River. ICW = Intracoastal Waterway, SJR = St. Johns River.

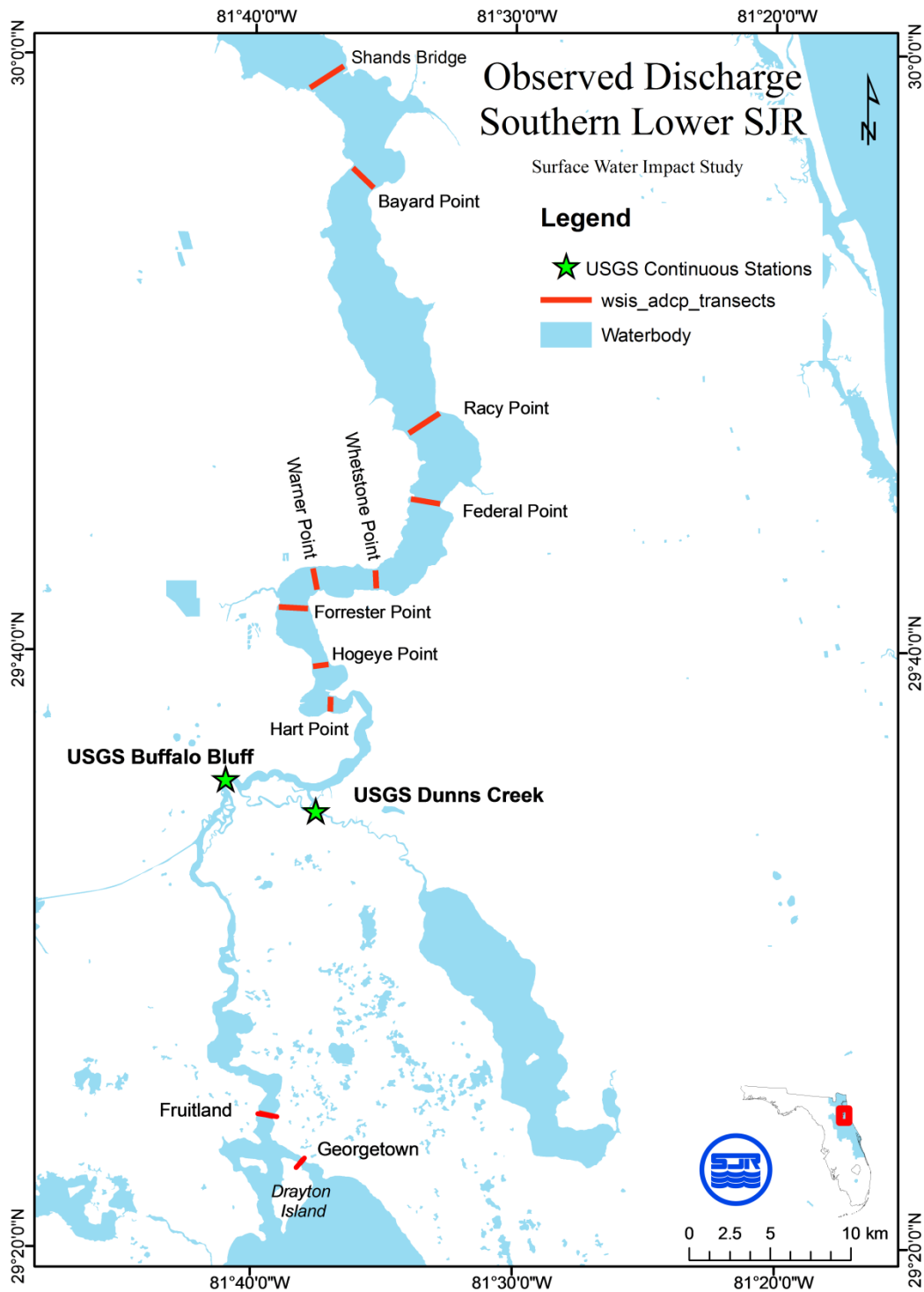


Figure 3–6. Map showing locations of observed tidal discharge for the southern portion of the lower St. Johns River. SJR = St. Johns River, ADCP = Acoustic Doppler Current Profiler.

Table 3–10. Acoustic Doppler Current Profiler (ADCP) tidal discharge monitoring sites.

Agency	Station Name	Collection Dates
USGS	Marker 22	8/23/1995, 8/6/1996, 9/22/1997
USGS	Marker 26	9/22/1997
USGS	Marker 35	8/23/1995, 9/22/1997
USGS	Marker 36	8/7/1996
SJRWMD	Sisters Creek	5/2/2006
SJRWMD	Pablo Creek	10/14/2004
SJRWMD	Browns Creek	5/2/2006
USGS	Clapboard Creek	9/17/1996
SJRWMD	Clapboard Creek	5/2/2006
USGS	Marker 38	8/7/1996
USGS	Blount I	9/17/1996
USGS	Dames Point	8/23/1995, 8/7/1996, 9/17/1996, 9/22/1997
USGS	Quarantine I	9/22/1997
USGS	Navy Fuel Dock	9/23/1997
USGS	Corp Dock	9/17/1996, 9/23/1997
USGS	Commodore Point	8/16/1995, 8/17/1995
USGS	Jaguar Stadium	9/23/1997
USGS	Main Street Bridge	8/16/1995, 8/17/1995, 7/31/1996, 9/18/1996
USGS	I-95 Bridge	8/16/1995, 8/17/1995
USGS	Ortega River	8/18/1995
USGS	Sadler Point	9/23/1997
USGS	Piney Point	9/24/1997
USGS	Black Point	9/24/1997
USGS	Holly Point	9/24/1997
USGS	Near Doctors Inlet	9/18/1996, 9/24/1997

Agency	Station Name	Collection Dates
USGS	Hibernia Point	9/24/1997
USGS	Popo Point	9/25/1997
USGS	Shands Bridge	9/25/1997
USGS	Bayard Point	9/18/1996, 9/25/1997
USGS	Racy Point	9/25/1997
USGS	Federal Point	9/25/1997
USGS	Whetstone Point	9/26/1997
USGS	Warner Point	9/26/1997
USGS	Forrester Point	9/26/1997
USGS	Hog Eye Point	9/26/1997
USGS	Hart Point	9/26/1997
SJRWMD	Fruitland	5/29/2002
SJRWMD	Georgetown	5/29/2002

3.4 SALINITY IN THE ST. JOHNS RIVER MAIN STEM

3.4.1 THE PRACTICAL SALINITY SCALE 1978

The Practical Salinity Scale 1978 (PSS78) was established to provide a practical means of measuring salinity by conductivity that is reproducible, conservative, and provides accurate computation of density differences (Lewis and Perkin, *Salinity: Its definition and calculation* 1978). PSS78 defines salinity as a unitless number based on a conductivity ratio between the conductivity of a water sample and conductivity of a standard solution. This definition of salinity differs from the common limnological definition as the sum concentration of all the ionic constituents (Wetzel 2001), which is expressed as mg L^{-1} . The limnological definition of salinity, though precise, is decidedly impractical because of the immense burden required to obtain observations by direct laboratory analysis. The PSS78 definition of salinity also differs from previous oceanographic definitions that related salinity to chlorinity. Chlorinity is the sum of halogens dissolved in seawater (expressed as g kg^{-1}), can be readily measured by titration or conductivity, and is linearly related to salinity. However, the use of chlorinity to define salinity is less accurate for determining density than salinity defined by PSS78 when the chemical composition of the salts differs from that of seawater. PSS78 salinity has an additional advantage of uniformity compared with chlorinity-defined salinity in that “all waters of the same conductivity have the same salinity” (Lewis, *The practical salinity scale and its antecedents* 1980). Although unitless, PSS78 salinity values are functionally equivalent to both the limnological expression of salinity as mg L^{-1} for the practical application of salinity to biological analysis, and the oceanographic expression of salinity as g kg^{-1} or ppt when the composition of salts is the same as that of seawater.

PSS78 provides the following advantages for hydrodynamic modeling of the system:

- Ease of field measurement by means of conductivity sensors—Nearly all the salinity values used for model development were obtained by conductivity measurement and converted to salinity as PSS78 following Standard Methods (APHA 1995). The simplicity of this observational technique means conductivity measurements are available throughout the study area as both synoptic grab samples and continuous monitoring at fixed locations.
- Accurate calculation of density differences within the hydrodynamic model—The advantage of conductivity-derived (PSS78) salinity over chlorinity-derived salinity for calculating density differences for waters with variable salt composition was explained by Lewis (1980) who noted that “changes in the ionic content ... are thus corrected for in conductivity-derived densities, at least in part, whereas an exchange of some ions in seawater materially affecting the density could leave the chlorinity unchanged.” Lewis further concluded that “differences of [conductivity-derived] density were ... not affected by the densities themselves being not quite accurate.” This last conclusion is quite important to the present modeling study because dynamic effects are governed by density differences.
- Use as a conservative tracer when major salt constituents are themselves conservative—Salinity derived from conductivity is a better conservative tracer than chloride in waters where salt composition changes due to mixing of waters of varying salt composition. Chloride would be a useful tracer if it could be measured directly because the chloride

ion is conservative. Direct chloride measurements are sparse in the St. Johns River, however. Indirect measurements of chloride can be made from conductivity, but chloride derived from conductivity is less accurate than salinity because salinity derived from conductivity compensates for shifting salt composition when waters are mixed. The use of salinity as a conservative tracer requires that the major salt constituents themselves be conservative, however. They cannot be appreciably lost or gained by chemical or biological reaction. Most major salt constituents are conservative, but HCO_3 (bicarbonate) and CO_3 (carbonate), (i.e., alkalinity), are not conservative.

In summary, salinity is properly a unitless value because its measurement is based on a conductivity ratio. PSS78 salinity provides accurate calculation of density differences for simulation of dynamic effects within the hydrodynamic model application regardless of shifting salt composition when waters dominated by ocean salts are mixed with waters dominated by terrestrial salts. PSS78 salinity can be used as a conservative tracer even with shifting salt composition as long as the ions predominately contributing to the salinity are themselves conservative. In this case, salinity is superior to chlorinity because of the greater accuracy in measuring salinity compared with chlorinity by means of conductivity. The caveat that the major ions accounting for salinity are themselves conservative is addressed in Section 4.4.2 by examination of the salt composition of the St. Johns River main stem over varying flow conditions.

3.4.2 OBSERVED SALINITY

Observed salinity is available from both continuous and synoptic stations. Eight continuous stations are maintained by USGS and record hourly salinity. There are 29 synoptic stations observed at (usually) monthly intervals as part of SJRWMDs Water Quality Monitoring Network (WQMN). The synoptic stations have high spatial resolution, while the continuous stations provide high temporal resolution. Together these two networks capture salinity variability of the lower and middle St. Johns River over ecologically relevant time scales.

Salinity gauges cover both the lower (Figure 3–7) and middle (Figure 3–8) St. Johns River. The synoptic stations were selected from a larger set of stations based on record length and location. Metadata (Table 3–11) and descriptive statistics (

Table 3–12) for each station are provided below.

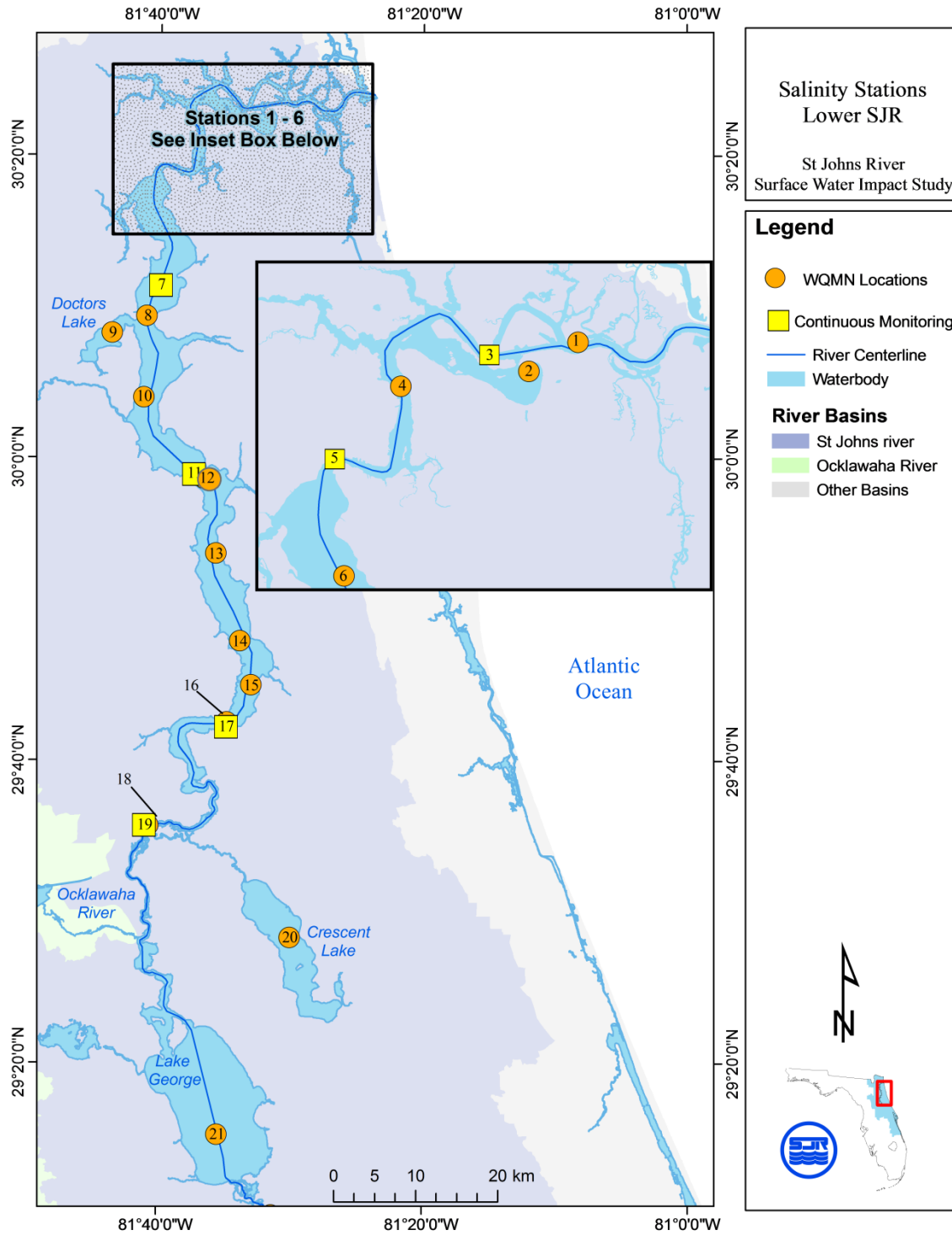


Figure 3–7. Locations of observed salinity stations (#1 to 21) in the lower St. Johns River. Orange circles denote Water Quality Monitoring Network (WQMN) locations and yellow squares denote locations of continuous monitoring. SJR = St. Johns River.

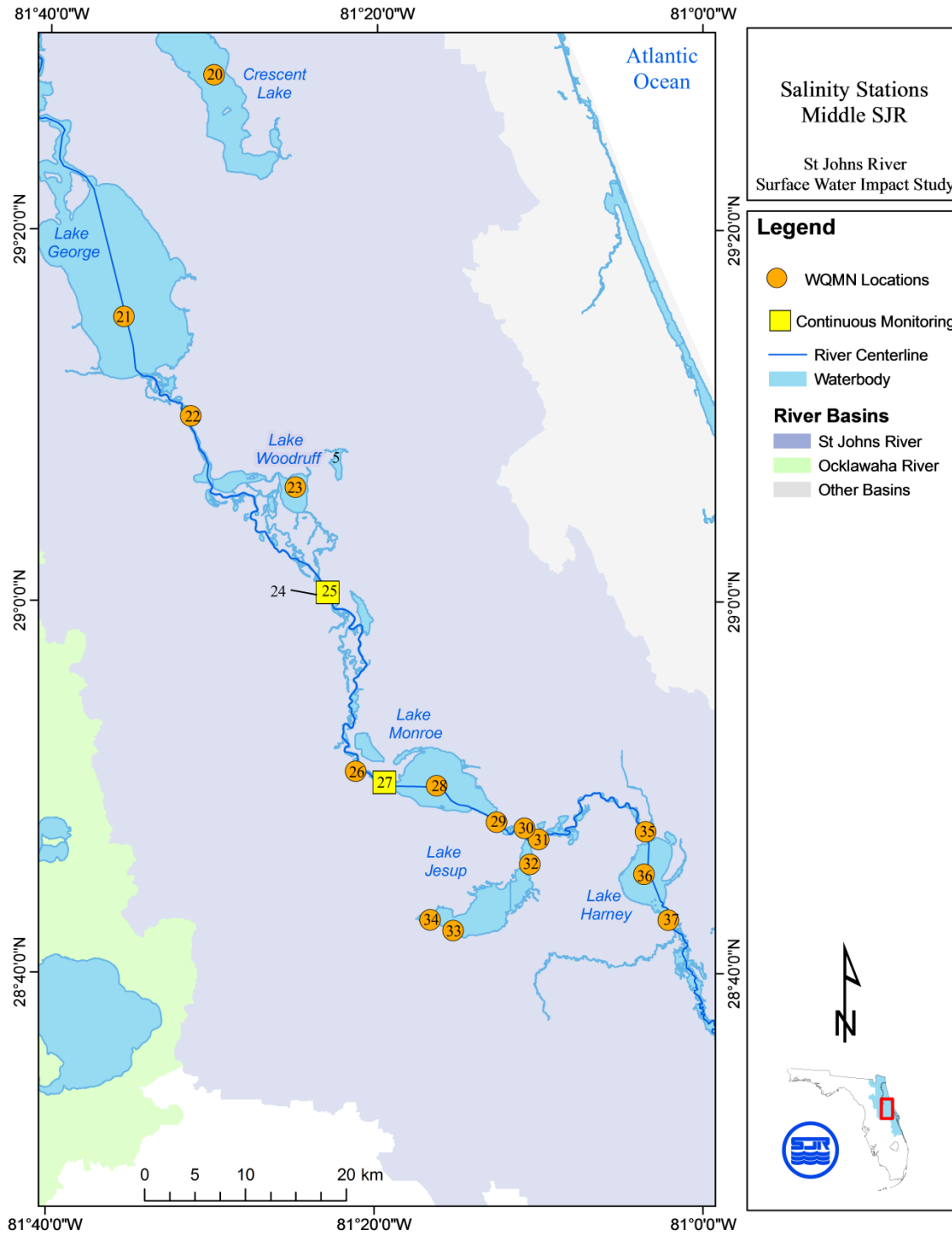


Figure 3–8. Locations of observed salinity stations (22 to 37) in the middle St. Johns River. Orange circles denote Water Quality Monitoring Network (WQMN) locations and yellow squares denote locations of continuous monitoring. SJR = St. Johns River.

Table 3–11. St. Johns River salinity stations arranged in downstream to upstream order. Map numbers refer to Figure 3–7 and Figure 3–8.

Map #	Station ID	Agency	Period of Record	Lat	Long	River km
1	JAXSJR04	SJRWMD	1998–2007	30 23.6	81 29.8	11.1
2	SAVMILCO	SJRWMD	1998–2002	30 23.6	81 31.8	17.2
3	Dames Point	USGS	1995–2006	30 23.2	81 33.5	17.3
4	JAXSJR17	SJRWMD	1998–2007	30 22.0	81 37.1	29.0
5	Acosta Bridge	USGS	1995–2003	30 19.2	81 39.5	38.1
6	JAXSJR40	SJRWMD	1997–2007	30 15.1	81 39.1	47.0
7	Buckman Bridge	USGS	1995–2003	30 11.5	81 41.4	55.0
8	MP72	SJRWMD	1993–2007	30 9.4	81 41.0	58.2
9	DTL	SJRWMD	1984–2007	30 8.3	81 39.1	63.1
10	SJRHBP	SJRWMD	1991–2007	30 4.0	81 41.2	68.9
11	Shands Bridge	USGS	1995–2001	29 59.0	81 38.0	79.3
12	SJSR16	SJRWMD	1991–2007	29 58.6	81 36.6	81.7
13	SJWSIL	SJRWMD	1997–2007	29 53.7	81 35.7	91.7
14	SRP	SJRWMD	1986–2007	29 47.9	81 33.9	101.6
15	SJM37	SJRWMD	1993–2007	29 45.0	81 33.0	108.8
16	FP42	SJRWMD	1993–2007	29 42.6	81 34.8	114.7
17	Dancy Point	USGS	1998–2005	29 42.6	81 34.8	115.0
18	BB22	SJRWMD	1993–2007	29 35.6	81 40.9	145.3
19	Buffalo Bluff	USGS	1995–2002	29 35.6	81 40.9	145.3
20	GF33	SJRWMD	1978–2007	29 28.3	81 30.0	160.0
21	LAG	SJRWMD	1989–2007	29 15.3	81 35.5	190.7
22	20010002	SJRWMD	1996–2007	29 10.6	81 31.4	204.4
23	LKWOOD	SJRWMD	1992–2006	29 3.7	81 14.7	223.1
24	2236000	SJRWMD	1996–2006	29 0.5	81 23.0	231.4

Map #	Station ID	Agency	Period of Record	Lat	Long	River km
25	02236000	USGS	2000–2002	29 0.5	81 23.0	231.4
26	SJR-DPP	SJRWMD	2003–2007	28 50.9	81 21.3	258.6
27	02234500	USGS	2000–2002	28 50.3	81 19.5	262.0
28	LMAC	SJRWMD	1995–2007	28 50.1	81 16.3	267.2
29	SJR-415	SJRWMD	2003–2007	28 48.2	81 12.6	274.5
30	OW-SJR-2	SJRWMD	1996–2003	28 47.8	81 10.9	278.4
31	OW-SJR-1	SJRWMD	1996–2007	28 47.2	81 10.0	281.3
32	OW-2	SJRWMD	1995–2007	28 45.9	81 10.6	282.1
33	OW-4	SJRWMD	1995–2007	28 42.3	81 15.2	292.8
34	OW-6	SJRWMD	1995–2007	28 42.9	81 16.7	295.6
35	SJR-OLH	SJRWMD	2003–2007	28 47.6	81 3.6	299.6
36	CLH	SJRWMD	2002–2007	28 45.4	81 3.6	300.6
37	SRN	SJRWMD	1995–2007	28 42.8	81 2.1	310.1

Table 3–12. Descriptive statistics for St. Johns River salinity stations. Map numbers refer to Figure 3–7 and Figure 3–8.

Map #	River km	Station ID	<i>NRECS</i>	<i>Mean</i>	<i>STDEV</i>	5%	<i>1Q</i>	<i>Median</i>	<i>2Q</i>	95%
1	11.1	JAXSJR04	1,110	25.0	7.9	9.4	20.3	27.0	31.3	34.4
2	17.2	SAVMILCO	101	16.6	8.4	2.9	9.3	16.7	22.8	29.8
3	17.3	Dames Point	173,765	22.8	6.8	10.1	18.6	23.7	27.9	32.3
4	29.0	JAXSJR17	1,085	13.8	8.5	1.0	6.4	13.8	20.2	28.3
5	38.1	Acosta Bridge	190,765	6.9	6.3	0.29	1.6	5.2	10.8	19.3
6	47.0	JAXSJR40	661	5.5	5.7	0.26	0.61	3.3	8.5	16.2
7	55.0	Buckman Bridge	170,075	3.0	3.8	0.27	0.40	1.0	4.4	11.1
8	58.2	MP72	588	3.1	3.9	0.24	0.32	0.64	4.8	10.9
9	63.1	DTL	686	2.8	3.0	0.27	0.51	1.3	4.7	8.9
10	68.9	SJRHBP	727	2.0	2.7	0.21	0.30	0.44	2.8	8.1
11	79.3	Shands Bridge	144,758	0.84	1.2	0.27	0.38	0.44	0.60	4.1
12	81.7	SJSR16	454	1.0	1.5	0.26	0.33	0.42	0.66	4.6
13	91.7	SJWSIL	355	0.67	0.72	0.26	0.35	0.44	0.63	2.2
14	101.6	SRP	614	0.51	0.31	0.27	0.35	0.46	0.60	0.75
15	108.8	SJM37	351	0.48	0.18	0.27	0.35	0.45	0.59	0.71
16	114.7	FP42	213	0.48	0.13	0.27	0.38	0.47	0.57	0.71
17	115.0	Dancy Point	115,557	0.47	0.13	0.27	0.37	0.44	0.58	0.70
18	145.3	BB22	558	0.49	0.15	0.28	0.36	0.47	0.63	0.75
19	145.3	Buffalo Bluff	57,420	0.49	0.13	0.28	0.39	0.48	0.59	0.72
20	160.0	GF33	203	0.25	0.13	0.10	0.14	0.22	0.36	0.48
21	190.7	LAG	158	0.53	0.18	0.26	0.36	0.55	0.68	0.84
22	204.4	20010002	255	0.50	0.21	0.23	0.34	0.50	0.63	0.76
23	223.1	LKWOOD	127	0.42	0.15	0.20	0.30	0.42	0.55	0.69

Map #	River km	Station ID	NRECS	Mean	STDEV	5%	1Q	Median	2Q	95%
24	231.4	2236000	131	0.47	0.18	0.20	0.32	0.47	0.63	0.75
25	231.4	02236000	621	0.58	0.64	0.22	0.42	0.64	0.73	0.86
26	258.6	SJR-DPP	63	0.49	0.23	0.18	0.28	0.49	0.63	0.91
27	262.0	02234500	829	0.65	0.70	0.22	0.40	0.70	0.83	1.12
28	267.2	LMAC	112	0.52	0.25	0.20	0.30	0.47	0.73	0.93
29	274.5	SJR-415	67	0.58	0.32	0.19	0.30	0.52	0.82	1.13
30	278.4	OW-SJR-2	348	0.54	0.27	0.20	0.34	0.49	0.73	1.08
31	281.3	OW-SJR-1	282	0.58	0.32	0.19	0.34	0.53	0.80	1.18
32	282.1	OW-2	240	0.50	0.24	0.25	0.31	0.41	0.60	0.98
33	292.8	OW-4	280	0.39	0.17	0.19	0.25	0.36	0.49	0.77
34	295.6	OW-6	280	0.34	0.16	0.15	0.21	0.31	0.38	0.53
35	299.6	SJR-OLH	63	0.60	0.32	0.17	0.32	0.52	0.84	1.17
36	300.6	CLH	73	0.60	0.32	0.17	0.32	0.51	0.84	1.14
37	310.1	SRN	168	0.53	0.35	0.11	0.23	0.43	0.83	1.11

NRECS = Number of records

1Q = first quartile of distribution (25th percentile)

2Q = second quartile of distribution (75th percentile)

3.4.3 UPSTREAM EXTENT OF OCEAN SALINITY

The farthest observed upstream extent of ocean salinity over the period 1986 to 2007 was to river km 108.8 during May 2007. Salinity for stations between river km 81 (Shands Bridge and SJSR16) and river km 145.3 (BB22 and Buffalo Bluff) show the high salinity event of May 2007 (Figure 3–9). The salinity event is clearly an intrusion of seawater at both SJSR16 (river km 81.7) and SRP (river km 101.6) because salinity at these locations rises above 2. During this same period the background upstream salinity level at BB22 (river km 145.3) was unaffected by the intrusion. Salinity for a few observations at SJM37 (river km 108.8), however, are above the upstream background level and correlated with the intrusion event. By inference, these observations likely resulted from the intrusion event and place the farthest upstream extent of ocean salinity to river km 108.8.

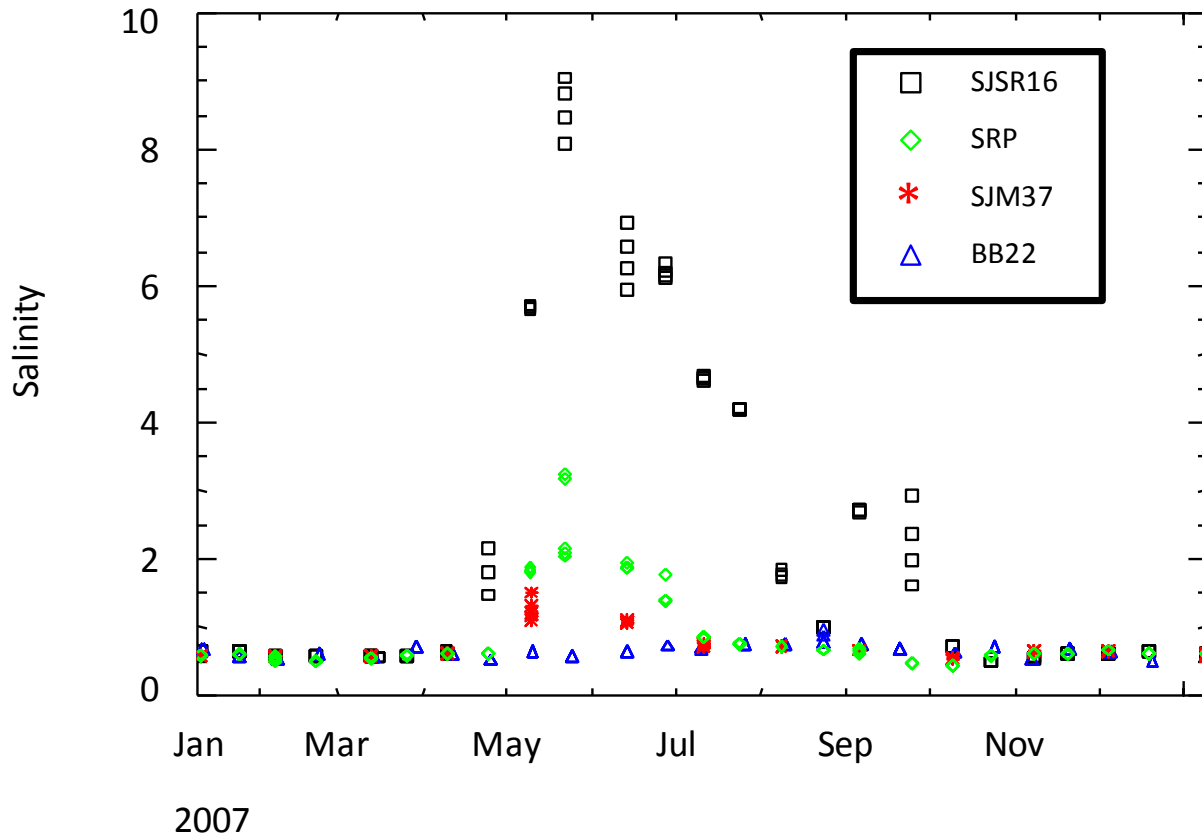


Figure 3–9. Comparison of salinity between Shands Bridge and Buffalo Bluff during the greatest observed upstream extent of salinity in May 2007. SJSR16, SRP, SJM37, and BB22 are salinity stations.

3.4.4 SEASONAL VARIATION OF SALINITY

On average, salinity in the St. Johns River is highest in summer and lowest in winter (Table 3–13). Seasonal variation of salinity is characterized by calculating mean values for all observations at a station falling within a given month irrespective of year. The station indicated as “MSJR” is a composite of data taken from stations 2236000, LMAC, and OW-SJR-1. These three stations are all upstream of the confluence of the St. Johns River with the Wekiva River and together represent salinity conditions in the uppermost reach of the study area. Aggregating data from these stations was required to have a sufficient number of records within a selected month to produce a meaningful mean value.

Table 3–13. Monthly averaged salinity for all months available within station record. The middle St. Johns River (MSJR) is calculated from pooled observations using stations 2236000, LMAC, and OW-SJR-1.

Station	Jan	Feb	Mar	Apr	May	Jun	Jul	Aug	Sep	Oct	Nov	Dec
Dames Surface	21.1	21.5	21.0	20.9	24.4	25.1	22.2	22.8	21.6	19.5	19.4	19.9
Acosta Surface	4.6	6.1	6.9	8.2	11.6	10.8	7.8	8.0	6.6	4.8	3.8	4.0
Buckman Surface	0.9	1.2	2.0	3.3	4.6	5.7	8.3	2.7	2.2	1.6	0.9	1.3
Shands Surface	0.4	0.4	0.5	0.5	1.2	1.6	1.2	0.9	1.1	0.6	0.4	0.4
Dancy Point	0.4	0.4	0.4	0.5	0.5	0.5	0.5	0.5	0.5	0.4	0.4	0.4
Buffalo Bluff	0.4	0.4	0.5	0.5	0.5	0.6	0.6	0.6	0.6	0.5	0.5	0.4
MSJR	0.4	0.5	0.6	0.7	0.7	0.8	0.6	0.5	0.4	0.3	0.4	0.5

3.5 SPRINGS

Probably the most charismatic expression of the connection between ground and surface waters within SJRWMD is spring discharge (Ferguson 1947). Springs are primarily found in the middle St. Johns River downstream of Lake Monroe and along the west shore of Lake George (Figure 3–10). The largest spring within SJRWMD is Silver Springs that flows to the St. Johns River through the Ocklawaha River.

There is substantial variation in the quantity, type, and time scale of data available for each spring. Details regarding estimation of time-varying discharge and salinity for model boundary conditions are presented in Section 0. Mean discharge of springs varies over four orders of magnitude and conductivity (a measure of salinity) varies over two orders of magnitude (Figure 3–11).

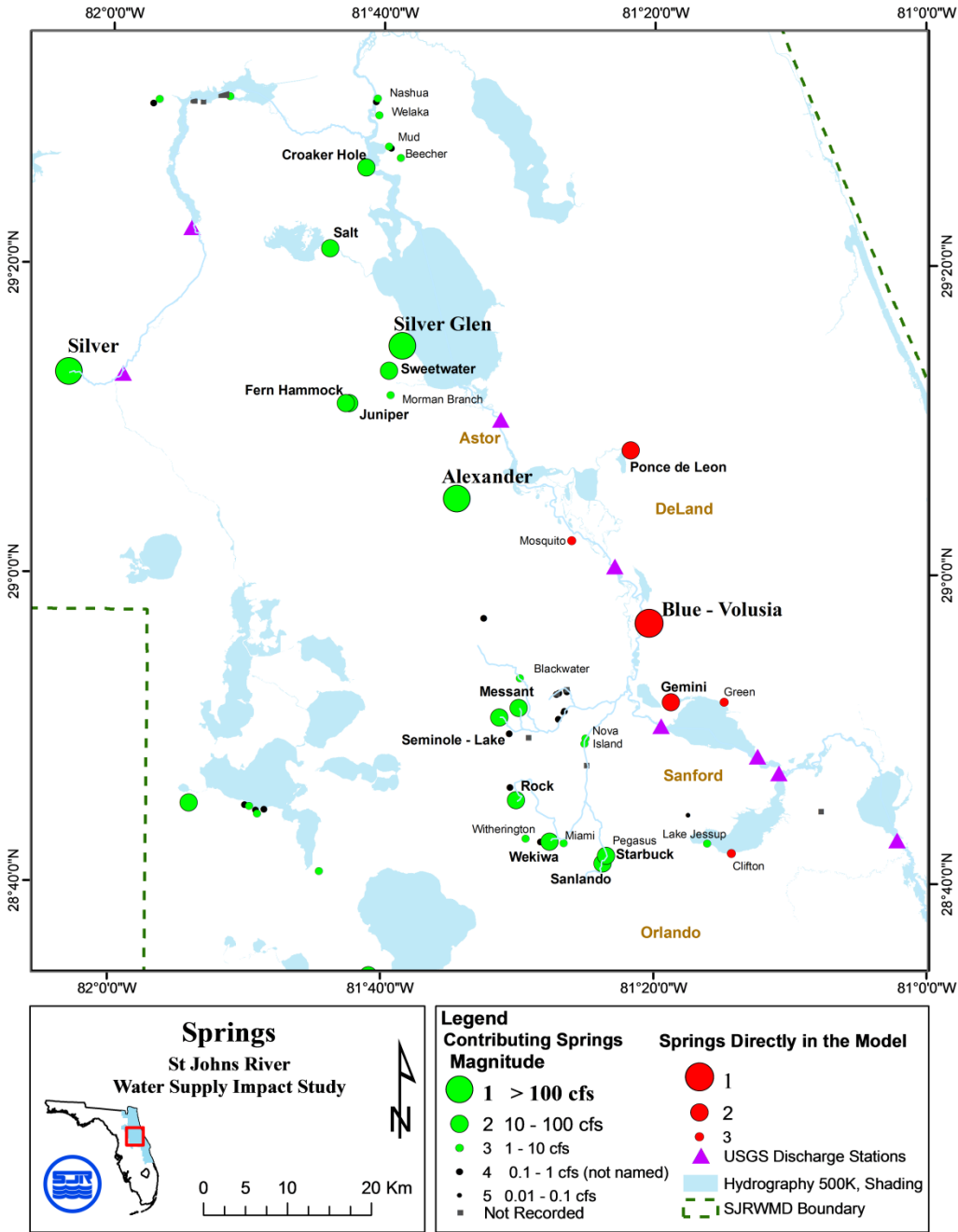


Figure 3–10. Location and magnitude of St. Johns River Water Management District springs with measured discharge.

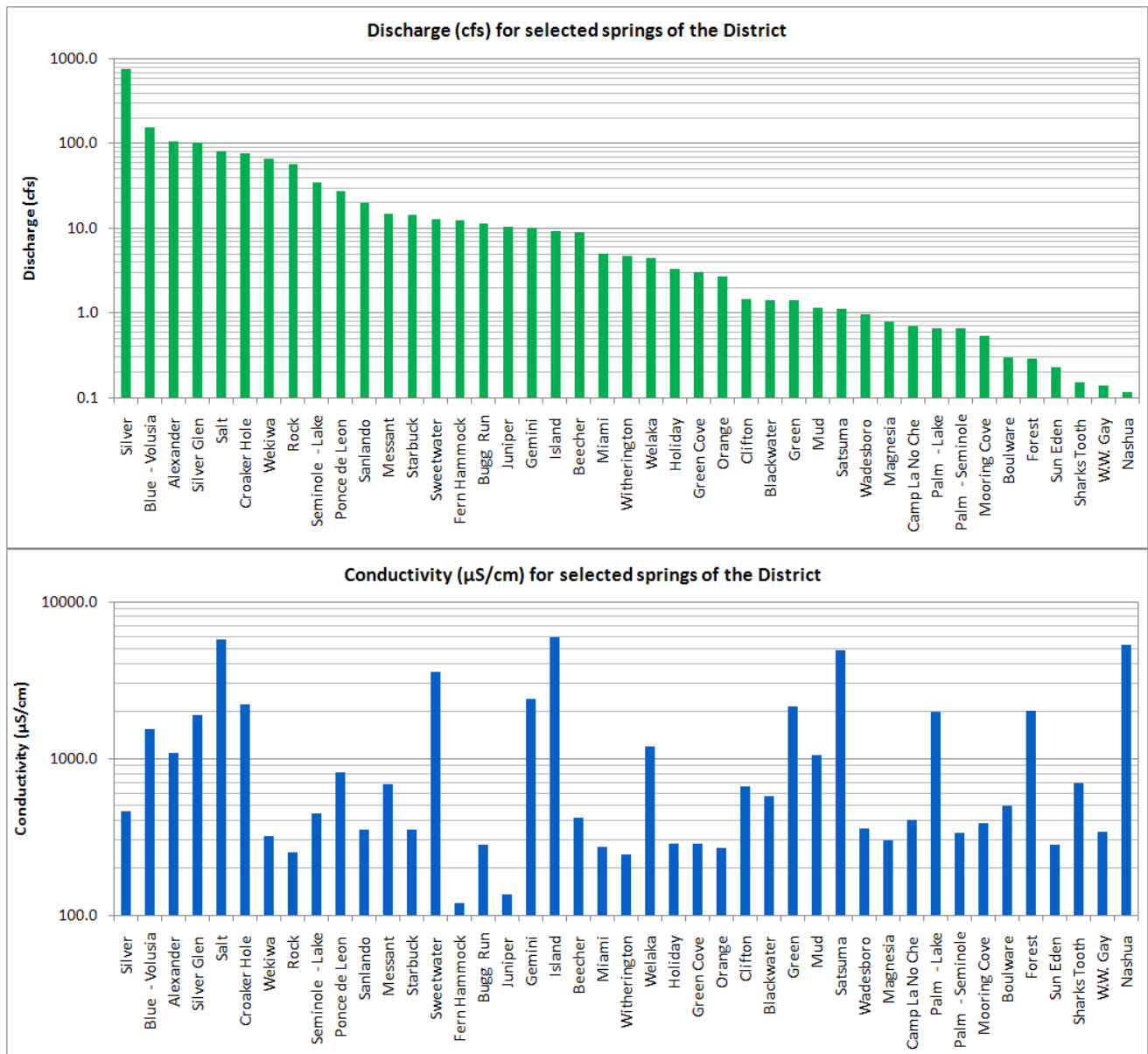


Figure 3–11. Mean discharge and conductivity of selected SJRWMD springs sorted by discharge.

The mass loading rate of salts from a spring to the river is determined by the product of discharge and salinity. Silver Springs has the greatest discharge among all springs but a relatively low salinity (conductivity). The total mass contribution of salts from Silver Springs is relatively small, then, although it is the largest single point source of bicarbonate alkalinity (HCO₃) to the St. Johns River. Salt Springs is the largest single point source of salt load to the St. Johns River. The salt load from Salt Springs is greater than the combined salt load of all surface runoff downstream of that point.

3.6 WASTEWATER TREATMENT PLANTS

In 1995, 36 wastewater treatment plants with average flow exceeding 0.1 mgd discharged directly to the St. Johns River (Figure 3-12). All these wastewater treatment plants discharged to the lower St. Johns River. The total average discharge for all 36 plants was 136.5 mgd.

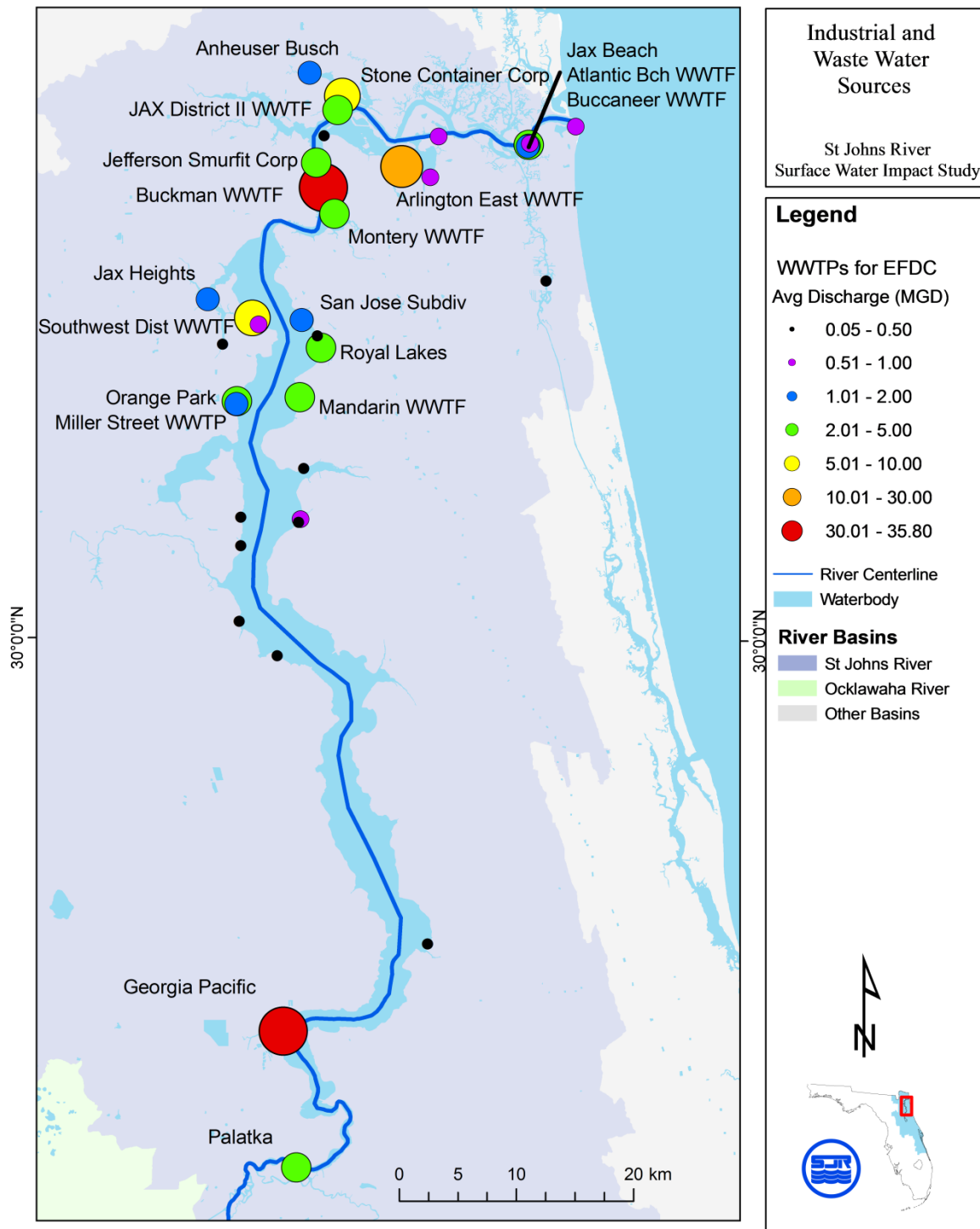


Figure 3–12. Locations and sizes of wastewater treatment plants discharging directly to the St. Johns River main stem during the year 1995. WWTP = wastewater treatment plant, WWTF = wastewater treatment facility.

3.7 RAINFALL

Daily averaged rainfall was available at seven stations near the St. Johns River main stem (Figure 3–13). These seven stations are a subset of the stations used to input rainfall for the hydrologic modeling (Chapter 3. Watershed Hydrology). All rain gauge stations are maintained by the National Weather Service. Metadata for the stations are shown in Table 3–14.

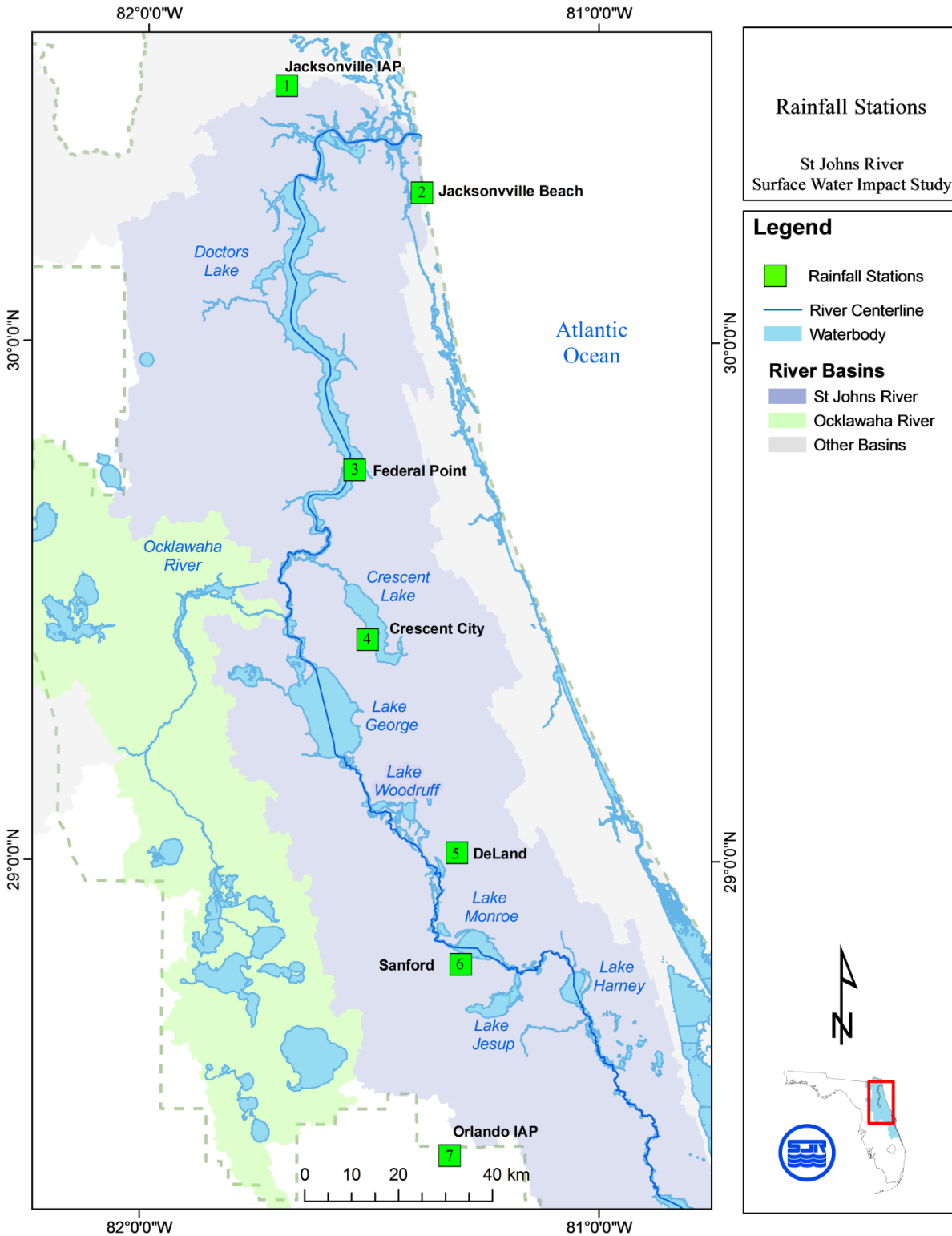


Figure 3–13. Locations of rain gauge stations near the St. Johns River.

Table 3–14. Rain gauge stations near the St. Johns River listed in north-to-south order. Map numbers refer to Figure 3–13.

Map #	Station ID	Station Name	Period of Record	Lat	Long
1	4538	Jacksonville International Airport	1948–Present	30 29.7	81 41.6
2	4366	Jacksonville Beach	1948–Present	30 17.3	81 23.6
3	2915	Federal Point	1931–Present	29 45.3	81 32.3
4	1978	Crescent City	1931–Present	29 25.0	81 30.8
5	2229	DeLand	1931–Present	29 01.1	81 18.6
6	7982	Sanford	1956–Present	28 48.9	81 16.7
7	6628	Orlando International Airport	1974–Present	28 26.0	81 19.5

Mean Annual Rainfall

Mean annual rainfall over 1975 to 2006 ranged from 948 to 1628 mm, with the lowest rainfall occurring in 2000 and the highest rainfall in 1994 (Figure 3–14). Mean annual rainfall anomalies referenced to the 30-yr period show how rainfall over the model simulation period compares with average rainfall conditions (Table 3–15). The anomalies indicate that an extended dry period occurred during the model simulation period from 1998 through 2000.

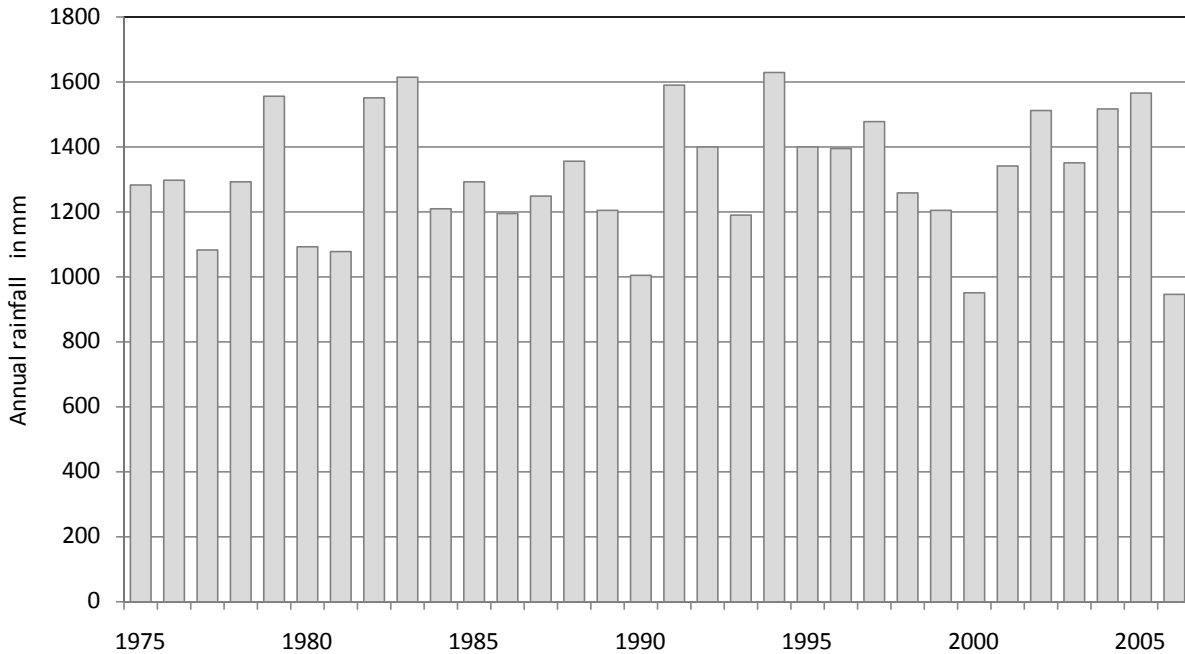


Figure 3–14. Annual rainfall averaged over all stations, 1975 to 2006.

Table 3–15. Mean annual rainfall anomalies (mm) referenced to base period 1975 to 2006. Negative values indicate that mean annual rainfall is lower than the average value.

Station Name	1995	1996	1997	1998	1999	2000	2001	2002	2003	2004	2005
Crescent City	-66	-28	284	30	-164	-134	115	41	203	10	280
DeLand	-214	1	157	-242	-39	-373	499	144	-121	457	296
Federal Point	-78	-323	-191	-284	-85	-267	90	-53	-121	73	308
Jax IAP	-53	215	125	111	-255	-319	-81	60	-200	435	308
Jax Beach	809	-150	220	-226	-412	-130	-160	43	-215	-186	144
Orlando IAP	-135	211	410	-117	164	-456	167	458	110	277	309
Sanford	203	292	71	-63	-108	-469	36	379	90	366	238
Overall	34	252	241	-90	28	-463	102	419	100	322	274

Seasonal Variation of Rainfall

Rainfall over the study area has a distinct seasonal pattern of wet summers and dry springs and winters (Figure 3–15). The highest monthly rainfall occurs June to September. The low rainfall months are November to May.

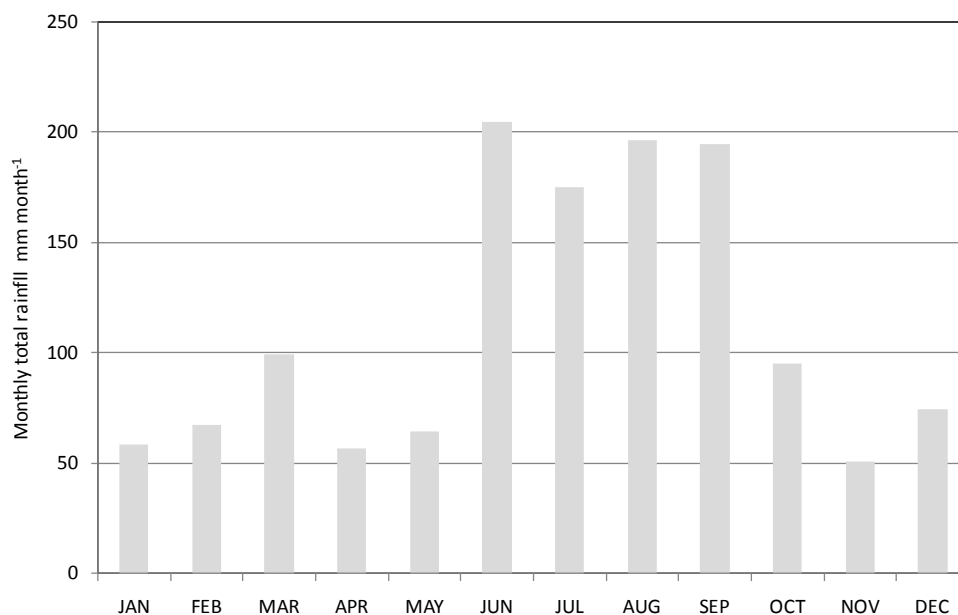


Figure 3–15. Average monthly total rainfall within the EFDC model area (1995 to 2005).

3.8 EVAPORATION

Potential evaporation is estimated using the 1985 Hargreaves Method (Hargreaves and Allen 2003) at the same locations as the rain gauge stations above. Potential evaporation is a direct estimate of actual evaporation over open water and is directly applied to the hydrodynamic model. Potential evaporation is identical to that used for the hydrologic modeling (Chapter 3). The Hargreaves Method requires only observed minimum and maximum air temperature and estimated extraterrestrial (solar) radiation and is the highest ranked temperature-based method for calculating potential evaporation (Jensen, Burman and Allen 1990). Inclusion of wind and relative humidity to the Hargreaves Method provides only minor improvement to evaporation estimates (Allen 1993)—wind and relative humidity explain only 10% and 9% of the variance, respectively (Hargreaves and Allen 2003).

Monthly Potential Evaporation

Monthly averaged estimates of potential evaporation ranged from 2 to 6 mm day⁻¹. Potential evaporation was relatively uniform among stations, although potential evaporation for Jacksonville Beach was lower than for the other stations. Monthly averaged potential evaporation is highest in summer and lowest in winter (Figure 3–16).

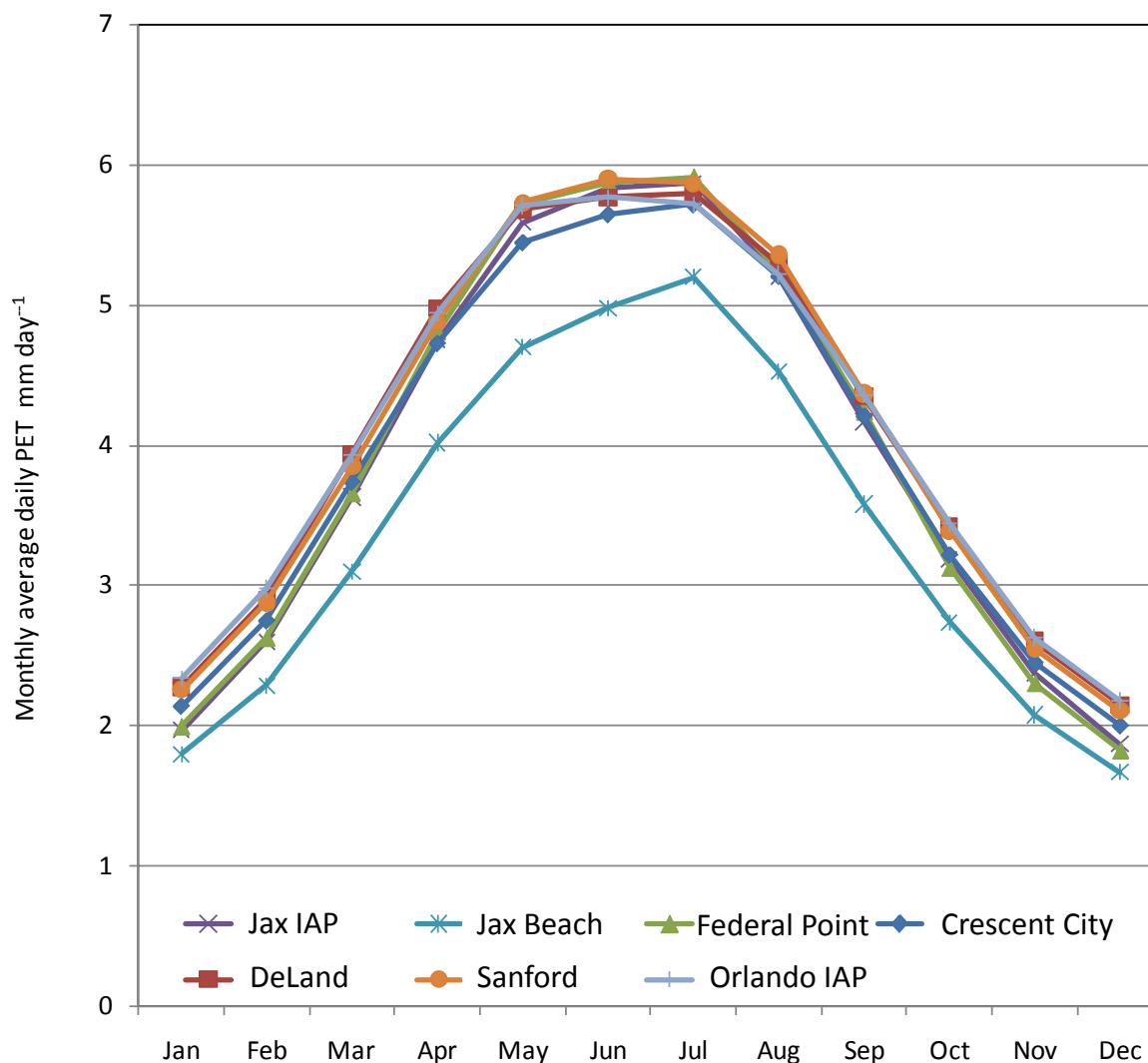


Figure 3–16. Monthly averaged potential evaporation (1975 to 2005) estimated by Hargreaves Method for rain gauge stations near the St. Johns River.

Net Rainfall

Net rainfall is the difference between rainfall and evaporation (potential evaporation). Net rainfall varies seasonally with positive values in early autumn and negative values in late spring (Figure 3–17). The autumn peak occurs because the high summer rainfall rates lag behind but eventually overcome the high summer potential evaporation. Negative values in April and May occur because rainfall rates are minimum and evaporation rates are approaching maximum during these months.

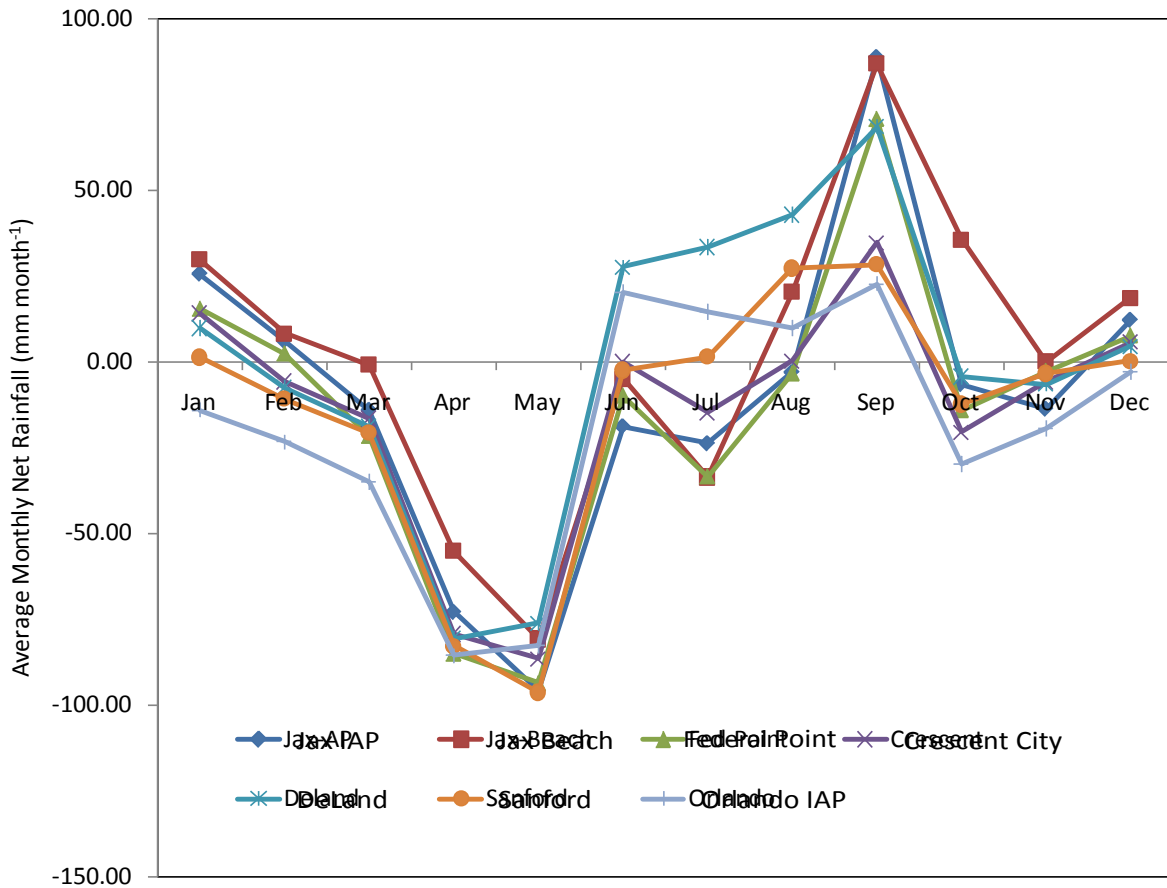


Figure 3–17. Average monthly net rainfall (1975 to 2005) for rain gauge stations near the St. Johns River main stem.

Annual net rainfall (mm) over the model simulation period shows that the 1998 to 2000 period was distinctly dry (Table 3–16). Net rainfall was slightly negative over the 11-yr period (-115 mm yr^{-1}). This net rainfall represents an average rate of water loss from the river of 70 mgd ($3 \text{ m}^3 \text{ s}^{-1}$) given the combined model surface area of $827 \times 10^6 \text{ m}^2$. For the driest year of 2000, the average annual loss rate was 450 mgd ($19.7 \text{ m}^3 \text{ s}^{-1}$).

Table 3–16. Annual net rainfall (mm) for rain gauge stations near the St. Johns River main stem. Negative numbers indicate that annual evaporation exceeded annual rainfall.

Station	1995	1996	1997	1998	1999	2000	2001	2002	2003	2004	2005
Jax IAP	-163	138	71	10	-354	-462	-170	-6	-258	337	257
Jax Beach	933	-50	324	-175	-298	-68	-57	121	-102	-86	278
Federal Point	-187	-423	-296	-423	-387	-414	0	-117	-207	-39	247
Crescent City	-162	-148	173	-110	-267	-281	-5	-55	78	-148	190
DeLand	-144	67	172	-270	-68	-425	489	121	-122	351	281
Sanford	32	105	-129	-318	-377	-707	-151	235	-67	177	121
Orlando IAP	-351	-54	151	-413	-116	-799	-81	216	-118	13	101
Overall Mean	-160	26	11	-366	-246	-753	-116	226	-93	95	111

Note:

Jax = Jacksonville, Florida

IAP = International Airport

3.9 WIND

Wind imparts a direct stress to the surface of the river. Wind stress can drive flows in the direction of the wind, and cause countercurrents in a direction opposite the direction of wind by the mechanism of wind setup of water level. Hourly wind data are available at eight locations near the study area (Figure 3–18). Four stations are located at airports and maintained by the National Oceanic and Atmospheric Administration (NOAA), three stations are located in agricultural areas and maintained by the Florida Automated Weather Network (FAWN) (University of Florida IFAS Extension 2010), and one station is located on a highway bridge spanning the Indian River Lagoon and maintained by the Florida Department of Environmental Protection (FDEP).

All stations provide hourly wind speed and direction. The NOAA stations report wind speeds in 1-knot intervals with a minimum recording threshold of 3 knots, and directions in 10-degree increments. At the time of retrieval, the FAWN stations reported wind speeds in 1-mph increments and directions in 1-degree increments. The FDEP station at Titusville reported wind speed in knots to two decimal places and direction in 1-degree increments. All stations record wind at a standard height of 10 m, except Titusville, which is higher because it is located on top of a bridge span. Metadata for the stations are provided below (Table 3–17).

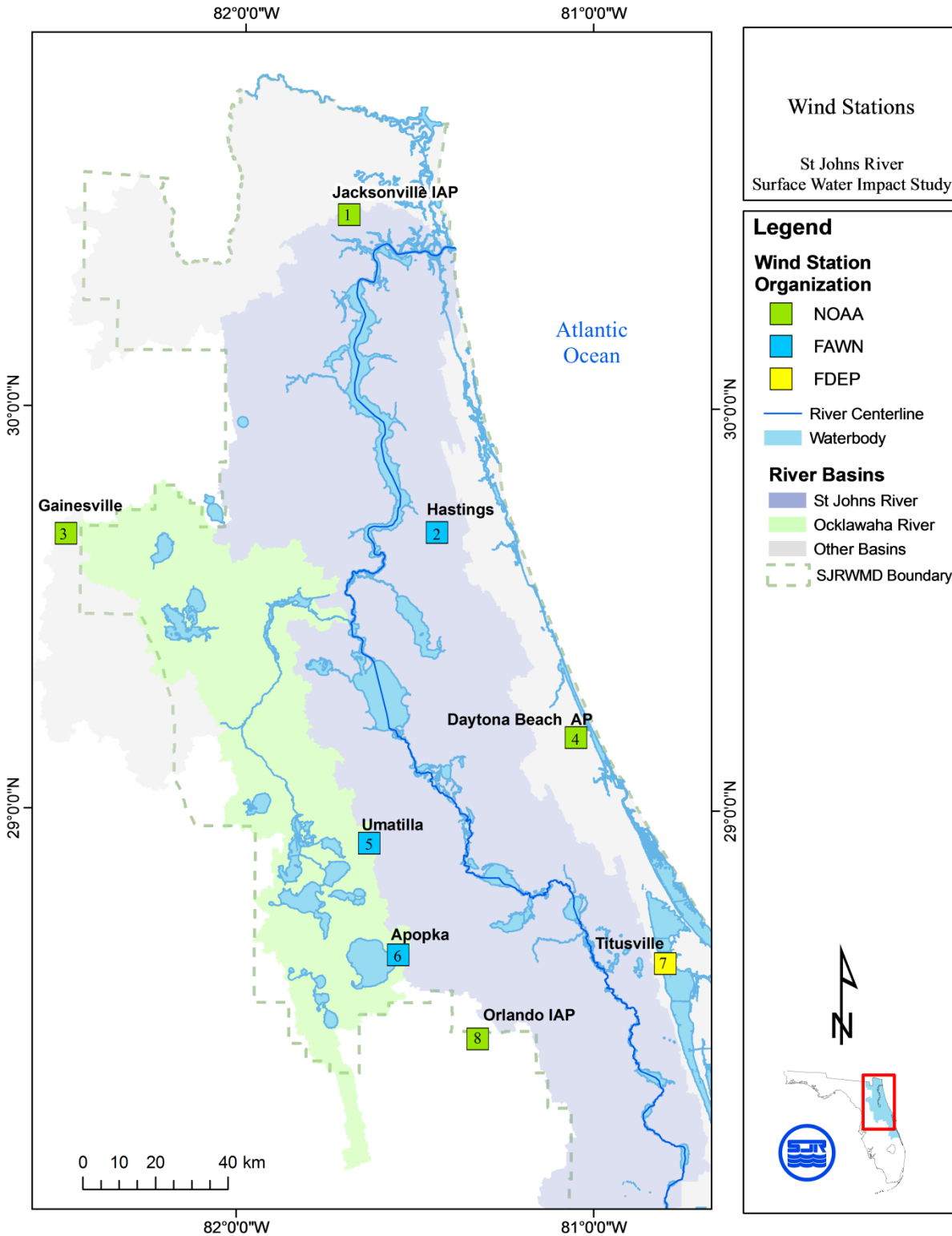


Figure 3–18. Locations of stations with observed hourly wind. IAP = International Airport, AP = airport.

Table 3–17. Wind stations near St. Johns River listed in north-to-south order. Map numbers refer to Figure 3–18.

Map #	Station ID	Station Name	Agency	Period of Record	Lat	Long
1	13884	Jacksonville International Airport	NOAA	1948–Present	30 29.7	81 41.6
2	270	Hastings	FAWN	1999–Present	29 41.6	81 26.7
3	12816	Gainesville Regional Airport	NOAA	1984–Present	29 41.5	82 16.5
4	12834	Daytona Beach International Airport	NOAA	1948–Present	29 11.0	80 2.9
5	302	Umatilla	FAWN	1998–Present	28 55.2	81 37.9
6	320	Apopka	FAWN	1998–Present	28 38.5	81 33.0
7	872-1456	Titusville-Brewer Causeway	FDEP	1996–2007	28 37.4	80 48.0
8	12815	Orlando International Airport	NOAA	1952–Present	28 26.0	81 19.5

The distribution of wind speeds differs among the eight stations. The distribution of wind speeds for the FDEP and NOAA stations are compared using 3-knot intervals (Table 3–18), while the distribution of wind speeds for the FAWN stations are compared using 3-mph intervals (

Table 3–19). The placement of wind speed values into bins was done in the native unit for each station to avoid the need for interpolation. The three southernmost stations—Titusville, Orlando, and Apopka—have a distinctly lower frequency of low wind events compared with the other five stations.

Table 3–18. Percentage of occurrence of wind speed by 3-knot intervals for NOAA stations and the FDEP station. Map numbers refer to Figure 3–18.

Map #	Station Name	0–2 knots	3–5 knots	6–8 knots	9–11 knots	> 11 knots
1	Jacksonville International Airport	30.6	30.3	20.6	11.5	7.0
3	Gainesville Regional Airport	31.5	33.6	20.7	10.1	4.1
4	Daytona Beach International Airport	31.5	27.6	21.2	12.3	7.4
7	Titusville-Brewer Causeway	13.2	33.2	30.8	14.4	8.4
8	Orlando International Airport	19.8	33.6	24.9	13.5	8.2

Table 3–19. Percentage of occurrence of wind speed by 3-mph intervals for FAWN stations. Map numbers refer to Figure 3–18.

Map #	Station Name	0–2 mph	3–5 mph	6–8 mph	9–11 mph	> 11 mph
2	Hastings	29.1	29.1	19.8	12.7	9.3
5	Umatilla	30.7	42.2	18.3	6.7	2.1
6	Apopka	16.7	40.0	25.0	11.7	6.6

Correlation between stations for daily averaged wind speed is strong. Figure 3–19 compares daily averaged wind speed at Hastings and Apopka over a 1-yr period and illustrates the strong correlation ($r^2 = 0.71$) of daily wind speed over a large distance relative to the length scale of the study area (Figure 3–19).

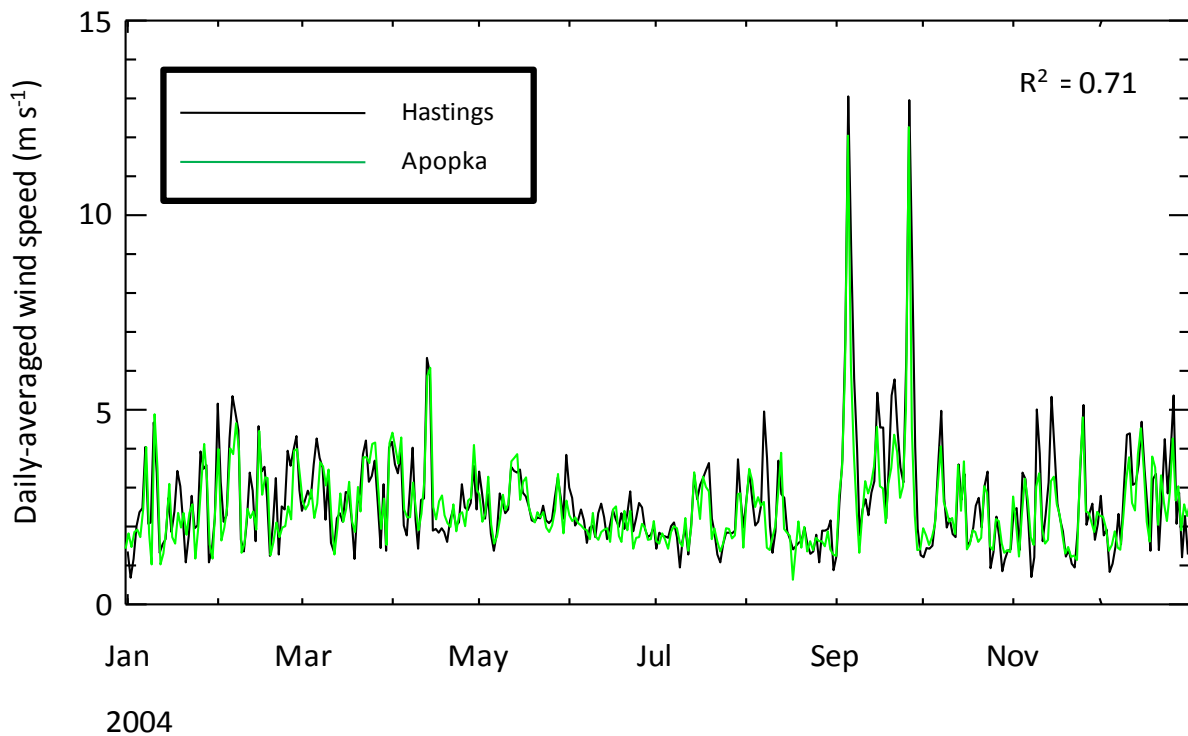


Figure 3–19. Comparison of daily averaged wind speed at Hastings and Apopka for 2004.

In order to examine spatial and temporal patterns of directional flow, time series of hourly wind vectors at each station are resolved into north and east components. Table 3–20 shows monthly averaged speed for the east-west component of wind over the 6-yr period of 2000 to 2005. Positive values indicate a net flow towards the east—or a westerly wind—and a negative value indicates a net easterly flow. Cells with a net westerly wind exceeding 0.1 m s⁻¹ are colored green and cells with a net easterly wind are colored yellow.

Table 3–20 indicates that the dominant east-west flow direction exhibits strong seasonality that shows good agreement between all stations. In general, there is a net flow towards the west (net easterly winds) from April through November and a net flow towards the east from December to March, although easterly winds are weak during April, and the easterly pattern is briefly disrupted in July.

Table 3–21 shows monthly averaged wind speeds for the north-south wind component over the same 6-yr period. Positive values indicate net flow towards the north (southerly winds) and negative values indicate net flow towards the south. These results also show a strong seasonality with generally good agreement between stations. In general there is net flow towards the south (northerly winds) from September through February, and net flow from the north (southerly winds) from March through August. The most notable deviations from the general pattern are the stronger northerly winds at Daytona, and to some extent Titusville, from March to May.

Table 3–20. Monthly averaged wind speed (m s^{-1}) for east-west component of wind, 2000 to 2005. Map numbers refer to Figure 3–18.

Map #	Jan	Feb	Mar	Apr	May	Jun	Jul	Aug	Sep	Oct	Nov	Dec
1	+0.99	+0.18	+0.36	+0.08	-0.20	-0.28	+0.22	-0.34	-1.21	-0.69	-0.08	+0.54
2	+0.83	+0.21	+0.29	-0.10	-0.43	-0.42	-0.07	-0.40	-1.05	-0.53	-0.14	+0.49
3	+0.86	+0.23	+0.51	+0.35	-0.01	-0.15	+0.15	-0.17	-0.92	-0.56	-0.10	+0.39
4	+0.96	+0.34	+0.20	-0.16	-0.82	-0.50	-0.15	-0.53	-1.35	-0.96	-0.17	+0.59
5	+0.31	-0.14	+0.07	-0.17	-0.41	-0.33	-0.03	-0.29	-0.85	-0.72	-0.41	-0.10
6	+0.19	-0.11	+0.28	-0.04	-0.37	-0.43	+0.04	-0.18	-0.73	-0.74	-0.64	-0.04
7	+0.81	+0.12	+0.20	-0.25	-0.60	-0.69	-0.19	-0.58	-1.48	-1.08	-0.56	+0.30
8	+0.56	-0.08	+0.22	-0.32	-0.93	-0.74	-0.27	-0.53	-1.38	-1.17	-0.67	+0.01
Avg	+0.69	+0.10	+0.27	-0.08	-0.47	-0.44	-0.04	-0.38	-1.12	-0.80	-0.35	+0.27

Table 3–21. Monthly averaged wind speed (m s^{-1}) for north-south component of wind, 2000 to 2005. Map numbers refer to Figure 3–18.

Map #	Jan	Feb	Mar	Apr	May	Jun	Jul	Aug	Sep	Oct	Nov	Dec
1	-0.43	-0.56	+0.04	+0.25	+0.34	+0.69	+0.65	+0.22	-0.67	-1.04	-0.45	-0.68
2	-0.20	-0.14	+0.33	+0.36	+0.43	+0.90	+0.76	+0.48	-0.16	-0.55	-0.21	-0.31
3	-0.35	-0.42	+0.17	+0.08	+0.11	+0.40	+0.40	+0.11	-0.79	-1.21	-0.63	-0.64
4	-0.63	-0.87	-0.25	-0.27	-0.32	+0.38	+0.37	-0.06	-1.04	-1.62	-1.01	-0.87
5	-0.16	-0.25	+0.10	+0.13	+0.03	+0.38	+0.37	+0.19	-0.36	-0.77	-0.43	-0.42
6	-0.21	-0.08	+0.34	+0.29	+0.18	+0.66	+0.62	+0.57	+0.04	-0.43	-0.23	-0.25
7	-0.93	-0.63	-0.10	+0.01	+0.10	+0.86	+0.71	+0.32	-0.52	-1.57	-1.12	-1.16
8	-0.45	-0.78	+0.08	+0.12	-0.01	+0.71	+0.83	+0.48	-0.73	-1.47	-0.86	-0.77
Avg	-0.42	-0.47	+0.09	+0.12	+0.11	+0.62	+0.59	+0.29	-0.53	-1.08	-0.62	-0.64

An examination of both Table 3-20 and Table 3-21 and shows four distinct combinations of east-west and north-south flow patterns producing the following counter-clockwise seasonal rotation of net winds: flow from the northwest from December to February, flow from the southwest during March, flow from the southeast from April to August, and flow from the northeast from September to November.

The time variation of general wind flow patterns between stations can be visualized using wind run plots. Wind run is the cumulative distance of travel for a given directional component of wind. Hourly wind run is calculated as the product of the hourly averaged wind speed (m s^{-1}) and the quantity of time in the appropriate units representing 1 hr (3600 s). The wind run plots show the accumulation, or running sum, of daily wind run over a 6-yr period (2001 to 2006). Because wind run is a product of speed and time, it has units of length (meters).

Wind run for the east-west component is plotted in Figure 3–20 for three stations, Hastings, Umatilla, and Orlando, over the 6-yr period of 2000 to 2005. These three stations envelope the range of response for all stations. The plot shows a downward trend at all stations indicating that the long-term average flow across the study area was from the east. The oscillations in the time series reflect the shifting seasonal patterns of east-west flows shown in Table 3–20. The seasonal variability visually shows strong correlation between the three stations; the same degree of correlation, although not shown, holds for all eight stations.

The plot shows that the net easterly flow increases from north to south. This phenomenon holds also for the stations not shown. Plots of east-west wind, run for all stations, showed that Gainesville and Jacksonville are similar to Hastings, Daytona and Apopka are similar to Umatilla, and Titusville is similar to Orlando.

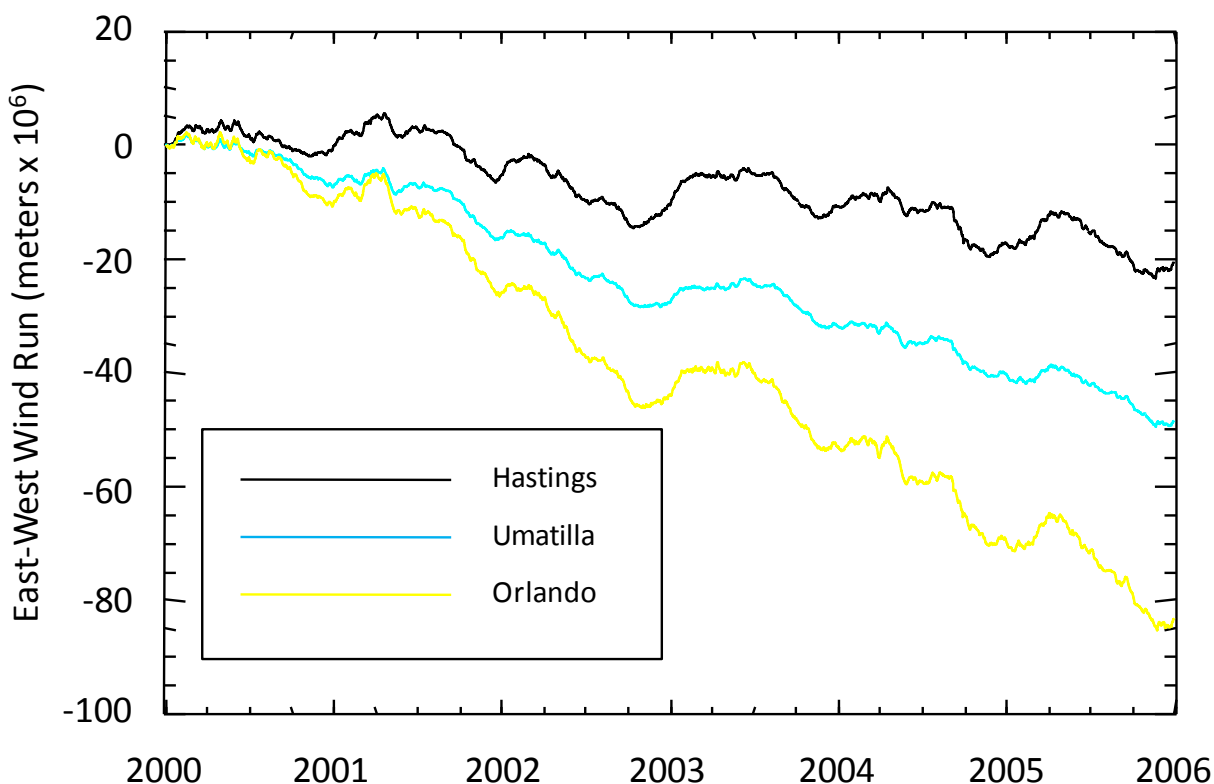


Figure 3–20. Comparison of east-west wind run at Hastings, Umatilla, and Orlando, 2000 to 2005.

Wind run for the north-south component is plotted in Figure 3–21 for the same three stations and period as above. Again, these three stations envelope the range of response for all stations. Hastings had a long-term average flow from the south, while Umatilla and Orlando had long-term average flows from the north.

Although these three stations show net northerly flow increasing from north to south, this trend does not apply to all stations. Plots of north-south wind run for all stations showed that Apopka is the only other station besides Hastings to exhibit a long-term average flow from the south. Stations similar to Umatilla, with moderate northerly flow, included two northern stations, Jacksonville and Gainesville, and a southerly station, Titusville. Daytona is similar to Orlando. Net north-south flow, then, varies between stations but has no discernible spatial pattern.

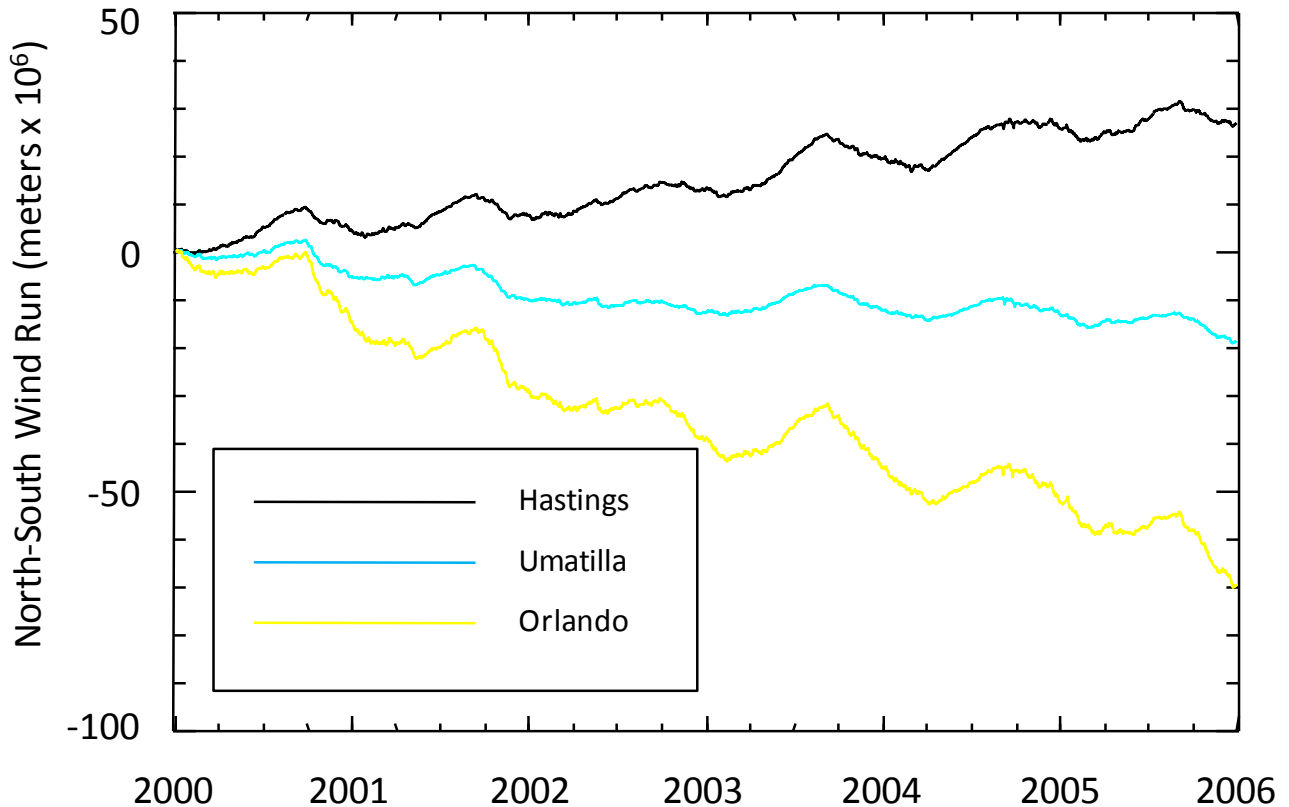


Figure 3–21. Comparison of north-south wind run at Hastings, Umatilla, and Orlando, 2000 to 2005.

The general variability of the strength and direction of monthly wind over the Florida Peninsula is mostly due to shifts in location and relative strengths of (a) the Bermuda-Azores High and Icelandic Low that form the North Atlantic Oscillation, and (b) the Ohio Valley High (Blanton, et al. 1985). The strong flow from the southeast during summer is explained by the typical westward shift of the Bermuda-Azores High during this time. The abrupt shift to strong flow from the northeast during autumn is caused by the subsequent eastward shift of the Ohio Valley High that replaces the Bermuda-Azores High as the dominant influence on wind flow.

Winds over the study area contain distinct seasonal, daily, and hourly time scales. The seasonal scales are primarily modulated by shifting pressure systems occurring over large spatial scale relative to the study area; as a result wind stations within the study area show strong correlation for seasonal wind variability. Wind at daily time scales are likely a result of the passage of synoptic weather systems. Because daily wind speed over the study area generally showed strong correlation ($r^2 = 0.47$ to 0.89), the synoptic weather systems must have length scales at least as large as the horizontal scale of the study area. Hourly time scales are influenced by land-sea breezes, small-scale convection (e.g., thunderstorms), and other local conditions and, not surprisingly, show weaker correlation between stations ($r^2 = 0.31$ to 0.60).

3.10 WATER QUALITY

Water quality data are used for setting salinity boundary conditions for tributaries, springs, and diffuse groundwater discharge. In order to establish that salinity can be treated as a conservative tracer (a substance that does not undergo transformations), we needed to examine the relationships between salinity, chloride, and salt composition. Water quality stations containing observations of the concentrations of major salt ions are used for this purpose (Figure 3–22). Water quality data were primarily obtained from SJRWMDs Water Quality Monitoring Network (Winkler 2004) and supplemental data were obtained from FDEP, USGS, Orange County, Orlando Utilities Commission, and City of Titusville. Water quality data are collected by SJRWMD at monthly to quarterly intervals and data collection methodologies are described by Winkler (2004). USGS collects water quality data as part of the National Water Information System (USGS, 2010) and data collection methodologies follow a standard protocol (Hem 1992). Kroening (2004) provides an excellent summary of water quality data available from both USGS and SJRWMD within the middle St. Johns River.

Most water quality stations span the model simulation period (1996 to 2005) (Table 3-22, Table 3-23). Summary statistics for chloride (Table 3-23) illustrate the generally high levels of salt concentrations found throughout the St. Johns River main stem relative to typical fresh surface waters. The source of high chloride over the lower 100 km of the river is seawater. The bulk of the river, from river km 100 to 400, is predominately oligohaline, with the source of chloride being groundwater entering the river through springs and as diffuse groundwater discharge. A relative maximum for chloride levels occurs near river km 330 in the upper St. Johns River.

Water quality sites off the St. Johns River main stem are shown separately in

Table 3–23. These sites include representative tributaries, a spring, several offline lakes, and two wastewater treatment plants. In general, tributaries have low chloride levels, more typical of fresh surface water. Station DPB is an exception because it is located in a tributary that receives reject water from a reverse osmosis plant. The offline lakes tend to have high chloride levels because they have low flushing and receive salt loading from groundwater. Blue Spring has high chloride typical of springs near the St. Johns River main stem. Wastewater treatment plants discharge low chloride waters because the sources of this water are primarily from domestic supply that necessarily requires low chloride levels as a secondary water quality standard. In summary, tributaries and wastewater treatment plants discharge low chloride waters to the river, but the St. Johns River main stem generally maintains its oligohaline character because of salt loading from relict seawater derived from groundwater.

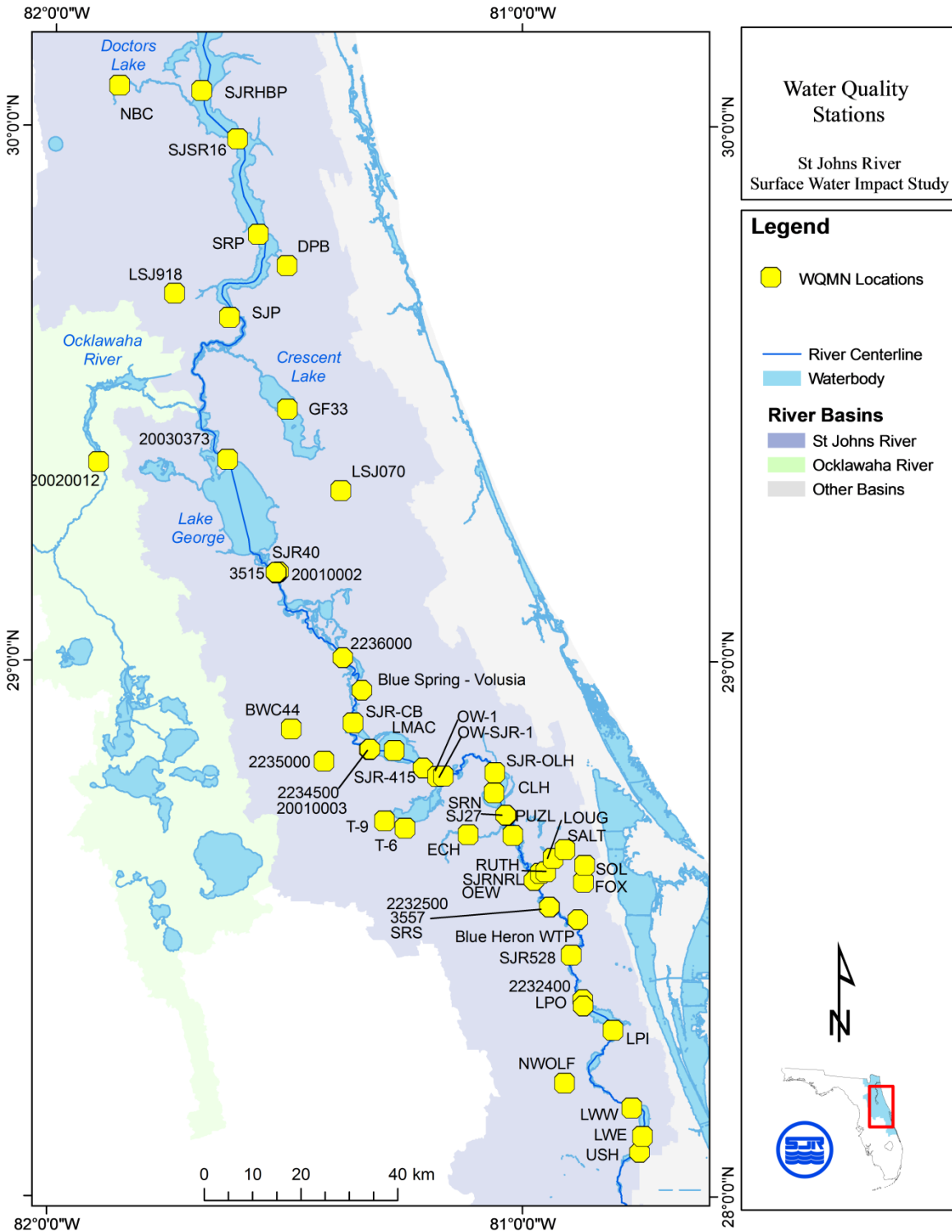


Figure 3–22. Water Quality Monitoring Network (WQMN) stations used for examination of salinity, chloride, and salt composition.

Table 3–22. Water quality sites along the St. Johns River main stem with summary chloride statistics.

Station ID	River km	Agency	NRECS	Period of Record	Chloride (mg L ⁻¹)		
					Min	Mean	Max
SJRHBP	68.7	SJRWMD	435	1995–2007	20	925	9,870
SJSR16	81.8	SJRWMD	201	1995–2007	83	425	4,944
SRP	102.7	SJRWMD	205	1995–2007	83	220	1,283
SJP	126.7	SJRWMD	254	1995–2007	86	194	353
20030373	176.8	SJRWMD	79	1995–2007	96	248	431
SJR40	204.3	SJRWMD	47	1999–2007	77	227	382
20010002	204.3	SJRWMD	136	1995–2007	78	225	380
3515	204.3	FDEP	83	1998–2006	78	212	380
2236000	232.3	SJRWMD	94	1995–2007	21	223	393
SJR-CB	251.0	SJRWMD	18	2002–2007	103	181	388
2234500	262.2	USGS	72	2000–2002	81	285	560
20010003	262.2	SJRWMD	49	1995–2001	85	257	580
LMAC	267.4	SJRWMD	82	1995–2007	69	250	573
SJR-415	274.6	SJRWMD	67	2002–2007	79	267	647
OW-1	279.7	SJRWMD	64	1995–2007	101	224	623
OW-SJR-1	281.4	SJRWMD	144	1996–2007	68	300	835
SJR-OLH	299.7	SJRWMD	63	2002–2007	77	282	700
CLH	303.9	SJRWMD	39	2001–2007	63	273	662
SRN	309.9	SJRWMD	167	1995–2007	15	272	866
SJ27	309.9	Orange County	13	1995–2000	126	246	523
PUZL	315.4	SJRWMD	2	1990	367	488	609
SJRNRL	330.0	SJRWMD	76	1996–2001	103	803	4,530
2232500	343.5	USGS	72	2000–2002	57	339	1,150

Chapter 5. River Hydrodynamics Calibration

SRS	343.5	SJRWMD	217	1995–2007	12	329	3,750
3557	343.5	FDEP	83	1998–2006	49	243	940
SJR528	364.2	SJRWMD	77	1996–2001	44	196	595
2232400	378.0	USGS	87	2000–2006	30	209	647
LPO	379.5	SJRWMD	157	1995–2007	12	161	708
LPI	388.0	SJRWMD	159	1996–2007	11	142	612
LWW	413.9	SJRWMD	160	1996–2007	24	71	166
LWE	422.0	SJRWMD	171	1996–2007	18	63	160
USH	425.8	SJRWMD	63	2003–2007	17	67	138

Table 3–23. Water quality stations off the St. Johns River main stem, with summary chloride statistics.

Station ID	Type	River km	Agency	NRECS	Period of Record	Chloride (mg L ⁻¹)		
						Min	Mean	Max
NBC	Tributary	71.0	SJRWMD	159	1995–2007	1	15	172
DPB	Tributary	106.4	SJRWMD	160	1995–2007	18	299	794
LSJ918	Tributary	121.4	SJRWMD	100	1995–2007	11	31	59
20020012	Tributary	162.7	SJRWMD	138	1995–2007	7	13	73
GF33	Lake	144.7	SJRWMD	82	1999–2007	29	119	236
LSJ070	Tributary	144.7	SJRWMD	72	1995–2007	8	16	57
Blue Spring–Volusia	Spring	243.2	USGS	76	1996–2007	161	353	553
BWC44	Tributary	253.2	SJRWMD	78	1995–2007	9	13	18
2235000	Tributary	253.2	SJRWMD	88	1995–2007	18	37	92
T-9	Tributary	279.6	SJRWMD	61	1995–2000	12	24	35
T-6	Tributary	279.6	SJRWMD	63	1995–2000	15	26	38
ECH	Tributary	311.4	SJRWMD	160	1995–2007	12	48	111
RUTH	Lake	330.4	SJRWMD	2	1990	204	450	696
LOUG	Lake	330.4	SJRWMD	2	1990	1,360	1745	2,130
SALT	Lake	330.4	SJRWMD	2	1990	1,200	1716	2,232
SOL	Lake	337.5	SJRWMD	11	1989–1991	172	214	289
FOX	Lake	337.5	SJRWMD	11	1989–1991	231	337	504
OEW	WWTP	331.2	Orlando Utilities Commission	137	1995–2006	23	74	100
Blue Heron	WWTP	353.1	City of Titusville	55	1998–2007	85	167	356
NWOLF	Tributary	399.7	SJRWMD	373	1996–2007	6	16	30

Quality Assurance of SJRWMD Water Quality Data

The SJRWMD laboratory performs the majority of salt composition analyses for SJRWMD water quality data. Precision, accuracy, and analysis methods are summarized below (Table 3–24). Precision is calculated from replicate samples and accuracy is determined from matrix spikes (J Applewhite, SJRWMD, pers. com. 2009).

Table 3–24. Precision and accuracy of chemical analytes for SJRWMD data.

Laboratory Analysis			
Analytes	Precision	Accuracy	Method
Chloride	2%	90%–110%	EPA300.0 R2.1 1993
Sulfate	3%	90%–110%	EPA300.0 R2.1 1993
Magnesium	30%	85%–115%	EPA200.7 R4.4 1994
Sodium	30%	80%–120%	EPA200.7 R4.4 1994
Potassium	30%	85%–115%	EPA200.7 R4.4 1994
Calcium	30%	85%–115%	EPA200.7 R4.4 1994
Alkalinity	2%	85%–115%	Standard Methods 20th Edition 2320B

Conductivity and pH are collected by data sonde at the time of sampling. Conductivity corrected to a standard reference temperature of 25°C is called specific conductivity. The resolution and accuracy of specific conductivity and pH collected with a YSI model 600XL (YSI Inc., Yellow Springs, Ohio), is representative of other sonde data as well (Table 3–25).

Table 3–25. Resolution and accuracy of field data obtained using a data sonde.

Field Data Collection			
Measurement	Resolution	Accuracy	Field Measurement Device
Specific conductivity	1 $\mu\text{S cm}^{-1}$	$\pm 1\%$	YSI 600XL
pH	0.01 unit	± 0.2 unit	YSI 600XL

Salinity is calculated from specific conductivity. Different manufacturers use different algorithms for this calculation, and the algorithm used by a company may change through time. For this chapter, salinity is recalculated from observed specific conductivity data to ensure uniformity between measurements.

Total Solids Versus Dissolved Solids in Salts Analysis

The majority of available data for salt composition is provided as total solids concentration, although dissolved solids concentrations are preferred. For major salt ions, dissolved solids concentrations are typically equivalent to total solids concentrations unless the sample contains appreciable sediment. To avoid the inclusion of sediment in unfiltered samples, samples were limited to data obtained from the top 1.0 meter of the water column with most samples collected at 0.5 m depth. Total solids concentration, then, is assumed interchangeable with dissolved solids concentration.

3.11 BATHYMETRY

Bathymetry of the lower and middle St. Johns River is known from many bathymetric surveys collected at different times between 1935 and present. Bathymetry for much of the lower St. Johns River was collected in recent times from 1990 to present, whereas bathymetry for most of the middle St. Johns River was collected prior to 1940.

For ease of use in modeling, all the bathymetric surveys are combined into a single Digital Elevation Model (DEM) with a 10-m horizontal resolution. The major tasks in creating the DEM are as follows:

- Conversion of depths associated with individual surveys to a common vertical datum
- Quality assurance of older surveys against recent surveys
- Spatial interpolation of scattered survey points to the regular gridded locations of the DEM
- Spatial interpolation of surveyed transects to the regular gridded locations of the DEM

Finally, the interpolated bathymetry was merged with existing topography over the adjacent watersheds to complete the DEM. Although the EFDC hydrodynamic model uses only bathymetry and not topography, the merging of bathymetry with topography helped defined the shoreline of the river and lakes for creation of the EFDC hydrodynamic model grid.

3.11.1 BATHYMETRIC SURVEYS OF THE LOWER AND MIDDLE ST. JOHNS RIVER

Bathymetric survey data were available from four sources, the U.S. Army Corps of Engineers (USACE), the National Ocean Service (NOS), University of Central Florida (UCF), and the SJRWMD (Table 3–26). Bathymetry surveys for the adjacent shelf (Shelf in the table) were obtained from a finite element model application by the University of Central Florida (UCF) (Hagen and Parrish 2004). The principle bathymetric data set for the lower St. Johns River was collected by the USACE in 1995 between Buffalo Bluff and the mouth of the river (LSJR Transects). The USACE also provided many additional, intensive bathymetric surveys in the navigational channel and in Mill Cove downstream of Jacksonville. The USACE also provided a centerline bathymetric survey of the river channel from the river mouth through Lake Harney (Navigation Channel). The SJRWMD did an intensive bathymetric survey of the Cedar–Ortega River in 1995.

Nearly all bathymetric surveys of Crescent Lake, Lake George, and the middle St. Johns River were collected by NOS from 1935 to 1939. In 2007, the SJRWMD initiated a small bathymetric

survey of the middle St. Johns River, as part of the WSIS, as a check on the accuracy of the NOS bathymetry (see section 0).

Table 3–26. Bathymetric survey data used to create a DEM of the lower and middle St. Johns River.

Name	Spatial Extent	NRECS	Year(s)	Source	Mean Depth (m)	STDEV (m)
Shelf	Seaward of mouth to the 40-m contour	3,122	2004	UCF	11.97	6.54
LSJR Transects	Buffalo Bluff to mouth	285,371	1995	USACE	3.46	2.94
Navigation Channel	Navigation Channel from Main Street Bridge to mouth	252,946	1991–1993	USACE	12.10	2.84
Mill Cove	Mill Cove	48,191	1995	USACE	2.23	2.71
Cedar–Ortega	Tidal portions of Cedar–Ortega River	4,855	1995	SJRW MD	2.29	1.50
Centerline	Navigation channel from Lake Harney to mouth	24,588	2001	USACE	3.84	1.53
Crescent	Crescent Lake	12,436	1935–1937	NOS	2.34	0.93
George	Lake George to Welaka	27,815	1937–1939	NOS	2.45	1.12
Sanford–Astor	US 17 (Sanford) to SR 40 (Astor) including Lakes Dexter and Woodruff	30,835	1938	NOS	2.19	1.50
Monroe	Lake Monroe	9,570	1938	NOS	1.78	0.77
Jesup	Lake Jesup	8,754	1938	NOS	0.92	0.42
Channel Monroe-Harney	Outlet of Lake Harney to inlet of Lake Monroe	11,385	1939	NOS	1.38	1.17
Harney	Lake Harney	9,207	1939	NOS	1.31	0.62
SJRWMD 2007	Selective segments from Lake Harney through Lake Monroe	5,656	2007	SJRW MD	1.59	1.05

3.11.2 CHECK OF MIDDLE ST. JOHNS RIVER BATHYMETRY

As a check on the accuracy of the 1930s NOS bathymetry, additional bathymetry data were collected during 2007. Because budget constraints limited this effort to relatively few areas, the

new survey focused on areas of the river where the greatest alterations to morphology have occurred since the 1930s. Two areas were selected: (a) the natural channel entering Lake Monroe where river flow into Lake Monroe was subsequently diverted by construction of the Monroe Canal and (b) the river channel between Lake Jesup and Lake Monroe that has been modified by road construction and channel stabilization (Figure 3–23). Figure 3–23 shows differences in elevation at points where the 1939 NOS survey and 2007 WSIS survey coincide.

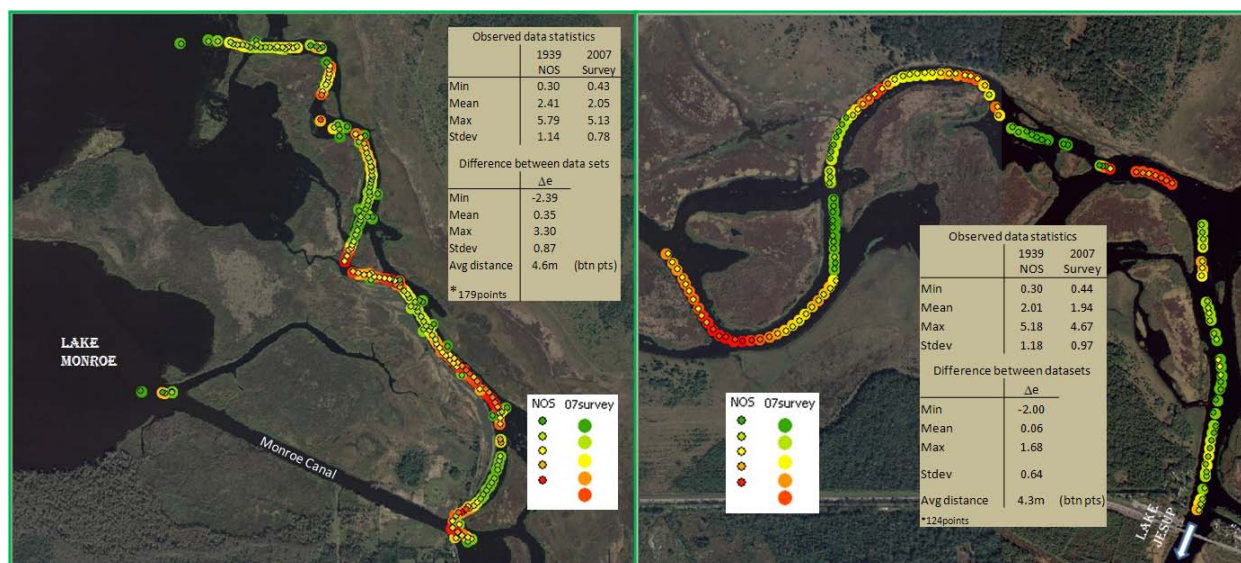


Figure 3–23. Comparison of bathymetry from 1939 National Ocean Service (NOS) and 2007 St. Johns River Water Management District SJRWMD surveys (m NAVD88). Left plot is the former river channel entering Lake Monroe that was cut off by the Monroe Canal. Right plot is the river channel between Lake Jesup and Lake Monroe. NAVD = North American Vertical Datum of 1988.

Because the Monroe Canal did not exist at the time of the NOS survey, we infer that the original river channel could have been subject to increased sedimentation due to reduction of velocity caused by diversion of flow through Monroe Canal. Bottom elevation increased in this channel by an average of 35 cm over 70 years (0.5 cm yr^{-1}). For the area downstream of Lake Jesup, morphological changes from the 1930s to present are evident, but the channel remained part of the main channel flow and the resultant changes in bottom elevation are much less than for the area near Monroe Canal. For the channel near Lake Jesup mean bottom elevation increased 6 cm (1 mm yr^{-1}), a decrease in depth of only 3%.

Aerial photography of the river extending back to the early 1940s indicates that river morphology has largely remained unchanged over most of the study area. We infer, then, that the 1930s bathymetry is still a useful representation of modern bathymetry. The river in the middle St. Johns River is characteristically sluggish with extremely low slope, and likely lacks sufficient energy to appreciably alter channel morphology and depth.

3.11.3 DIGITAL ELEVATION MODEL

A Digital Elevation Model (DEM) was developed for the lower and middle St. Johns River to facilitate the accurate transference of river geometry and bathymetry to the model. The DEM is a

gridded data set of topographic and river bottom elevations at a 10-m horizontal resolution. The topographic data are not used directly for modeling, because the model simulates only in-channel flows. Topography is included for completeness, for possible future work, and for assessment of stage–volume–area relationships across flood plains.

The primary source for topography of the river basins was an existing SJRWMD drainage-enforced, 10-m DEM (SJRWMD DEM). The SJRWMD DEM does not contain bathymetry, however, and most of the effort in creating the DEM for hydrodynamic modeling focused on addition of bathymetric data sets to define bathymetry at the same 10-m resolution. Because the middle St. Johns River has wide flood plains, topography of the flood plain in this area was improved from the SJRWMD DEM using surveyed transects, LiDAR, and elevations inferred from vegetative cover. Again, these topographic improvements were not used for the WSIS modeling, but could be useful for future modeling studies.

Bathymetry data were included in the DEM by spatial interpolation of points obtained from existing bathymetric surveys. For areas with a dense and relatively uniform coverage of bathymetric points, inverse-distance weighting of points were used to interpolate to the 10-m DEM cells. Throughout much of the lower St. Johns River, the observed bathymetry points are arranged in transects. Interpolation algorithms, such as inverse-distance weighting, can produce erroneous features when used for interpolation of data arranged as transects. Errors occur because the interpolation algorithms do not account for river topology, that is, they have no knowledge of the longitudinal direction of the river channel (thalweg). A common error is the creation of artificial “mounds” or “humps” between transects. To circumvent this problem, an algorithm was developed that creates a denser, more uniformly spaced set of transects between each pair of observed transects using a thalweg-enforced interpolation method that follows the river thalweg.

Interpolation of Bathymetry in the Middle St. Johns River

The 1930s NOS bathymetry data are relatively dense and evenly distributed over the surveyed areas. The raw bathymetric points for Lake Monroe (Figure 3–24) illustrate the spatial density typical of the NOS bathymetric surveys in the middle St. Johns River. These data were interpolated directly onto the DEM using an inverse-weighted distance methodology.

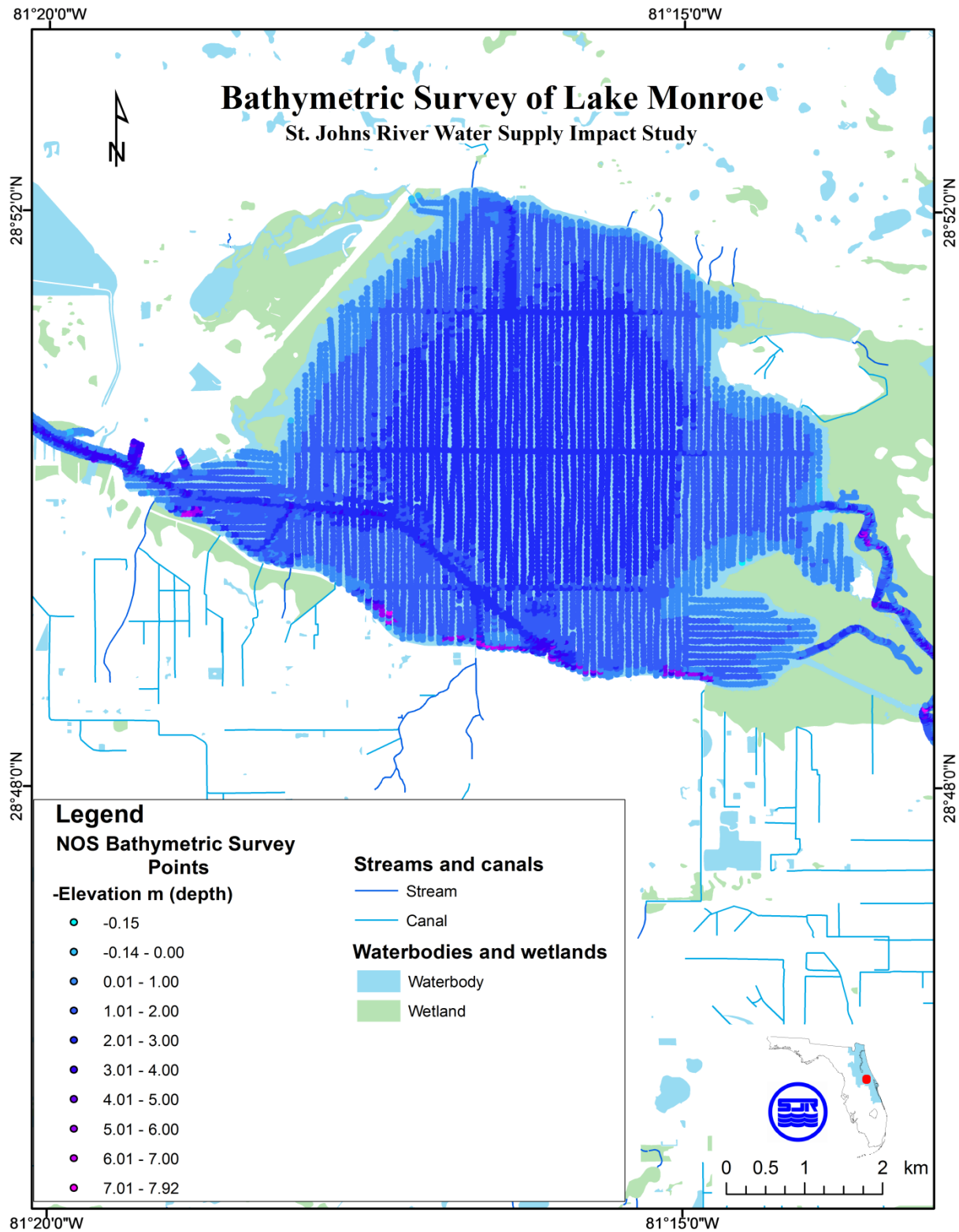


Figure 3–24. National Ocean Service (NOS) bathymetric survey of Lake Monroe in the middle St. Johns River.

Interpolation of Bathymetry in the Lower St. Johns River

The principle bathymetric data set for the lower St. Johns River was a 1995 survey collected as lateral transects at 500 to 1000 m spacing. These data were interpolated along the river thalweg to create 20 additional equally spaced transects between each pair of observed transects. Bottom elevations along the interpolated transects are assigned by linear interpolation longitudinally across transects. The interpolation is split at the centerline of the river channel to ensure that elevations along the main river channel are maintained. Figure 3–25 shows an example of the results of this thalweg-enforced interpolation of transects. The points created by the thalweg-enforced interpolation of transects were then used to interpolate bathymetry to the DEM using inverse-distance weighting.

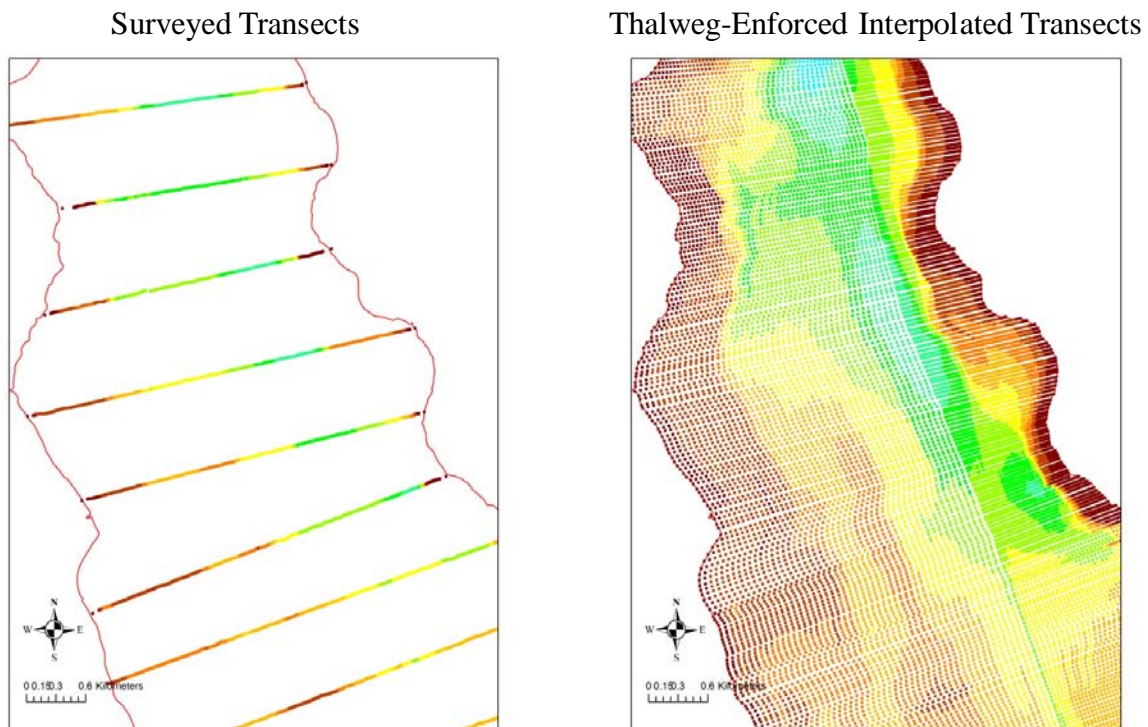


Figure 3–25. Surveyed transects at approximate 500 m spacing (left) and thalweg-enforced interpolated transects at approximate 25 m spacing (right). The thalweg-enforced transects were used to interpolate bathymetry to the DEM at 10-m horizontal resolution.

3.11.4 FINAL DIGITAL ELEVATION MODEL OF THE LOWER AND MIDDLE ST. JOHNS RIVER

The final DEM of the lower and middle St. Johns River is organized into 103 square tiles, where each tile contains 1000 x 1000 cells at 10-m spacing (Figure 3–26). This DEM is used to provide depths and shorelines for the EFDC hydrodynamic model.

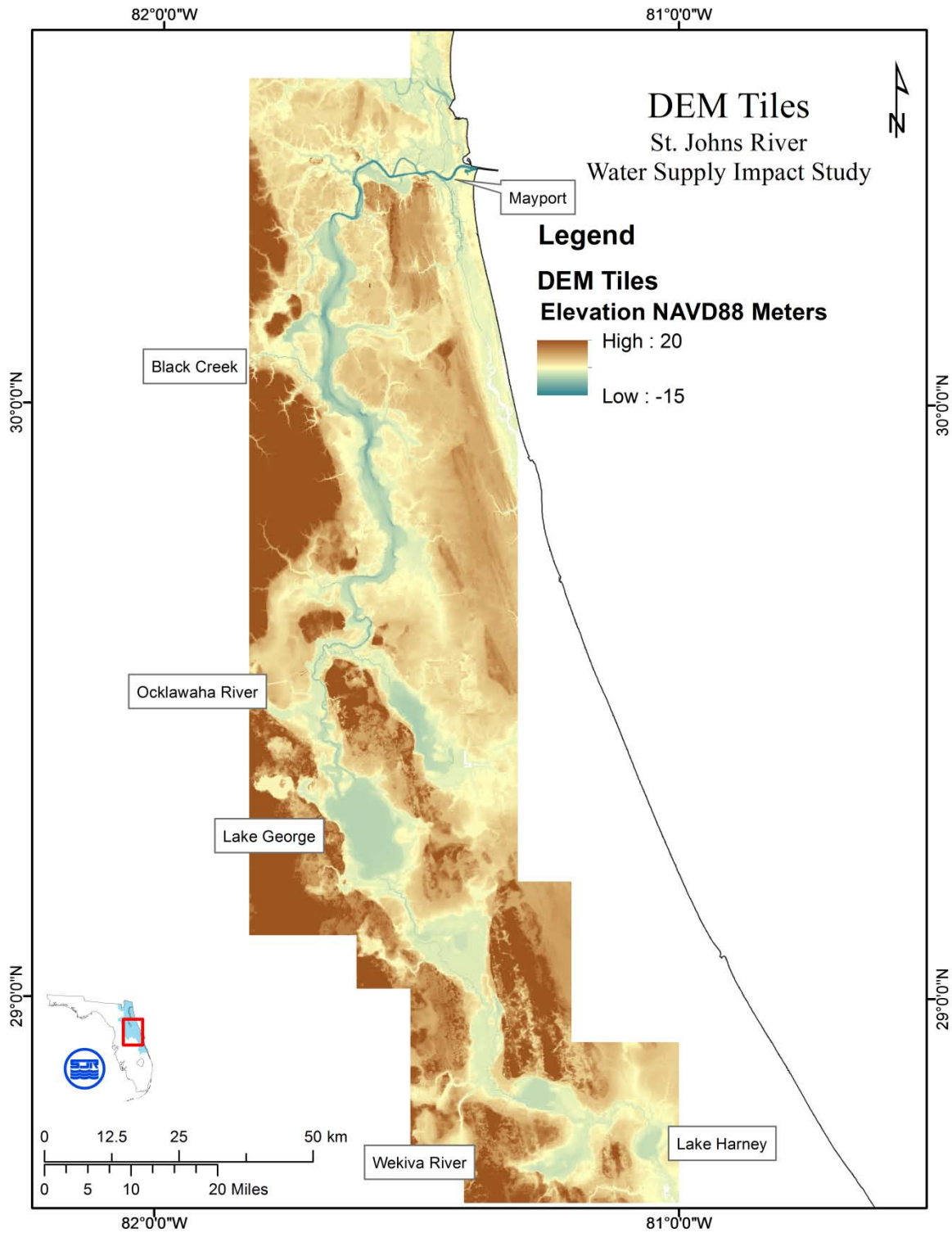


Figure 3–26. Final Digital Elevation Model (DEM) of lower and middle St. Johns River used to assign depths and shorelines for the EFDC hydrodynamic model.

4 MODEL FRAMEWORK

Models are approximations of the real world. Building a perfect model is not possible nor is it desirable. One advantage of a good model is that it reduces real world phenomena to the most important mechanisms relevant to the question at hand, and this simplifies analysis of the problem. The real St. Johns River is subject to forcings at a wide range of spatial and temporal scales. One can easily see boat wakes, the rapid wave motions created by boats, for example. Not so easily seen is the slow, steady rise of sea level that presently averages about 3 mm yr^{-1} . Yet the hydrodynamic model for this study ignores the former and incorporates the latter. This is not to say that boat wakes are never important—they may be critical to understanding shoreline erosion along a shipping channel, for example—but they are not important to understanding how river hydrodynamics are affected by water withdrawals. A model must not only include important factors needed to address the problem at hand, but also exclude unimportant factors. A model framework encompasses decisions regarding which processes are included and which processes are excluded from the model.

Many types of hydraulic and hydrodynamic models are commonly used for rivers (Martin and McCutcheon 1999). The model types vary largely due to simplifying assumptions of the underlying physical equations. Model selection depends on whether these simplifications are appropriate for a particular application. EFDC (Environmental Fluid Dynamics Code) (Hamrick 1992), a three-dimensional hydrodynamic model, was selected for the lower St. Johns River because this area is a tidally dominated, partially stratified estuary with complex geometry (Oey, Mellor and Hires 1985). The EFDC hydrodynamic model provides the capability to simulate changes in water level, velocity, discharge, salinity, and water age (a measure of flushing rate) due to changes in inflows from multiple sources and locations.

Model selection for the middle St. Johns River was not as straightforward, although ultimately the EFDC hydrodynamic model was also selected for this area also. The middle St. Johns River lies upstream of the tidally dominated portion of the river. Model simulation of non-tidal rivers commonly assumes one-dimensional flow. These models include simple hydrologic routing based only on conservation of mass (Bicknell, et al. 1997). The model application of the middle St. Johns River requires simulation of unsteady, nonuniform flows and backwater effects (section 4.2). This capability is provided by river hydraulic models such as the HEC-RAS hydraulic model. The EFDC hydrodynamic model was selected, however, because we felt the following additional model features were needed:

- Advective-diffusion calculations to simulate salinity and water age
- Surface wind stress at hourly time scales
- Two-dimensional horizontal flows and circulation in lakes
- Three-dimensional return flows generated by wind set-up in lakes

This section focuses on the important aspects of the system that formed the EFDC hydrodynamic model framework for hydrodynamic modeling of the lower and middle St. Johns River. Ocean tides are first discussed (Section 4.1), because both astronomical and meteorological tide are of paramount importance to the hydrodynamic processes of the lower St. Johns River. Meteorological tide is shown to influence also the middle St. Johns River (Section 4.2), which is important to understanding how middle St. Johns River water levels are affected by water

withdrawal. The influence of ocean water level on both the lower and middle St. Johns River makes a unified model of both systems desirable for predicting the total system response to flow reductions. The selection of the EFDC hydrodynamic model for both systems allows for this unification. Because of the character of the ocean influence on the middle St. Johns River, calibration of the EFDC hydrodynamic model for this area required a careful examination of slope–discharge relationships (Section 4.3). Finally, simulating salinity in oligohaline areas, where salt sources are from terrestrial groundwater, required an extensive analysis of sources of salts to the river, salt composition of the river, and relationship between chloride and salinity (Section 4.4).

4.1 OCEAN TIDE

The term ocean tide is used here to mean deviations of the ocean surface from mean sea level excluding wind waves. Ocean tide is dominated by astronomical tides, although meteorological tides are also present and play an important role in the hydrodynamics of the St. Johns River. Astronomical tides result from the gravitational attraction of the moon and sun on the rotating earth. The fundamental periods of these motions are derived with great precision from the analysis of the astronomical forces (Schureman 1988). Astronomical tidal periods are mainly semidiurnal (near 12 hrs) and diurnal (near 24 hrs). Meteorological tides are produced primarily by winds, atmospheric pressure changes, and shifts in large-scale ocean circulation. The dominant periods for meteorological tides occur at synoptic (2 to 12 days) and seasonal time scales. Both astronomical and meteorological tides are important to the dynamics of the St. Johns River and are treated separately for specification of model boundary conditions.

4.1.1 EFFECT OF OCEAN TIDE ON THE ST. JOHNS RIVER

The St. Johns River is strongly affected by ocean tide to Lake George, nearly 200 km from the mouth. Circulation, mixing, and transport within the lower St. Johns River to Lake George is dominated by short period semidiurnal and diurnal tide. Tidal range and phase varies throughout the river because of the interaction of the tidal wave entering the river mouth with the complex geometry and bathymetry of the river. The spatial variability of tide must be properly simulated to ensure that the important effects of tide on the fundamental physical processes affecting the hydrodynamics of the estuary are correctly modeled.

Although the lower St. Johns River is often described as a broad, sluggish river of low slope flowing slowly to the sea, we must recognize that tidal motions cause dynamic oscillations of water levels and flows throughout this reach of the river. The annual average discharge at Jacksonville is $240 \text{ m}^3 \text{ s}^{-1}$ and daily discharge exceeds $710 \text{ m}^3 \text{ s}^{-1}$ for only 10% of days, yet tidal discharge attains $9,000 \text{ m}^3 \text{ s}^{-1}$ on every tidal cycle, twice per day. In the navigational channel near Jacksonville, peak tidal velocities reach 150 cm s^{-1} . In the absence of tide, velocities would achieve only a tenth of this value.

Due to their magnitude, tidal flows are important to circulation and mixing of water and other materials carried with the flows. The mixing of freshwater and seawater by tides has important feedback mechanisms that can control the net movement of salt and pollutants. By the mechanisms of tidal diffusion and estuarine circulation, tidal currents both directly and indirectly cause transport of ocean salts and other material upstream against the downstream direction of

the freshwater flow. The simulation of intrusions of seawater into the St. Johns River, then, depends on proper simulation of tidal motions.

Tidal currents are sinusoidal and, in the absence of mixing, a particle moved upstream by the tide would return to its original position some 6 hrs later. The large velocities generated by tide also produce large velocity gradients both horizontally, between the river channel and shore, and vertically, between the surface and bottom. The movement of water at differing speeds causes rotation and shearing of water parcels, which causes adjacent water parcels to mix. The enhanced mixing of waters by tidal currents results in a diffusive process that allows dissolved material at high concentration in downstream waters to move into lower concentration waters upstream. This process, called tidal diffusion, is one mechanism for the upstream transport of ocean salt.

Vertical mixing of stratified waters by tides results in estuarine circulation. Estuarine circulation is also an important mechanism for upstream transport of ocean salt into an estuary. When tidal energy causes vertical mixing of salty, dense bottom waters with fresh, light surface waters, the potential energy of the water column increases as heavier bottom water is lifted vertically against the force of gravity. Vertical mixing by tides, then, results in conversion of the kinetic energy of the tidal motions into potential energy. The mixing creates an upstream, baroclinic (density-induced) pressure gradient opposing the downstream, barotropic (discharge-induced) pressure gradient of the freshwater discharge. Through the force of the baroclinic pressure gradient, potential energy is reconverted to the kinetic energy of an upstream-directed bottom current. This bottom current can transport large volumes of ocean water into the estuary. In the lower St. Johns River, estuarine circulation manifests itself as a density-driven movement of bottom waters upstream from the river mouth to near Jacksonville.

4.1.2 ASTRONOMICAL TIDE

Astronomical tide is specified at the model's ocean boundary by setting harmonic constants for the dominant short period tidal constituents. By this method, the amplitude and phase of the astronomical tide can be adjusted independently of the longer period meteorological tide. Long-period (> 30 hrs) astronomical tidal constituents are ignored because they are small relative to meteorological tides.

Although tides are caused by the gravitational attraction of the moon and sun on the earth, the direct effect of gravitational fields on the river is insignificant compared with the indirect forcing of ocean tide at the mouth. Direct gravitational forces of the moon and sun are thus ignored in the model. Tidal forcing is included in the model by forcing of ocean water level at the open ocean boundary. Ocean water level forcing results in the propagation of the tidal wave through the river mouth.

4.1.3 METEOROLOGICAL TIDE

Meteorological tides have long periods, typically greater than about 30 hrs. Meteorological tides are quasiperiodic; they are always present, but are not predictable as are astronomical tides. Forecasting meteorological tides using hydrodynamic models is possible (Vincent, Luther and Ross 2001), and is done in major harbors in a process that is similar to weather forecasts. Meteorological tides are not directly simulated by the EFDC hydrodynamic model for this study and must be specified at the model's ocean boundary using observed water level. Similar to

astronomical tides, meteorological tides are remotely forced motions that propagate into the river from the ocean.

Separation of Astronomical and Meteorological Tide

Meteorological tide can be functionally separated from astronomical tide within a time series of observed water levels. The separation of water level variability into these two components allows the astronomical tide to be adjusted independently from the meteorological tide for specification of the model open ocean boundary condition offshore from the point of observation. The amplitudes and phases of the astronomical tides are modified significantly as the tidal wave propagates across the shelf towards the shore, while the longer period meteorological tides are essentially unchanged.

Harmonic analysis is used to separate the astronomical tide from the meteorological tide entering the St. Johns River using observed hourly water level at Bar Pilot Dock (Figure 4–1). The astronomical tide essentially represents the results of a high-pass filter and the meteorological tide represents the results of a low-pass filter with a cutoff frequency of 0.033 hr^{-1} . The dominance of astronomical tide at Bar Pilot Dock is readily apparent relative to the smaller, more slowly varying meteorological tide.

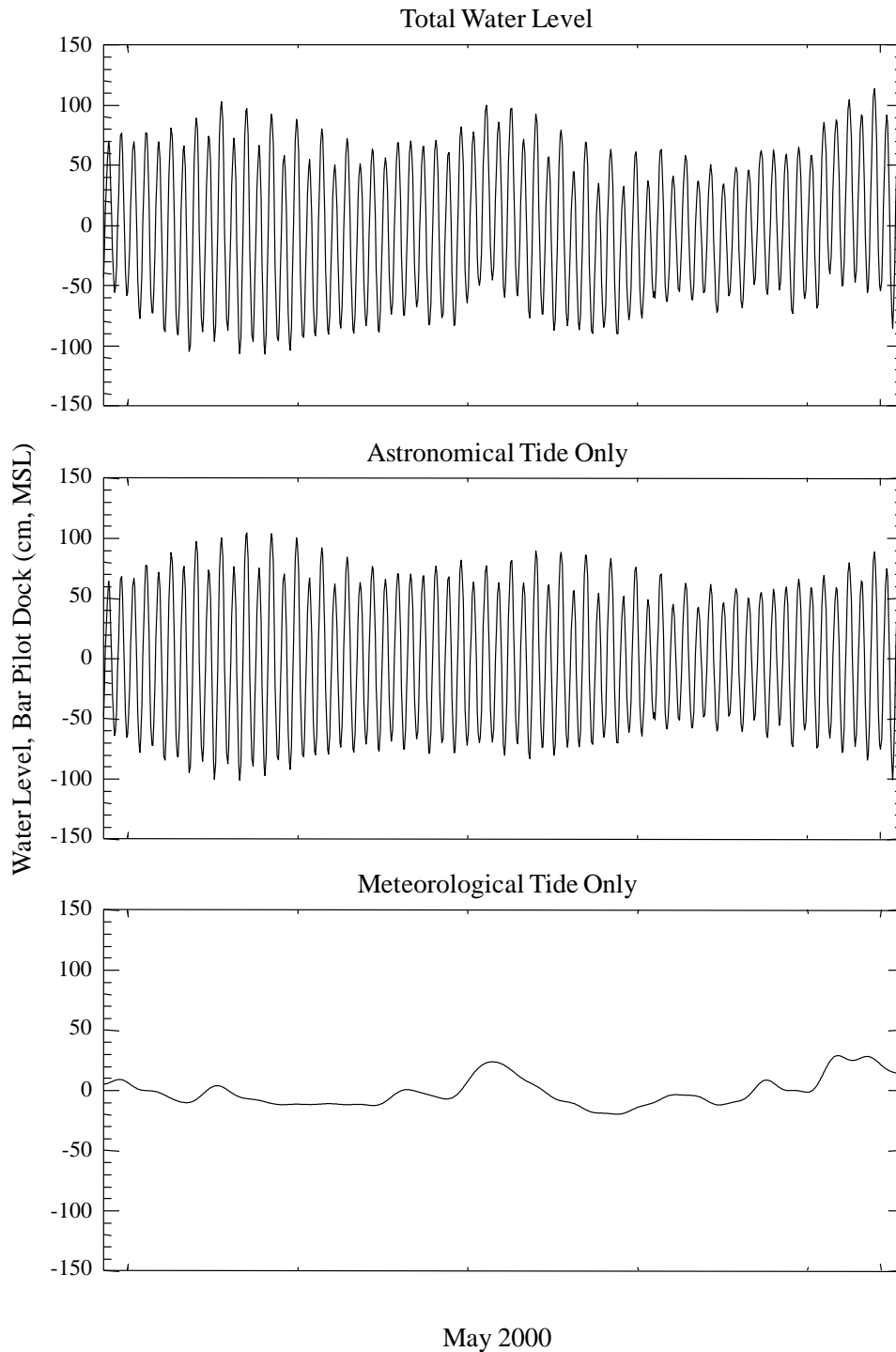


Figure 4–1. Separation of observed hourly water level at Bar Pilot Dock into astronomical and meteorological tide. For illustration, plots show time series over a 1-month period (May 2000) referenced to MSL. Total water level (top), astronomical tide (middle), and meteorological tide (bottom).

The variability of the meteorological tide is seen more clearly with an expanded y-scale and expanded over a 1-yr period (Figure 4–2). The dominant variability of the meteorological tide is

the synoptic scale, quasiperiodic motions at 2 to 12-day periods with characteristic amplitudes of 10 to 20 cm. Synoptic scale water level variability is caused principally by the response of the inner South Atlantic Bight to wind stress (Blanton, et al. 1985).

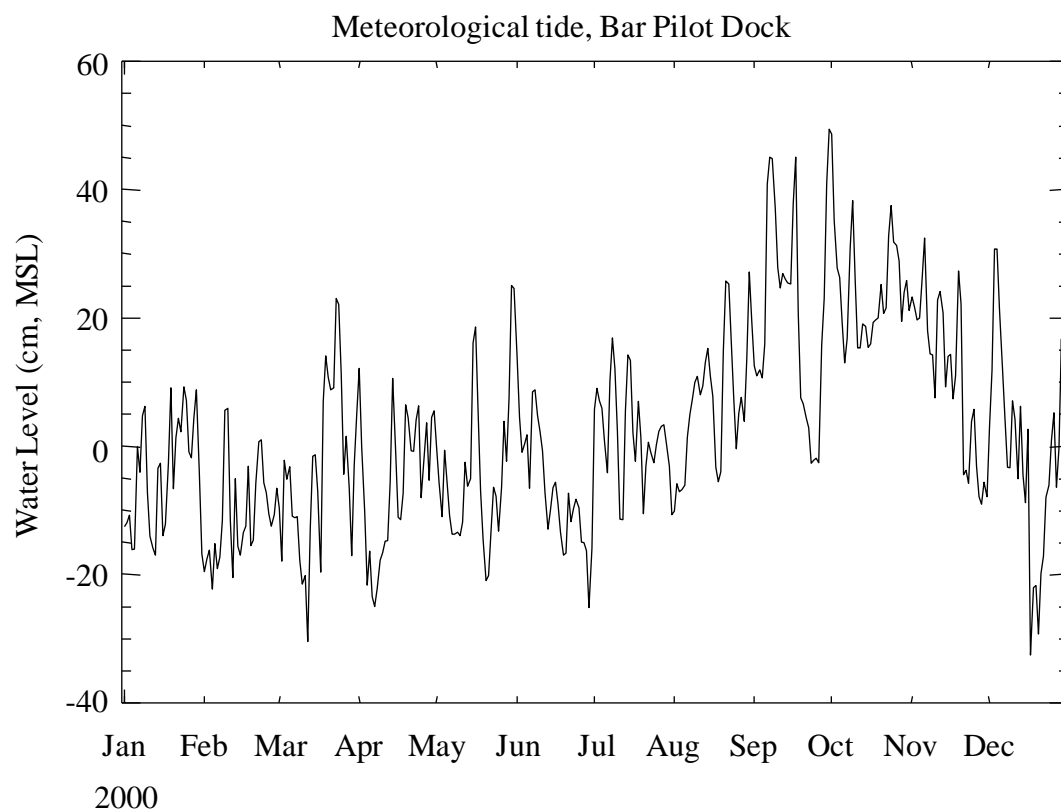


Figure 4–2. Meteorological tide over a 1-yr period (2000) at Bar Pilot Dock.

4.1.4 IMPORTANCE OF METEOROLOGICAL TIDE

Despite the smaller size of the meteorological tide relative to the astronomical tide, the meteorological tide is also important to the hydrodynamics of the river. Meteorological tide causes pulse-like intrusions of seawater into the lower St. Johns River (Sucsy and Morris, Salinity intrusion in the St. Johns River, Florida 2001). Because meteorological tidal motions have longer periods than the astronomical tide, their effects are transmitted much farther upstream, through Lake George and into the middle St. Johns River. Large synoptic events, such as occurred near 1 October 2000, cause a filling of the lower and middle St. Johns River as water levels rise 20 to 40 cm over several days. This filling causes daily averaged flow reversals far up the river and causes intrusion of seawater into normally oligohaline areas.

The typical seasonal variability of ocean water level at the St. Johns River mouth is evident in Figure 4–2; water levels were generally lower in January to August than in September to November for the year shown. A plot of monthly averaged water levels over an 80-yr period (Figure 4–3) shows that ocean levels typically increase from summer to autumn by 20 to 40 cm. These seasonal effects extend over 300 km up river from the river mouth to Lake Harney. The rise in ocean water level in autumn is coincident with, but independent of, higher river discharge

following north Florida's wet season. Increasing river stage in autumn is often mistakenly attributed to increasing discharge alone, but ocean water level is an important contributing factor.

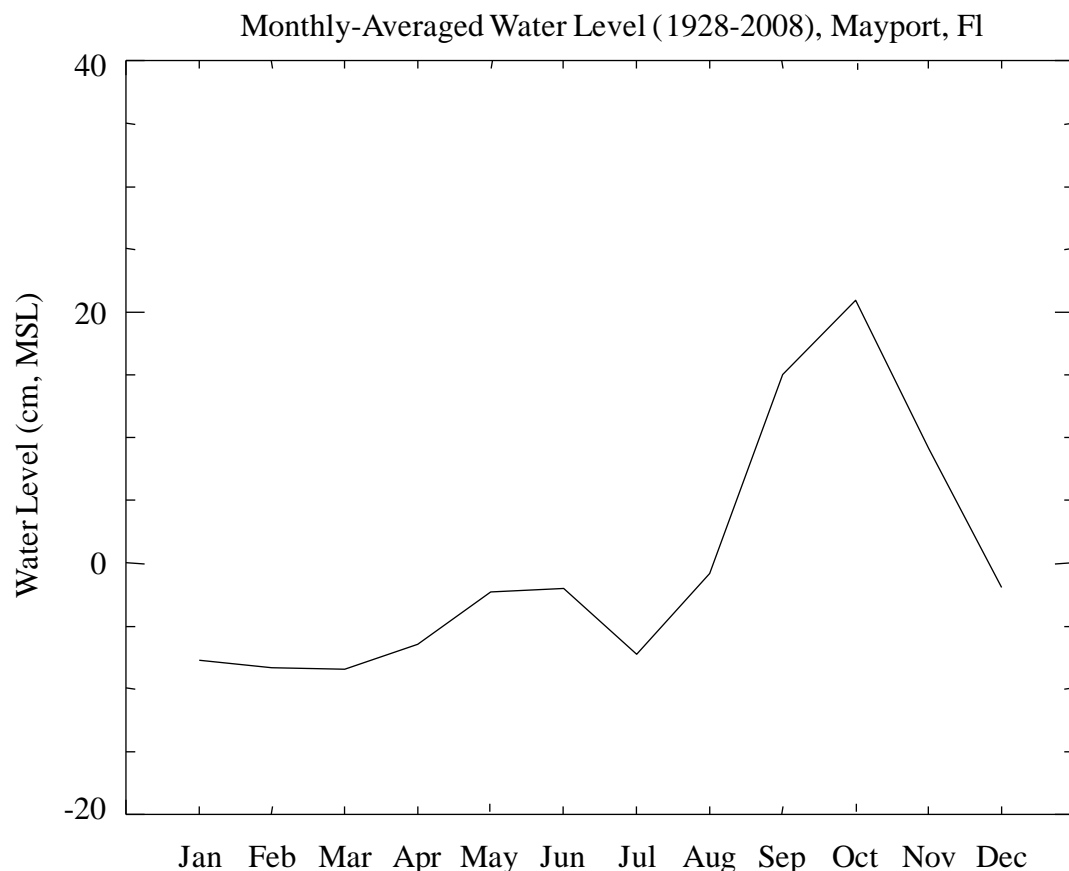


Figure 4-3. Monthly averaged water level (1928 to 2008) at Mayport, FL, near the mouth of the St. Johns River.

Sea Level Rise

Sea level rise is also present in the time series of meteorological tide. Sea level rise results from the gradual response of the world oceans to both natural and human-induced global climate change. Accounting for sea level rise is not necessary for model calibration, but is important for projecting the river's response to water withdrawal into the future. The model setup needs to account for simulation of sea level rise in anticipation of this future scenario (for WSIS Scenarios, see Chapter 6. River Hydrodynamics Results).

Although sea level rise occurs slowly, about 3 mm yr^{-1} , the effects are readily seen in an observed record of annual averaged sea level (Figure 4-4). Prior to 1940, annual averaged sea level at the river mouth was 15 to 25 cm lower than present. The average rate of sea level rise at this location was 25 cm (~1 ft) per century over the period of record (1928 to 2008). Prediction of water level change for the period 1995 to 2030 also requires accounting for sea level rise.

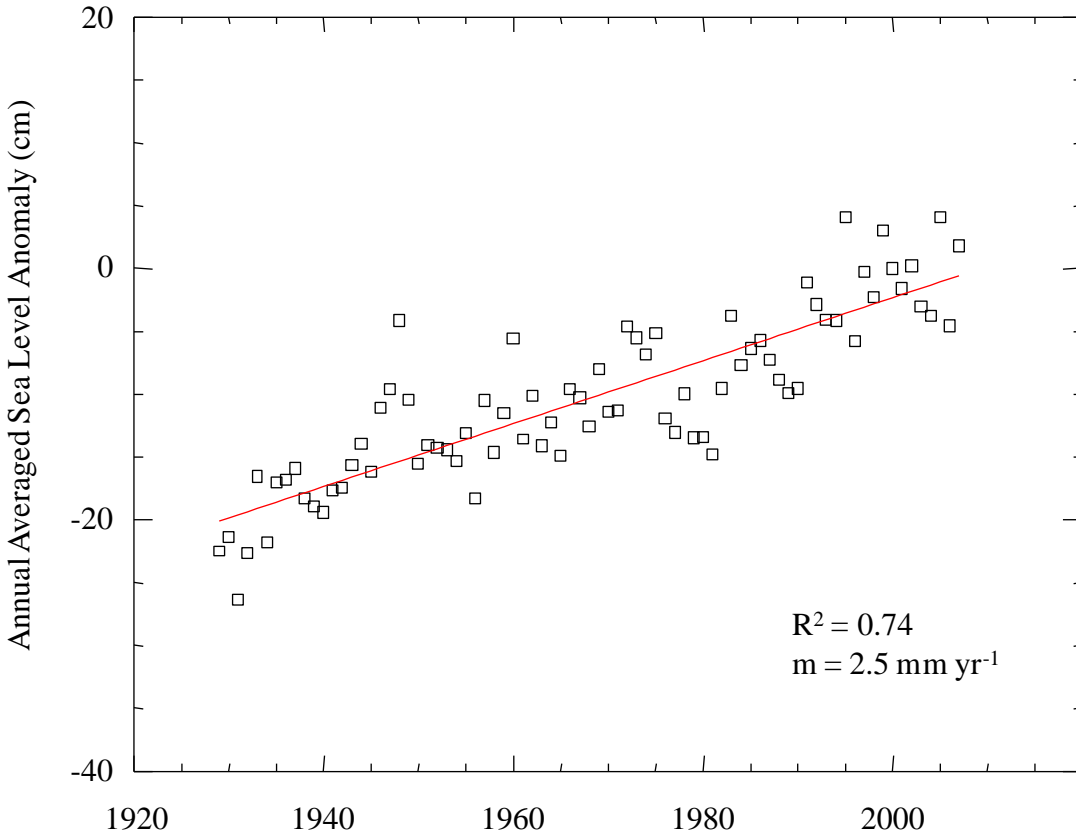


Figure 4–4. Annual averaged sea level anomaly (referenced to the year 2000), Mayport, FL.

4.2 OCEAN INFLUENCE ON MIDDLE ST. JOHNS RIVER STAGE

4.2.1 INTRODUCTION

The low gradient of the St. Johns River allows the Atlantic Ocean to exert a backwater effect well upstream into the middle St. Johns River (Robison 2004). Selection of an appropriate numerical model for simulating water withdrawals within the middle St. Johns River depends on an understanding of this ocean influence. If ocean influences are only of secondary importance compared to discharge, a simple hydrologic routing model (e.g., Hydrologic Simulation Program–FORTRAN [HSPF] hydrologic model) could be used for simulating withdrawal effects on water levels, whereas a strong ocean influence requires a hydrodynamic model. The conditions under which the ocean influences middle St. Johns River water level, and the relative contribution of ocean effects in comparison to discharge, helped determine our model selection.

Discharge and stage at State Road (SR) 44 near DeLand and ocean water level at Mayport are used to quantify ocean influences within the middle St. Johns River. The middle St. Johns River, although lying 200 to 300 km upstream of the river mouth, forms a pool with bottom elevation below MSL. This pool would remain filled with ocean water even in the absence of any freshwater inflow. The gauging station at SR 44 near DeLand lies within this reach, has a long period of record (1934 to present) for discharge and stage, and is representative of the middle St.

Johns River as a whole. The tide gauge at Mayport is close to the river entrance, has an equally long period of record (1928 to 2008) and measures ocean water level.

Although the period of records of both the DeLand and Mayport gauges extends nearly 70 years, early periods were removed from the analysis because discharge measurement methodology at DeLand did not allow observation of reverse flows prior to 1956 (Kroening 2004).

Quantification of ocean influence on the middle St. Johns River stage demonstrates that ocean effects dominate stage variability throughout much of the middle St. Johns River when river discharge is below its mean value. Comparison of long-term DeLand and Mayport stage observations shows that water levels in the middle St. Johns River are likely rising in response to sea level rise. The dominate ocean influence on stage in the middle St. Johns River means that a hydrodynamic model is appropriate for simulating the effects of water withdrawals in this area. A hydrodynamic model is also needed to simulate the effects of sea level rise for examining system response to water withdrawals under future conditions.

4.2.2 COMPARISON BETWEEN RIVER STAGE AT DELAND AND MAYPORT

River stage at DeLand often falls quite close to ocean water level at Mayport even though these gauges are separated by 230 km (Figure 4–5). For the 2000 to 2007 periods, the average slope between these locations was 1.09 mm km^{-1} . The periods of largest separation between river stage at DeLand and Mayport coincide with periods of high freshwater discharge. For several extended periods, river stage at DeLand and Mayport are nearly identical. During the low-flow periods of January 2000 to July 2001 and July 2006 to 2007, the average slope between these locations was 0.45 mm km^{-1} , only a 10 cm drop in elevation over 200 km. The extreme low slope of the river over seasonal durations suggests that ocean influence on the middle St. Johns River is common.

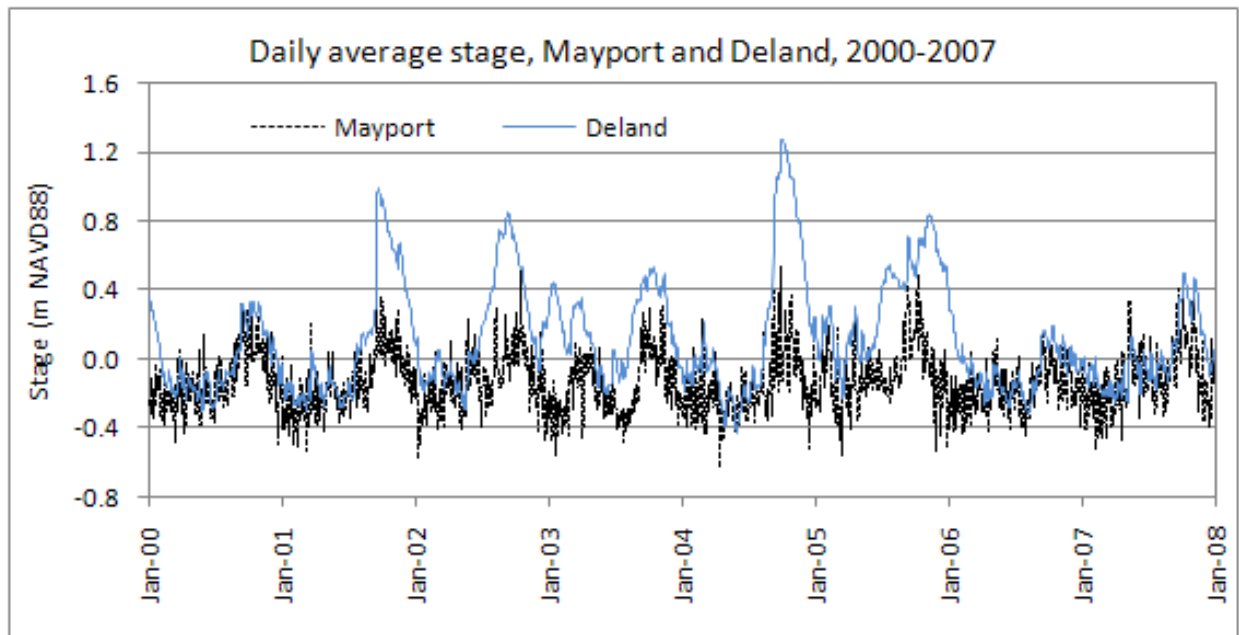


Figure 4–5. Comparison of daily averaged river stage at Mayport and DeLand, 2000 to 2007.

4.2.3 COMPARISON BETWEEN RIVER STAGE AND DISCHARGE AT DELAND

A comparison of daily averaged river stage with discharge at DeLand shows a generally positive correlation between stage and discharge (Figure 4–6). During high discharge, there is a strong positive correlation between stage and discharge for the high-flow year of 2004. For low discharges, the correlation is weak. For example, compare stage and discharge for the low-flow year of 2007. Frequent reverse flows occur when river stage is as high as 0.5 m, which is well above the mean stage of 0.08 m.

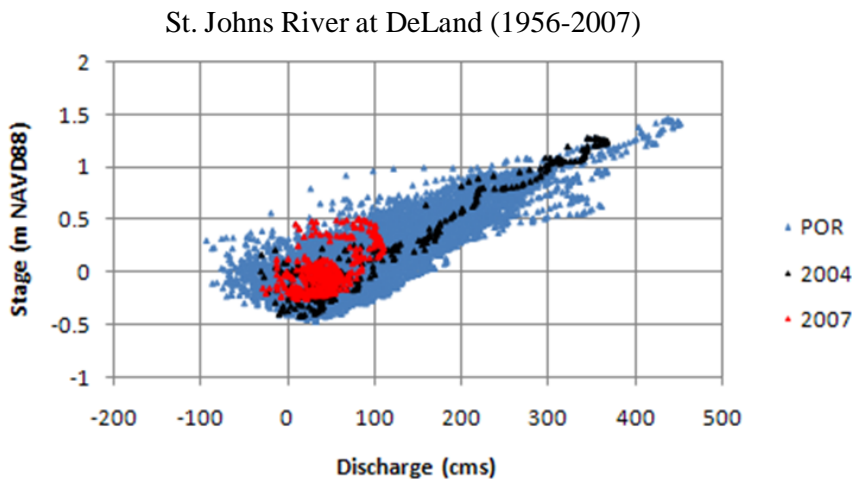


Figure 4–6. Comparison of river stage and discharge at DeLand (USGS 02236000).

4.2.4 CORRELATION OF RIVER STAGE AND DISCHARGE AT DELAND BY Q-LIMIT

Stage and discharge are visually correlated for high discharge, but weakly correlated or uncorrelated for low discharge. The discharge for which stage and discharge become uncorrelated is determined by computation of the Pearson correlation and coefficient of determination (r^2) for stage-discharge (HQ) pairs with discharge less than a given discharge limit (Q-Limit) (Figure 4–7). Discharge limits ranged from 10 to 400 m^3s^{-1} in 10 m^3s^{-1} increments. The Pearson Correlation is less than 0.273 and r^2 is less than 0.1 for discharge below 90 m^3s^{-1} . Because the average discharge at this location is 83.95 m^3s^{-1} , less than 10% of water level variation is explained by discharge below the average discharge. r^2 is greater than 0.5 only when discharge exceeds 200 m^3s^{-1} . This level of discharge is the 93rd percentile of the distribution of discharge observed at DeLand. These results show that under most flow conditions, factors other than discharge predominately control stage in the middle St. Johns River.

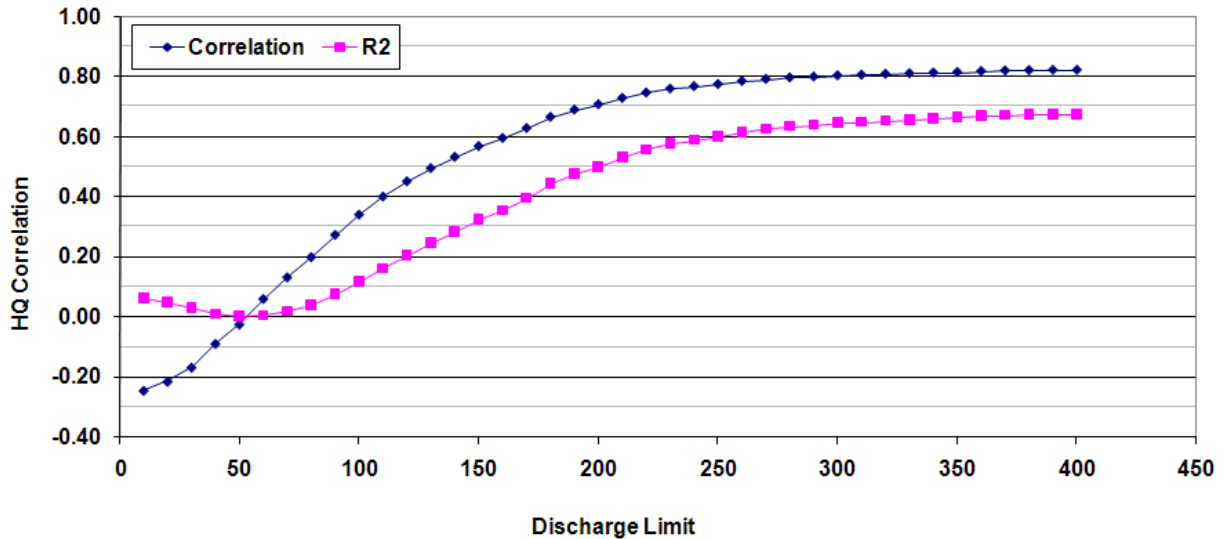


Figure 4–7. Pearson Correlation and coefficient of determination (r^2) versus discharge limit (Q-Limit) at DeLand.

Relative Importance of Ocean Stage and River Discharge on Stage at DeLand

A multiple regression analysis was run using river stage at DeLand (H) as the dependent variable with discharge at DeLand (Q) and ocean water level at Mayport (M) as the explanatory variables (Figure 4–8) to determine the relative importance of ocean water level versus river discharge on river stage at DeLand. The multiple regression analysis determines which explanatory variable (Q or M) has a greater effect on the dependent variable (H) for a range of Q-Limits. Regression coefficients are scaled using standardized regression coefficients (β) to permit the comparison of the different magnitude of the independent variables Q and M, (Montgomery 2006). For all HQ pairs the standardized regression coefficient of Q ($\beta= 0.771$) is nearly twice that of M ($\beta= 0.411$), indicating discharge (Q) dominance of stage at DeLand. However, at low discharges (Q) ocean water level at Mayport (M) becomes the dominant explanatory variable. The inflection point between Q and M dominance occurs near $140 \text{ m}^3\text{s}^{-1}$ indicating that, for discharge conditions well above the mean discharge, ocean water level has greater dominance on river stage at DeLand than does discharge at DeLand.

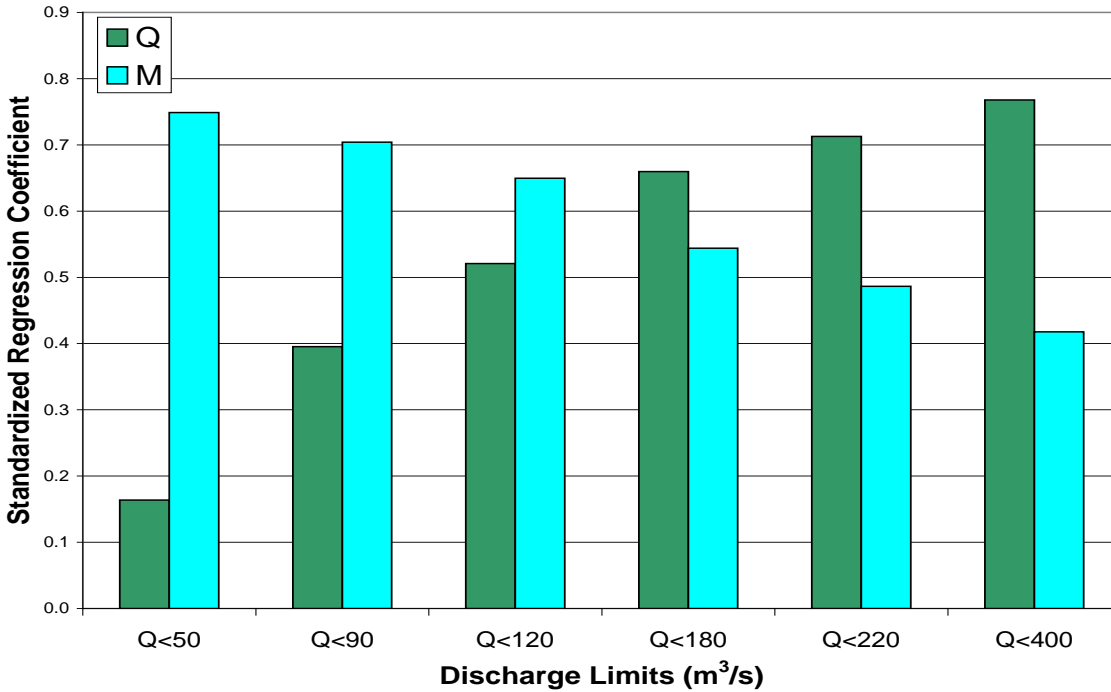


Figure 4–8. Standardized Regression Coefficient (β) versus Q-Limits, Mayport (M) versus DeLand (Q).

4.2.5 EVIDENCE FOR SEA LEVEL RISE IN THE MIDDLE ST. JOHNS RIVER

Direct evidence for sea level rise in the middle St. Johns River is evaluated by comparison of temporal trends for annual averaged stage (H) with discharge at DeLand (Q) and ocean water level at Mayport (M) for the period 1956 to 2008 (Figure 4–9). Ocean water level at Mayport has an increasing trend of 2.7 mm yr⁻¹, consistent with estimates of local sea level rise (Zervas 2001). Stage at DeLand has an increasing trend of 1.6 mm yr⁻¹. Discharge at DeLand has a decreasing trend caused by the high discharge year of 1960 (Hurricane Donna). When this year is removed from analysis, the discharge trend is essentially zero, consistent with Kroening (2004). Given no apparent change in river discharge, the rising trend of stage at DeLand is likely caused by sea level rise. The slower rate of rise of stage at DeLand compared with Mayport may be due to the hydraulics of the stage-discharge relationships under varying discharge conditions and further emphasizes the need for a hydrodynamic model for simulating the effects of sea level rise.

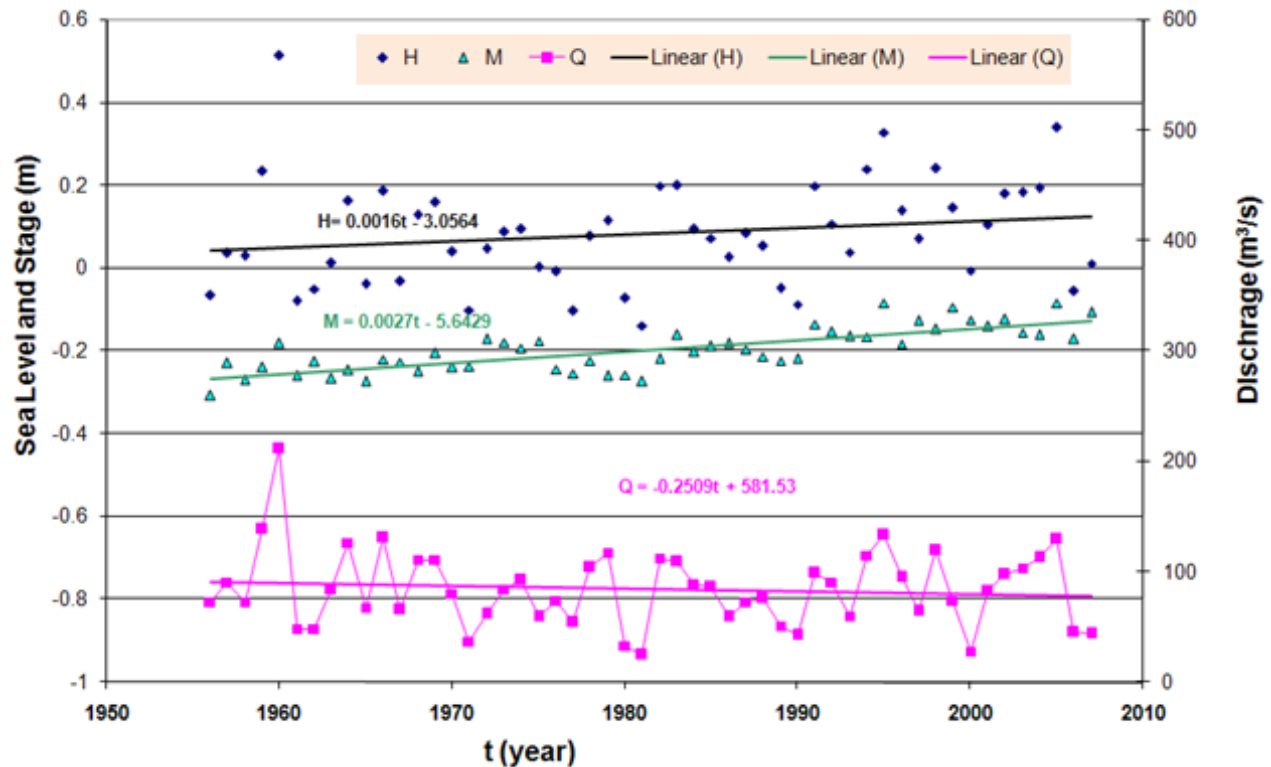


Figure 4–9. Temporal trends in stage (H) and discharge (Q) at DeLand and stage (M) at Mayport, 1956 to 2007.

4.2.6 SUMMARY

Middle St. Johns River stage is dominated by ocean water level for periods when river discharge is less than the average discharge. The dominance of ocean water level on river stage occurs over the entire 300 km of the lower and middle St. Johns River. Prediction of the physical effects of water withdrawals over this river reach requires a hydrodynamic model to account for the effects of ocean water level on flow, circulation, and mixing throughout this system. The dominance of ocean water level on stage in the middle St. Johns River under low flow conditions has direct application to the effects of water withdrawals on river stage. Under low flow conditions, the fraction of flow removed by withdrawals is greatest, yet a reduction in discharge has the least effect on stage because stage is predominately governed by ocean water level and not by discharge at these times. During low flow periods, large fractional reductions in discharge have a relatively small effect on river stage.

In this context, an evaluation of the effects of reduction of discharge at DeLand, whether by direct surface water withdrawals for water supply or by diversion of waste streams for reuse, should not focus on reduction of river stage, but on possible increases to residence time, frequency of reverse flow events, and salinity.

Stage in the middle St. Johns River is increasing in response to global ocean sea level rise at a rate of 1 to 3 mm yr⁻¹. Given that the average slope from DeLand to Mayport was only 1.21mm km⁻¹ for the period of record (1956–2007), sea level rise should be considered in any long-term strategies for management of both the lower and middle St. Johns River.

4.3 SLOPE–DISCHARGE RELATIONSHIPS IN THE MIDDLE ST. JOHNS RIVER

Introduction

Although river stage and discharge in the middle St. Johns River are generally uncorrelated during low flows, surface water slope is positively correlated with river discharge (Robison 2004). This slope–discharge relationship is a fundamental hydrodynamic characteristic of the middle St. Johns River system and is used to calibrate the frictional resistance of the hydrodynamic model. Frictional resistance is adjusted in the calibration process by adjustment of spatially varying bottom roughness parameters.

In the lower St. Johns River, bottom roughness is adjusted by calibration to tidal amplitude and phase. However, in the middle St. Johns River the astronomical tide is too small to be used for calibration, and bottom roughness is instead adjusted by calibration to slope–discharge relationships. This section describes how the slope–discharge relationships of the middle St. Johns River are determined from existing observed data.

Contrast Between Upper and Middle St. Johns River Stage–Discharge Relationships

For many rivers, there is a correlation between stage and discharge so that one variable can be predicted from the other. In the St. Johns River, such stage–discharge relationships are only found in the upper St. Johns River, as illustrated by St. Johns River at Christmas (Figure 4–10). Note that stage at Christmas declines to a well-defined minimum level as discharge declines to zero. In contrast to Christmas, stage and discharge at Sanford in the middle St. Johns River are uncorrelated below the median discharge (Figure 4–11).

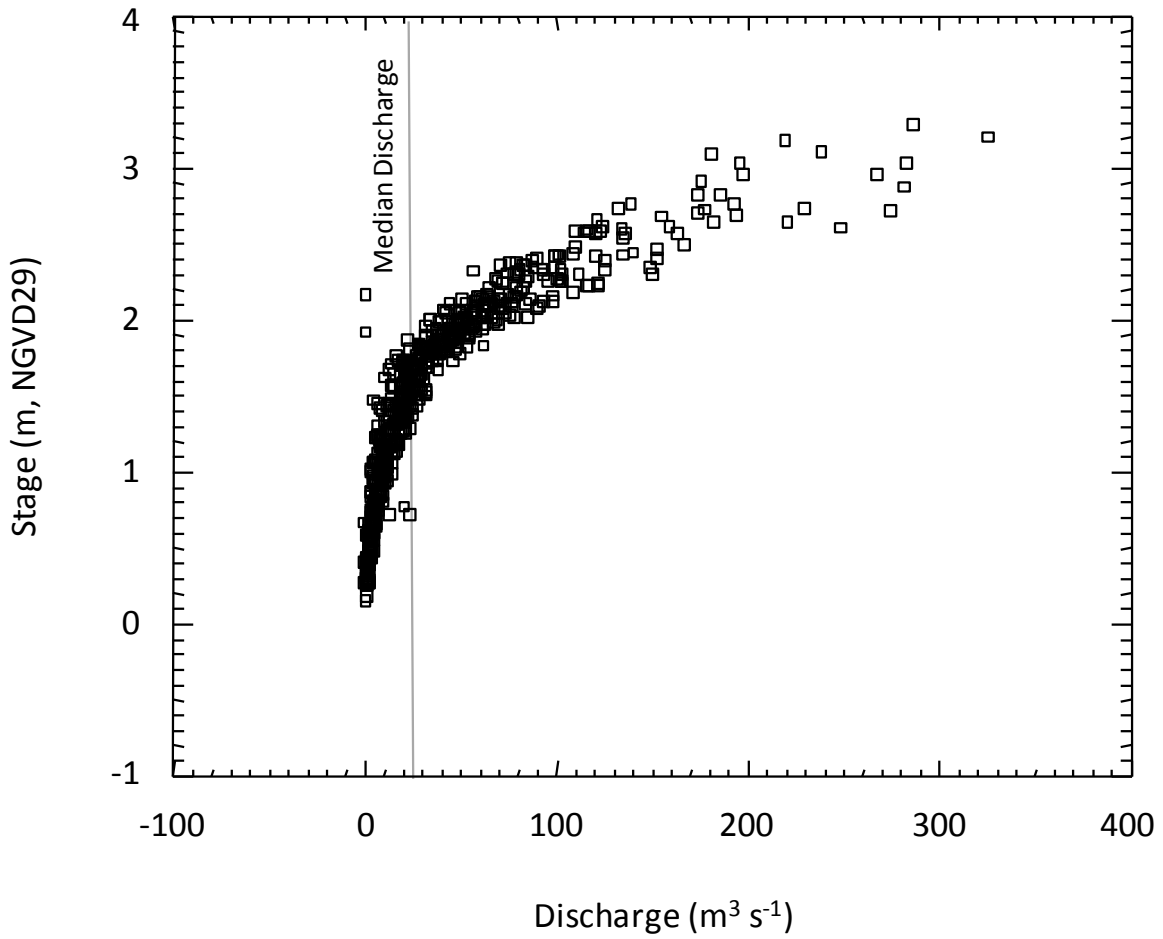


Figure 4–10. Manual observations of discharge and stage at St. Johns River at Christmas (SR 50), 1933 to 2010. Source: USGS.

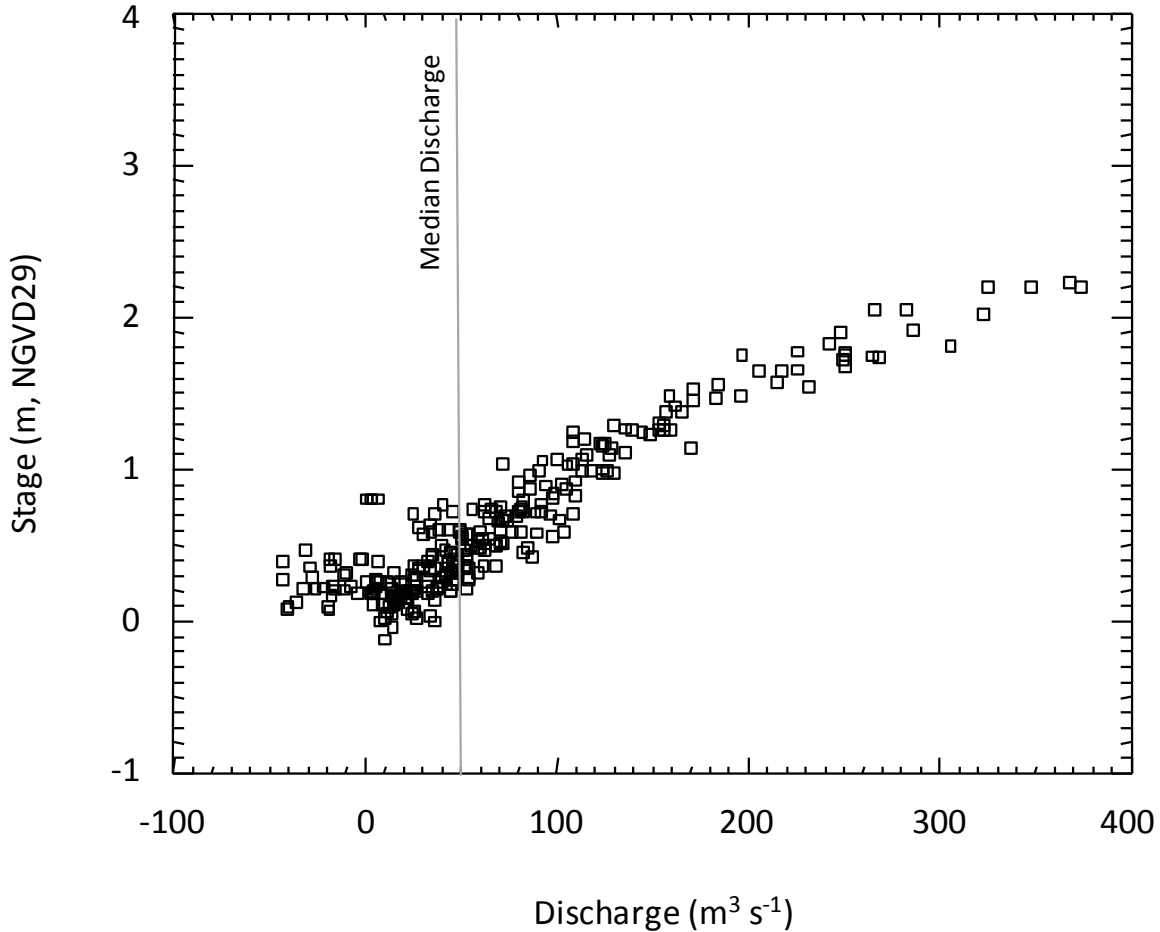


Figure 4–11. Manual observations of discharge and stage at St. Johns River at Sanford (US 17), 1941 to 2010. Source: USGS.

4.3.1 SLOPE–DISCHARGE RELATIONSHIP IN MIDDLE ST. JOHNS RIVER

Discharge in the middle St. Johns River is related to surface slope, which can be determined by the difference in stage between gauges. The slope–discharge relationship for the river reach between Astor and DeLand is shown in Figure 4–12. Paired values of daily averaged discharge and surface slope are shown. The theoretical form of the slope–discharge relationship, estimated from Manning’s Equation (Munson, Young and Okiishi 1990) using reasonable length scales for the local river channel (width = 300 m and depth = 3 m) with a Manning’s n of 0.04, is shown as the solid red curve in the figure. The theoretical form illustrates the similarity in form between the observed slope–discharge relationship and the theoretical Manning’s relationship where discharge is related to the square root of surface slope.

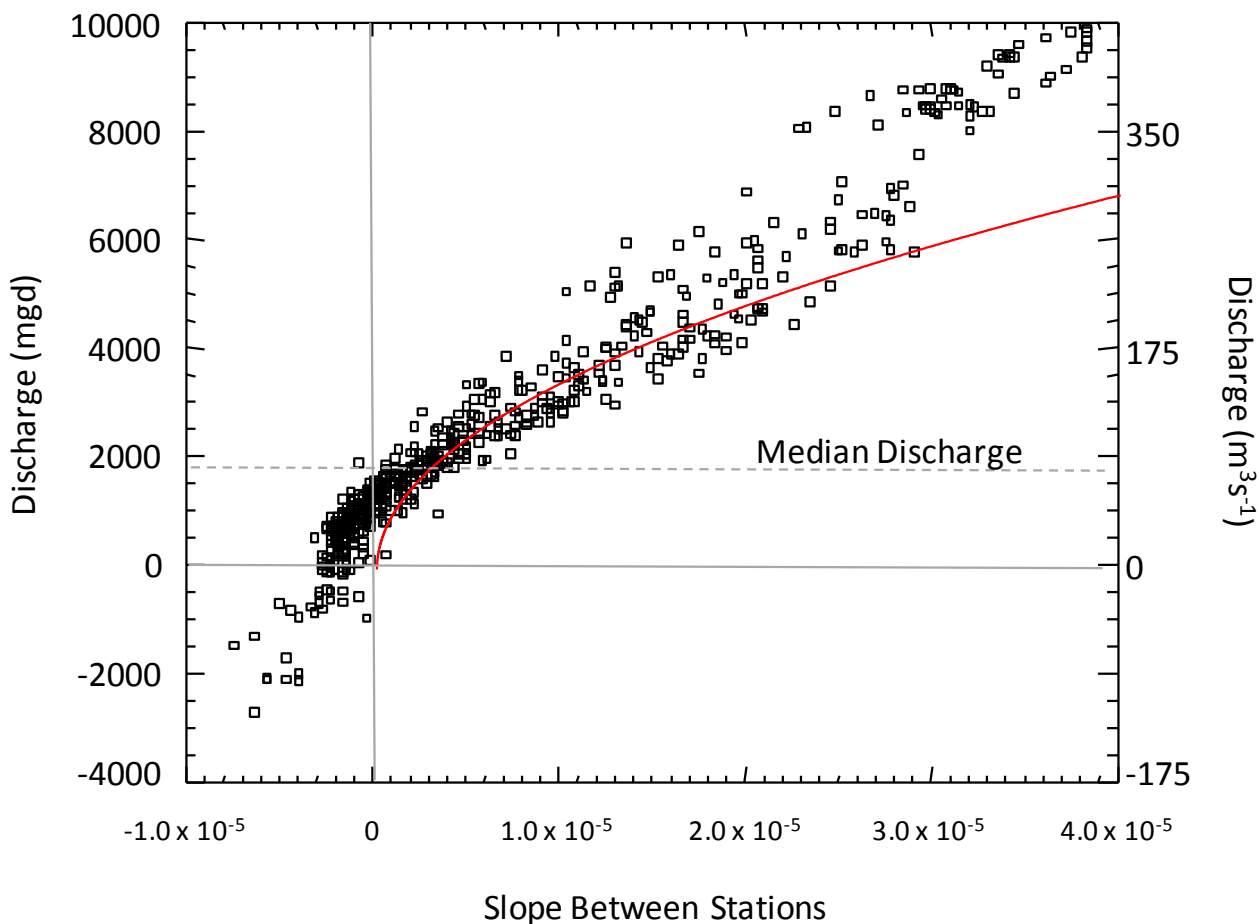


Figure 4–12. Slope–discharge relationship between DeLand (SR 44) and Astor (SR 40), 1994 to 2009. The red line shows a classical Manning’s relationship where discharge (Q) is proportional to the square root of surface slope ($\text{Slope}^{1/2}$).

4.3.2 EVIDENCE FOR ERRORS IN VERTICAL LEVELS BETWEEN STATIONS

Manning’s Equation (see Figure 4–12) produces 0 discharge for 0 slope; without energy to drive the flow, no flow occurs. The observed data consistently show considerable positive, downstream discharge at 0 slope. Downstream discharge at 0 slope could result, for a single observation, from downstream-directed wind stress, inertial motions (e.g., seiche), or time averaging of asymmetric flow oscillations (e.g., for ebb-dominated inlets). However, the first two factors would result in both positive and negative discharges at 0 slope, not a consistently positive discharge. The (daily) averaging of asymmetric flow oscillations would require sinusoidal discharge variability of amplitude much greater than the daily averaged observations. It seems highly unlikely, then, that the apparent condition of positive discharge at 0 slope is physically realistic. This discrepancy is likely caused by inaccuracy of the surveyed datum between the two stations relative to a geoidal surface, which results in leveling errors.

4.3.3 CORRECTING FOR LEVELING ERRORS BETWEEN STATIONS

In the river reach between Sanford and DeLand, the slope–discharge relationship for pre-2005 observations is linearly offset along the x-axis relative to the post-2005 observations (Figure 4–

13). The offset in the observed slope probably resulted from an adjustment to the gauge datum. The two data sets suggest, however, that a simple translation of slope (x) would force the point of 0 slope to have 0 discharge.

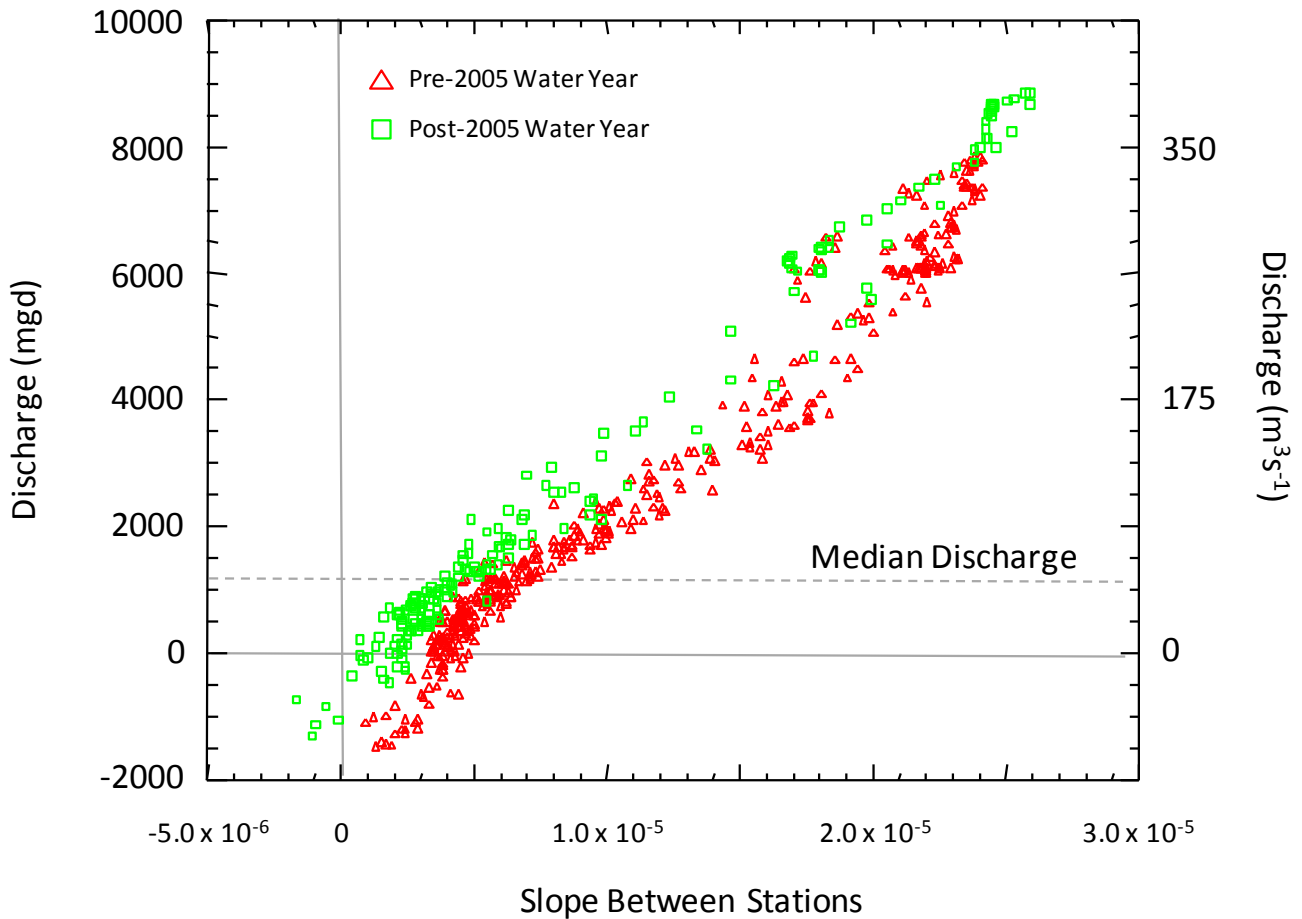


Figure 4–13. Slope–discharge relationship between Sanford (US 17) and DeLand (SR 44), 1987 to 2009.

Translation of the slope to force 0 discharge at 0 slope is complicated by the considerable scatter in observed discharge when slope is near 0 (Figure 4–14). At 0 slope, observed discharge between DeLand and Astor during the year 2000 ranged from near 0 to nearly 1500 mgd. Variability is expected in a dynamic system subject to wind forcing and inertial effects, but the central tendency for discharge should be near 0 at 0 slope. Because the problem requires adjustment of slope, the problem is better addressed by making slope the dependent variable and discharge the independent variable. A further, practical consideration is to use the numerical difference in stage (cm) between two gauges in place of slope. The inverse problem is then to find the central tendency of stage differences for discharges sufficiently close to zero.

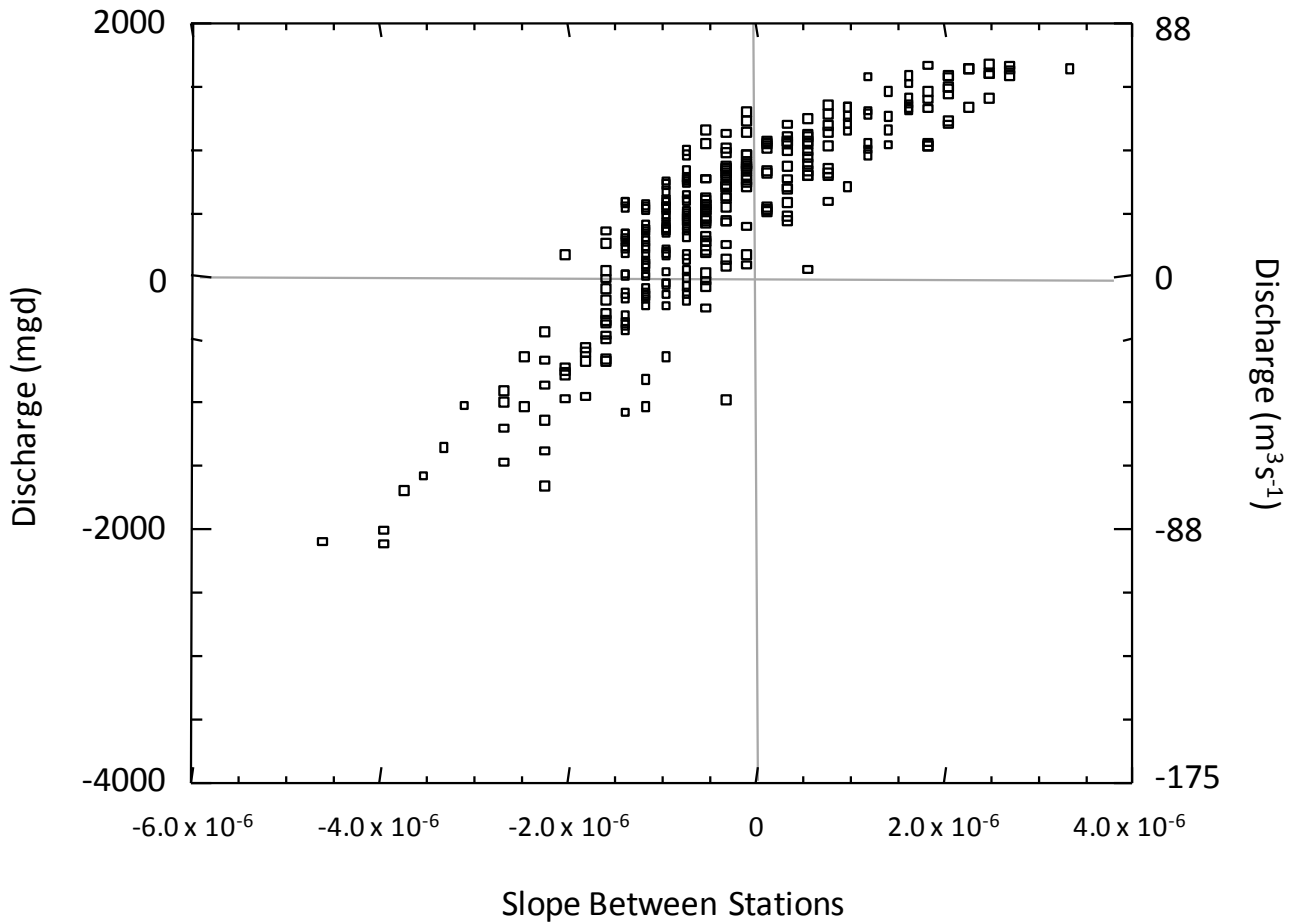


Figure 4–14. Slope–discharge relationship between DeLand (SR 44) and Astor (SR 40) for the year 2000 and limited to discharge below the long-term median.

The central tendency for stage differences over a range of discharge is determined by calculating the mean stage difference, along with the 95-th percentile for upper and lower confidence limits on the mean, for stage differences falling within 100 mgd discharge bins (Figure 4–15).

Discharge bins with fewer than 15 observations are excluded. Mean stage differences exhibit a high degree of confidence below the median discharge (blue line). For this reach, the mean stage difference at 0 discharge is -1.94 ± 0.53 cm. The vertical error in level is small, less than 2 cm over a 14-km distance.

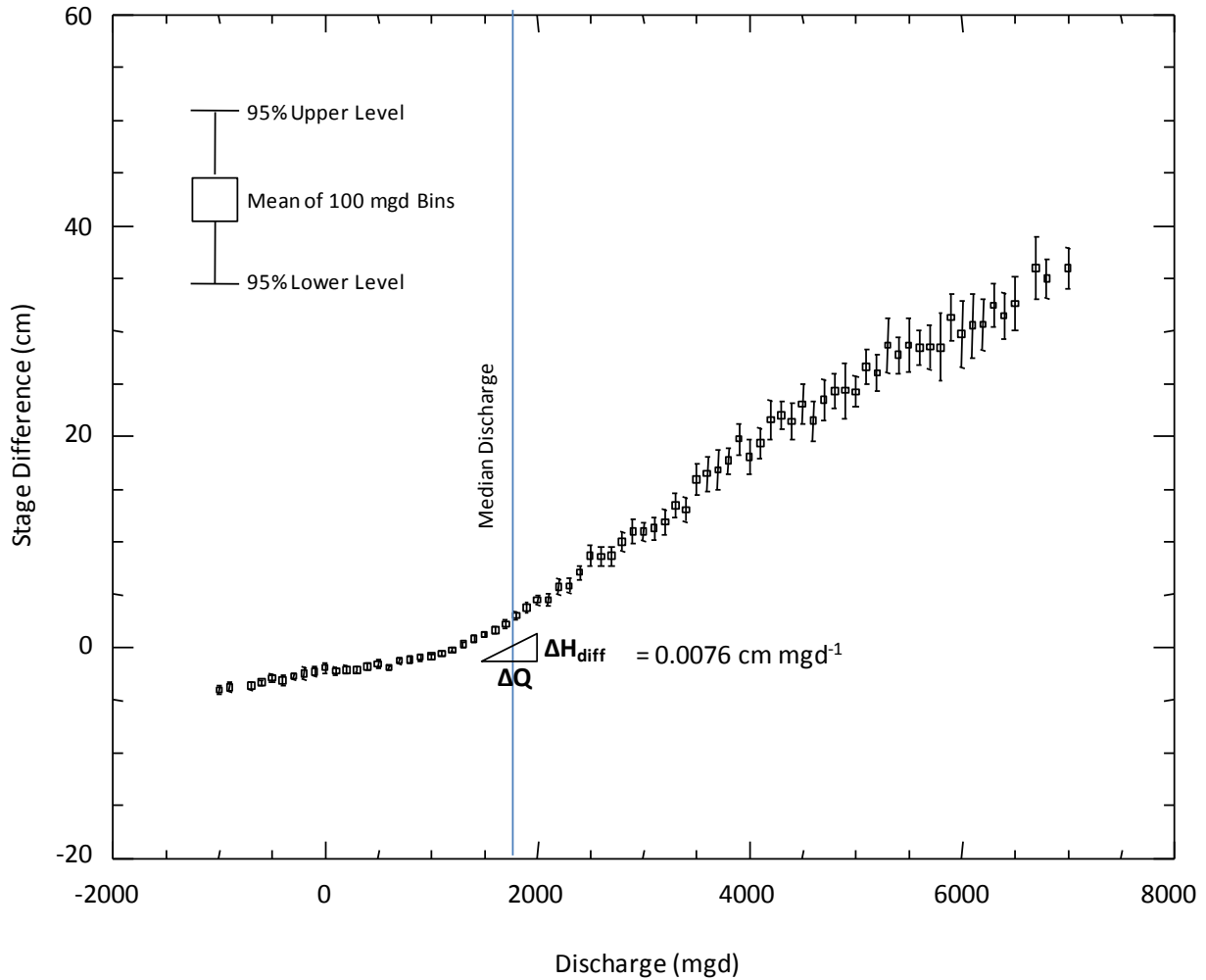


Figure 4–15. Relationship between discharge at Astor and the difference in stage between DeLand (SR 44) and Astor (SR 40), 1994 to 2009. Stage differences are presented as box plots representing the mean stage difference with 95% confidence limits within 100 mgd bins.

The curve in Figure 4–15 can be forced to have 0 slope at 0 discharge by a simple translation of the y-axis values (stage difference) by +1.94 cm. The adjusted curve is subsequently used for comparison with model results for model calibration.

Similar relationships are also developed for two other river reaches, Sanford–DeLand and Lake Harney–Sanford. For the Sanford–DeLand reach, stage difference is adjusted -8.94 cm (Figure 4–16). This offset of vertical level occurs over a distance of 30.6 km. For Lake Harney–Sanford, the required adjustment is -8.74 cm (Figure 4–17). This offset of vertical level occurs over a distance of 48 km.

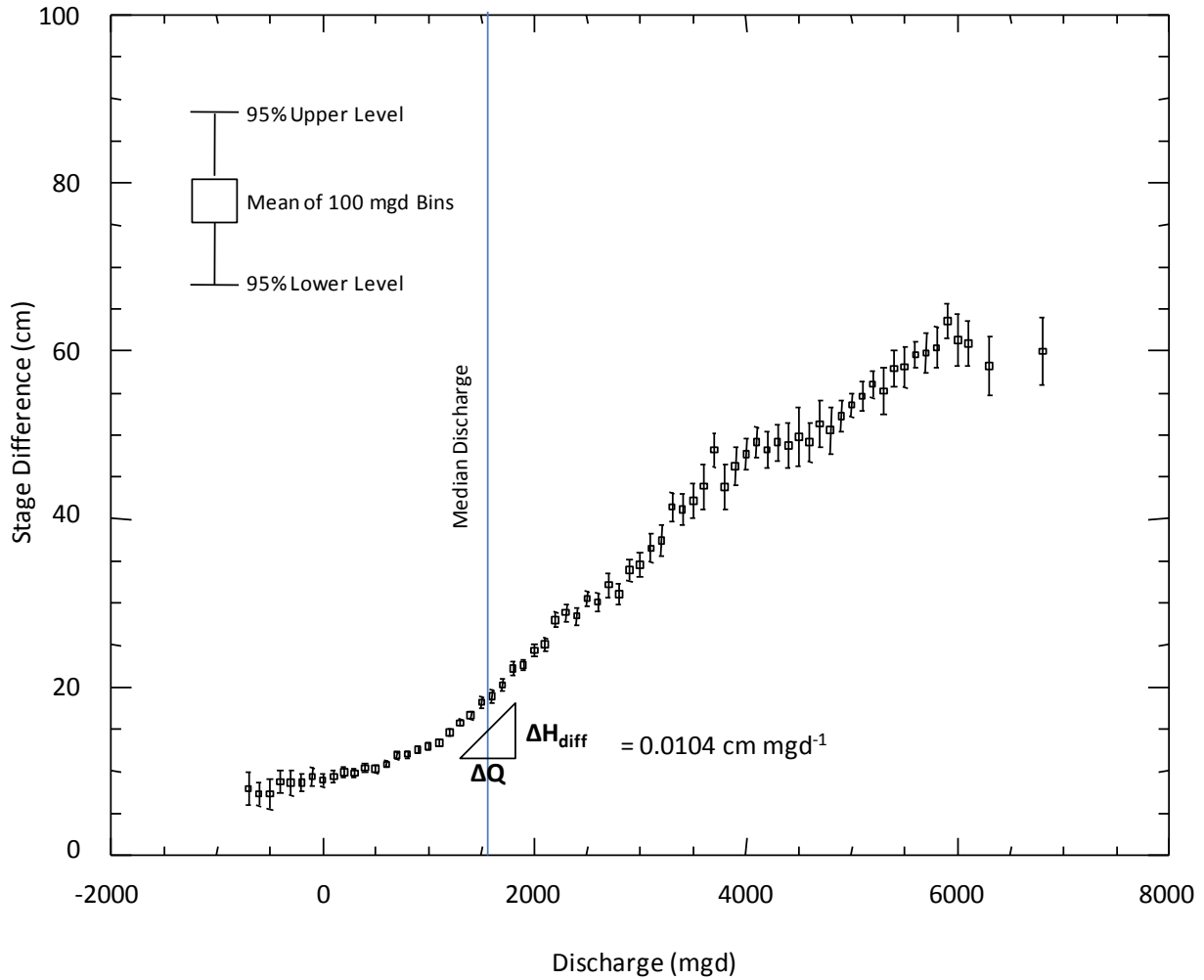


Figure 4–16. Relationship between discharge at DeLand and the difference in stage between Sanford (US 17) and DeLand (SR 44), 1987 to 2009. Stage differences are presented as box plots representing the mean stage difference with 95% confidence limits within 100 mgd bins.

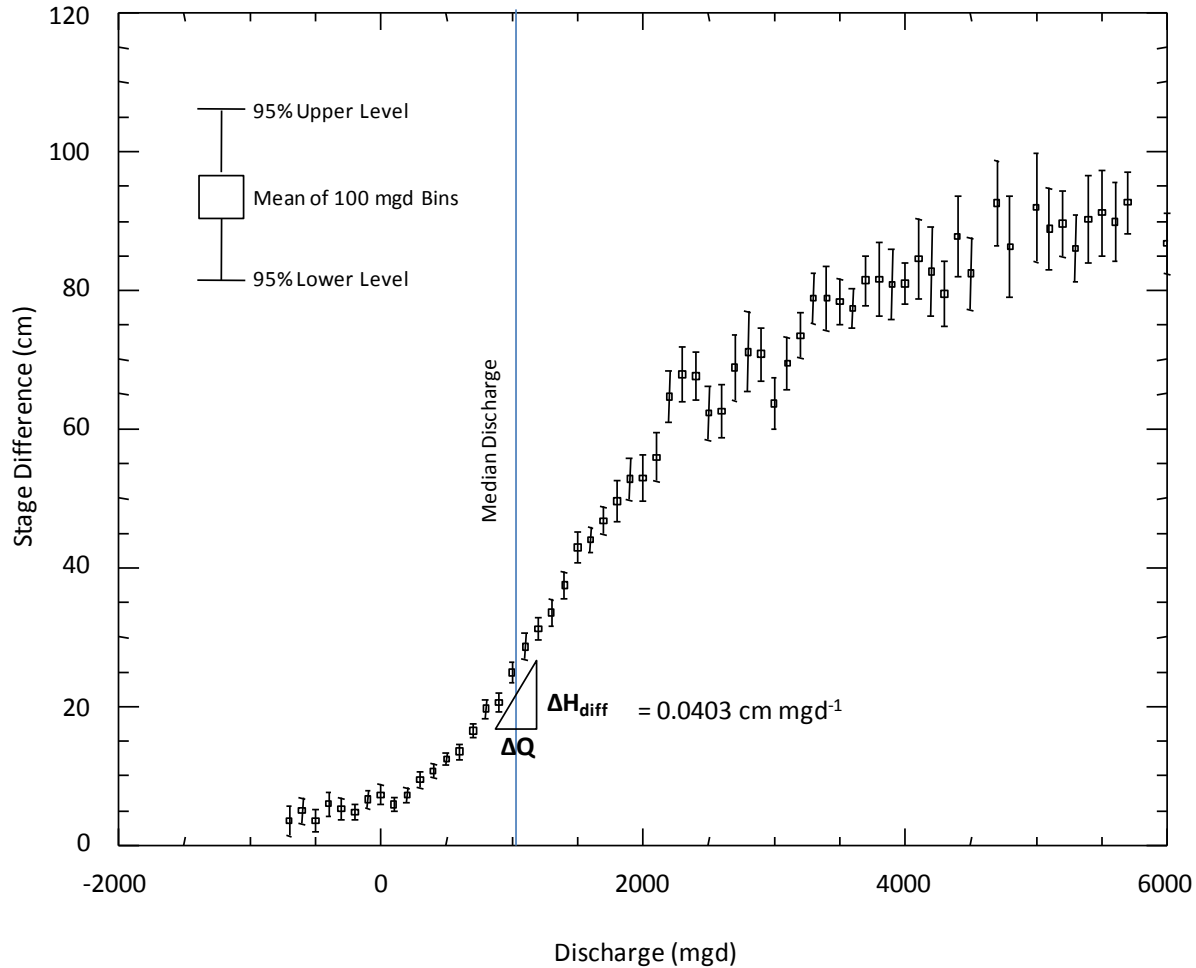


Figure 4–17. Relationship between discharge at Sanford and the difference in stage between Lake Harney (SR 46 near Geneva) and Sanford (US 17), 1987 to 2009. Stage differences are presented as box plots representing the mean stage difference with 95% confidence limits within 100 mgd bins.

Importantly, translation of the y-axis to correct for a bias in vertical level between gauges does not change the slope of the curve ($\Delta H/\Delta Q$) for a given discharge level. This means that the adjusted curves accurately represent, in an averaged sense, the change in stage per unit change in discharge. The errors in vertical levels, then, do not affect the model calibration. In addition, the slope of the curves can be used to estimate the effect of discharge reduction on stage, at least in an averaged sense.

Simple Estimation of the Effect of a Water Withdrawal on River Stage

The slope of the discharge-stage difference curves shown above can be used as a first order estimate of the expected change in stage caused by a water withdrawal. For the Astor-DeLand curve, the slope of the curve is $0.0076 \text{ cm mgd}^{-1}$ at median discharge (see Figure 4–15). A 155 mgd withdrawal under a median discharge condition would thus result in a reduction of stage of about $0.0076 \times 155 \text{ mgd} = 1.2 \text{ cm}$.

A water withdrawal causes the greatest reduction in stage where the slope of the discharge-stage difference curve is greatest. The largest slope, and thus the largest withdrawal effect on stage, occurs for discharges above the median discharge. This result is contrary to the common belief that the largest effect on stage would occur under low flow conditions, when a withdrawal removes the greatest fraction of discharge. For low discharges, the slope of the discharge-stage difference curve becomes quite flat so that water withdrawals have minimal effect on stage at low discharge.

For the Sanford to DeLand reach the greatest slope again occurs above the median discharge. A first order estimate of water level reduction resulting from a 155 mgd withdrawal in this reach is 1.6 cm at the median discharge.

For the Lake Harney to Sanford reach, the slope of the curve at median discharge is greater than for the downstream reaches and is maximal between a discharge of 500 to 2,000 mgd. Slope is considerably reduced both above 2,000 mgd and below 500 mgd. A first order estimate of water level reduction resulting from a 155 mgd withdrawal in this reach is 6.2 cm at the median discharge. This is likely an overestimate, however, because much of the proposed 155 mgd withdrawal would occur downstream of this reach. The geometry of the river causes the local discharge-stage difference curve to have the greatest slope in the river reaches upstream of Sanford. Stage in these upstream reaches is more sensitive to water withdrawals than is stage downstream of Sanford.

Summary

The adjustments of stage differences for the three reaches is +1.94, -8.94, and -8.74 cm for DeLand–Astor, Sanford–DeLand, and Lake Harney–Sanford, respectively. The overall offset in vertical level between the downstream gauge at Astor and the upstream gauge at Lake Harney is -15.74 cm. Although water level measurements at individual gauges are very precise (≈ 1 mm), this total offset is an estimate of the possible bias in vertical leveling across the region. Any study requiring comparison of water levels at two separate locations should account for a possible error between gauge datums of ± 15 cm.

The discharge-stage difference relationships are central to calibration of the hydrodynamic model within the middle St. Johns River. The vertical offsets of stage difference near 0 discharge are used to adjust the discharge-stage difference curves to force 0 discharge for 0 slope. The adjustment of stage difference by vertical translation does not affect the slope of the discharge-stage difference curve at a given level of discharge, however, and a model calibrated to the adjusted curves will predict the correct response of water level to discharge reduction.

4.4 MODELING SALINITY IN THE LOWER AND MIDDLE ST. JOHNS RIVER

4.4.1 INTRODUCTION

Salinity is a measure of the salt content of water. Salinity is used for hydrodynamic modeling of the lower and middle St. Johns River in two ways: as a means to estimate water density, and as a conservative tracer to demonstrate that water masses entering the model at different times and locations are mixing and moving through the model properly (Mangelsdorf 1964).

Salinity largely determines the water density in estuaries. Density differences, when sufficiently large, affect estuarine hydrodynamics. Horizontal density differences can drive circulation and contribute to constituent transport within the estuary. Vertical density differences can control mixing of the stratified water column. Both types of density differences are important to the hydrodynamics of a partially stratified estuary. The portions of the lower St. Johns River mixed with ocean water are nearly always partially stratified; thus, simulation of salinity is required for hydrodynamic modeling of this river reach.

Use of salinity as a conservative tracer for hydrodynamic modeling studies is generally restricted to areas having diluted seawater (waters with salts predominately derived from ocean waters). A conservative tracer is a substance that does not diminish or decay by chemical or biological processes when carried by and mixed within a fluid. The principle ionic constituents of seawater, mostly sodium and chloride, contributing to salinity are themselves conservative, so that salinity of dilutions of seawater is also conservative. Salinity of upstream freshwaters is often omitted from use as a tracer because the ions accounting for the salinity in these areas may not be conservative (particularly those contributing alkalinity)— they may be lost or gained by chemical or biological transformation. For this study, salinity is used as a conservative tracer throughout the entire study area because of the unique oligohaline character of the upstream waters. Use of salinity as a conservative tracer required careful analysis of salt composition of both the St. Johns River main stem and predominate inflows from tributaries, springs, and diffuse groundwater (see Chapter 4. Groundwater Hydrology).

4.4.2 SALT COMPOSITION OF THE ST. JOHNS RIVER MAIN STEM

Introduction

Salinity along the lower and middle St. Johns River main stem ranges from 0.1 in upstream areas under high flow conditions to over 36 near the mouth. High salinity waters near the mouth are derived from ocean salts and salt composition is nearly identical to seawater. Of particular interest here are upstream oligohaline waters where salinity ranges from 0.1 to 1.5. High salinity in these upstream areas occurs during extended periods of low flow when river water is most affected by groundwater inflow and the associated flux of chlorides from relict seawater (Odum 1953). However, salinity can decline 80% to 90% during the transition from low to high flow conditions and the question of whether this rapid dilution by surface water runoff shifts salt composition away from sodium-chloride dominance to the typical calcium-bicarbonate dominance of fresh surface waters is important for use of salinity as a conservative tracer. Sodium and chloride are conservative, while carbonate and bicarbonate, because they participate in acid base reactions, are not conservative.

Salt composition at 13 mainstem locations under low, median, and high discharge conditions is examined using Maucha diagrams to show relative abundance of major ions. The analysis extends upstream of the study area to include the upper St. Johns River for a better understanding of salt composition and sources entering the upstream model boundary. The examination of salt composition showed that the St. Johns River main stem is dominated by sodium, chloride, and sulfate ions over a wide range of discharge conditions. Because these are conservative ions, the associated salinity is also conservative.

The Maucha Diagram

The Maucha diagram, or ionic polygonic diagram, shows the relative abundance of the major cations and anions in water (Maucha 1932). Relative abundance is the ratio or percent of each constituent in solution. The same eight major cations and anions are found in both ocean and fresh waters—chloride (Cl⁻), sulfate (SO₄²⁻), potassium (K⁺), sodium (Na⁺), magnesium (Mg²⁺), calcium (Ca²⁺), bicarbonate (HCO₃⁻), and carbonate (CO₃²⁻). (For the remainder of this chapter the charge is omitted.) The Maucha diagram is a useful method of comparing the relative abundance of ions for locations with widely varying concentrations (Silberbauer and King 1991).

Creation and use of the Maucha diagram is illustrated by comparing the average salt composition of the middle and upper St. Johns River to the salt composition of ocean water. Mean concentrations of the eight major ions from 612 samples between U.S. 192 and SR 40 is compared to the ocean standard in the top of Table 4–1. CO₃ and HCO₃ concentrations were calculated from observed alkalinity and pH. Ocean concentrations generally exceed the mean concentrations of the oligohaline reach of the St. Johns River by one to two orders of magnitude.

Relative abundance is shown by normalizing a set of eight concentrations by the average of the eight concentrations. The average of a set of normalized values, then, equals one and the sum of a set of normalized values equals eight. Normalized values for the ocean standard and oligohaline reach of the St. Johns River are shown in the bottom of Table 4–1. The normalized values show similarities between the relative abundance of ions in ocean water compared with the waters of the oligohaline reach of the St. Johns River. Finally, the normalized values are used to create Maucha diagrams for visual comparison of the relative abundance of salts between these two data sets (Figure 4–18).

Table 4–1. Comparison of eight main salt constituents in the ocean standard to average values for the St. Johns River.

	Observed Concentration (mg L ⁻¹)						Calculated Concentration (mg L ⁻¹)	
	Cl	SO ₄	K	Na	Mg	Ca	HCO ₃	CO ₃
Ocean Standard	19,354	2,712	399	10,770	1,290	412.1	140.67	1.66
Average U.S. 192 to SR 40	222.4	73.7	5.5	116.4	17.4	48.8	60.18	0.09
	Observed (Normalized)						Calculated (Normalized)	
	Cl	SO ₄	K	Na	Mg	Ca	HCO ₃	CO ₃
Ocean Standard	4.4138	0.6185	0.0910	2.4561	0.2942	0.0940	0.0321	0.0004
Average U.S. 192 to SR 40	3.2684	1.0825	0.0811	1.7098	0.2551	0.7176	0.8843	0.0013

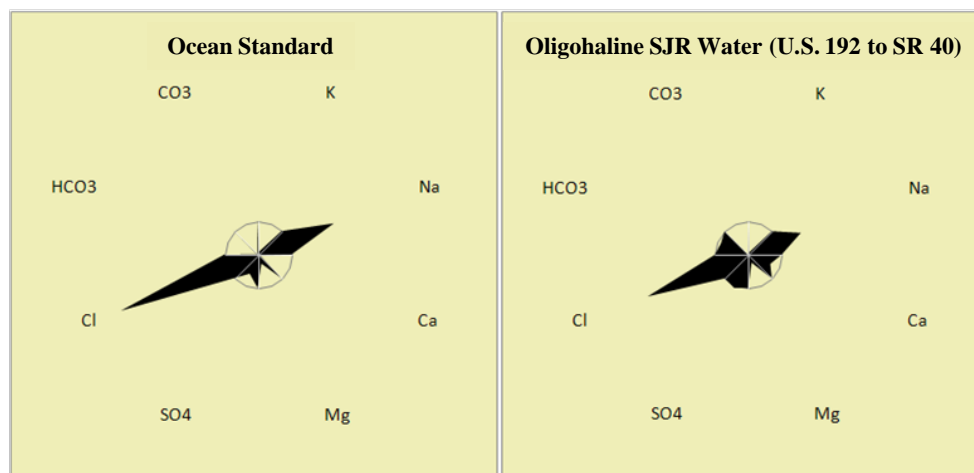


Figure 4–18. Maucha diagrams comparing relative abundance of eight major ions in ocean water with the oligohaline reach of the St. Johns River (U.S. 192 to SR 40).

The Maucha diagram shows that Cl, Na, and SO₄ are the dominant constituents of both ocean water and waters of the oligohaline reach of the St. Johns River. This similarity exists even though the salts of the oligohaline reach of the St. Johns River are terrestrial in origin and not derived from mixing with seawater. The St. Johns River water contains some Ca and HCO₃, whereas the ocean water contains almost none. Still, the dominance of the conservative Na, Cl, and SO₄ ions in the St. Johns River water is clearly shown.

Relative Abundance Over a Range of Flow Conditions

Salt composition along the St. Johns River main stem was evaluated over a range of flow conditions to determine whether relative abundance of salts shifts within any portions of the river because of dilution by surface water runoff. Specific months representing low-, median-, and high-discharge conditions were selected for analysis. The low-flow condition (April 2001) represents a period of extended drought when flow was primarily derived from groundwater and springs, making salinity correspondingly high. The median flow condition (April 2003) had a monthly median discharge at State Road (SR) 46 above Lake Harney similar to the median discharge for the period 1996 to 2006 (USGS 2004). Flow during this period is nearly equally derived from groundwater, springs, and surface water runoff. The high-flow condition (November 2004 and March 1998) represents a period following a major precipitation event when surface water runoff dominates flow and salinity is correspondingly low. (March 1998 was used to replace unavailable data for the four northern sites.) Maucha diagrams were created at 13 locations for each of these flow conditions to show the spatial and temporal variability of salt composition (Figure 4–19).

Salt composition within the study area, from SR 46 northward, is dominated by Na and Cl under all flow conditions. The only location where HCO₃ is dominant is for the median- and high-flow conditions at U.S. 192, outside the study area in the upper St. Johns River. The entire river reach upstream of the study area, from U.S. 192 to SR 46, exhibits a mixed character of salt composition under high-flow conditions with a significant fraction of Ca and HCO₃ in addition to Na and Cl. Downstream of SR 46, and within the study area, chloride dominates for all flow conditions.

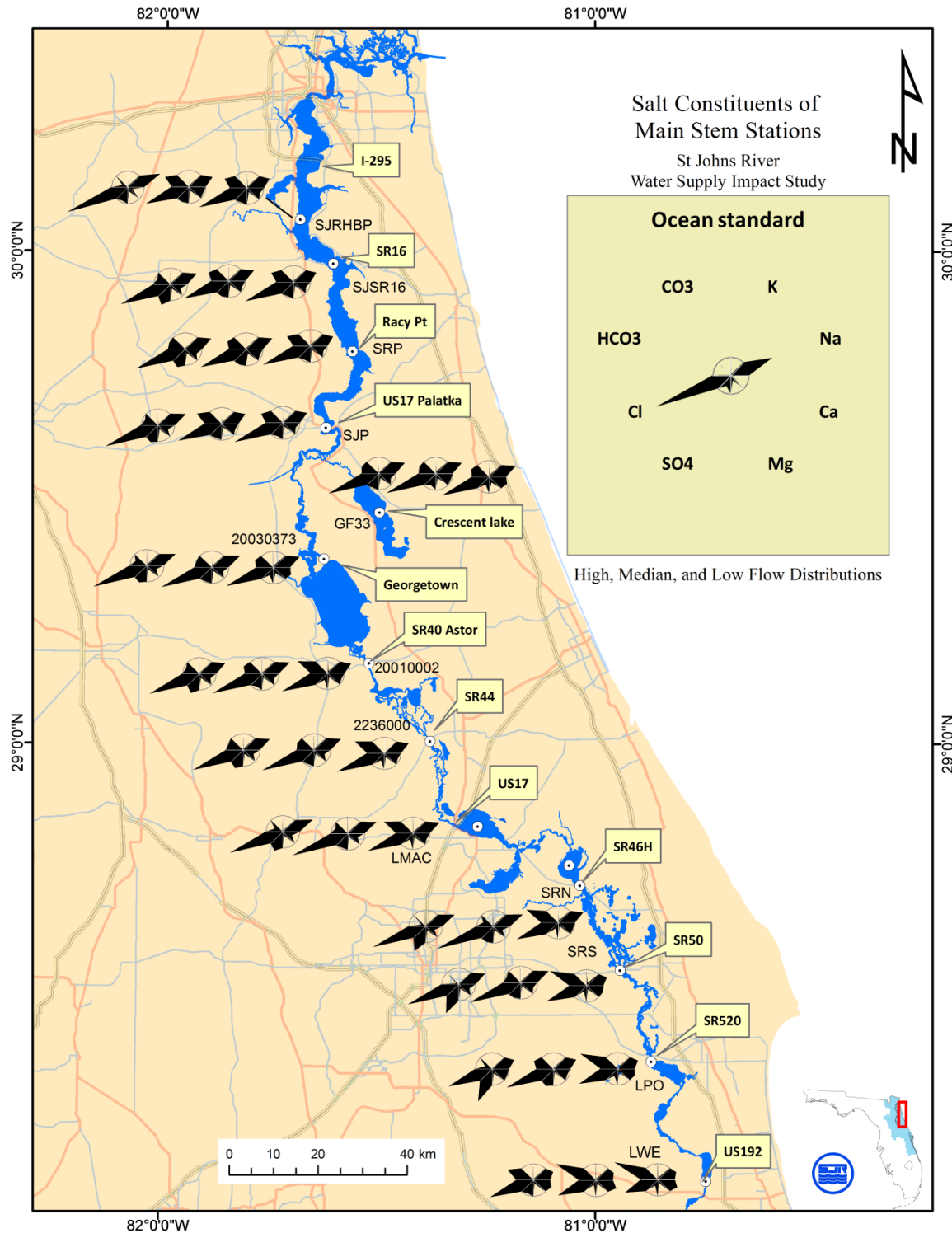


Figure 4–19. Maucha diagrams for the St. Johns River main stem. For each location the Maucha diagrams show, from left to right, relative salt abundance under low-, median-, and high-flow conditions.

The spatial shift in relative abundance of salts along the river is due to the principle source of salts within each river reach. At U.S. 192, the salt composition is characteristic of surface water

runoff. Just upstream of U.S. 192, at an elevation of about 6 m above sea level, the St. Johns River becomes a defined surface drainage feature. The salt composition is dominated by dissolution of CaCO_3 and, to a lesser extent, MgSO_4 . Salt composition changes abruptly to NaCl dominance between State Road (SR) 50 to SR 46. Because this reach has no tributaries contributing chlorides, and no springs at all, the source of this chloride can only come from diffuse groundwater discharge and associated flux of chlorides from relict seawater. The Georgetown site shows a consistent decrease in relative abundance of HCO_3^- compared with SR 40 and this feature is due to the proximity of Salt Springs, *the* major contributor of terrestrially derived NaCl mass to the river. HCO_3^- abundance increases at U.S. 17 (near Palatka) due to the addition of Silver Springs waters by way of the Ocklawaha River. Silver Springs is the largest point source for bicarbonate to the St. Johns River. Downstream of State Road (SR) 16 ocean salts begin to dominate relative abundance. The salt composition at SJRHBP during low flow conditions is essentially that of seawater.

Relative abundance of salts in Crescent Lake is similar to the adjacent St. Johns River, yet Stewart (2008) demonstrated that mixing of Crescent Lake waters with St. Johns River waters through Dunns Creek is insufficient to control salt composition of the lake. Crescent Lake instead derives its salts from local runoff. The salt composition of Crescent Lake is similar to that of Little Haw Creek, which drains north from the DeLand Ridge along the relict path of the St. Johns River through the Eastern Valley (Figure 2–9). The importance of local sources of salt to determining salt composition of such a large lake illustrates the importance of examining the salt composition of surface tributaries to the St. Johns River for the purposes of establishing proper salinity boundary conditions for the hydrodynamic model. This question is revisited later in this chapter.

Summary

The salt composition of the St. Johns River main stem and major lakes throughout the study area—the middle St. Johns River, Lake George, Crescent Lake, and lower St. Johns River—is dominated by Na and Cl under all flow conditions. NaCl dominance is maintained even when salinity in the upstream oligohaline river declines over 80% during periods of high tributary discharge. The stable salt composition dominated by conservative ions justifies the use of salinity as a conservative tracer for hydrodynamic modeling of the oligohaline reaches of the St. Johns River.

4.4.3 CONDUCTIVITY-CHLORIDE RELATIONSHIPS IN THE OLIGOHALINE REACHES

Introduction

Although chloride is not used as an independent variable in the hydrodynamic model, chloride has importance to biological processes. Conductivity–chloride relationships were examined as part of the model development process to understand the possible utility of chloride as a direct conservative tracer and to develop an understanding of the sources of salinity to the study area. The conductivity–chloride relationships for the oligohaline river are summarized here to demonstrate that chloride concentrations in the river main stem can be reasonably estimated from conductivity observations. These results have general applicability to future studies of the chemical and biological characteristics of the river system.

General Conductivity–Chloride Relationship in the Middle St. Johns River

Matched pairs of conductivity and chloride taken from 20 locations between U.S. 192 and SR 40 have a strong linear relationship with a slope less than that of diluted ocean water (Figure 4–20). The Seawater Line in Figure 4–20 shows the conductivity–chloride relationship of diluted seawater estimated from the salinity:chlorinity ratio of 1.80655 for seawater (Lewis, The practical salinity scale and its antecedents 1980). The Seawater Line is the line for which the ratio of conductivity to chloride is identical to that of diluted seawater. The conductivity–chloride curve for seawater actually has a slightly increasing slope for increasing conductivity. Over the range of conductivities shown, the Seawater Line has a slope of 0.27 to 0.30. The pooled conductivity–chloride pairs for the oligohaline St. Johns River have a slope of 0.25.

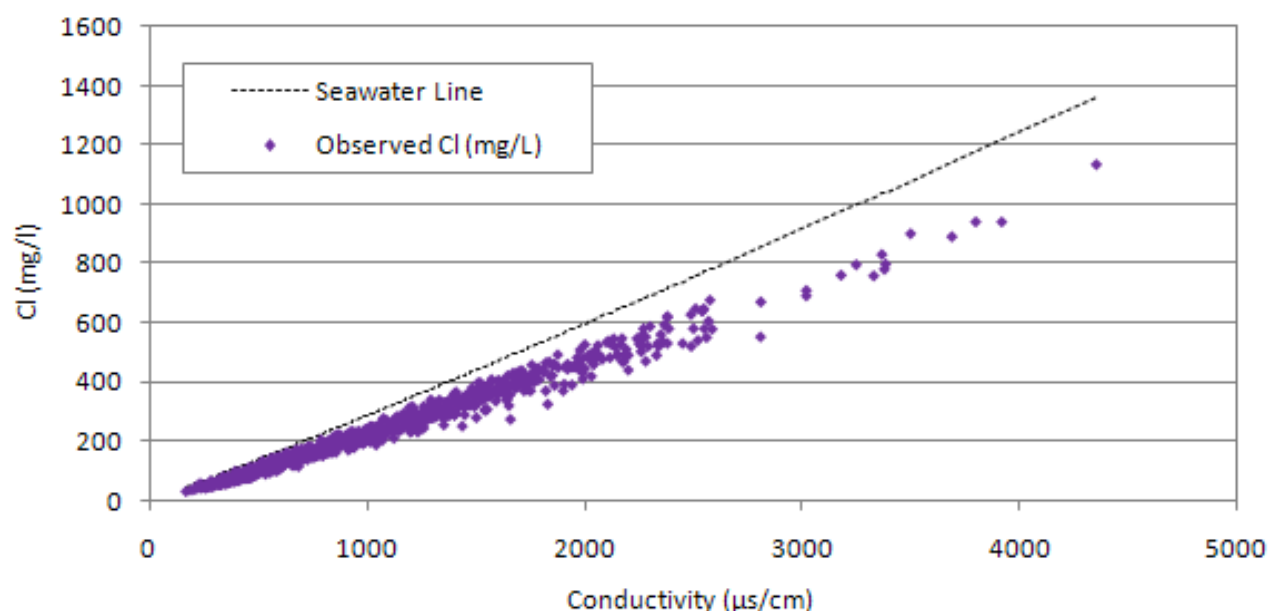


Figure 4–20. Observed conductivity and chloride, U.S. 192 to SR 40, compared with chloride of diluted seawater at the same conductivity (Seawater Line).

The lower slope for the observed St. Johns River data compared with the Seawater Line is due to a greater proportion of divalent ions in the St. Johns River waters, primarily from the dissolution of limestone (CaCO_3), dolomite ($\text{CaMg}(\text{CO}_3)_2$), and gypsum (CaSO_4). Use of a chloride:conductivity ratio of 0.25 provides a reasonable estimate of chloride from observed conductivity for the oligohaline St. Johns River. This site-specific ratio improves the estimate of chloride concentration from conductivity about 20% compared with estimating chloride by assuming chloride is in proportion to diluted seawater.

Spatial Variation of Conductivity–Chloride Relationship in Upper and Middle St. Johns River

The estimation of chloride from conductivity along the St. Johns River can be slightly improved over the constant ratio shown above by considering spatial variation of the chloride:conductivity ratio. Chloride:conductivity ratios for each of the observed locations vary from 0.21 to 0.30 (Figure 4–21). The spatial variation of the chloride:conductivity ratios are also indicators of

notable shifts in salt composition caused by local salt sources or the diluting effects of tributary inflows.

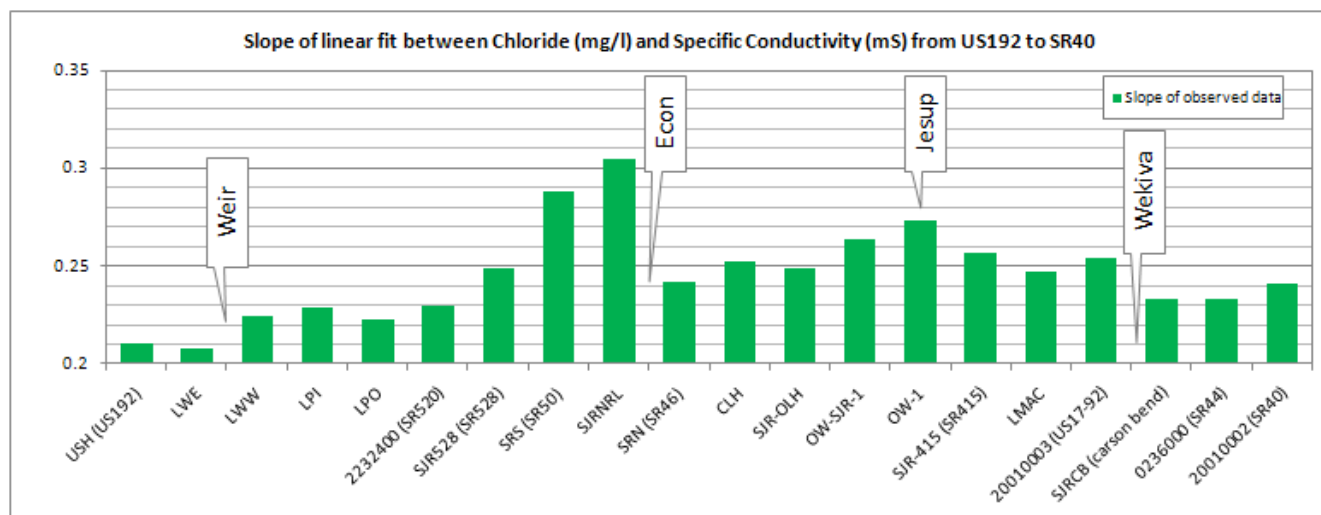


Figure 4–21. Spatial variation of chloride:conductivity ratio along the St. Johns River from U.S.192 to SR 40. The ratio for diluted seawater ranges from 0.21 to 0.30 for the ranges of conductivity considered.

A weir controlling the water level (stage) of Lake Washington exists between LWE and LWW and low conductivity:chloride ratios occur upstream of the weir. The conductivity:chloride ratio increases abruptly between SR 520 and SJRNRL in an area of high groundwater discharge. The conductivity:chloride ratio here reaches that of diluted seawater. The decline in the ratio at SRN is due to the introduction of low chloride water from the Econlockhatchee River. The ratio increases to a relative maximum near the mouth of Lake Jesup. A notable decline in the ratio occurs at the confluence of the Wekiva River near SJRCB.

The conductivity:chloride ratio varies spatially along the upper and middle St. Johns River. The spatial-variability of the ratio is consistent with major sources of salt or the diluting effects of tributaries along the river. The site-specific chloride:conductivity ratios are sufficient to calculate chloride from conductivity to within a few percent of observed values.

4.4.4 DOMINANCE OF RELICT SEAWATER IN THE SALT COMPOSITION OF THE OLIGOHALINE REACH OF THE ST. JOHNS RIVER

Introduction

The previous sections of this chapter demonstrated that the salt composition of the St. Johns River main stem is dominated by NaCl throughout the study area. The dominance of NaCl in the oligohaline reach of the river is of particular interest because these areas are far removed from direct influence of seawater. The source of salts to these areas must be known to properly set the model boundary conditions. In this section ionic ratios of river water are used to infer that the predominate source of salts to the oligohaline reach of the river is relict seawater.

Plots comparing chloride concentration with the concentration of three divalent salt species (Ca, Mg, and SO₄) are used to show deviation of salt composition from seawater for the river main stem and both springs and tributaries, which are the principle surface water sources of salt to the river (Figure 4–22). As a non-reactive constituent, chloride provides a conservative reference to the relative abundance of salts, as well as their spatial and temporal distribution, in surface waters (Sawyer, McCarthy and Parkin 1994). The data pairs for the St. Johns River main stem and tributaries are stratified by discharge into categories of high-flow (above the median discharge) and low-flow (below the median discharge). Springs are stratified by elevation relative to MSL into three categories, < 5 ft, 5 to 25 ft, and > 25 ft.

Within each plot, deviation from the composition of seawater is indicated by location of points above a Seawater Line. The Seawater Lines shown here are similar to those used for the previous conductivity–chloride analysis. The Seawater Line is the line for which the ratio of the independent chloride variable with the dependent ion would be identical to the ratio for diluted seawater. The Seawater Line defines a lower limit of ion:chloride ratio for comparison with observed ratios. Ratios exceeding the ion:chloride ratio of seawater are seen as points that plot above the Seawater Line and indicate the addition of salts from dissolution rather than direct flushing of salts from relict seawater (Sacks and Tihansky 1996).

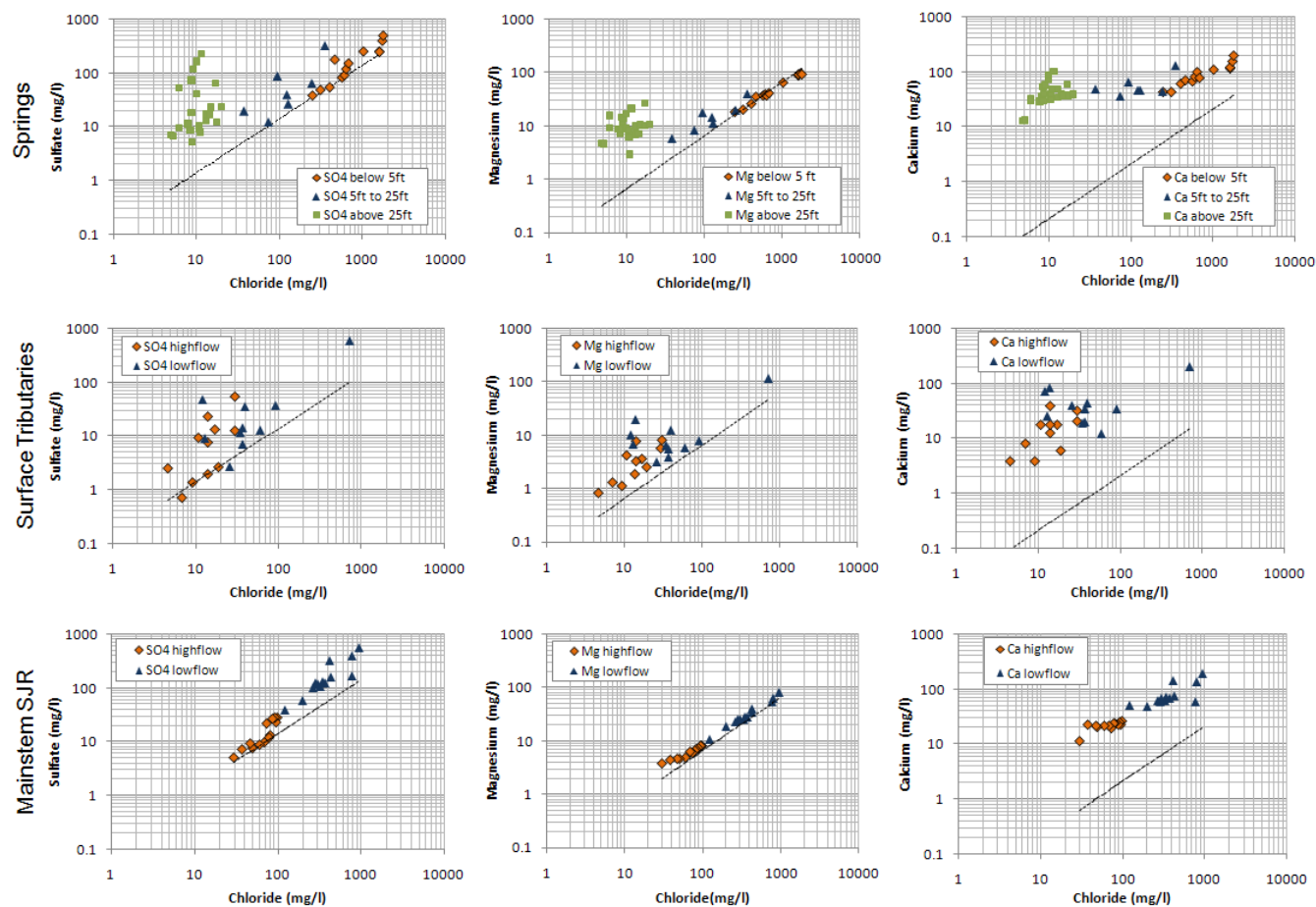


Figure 4–22. Ratios of Cl concentration with concentrations of SO₄, Mg, and Ca for springs, surface tributaries, and the middle St. Johns River main stem. The Seawater Line (dashed) is the ratio of diluted seawater.

Salt Composition of Springs

The SO₄:Cl ratio for springs shows a distinct shift to dissolution for springs above 25 ft. Springs between 5 and 25 ft have a mixed character but tend to converge with the Seawater Line, while springs below 5 ft (including submerged springs) all converge with the Seawater Line. The SO₄:Cl ratio for springs shows clearly that the dominant source of salts from springs shifts from relict seawater to dissolution above 25 ft elevation. The Mg:Cl ratio for springs confirms the shift in salt dominance above 25 ft elevation.

Because Calcium (Ca) is almost a trace element in ocean water, observed Ca:Cl ratios are greater than that of seawater and points on the plots of the Cl-Ca relationship lie above the Seawater Line, showing that dissolution of Ca is present throughout the system. Ca concentrations remain fairly constant over the range of spring elevations, however, while Cl concentration shifts two orders of magnitude, an indication of increased dominance of relict seawater in salt composition for increasing spring salinity.

Salt Composition of Tributaries

Ratios for tributaries had no distinct pattern, some tributaries fall close to the Seawater Line and some do not. Tributaries that fell on the Seawater Line generally remained along the line under both high- and low-flow conditions, showing a constancy of salt composition. Some tributaries, however, showed a shift towards the Seawater Line under high-flow conditions and a shift away from the Seawater Line under low-flow conditions. For these tributaries, a greater fraction of groundwater under low-flow conditions results in an increase in the abundance of salts attributable to dissolution.

Salt Composition Along the St. Johns River Main Stem

The plotted ratios along the St. Johns River main stem show greater similarity to seawater than either the tributaries or springs. The $\text{SO}_4:\text{Cl}$ ratios are closer to the Seawater Line under high-flow than low-flow conditions. This feature indicates an increase in salts from dissolution when the fraction of groundwater increases. The $\text{Mg}:\text{Cl}$ ratios along the St. Johns River main stem fall almost directly on the Seawater Line. The slight drift towards dissolution of Mg under high-flow conditions occurred only for the upper St. Johns River sites. The $\text{Ca}:\text{Cl}$ ratio shifts towards the Seawater Line with increasing Cl under low-flow conditions indicating increased influence of relict seawater at these times. The greater similarity of the salt composition of the St. Johns River main stem to seawater compared with either springs or tributaries indicates the importance of a third source of salts, in this case, relict seawater entering the river by diffuse groundwater discharge.

Maucha Diagrams of the Upper St. Johns River

Chloride concentration and conductivity within the oligohaline reach of the river exhibit a relative maximum in the lower portions of the upper St. Johns River between SR 50 and SR 46 (Figure 4–21). This river reach has no springs and few tributaries upstream of the Econlockhatchee River, so that salt composition is dominated by relict seawater from diffuse groundwater discharge. Artesian wells in this area have the highest chloride concentrations in the upper St. Johns River (Brown 1962). An analysis of the salt composition of these waters, using Maucha diagrams, confirms that the salt composition of waters dominated by relict seawater are nearly identical to the salt composition of seawater. This means also that the salt composition of relict seawater is identical to modern seawater.

Maucha diagrams for six lakes in this reach confirm the strong similarity of the salt composition to seawater (Figure 4–23). The salt composition of three of the lakes, Salt (Site SALT), Loughman (Site LOUG), and Fox (Site FOX), is closest in character to seawater of any location examined along the St. Johns River Valley upstream of the direct influence of seawater. This result is additional evidence that the dominant source of salts to the oligohaline reach of the St. Johns River is relict seawater and that diffuse groundwater discharge is an important mechanism for movement of relict seawater into the river.

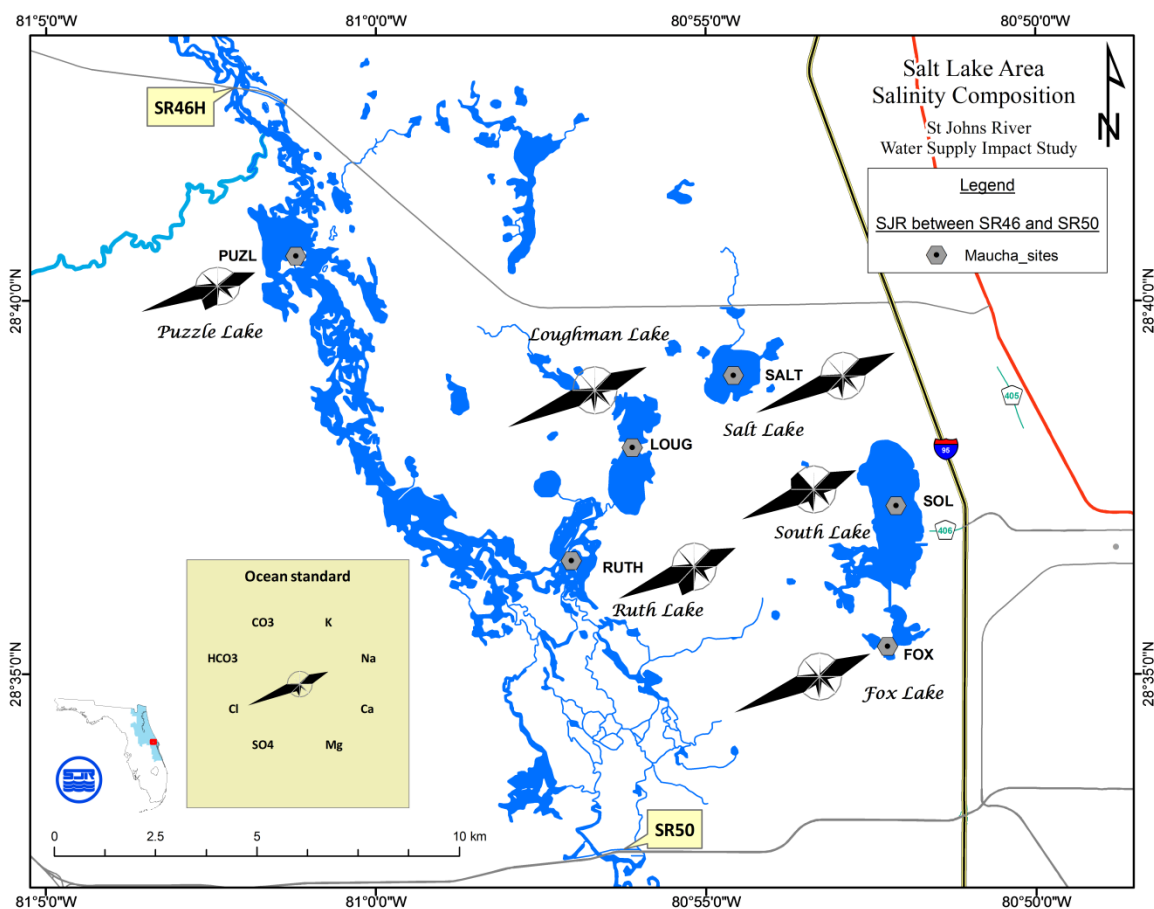


Figure 4–23. Maucha diagrams for lakes in the St. Johns River valley between SR 50 and SR 46.

Summary

The greater similarity of the salt composition of the St. Johns River main stem to seawater compared with either springs or tributaries indicates, by inference, the importance of a third source of salts, in this case, relict seawater entering the river by diffuse groundwater discharge. If the dominant source of salts were from springs or tributary runoff alone, then the salt composition of the St. Johns River main stem would be characteristically like those sources in both composition and concentration.

An understanding of the salt composition of various sources of salt to the river is useful for setting model boundary conditions in areas lacking sufficient direct observations of salinity. For springs, salt composition is closely associated with spring elevation, and both concentration (salinity) and composition of salts from springs can be inferred, in the absence of observed data, from spring elevation. Given the wide range of salt characteristics of the tributaries shown here, and need for estimating salinity of ungauged watersheds for model boundary conditions, a further understanding of the salt composition of tributaries is needed, particularly in areas where tributaries supply relict seawater. This information is developed in Section 4.4.5. The nearly identical salt composition of relict seawater and modern seawater means that groundwater salinity can be calculated from observed chloride where that is the only measured parameter.

4.4.5 CLASSIFICATION OF SOURCES OF SALT BY SALT COMPOSITION

A thorough understanding of the salt composition of sources of salt to the river is useful for developing salinity boundary conditions for the hydrodynamic model. Salt composition is used, for example, to infer properties of salinity from ungauged tributaries and springs. Expected salinity levels, stability of salinity in time, and relationship between salinity and discharge can all, to an extent, be inferred from knowledge of salt composition. Rather than considering salt composition as a continuous spectrum of ionic concentrations, additional order is gained by a classification of salt composition into a few meaningful categories. USGS classified Florida springs by salt composition (Slack and Rosenau 1979) and this classification is applied here for both springs and tributaries by means of Maucha diagrams.

Classification of Springs by Salt Composition

Springs within the study area can be classified into one of four categories of salt composition (Figure 4–24). The four categories are summarized by the following dominant salt characteristics:

- NaCl (Chloride): Sodium-chloride dominance
- Ca-Mg-HCO₃ (Bicarbonate): Calcium-Magnesium-Bicarbonate dominance
- Mixed Cl- HCO₃ (Mixed): No distinction between NaCl or Ca-Mg-HCO₃ dominance
- Ca-SO₄ (Sulfate): Sulfate dominance

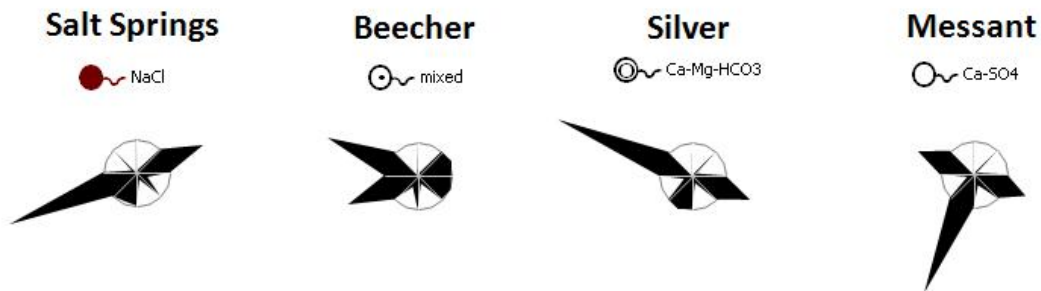


Figure 4–24. Springs representative of the four categories of salt composition used to classify springs.

Classification of major springs throughout the study area shows the predominance of chloride springs near the St. Johns River main stem and concentrated in the middle St. Johns River and Lake George (Figure 4–25). Bicarbonate springs are more distant from the river and above 25 ft elevation. Blackwater Creek is unusual in having sulfate springs in its upper reaches.

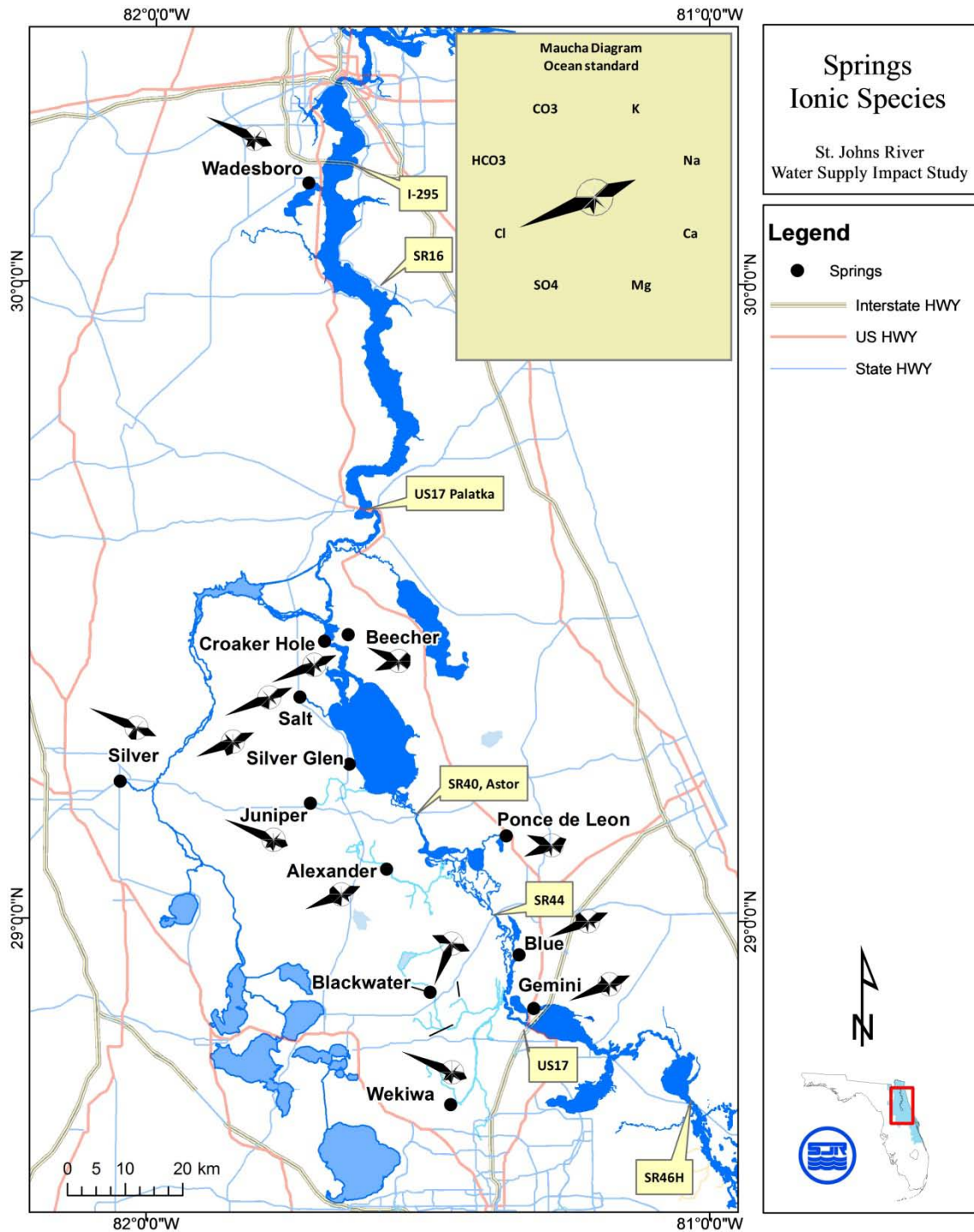


Figure 4–25. Maucha diagrams for major springs in the study area.

Classification of Surface Tributaries

Surface water tributaries can be classified by salt composition using the same four categories used for springs (Kaufman 1975). Salt composition of some tributaries shifts categories when

discharge conditions shift from low to high discharge. Maucha diagrams representative of surface tributaries falling within the four categories of salt composition are shown in Figure 4–26.

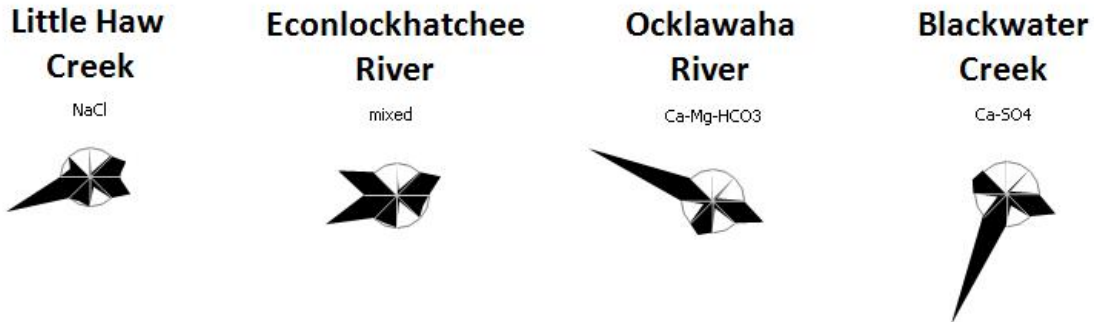


Figure 4–26. Tributaries representative of the four categories of salt composition used to classify St. Johns River tributaries under low-flow conditions.

Maucha diagrams of representative tributaries show the differences between salt compositions of tributaries under low- and high-flow conditions (Figure 4–27). Salt composition under low-flow conditions is generally representative of base flow. Base flow is the groundwater contribution where the water table intersects a stream channel (Linsley 1982). For some tributaries that are highly disturbed by agricultural or urban activities, base flow is partly maintained by the addition of water from irrigation or wastewater treatment discharge (e.g., Site DPB near Racy Point). In Black Creek (Site NBC near SR 16), the salt composition during low-flow conditions becomes chloride dominated because of direct intrusion of seawater from the adjacent St. Johns River.

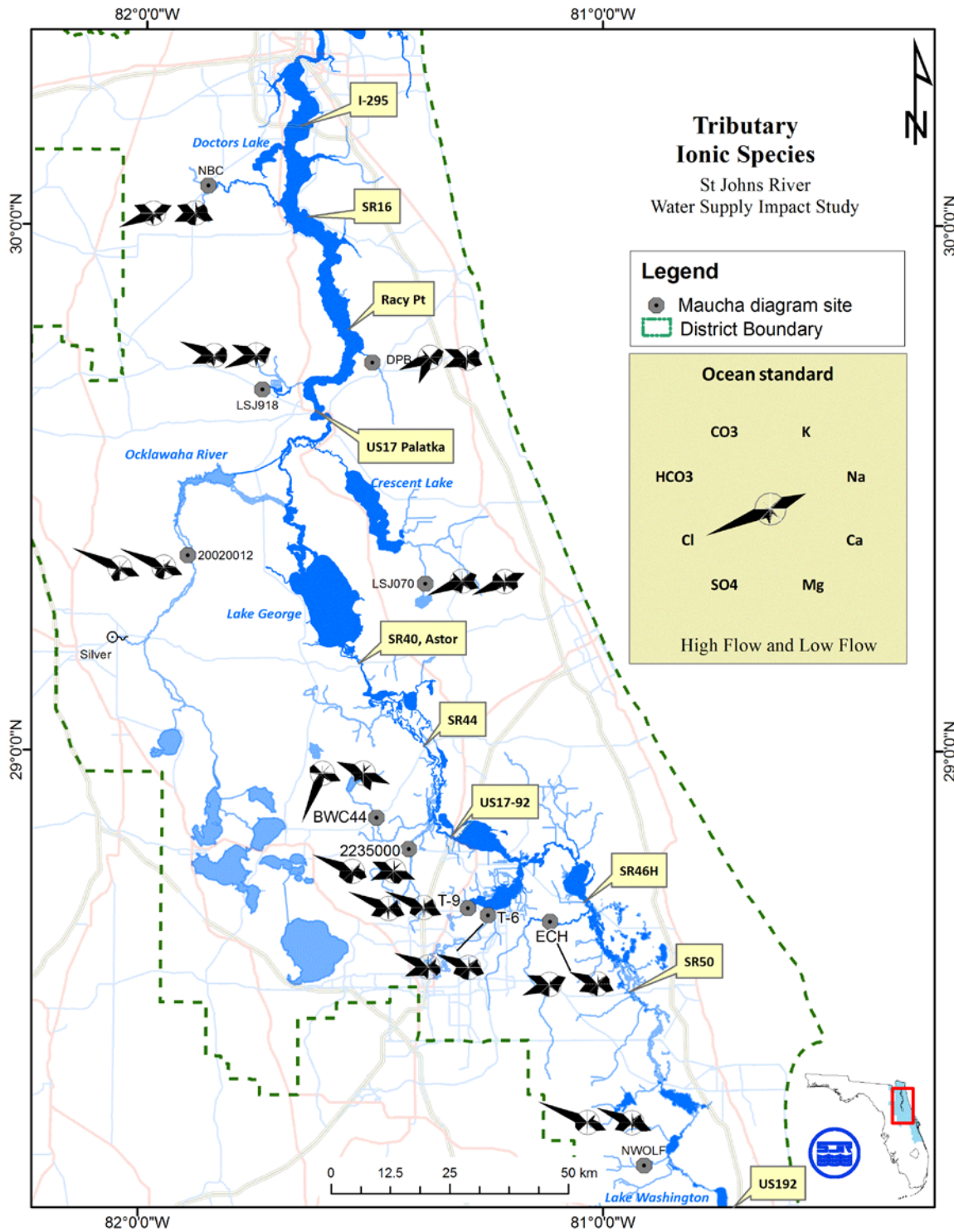


Figure 4–27. Maucha diagrams of selected tributaries to the St. Johns River under low-flow (left) and high-flow (right) conditions.

The salt composition of tributaries tends towards the typical bicarbonate dominance of surface waters because tributaries generally drain higher areas above 25 ft elevation. A clear example of

bicarbonate dominance is the Ocklawaha River, the largest tributary of the St. Johns River. The Ocklawaha River (Site 20020012) is a stable bicarbonate tributary, first, because it drains the areas of highest elevation in the watershed, and second, because of the dominance of Silver Springs—on average Silver Spring accounts for 70% of the river flow. Wolf Creek (Site NWOLF) in the upper St. Johns River and Gee Creek (Site T-9) entering Lake Jesup are the most stable bicarbonate tributaries in the study area.

Two urbanized tributaries, the Econlockhatchee River (Site ECH) and Howell Creek (Site T-6), are adjacent to Wolf Creek and Gee Creek, yet are mixed tributaries. The mixed salt composition of these highly urbanized watersheds illustrates the importance of land use to salt composition. Salt composition in urban runoff can be altered from natural conditions by direct discharge of treated municipal wastewater, runoff of municipal water being used for lawn irrigation, or relict agricultural wells (FDEP 1997). The Econlockhatchee River receives inflow from Iron Bridge, a regional wastewater treatment system. On average (1995 to 2006) discharge from Iron Bridge is about 4% of the total Econlockhatchee River discharge, but the proportion rises during drought. Iron Bridge accounts for 20% of the flow for 10% of days.

Little Haw Creek (Site LSJ070) drains into Crescent Lake and is a stable chloride tributary. This creek drains a watershed that was an island during a previous high stand of sea level, when the St. Johns River Valley was inundated by seawater. The chloride dominance of the tributary is an indication of the continued flushing of relict seawater from groundwater (Tibbals 1990) that may be enhanced by artesian pumping (Munch 1979). The contribution of relict seawater from some tributaries, in addition to springs and diffuse groundwater, points to the need to account for this additional source of salts when setting model boundary conditions.

4.4.6 DISCHARGE-CHLORIDE RELATIONSHIPS

St. Johns River Main Stem

The oligohaline reach of the St. Johns River main stem contains salts derived primarily from relict seawater and has a salt composition dominated by chloride. Relict seawater enters the river through springs and diffuse groundwater discharge where it is mixed with low-chloride surface waters. This mixing process can be conceptualized as a small discharge with high chloride concentration (relict seawater) mixing with a larger discharge of low chloride concentration (surface water runoff). The resultant dynamics of mixing process produces a well-defined discharge–chloride relationship. The discharge–chloride relationship typical of waters influenced by relict seawater is demonstrated here for the oligohaline reach of the middle and upper St. Johns River main stem because this reach has good discharge gauging coupled with reliable chloride observations (see Chapter 4. Groundwater Hydrology).

Plots of matched pairs of discharge and chloride for six mainstem locations between U.S.192 and SR 40 produce an L-shaped pattern (Figure 4–28). In upstream areas most affected by relict seawater (SR 520 to SR 46) chloride and discharge are strongly correlated and are related by a power law. A power law relates chloride concentration (Cl) to discharge (Q) raised to a power ($Cl \sim Q^n$). At downstream sites, the characteristic L-shaped pattern becomes more diffuse, but the power law relationship is still evident.

The L-shaped pattern for the discharge–chloride relationship results because of the balance between the rate of input and rate of flushing of relict seawater. For a typical range of discharge

conditions, surface water discharge (Q_{SW}) is much larger than total groundwater discharge from springs and diffuse groundwater (Q_{GW}). Although the groundwater chloride concentration (Cl_{GW}) is much greater than surface water chloride concentration (Cl_{SW}), Q_{SW} dominates and the resultant chloride mixture of the river is driven towards a steady-state only slightly greater than Cl_{SW} . The time to achieve steady-state is proportional to the hydraulic residence time, $HRT = \text{Volume}/Q_{river}$, where $Q_{river} = Q_{SW} + Q_{GW}$. For typical discharge conditions, HRT is small and the chloride concentration of the river is driven to Cl_{SW} rapidly.

Under drought conditions, total discharge to the St. Johns River is dominated by groundwater discharge (Q_{GW}) as surface water discharges (Q_{SW}) decline. River chloride concentration then rises towards the chloride concentration of the inflowing groundwater (Cl_{GW}). However, the total river discharge (Q_{river}) is now small, HRT is correspondingly large, and the time to steady-state is very long. Steady-state is likely never achieved during droughts, so that the *duration* of the drought governs the maximum chloride level achieved. The variability of drought durations, then, produces the wide spread of chloride concentration when discharge is near 0, thus forming the left-hand side of the L-shaped pattern.

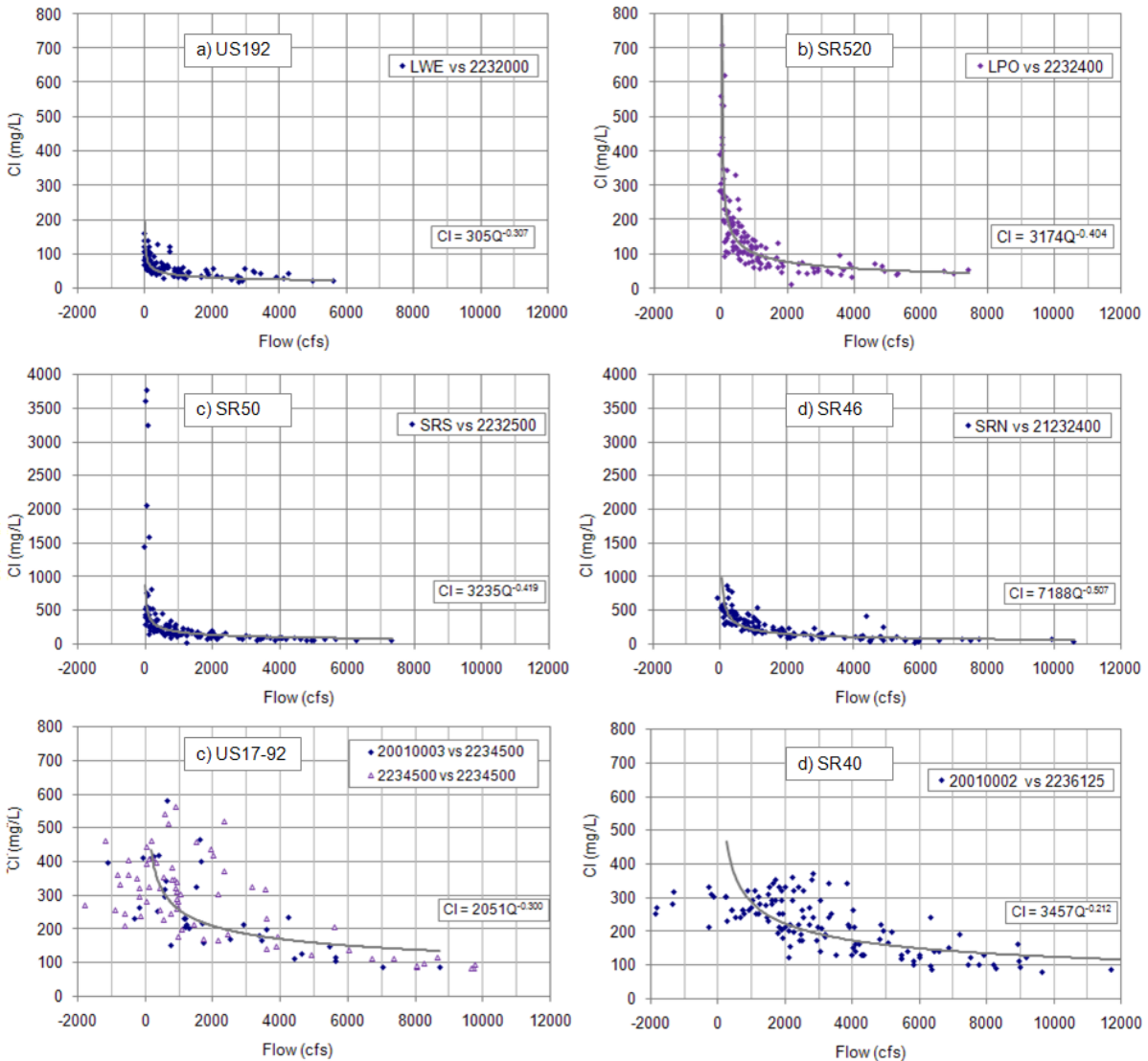


Figure 4–28. Cl (mg L⁻¹) versus flow (cfs) proceeding downstream, (a) U.S.192 (Site LWE), (b) SR 520 (Site LPO), (c) SR 50 (Site SRS), (d) SR 46 (Site SRN), (e) U.S.17 (Site 20010003), and (f) SR 40 (Site 20010002).

Low-lying Tributaries

Low-lying tributaries to the middle St. Johns River follow a power law relationship for chloride and discharge because relict seawater enters these tributaries as diffuse groundwater discharge. Because relict seawater is a dominant source of salts in the St. Johns River main stem, the quantification of salts entering the river from low-lying tributaries is important to setting model boundary conditions that account for the river’s salt budget. Salinity boundary conditions for low-lying tributaries entering the middle St. Johns River were developed from discharge–chloride relationships.

Tributaries have surface water inflows, and sometimes spring inflows, that are large in comparison to diffuse groundwater discharge. The overwhelming volume of surface water or spring flow can “blur” the power law of the discharge–chloride relationship in tributaries. An

example is shown for the Wekiva River, which has a large upstream contribution of discharge from springs (Figure 4–29). The top plot of Figure 4–30 is the discharge–chloride relationship for the Wekiva River at SR 46 (Site 2235000). The discharge–chloride relationship follows a power law, but the correlation is weak.

Discharge and chloride concentrations for the named springs in the Wekiva system are measured. When these observed sources are removed from the discharge–chloride relationship at SR 46, the resultant adjusted relationship follows the L-shape pattern previously shown to result from relict seawater (bottom plot, Figure 4–30).

With the removal of the upstream spring discharge, the adjusted Wekiva River discharge approaches zero under drought conditions, showing that the named springs account for nearly all the base flow at SR 46. The L-shaped pattern of the adjusted discharge–chloride relationship indicates the presence of an unobserved small discharge of high chloride concentration. The unobserved discharge is likely diffuse groundwater discharge containing relict seawater. Diffuse groundwater discharge to the Wekiva River was also noted by Tibbals (1990), who called it pick-up water.

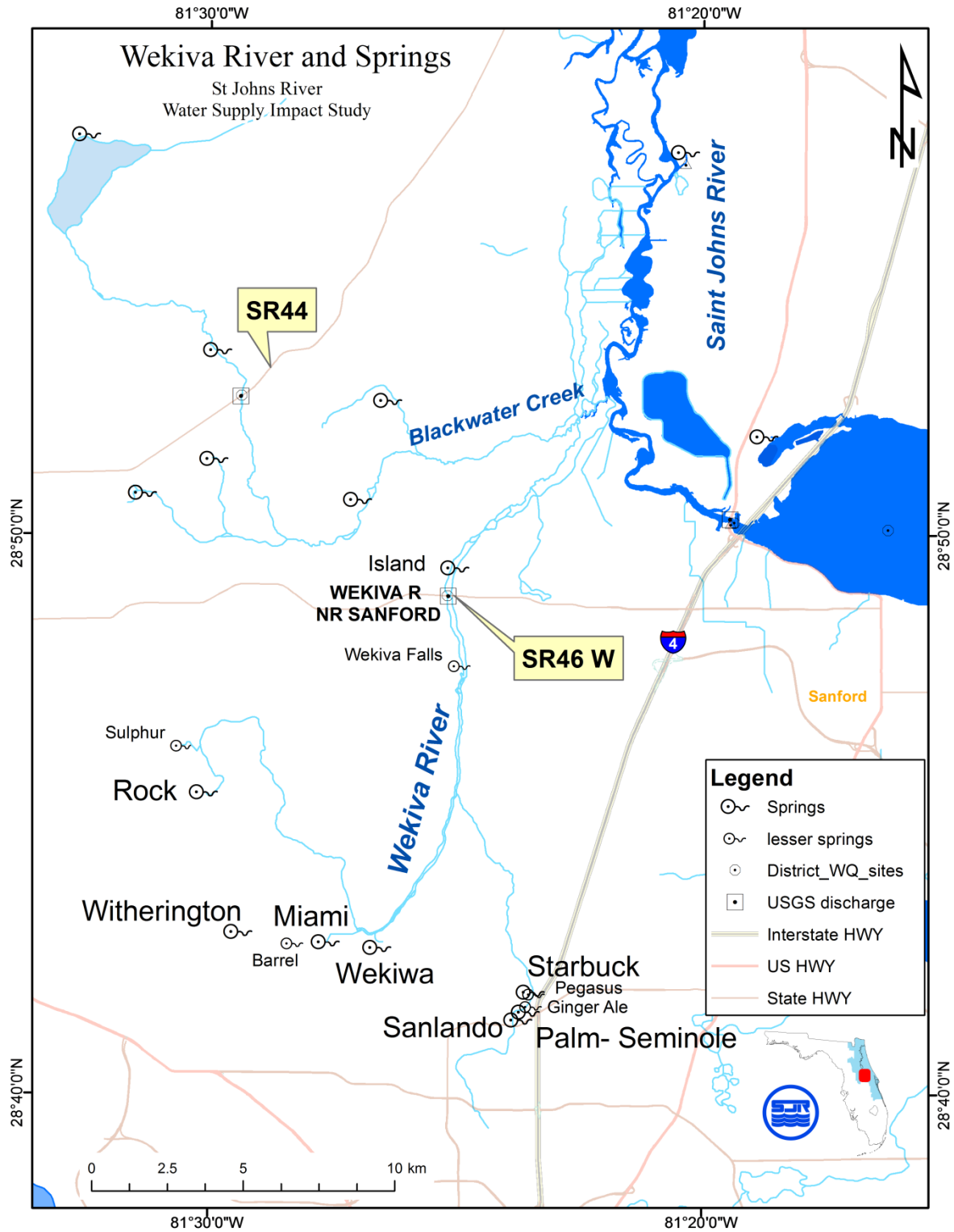


Figure 4–29. Gauge location at SR 46 in the Wekiva River and locations of major springs upstream of the gauge.

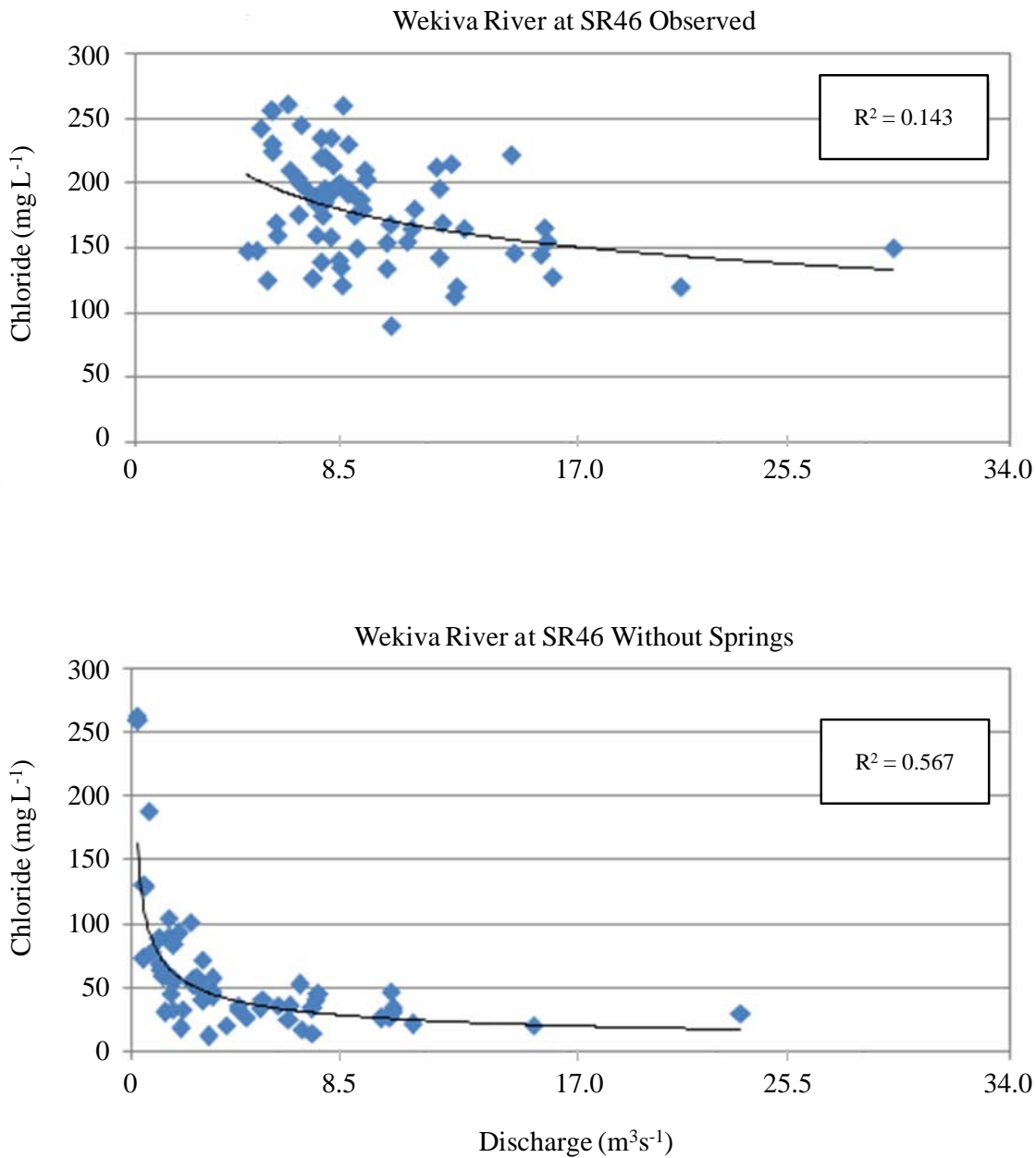


Figure 4–30. Discharge–chloride relationship for Wekiva River at SR 46 (Site 2235000). Relationship for total flow (top) and relationship without springs (bottom).

Summary

Relict seawater is a dominant source of salts to the St. Johns River main stem and quantification of the inflow of relict seawater to the river is required for setting model boundary conditions that account for the river’s salt budget. Relict seawater enters the river through spring discharge, diffuse groundwater discharge entering the river directly, and diffuse groundwater discharge entering the river from tributaries as pick-up water. This latter source is accounted for in the hydrodynamic model by use of a power law describing the chloride-discharge relationship for

low-lying tributaries. Use of the power law relationship allows for the estimation of daily salinity for a tributary from either observed or simulated daily discharge. The estimated salinity accounts for the salt contribution of diffuse groundwater discharge to low-lying tributaries that ultimately enters the St. Johns River main stem as tributary discharge.

4.5 SUMMARY

The EFDC hydrodynamic model was selected for simulating the effects of water withdrawals on water level, discharge, velocity, salinity, and water age throughout the lower and middle St. Johns River. A hydrodynamic model is needed for the lower St. Johns River because this area is a tidally dominated, partially stratified estuary. The EFDC hydrodynamic model was also selected for the middle St. Johns River, despite the absence of astronomical tide or vertical stratification, because of the desire to simulate the following features:

- Three-dimensional wind-driven flow structure within the large flow-through lakes,
- Influence of low frequency ocean water level variability on river stage,
- Sea level rise throughout the middle St. Johns River,
- Advective-diffusion of salinity and water age.

Ocean tide entering the river mouth is separated into astronomical tide and meteorological tide. Astronomical tide is functionally defined as having periods less than 30 hrs. Meteorological tide is primarily synoptic scale, with periods of 2 to 12 days although seasonal and annual variability is also present. The separation of observed ocean water level into astronomical and meteorological tide allows for separate adjustment of the astronomical tide at the open model boundary located on the shelf. Inclusion of the low frequency, meteorological tide is important for simulating the hydrodynamics of both the lower and middle St. Johns River because this low frequency ocean forcing affects water levels and river flows throughout the area.

River stage in the middle St. Johns River is dominated by low frequency ocean water level for periods when river discharge is below the average discharge. River stage and discharge are uncorrelated under these conditions. River slope and discharge are related, in an average sense, and this relationship is developed for subsequent calibration of the EFDC hydrodynamic model within the middle St. Johns River. The analysis used to develop the slope–discharge relationships shows that water level gauges across this area have biases in vertical level of about ± 15 cm. The resultant slope–discharge relationships also show that water withdrawals have the least effect on river stage when river discharge is below average discharge.

Salinity is simulated in both the lower and middle St. Johns River. In the lower St. Johns River, salinity is required for proper simulation of density effects on vertical mixing and estuarine circulation. In both systems, salinity is used as a conservative tracer to infer that mixing and circulation are accurately modeled. A careful analysis of salinity and salt composition is provided for the middle St. Johns River to ensure that salinity is appropriate as a conservative tracer in the oligohaline river and to understand the sources of salts for proper setting of model boundary conditions.

This modeling study used salinity determined from conductivity as defined by the Practical Salinity Scale 1978 (PSS78). Salinity thus defined is unitless, but is numerically equivalent (in

practice) to the conventional limnological definition as the total concentration of salt ions in mg L^{-1} . Conductivity-derived salinity (defined using PSS78) is used because of its ease of measurement, accurate determination of water density differences within the model, and applicability as a conservative tracer. Conductivity-derived salinity as a conservative tracer in low-salinity areas (such as the middle St. Johns River) depends on salt composition. Salinity in the middle St. Johns River is shown to be conservative because the salt composition of the middle St. Johns River is chloride-dominated under all flow conditions due to the presence of relict seawater

Finally, analysis of salt composition of inflows to the river, tributaries and springs, is useful for setting model boundary conditions. This information is used in two ways: first, to infer properties of salt composition and salinity levels for ungauged areas and second, as a means to create discharge-salinity relationships to estimate salt loads derived from pick-up water in tributaries.

5 MODEL BOUNDARY CONDITIONS

The EFDC hydrodynamic model is designed for application to a wide range of systems. The application of the EFDC hydrodynamic model to the St. Johns River required development of a model grid and model boundary conditions specific to that system.

The following boundary conditions were used for the EFDC hydrodynamic model application of the St. Johns River:

- Ocean water level and salinity at the open ocean boundary
- Tributary discharge and salinity
- Spring discharge and salinity
- Diffuse groundwater discharge and salinity
- Wastewater treatment plant discharge and salinity
- Rainfall and evaporation
- Wind

From these specified boundary conditions, the model calculates water level, velocity, discharge, salinity, and water age at each interior model cell at 30-s time intervals over the model simulation period of 1996 to 2005.

5.1 MODEL GRIDS

The EFDC hydrodynamic model of the lower and middle St. Johns River was developed in two sections. The downstream section covers the lower St. Johns River from the river entrance to Astor, just upstream of Lake George. This section includes a portion of the adjacent ocean shelf. The upstream section covers the middle St. Johns River from Astor to Geneva, just upstream of Lake Harney. Astor is the upstream boundary of the lower St. Johns River grid and the downstream model boundary of the middle St. Johns River grid. The two models were developed and calibrated independently for practical considerations. The model calibration process entails making numerous model runs and computer run-times are long, about 17 hrs^{-1} of simulation for the lower St. Johns River grid and 6 hrs yr^{-1} of simulation for the middle St. Johns River grid.

Developing the models separately allowed quicker turn-around of model results and facilitated the calibration process.

5.2 OCEAN WATER LEVEL AND SALINITY

Fifty-two cells along the eastern side of the block of ocean cells in the lower St. Johns River grid form the open ocean boundary. Ocean tide and salinity are specified along this boundary. These model boundary conditions account for the astronomical and meteorological tidal energy throughout the river, as well as ocean-derived salinity.

Ocean Water Level

Ocean water level along the open ocean boundary is specified as time series of hourly heights. The total time series is created by a superposition of predicted astronomical tide and observed meteorological tide. The astronomical tide was obtained by harmonic tidal prediction using 32 short period tidal constituents. The phase and amplitude of the largest five tidal constituents were adjusted using trial-and-error by comparison of simulated and observed harmonic constants at Bar Pilot Dock (Table 5–1). The meteorological tide was obtained from observed hourly heights at Bar Pilot Dock using a low-pass filter with a 30-hr cutoff.

Table 5–1. Five largest harmonic constituents adjusted for astronomical tidal prediction at open ocean boundary. Tidal constituents are defined in Table 3–5.

Tidal Constituent	Amplitude (cm)	Phase (degrees)
M ₂	65.9	229.6
S ₂	10.8	248.2
N ₂	15.8	216.1
K ₁	10.2	121.6
O ₁	7.0	141.6

Ocean water level ranged from -1.63 to 1.36 m NAVD88 (North American Vertical Datum of 1988) during the model simulation period (1996 to 2005). Water level distributions at the open ocean boundary are shown in Table 5–2.

Table 5–2. Distribution of ocean water level at open ocean boundary.

% Exceedance	Min	1	5	10	25	50	75	90	95	99	Max
m, NAVD88	-1.63	-1.16	-0.98	-0.87	-0.63	-0.18	0.26	0.51	0.64	0.87	1.36

Ocean Salinity

Ocean salinity was set at a constant value of 35.5. Surface salinity of the open ocean has a salinity of 35 to 36.5 (Apel 1987). The shelf waters seaward of the St. Johns River mouth have a salinity range of about 32 to 36 with lower values occurring in autumn (Atkinson 1985).

5.3 TRIBUTARY DISCHARGE AND SALINITY

5.3.1 TRIBUTARY DISCHARGE

Tributary discharge is obtained from either USGS gauging stations or from hydrologic modeling (Chapter 3). Twenty-one USGS gauges were active during the model simulation period and account for discharge from about 60% of the St. Johns River Basin area (Figure 5–1, Table 3–8). Tributary discharges enter the lower St. Johns River model in 100 separate locations and the middle St. Johns River model in 51 locations. Average tributary discharge for the model simulation period (1996 to 2005) was 2,494 mgd ($109.3 \text{ m}^3\text{s}^{-1}$) to the lower St. Johns River and 586 mgd ($25.7 \text{ m}^3\text{s}^{-1}$) to the middle St. Johns River. The middle St. Johns River received an additional 1371 mgd ($60.1 \text{ m}^3\text{s}^{-1}$) of discharge from the upper St. Johns River (SR 46 at Lake Harney).

Distributions of daily averaged discharge from tributaries is skewed towards higher values, so that median discharges are lower than means (Table 5–3).

Table 5–3. Distribution of daily averaged discharge (m^3s^{-1}) from in the upper St. Johns River at SR 46 at Lake Harney (SR46H), middle St. Johns River (SJR) tributaries, and lower St. Johns River tributaries (1996 to 2005).

% Days Exceeded	SR46H	Middle SJR Tributaries	Lower SJR Tributaries	Total
Max	333.0	372.7	1,567.0	2,000.2
1	258.6	146.1	611.6	909.6
2	229.2	113.3	452.3	698.9
5	191.1	81.1	316.2	535.6
10	159.6	61.4	232.7	429.0
25	96.0	35.4	132.7	272.7
50	39.0	16.5	74.1	142.3
75	16.7	8.3	45.9	80.1
90	6.0	4.0	27.4	42.5
95	3.9	2.6	21.3	29.5
98	1.4	1.8	18.8	24.6
99	0.4	1.4	17.6	22.0
Min	-2.3	1.0	13.8	14.7

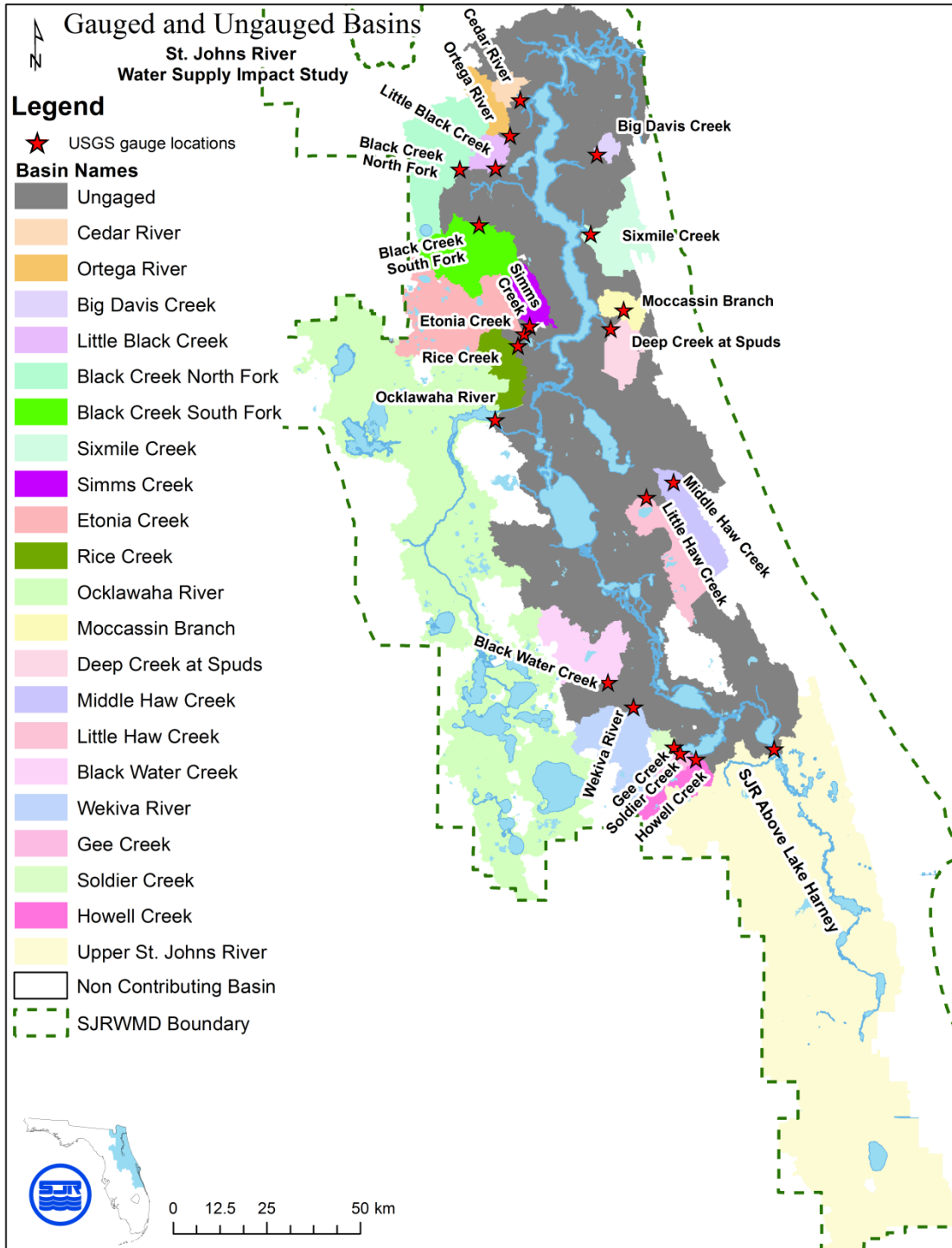


Figure 5–1. Gauged and ungauged watersheds of the middle and lower St. Johns River. For this study, the entire upper St. Johns River and Ocklawaha River are gauged where they enter the middle and lower St. Johns River, respectively.

5.3.2 TRIBUTARY SALINITY

Salinity boundary conditions are assigned to each of the 151 tributary inflows. Time series of salinity used for boundary conditions are developed from four methods: observed data, site-specific discharge-salinity relationship, generic discharge-salinity relationship, or constant. Observed salinity is used for locations where observations span the entire model simulation period (1996 to 2005) with adequate temporal resolution. In the middle St. Johns River, adequate observed salinity is found only for the mainstem location at SR 46 at Lake Harney. In the lower St. Johns River, adequate observed salinity is found at the mainstem locations at SR 40 Astor, and for two tributaries, Rice Creek and Deep Creek (St. Johns County). Site-specific discharge-salinity relationships are developed for tributaries with limited periods of observed salinity. Generic discharge-salinity relationships are used in areas with no observed data. Discharge-salinity relationships are only developed in the oligohaline reaches of the river where salinity in the main stem river is sensitive to small changes in salinity boundary conditions. These oligohaline reaches include the entire middle St. Johns River and Crescent Lake. Finally, a constant salinity of 0.04 is assigned to all lower St. Johns River surface tributaries downstream of Rice and Deep Creeks.

Discharge–Salinity Relationships in the Middle St. Johns River

Discharge-salinity relationships were first developed for 12 middle St. Johns River tributaries that have sufficient coincident discharge and conductivity observations to calculate a site-specific relationship. Regression equations are developed using conductivity as a proxy for salinity. In some cases, simulated discharge from the HSPF hydrologic model was used to fill missing discharge records. The conductivity-discharge relationships are expressed as either a power law or linear function of conductivity dependent on discharge (Table 5–4).

Where observed conductivity data are insufficient to develop a site-specific relationship, conductivity-discharge relationships are estimated from the composite of relationships developed for characteristically similar watersheds. These generic conductivity-discharge relationships are selected from between three classes of watersheds representative of low-conductivity (bicarbonate), medium-conductivity (mixed salts), and high conductivity (NaCl and SO₄ dominated) tributaries (Figure 5–2).

Table 5-4. Equations relating conductivity to discharge for middle St. Johns River surface tributaries

Tributary	Site ID	Equation Form	a	b
Deep Creek	DCR-MRD	Power*	875.0	-0.600
Wekiva River	2235000	Power	5,000.0	-0.450
Blackwater Creek	2235200	Power	628.5	-0.295
Salt Creek	T2	Power	2,900.0	-0.320
Sixmile Creek	T3	Power	625.0	-0.230
Howell Creek	2234324 (T5)	Power	458.4	-0.174
Gee Creek	2234400 (T9)	Power	329.9	-0.153
Soldier Creek	2234384 (T10)	Power	287.2	-0.132
Phelps Creek	T12	Power	316.2	-0.131
Sweetwater Creek	T4	Linear†	142.2	3,525
Chub Creek	T13	Linear	-286.6	1,149

Note:

* Power: $Cond = a \times Q^b$

† Linear: $Cond = a \times Q + b$

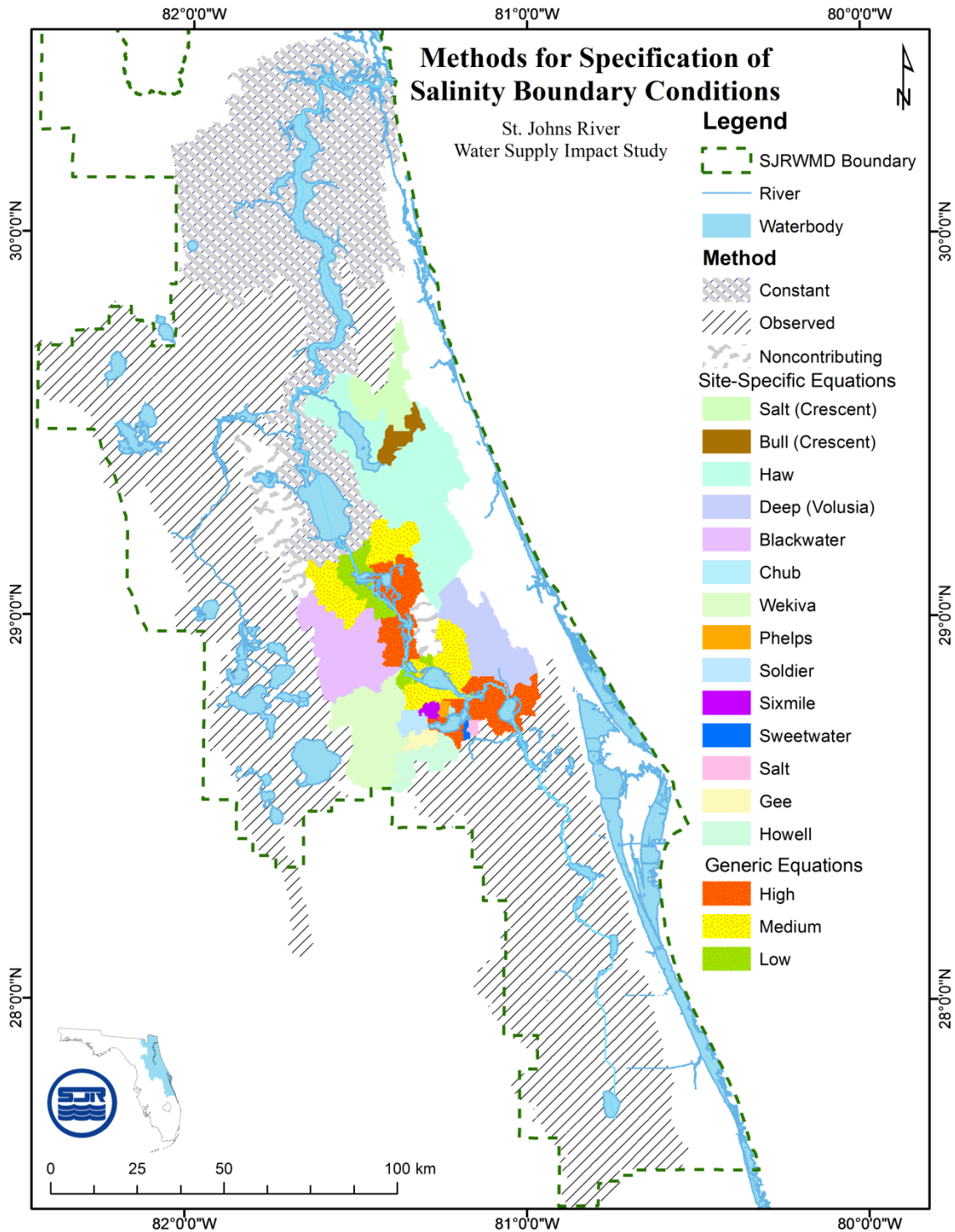


Figure 5–2. Method of assigning salinity boundary conditions to watersheds.

Several creeks upstream of SR 46 at Lake Harney, in the upper St. Johns River, are used to characterize low-conductivity tributaries typical of undeveloped, bicarbonate runoff from small rural watersheds. Medium-conductivity tributaries are typically urban or have mixed land use

that result in a mixed salt characteristic (both NaCl and bicarbonate). High-conductivity watersheds typically drain areas below 25 ft elevation, and are former agricultural areas that have converted to rural residential or silviculture. These watersheds are usually canalized, have a strong NaCl salt characteristic, and often contain sulfate. Parameters used to represent conductivity-discharge relationships for low-, medium-, and high-conductivity tributaries are summarized in Table 5–5.

Table 5–5. Coefficients used to represent conductivity-discharge relationships for low-, medium-, and high-conductivity tributaries. The coefficients (*a* and *b*) determine conductivity ($\mu\text{S cm}^{-1}$) from discharge (*Q*, cfs) according to the equation conductivity = aQ^b .

USGS Classification	Tributary	<i>a</i>	<i>b</i>
Bicarbonate	Penneywash Creek	190.7	-0.160
	Wolf Creek	260.0	-0.270
	Taylor Creek	255.0	-0.260
	Jim Creek	164.3	-0.118
	Low-conductivity tributaries	217.5	-0.201
Mixed salt character	Soldier Creek	287.2	-0.132
	Gee Creek	329.8	-0.153
	Phelps Creek	316.2	-0.131
	Howell Creek	458.4	-0.174
	Medium- conductivity tributaries	347.9	-0.147
NaCl, SO ₄ dominated	Rotten Egg Slough	840.0	-0.340
	Salt Creek	2,900.0	-0.320
	High-conductivity tributaries	1,455.0	-0.323

The dominant surface flow to the middle St. Johns River is from the upper St. Johns River at the SR 46 at Lake Harney upstream model boundary (Table 5–6). This inflow also has a high salinity and this source often dominates the salinity signal of the middle St. Johns River main stem. Deep Creek (Volusia County) and Blackwater Creek are large tributaries to the middle St. Johns River with low-conductivity surface water inflows.

Table 5–6. Summary of salinity boundary conditions used to represent surface water runoff to tributaries in the middle St. Johns River (MSJR) model.

Tributary	Method for Salinity Boundary Conditions	Mean Salinity	STDEV of Salinity	Mean Discharge (m³s⁻¹)
SR 46 at Lake Harney Geneva	Observed	0.52	0.34	58.2
Deep (Volusia County)	Power*	0.11	0.18	5.15
Medium	Power	0.13	0.03	5.01
Blackwater	Power	0.09	0.03	3.79
Wekiva	Power	0.36	0.17	3.26
High	Power	0.54	0.22	3.16
Howell	Power	0.12	0.03	2.14
Low	Power	0.09	0.02	1.72
Gee	Power	0.11	0.02	0.56
Soldier	Power	0.10	0.02	0.50
Sixmile	Power	0.98	0.42	0.35
Phelps	Power	0.12	0.02	0.34
Sweetwater	Linear [†]	1.55	0.25	0.23
Salt	Power	1.04	0.45	0.19
Chub	Linear	0.30	0.15	0.07
Total		0.43		84.7

Note:

* Power: $\text{Cond} = a \times Qb$

† Linear: $\text{Cond} = a \times Q + b$.

Salinity at SR 46 at Lake Harney Upstream Boundary

The model boundary condition for salinity at the upstream boundary is specified using observed monthly salinity. Observed salinity is used at this location, rather than a discharge-salinity relationship, because the discharge-salinity pattern can be disrupted, particularly under low flow conditions, by urban runoff from the Econlockhatchee River and treated municipal wastewater. As a result, under low flow conditions salinity at the model boundary (SR 46 at Lake Harney) is diluted relative to St. Johns River mainstem stations farther upstream (SR 50).

Treated wastewater from the Orlando Regional Treatment System (ORTS) enters the river directly upstream of SR 46 at Lake Harney and downstream of SR 50. The wastewater enters the river by two pathways. The first is through the Orlando Easterly Wetlands (OEW), a treatment wetland that discharges directly to the river upstream of the confluence with the Econlockhatchee. The second is through the principle wastewater treatment plant, Iron Bridge, which discharges to the Little Econlockhatchee River, which ultimately discharges to the St. Johns River just upstream of SR 46 at Lake Harney.

Under average flow conditions, the St. Johns River dominates salinity at SR 46 at Lake Harney. Under low flow conditions, however, flows from the Econlockhatchee and ORTS contribute an increasingly greater fraction of the total discharge at SR 46 at Lake Harney (Figure 5–3). A comparison of the ratio of the combined Econlockhatchee and ORTS discharge to St. Johns River discharge at SR 50 shows that combined discharge of the Econlockhatchee and ORTS is nearly equivalent in magnitude to SR 50 discharge for 10% of days. Treated wastewater discharge is about one-fifth of SR 50 discharge for 10% of days, a ratio sufficient to exert an influence on salinity at SR 46 at Lake Harney at these times. Because of the complexity of the mixing of sources upstream of the model boundary, the salinity boundary condition is based on observed data.

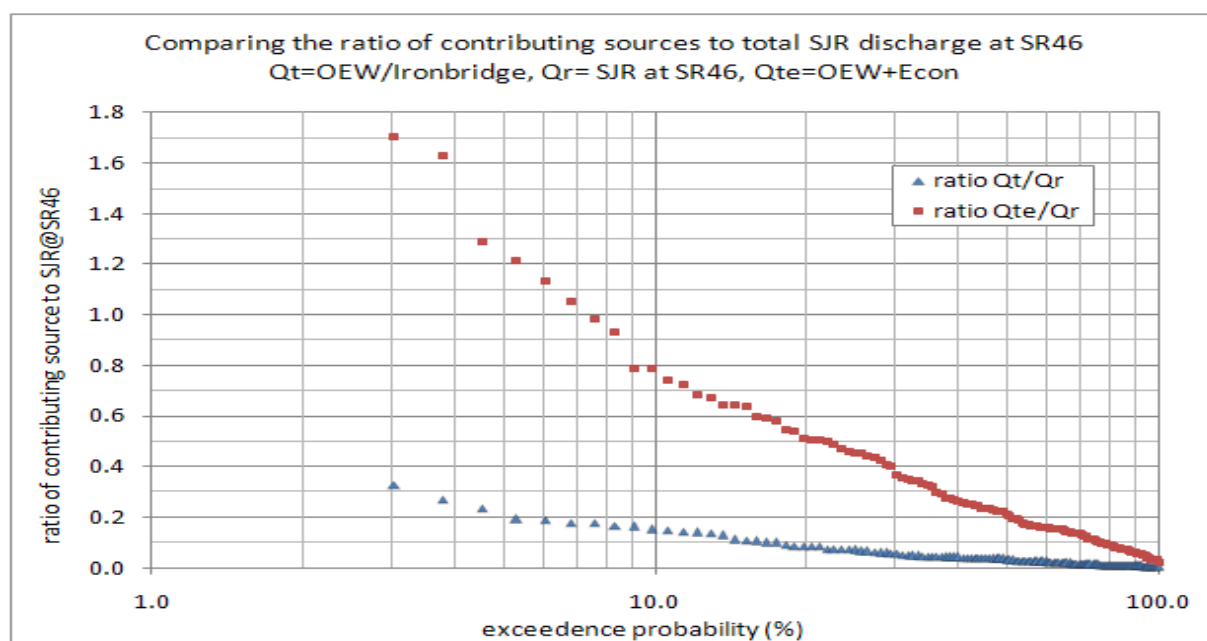


Figure 5–3. Comparison of anthropogenic sources of discharge (OEW and Iron Bridge) and their receiving bodies (St. Johns River and the Econlockhatchee River)

Discharge-Salinity Relationships in lower St. Johns River

Site-specific discharge-salinity relationships were developed for three watersheds in the lower St. Johns River that enter Crescent Lake. These relationships are polynomial functions of salinity dependent on discharge. The relationships are $S = 0.075 + 0.232 Q^{-1} - 0.055 Q^{-2}$ for Haw Creek, $S = 0.125 + 0.232 Q^{-1} - 0.055 Q^{-2}$ for Salt Creek, and $S = 0.26 + 0.28 Q^{-1}$ for Bull Creek. These watersheds have relatively small discharge compared with total tributary discharge to the entire

lower St. Johns River (Table 5–7), but they are important to establishing the salinity of Crescent Lake.

Salinity boundary conditions used for surface water runoff to tributaries in the lower St. Johns River are summarized in Table 5–7.

Table 5–7. Summary of salinity boundary conditions used to represent surface water runoff to tributaries in the lower St. Johns River model.

Tributary	Method for Salinity Boundary Conditions	Mean Salinity	STDEV of Salinity	Mean Discharge mgd (m³s⁻¹)
SR 40 Astor	Observed	0.46	0.17	2,296.1 (100.6)
All others	Constant	0.04	0.00	1,205.1 (52.8)
Ocklawaha River	Observed	0.24	0.06	819.4 (35.9)
Haw Creeks	Polynomial	0.20	0.09	226.0 (9.9)
Rice Creek	Observed	0.45	0.16	118.7 (5.2)
Bull Creek	Polynomial	0.74	0.54	95.9 (4.2)
Deep Creek	Observed	0.81	0.38	93.6 (4.1)
Salt Creek	Polynomial	0.25	0.09	63.9 (2.8)
Total		0.32		4,941.4 (216.5)

5.4 SPRING DISCHARGE AND SALINITY

Springs enter the hydrodynamic models at 20 locations, nine for the MSJR model and 11 for the lower St. Johns River. Time series of discharge and constant salinity are provided as boundary conditions at each location. Although discharge from springs varies much less than for surface tributaries, spring discharges vary seasonally in response to the effect of meteorological variability of precipitation on the potentiometric pressure of the contributing aquifer (Copeland 2009). Boundary conditions for most springs are thus supplied monthly discharge to capture seasonal variability. A few small springs are assumed to have constant discharge. Salinity associated with spring flows has low temporal variability and salinity boundary conditions for springs are supplied as constant values.

Three of the spring inflows represent a group of springs that enter the model at a single location. The three spring groups enter through the Wekiva River, Blackwater River, and Juniper Creek. Major springs of the Wekiva Group include Island, Nova, Miami, Wekiwa, Witherington, Rock, Starbuck, and Sanlando springs. Major springs of the Blackwater Group include Palm (Lake), Messant, Seminole (Lake), and Blackwater springs. Major springs of the Juniper Group include Juniper, Fern Hammock, Mormon Branch, and Sweetwater springs.

Spring discharge observations are sparse for most springs within SJRWMD. Only four of the largest springs—Blue (Volusia County), Alexander, Silver Glen, and Salt—have sufficient monthly or bi-monthly (6 times per year) observations for directly setting model boundary conditions. Only Blue Spring (Volusia County) has continuous, daily discharge observations (Figure 5–4). For springs with insufficient discharge data, time series of discharge were estimated either by correlation to stage within a nearby well or by correlation to a neighboring spring discharge.

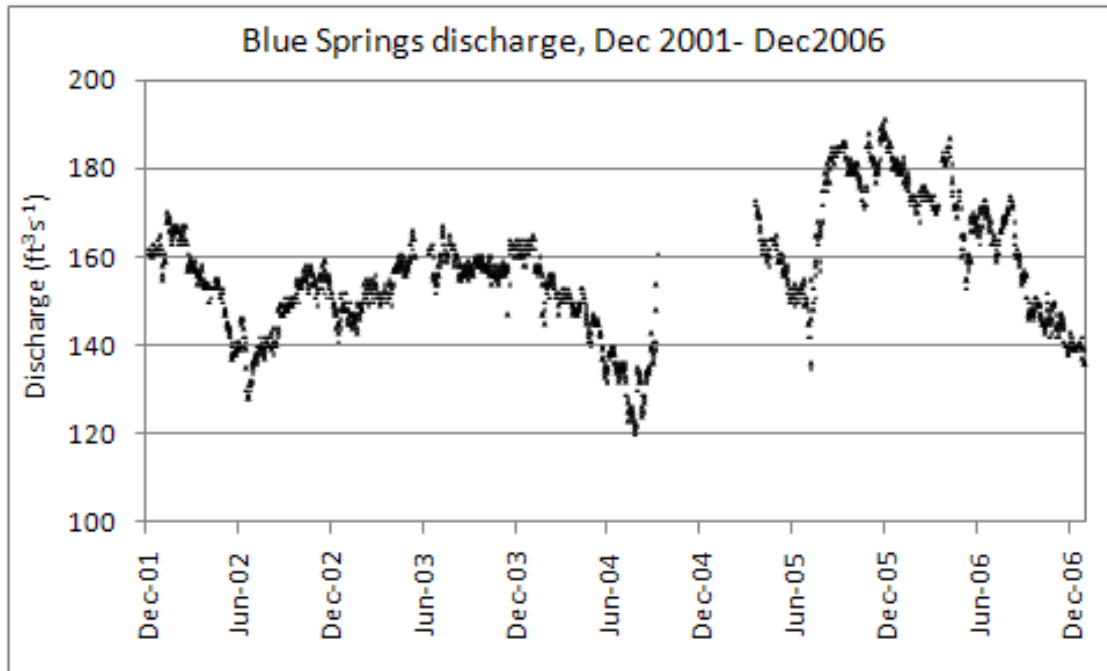


Figure 5–4. Continuous, daily observed discharge for Blue Springs (Volusia County), December 2001 to December 2006.

5.4.1 METHODS OF ESTIMATING SPRING DISCHARGE

The methodology for estimating spring discharge by correlation to stage in a nearby well was developed by Intera (Intera 2007a) (Intera 2007b) under contract with SJRWMD. Intera previously estimated spring discharges for five springs used for model boundary conditions. The Intera Model is used in this study to estimate discharge for seven additional springs. For springs without a representative groundwater well, discharge was estimated by correlation to a neighboring spring. In all, we distinguish three methods for setting spring discharge boundary conditions: (a) using observations, (b) using the Intera Model of correlation to stage in a nearby well, and (c) by correlation to discharge from a neighboring spring. The three methodologies are termed Observation, Intera Model, and Correlation to Discharge, respectively.

Intera previously estimated spring discharge for three springs directly entering the river (Ponce de Leon, Gemini, and Green Springs) and for Wekiwa and Rock springs in the Wekiwa Group. The Intera Model captures spring discharge magnitude and variability well (Figure 5–5).

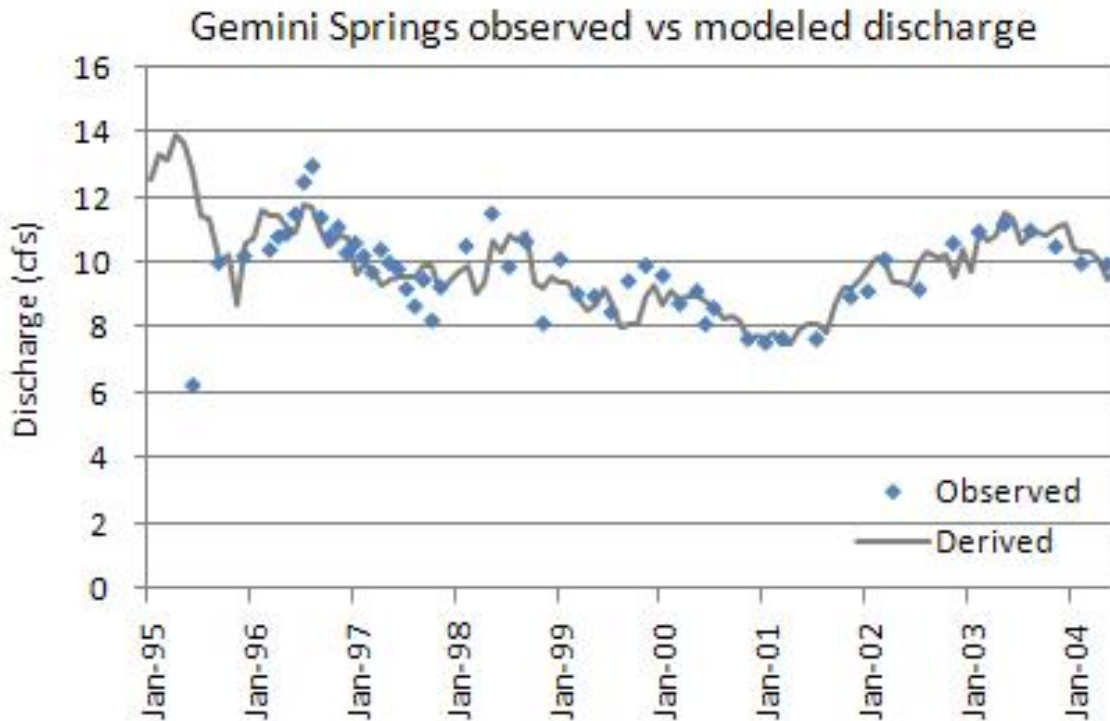


Figure 5–5. Comparison of observed discharge with discharge estimated by the Intera Model for Gemini Springs.

The Intera Model is used to estimate discharge for seven springs: Clifton, Juniper, Croaker Hole, Beecher, Nashua, Satsuma, and Wadesboro. Discharge estimated by the Intera Model captures spring discharge variability well (Figure 5–6).

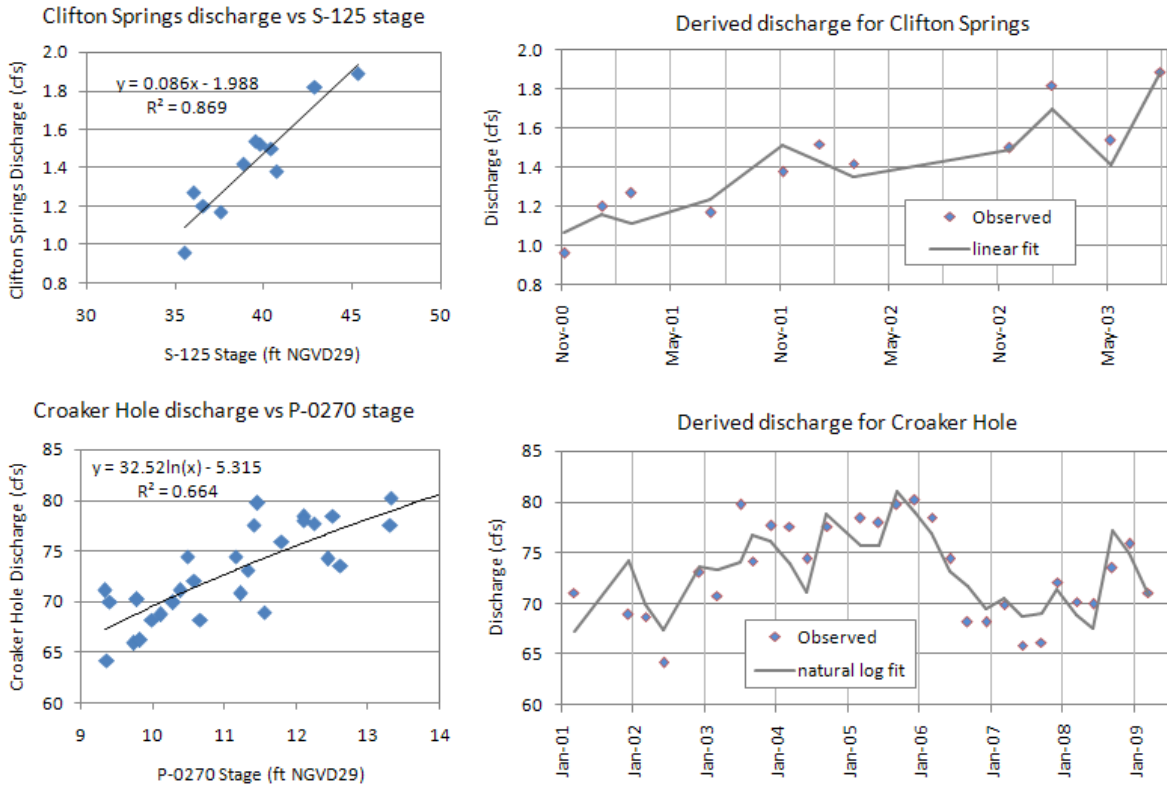


Figure 5–6. Correlation between well stage and spring discharge (left) and comparison of observed and predicted discharge (right) for Clifton Springs (top) and Croaker Hole (bottom).

Discharge for the remaining springs are estimated by nonlinear correlation to neighboring spring discharge. As an example, Figure 5–7 shows the correlation between Rock Spring discharge (independent) and Seminole Spring discharge (dependent).

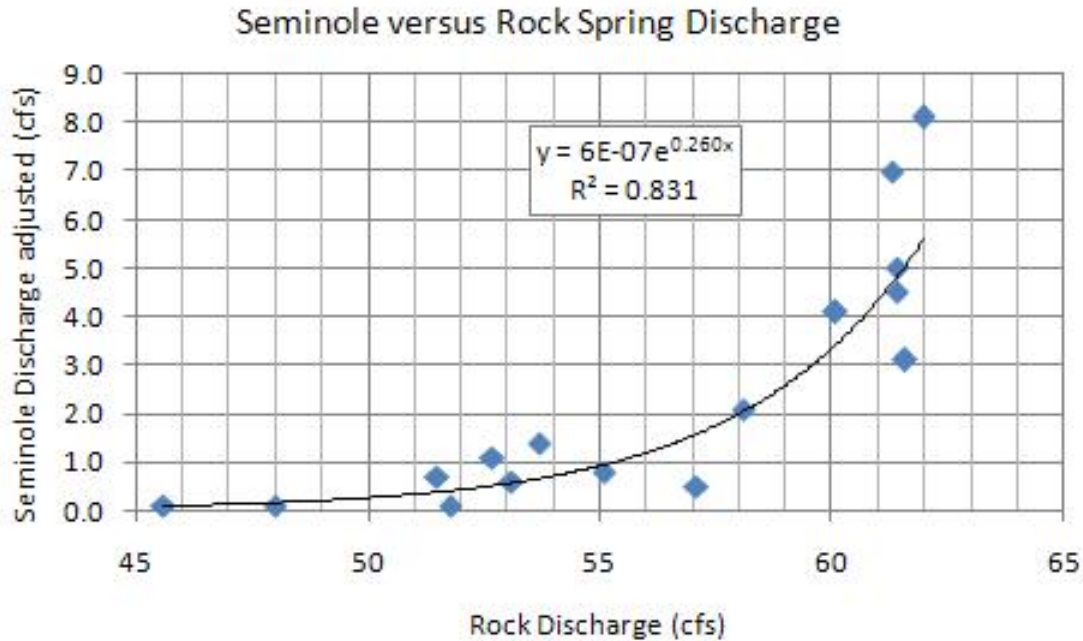


Figure 5-7. Correlation between Rock and Seminole Spring discharge. (Seminole discharge is adjusted +35 cfs).

5.4.2 SUMMARY OF SPRING BOUNDARY CONDITIONS

Spring boundary conditions for discharge and salinity are summarized in Table 5-8 for all 20 springs. Springs are sorted by mean discharge over the model simulation period (1995 to 2005). The table provides standard deviation of discharge as an indicator of temporal variability, constant salinity associated with each spring, the model that the spring enters, and the method of determining discharge.

Table 5–8. Summary of spring boundary conditions for the lower St. Johns River (LSJR) and middle St. Johns River (MSJR) hydrodynamic models.

Spring Name	Discharge mgd (m ³ s ⁻¹)		Salinity	EFDC Model	Method of Estimating Discharge
	Mean	Standard Deviation			
Wekiva Group	141 (6.19)	13.7 (0.60)	0.40	MSJR	Intera Model, Correlation to Discharge
Blue (Volusia County)	105 (4.61)	13.5 (0.59)	0.83	MSJR	Observed
Juniper Group	72.8 (3.19)	2.97 (0.13)	0.81	LSJR*	Intera Model (Well P-0820)
Silver Glen	72.1 (3.16)	10.0 (0.44)	0.95	LSJR	Observed
Alexander	71.4 (3.13)	6.85 (0.30)	0.58	MSJR	Observed
Salt	55.7 (2.44)	5.93 (0.26)	2.85	LSJR	Observed
Croaker	50.2 (2.20)	2.97 (0.13)	1.08	LSJR	Intera Model (Well P-0820)
Blackwater Group	50.0 (2.19)	5.02 (0.22)	0.28	MSJR	Intera Model, Correlation to Discharge
Ponce de Leon	17.8 (0.78)	5.25 (0.23)	0.43	MSJR	Intera Model
Gemini	6.85 (0.30)	0.91 (0.04)	1.33	MSJR	Intera Model
Beecher	6.85 (0.30)	0.91 (0.04)	0.23	LSJR	Intera Model (Well P-0270)
Welaka	5.48 (0.24)	0.91 (0.04)	0.67	LSJR	Correlated to Discharge (Beecher)
Green Cove	2.05 (0.09)	0.23 (0.01)	0.07	LSJR	Correlated to Discharge (Wadesboro)
Mosquito	1.14 (0.05)	0.00 (0.00)	0.15	MSJR	1 observation, used constant Q
Green	1.14 (0.05)	0.46 (0.02)	1.65	MSJR	Intera Model
Clifton	1.14 (0.05)	0.23 (0.01)	0.35	MSJR	Intera Model (Well S-125)
Mud	0.91 (0.04)	0.23 (0.01)	1.11	LSJR	Correlated to Discharge (Beecher)
Wadesboro	0.91 (0.04)	0.00 (0.00)	0.07	LSJR	Intera Model (Well C-0094)
Satsuma	0.68 (0.03)	0.00 (0.00)	3.36	LSJR	Intera Model (Well P-0270)
Nashua	0.05 (0.002)	0.00 (0.00)	2.39	LSJR	Intera Model (Well P-0270)
Total	663 (29.08)		0.86		

*LSJR means spring enters the lower St. Johns River model grid, MSJR mean spring enters the middle St. Johns River model grid.

5.5 DIFFUSE GROUNDWATER DISCHARGE

Diffuse groundwater discharge is Upper Floridan aquifer water that flows into the river through the river bottom. It enters broad areas of the river throughout the middle St. Johns River, Lake George, and Crescent Lake. Diffuse groundwater discharge is nominal to the lower St. Johns River downstream of Lake George and Crescent Lake (Spechler 1994). Diffuse groundwater discharge boundary conditions were developed using groundwater modeling (Chapter 4. Groundwater Hydrology) and are provided as constant discharge and salinity.

Diffuse groundwater discharge and salinity are assigned to 20 river segments. Sixteen segments fall in the EFDC hydrodynamic model application to the middle St. Johns River (EFDC-MSJR

hydrodynamic model) and four segments fall in the EFDC hydrodynamic model application to the lower St. Johns River (EFDC-LSJR hydrodynamic model) (Figure 5–8). Groundwater discharge enters the bottom cells of the EFDC hydrodynamic model. Groundwater discharge is areally weighted across model cells within each segment, so that each model cell within a segment receives an identically constant discharge per unit area. Because salinity is also uniform across each segment, each cell has an identically constant salt flux.

Table 5–9 contains the area, total diffuse groundwater discharge, and associated salinity assigned to each of the 20 groundwater segments. Segments 1 to 16 are within the EFDC-MSJR hydrodynamic model and segments 17 to 20 are within the EFDC-LSJR hydrodynamic model. Although the contribution of discharge from diffuse groundwater is small relative to other sources, the associated salt flux is important to the salt budget of the river.

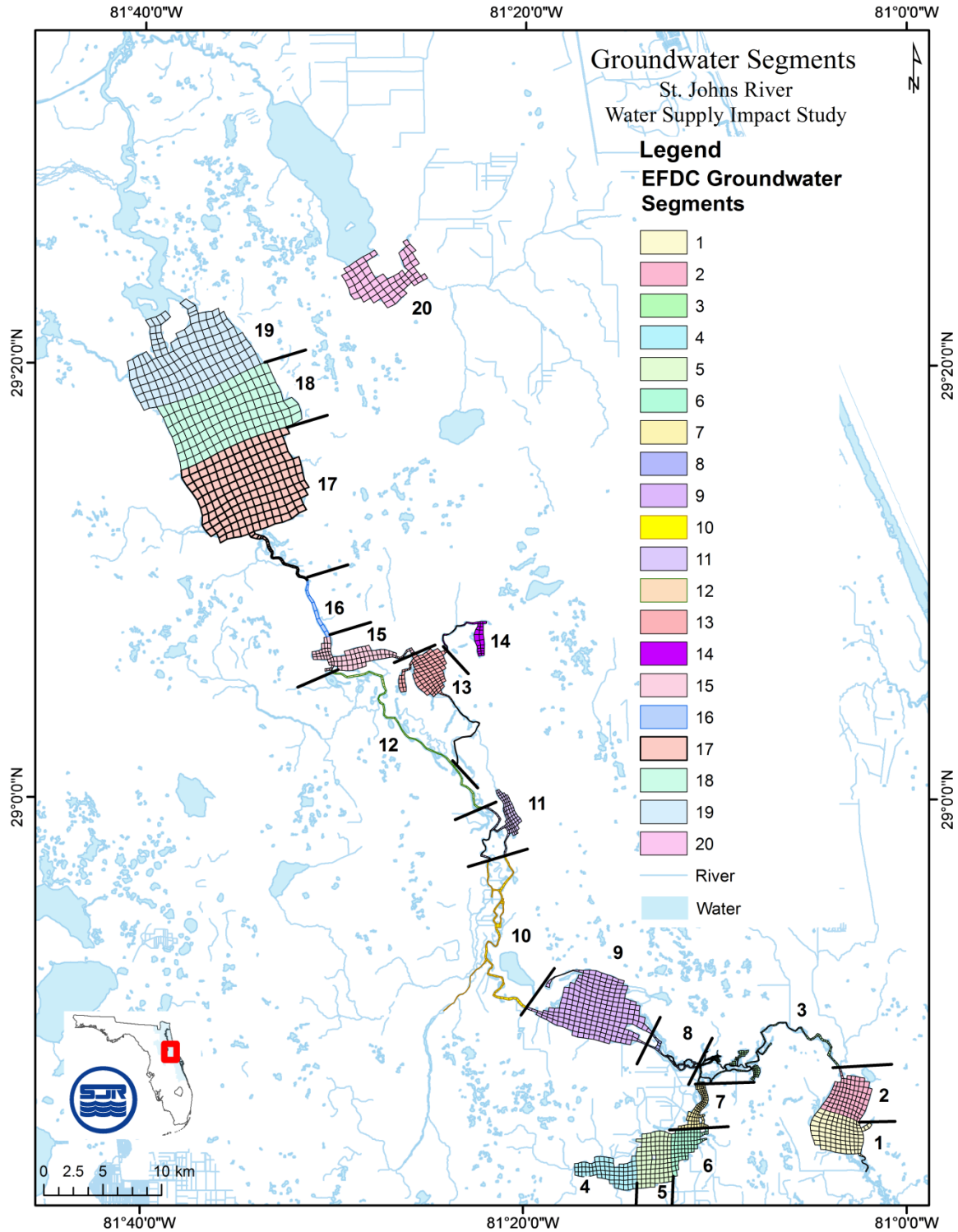


Figure 5–8. Groundwater segments used for input of diffuse groundwater discharge and associated salinity as model boundary conditions.

Table 5–9. Discharge and salinity assigned to 20 EFDC groundwater segments as diffuse groundwater discharge boundary conditions.

EFDC Segment	Segment Name	Segment Area (km ²)	Discharge mgd (m ³ s ⁻¹)	Salinity
1	Lake Harney South	13.6	11.182 (0.490)	2.50
2	Lake Harney North	10.9	4.609 (0.202)	2.25
3	Upper River Channel East	4.1	10.178 (0.446)	2.00
4	Lake Jesup West	9.3	5.477 (0.240)	1.25
5	Lake Jesup Middle	12.7	5.249 (0.230)	1.50
6	Lake Jesup Mid-East	6.5	5.317 (0.233)	1.75
7	Lake Jesup East	3.7	5.705 (0.250)	1.80
8	Upper River Channel West	1.2	3.537 (0.155)	1.49
9	Lake Monroe	35.0	14.240 (0.624)	1.80
10	Wekiva Region	1.8	13.714 (0.601)	1.75
11	Lake Beresford	3.9	3.423 (0.150)	1.55
12	River Channel Sanford-DeLand	2.2	7.896 (0.346)	2.25
13	Nelson Deadwater	10.4	9.539 (0.418)	1.00
14	Spring Garden Lake	2.3	9.630 (0.422)	1.00
15	Lake Dexter	8.9	5.226 (0.229)	1.80
16	River Channel DeLand-Astor	1.3	9.835 (0.431)	0.58
17	Lake George South	67.8	6.458 (0.283)	0.45
18	Lake George Center	56.8	9.700 (0.425)	0.65
19	Lake George North	57.0	9.700 (0.425)	0.45
20	Crescent Lake	0.3	10.337 (0.453)	0.36
Totals	LSJR–MSJR	309.7	160.950 (7.053)	1.38

5.6 WASTEWATER TREATMENT PLANTS

The model includes discharge from 36 wastewater treatment plants (Figure 3–12). Boundary conditions for discharge are specified as constant for each plant (Table 5–10). In general, treated wastewater has low salinity because the source of the wastewater is domestic water supply that must be low in ionic content for human consumption. Salinity for all wastewater treatment plants, then, is assigned a constant value of 0.04.

Table 5–10. Average discharge of 36 wastewater treatment plants entering the lower St. Johns River (EFDC-LSJR) model.

Plant Name	Plant ID	Discharge (mgd)
Georgia Pacific	FL0002763	35.8
Buckman	FL0026000	32.1
Arlington East	FL0026441	10.3
Stone Container Corp	FL0000400	7.6
Southwest District	FL0026468	6.2
Mandarin	FL0023493	4.8
Jefferson Smurfit Corp	FL0000892	4.7
Jacksonville District II	FL0026450	4.1
Miller Street	FL0025151	3.4
Jacksonville Beach	FL0020231	2.9
Monterey	FL0023604	2.9
Palatka	FL0040061	2.7
Royal Lakes	FL0026751	2.4
Orange Park	FL0023922	1.9
Atlantic Beach	FL0038776	1.9
San Jose Subdivision	FL0023663	1.9
Jacksonville Heights	FL0023671	1.1
Anheuser Busch	FL0041530	1.0
Buccaneer	FL0023248	1.0
USN Mayport	FL0011427	1.0
NAS Jacksonville	FL0011429	1.0
Neptune Beach	FL0020427	1.0
Holly Oaks Subdivision	FL0023621	0.7
Beacon Hills	FL0026778	0.7

Julington	FL0043591	0.6
Green Cove Springs	FL0020915	0.5
Fleming Island	FL0043834	0.5
San Pablo	FL0024767	0.4
Beauclerc	FL0111111	0.4
Woodmere Subdivision	FL0026786	0.3
South Green Cove	FL0030210	0.3
United Water FL	FL0117668	0.2
Fleming Oaks	FL0032875	0.2
Ortega Hills Subdivision	FL0025828	0.1
Hastings	FL0042315	0.1
Wesley Manor Retire Village	FL0022489	0.1
Totals		136.7

5.7 METEOROLOGY: RAINFALL, EVAPORATION, AND WIND

Rainfall, evaporation, and wind are supplied to the model as spatially varying fields. The value assigned to a model cell is determined by inverse-distance interpolation to the nearest three stations. Seven rain gauge and evaporation stations (see Figure 3–13) and eight wind stations (see Figure 3–18) are used for model boundary conditions. For rainfall and evaporation, the EFDC-LSJR hydrodynamic model uses the northern five stations and the EFDC-MSJR hydrodynamic model uses the southern four stations. Two central stations (Crescent City and DeLand) are common to both model applications. For wind, both model applications each use five wind stations. The two common stations are Daytona Beach Airport and Umatilla.

6 MODEL CALIBRATION

6.1 INTRODUCTION

Model calibration is the process of adjusting model parameters so that the model simulation matches observed data. Model calibration is distinct from either model confirmation or model prediction in that model calibration uses the model output to adjust model inputs. For model confirmation and model prediction, changes to model inputs are used to assess model outputs. For the EFDC hydrodynamic model the principle calibration parameter is spatially varying bottom roughness. This parameter largely controls the amount of frictional resistance simulated

by the model. Bottom roughness is not measured and must be identified in the calibration process by trial-and-error.

Model calibration requires examination of hydrodynamic variables at various time scales to demonstrate that the model is correctly capturing important dynamic properties of the system. Observed hourly water levels in the lower St. Johns River, for example, are used to compare the model response to astronomic ocean tide and this comparison demonstrates the proper propagation of long-wave tidal energy through the system. Observed daily discharge is useful for demonstrating the integrated model response to low frequency, meteorologically induced ocean variability, local wind stress, and tributary inflows.

Salinity is an important output variable for calibration, first, because the extent of alterations to salinity in the estuarine zone of the river from water withdrawals is a central question to the WSIS, and second, because salinity is a useful conservative tracer that integrates the hydrodynamic effects of circulation and mixing throughout the model domain.

Model calibration depends on a rigorous definition of the geometry and bathymetry of the system. A digital elevation model (DEM) at 10-m resolution was first developed to aid this calibration task. Following the development of the DEM, model grids were developed to discretize the region and establish the spatial resolution of the model.

The principle calibration parameter used for this study was spatially varying bottom roughness. The lower St. Johns River and middle St. Johns River areas are calibrated separately because the methods for calibrating bottom roughness were necessarily different for the two regions. For the model of lower St. Johns River (EFDC-LSJR hydrodynamic model), bottom roughness is optimized to minimize the difference between observed and simulated harmonic tide. Proper simulation of tidal dynamics is essential to the model calibration in this region because the dominant tidal motions are of fundamental importance to circulation and mixing. For the middle St. Johns River model (EFDC-MSJR hydrodynamic model), bottom roughness is calibrated to match observed surface slope–discharge relationships. These relationships are direct manifestations of the effects of bottom roughness on the frictional resistance to flow that establishes the surface slope–discharge relationships. The calibrated lower and middle St. Johns River models are shown to well represent the hydrodynamics of the river.

6.2 EFDC MODEL GRID DEVELOPMENT

6.2.1 INTRODUCTION

The horizontal resolution of the model grids was determined first for the EFDC-LSJR hydrodynamic model and this resolution was then followed for the EFDC-MSJR hydrodynamic model. This order of development was followed for two reasons: first, because the lower St. Johns River had an existing, calibrated EFDC hydrodynamic model application to use as a starting point and second, because the horizontal resolution in the lower St. Johns River could be practically tested for convergence using observed tidal harmonics. The existing model grid of the lower St. Johns River was expanded to include some additional features deemed important for the WSIS: (a) expansion of the model grid upstream to include Lake George and Crescent Lake, (b) expansion of the model grid offshore to include a greater portion of the shelf, and (c) adjustment of the cell areas representing adjacent tidal marshes to better simulate the tidal prisms

of the salt marsh areas. These changes established a base grid for the EFDC-LSJR hydrodynamic model. A convergence test of the horizontal resolution of the base grid was performed that established that this grid has sufficient horizontal resolution to capture M_2 tidal dynamics. A similar horizontal resolution was then followed to create the grid for the EFDC-MSJR hydrodynamic model.

6.2.2 DEVELOPMENT OF THE BASE GRID OF THE LOWER ST. JOHNS RIVER

Expansion of Existing Model Grid

An existing EFDC hydrodynamic model application of the lower St. Johns River (EFDC-TMDL hydrodynamic model) was previously developed for setting Pollutant Load Reduction Goals (PLRGs) and Total Maximum Daily Loads (Sucsy and Morris 2002). The EFDC-TMDL hydrodynamic model grid extended from just offshore of Mayport to Buffalo Bluff. This grid was expanded upstream to include Crescent Lake and Lake George and seaward to contain a greater portion of the shelf for the WSIS (Figure 6–1). The seaward expansion of the EFDC-TMDL hydrodynamic model grid allows for a more realistic representation of the plume of freshwater exiting the river mouth without artificial interference from the model ocean boundary. The expanded grid also better represents the jetties at the mouth of the river as thin-walled barriers that block lateral flow across the cell faces representing these features.

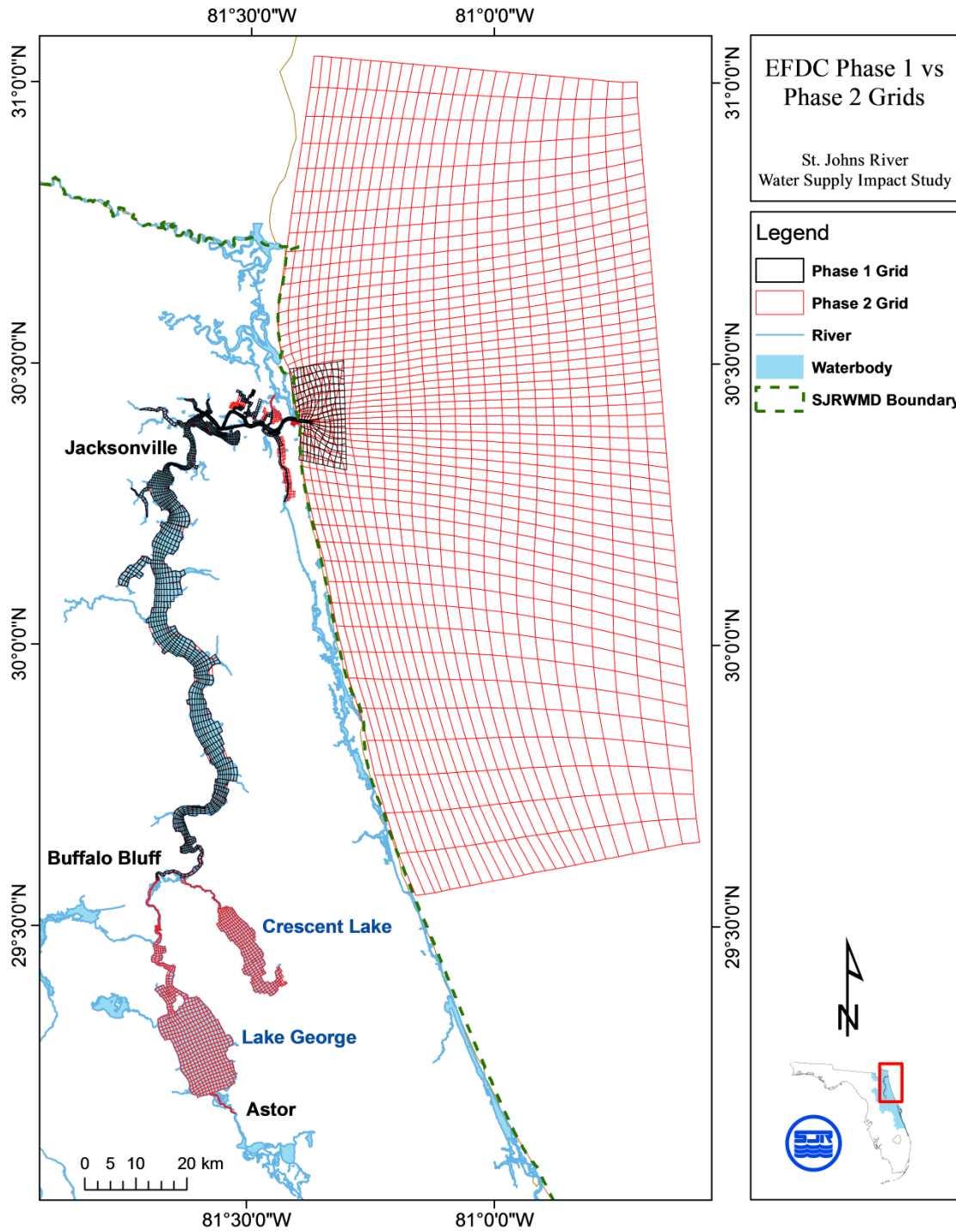


Figure 6–1. Comparison of EFDC-TMDL hydrodynamic model grid (black) with the expanded base grid (red) established for the EFDC-LSJR hydrodynamic model.

Adjustment of Tidal Marshes

Tidal marshes downstream of Jacksonville are represented in both the EFDC-TMDL hydrodynamic model and EFDC-LSJR hydrodynamic model as simple storage areas that fill and

drain over a tidal cycle; flooding and drying of marsh areas are not simulated. Recent ADCP discharge measurements at the mouths of the major tidal creeks showed that the EFDC-TMDL hydrodynamic model generally underpredicted the observed tidal prisms of the salt marshes. The marsh areas were adjusted for the EFDC-LSJR hydrodynamic model to match better the observed tidal prisms.

Nearly all the flow entering marshes occurs through just four tidal creeks (Figure 6–2). Figure 6–2 shows the values of effective tidal area estimated from observed ADCP discharge, the effective tidal area of the EFDC-TMDL hydrodynamic model, and the cells (red) modified to represent better the tidal marsh areas in the EFDC-LSJR hydrodynamic model. (The small area of red cells nearest the river mouth is the Mayport turning basin that was also added to the EFDC-LSJR hydrodynamic model.)

Effective tidal area is defined as the area that yields the observed tidal prism for the local tidal range. Effective tidal area is calculated from observed values of peak tidal discharge (Q_{peak}) and tidal range (H_r) by the following method:

First, the tidal prism (TP) is calculated from Q_{peak} by integrating over ½ a tidal period (22358 sec.) assuming tidal discharge varies sinusoidally,

$$TP = \int_0^{22358} Q_{peak} \sin\left(\frac{\pi}{22358} t\right) dt = 2(Q_{peak} \frac{22358}{\pi}) \tag{6-1}$$

The effective tidal area (A_{eff}) is then calculated as tidal prism divided by tidal range,

$$A_{eff} = \frac{TP}{H_r} \tag{6-2}$$

Calculated values of effective tidal area for the four principle tidal creeks are shown in Table 6–1.

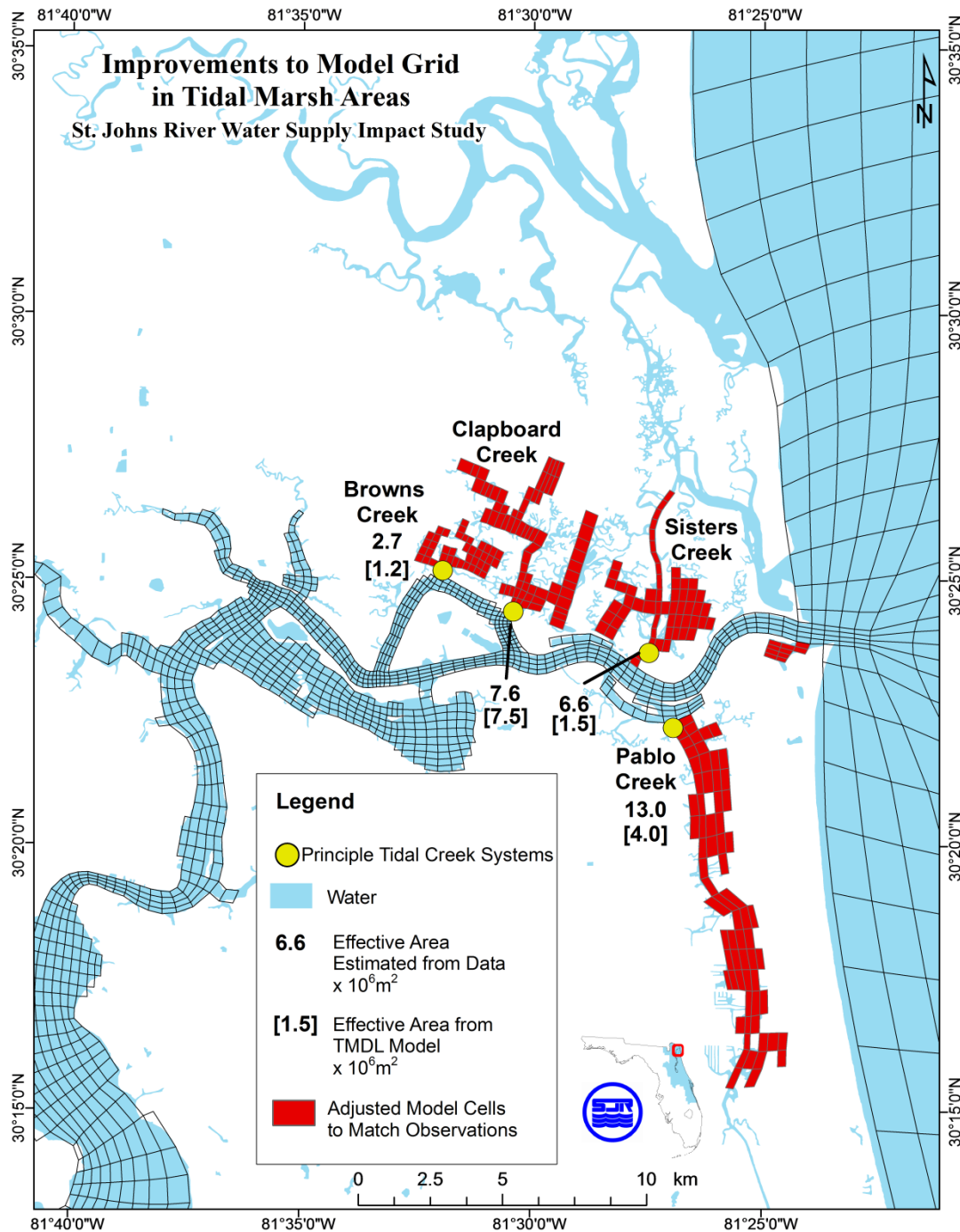


Figure 6–2. Effective tidal area ($\times 10^6 m^2$) estimated from observed ADCP tidal discharge at mouths of four principle tidal creeks. Numbers in brackets are effective tidal areas for the EFDC-TMDL hydrodynamic model. Cells in red are areas adjusted for the EFDC-LSJR hydrodynamic model to match ADCP tidal discharge.

Table 6–1. Observed peak tidal discharge (Q_{peak}), estimated tidal prism (TP), and effective tidal area (A_{eff}) for four principle marsh areas in the lower St. Johns River. (Tidal range is assumed 1.2 m.)

Tidal Marsh Name	Q_{peak} ($\text{m}^3 \text{s}^{-1}$)	TP ($\times 10^6 \text{ m}^3$)	A_{eff} ($\times 10^6 \text{ m}^2$)
Pablo Creek	1,100	15.7	13.0
Sisters Creek	560	8.0	6.6
Clapboard Creek	670	9.5	7.6
Browns Creek	230	3.3	2.7

Because marsh cells are used only for volume storage, they are assigned a uniform depth of 2 m. A 2-m depth ensures these cells will have sufficient depth over a tidal cycle to prevent drying of cells and maintain model stability.

The adjustment of the marsh cells, together with the upstream expansion to Lake George and Crescent Lake and the seaward expansion on the shelf, completes the base grid for the EFDC-LSJR hydrodynamic model. This base grid was next used for testing grid convergence.

6.2.3 GRID CONVERGENCE

Grid convergence was tested using the base grid of the EFDC-LSJR hydrodynamic model described above. Two successively finer grids were created from the base grid by dividing each cell into first four (4X) and then 16 (16X) new cells (Figure 6–3). The base grid becomes the 1X grid for testing grid convergence.

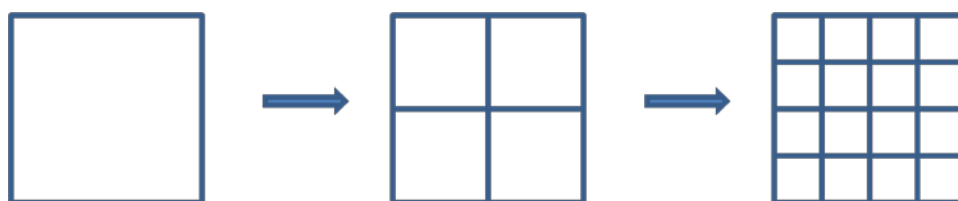


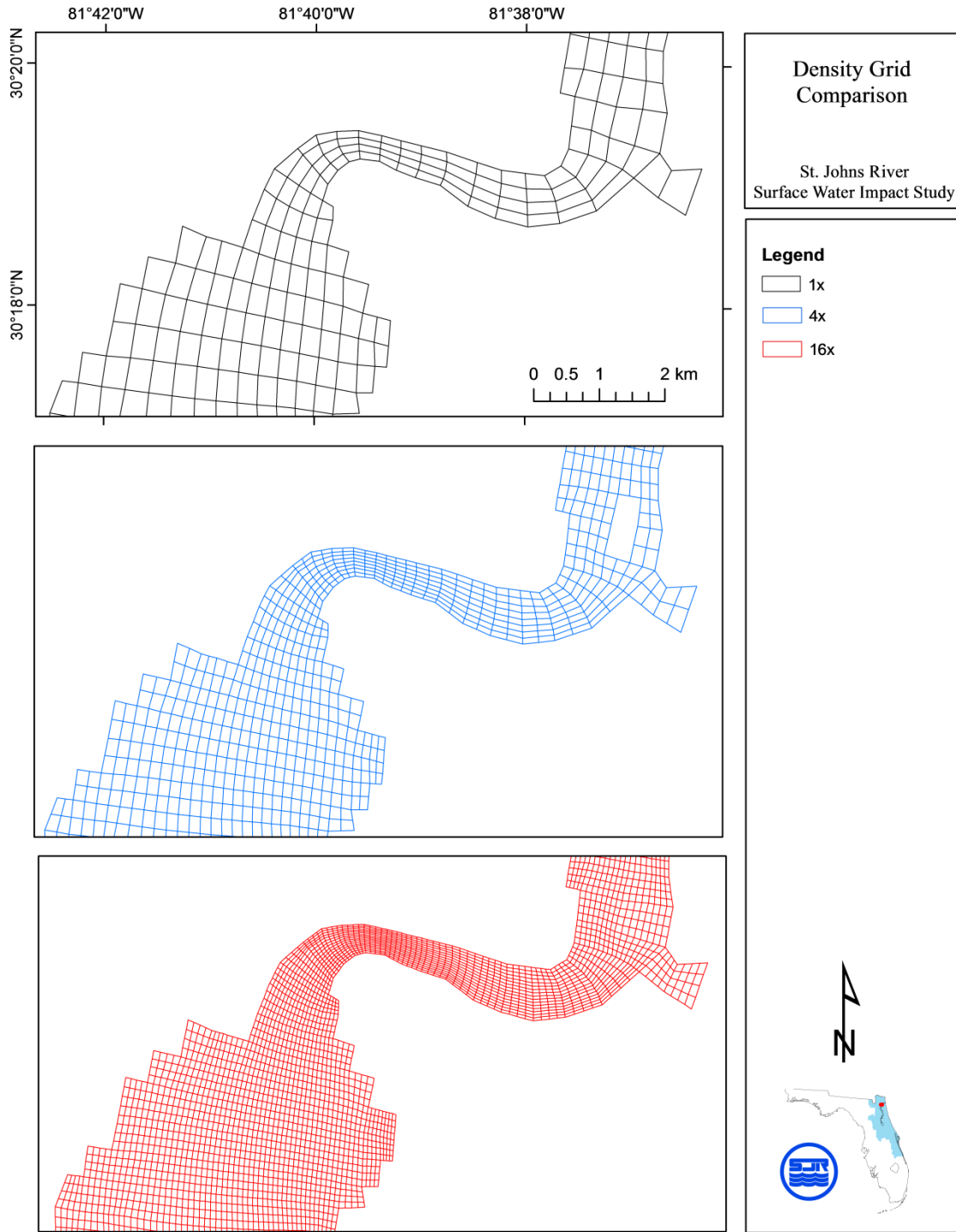
Figure 6–3. Cell divisions used to create successively finer model grids for testing grid convergence.

Bathymetry was independently interpolated onto each grid from the DEM, so that the finer grids also have finer resolution of bathymetric features. Table 6–2 shows the characteristics of each grid. An example of the difference in horizontal resolution between the 1X, 4X, and 16X model grids is shown in Figure 6–4 for the area near Jacksonville.

Running the 4X and 16X grids as six-layer, three-dimensional models with salinity was impractical due to computational constraints. Grid convergence tests instead used vertically averaged, barotropic tidal simulations. Precipitation, wind, and tributary inputs were neglected. Each grid was tested by forcing with an identical harmonic tide at the ocean boundary. The model time-step was 10 s for all grids.

Table 6–2. Grid characteristics for three successively finer grids used for testing grid convergence. IC and JC are dimensions of the computational EFDC hydrodynamic model grid. The number of horizontal cells includes wet cells only.

Grid	IC	JC	Number Horizontal Cells	Mean Cell Length in X-direction (m)	Mean Cell Length in Y-direction (m)
1X	121	259	3,013	434	577
4X	241	517	12,052	217	289
16X	481	1033	48,208	109	144



+
 Figure 6–4 Comparison of horizontal resolution near Jacksonville for the 1X (top, black), 4X (middle, blue), and 16X (bottom, red) grids used for testing grid convergence.

Model runs employed a 10-day spin-up followed by output of 696 hourly (29 days) water level heights for harmonic analysis. Water level was output at 23 locations having observed tidal

constituents (Table 3–3, Figure 3–2). Because the EFDC hydrodynamic model calculates water level at the cell centers, the water level output for all three grids is not at the exact same locations and the nearest locations were used (Figure 6–5).

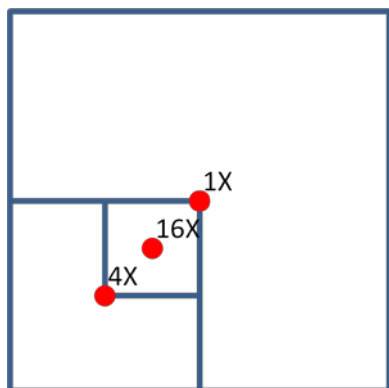


Figure 6–5. Cell center locations used for water level output.

Tidal harmonics (M_2 , S_2 , N_2 , O_1 , and K_1) were calculated using the Tidal Analysis Package Python–TAPPY (Cera 2010). Only results for M_2 amplitudes and phases are presented below, because M_2 is the dominant tidal constituent in the St. Johns River and results for the other tidal constituents are similar to M_2 .

Differences in M_2 amplitudes (Table 6-3) and phases (Table 6-4) between the three grids are small. Only the six most upstream sites (18 to 23) have greater than 5% difference in M_2 amplitude between the 16X and 1X grids. The absolute differences in M_2 amplitude for these six sites are all less than 1 cm. M_2 amplitudes for sites downstream of Palatka (1 to 17) differ by less than 4% between the 1X and 16X grids. Only two sites (20 and 21) have M_2 phase differences greater than 5° (approximately a 10 min. difference) and only site 20 has a phase difference exceeding 10° (20 minutes). At all other locations, M_2 phase differences between the 1X and 16X grids differ by less than 4° (8 min).

Convergence plots for M_2 amplitude and phase are shown for four representative locations: Main Street Bridge (Site 10, Figure 6–6), Shands Bridge (Site 15, Figure 6–7), Buffalo Bluff (Site 18, Figure 6–8), and Moccasin Landing (Site 20, Figure 6–9). The phases for Sites 10, 15, and 20 show convergence from the coarse to fine grid, but the amplitudes do not converge in the classical sense of the slope of the curve tending toward zero to the left. The differences in amplitudes, however, are smaller than the practical requirements of model calibration.

These results indicate that the 1X grid resolution is sufficient to capture tidal motions within the model area for achieving an accurate calibration to observed tidal harmonics. The 1X grid resolution has horizontal length scales of 100 to 1000 m, and this horizontal resolution was used as a guideline for creation of the grid for the EFDC-MSJR hydrodynamic model. The horizontal resolution of the EFDC-MSJR hydrodynamic model grid is slightly finer, 50 to 500 m.

Table 6-3. Differences in M_2 amplitudes (cm) between grids. Map # refers to Figure 3-2.

Map #	Station Name	1X to 4X		4X to 16X		1X to 16X	
		Magnitude (cm)	Percentage	Magnitude (cm)	Percentage	Magnitude (cm)	Percentage
1	Bar Pilot Dock	0.16	0.25	0.03	0.05	0.19	0.30
2	Mayport	0.07	0.11	0.21	0.33	0.28	0.44
3	Pablo Creek Entrance	0.67	1.26	0.43	0.82	1.10	2.06
4	Fulton	0.07	0.15	0.09	0.19	0.16	0.34
5	Clapboard Creek	-0.45	-1.00	0.06	0.13	-0.39	-0.86
6	Blount Island	-0.42	-0.99	-0.28	-0.65	-0.70	-1.65
7	Dames Point	-0.36	-0.87	-0.25	-0.60	-0.61	-1.47
8	Navy Fuel Depot	-0.79	-2.27	-0.44	-1.24	-1.23	-3.54
9	Long Branch	-0.22	-0.70	-0.36	-1.13	-0.58	-1.84
10	Main Street Bridge	-0.06	-0.25	-0.23	-0.97	-0.29	-1.23
11	Ortega River Entrance	-0.06	-0.33	-0.12	-0.66	-0.18	-1.00
12	Piney Point	-0.08	-0.64	-0.15	-1.20	-0.23	-1.85
13	Buckman Bridge	0.00	0.00	-0.09	-0.87	-0.09	-0.87
14	Doctors Lake	-0.10	-0.96	-0.08	-0.76	-0.18	-1.73
15	Shands Bridge	-0.06	-0.86	-0.08	-1.14	-0.14	-2.01
16	Racy Point	-0.21	-2.83	-0.07	-0.92	-0.28	-3.77
17	Palatka	-0.14	-1.79	-0.13	-1.63	-0.27	-3.45
18	Buffalo Bluff	-0.32	-5.40	-0.18	-2.88	-0.50	-8.43

Chapter 5. River Hydrodynamics Calibration

19	Sutherland Still	0.20	3.98	0.39	8.09	0.59	11.75
20	Moccasin Landing	0.04	8.70	0.01	2.38	0.05	10.87
21	Welaka	-0.33	-16.18	-0.10	-4.22	-0.43	-21.08
22	Georgetown	-0.04	-11.43	0.00	0.00	-0.04	-11.43
23	Silver Glen	-0.03	-5.45	-0.01	-1.72	-0.04	-7.27

Table 6–4. Differences in M₂ phases (degrees) between grids. Map # refers to Figure 3–2.

Map #	Station Name	1X minus 4X	4X minus 16 X	1X minus 16X
1	Bar Pilot Dock	-1.0134	-0.1498	-1.1632
2	Mayport	-0.9131	-0.2218	-1.1349
3	Pablo Creek Entrance	2.9898	0.7119	3.7017
4	Fulton	-0.3435	-0.0550	-0.3985
5	Clapboard Creek	0.4330	-0.4728	-0.0398
6	Blount Island	0.3059	0.0718	0.3777
7	Dames Point	-0.0142	-0.0791	-0.0933
8	Navy Fuel Depot	-0.3856	-0.1471	-0.5327
9	Long Branch	-0.6413	-0.1078	-0.7491
10	Main Street Bridge	-0.6864	-0.1409	-0.8273
11	Ortega River Entrance	0.2419	0.0688	0.3107
12	Piney Point	-0.6499	-0.1061	-0.7560
13	Buckman Bridge	-0.8608	-0.0712	-0.9320
14	Doctors Lake	-1.8902	-1.1088	-2.9990
15	Shands Bridge	-1.3949	0.3891	-1.0058
16	Racy Point	-0.8895	-0.4045	-1.2940
17	Palatka	-0.2691	-0.7333	-1.0024
18	Buffalo Bluff	-1.0431	-1.3798	-2.4229
19	Sutherland Still	-0.8254	-0.0396	-0.8650
20	Moccasin Landing	-9.6938	-0.8661	-10.5599
21	Welaka	-3.7310	-1.5102	-5.2412
22	Georgetown	-2.3559	-0.7254	-3.0813
23	Silver Glen	-2.5609	-1.3547	-3.9156

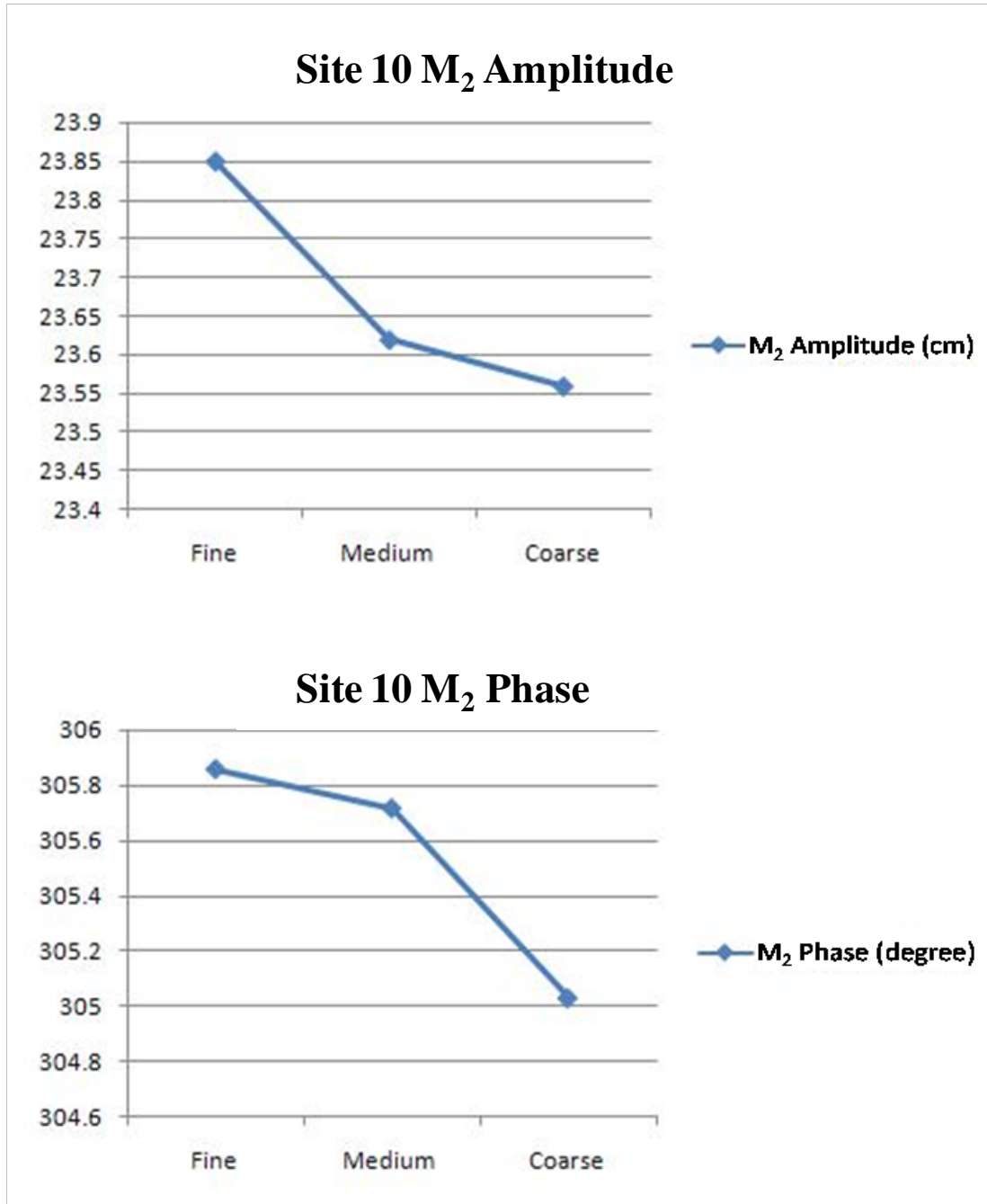


Figure 6–6. M₂ amplitude and phase simulated for each of three successively finer grids at Main Street Bridge, Site 10.

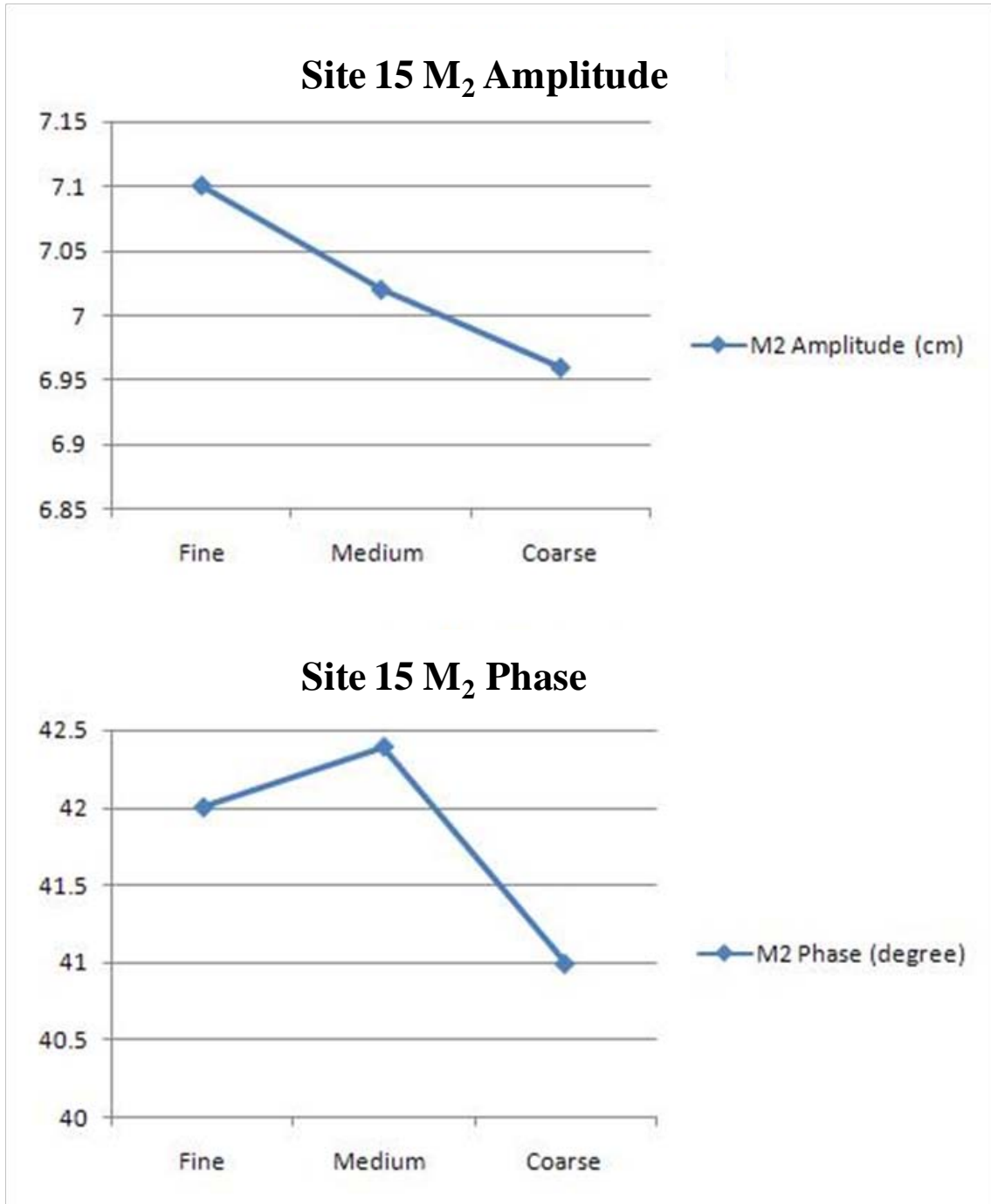


Figure 6–7. M₂ amplitude and phase simulated for each of three successively finer grids at Shands Bridge, Site 15.

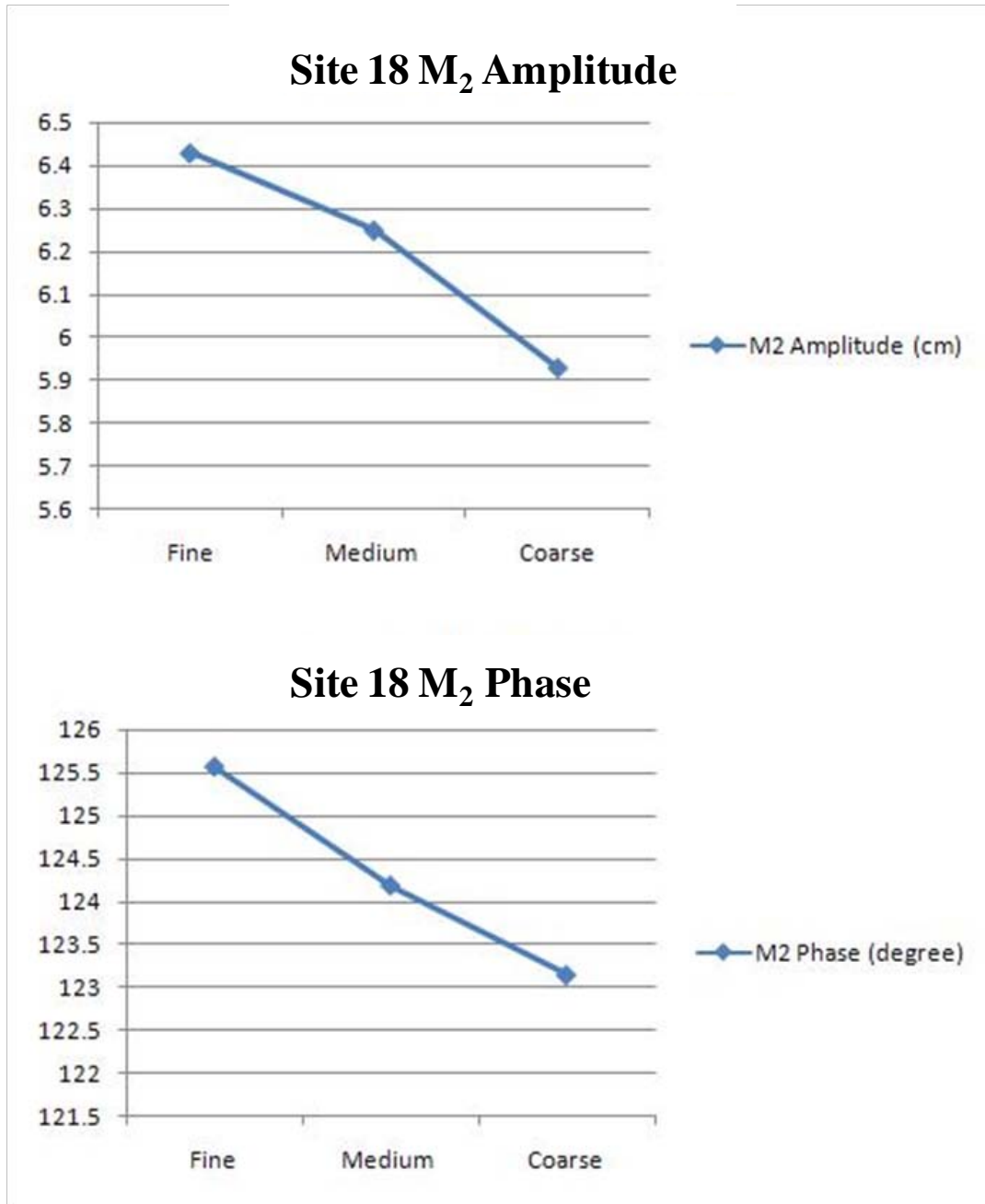


Figure 6–8. M₂ amplitude and phase simulated for each of three successively finer grids at Buffalo Bluff, Site 18.

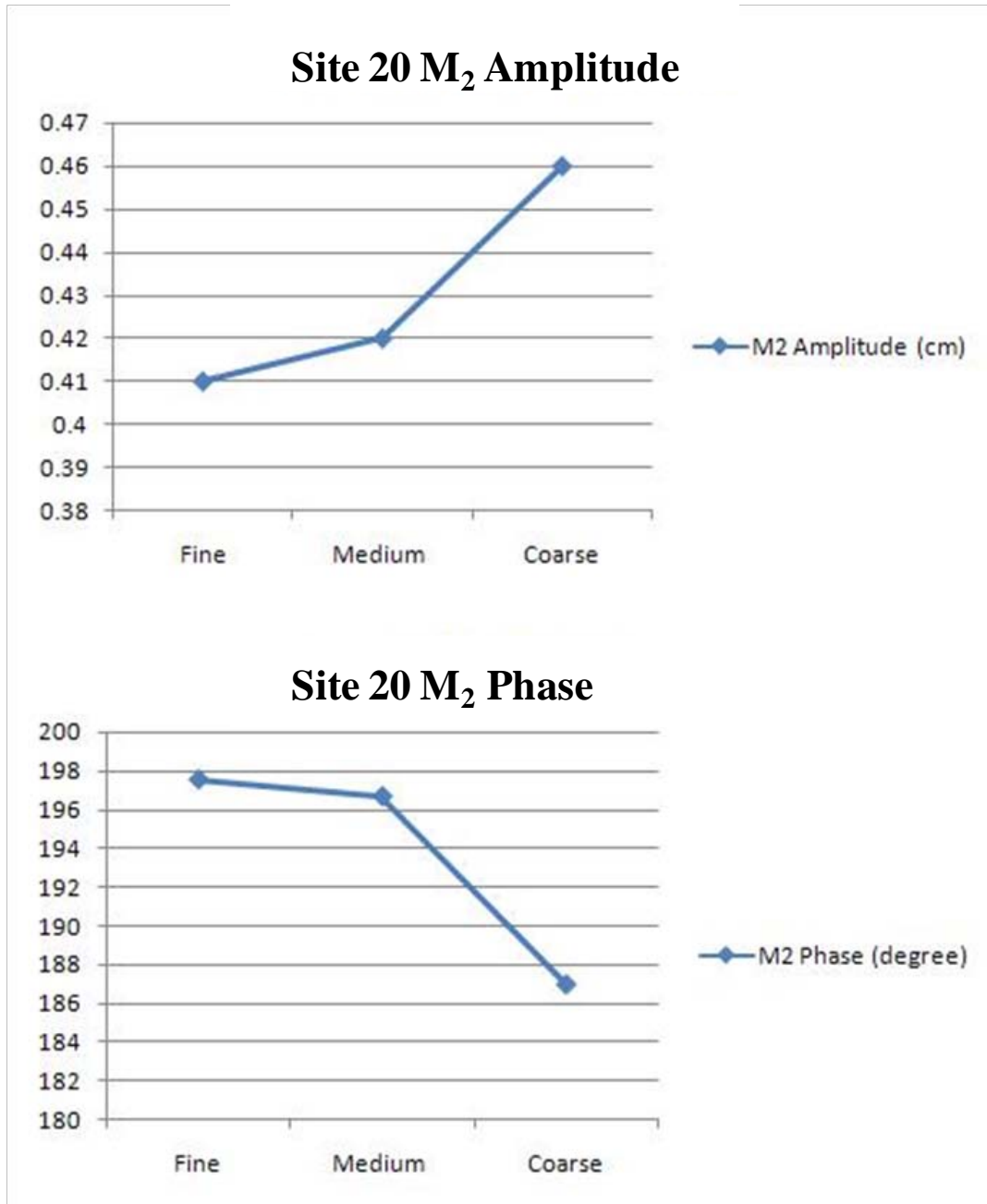


Figure 6–9. M₂ amplitude and phase simulated for each of three successively finer grids at Moccasin Landing, Site 20.

6.2.4 ADDING DEPTHS TO THE MODEL GRIDS

A depth was first assigned to each model cell by simple interpolation from the 10-m DEM. The depth assigned to each cell was interpolated in two possible ways. If one or more DEM points fell directly inside a cell, then the cell was assigned the mean depth of those points. If no points fell within the cell, then the cell depth was calculated by inverse-weighted distance from the cell center to the nearest three DEM points. This initial depth field was then adjusted in two additional steps: first, by a programmatic adjustment to each row or column of cells lateral to the

river channel that minimized the difference in cross-sectional area between the model and the DEM, and second, by manual adjustment of cells representing the navigational channel.

Programmatic Adjustment to Minimize Differences in Cross-Sectional Area

Following the initial interpolation of depth to the model cells, a computer program was used to adjust the depths across cells lateral to the river to match the cross-sectional area of the DEM. The methodology for adjustment begins by identifying the model cells that lie along a transect lateral to the river flow (Figure 6–10). The model cells are then overlain on the DEM (Figure 6–11). The program next establishes the real world coordinates of the model cell centers and middle of the model cell sides and connects these points with line segments (Figure 6–12). Each line segment is then sub-divided into 10 segments of equal length (Figure 6–13) and a depth is assigned to each of the segment endpoints using the depth of the nearest 10-m DEM cell (Figure 6–14). The result of the previous interpolation is a set of 21 points, aligned precisely along the model cells, whose depths define the shape of the river transect at this location (Figure 6–15). The cross-sectional area of the transect is calculated by numerical integration using Simpson’s Rule (Thomas 1972).

The model cell representing the navigational channel is determined by finding the 80th percentile (H80) of the 21 depths within each model cell. The model cell with the largest H80 value is defined as the navigational channel and is assigned a depth equal to that model cell’s H80 value. The depth within the cell representing the navigational channel remains fixed, while the depths of the remaining cells are iteratively adjusted by equal percentages of depth until the aggregate cross-sectional area of all model cells matches the cross-sectional area derived directly from the DEM to within 1% error.

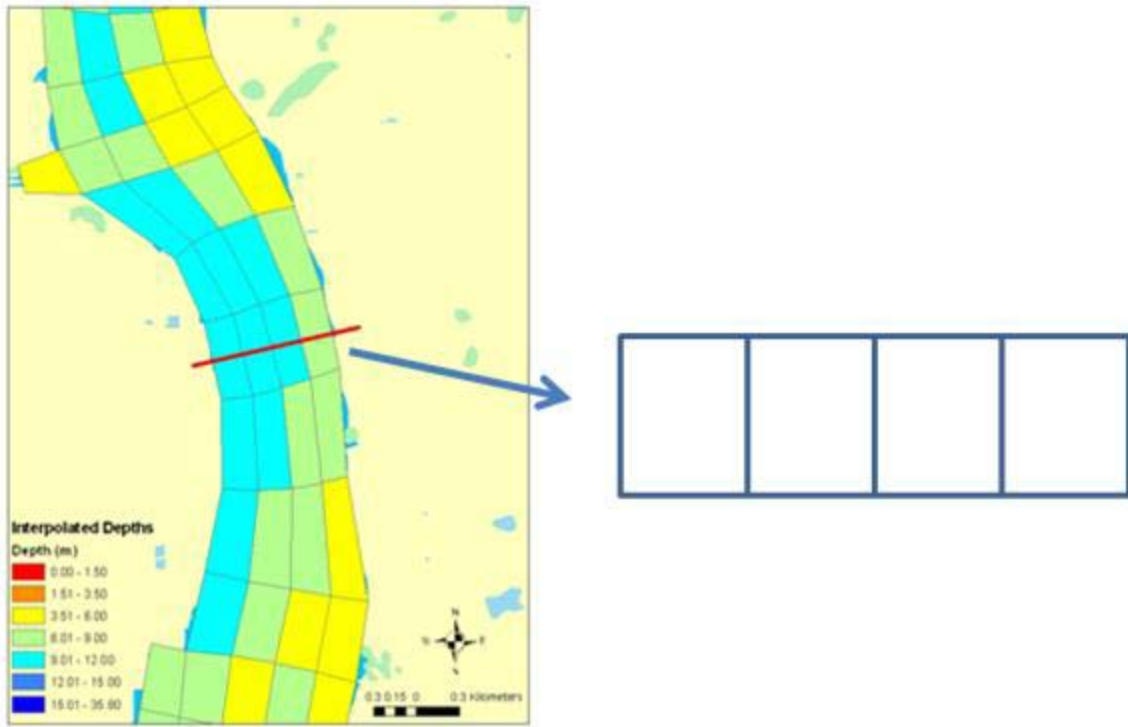


Figure 6–10. Model cells defining a lateral transect.

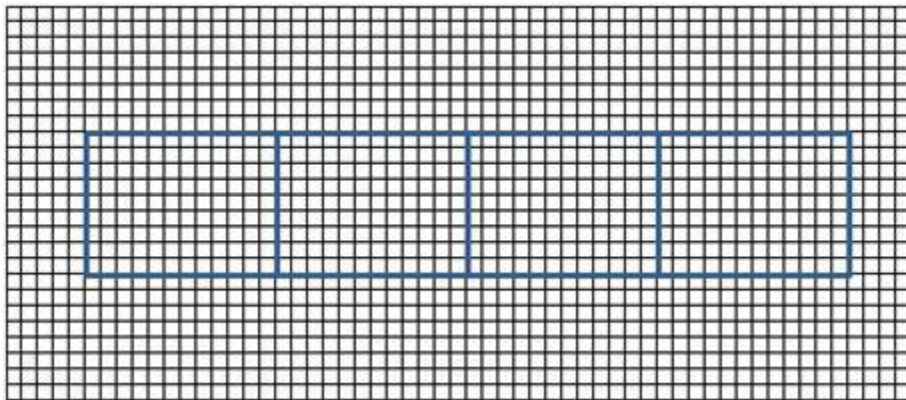


Figure 6–11. Model cells along a transect overlain on the 10-m DEM.

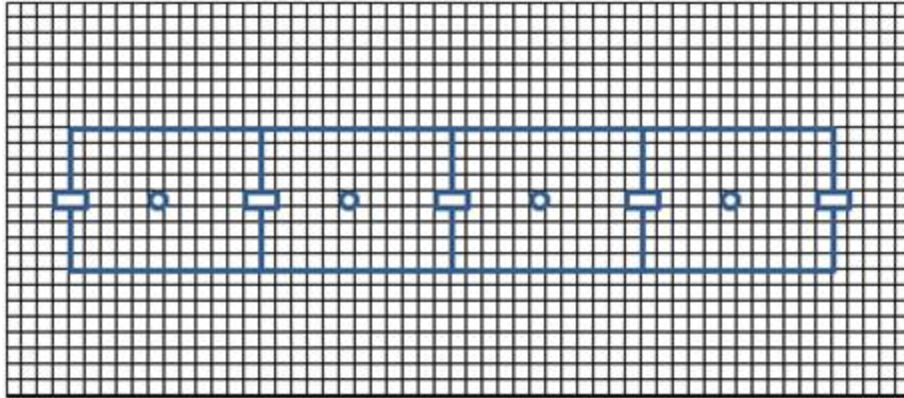


Figure 6-12. Points used to draw a continuous set of line segments across the river transect.

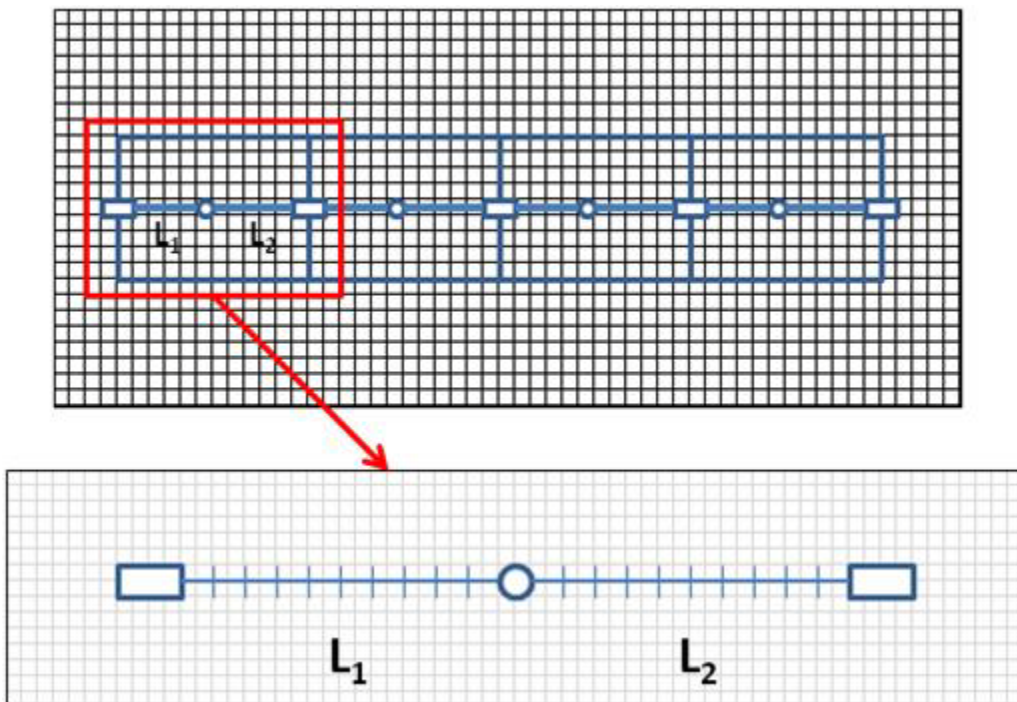


Figure 6-13. Sub-division of each line segment into 10 equal sections.

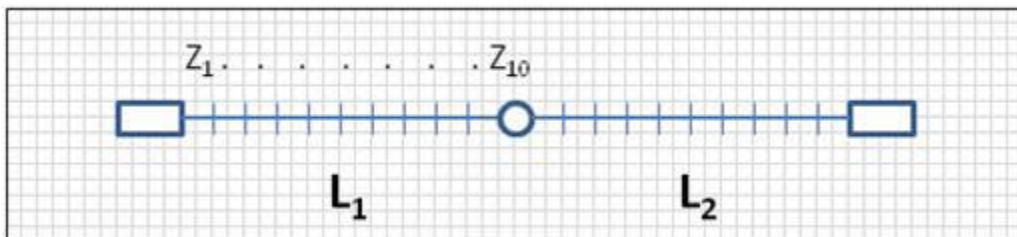


Figure 6-14. A z-value is assigned to each endpoint of the sub-divided sections using the depth of the nearest 10-m DEM cell.

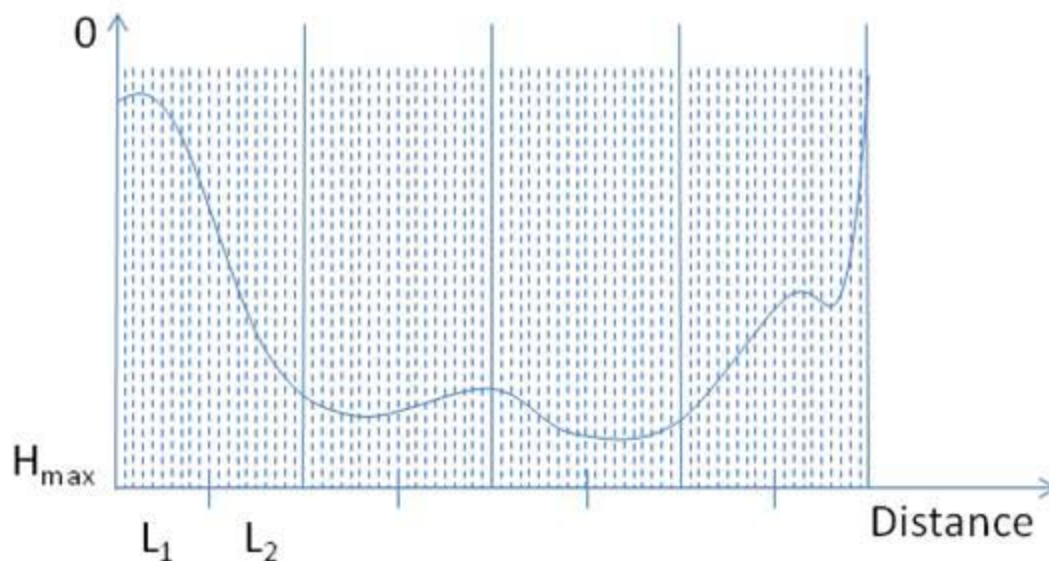


Figure 6–15. Equally spaced z-values plotted along the grid transect by distance. The cross-sectional area of the transect is calculated by numerical integration using Simpson’s Rule.

Manual Adjustments to Channel Cells

A final manual adjustment of model depths was required to (a) align the navigational channel as much as possible along a continuous row of model cells and (b) adjust the cross-sectional areas of narrow channels represented by a single model cell. In the lower St. Johns River, the programmatic assignment of depth sometimes caused cells representing the navigational channel to be staggered longitudinally along different columns of model cells. We preferred that the navigational channel be longitudinally continuous along the same column of model cells, as much as possible, to allow continuous unidirectional flow through the navigational channel. Manual adjustment of cell depths was needed between the Fuller Warren Bridge and the river mouth to align the navigational channel with the same longitudinal column of model cells.

In the middle St. Johns River, the navigational channel is represented by a single cell width in narrow areas of the river interconnecting the major lakes. Many points in the DEM fall within these channel cells and the mean of the DEM depths falling within each model cell was initially assigned as the model cell depth. The range of depth for points falling in a single model cell is often large (Figure 6–16) and the mean depth is not always the best representation of the cross-sectional area of the model cell. Programmatic adjustment of the cross-sectional area using the DEM will also fail to represent the cross-sectional area of the model cell accurately if the model cell is not perfectly aligned with the real world navigational channel. Manual adjustments to model cell depths were thus required where the width of the river channel is represented by a single model cell.

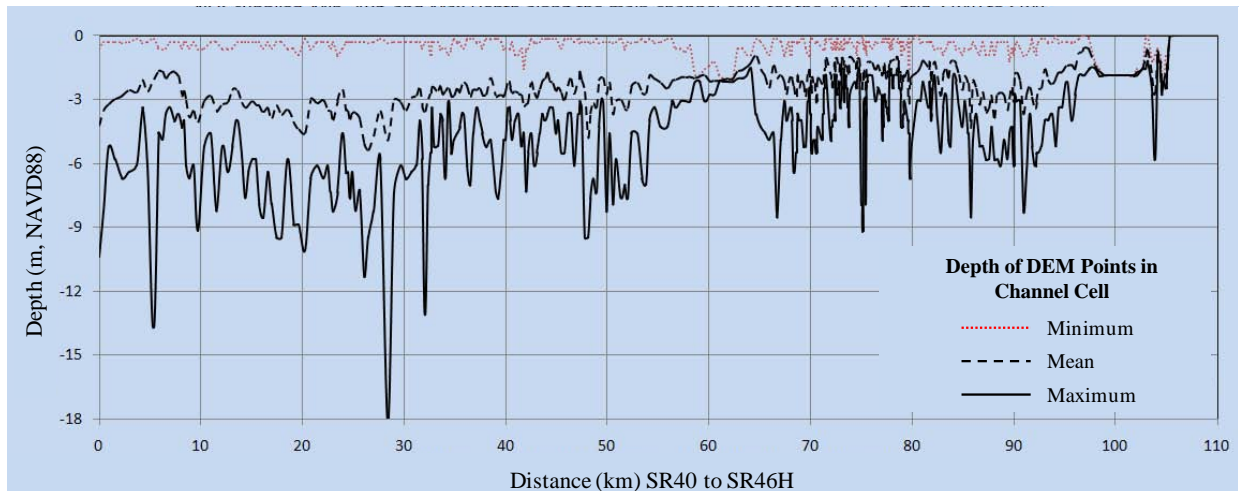


Figure 6–16. Minimum, average, and maximum bottom elevation of DEM points falling within model cells along the thalweg of the middle St. Johns River.

Comparison of Model Cell Depths with DEM Cell Depths

As a final check on the model’s resolution of bathymetry, model cell depths were plotted against DEM cell depths at various river cross-sections. Eight representative cross-sections are shown below. The selected cross-sections extend from the mouth near Mayport to Lake Harney (Figure 6–17).

Comparisons between model cell depths and DEM cell depths for the four northern cross-sections (Figure 6–18) and four southern cross-sections (Figure 6–19) show good agreement.

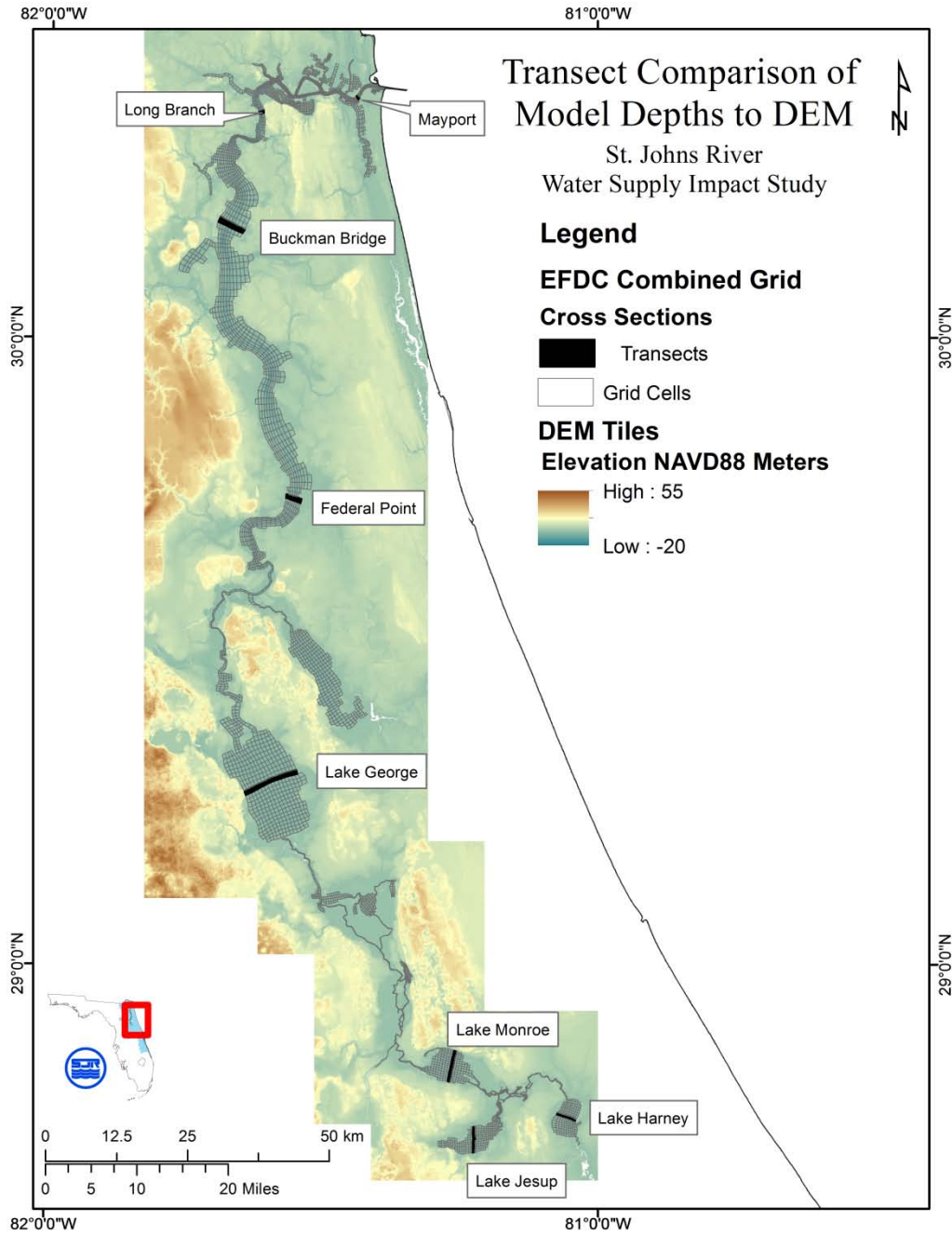


Figure 6–17. Locations of transects where model cell depths are compared to DEM cell depths.

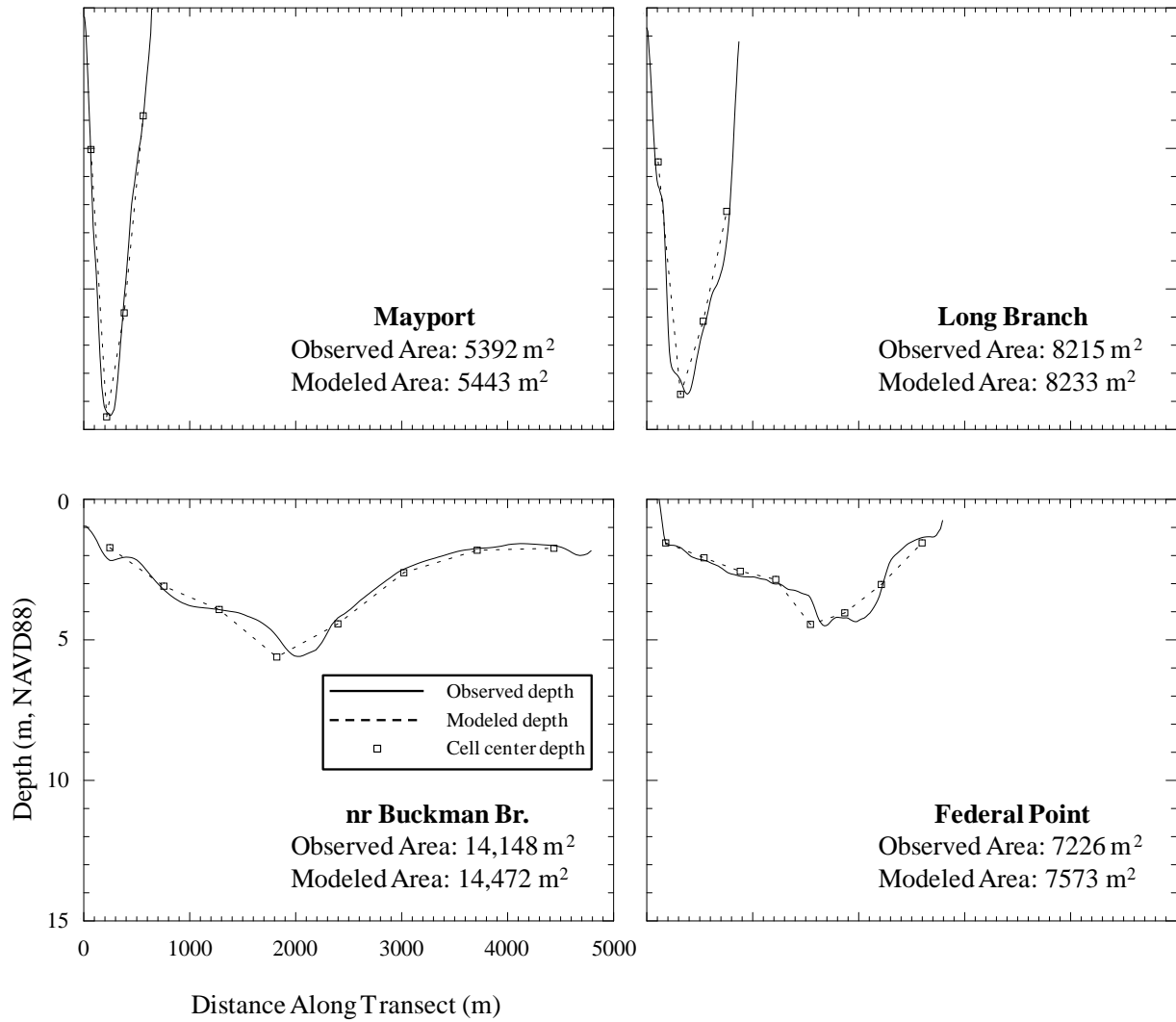


Figure 6–18. Comparison of model cell depths with DEM cell depths across four representative transects in the lower St. Johns River. Equivalent x- and y- scales are maintained for ease of comparison between plots.

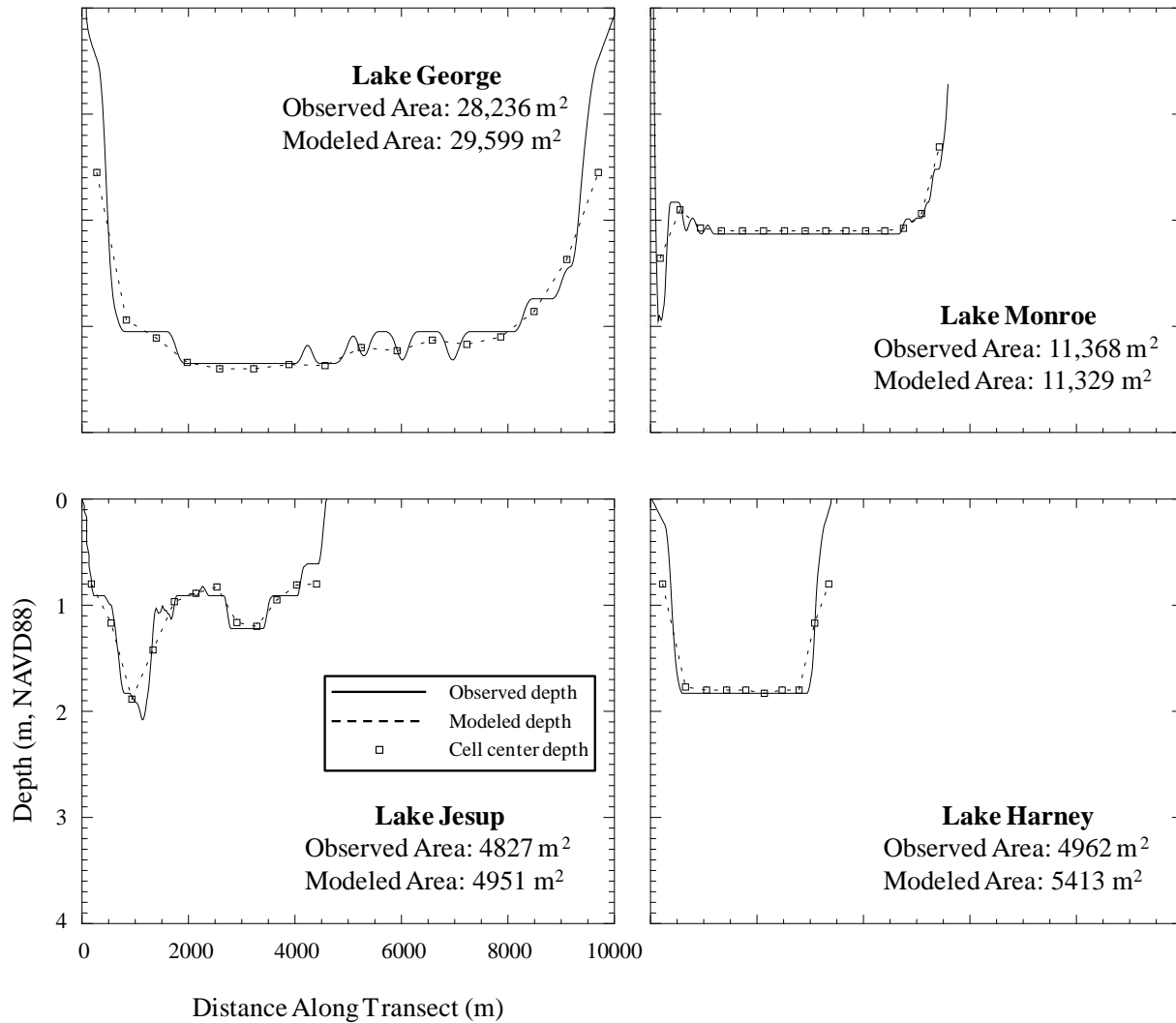


Figure 6–19. Comparison of model cell depths with DEM cell depths across four major lakes in the lower and middle St. Johns River. Equivalent x- and y- scales are maintained for ease of comparison between plots.

6.2.5 FINAL MODEL GRIDS

Final model grids are plotted below for the shelf region of the lower St. Johns River (Figure 6–20), the river region of the lower St. Johns River (Figure 6–21), and the middle St. Johns River (Figure 6–22). The surface area of the EFDC-LSJR hydrodynamic model grid is 11,400 km² and is considerably larger than the surface area of the EFDC-MSJR hydrodynamic model grid of 130.1 km². The shelf area (10,690 km²) accounts for most of the surface area of the EFDC-LSJR hydrodynamic model grid. The EFDC-LSJR hydrodynamic model grid resolves the area by 4295 horizontal cells of which 1356 are shelf cells and 2939 are river cells. The EFDC-MSJR hydrodynamic model grid contains 1713 river cells.

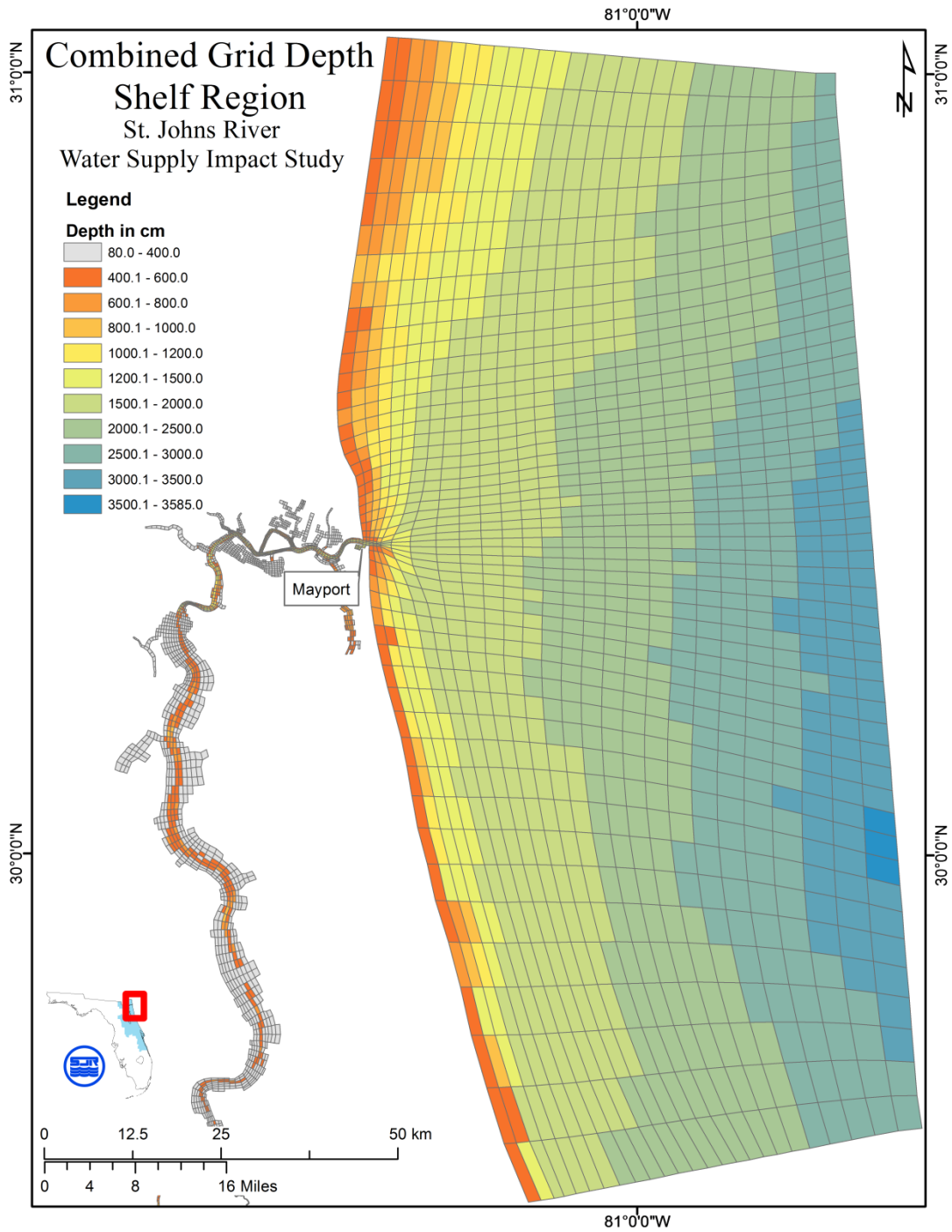


Figure 6–20. Final grid for the EFDC-LSJR hydrodynamic model with emphasis on the shelf region.

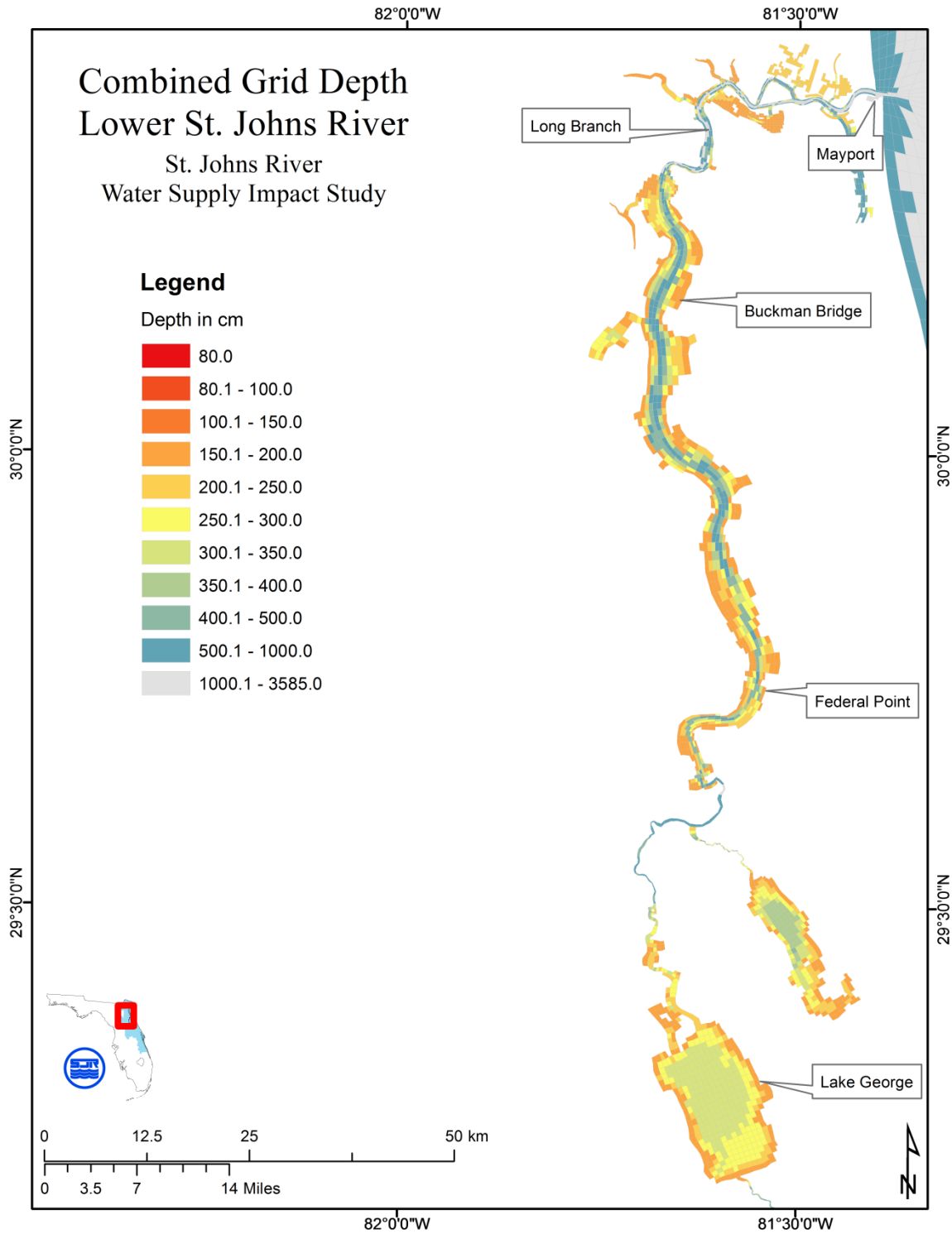


Figure 6–21. Final grid for the EFDC-LSJR hydrodynamic model with emphasis on the river region.

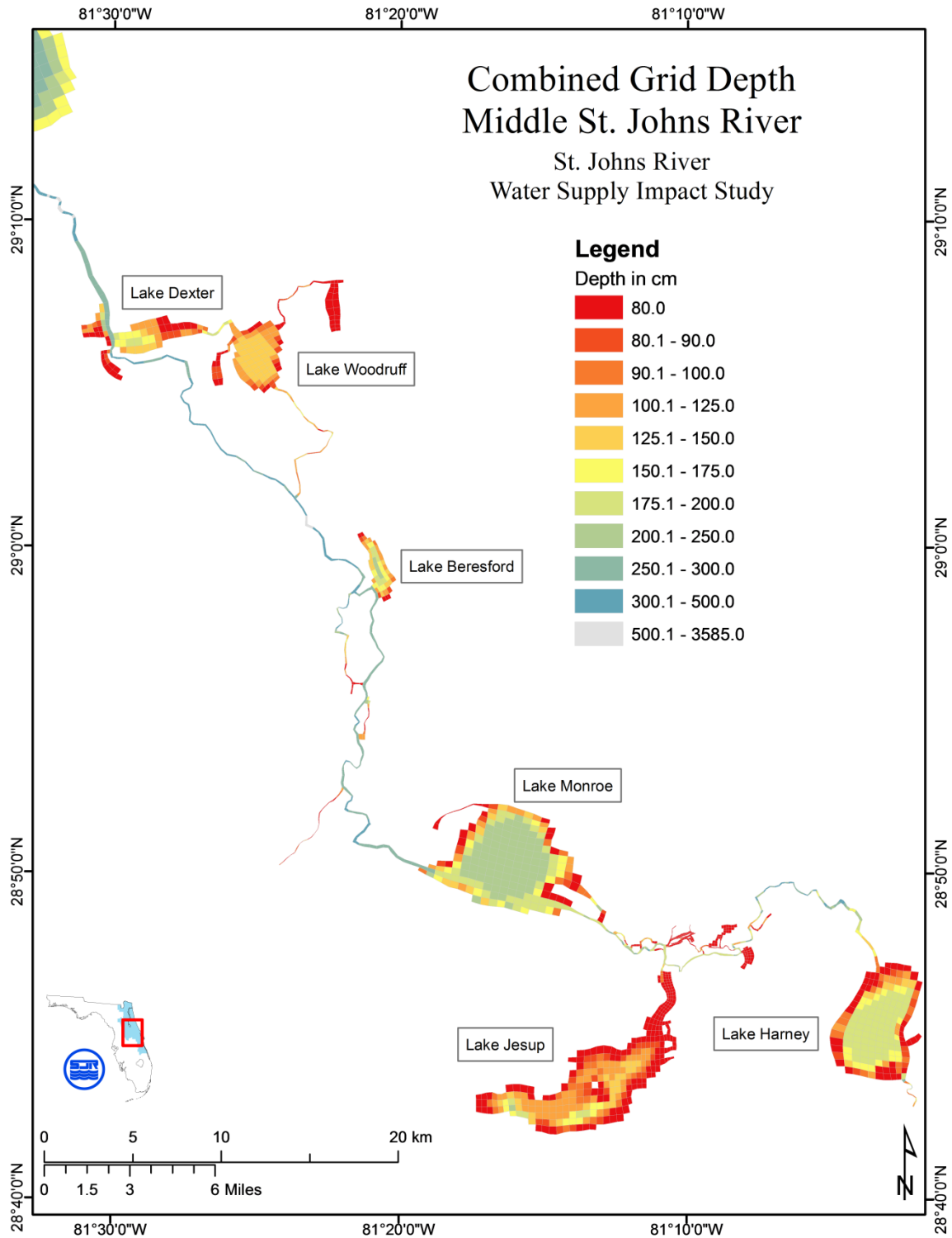


Figure 6–22. Final grid for the EFDC-MSJR hydrodynamic model.

6.3 VERTICAL GRID RESOLUTION

Vertical grid resolution is provided in the EFDC hydrodynamic model by division of each horizontal model cell into an equal number of vertical layers. For the WSIS application of the EFDC hydrodynamic model, the vertical layers are equally spaced. The vertical layers expand and contract to conform to the temporally varying total depth of the water column in each model cell. Such vertical layers are termed “sigma layers” taken from the transform of the underlying differential equations from a z-axis scale to a uniform sigma-axis scale of (usually) zero to one.

Both the lower St. Johns River (EFDC-LSJR) and middle St. Johns River (EFDC-MSJR) hydrodynamic models use six vertical layers. This vertical resolution was needed primarily to account for vertical stratification of salinity in the marine end of the lower St. Johns River. Because the two models are ultimately meant to be combined into a single model application, the same vertical resolution is used for both models. Use of vertical layers for the EFDC-MSJR hydrodynamic model has the added advantage of allowing simulation of vertical velocity profiles, such as might develop within even a homogenous lake due to surface wind stress.

The choice of six vertical layers was determined by a sensitivity test of the EFDC-LSJR hydrodynamic model for salinity. The model simulation period was 1-yr (1997). Runs were made using four, six, eight, and 10 vertical layers. Results show that both average salinity and salinity stratification increased from four to six vertical layers (Figure 6–23). Salinity simulated using six layers was nearly indistinguishable to salinity simulated using eight or 10 layers. Because model run time increases linearly with the number of vertical layers, six vertical layers was deemed optimal for this study.

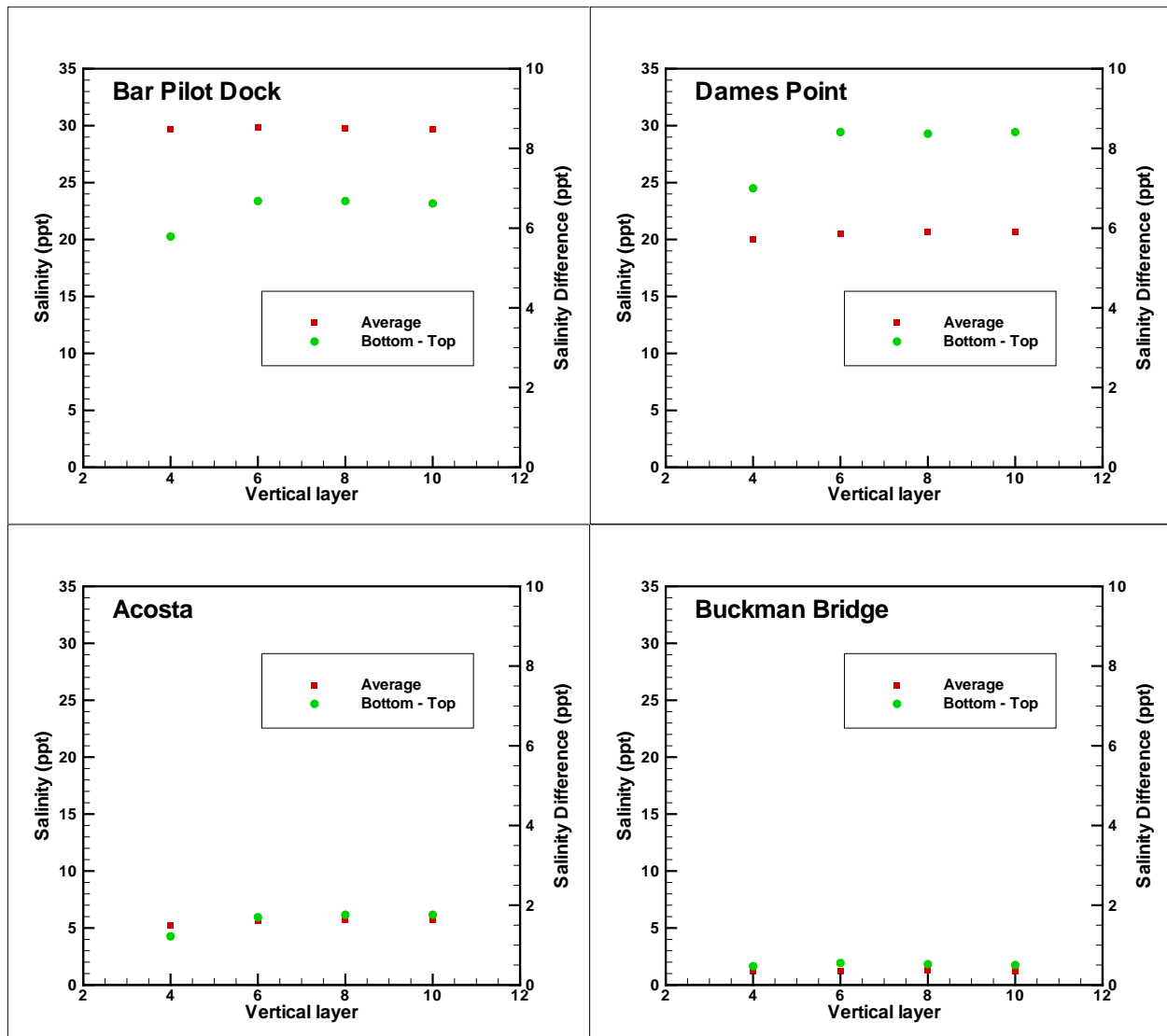


Figure 6–23. Sensitivity of mean salinity and salinity stratification to number of vertical layers for a 1-yr period (1997).

6.4 SELECTION OF CALIBRATION PERIOD

The model simulation period spans 10 years from 1996 to 2005. This period contains complete boundary conditions required to run both the EFDC-LSJR and EFDC-MSJR hydrodynamic models (see Section 5). A shorter calibration period was selected from this period for each model. Using a shorter calibration period allows model confirmation using the larger 10-yr data set. This method satisfies the general modeling principle of using a given set of conditions for model calibration followed by use of an independent set of conditions for model confirmation. Model confirmation tests the robustness of the model under conditions statistically distinct from the calibration period to show that the model is capable of prediction under conditions different than the calibration period. We show below that the 10-yr model simulation period contains more extreme events than the selected calibration periods.

Middle St. Johns River Calibration Period

The calibration period selected for the EFDC-MSJR hydrodynamic model is March to September 2001. This period is selected primarily because it is contained within the period of record for the continuous USGS salinity gauges at DeLand and Sanford (see Table 3–11).

The calibration period contains a period of slowly increasing salinity followed by a rapid decline. The daily averaged salinity at Sanford (USGS 02236000) fell from a maximal value of 1.35 on 8 July 2001 to 0.22 at the end of September 2001 (Figure 6–24). The first 3 months, March to May, of the period had low discharge with several periods of reverse flow; salinity was generally below about 0.8 and showed several freshening events. Discharge rose slightly in June and July and reverse flow events were no longer observed. Salinity, however, continued to increase from near 1.0, at the beginning of June, to a maximum value of 1.35 in early July. Discharge rose again, from mid-July through September, reaching $250 \text{ m}^3 \text{ s}^{-1}$ by the end of September.

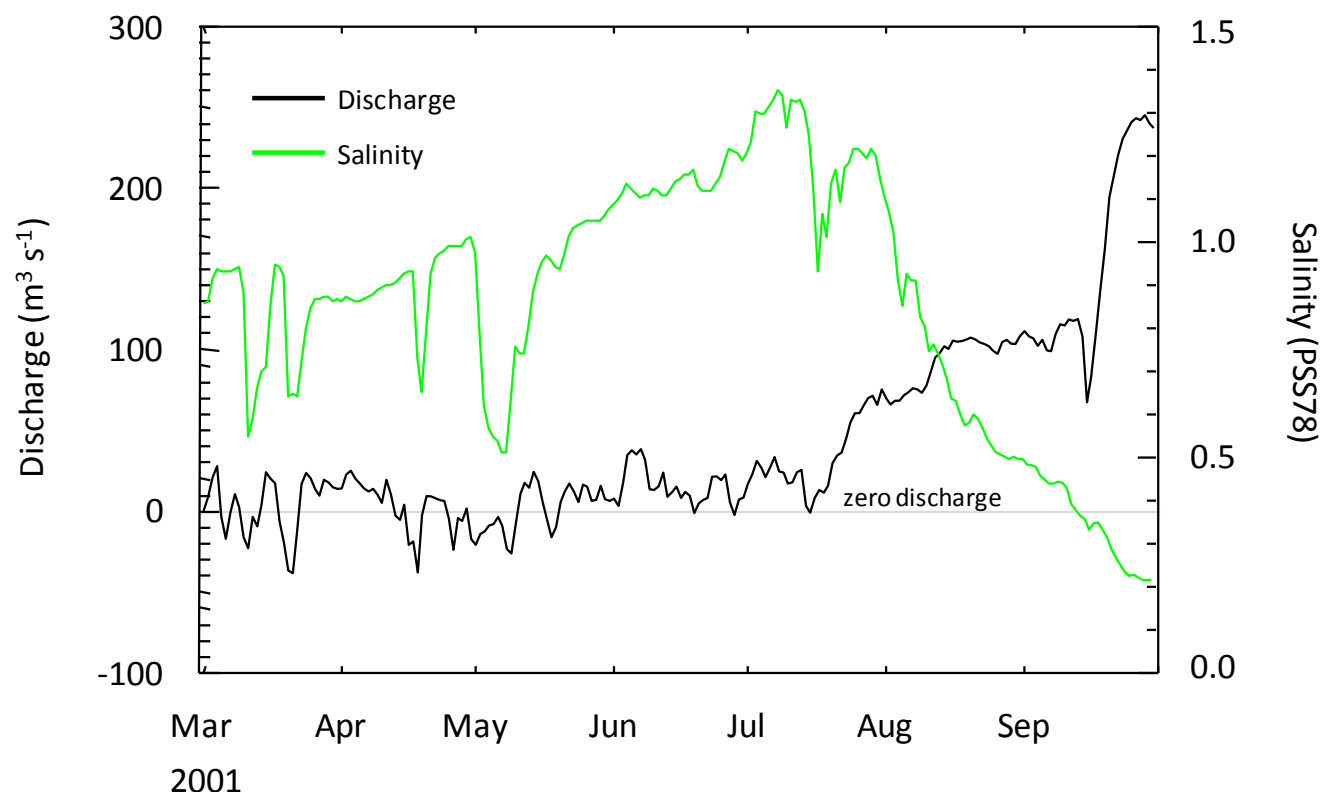


Figure 6–24. Observed daily averaged discharge and salinity at Sanford, U.S.17 (USGS 02236000), for the middle St. Johns River calibration period.

Discharge during the calibration period is placed in context to long-term discharge by comparing various N-day averages of discharge for the calibration period to duration frequency curves developed from a long-term discharge record. Comparisons are made at DeLand because of its long-period of record for discharge (1957 to 2008). Low flow duration frequency curves for DeLand are shown as solid lines in Figure 6–25. The minimum N-day average discharge over the calibration period are shown as square symbols for $N = 1, 2, 5, 10, 20, 50, 100,$ and 200 days.

Minimum discharge during the calibration period has moderate return periods. The highest return period of 5 yrs occurs for 50 to 100-day averaging periods. In contrast, minimum N-day averages of discharge for the 10-yr model confirmation period (1996 to 2005) have return periods equal or greater than 25 years. The model confirmation period has periods of low flow that are significantly more extreme than for the model calibration period.

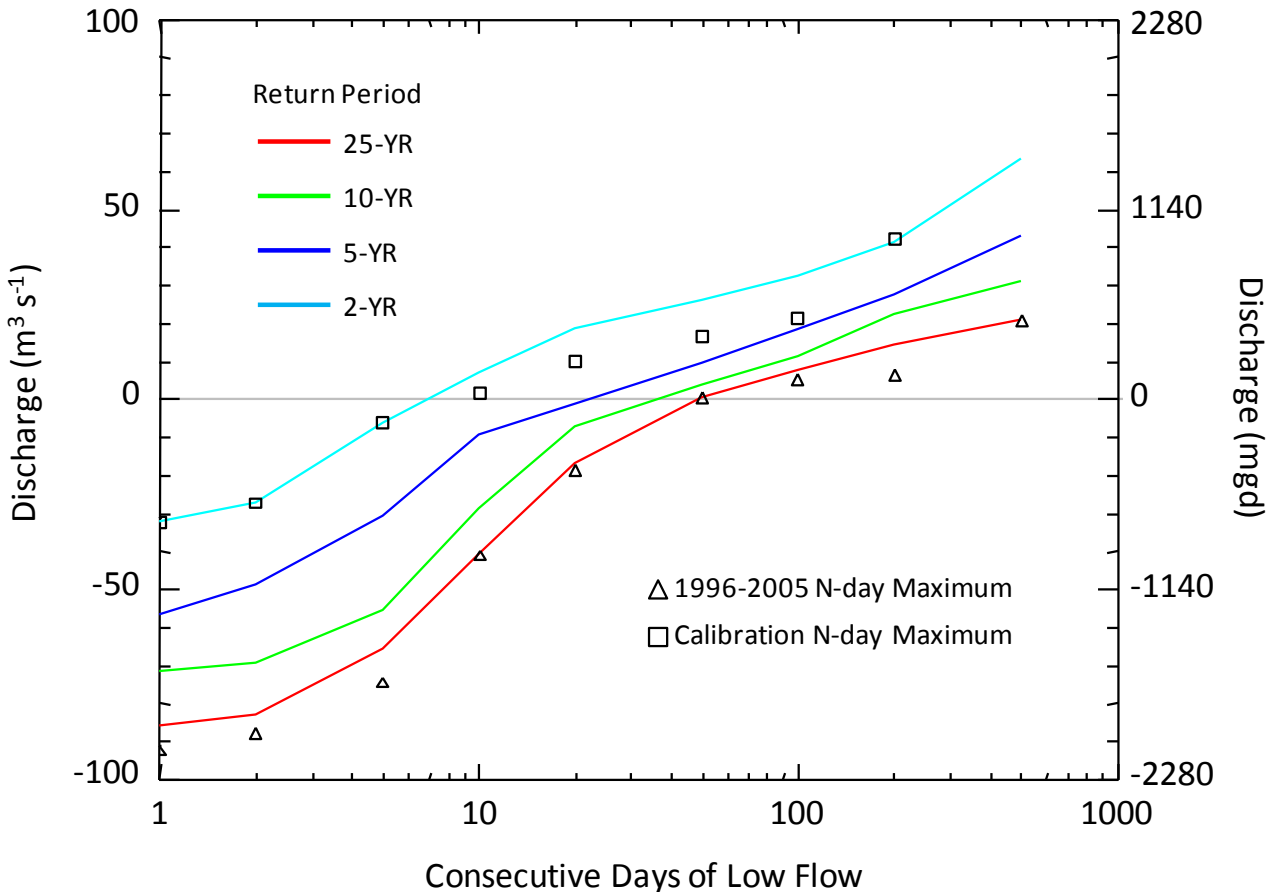


Figure 6–25. Low flow duration frequency curves for DeLand with minimum N-day averages over the model confirmation period (1996 to 2005) and middle St. Johns River calibration period (March to September, 2001). Duration frequency curves use the DeLand long-term record of 1957 to 2008.

High flow duration frequency curves for DeLand are shown in Figure 6–26, with maximum N-day averages of discharge for the calibration period shown by square symbols. High flow events during the calibration period for averaging periods less than 10 days are high, with return periods of 5 to 10 years. High flow events during the calibration period are modest for averaging periods greater than 10 days, however, with return periods of 2 years or less. By contrast, the confirmation period (1996 to 2005) exhibits 25-yr extreme high flows for averaging periods greater than 50 days. The confirmation period has long-duration periods of high flow that are significantly more extreme than for the model calibration period.

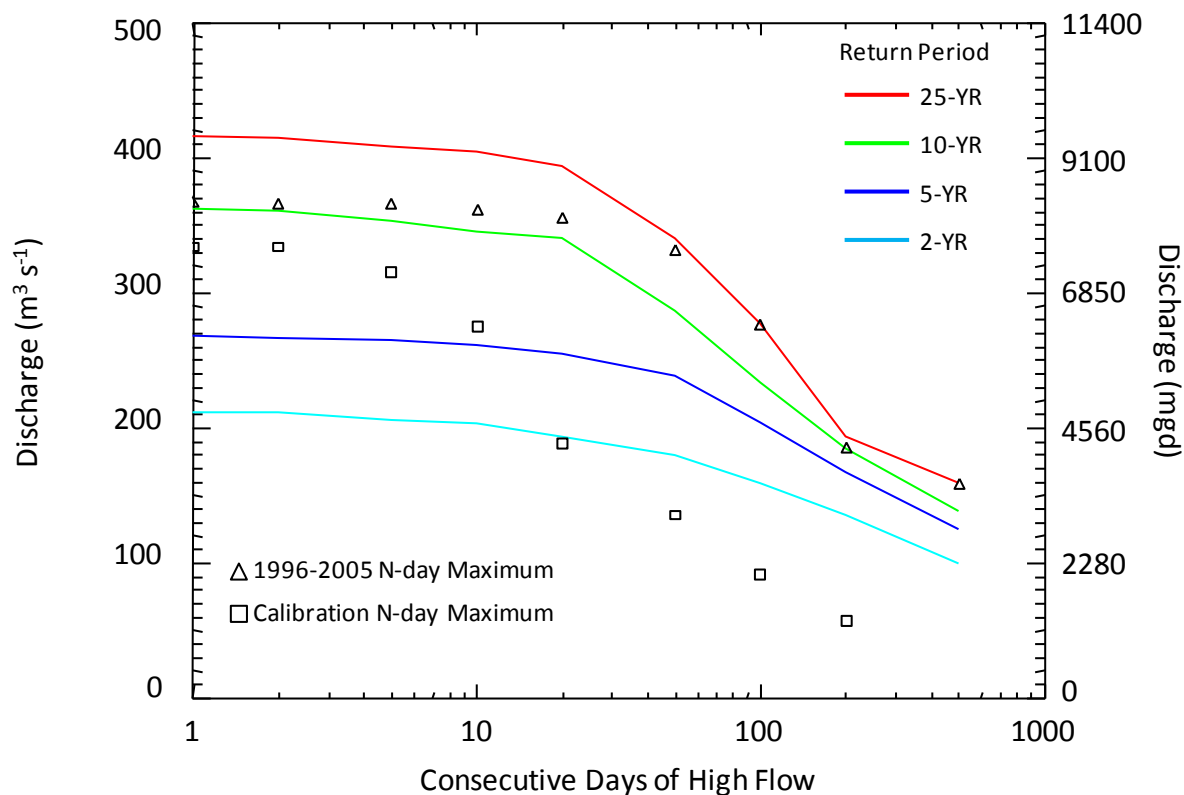


Figure 6–26. High flow duration frequency curves for DeLand with minimum N-day averages over the confirmation period (1996 to 2005) and middle St. Johns River calibration period (March to September, 2001). Duration frequency curves use the DeLand long-term record of 1957 to 2008.

Lower St. Johns River Calibration Period

The calibration period selected for the EFDC-LSJR hydrodynamic model is August 1997 to April 1999. This period is selected because of the following features:

- A comprehensive set of ADCP tidal discharge observations collected in September 1997 (Table 3–10)
- Five additional WQMN salinity stations and one additional USGS continuous discharge stations that went online in 1997 to 1998 (Table 3–11)
- This period was previously used for calibration of the EFDC-TMDL hydrodynamic model (Sucsy and Morris 2002)

The calibration period includes an extremely wet winter during December 1997 to April 1998 (Figure 6–27). 30-day averaged discharge at Main Street Bridge near Jacksonville reached over $800 \text{ m}^3 \text{ s}^{-1}$ during that period, while salinity dropped to near zero. The calibration period contains two periods of high salinity in the summer of 1998 and spring of 1999. Mean discharge for the calibration period is $285.6 \text{ m}^3 \text{ s}^{-1}$ with a range of 38.6 to 836.7 for 30-day averaged discharge. Mean salinity is 4.9, with a range of 0.2 to 16.7 for 30-day averaged salinity.

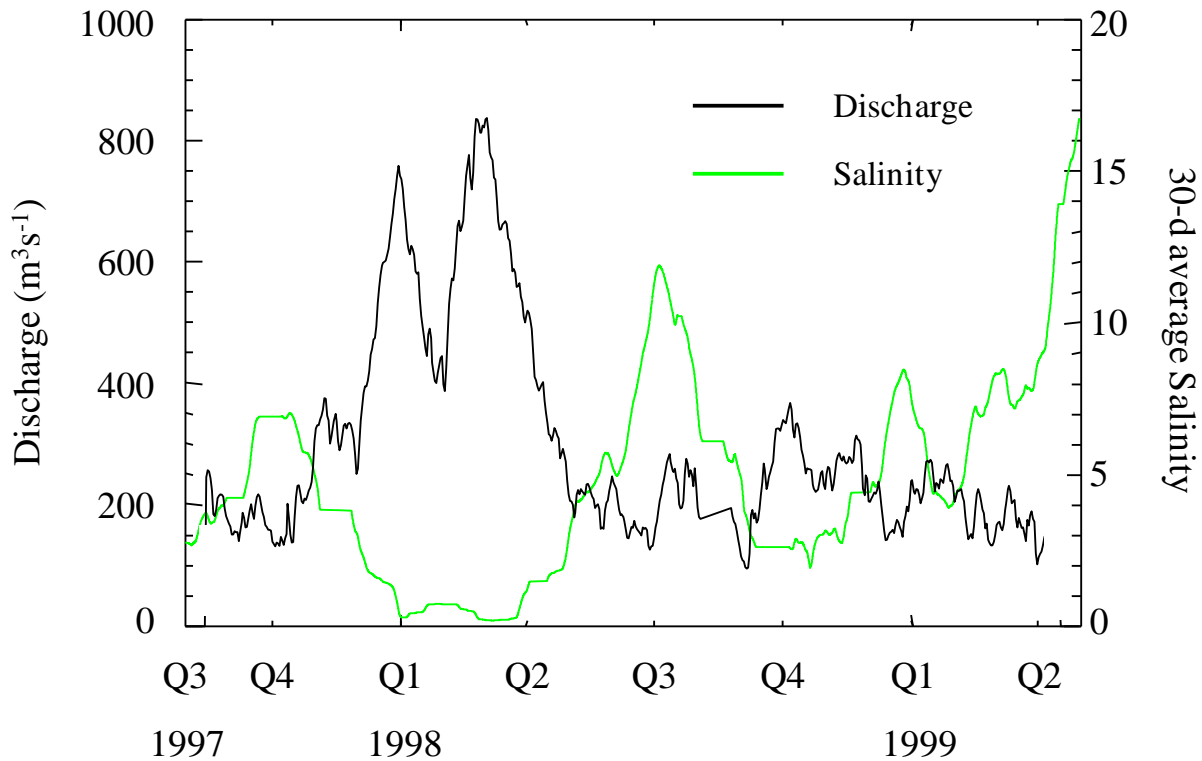


Figure 6–27. Observed 30-day averaged discharge and salinity at Main Street Bridge near Jacksonville (USGS) for the lower St. Johns River calibration period.

Discharge and salinity records in the lower St. Johns River have insufficient length to create duration frequency curves as shown above for DeLand discharge. A comparison of the magnitude of salinity events shows that the 10-yr confirmation period has significantly larger salinity events than the calibration period (Table 6–5). The maximum 30-day averaged salinity at Buckman Bridge was 4.0 during the model calibration period, but 13.9 during the confirmation period. Shands Bridge had no appreciable salinity events during the calibration period, but had a 1-day salinity of 8.8 and 30-day salinity of 5.0 during the confirmation period.

Table 6–5. Comparison of 1-, 7-, and 30-day high salinity events for the confirmation period (1996 to 2005) and calibration period (August 1997 to April 1999) at four locations in the lower St. Johns River (LSJR).

Station	Period	Max 1-Day Surface Salinity	Max 7-Day Surface Salinity	Max 30-Day Surface Salinity
Dames Point	10-yr Simulation	35.7	34.4	30.8
	LSJR Calibration	32.7	29.8	25.6
Acosta Bridge	10-yr Simulation	33.7	29.1	20.7
	LSJR Calibration	25.3	17.2	11.9
Buckman Bridge	10-yr Simulation	18.7	15.9	13.9
	LSJR Calibration	11.4	6.4	4.0
Shands Bridge	10-yr Simulation	8.8	6.2	5.0
	LSJR Calibration	1.7	0.8	0.7

6.5 COMPARATIVE STATISTICS

The model calibration was evaluated by statistical comparison of matched pairs of simulated and observed time series. Comparative statistics calculated were the coefficient of determination (r^2), the slope of the linear regression line (m), the Nash–Sutcliffe coefficient (NS), the average relative error ($AVRE$), the average absolute error ($AVAE$), and the root-mean-square error ($RMSE$).

r^2 and m were calculated using built-in functions from the Visual Numerics library (Visual Numerics 2001). The remaining comparative statistics were calculated using the formulas below. The Nash–Sutcliffe statistic is defined following an ASCE Watershed Management Committee report (ASCE 1993) and $AVRE$, $AVAE$, and $RMSE$ are defined by Thomann (1982).

If O_i represent the observed values and P_i the simulated (predicted) values for $i = 1$ to N , where N is the number of match pairs, then statistics are defined as follows:

$$NS = 1.0 - \frac{\sum_{i=1}^N (O_i - P_i)^2}{\sum_{i=1}^N (O_i - \bar{O})^2} \tag{6-3}$$

$$AVRE = \frac{\sum_{i=1}^N \frac{|O_i - P_i|}{|O_i|}}{N} \tag{6-4}$$

$$AVAE = \frac{\sum_{i=1}^N |O_i - P_i|}{N} \tag{6-5}$$

$$RMSE = \sqrt{\frac{\sum_{i=1}^N (O_i - P_i)^2}{N}} \quad (6-6)$$

Guidance for the interpretation of the Nash–Sutcliffe statistic is provided in Chapter 3 as:

Very Good	0.75 to 1.0
Good	0.65 to 0.75
Satisfactory	0.50 to 0.65
Unsatisfactory	<0.50

Although these categories apply particularly to monthly discharge, they serve as a useful frame of reference.

6.6 CALIBRATION OF BOTTOM ROUGHNESS

Bottom roughness is the principle calibration parameter for the EFDC hydrodynamic model. However, calibration cannot be accomplished by adjustment of bottom roughness alone. Proper specification of system geometry, bathymetry (see Section 6.2), and model boundary conditions (see Section 5) must be included when calibrating a model. For the WSIS, adjustment of bottom roughness followed careful attention to these factors and essentially produced the final calibrated model excepting a few adjustments to boundary conditions.

The calibration of bottom roughness was done differently for the EFDC-LSJR and EFDC-MSJR hydrodynamic models. Calibration of the two models focused on different dynamical responses to bottom roughness. For the EFDC-LSJR hydrodynamic model, the adjustment of bottom roughness focused on matching tidal dynamics. This choice reflects the importance of tidal dynamics to the overall hydrodynamics of the lower St. Johns River (Section 4.1). For the EFDC-MSJR hydrodynamic model, the adjustment of bottom roughness focused on simulating observed discharge-surface slope relationships. This choice is based on a previous hydraulic calibration by Robison (2004), the lack of tide in the middle St. Johns River, and the importance placed on simulation of discharge-stage (surface slope) responses for the evaluation of water withdrawals (Section 4.3).

The calibration methodologies for the two grids also differed because of the different goals of the calibration. For the EFDC-LSJR hydrodynamic model, the adjustment of bottom roughness to match system-wide tidal dynamics was conducive to use of a spatial optimization method for bottom roughness. For this model application, we used PEST (Doherty 2004), a parameter optimization model, to determine spatially varying bottom roughness that minimizes the differences between observed and simulated tidal constituents throughout the model domain. For the EFDC-MSJR hydrodynamic model bottom roughness and the spatial variation of bottom roughness is developed by use of well-established Manning's n values as a starting point, followed by numerical experiments using the EFDC-MSJR hydrodynamic model.

6.6.1 CALIBRATION OF LOWER ST. JOHNS RIVER BOTTOM ROUGHNESS

To implement parameter optimization, grid cells were grouped into 10 segments (Figure 6–28) within which bottom roughness is optimized. Initial bottom roughness for the segments was set to match the EFDC-TMDL hydrodynamic model (Sucsy and Morris 2002) and varied from 1.0×10^{-4} to 0.025 m. Bottom roughness within each segment was allowed to vary over this same

range. Bottom roughness within cells along segment boundaries were smoothed to prevent sharp discontinuities of bottom roughness between segments that could introduce artificial reflections within the model. Marsh cells, cells in tributaries, and ocean cells were not optimized by PEST and were assigned a constant bottom roughness of 2.5×10^{-2} m.

For each instance of parameter selection within PEST, the EFDC hydrodynamic model was run for 28 days. Following 21 days of spin-up, the last 7 days were used for harmonic tidal analysis of water levels. M_2 and K_1 tidal constituents were calculated using the Tidal Analysis Program Python (Cera 2010).

PEST minimized the differences between observed and simulated tidal constituents for 12 stations. The stations selected were the 10 active water level stations in the lower St. Johns River (stations 1 to 10, see Table 3–1) and two stations leading into Crescent Lake (stations 19 to 20, see Table 3–3). PEST generally lowered bottom roughness from the initial supplied values (Table 6–6). Bottom roughness in the lacustrine lower St. Johns River (segments 2 and 3) and in portions of Crescent Lake (segment 5) were reduced to (or maintained at) minimum allowable values.

Table 6–6. Initial and optimized bottom roughness for each segment provided to PEST. Segment numbers refer to Figure 6–28.

Segment	Initial Bottom Roughness (m)	PEST Optimized Bottom Roughness (m)
1	3.00E-03	6.14E-04
2	1.00E-03	1.00E-04
3	1.00E-04	1.00E-04
4	1.00E-02	1.25E-02
5	1.00E-02	1.00E-04
6	1.00E-04	2.50E-02
7	2.50E-02	2.50E-02
8	2.50E-02	1.92E-02
9	1.00E-02	2.50E-02
10	1.00E-02	7.78E-03

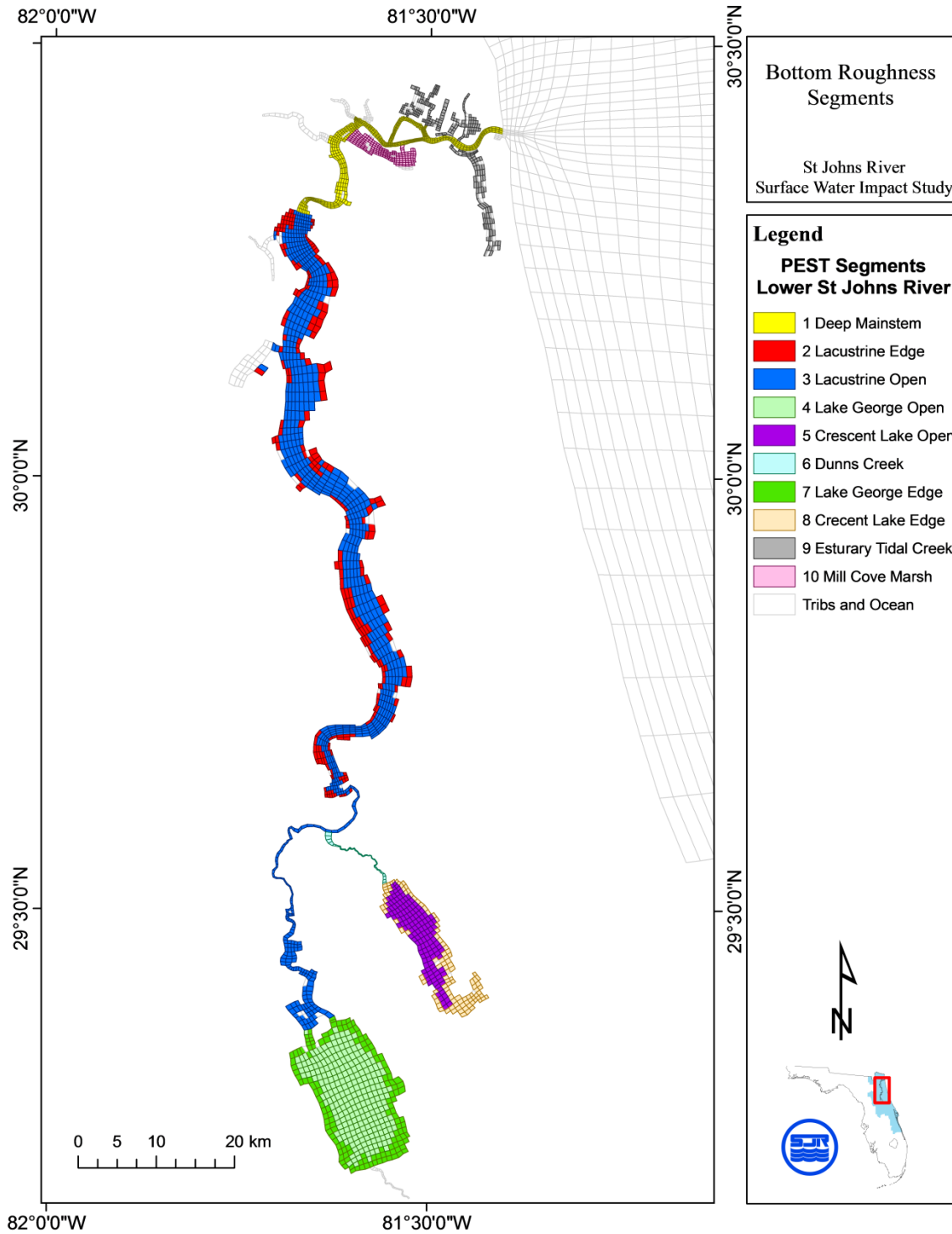


Figure 6–28. Segments used for Parameter ESTimation (PEST) optimization of bottom roughness.

6.6.2 CALIBRATION OF MIDDLE ST. JOHNS RIVER BOTTOM ROUGHNESS

Calibration of middle St. Johns River bottom roughness was done in three steps. Initial estimates of bottom roughness were first made from estimates of Manning's n (Sturm 2001) for various river segments. Manning's n was estimated in two ways: first, by use of observed slope and discharge, and second, by use of standard hydraulic tables. The use of Manning's n as a starting point for bottom roughness provided both initial estimates and established the relative spatial variation of bottom roughness over the model domain.

Following the initial estimation of bottom roughness by Manning's n , bottom roughness was calibrated using constant, steady-state discharge scenarios. Bottom roughness was iteratively adjusted for each discharge scenario so that simulated water levels matched the observed surface slope–discharge relationships developed in Section 4.3. The relative spatial variation of initial bottom roughness was maintained in this step.

Finally, the initial bottom roughness and calibrated bottom roughness were compared for a completely dynamic simulation over the calibration period. This last step is to ensure that the calibrated bottom roughness parameters developed using the steady-state discharge tests are applicable to the dynamic simulation.

Initial Estimation of bottom roughness based on Manning's n

Initial values of bottom roughness were assigned to the middle St. Johns River grid cells from estimates of the common hydraulic friction parameter, Manning's n (Sturm 2001). Manning's n values were estimated for the main channel by application of Manning's equation to observations of surface water slope and discharge. Higher values of Manning's n were assigned to shallow, vegetated areas off the main channel using standard tables. The Manning's n values were then converted to bottom roughness for input to the hydrodynamic model. This methodology supplied both initial values of bottom roughness to the EFDC-MSJR hydrodynamic model grid, and established the relative spatial variation of bottom friction throughout the model.

An example of estimating of Manning's n from observed slope and discharge is presented for both a high and low discharge event at U.S.17. The low discharge event of $32.6 \text{ m}^3 \text{ s}^{-1}$ occurred on 9 November 2005 and the high discharge event of $251.8 \text{ m}^3 \text{ s}^{-1}$ occurred on 7 June 2007.

Discharge on these days was determined from ADCP velocity measurements (Figure 6–29). The ADCP data also shows that the velocities are relatively uniform over the bulk of the water column, although weaker velocities occur along the river margins. Typical current speeds were 0.1 m s^{-1} for the low-flow event and 0.4 m s^{-1} for the high-flow event. Observed discharge, velocity, and river stage for these two days is shown in Table 6–7 for the U.S.17 location and for stations both upstream (SR 46) and downstream (SR 44) of U.S.17.

Geometric parameters required for Manning's Equation are also available from the ADCP measurements (Table 6-8).

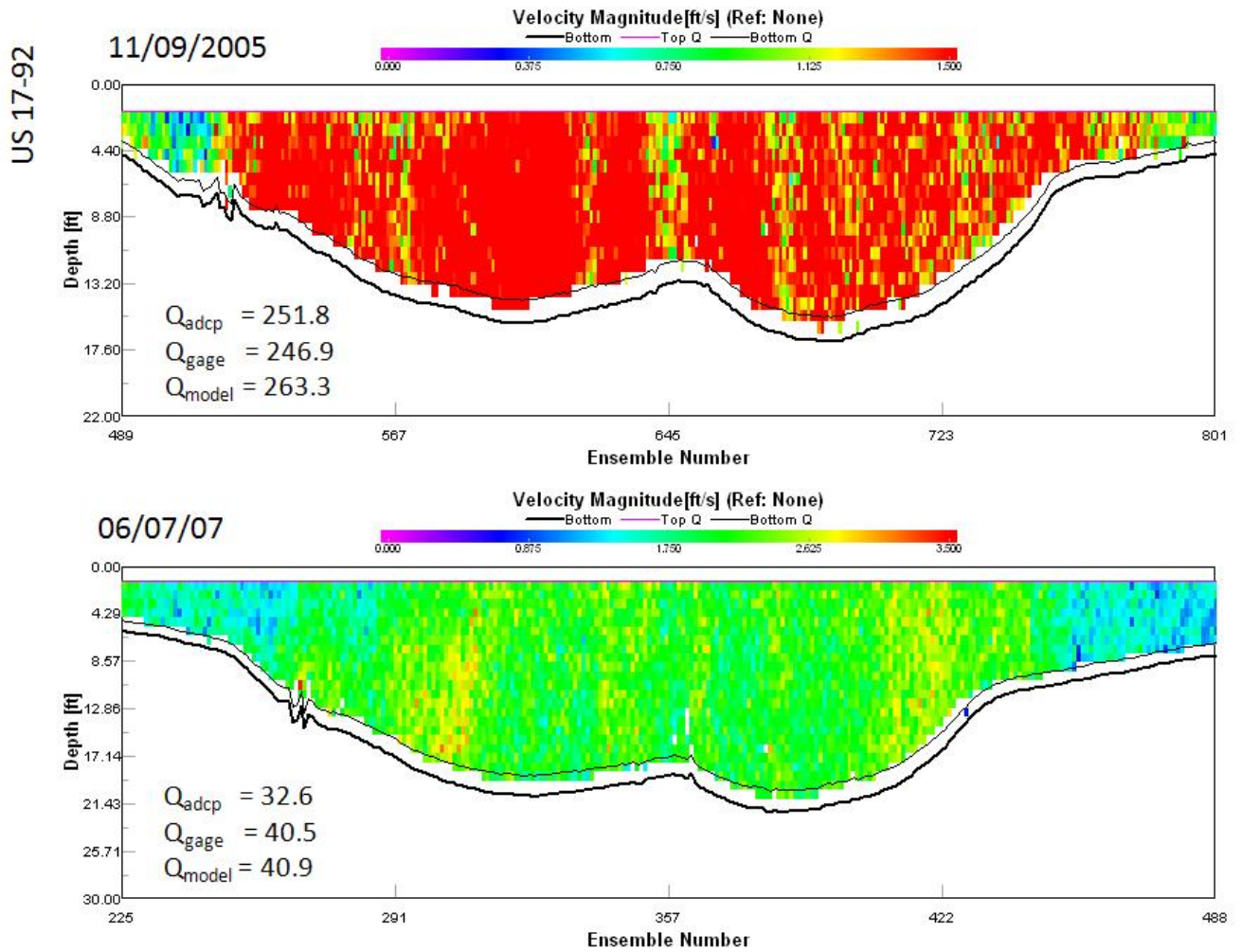


Figure 6–29. Acoustic Doppler Current Profiler (ADCP) profile of velocity at U.S.17 for a low discharge and high discharge period.

Table 6–7. Observed stage, discharge, and velocity at U.S.17 and at upstream (SR 46) and downstream (SR 44) sites for high flow (9 November 2005) and low flow (7 June 2007) events.

Event	Observation	SR 46	US 17	SR 44
11/09/05	Stage (m NAVD88)	2.29	1.43	0.86
	Discharge (m ³ s ⁻¹)	219.3	246.8	268.6
	Velocity (m s ⁻¹)	0.18	0.40	0.42
06/07/07	Stage (m NAVD88)	-0.15	-0.09	-0.17
	Discharge (m ³ s ⁻¹)	4.4	40.5	54.9
	Velocity (m s ⁻¹)	0.01	0.10	0.10

Table 6–8. Geometric parameters for the U.S.17 gauged cross section derived from Acoustic Doppler Current Profiler (ADCP) measurement.

US 17 near Sanford	Measurement Day	
	9 November 2005	7 June 2007
Max Depth (m)	6.82	5.24
Width (m)	434.04	376.85
Area (m ²)	657.73	442.13
Wetted Perimeter (m)	135.51	116.81
Hydraulic Radius (m)	4.85	3.79
Average Depth (m)	4.67	3.62

Manning’s *n* for these two flow conditions is estimated as 0.032 to 0.039 (Table 6–9), comparable to literature values for natural channels (Sturm 2001).

Manning’s *n* is converted to bottom roughness *z*₀ through equivalence with *K*, the dimensionless drag coefficient of the quadratic stress law, using the following two relationships:

$$K = \frac{g \times n^2}{H^{1/3}} \tag{6-7}$$

$$K = (0.4)^2 \left[\frac{(\frac{\Delta H}{2})}{z_0} \right]^{-2} \tag{6-8}$$

where

$$g = 9.81 \text{ m/s}^2$$

$$H = \text{depth (m)}$$

Depth in Equation 6.4 is denoted ΔH to indicate that it is selected here as the mid-depth value of the water column without consideration of the vertical velocity profile. This assumption can lead to order-of-magnitude deviations in the estimation of z_o from n .

Bottom roughness ranges from 0.014 to 0.031 m for these two events (Table 6–9).

Table 6–9. Manning’s n , drag coefficient, bottom roughness, and bottom stress estimated from observed Acoustic Doppler Current Profiler (ADCP) data at U.S.17.

Observed and Calculated Parameters Obtained from ADCP Data and Surface Slope	9 November 2005	7 June 2007
ADCP velocity (m/s)	0.38	0.07
Velocity head upstream station (m)	1.6E-03	6.3E-06
Velocity head downstream station (m)	7.5E-03	2.7E-04
Vel Hv (difference v-head)	-5.9E-03	-2.6E-04
Del H (diff in stage, m)	0.86	0.06
Slope (m/m)	1.8E-05	1.3E-06
Manning’s n	0.032	0.039
Drag coefficient (K)	0.0060	0.0097
Bottom roughness (m)	0.014	0.031
Bottom stress (Pa)	0.8839	0.0507

A nomograph comparing Manning’s n , depth, and bottom roughness (z_o) was created to estimate initial bottom roughness in model cells from calculated Manning’s n and Manning’s n assigned by reference to standard tables (Figure 6–30).

Initial values of bottom roughness assigned to the precalibrated middle St. Johns River model ranged from 0.001 to 0.1 m (Figure 6–31).

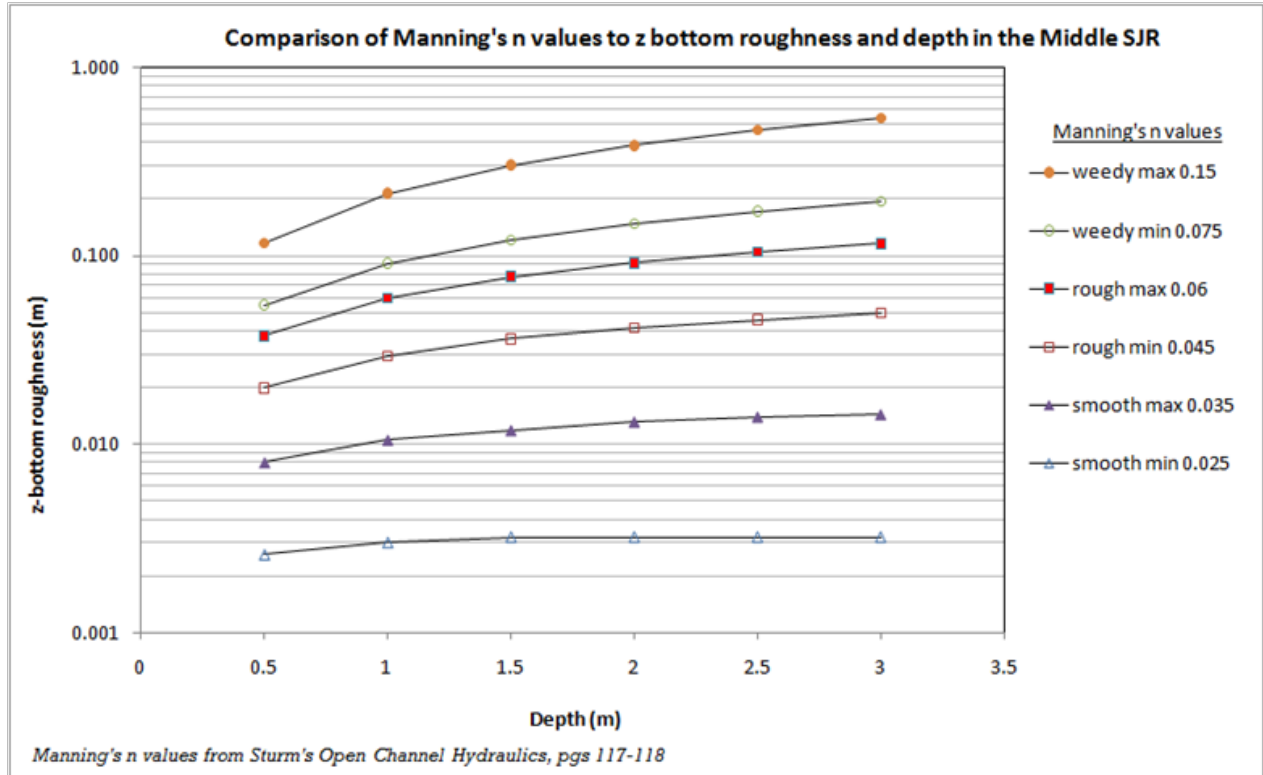


Figure 6–30. Nomograph comparing Manning's n values to bottom roughness z_0 and depth for ranges of values within the middle St. Johns River.

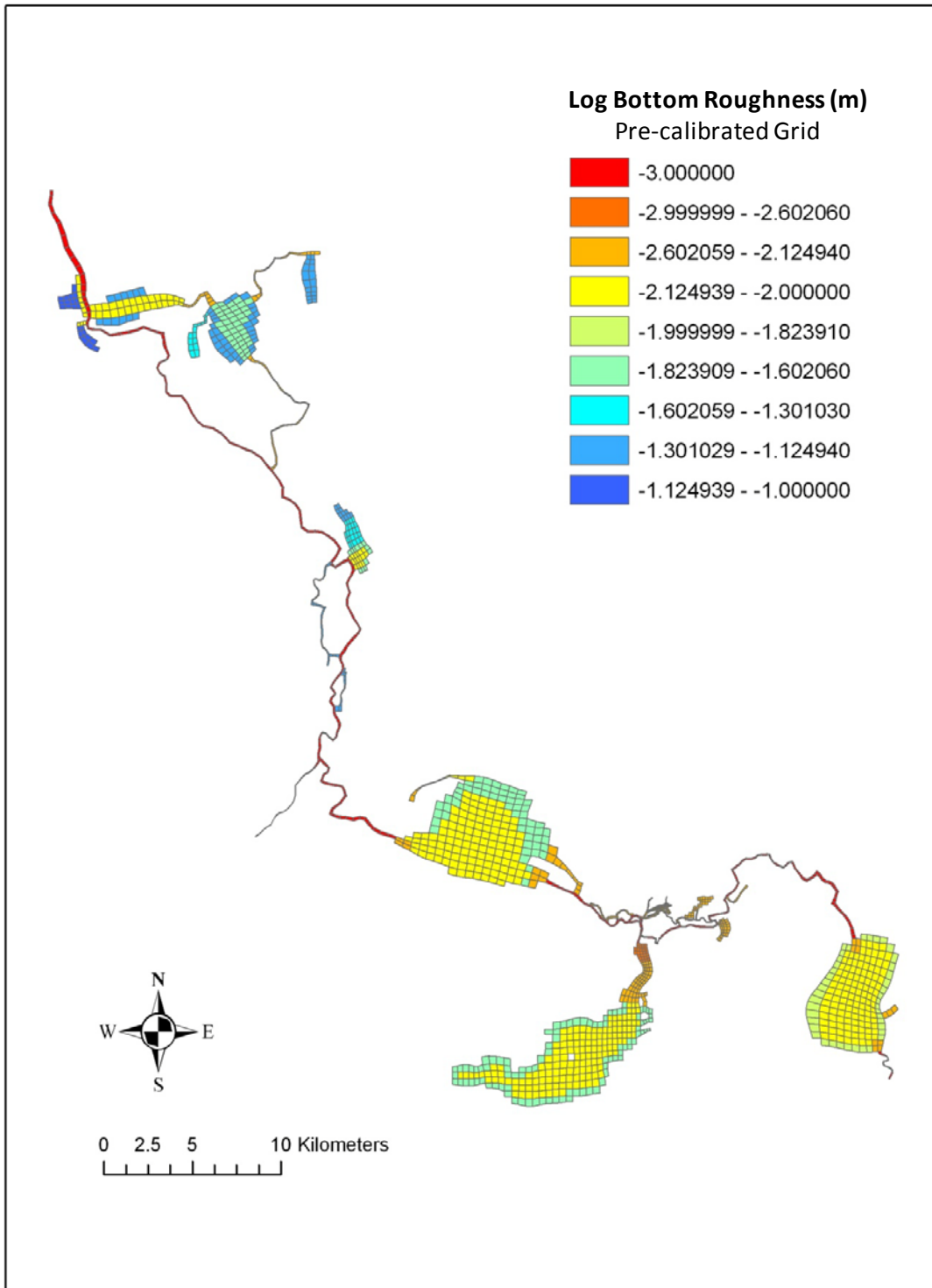


Figure 6–31. Initial bottom roughness assigned to precalibrated middle St. Johns River model (EFDC-MSJR).

Calibration of Bottom Roughness By Steady-State Numerical Experiments

Bottom roughness was calibrated by comparison of simulated slope–discharge relationships with the observed relationships shown in Section 4.3. The adjustment of bottom roughness was a trial-and-error process that entailed running numerous calibration scenarios, where each calibration scenario tested a different field of spatially varying bottom roughness parameters. To facilitate this process, the slope–discharge relationships for each calibration scenario were estimated using a range of steady-state discharge entering Lake Harney. All other model boundary conditions were removed including groundwater and spring inflows, rainfall and evaporation, and wind stress; advective-diffusion calculations for salinity were also turned off.

For the steady-state model tests, discharge entering Lake Harney was varied from 200 to 1200 mgd in 200 mgd intervals (8.8 to 52.6 m³ s⁻¹). (The upper limit of discharge tested corresponds roughly to the median discharge at U.S.17, Sanford). The model achieved steady-state for water level within 30 simulation days. Water level differences relative to Astor were output at DeLand, Sanford, and Lake Harney for comparison with observed values at the same level of discharge (see, for example, Figure 4–15).

Bottom roughness was varied globally between calibration scenarios using:

- A linear transfer function between the calibration scenario and precalibration bottom roughness.
- A constant value of bottom roughness (BR) for the channel cells (BR_{channel}).

The linear transfer function used was

$$BR_{new} = m \cdot BR_{old} + b \quad (6-9)$$

where:

BR_{new} = new bottom roughness

BR_{old} = old bottom roughness

m (slope) and *b* (intercept) are the variables adjusted for calibration.

Adjustment of bottom roughness by this method preserved, for the new bottom roughness values, the relative spatial variation of the old bottom roughness values. In addition, this method allowed for adjustment of all 1,671 bottom roughness cell values using just three variables for the calibration process.

Variables used for the final adjustment to bottom roughness were $m = 0.04 \text{ m m}^{-1}$, $b = 0.001 \text{ m}$, and BR_{channel} = 0.0001 m. The linear transfer function maps the old bottom roughness range of 0.001 to 0.1 m to 0.001 to 0.004 m. Bottom roughness in the channel cells were reduced from 0.001 m to 0.0001 m. Final bottom roughness values for each cell are shown in Figure 6–32.

Because this part of the calibration process resulted in a lowering of bottom roughness compared with the initial estimates of bottom roughness, we refer to the precalibrated model using initial bottom roughness as the High Roughness model and the model using the lower, adjusted values as the Low Roughness model.

The discharge–slope relationships for the High Roughness and Low Roughness models are compared in Figure 6–33 for DeLand, Sanford, and Lake Harney. The dashed lines show the stage differences at each location relative to the fixed downstream stage at Astor for the High Roughness model and the solid lines show the stage differences for the Low Roughness model. The symbols show observed values. The Low Roughness model produced more realistic stage–discharge relationships throughout the system.

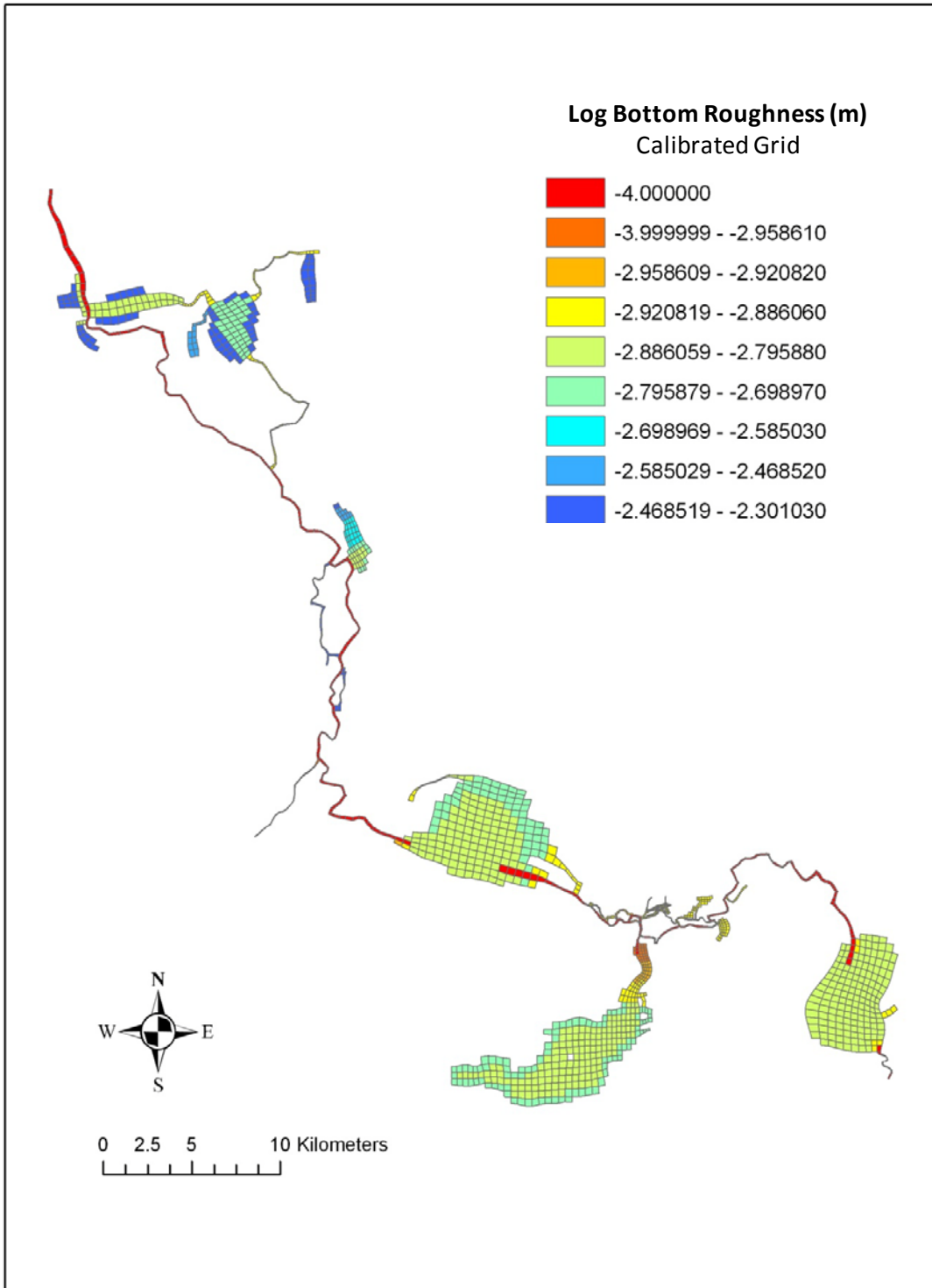


Figure 6–32. Calibrated bottom roughness assigned to calibrated model of the middle St. Johns River model (EFDC-MSJR).

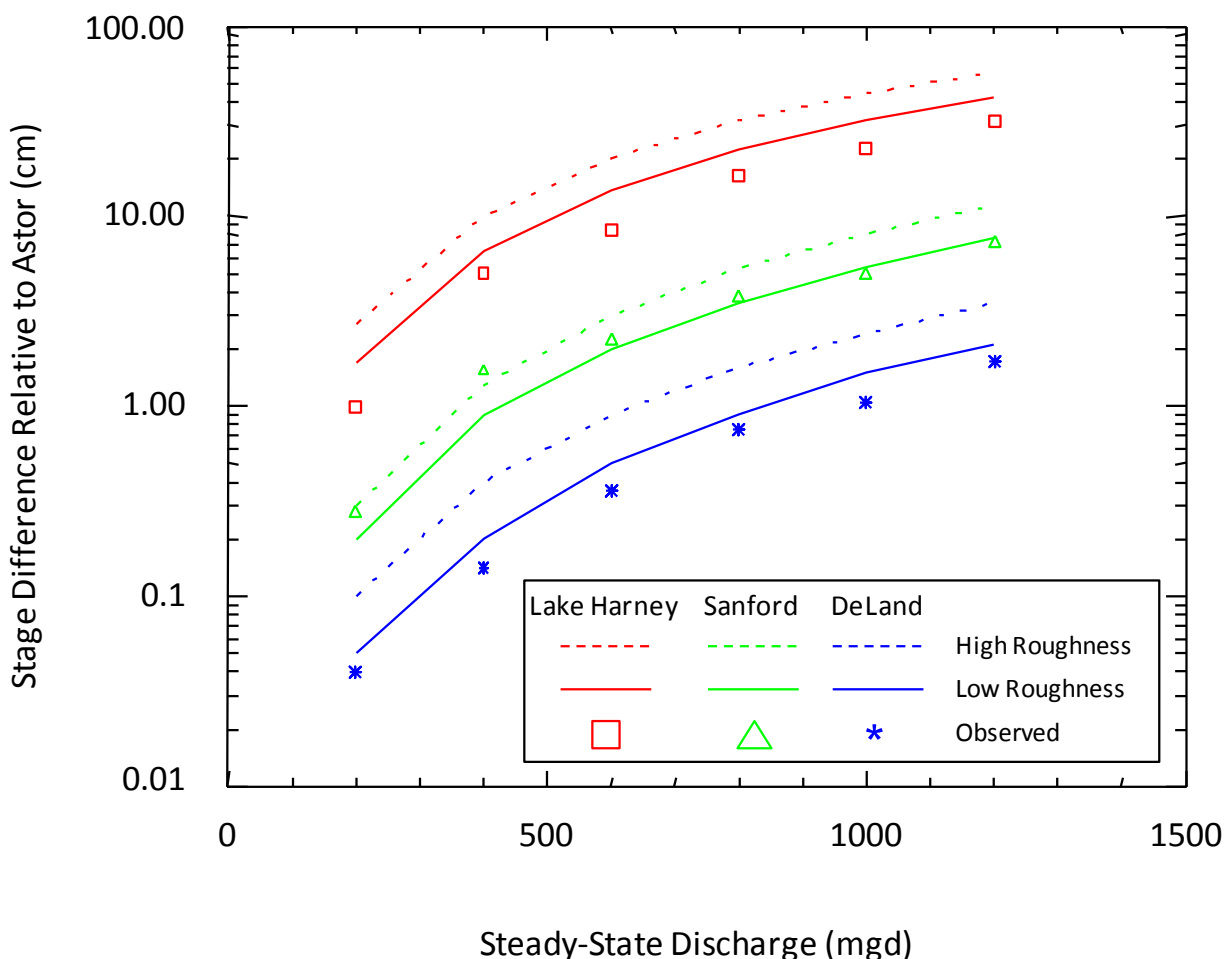


Figure 6–33. Steady-state discharge tests used for model calibration of the EFDC-MSJR hydrodynamic model.

Comparison of High and Low Roughness Models During Calibration Period

The High and Low Roughness models were run over the calibration period as fully dynamic simulations, using tributary discharge, spring discharge, rainfall, evaporation, wind, groundwater inflow, and advective-diffusion of salinity. The models were compared for a range of output variables to (a) develop confidence that the calibration parameters developed using steady-state numerical tests are robust for a dynamic simulation, and (b) illustrate the relative importance of bottom roughness on output variables.

Slope–Discharge Relationships

Comparisons of observed and simulated discharge–slope relationships are shown below for Astor-DeLand (Figure 6–34), DeLand-Sanford (Figure 6–35), and Sanford-Lake Harney (Figure 6–36). In the first two river reaches, the Low Roughness model performs considerably better than the High Roughness model.

The visual comparison for the Sanford-Lake Harney reach yields mixed results for model performance because the High and Low Roughness models yield similar results for this reach. The Low Roughness model matches observed data best during low discharge (< 1000 mgd).

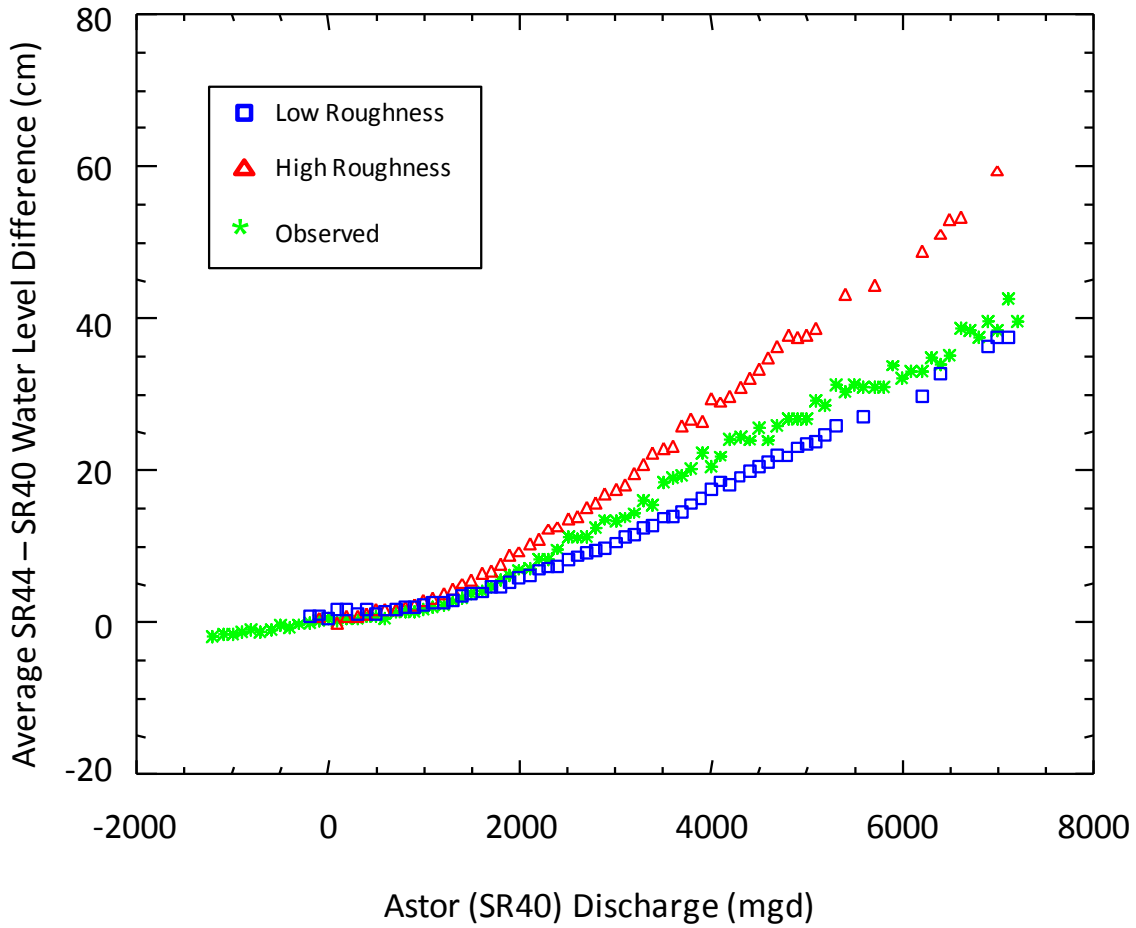


Figure 6-34. Comparison of observed and simulated discharge-slope relationships between DeLand (SR 44) and Astor (SR 40) for High and Low Roughness models.

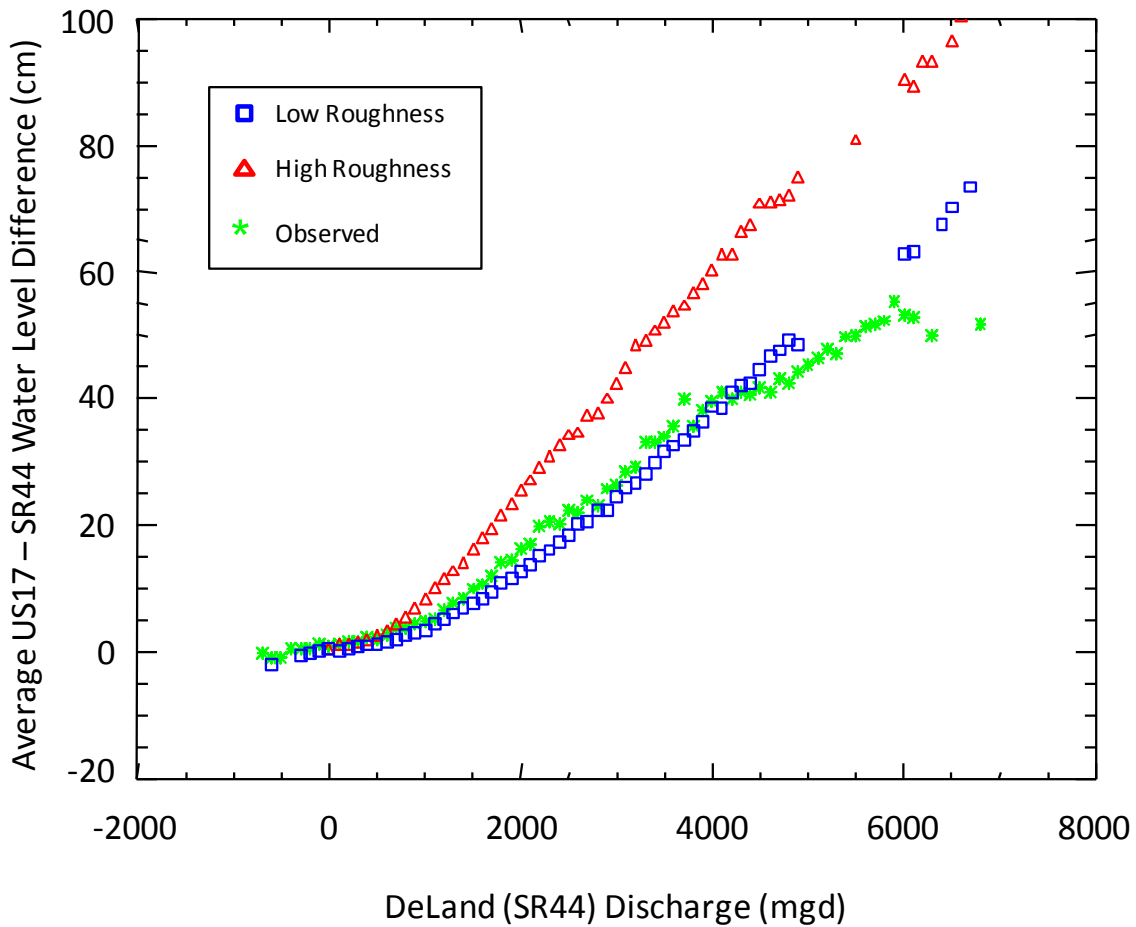


Figure 6-35. Comparison of observed and simulated discharge-slope relationships between Sanford (US 17) and DeLand (SR 44) for High and Low Roughness models.

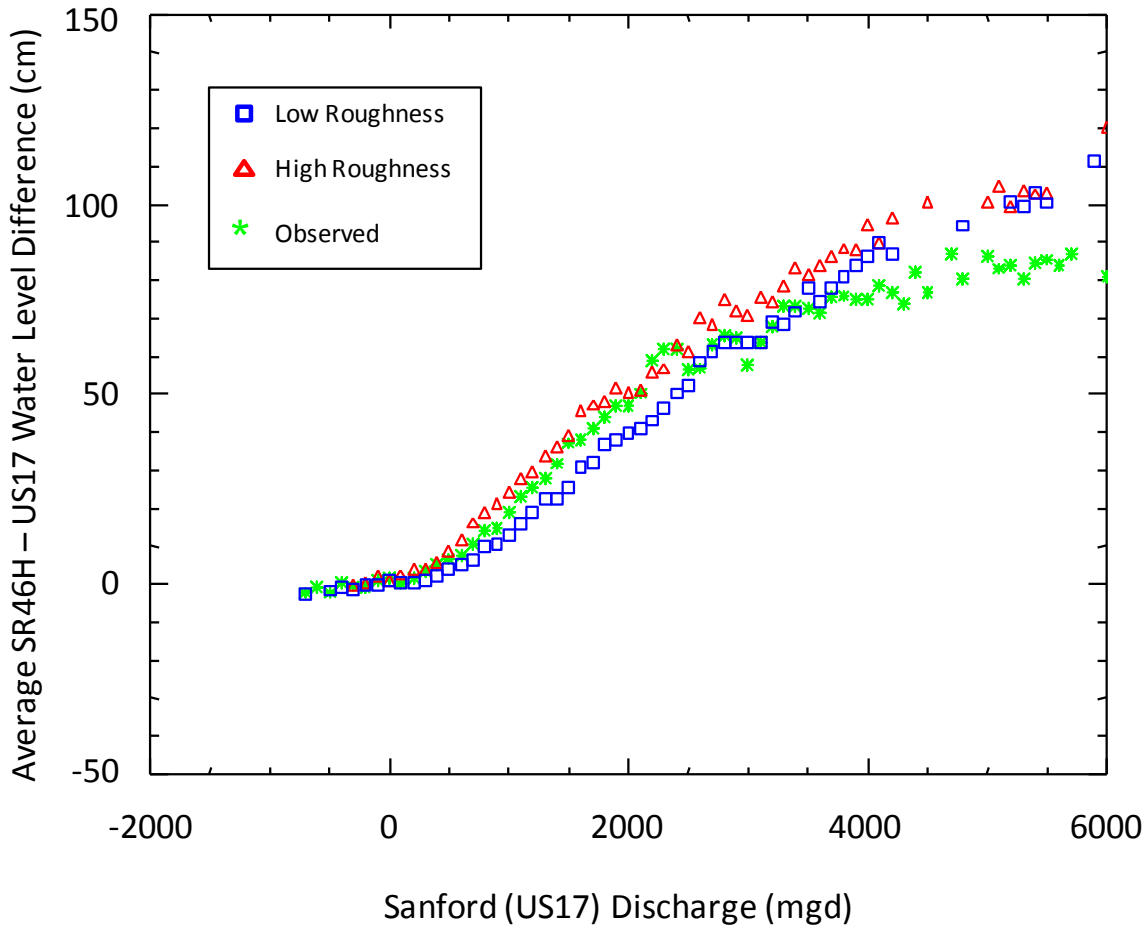


Figure 6–36. Comparison of observed and simulated discharge–slope relationships between Lake Harney (SR 46 at Lake Harney) and Sanford (US 17) for High and Low Roughness models.

Daily Water Level

Statistical comparisons between observed and simulated daily water level for both the High and Low Roughness models are shown in Table 6–10 at four locations for the EFDC-MSJR hydrodynamic model calibration period. Correlation coefficients (R) are very high, exceeding 0.98, for both models at all stations. The slopes of the regression line (m) are generally near 1 for both models, but the Low Roughness model shows improvement over the High Roughness model at all locations. The Nash–Sutcliffe statistic ($N-S$) ranges from 0.789 to 0.960 for the High Roughness model and improves considerably, to 0.958 to 0.994, for the Low Roughness model. $AVAE$, $AVRE$, and $RMSE$ are all improved for the Low Roughness model compared with the High Roughness model.

Although the slope–discharge results (Figure 6–36) between Sanford and Lake Harney do not show an advantage of the Low Roughness model over the High Roughness model, the

quantitative statistics generated from the time series of water level do show an advantage for the Low Roughness model at both locations.

Table 6–10. Statistical comparison of simulated and observed water level for High and Low Roughness models at four locations.

	DeLand		Sanford		Lake Jesup Outlet		Lake Harney	
	High	Low	High	Low	High	Low	High	Low
<i>NRECS</i>	214		214		208		214	
r^2	0.994	0.996	0.990	0.988	0.990	0.980	0.986	0.974
<i>m</i>	1.180	1.047	1.437	1.162	1.381	1.091	1.268	1.074
<i>NS</i>	0.960	0.994	0.789	0.958	0.836	0.968	0.905	0.964
<i>AVAE</i> (m)	0.051	0.017	0.156	0.057	0.139	0.048	0.179	0.088
<i>AVRE</i> (%)	18.4	7.3	37.5	17.5	38.8	15.7	35.0	17.3
<i>RMSE</i> (m)	0.062	0.025	0.189	0.084	0.175	0.077	0.23	0.14

Note:

<i>NRECS</i>	=	Number of records
r^2	=	Coefficient of determination
<i>m</i>	=	slope of the regression line
<i>NS</i>	=	Nash–Sutcliffe
<i>AVAE</i>	=	Average absolute error
<i>AVRE</i>	=	Average relative error
<i>RMSE</i>	=	Root-mean-square error

Time series plots comparing observed and simulated daily water level values are shown below for DeLand (Figure 6–37), Sanford (Figure 6–39), Lake Jesup outlet (Figure 6–41), and Lake Harney (Figure 6–43). Corresponding scatter plots are Figure 6–38, Figure 6–40, Figure 6–42, and Figure 6–44. These series of plots visually show the slight, but consistent, improvement in prediction of daily water level for the Low Roughness model compared with the High Roughness model.

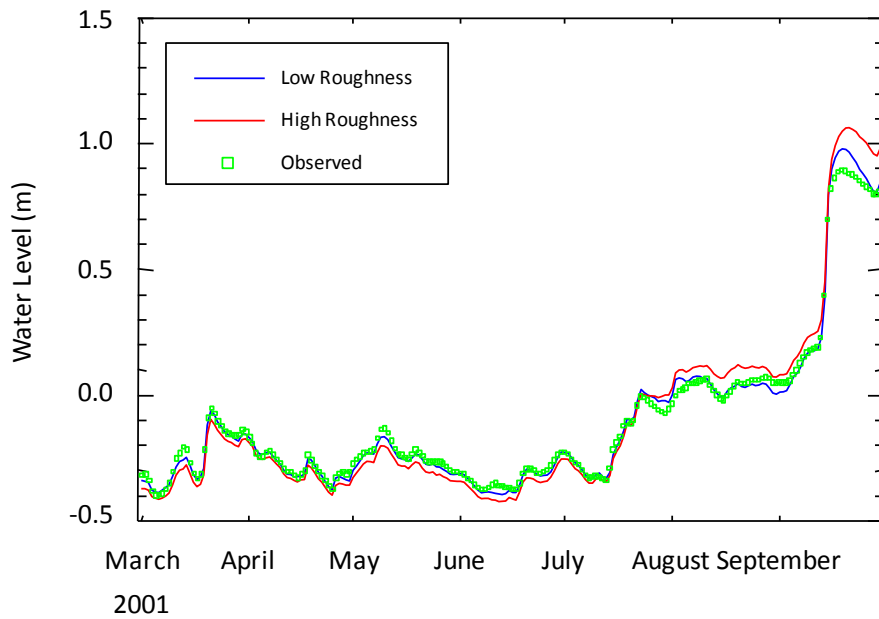


Figure 6–37. Simulated versus observed daily water level at DeLand (SR 44) over the calibration period.

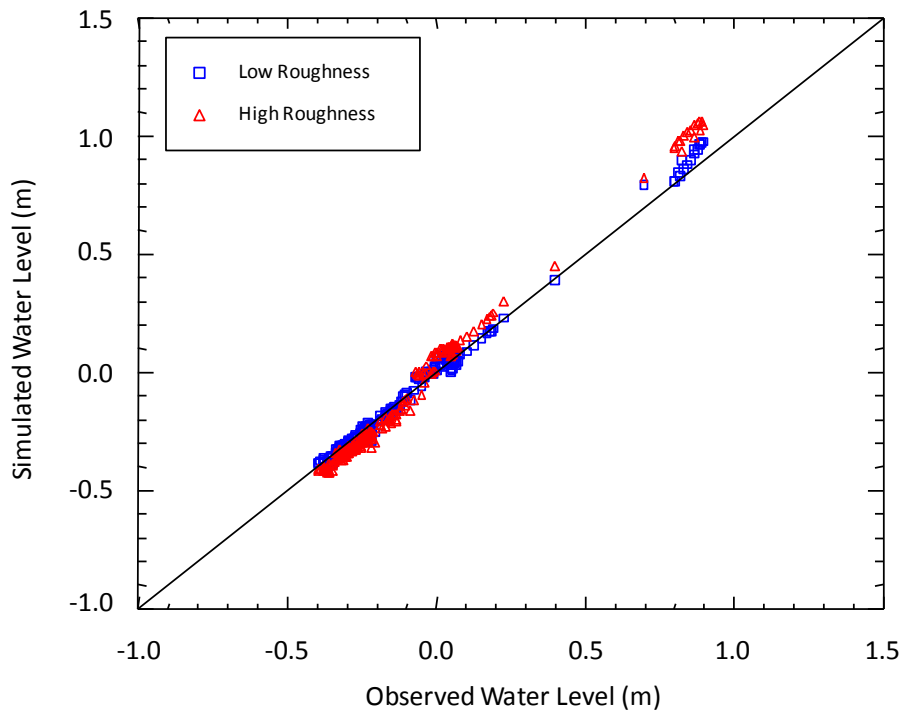


Figure 6–38. Scatter plot of paired values of observed and simulated daily water level at DeLand (SR 44) over the calibration period, March to September, 2001.

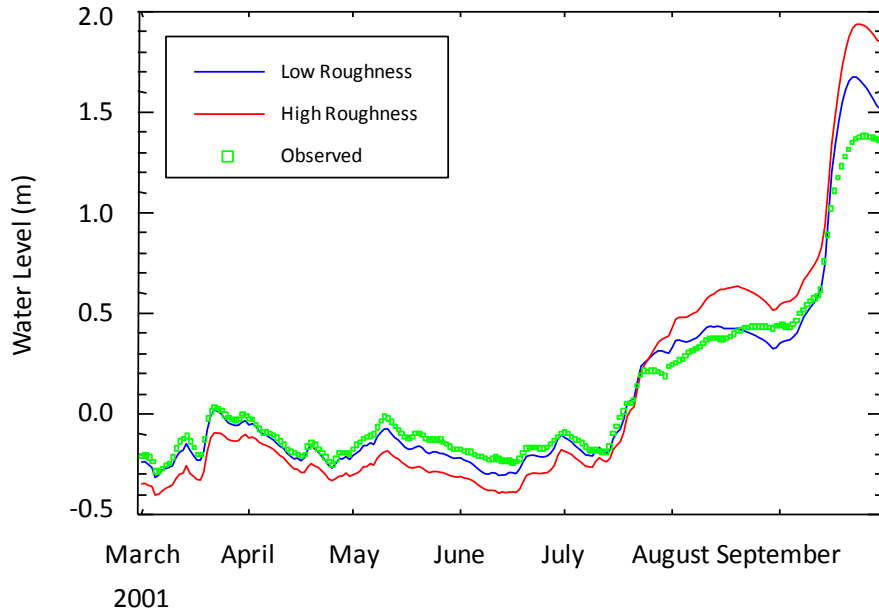


Figure 6–39. Simulated versus observed daily water level at Sanford (US 17) over the calibration period.

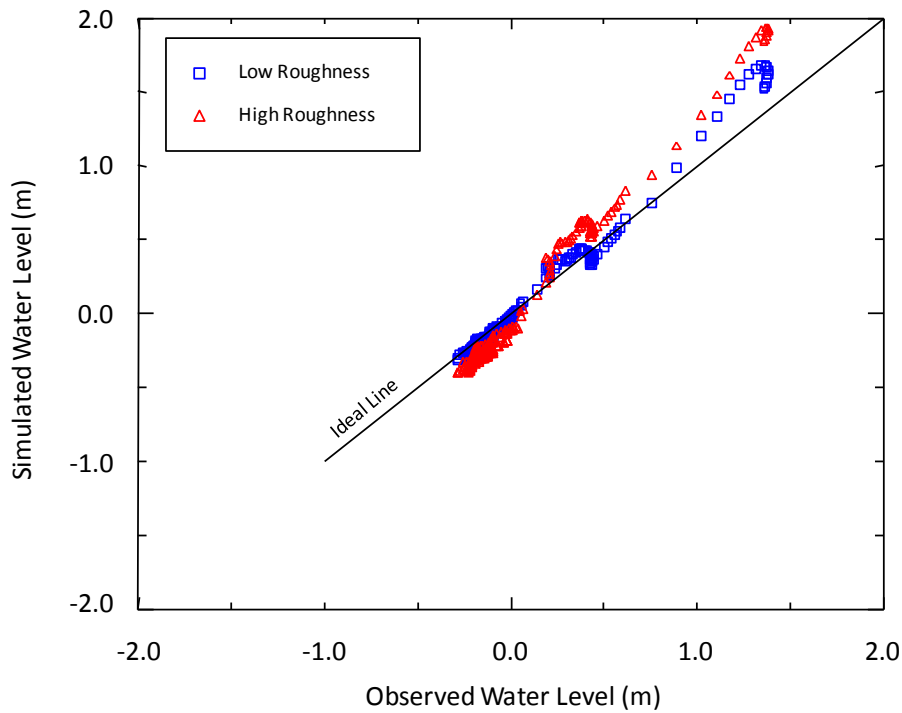


Figure 6–40. Scatter plot of paired values of observed and simulated daily water level at Sanford (US 17) over the calibration period, March to September 2001.

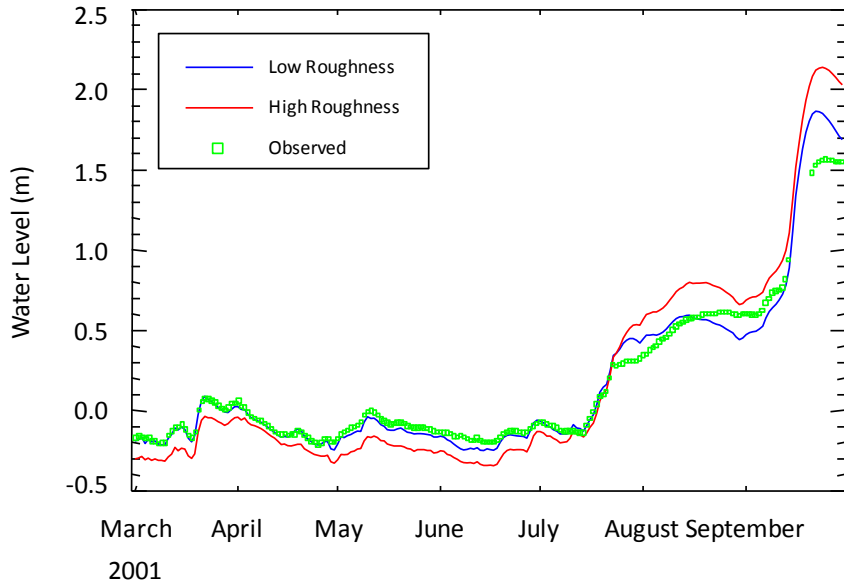


Figure 6–41. Simulated versus observed daily water level at Lake Jesup outlet (SR 46 at Lake Jesup) over the calibration period.

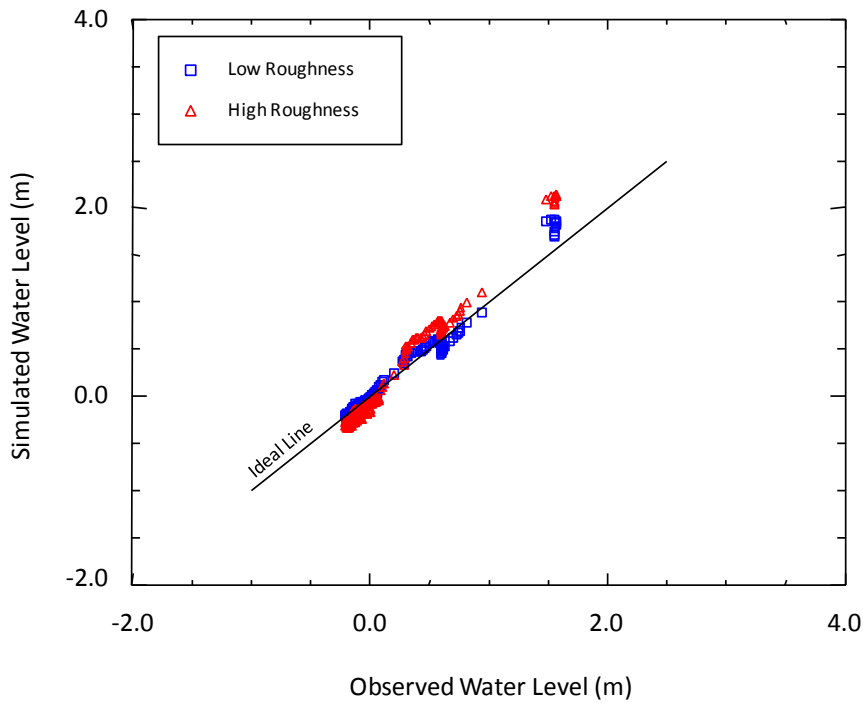


Figure 6–42. Scatter plot of paired values of observed and simulated daily water level at Lake Jesup outlet (SR 46 at Lake Jesup) over the calibration period, March to September, 2001.

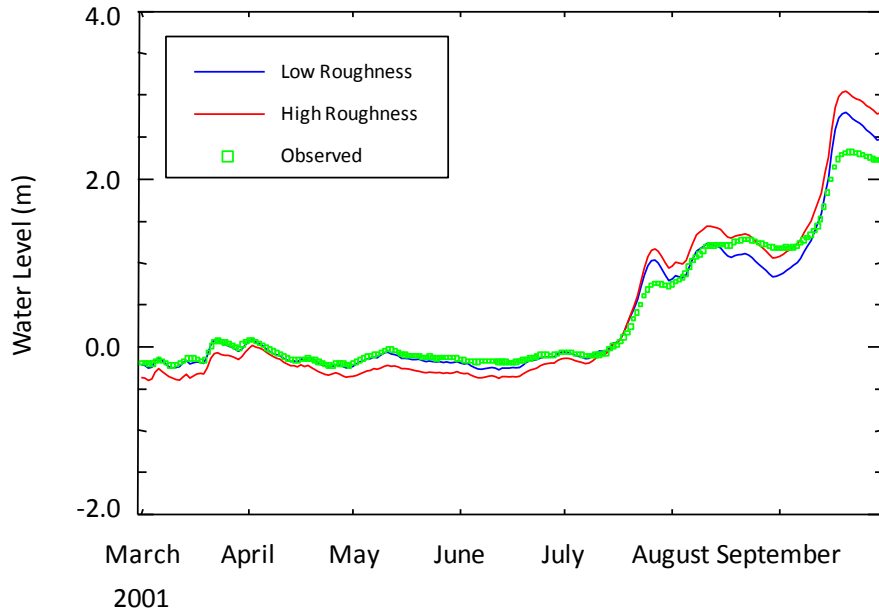


Figure 6–43. Simulated versus observed daily water level above Lake Harney (SR 46 at Lake Harney) over the calibration period.

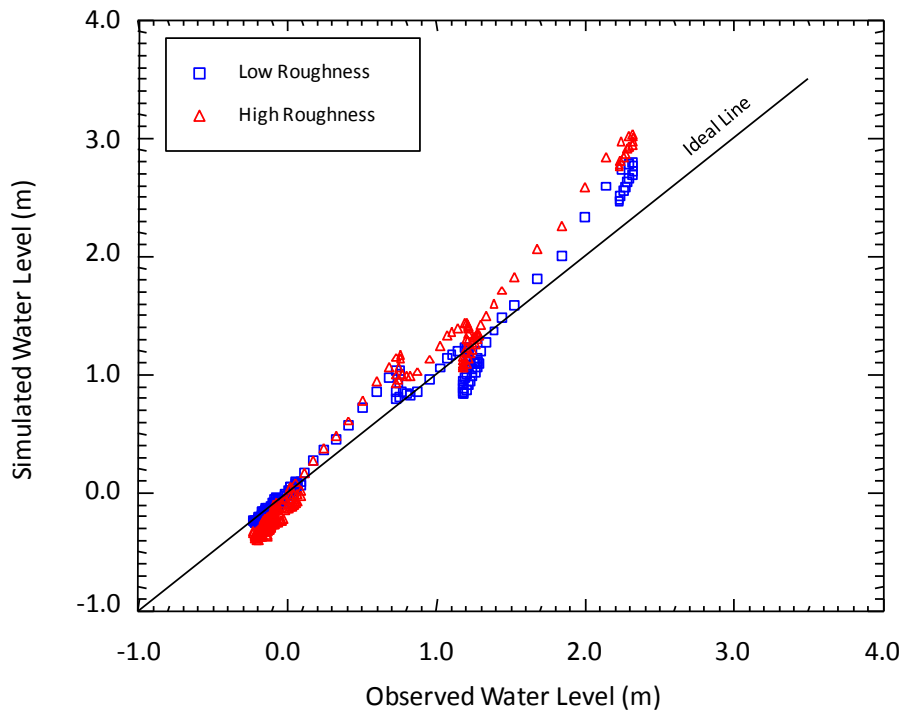


Figure 6–44. Scatter plot of paired values of observed and simulated daily water level above Lake Harney (SR 46 at Lake Harney) over the calibration period, March to September 2001.

Daily Discharge

Comparative statistics between observed and simulated daily discharge are quite similar for both the High and Low Roughness models (Table 6–11). Daily discharge is essentially insensitive to changes in bottom roughness and is likely governed instead by boundary inflows.

Nash–Sutcliffe statistics are unsatisfactory at Astor and Lake Jesup, although this statistic is very good for DeLand and Sanford. The lower Nash–Sutcliffe statistic at Astor as compared with DeLand and Sanford is because of the high percentage of missing records at Astor during the calibration period. The only observed discharge at Astor occurs during periods when discharge is overpredicted. The poor statistics at Lake Jesup outlet are discussed below with reference to time series and scatter plots.

Table 6–11. Statistical comparison of simulated and observed daily discharge for High and Low Roughness model at four locations.

	Astor		DeLand		Sanford		Lake Jesup Outlet	
	High	Low	High	Low	High	Low	High	Low
<i>NRECS</i>	73		214		214		214	
r^2	0.763	0.731	0.902	0.906	0.964	0.962	0.512	0.432
<i>m</i>	0.827	0.878	1.042	1.097	1.005	1.056	0.378	0.385
<i>NS</i>	0.449	0.367	0.835	0.803	0.942	0.918	0.380	0.293
<i>AVAE</i> (cms)	41.3	47.3	17.65	19.54	11.5	13.6	7.1	7.4
<i>AVRE</i> (%)	26.5	29.5	23.9	26.9	39.6	31.5	122.3	138.7
<i>RMSE</i> (cms)	55.2	59.1	25.7	28.1	14.5	17.3	11.4	12.1

- NRECS* = Number of records
- r^2 = Coefficient of determination
- m* = Slope of the regression line
- NS* = Nash–Sutcliffe
- AVAE* = Average absolute error
- AVRE* = Average relative error
- RMSE* = Root-mean-square error

Observed discharge at Astor is only available during the last 2.5 months of the calibration period when simulated values underpredict discharge (Figure 6–45). Simulated and observed values are visually correlated, consistent with the R statistic of 0.855 for the Low Roughness model.

The scatter plot of Figure 6–46 shows again that both the Low and High Roughness models produce similar results for discharge but model test results are consistently higher than observed.

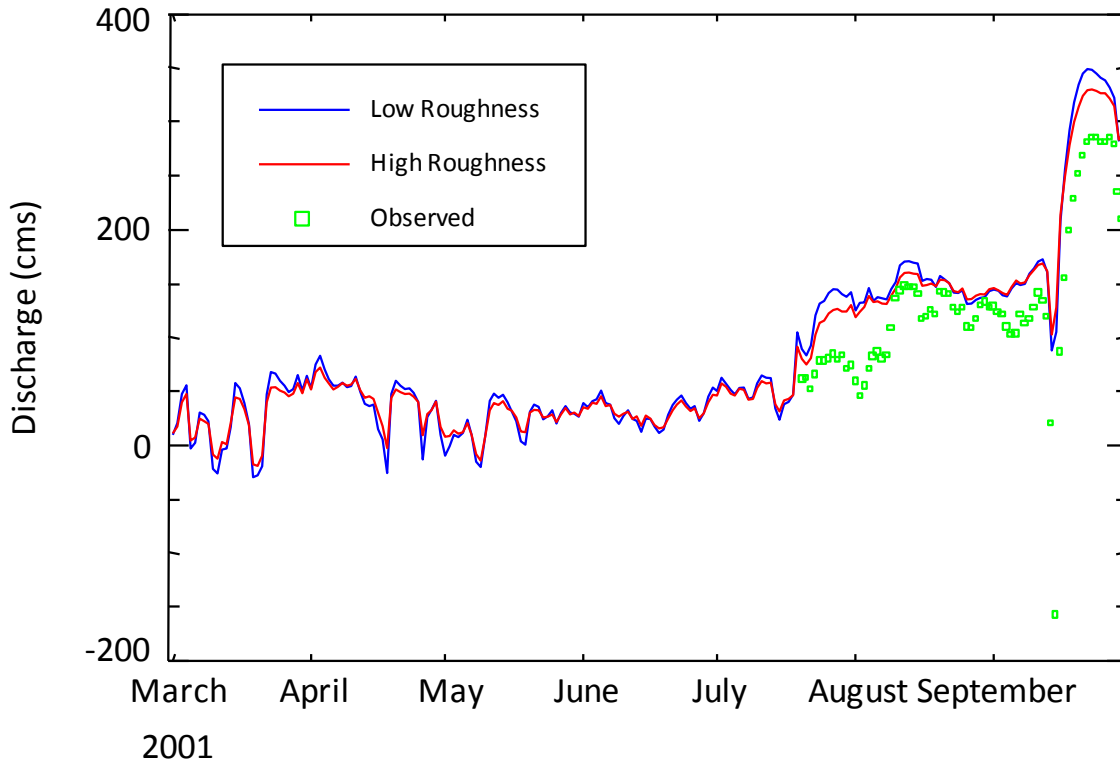


Figure 6–45. Simulated versus observed daily discharge at Astor (SR 40) over the calibration period.

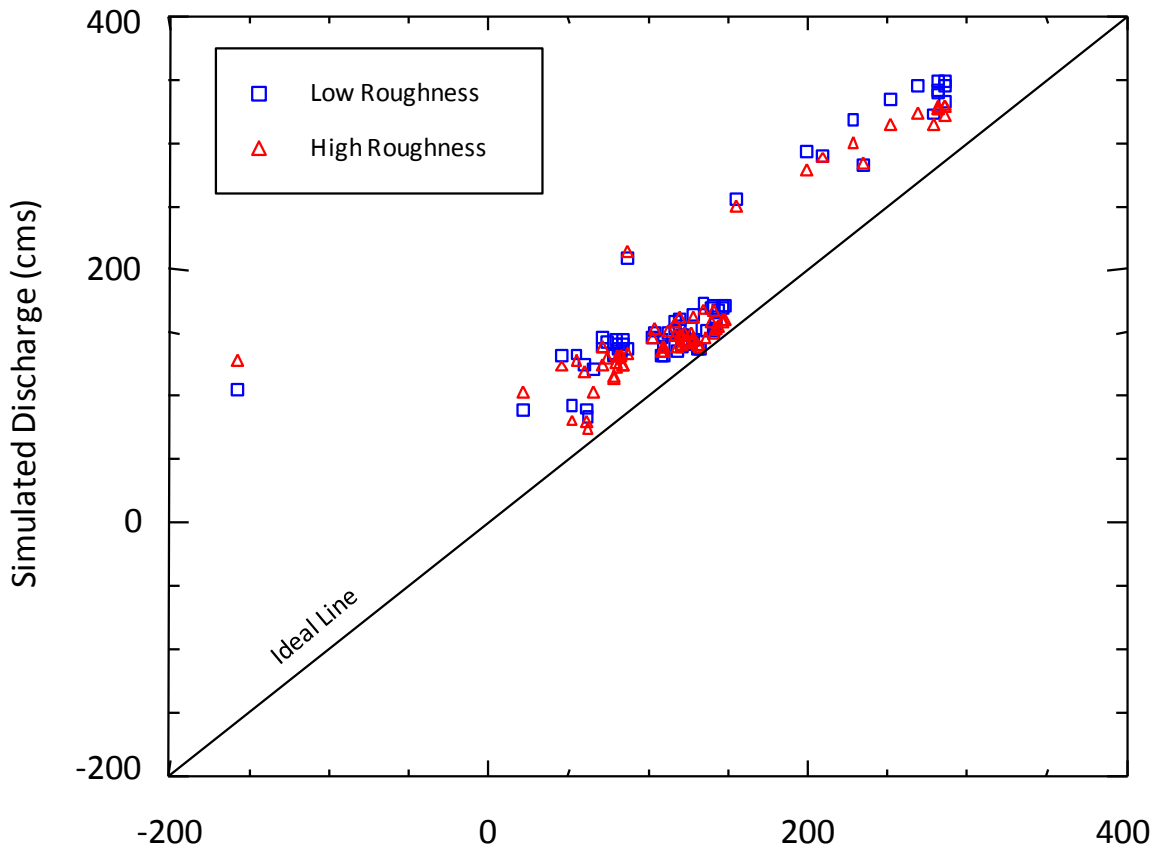


Figure 6–46. Scatter plot of paired values of observed and simulated daily discharge at Astor (SR 40) over the calibration period, March to September 2001.

Figure 6–47 compares time series of observed and simulated daily discharge at DeLand. The simulated values match discharge well for the low discharge period of March through June. Discharge values diverge for July through September because of an overprediction of inflowing tributary discharge. The high correlation between observed and simulated discharge during the low flow period, however, indicates that the model is correctly predicting the timing and magnitude of reverse flow events at this location.

The scatter plot of Figure 6–48 again shows the good match between observed and simulated discharge at low flows and overprediction of simulated values at high flows.

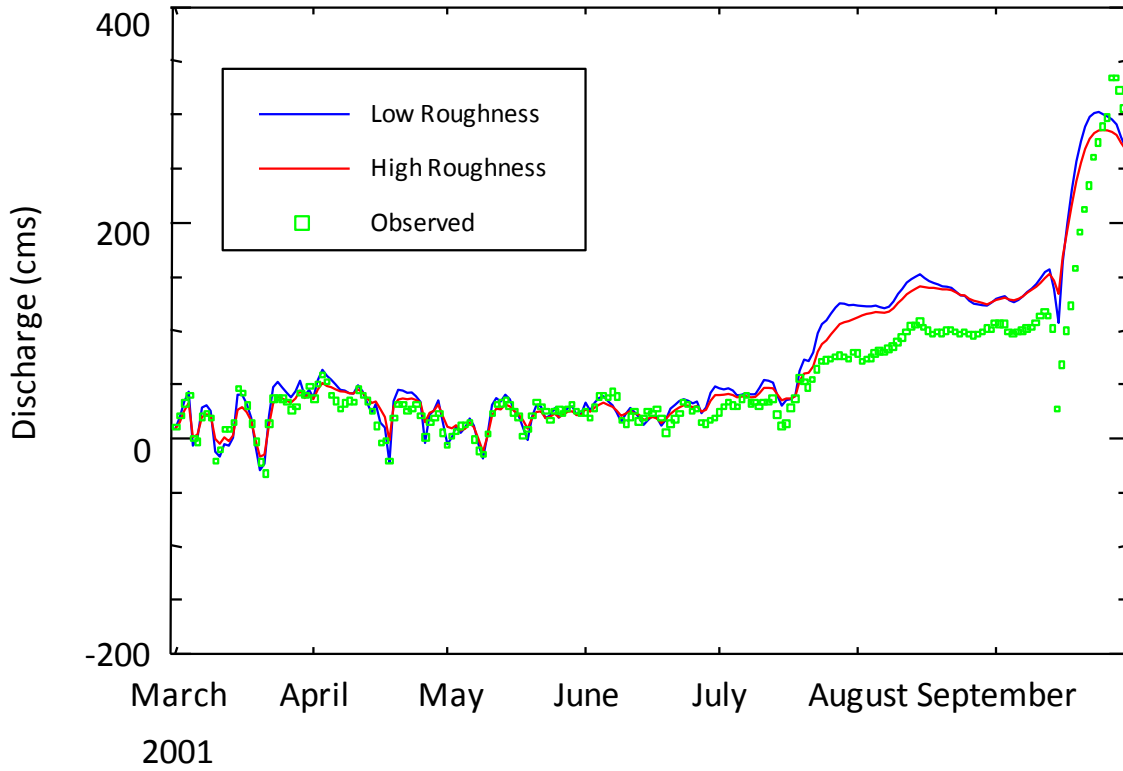


Figure 6–47. Simulated versus observed daily discharge at DeLand (SR 44) over the calibration period.

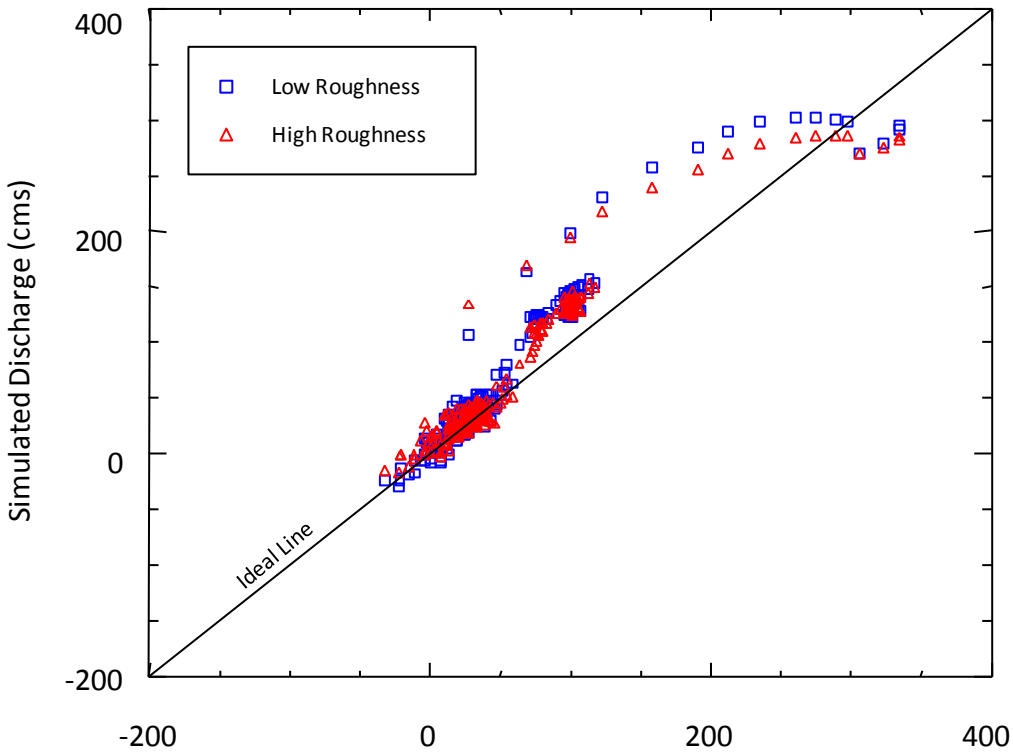


Figure 6–48. Scatter plot of paired values of observed and simulated daily discharge at DeLand (SR 44) over the calibration period, March to September 2001.

The time series plot for Sanford (Figure 6–49) is similar to DeLand. The lower discharge at Sanford allowed for expansion of the y-scale to show low discharge comparisons more clearly. The scatter plot of Figure 6–50 illustrates the generally high correlation between observed and simulated discharge.

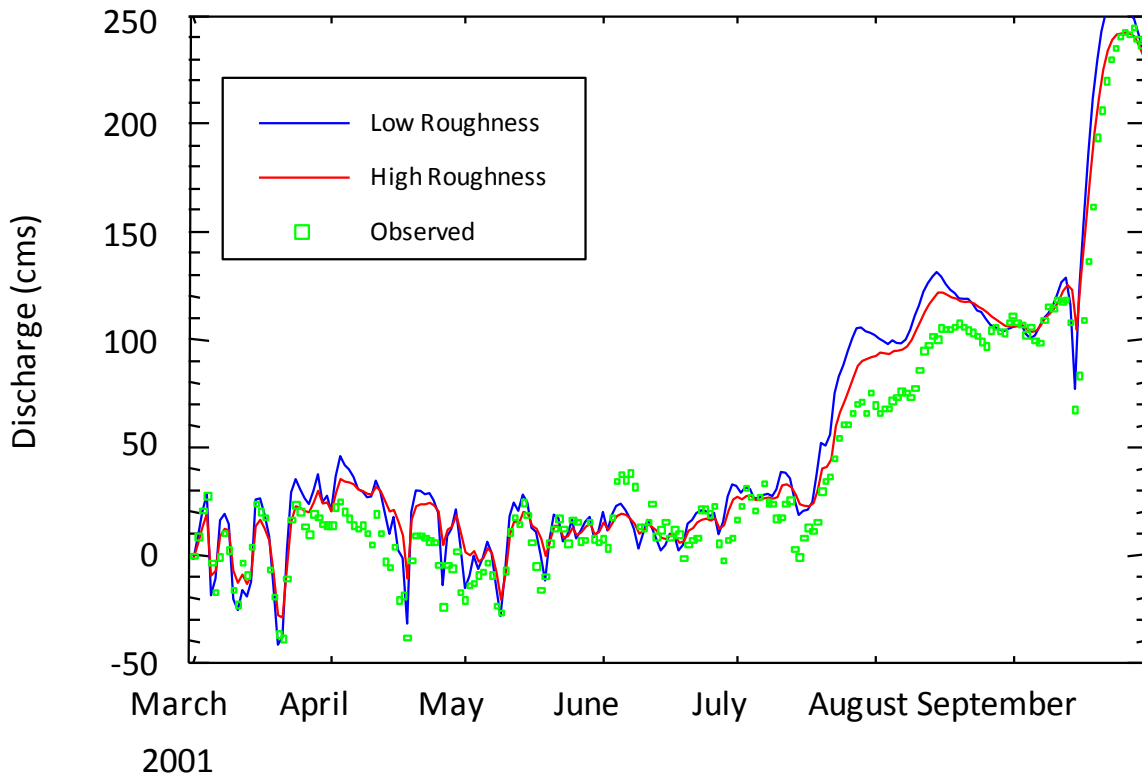


Figure 6–49. Simulated versus observed daily discharge at Sanford (US 17) over the calibration period.

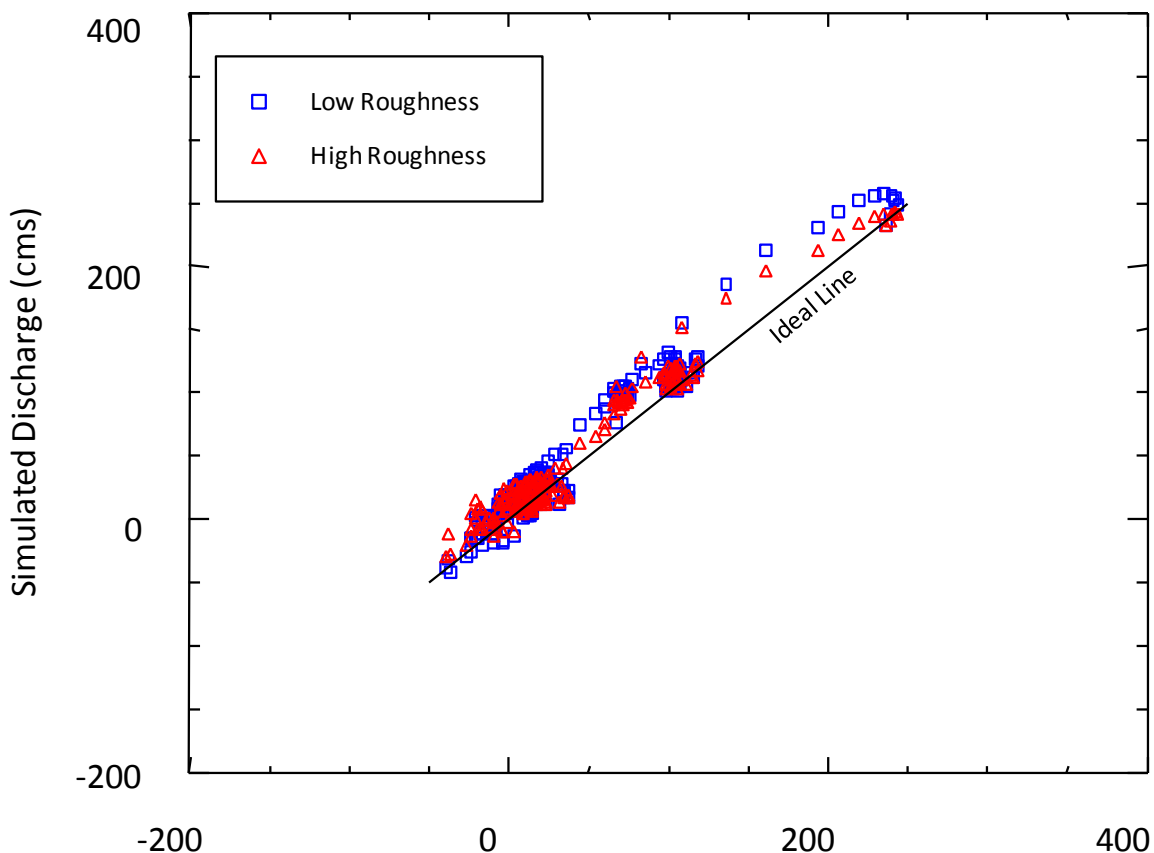


Figure 6–50. Scatter plot of paired values of observed and simulated daily discharge at Sanford (U.S. 17) over the calibration period, March to September 2001.

Figure 6–51 compares time series of observed and simulated daily discharge at Lake Jesup outlet. Discharge at this location measures flow into and out of the lake. The dominant feature of discharge at this location is a quasiperiodic motion about a very small mean value. The observed net discharge into the lake during this period had a magnitude of 68.5 mgd ($3 \text{ m}^3\text{s}^{-1}$). During low flow periods, discharge at this station responds to dynamic oscillations in the system likely caused by winds.

Simulated discharge matched observed discharge well for the lowest discharge period of March through May. The good match of daily discharge in the March to May period is evidence that the model physics are correctly specified, although they are subject to uncertainty of boundary conditions, notably tributary discharge and wind. When discharge is generally overpredicted in the latter portion of the calibration period, the oscillations of discharge are also poorly matched. It is possible that the magnitude of the reverse flow oscillations is sensitive to the specification of tributary discharge entering the lake, so that overestimation of tributary discharge suppresses simulated reverse flow events. Note that the model does predict the occurrence of the large reverse flow event in mid-September, although it underpredicts the magnitude by half.

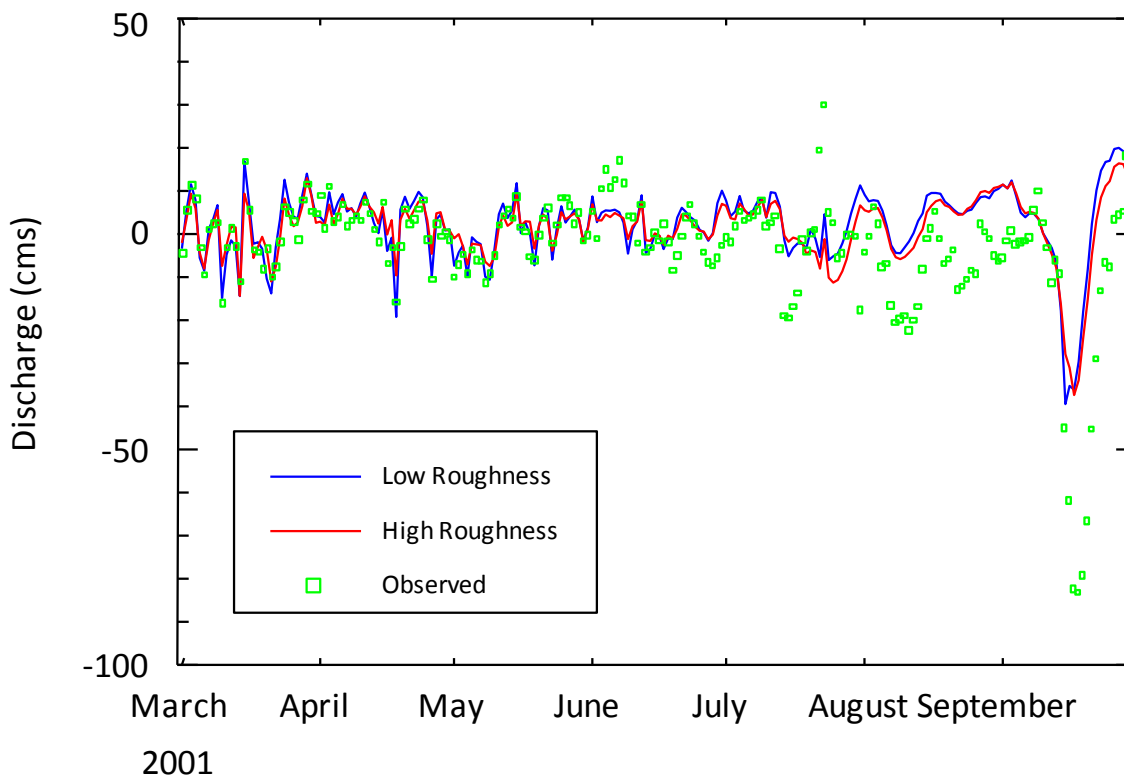


Figure 6-51. Simulated versus observed daily discharge at Lake Jesup outlet (SR 46 at Lake Jesup) over the calibration period.

The scatter plot of Figure 6-52 shows that the poor regression slope (0.385) at this location is largely caused by underprediction of the large observed reverse flow during September.

The overprediction of discharge during August and September 2001 is in part due to inaccuracies in the observed discharge at SR 46 at Lake Jesup. At SR 46 at Lake Jesup, the average observed monthly discharge for August was $-7.5 \text{ m}^3 \text{ s}^{-1}$, where the negative sign indicates net flow from the river into the lake. During September, the average observed monthly flow was $-16.4 \text{ m}^3 \text{ s}^{-1}$. The lake stage rose 25.6 cm during August and 94.4 cm during September. Because the lake area is about $32.5 \times 10^6 \text{ m}^2$, these stage changes indicate that the net inflow required to raise the lake stage during these months was 3.1 and $11.4 \text{ m}^3 \text{ s}^{-1}$, respectively. Even if there were no surface discharges entering the lake during these months (highly unlikely), the observed discharge indicates that 4.4 and $5.0 \text{ m}^3 \text{ s}^{-1}$ more discharge entered the lake during July and August, respectively, than is explained by the rise in stage. The only possible loss from the lake is through evaporation, which was estimated as 13.4 cm for August and 10.8 cm for September. These evaporative loss rates equate to discharges of -1.6 and $-1.3 \text{ m}^3 \text{ s}^{-1}$, far smaller in magnitude than the losses required to balance the observed rise in stage. We can only conclude that the monthly averaged observed discharge for these two months is underpredicted by at least 2.8 and $3.7 \text{ m}^3 \text{ s}^{-1}$ during August and September, with percent errors of 23% to 37%. Accounting for reasonable value of tributary discharge entering the lake would considerably increase these estimates of observed error in discharge at SR 46 at Lake Jesup.

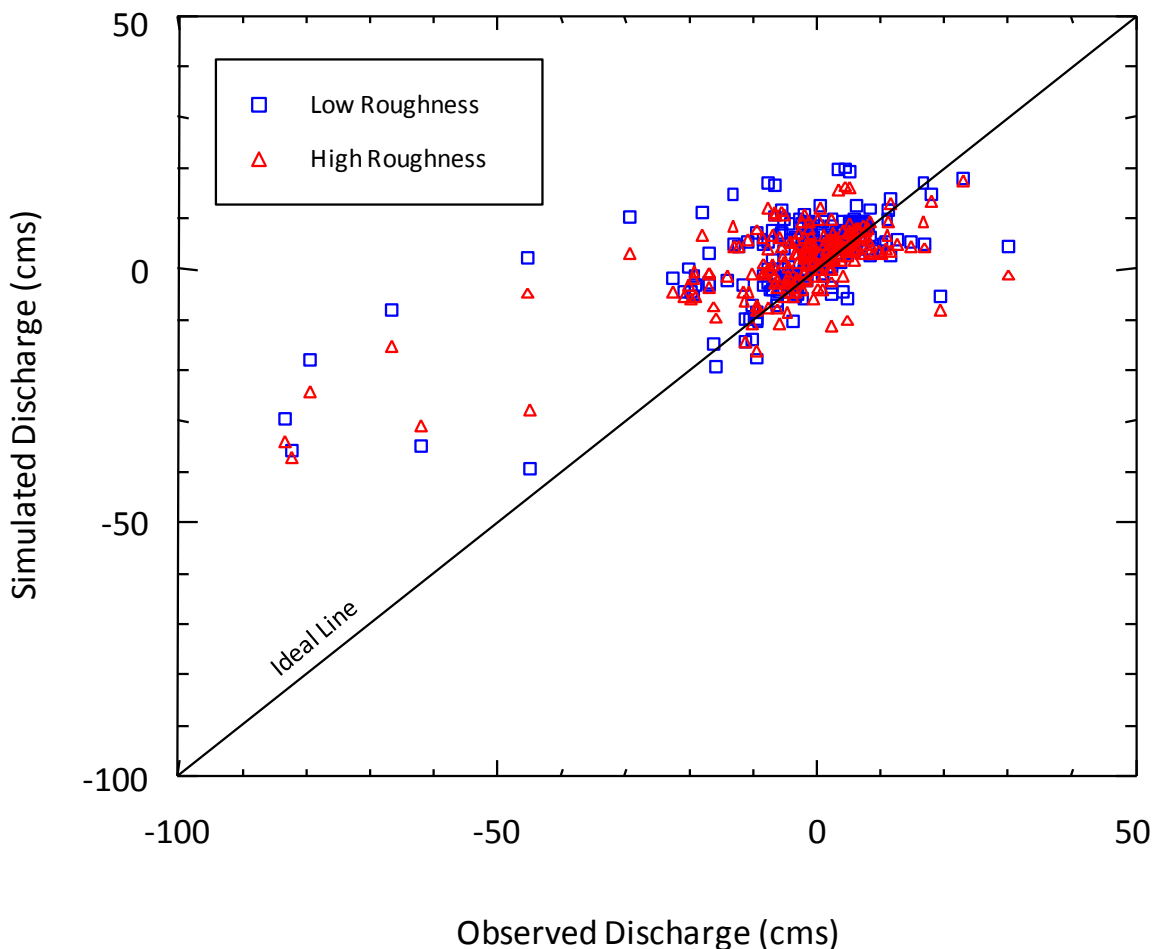


Figure 6–52. Scatter plot of paired values of observed and simulated daily discharge at Lake Jesup outlet (SR 46 at Lake Jesup) over the calibration period, March to September, 2001.

Monthly Discharge

Observed and simulated average monthly discharge is compared in Table 6–12 at Astor, DeLand, Sanford, and Lake Jesup outlet. Because monthly discharge is essentially identical for the High and Low Roughness models, only results for the Low Roughness model appear in the table. Monthly discharge is governed by the model boundary conditions, of which tributary and spring discharges dominate the discharge budget. These results, then, merely reflect the uncertainty inherent in estimating inflows to the river for specific months and the uncertainty of the observations as discussed above. Inflows during the calibration period are evidently overpredicted, because simulated average discharge at DeLand is 28.8% greater than observed; and simulated average discharge at Sanford is 26.5% greater than observed.

Table 6–12. Observed (Obs) versus simulated (Sim) (Low Roughness model) monthly averaged discharge over the calibration period, March to September 2001.

Month	Astor		DeLand		Sanford		Lake Jesup	
	Obs	Sim	Obs	Sim	Obs	Sim	Obs	Sim
March	—	27.8	18.5	20.2	2.9	7.4	0.15	1.2
April	—	43.6	25.8	34.4	2.5	21.6	1.6	3.6
May	—	21.9	17.0	17.8	1.4	6.5	-0.7	0.20
June	—	32.4	23.7	26.3	15.0	13.6	1.9	2.5
July	72.8	81.0	45.4	67.5	32.9	43.6	-0.4	2.4
August	114.7	142.9	92.9	129.1	92.1	108.6	-7.5	5.2
September	168.4	229.6	166.7	202.3	153.8	163.4	-16.4	0.73
Overall	—	83.0	55.5	71.5	42.7	54.0	-3.0	2.3

Hourly Discharge

Hourly discharge was examined as part of the calibration process because of its potential importance to mixing processes. In this low-slope system, hourly discharge variability can be large relative to mean daily discharge. The hourly discharge variability is manifested as quasiperiodic oscillations about the daily mean value. We assume that these quasiperiodic motions could act similarly to tidal motions in the estuarine river and affect mixing through enhanced vertical and horizontal velocity shear. For this reason, the sensitivity of bottom roughness to hourly discharge was examined as part of the calibration process.

Table 6–13 shows comparative statistics for simulated and observed hourly discharge over the calibration period. Similarly, for daily discharge, the hourly discharge comparative statistics were insensitive to bottom roughness, although the High Roughness model outperformed the Low Roughness model for the Nash–Sutcliffe statistic.

A visual comparison of observed and simulated values shows, however, that the Low Roughness model more closely matches the observed amplitudes of the quasiperiodic motions (Figure 6–53). The Low Roughness model, for example, captures the two large reverse flow events on 18 April 2001 and again on 26 April 2001.

Table 6–13. Statistical comparison of simulated and observed hourly discharge for High and Low Roughness models at four locations over the calibration period, March to September 2001.

	Astor		DeLand		Sanford		Lake Jesup Outlet	
	High	Low	High	Low	High	Low	High	Low
<i>NRECS</i>	1,764		5,009		5,136		5,019	
r^2	0.734	0.746	0.885	0.887	0.939	0.933	0.178	0.200
<i>m</i>	0.797	0.860	1.021	1.075	0.979	1.031	0.199	0.287
<i>NS</i>	0.461	0.374	0.821	0.787	0.919	0.892	0.133	0.094
<i>AVAE</i> (cms)	41.6	48.0	20.0	22.3	13.8	16.0	9.6	9.7
<i>AVRE</i> (%)	28.2	31.3	36.0	34.7	52.2	46.7	205.4	179.2
<i>RMSE</i> (cms)	57.2	61.6	27.3	29.9	17.4	20.1	13.8	14.1

- NRECS* = Number of records
- r^2 = Coefficient of determination
- m* = Slope of the regression line
- NS* = Nash–Sutcliffe
- AVAE* = Average absolute error
- AVRE* = Average relative error
- RMSE* = Root-mean-square error

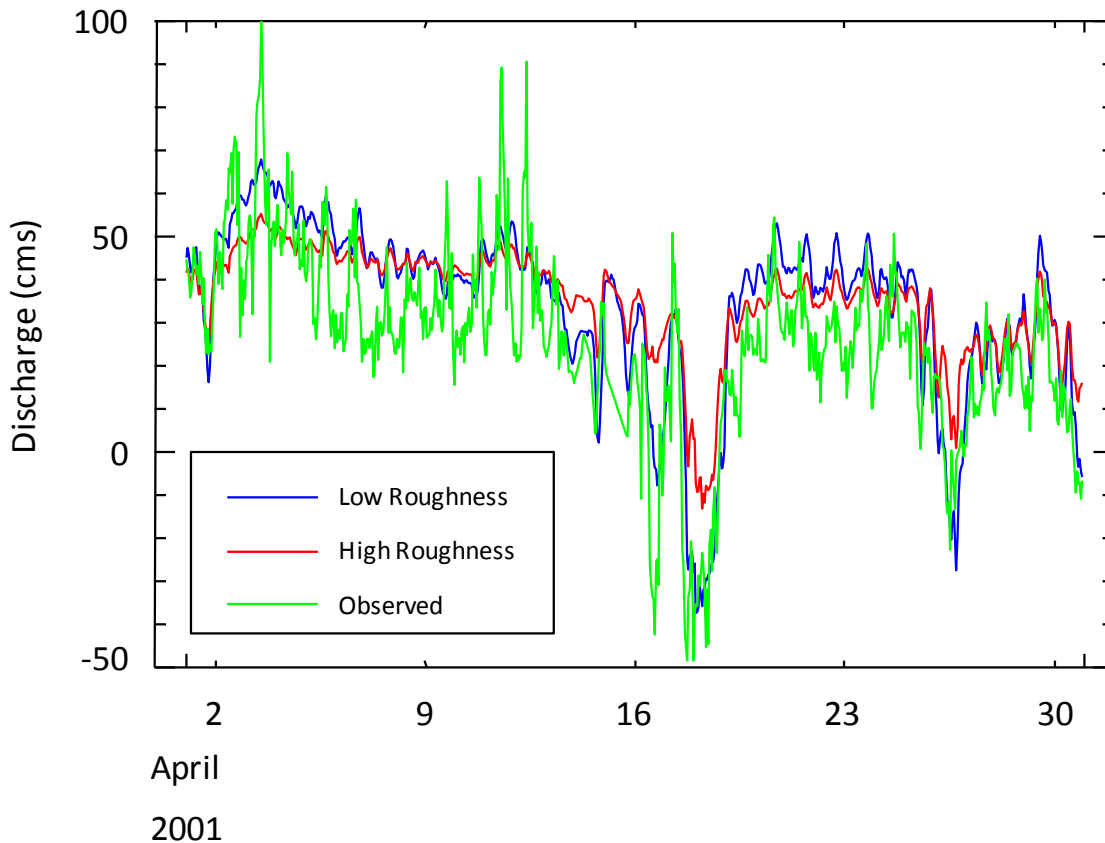


Figure 6–53. Simulated versus observed hourly discharge at DeLand during April 2001.

The comparative statistics for hourly discharge at Lake Jesup outlet were poor (see Table 6–13). Short period oscillations at this location are generally unaffected by net downstream discharge, particularly during dry periods when net discharge leaving the lake is near zero. During dry conditions diurnal oscillations of discharge are sometimes observed, presumably forced by winds. This phenomenon occurred during the first 2 weeks of May during the calibration period (Figure 6–54). The Low Roughness model does considerably better than the High Roughness model at capturing the diurnal variability of discharge. The Nash–Sutcliffe statistic for the High and Low Roughness models improves from 0.547 (satisfactory) to 0.698 (good) for this period.

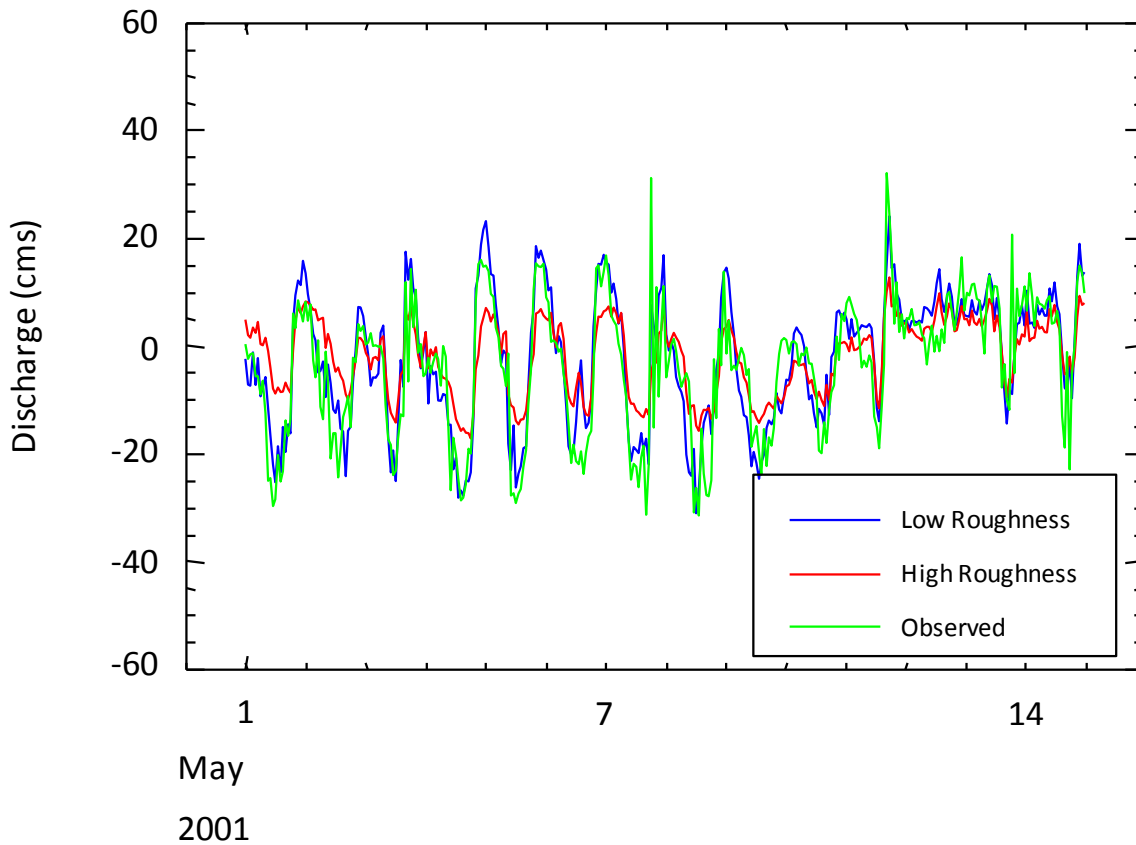


Figure 6–54. Simulated versus observed hourly discharge at Lake Jesup outlet during 1 to 14 May 2001.

Figure 6–55 illustrates the cause for the poor comparative statistics for hourly discharge at Lake Jesup outlet. Observed hourly discharge displays much larger variability than simulated discharges for either model. Observed discharge shows an appreciable net flow into the lake between 6 to 13 August. We previously showed that observed discharge is inconsistent with observed lake stage during this month and that the observed discharge is likely low. Hourly discharge measurements at this gauge need to be quality-assured to establish confidence in these observed data.

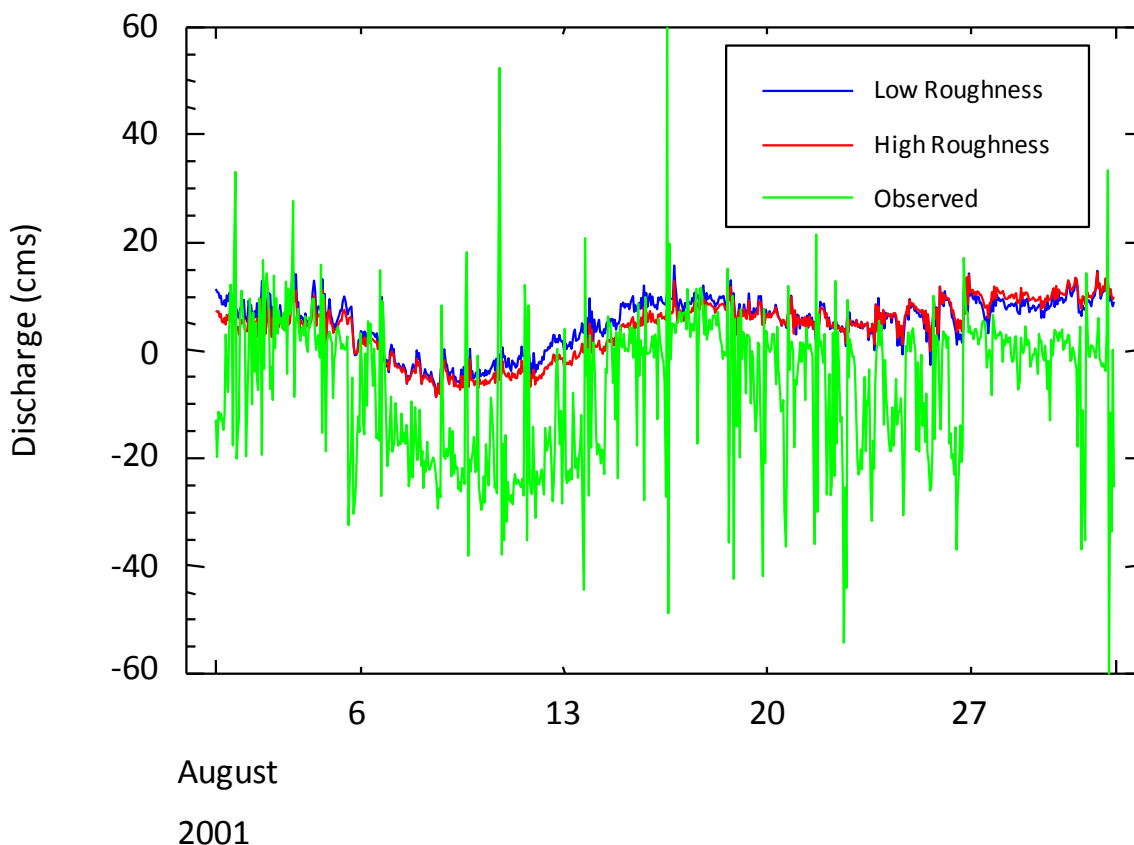


Figure 6–55. Simulated versus observed hourly discharge at Lake Jesup outlet during August 2001.

Daily Salinity

Comparative statistics between simulated and observed salinity are shown in Table 6–14 at DeLand and Sanford. The comparative statistics are similar between the High and Low Roughness models. The unsatisfactory Nash–Sutcliffe statistic is caused by the large mismatch in salinity during the August-September period.

The visual comparison of simulated salinity at DeLand between the High and Low Roughness models indicates that salinity is generally insensitive to bottom roughness at this location (Figure 6–56).

The High and Low Roughness model simulations are generally insensitive to bottom roughness at Sanford also, but the Low Roughness model captures the freshening events during April and May slightly better than the High Roughness model (Figure 6–57). These freshening events are caused by upstream movement during reverse flow events of fresher waters exiting the Wekiva River.

At both DeLand and Sanford, simulated and observed salinity visually compare well for the first 4 months of the calibration period. Salinity is notably underpredicted at Sanford in July and at

both locations during August and September. The mismatch of salinity during August-September is examined below and found to result from the upstream salinity boundary condition.

Table 6–14. Statistical comparison of simulated and observed daily salinity for High and Low Roughness models at DeLand and Sanford over the calibration period, March to September 2001.

	DeLand		Sanford	
	High	Low	High	Low
<i>NRECS</i>	214		214	
r^2	0.566	0.551	0.646	0.651
<i>m</i>	0.970	0.956	0.933	0.922
<i>NS</i>	0.210	0.163	0.476	0.461
<i>AVAE</i>	0.116	0.115	0.150	0.143
<i>AVRE (%)</i>	17.9	17.7	20.7	19.6
<i>RMSE</i>	0.159	0.164	0.211	0.214

- NRECS* = Number of records
- r^2 = Coefficient of determination
- m* = Meter
- NS* = Nash–Sutcliffe
- AVAE* = Average absolute error
- AVRE* = Average relative error
- RMSE* = Root-mean-square error

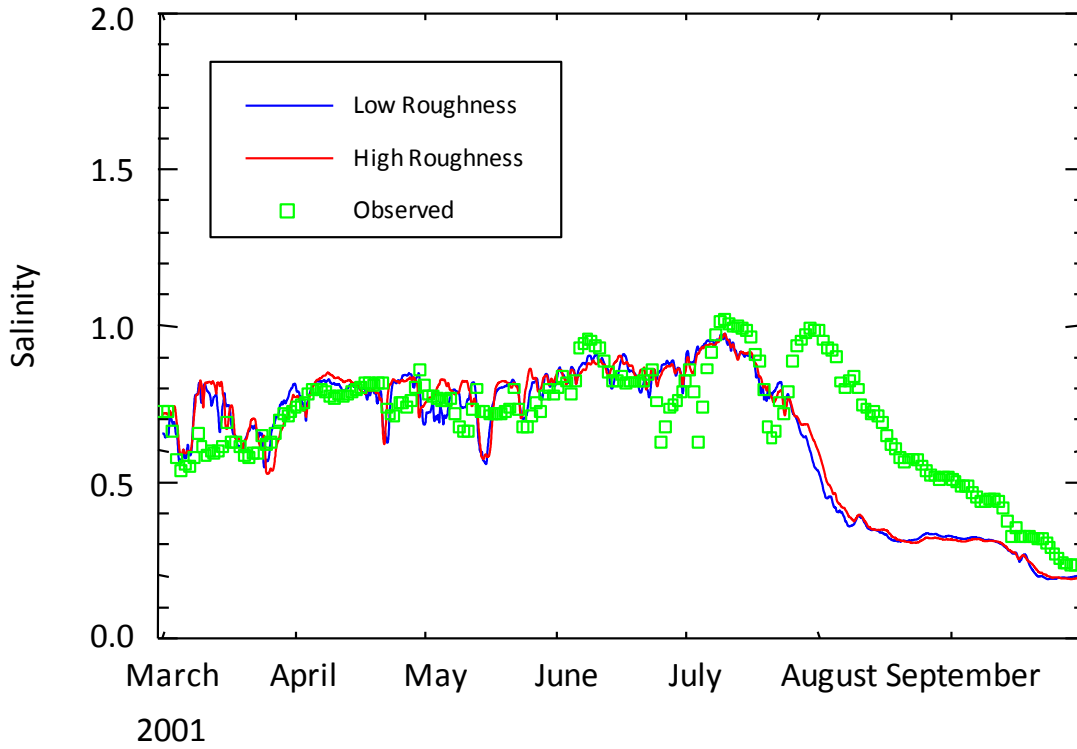


Figure 6–56. Simulated versus observed daily salinity at DeLand (SR 44) over the calibration period.

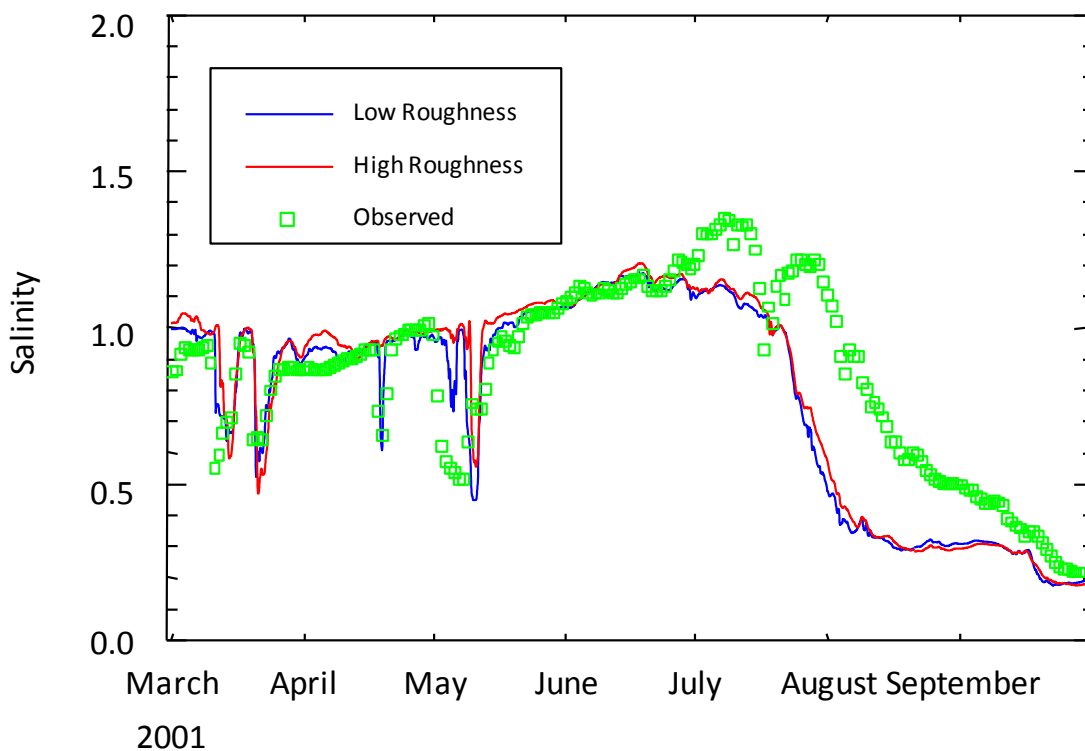


Figure 6–57. Simulated versus observed daily salinity at Sanford (US 17) over the calibration period.

6.6.3 SUMMARY OF BOTTOM ROUGHNESS CALIBRATION

Bottom roughness for the EFDC-LSJR hydrodynamic model was optimized using PEST to minimize the difference between observed and simulated tidal constituents throughout the model domain. Final bottom roughness parameters ranged from 0.0001 to 0.025 m with the lowest values occurring in the wide lacustrine portion of the river between Jacksonville and Palatka.

Bottom roughness for the EFDC-MSJR hydrodynamic model was first estimated from Manning's n values with a range of 0.001 to 0.2 m. Numerical tests, using a range of constant, steady-state discharge entering Lake Harney, were used to adjust the initial bottom roughness by comparison with observed surface slope–discharge relationships. Bottom roughness was reduced to a range 0.0001 to 0.004 m with the lowest values occurring in the main channel. Bottom roughness values for the EFDC-MSJR hydrodynamic model are consistent with values for the EFDC-LSJR hydrodynamic model even though both models were calibrated independently using different methodologies and calibration criteria.

For the EFDC-MSJR hydrodynamic model, the initial bottom roughness values (High Roughness model) were compared with the calibrated bottom roughness values (Low Roughness model) for a completely dynamic simulation over the calibration period. The dynamic simulation confirmed that the Low Roughness model is superior to the High Roughness model for simulation of daily water level and hourly discharge. Daily discharge and salinity are relatively insensitive to changes in bottom roughness over the range of values tested.

6.7 FINAL CALIBRATION

For the final calibration, output variables for each model were compared to observed data. For the EFDC-LSJR hydrodynamic model, the comparison showed that no further calibration is required. For the EFDC-MSJR hydrodynamic model, an unsatisfactory match of observed and simulated salinity (see Figure 6–57) is resolved by a modification to the upstream salinity boundary condition.

6.7.1 FINAL CALIBRATION OF THE EFDC-LSJR HYDRODYNAMIC MODEL

Hourly Water Level

Simulated and observed hourly water level for a 1-month period in September 1997 were plotted for Main Street Bridge (Figure 6–58) and Buffalo Bluff (Figure 6–59). These plots showed the dominance of the semidiurnal tide, although lower frequency variability is also evident. The simulated results (square symbols) closely match observed water level (lines) at both locations.

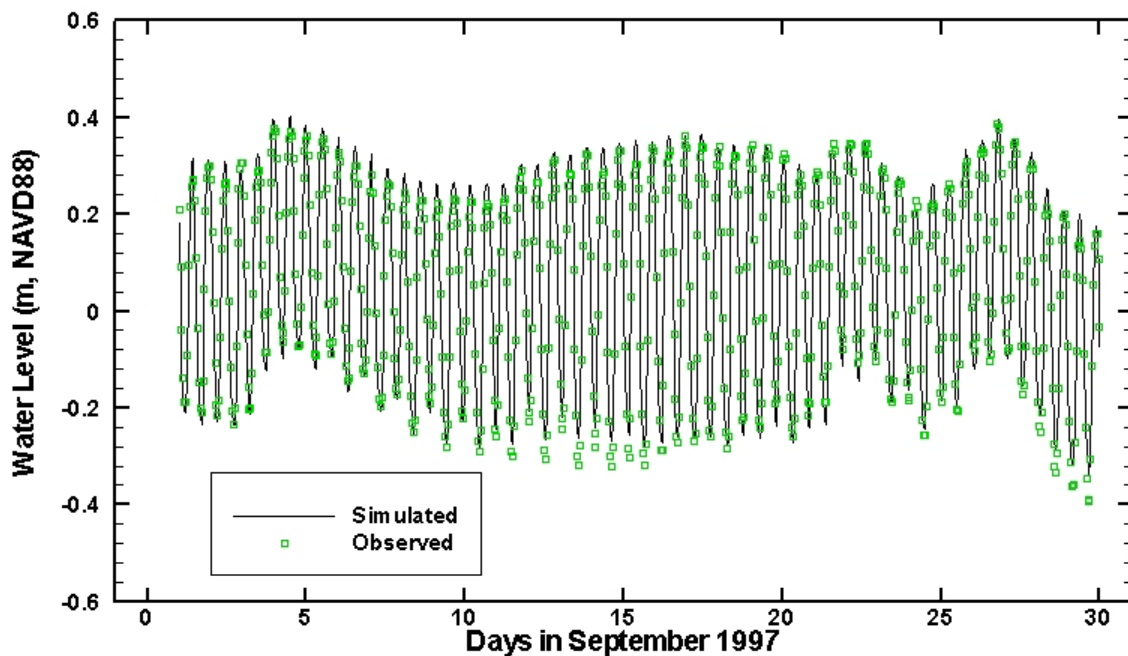


Figure 6–58. Simulated and observed hourly water level at Main Street Bridge, September 1997.

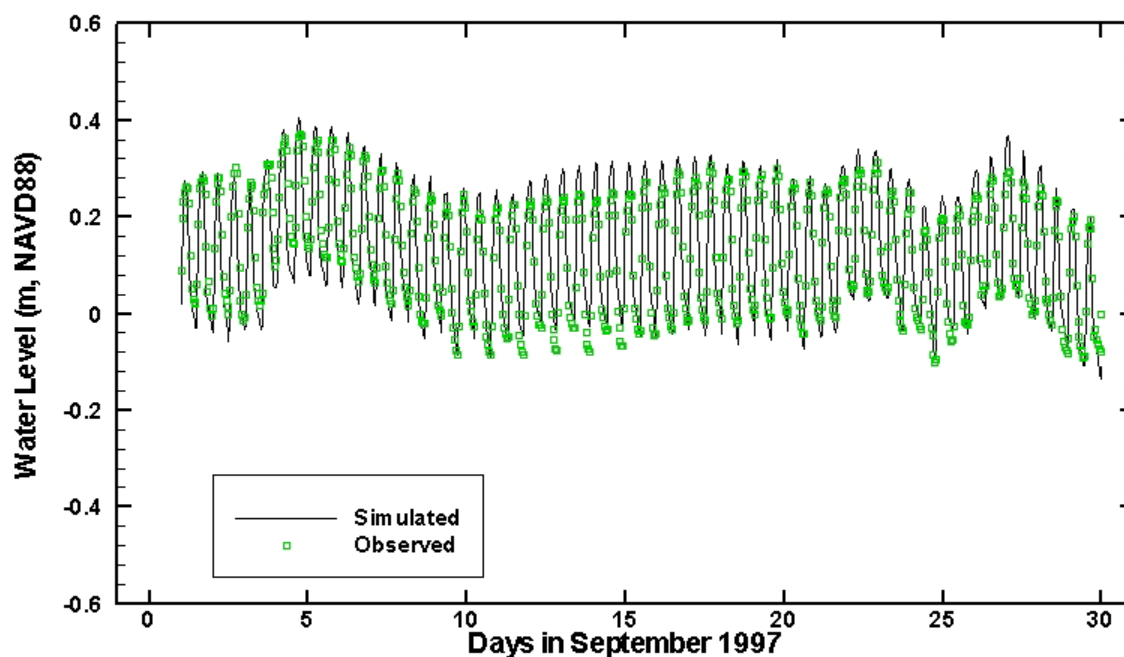


Figure 6–59. Simulated and observed hourly water level at Buffalo Bluff, September 1997.

Because of the dominance of the semidiurnal tide, comparison of observed and simulated M_2 tidal amplitude and phase are shown for stations throughout the lower St. Johns River (Table 6–15). For modern tidal stations in the river main stem, the largest percent error in M_2 amplitude is 8.5% at Main Street Bridge. Percent error at Silver Glen is larger, but the amplitude is approximately 1 cm and the small difference in amplitude explains the large percent error. M_2 phase errors are generally less than 5 degrees for the modern stations, with the highest being 5.9 degrees at Buckman Bridge. Simulated and observed M_2 amplitude and phase plotted against river kilometer show that the model correctly simulates the spatial variation of tidal amplitude and phase throughout the lower St. Johns River (Figure 6–60).

Table 6–15. Comparison of observed and simulated M₂ tidal amplitude and phase over the calibration period, August 1997 to April 1999.

Station	Amplitude (cm)			Phase (Degrees)		
	Observed	Simulated	% Error	Observed	Simulated	Difference
Mayport	67.0	64.9	-3.1	241.3	241.9	0.6
Bar Pilot Dock	66.8	65.7	-1.7	240.8	241.2	0.4
Pablo Creek Entrance	57.4	59.7	4.0	254.2	259.8	5.6
Fulton	56.5	55.7	-1.4	253.5	257.6	4.1
Clapboard Creek	54.6	55.0	0.8	261.1	262.8	1.7
Blount Island	53.3	53.5	0.3	261.2	264.2	3.1
Dames Point	53.7	51.9	-3.3	264.0	265.2	1.2
Navy Fuel Depot	40.5	41.0	1.3	278.4	274.8	-4.4
Long Branch	37.4	37.3	-0.4	278.1	279.2	1.1
Main Street Bridge	28.7	26.2	-8.5	290.0	290.8	0.8
Ortega River Entrance	17.4	19.8	13.7	304.7	304.7	0.0
Piney Point	13.3	15.3	15.3	319.5	317.5	-2.0
Buckman Bridge	12.7	13.5	6.2	324.7	330.6	5.9
Doctors Lake	12.1	13.6	12.1	334.0	348.5	14.5
Shands Bridge	11.7	11.7	0.0	25.1	30.0	4.9
Racy Point	15.7	16.0	1.9	65.6	69.5	3.9
Palatka	18.5	17.5	-5.2	83.0	85.6	2.6
Buffalo Bluff	15.6	14.7	-5.4	95.6	97.3	1.7
Sutherland Still	13.9	12.2	-11.9	94.5	95.8	1.3
Moccasin Landing	0.9	0.8	11.1	188.7	145.6	-43.1
Welaka	6.3	6.0	-4.6	109.7	114.0	4.3
Georgetown	0.9	1.2	32.2	231.8	192.0	-39.8
Silver Glen	1.0	1.4	40.0	232.2	232.8	0.6

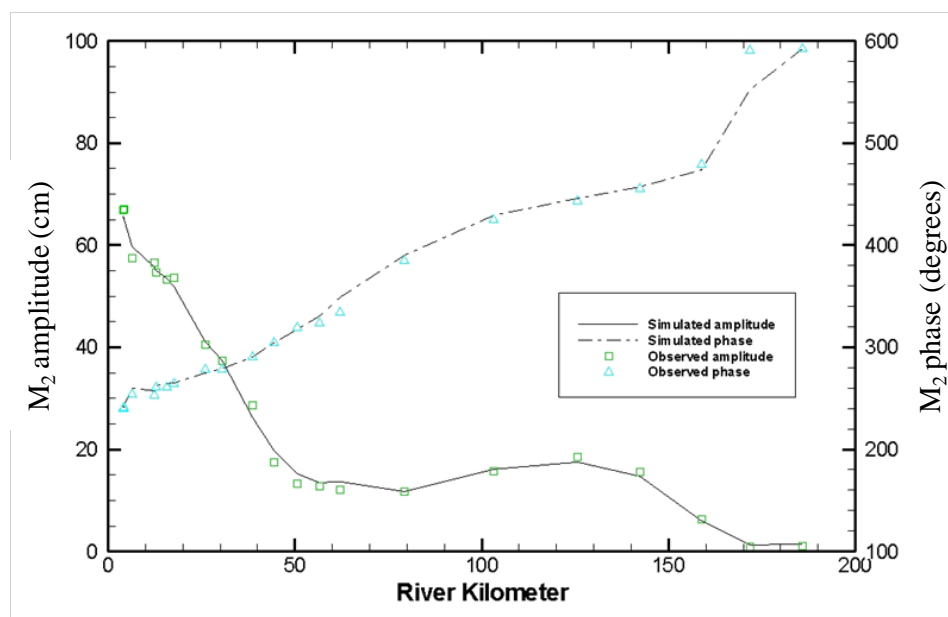


Figure 6–60. Simulated and observed M_2 amplitude and phase by river kilometer during the calibration period, August 1997 to April 1999.

The ratio of diurnal to semidiurnal amplitude, or form number, is also correctly simulated by the model. Form number is defined as the ratio $(K_1+O_1):(M_2+S_2)$. The model successfully captures the increase in form number from Main Street Bridge to Shands Bridge, the subsequent decrease to Welaka, and the increase in Lake George as represented by Georgetown and Silver Glen Springs (Table 6–16).

Comparative statistics for paired values of observed and simulated hourly water level are shown in Table 6-17. This comparison shows the goodness of fit between simulated and observed total water level, including sub-tidal variability. The squared correlation coefficients exceed 0.90 and root-mean square errors (*RMSE*) are less than 9 cm.

Frequency distributions for both observed and simulated water level are shown in Table 6–18, for all paired values. Before the calculations were done, the data and model results at each station were adjusted to the mean observed water level. Water level between the 10th and 90th percentile (80% of all values) provides a characteristic range of typical water level experienced at each station. Simulated results match low levels (10th percentile) within 2 cm and high levels (90th percentile) within 3 cm. Median water levels are also simulated to within 2 cm.

Table 6–16. Observed and simulated form number, $(K_1+O_1)/(M_2+S_2)$ during the calibration period, August 1997 to April 1999.

Station	Observed	Simulated
Mayport	0.18	0.19
Bar Pilot Dock	0.19	0.19
Pablo Creek Entrance	0.23	0.19
Fulton	0.16	0.17
Clapboard Creek	0.18	0.18
Blount Island	0.22	0.17
Dames Point	0.15	0.16
Navy Fuel Depot	0.18	0.16
Long Branch	0.17	0.16
Main Street Bridge	0.15	0.16
Ortega River Entrance	0.18	0.19
Piney Point	0.16	0.21
Buckman Bridge	0.25	0.24
Doctors Lake	0.28	0.25
Shands Bridge	0.26	0.28
Racy Point	0.21	0.20
Palatka	0.18	0.17
Buffalo Bluff	0.15	0.17
Sutherland Still	0.15	0.17
Moccasin Landing	0.36	0.32
Welaka	0.13	0.19
Georgetown	0.39	0.45
Silver Glen	0.33	0.34

Table 6–17. Comparison of observed and simulated hourly water level during the calibration period, August 1997 to April 1999.

Station	<i>NRECS</i>	r^2	<i>m</i>	<i>RMSE</i> (cm)
Bar Pilot Dock	15,337	0.97	0.95	8.7
Dames Point	11,410	0.97	0.98	7.9
Long Branch	12,343	0.97	1.00	5.9
Main Street Bridge	15,257	0.95	0.97	5.3
Buckman Bridge	14,910	0.94	1.00	4.2
Shands Bridge	13,101	0.91	0.97	4.8
Racy Point	12,833	0.93	0.98	4.7
Palatka	14,352	0.92	0.96	5.6
Buffalo Bluff	14,111	0.92	0.94	5.3
Welaka	15,337	0.95	0.94	3.9

NRECS = Number paired observed and simulated values

r^2 = Coefficient of determination

m = Slope of regression line

RMSE = Root-mean-square error

Table 6–18. Observed (Obs) and simulated (Sim) distribution of hourly water level for all paired values during the calibration period, August 1997 to April 1999, in m, NGVD29.

Station		<i>Min</i>	<i>10th Percentile</i>	<i>Median</i>	<i>90th Percentile</i>	<i>Max</i>
Bar Pilot Dock	Obs	-1.51	-0.85	-0.12	0.56	1.04
	Sim	-1.48	-0.83	-0.12	0.53	1.15
Dames Point	Obs	-1.07	-0.66	-0.09	0.43	0.81
	Sim	-1.02	-0.65	-0.11	0.44	0.91
Long Branch	Obs	-0.86	-0.46	-0.05	0.35	0.70
	Sim	-0.78	-0.45	-0.07	0.37	0.78
Main Street Bridge	Obs	-0.76	-0.40	-0.06	0.23	0.60
	Sim	-0.70	-0.39	-0.07	0.24	0.61
Buckman Bridge	Obs	-0.46	-0.23	-0.02	0.18	0.58
	Sim	-0.49	-0.24	-0.02	0.20	0.54
Shands Bridge	Obs	-0.52	-0.21	-0.01	0.20	0.52
	Sim	-0.48	-0.21	-0.01	0.20	0.52
Racy Point	Obs	-0.52	-0.22	0.00	0.21	0.71
	Sim	-0.50	-0.24	-0.01	0.23	0.62
Palatka	Obs	-0.52	-0.26	0.00	0.24	0.78
	Sim	-0.50	-0.25	-0.01	0.26	0.63
Buffalo Bluff	Obs	-0.47	-0.21	0.03	0.27	0.68
	Sim	-0.45	-0.20	0.03	0.27	0.62
Welaka	Obs	-0.06	0.15	0.36	0.58	0.90
	Sim	-0.06	0.15	0.37	0.57	0.91

Tidal Discharge

Representative plots of observed and simulated tidal discharge are shown below for Marker 22 (Figure 6–61), Shands Bridge (Figure 6–62), and Hog Eye Point (Figure 6–63) during September 1997. The model captures both the range and timing of tidal discharge at each of the stations.

The model also captures the much stronger flood tide (negative values) as compared to ebb tide that occurred at Marker 22 on that day.

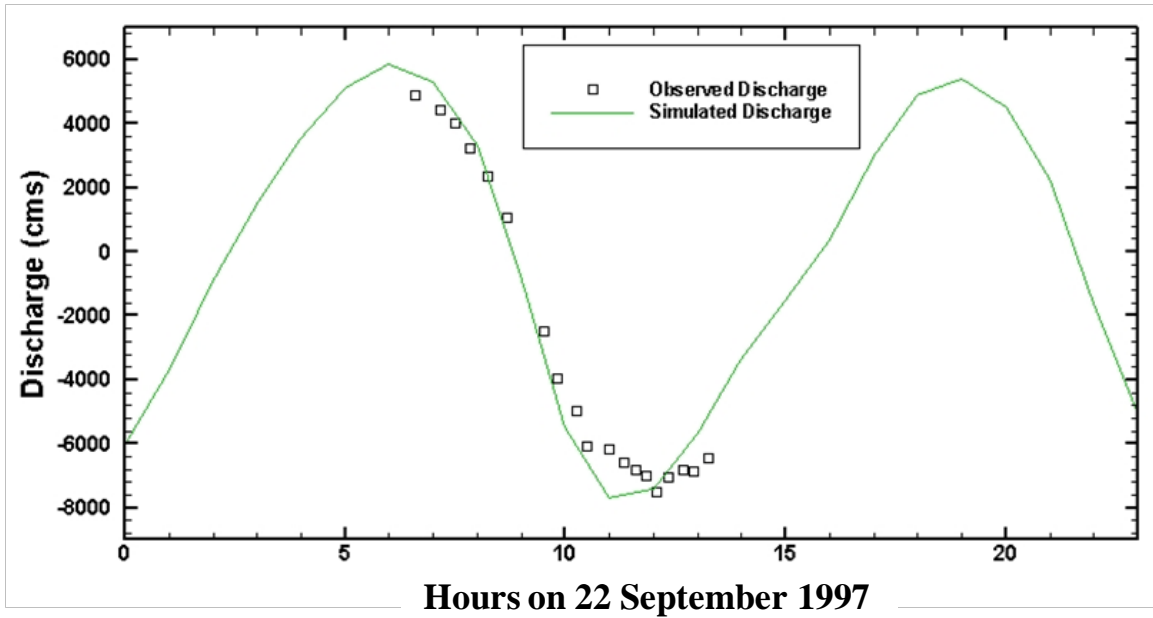


Figure 6–61. Comparison of observed and simulated tidal discharge at Marker 22 on 22 September 1997.

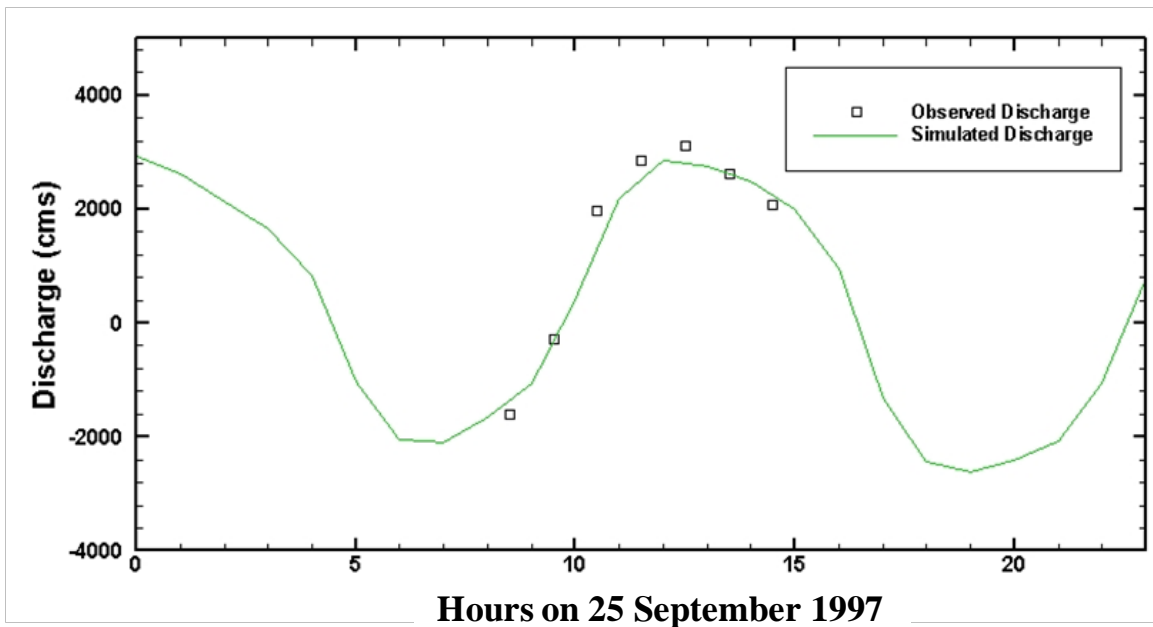


Figure 6–62. Comparison of observed and simulated tidal discharge at Shands Bridge on 25 September 1997.

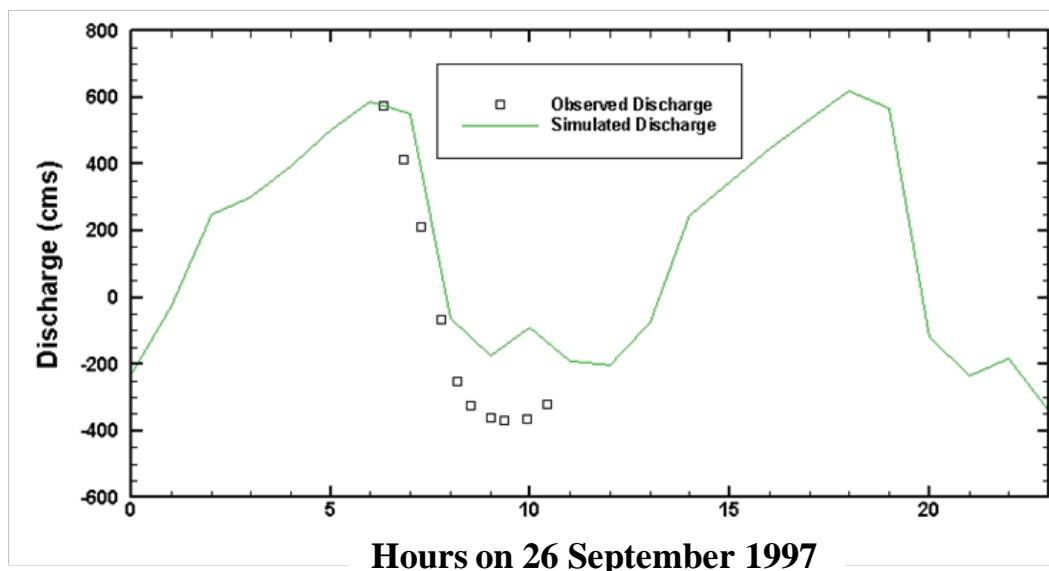


Figure 6–63. Comparison of observed and simulated tidal discharge at Hog Eye Point on 26 September 1997.

Tidal Harmonics for Continuous Discharge

Simulated and observed tidal harmonics for discharge at three USGS continuous discharge stations are compared below for six major tidal constituents (Table 6–19). These results show that the model captures the strength and timing of tidal discharge in both downstream and upstream areas of the lower St. Johns River.

Table 6–19. Comparison of observed (Obs) and simulated (Sim) tidal constituents for discharge at USGS continuous discharge stations during the calibration period, August 1997 to April 1999. Tidal constituents are defined in Table 3–5.

Station		M ₂		N ₂		S ₂		O ₁		K ₁		M ₄	
		A	P	A	P	A	P	A	P	A	P	A	P
Main Street Bridge	Sim	3969	114	718	98	524	133	324	319	434	327	291	30
	Obs	4017	113	700	95	428	130	326	328	431	321	213	4
Buffalo Bluff	Sim	340	302	58	284	41	329	41	70	47	84	16	348
	Obs	261	285	41	264	29	319	30	68	33	73	16	324
Dunns Creek	Sim	82	273	14	253	10	300	7	58	8	72	14	330
	Obs	105	292	17	260	12	308	9	75	11	72	11	355

A = Amplitude in m³s⁻¹
P = Phase in degrees.

Daily Averaged Discharge

Comparative statistics for observed and simulated daily averaged discharge are shown in Table 6–20 for each continuous discharge station. Daily discharge in this reach of the St. Johns River is particularly influenced by low frequency ocean water level variability (Sucsy and Morris 2001). Simulated values at the two mainstem stations at Main Street Bridge and Buffalo Bluff compare well with observed values. Both have high correlation ($r^2 > 0.80$). Simulated values at the Dunns Creek station have the highest *AVRE*. We expected that daily discharges would respond similarly at Dunns Creek and Buffalo Bluff because both should respond to the same ocean water level forcing. The higher *AVRE* for Dunns Creek could indicate that Dunns Creek is more influenced by local hydrology than Buffalo Bluff and that the simulated hydrology at daily time scales has a larger effect.

Table 6–20. Comparison of observed and simulated daily discharge over the calibration period, August 1997 to April 1999.

Station	<i>NRECS</i>	r^2	<i>m</i>	<i>b</i>	<i>AVAE</i>	<i>AVRE</i>	<i>RMSE</i>
Main Street Bridge	618	0.90	0.86	0.5	98.8	25.3	133.2
Buffalo Bluff	639	0.81	0.90	33.6	51.9	28.2	72.9
Dunns Creek	639	0.84	0.71	5.4	12.7	41.8	16.9

NRECS = Number of paired values of simulated and observed discharge.

r^2 = Coefficient of determination

m = Slope of regression line

b = Intercept of regression line

AVAE = Average absolute error ($\text{m}^3 \text{s}^{-1}$)

AVRE = Average relative error (%)

RMS = Root-mean-square error ($\text{m}^3 \text{s}^{-1}$)

Plots of observed and simulated daily averaged discharge at the three sites are shown in Figure 6–64, Figure 6–65, and Figure 6–66. Each figure compares observed and simulated daily averaged discharge during 1998. River discharge was much higher than average during the first 3 months of 1998. River discharge from April to November was about average and discharge in December was lower than average. The model correctly captures these seasonal discharge trends. Perhaps more importantly, the model exhibits strong correlation for daily variability of discharge at all three stations. In particular, the model simulates the frequent daily flow reversal (negative discharge) at each location.

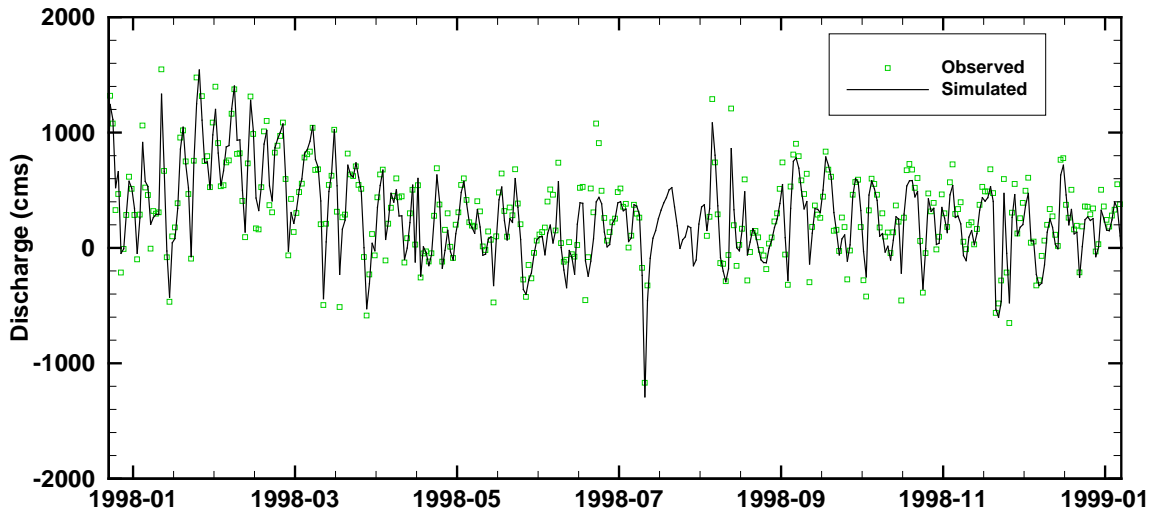


Figure 6–64. Simulated and observed daily averaged discharge at Main Street Bridge for 1998.

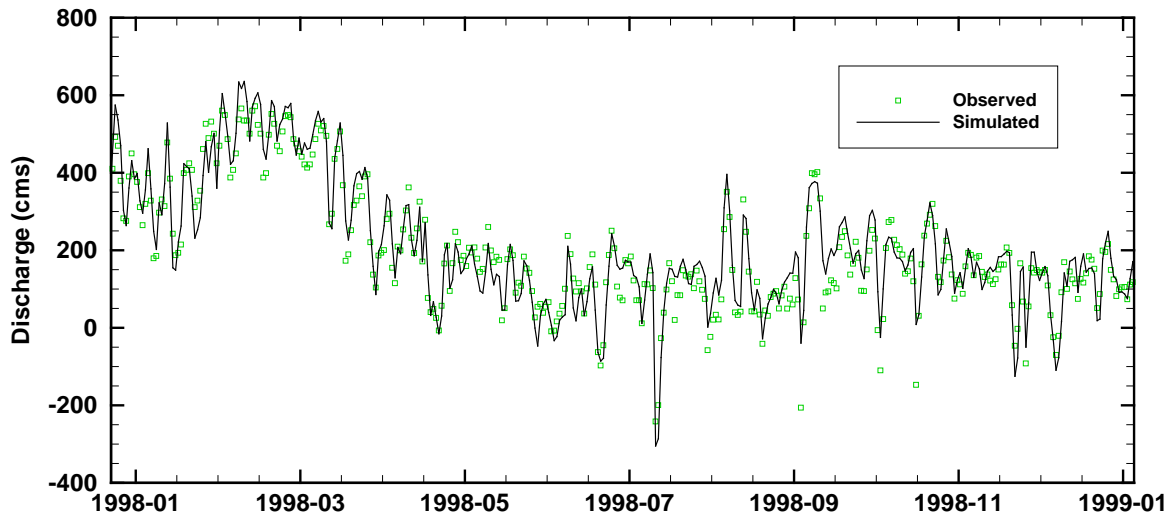


Figure 6–65. Simulated and observed daily averaged discharge at Buffalo Bluff for 1998.

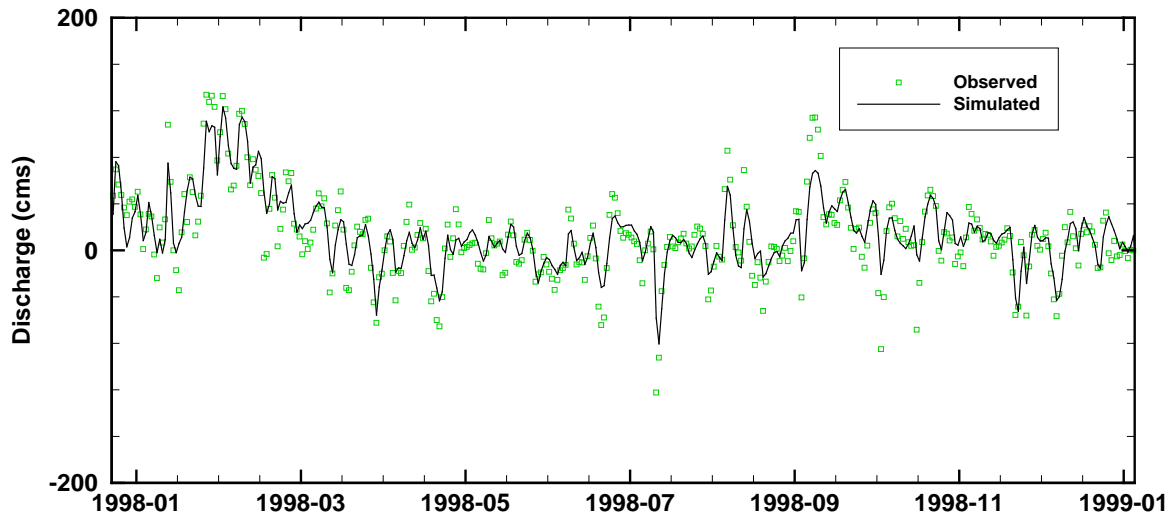


Figure 6–66. Simulated and observed daily averaged discharge at Dunns Creek for 1998.

Vertical Velocity Profile

NOAA collected vertical velocity profiles using upward-looking Acoustic Velocity Meters at three locations (Figure 6–67) in the lower St. Johns River during the calibration period. Observed and simulated velocities are compared at each site for a 48-hr period in the beginning of August 1998 (Figure 6–68). The model generally captures the timing and magnitude of both flood (negative velocities) and ebb (positive velocities) tides at all three locations. The model also captures the observed hourly variations of vertical velocity including periods on the flood tide when vertical velocity profiles are uniform, and periods on the ebb tide when vertical velocity profiles are steep. The strength of the flood tides is slightly overpredicted in the upper portions of the water column, particularly at Blount Island East and Dames Point. Two of the ebb tides at Dames Point are underpredicted near the bottom. Amplitude differences for velocities can be caused by mismatch of local bathymetry and grid resolution.

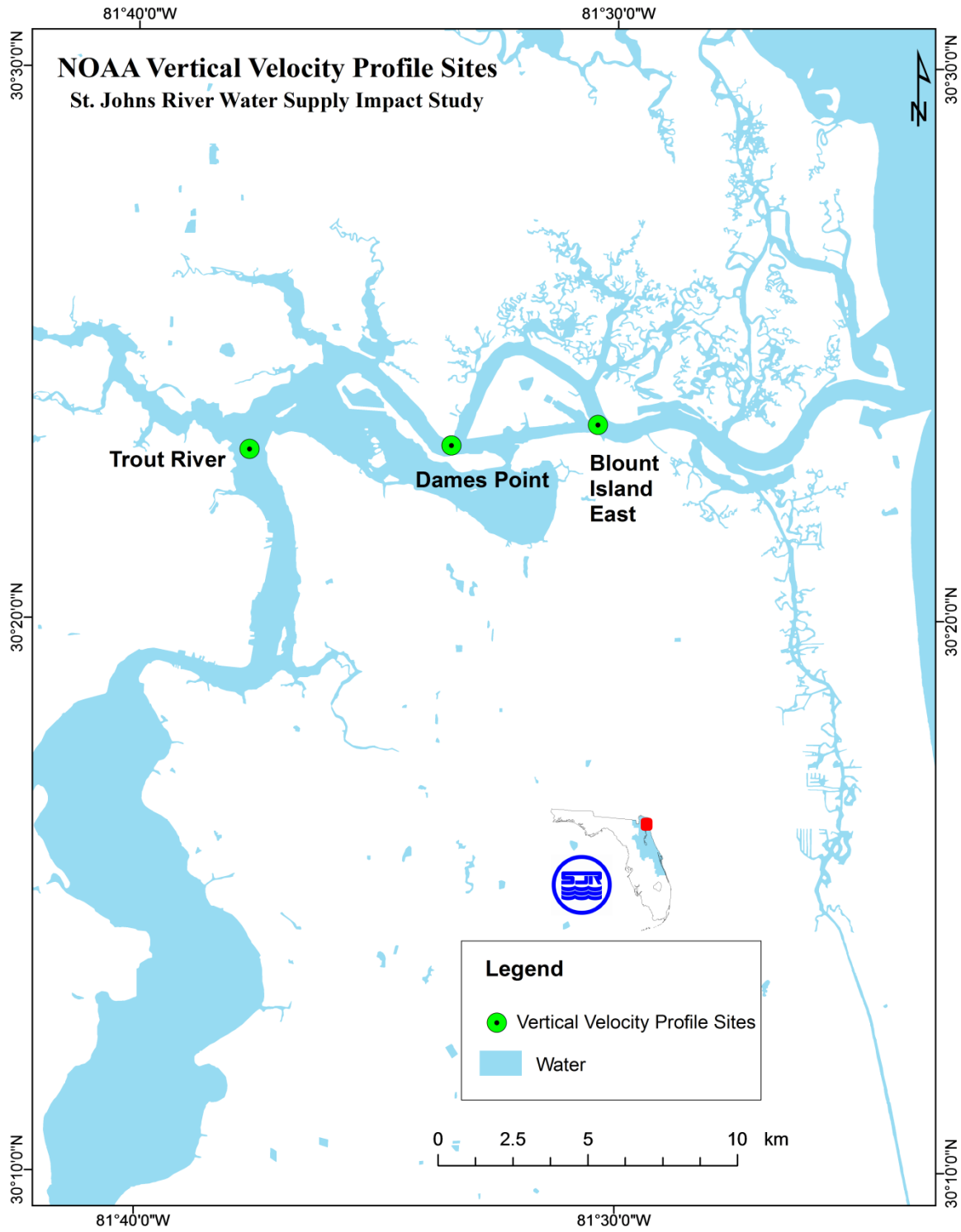


Figure 6–67. Locations for the NOAA vertical velocity profile measurements.

Simulated

Observed

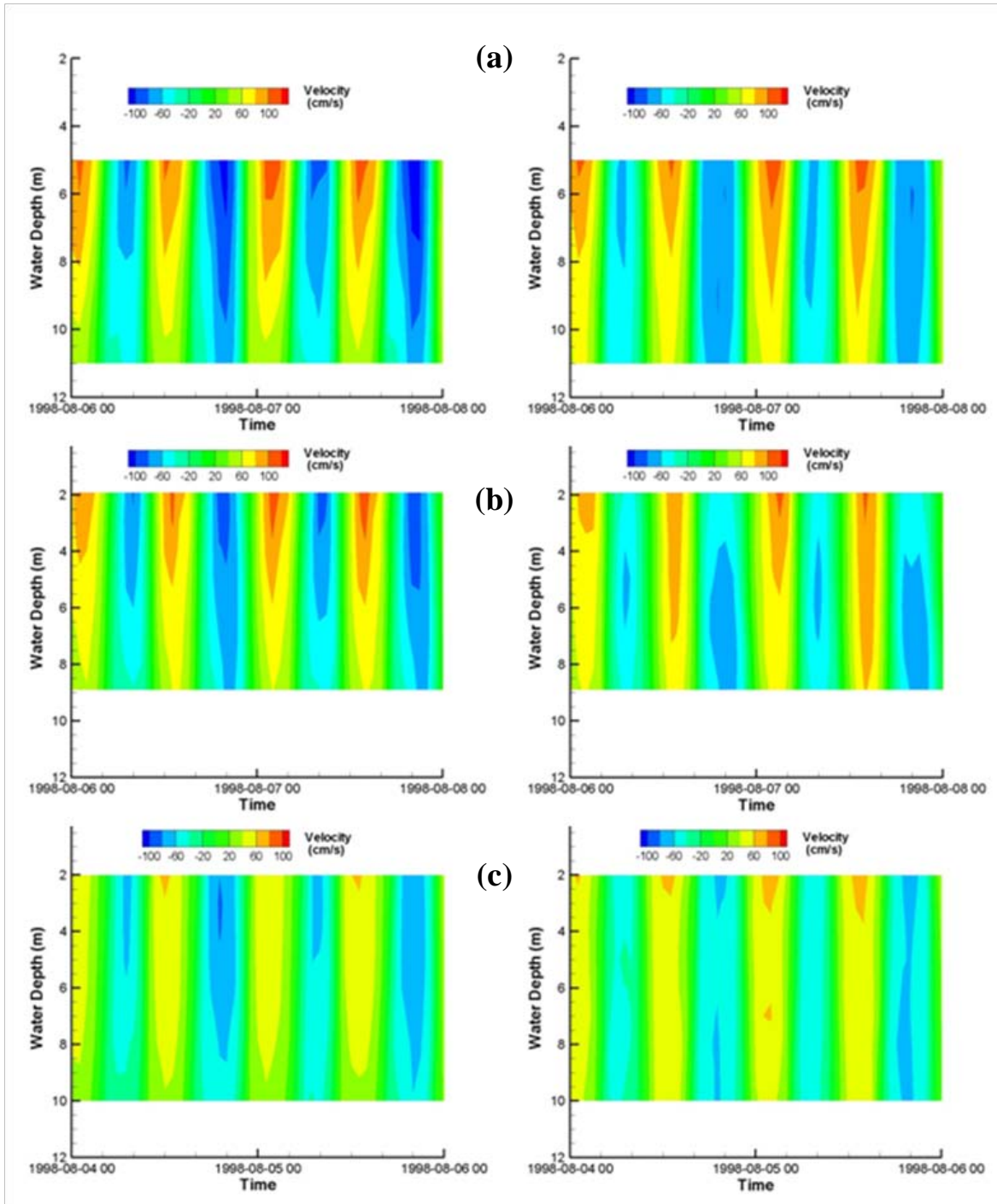


Figure 6–68. Vertical velocity profile comparison at (a) Blount Island East, (b) Dames Point, and (c) Trout River (simulated values left and observed values right).

Salinity

Accurate prediction of salinity is a key skill for the EFDC-LSJR hydrodynamic model because salt, as a conservative tracer, provides a means to assess the integration of all forces acting on the model that result in transport, circulation, and mixing processes. In addition, salinity is a key parameter that affects the biology of estuaries, and the response of salinity to water withdrawals and other factors must be quantified for the present study.

Comparative statistics for paired simulated and observed hourly salinity at the continuous salinity stations are shown in Table 6–21. Salinity at each of the stations is measured at either two or three depths. Observed salinity for stations with observations at three depths is designated top, middle, and bottom. For stations with two depths, the designation is top and bottom. (A designation of top should not be assumed to be a surface observation; the top sensor must be placed at a depth that will ensure that the sensor remains submerged under all expected tidal and meteorological conditions.) Observed salinity at each depth are matched by converting simulated salinity at the six sigma levels to fixed depths (z-levels) for each time of observation. The simulated z-level salinities are then linearly interpolated to determine simulated salinity at the fixed depths (i.e., top, middle, bottom) of observed salinity.

Correlations are high between simulated and observed hourly salinity, particularly upstream of Acosta Bridge where r^2 ranges from 0.82 to 0.93 and *AVAE* are less than 1. *AVAE* is higher (1.85 -3.03) in the marine segment at Dames Point, but because salinity is generally high at this station *AVRE* is less than 14%. At each station, simulated salinity generally matches observed salinity equally over all depths of observation. The exception is Buckman Bridge where *AVRE* increases from 22.9% at the top depth to 32.8% at the bottom depth.

Table 6–21. Comparison of observed and simulated hourly salinity at USGS continuous salinity stations over the calibration period, August 1997 to April 1999.

Station	<i>NRECS</i>	r^2	<i>m</i>	<i>b</i>	<i>AVAE</i>	<i>AVRE</i>	<i>RMSE</i>
Dames Point Top	11,116	0.84	0.91	1.48	1.85	9.1	2.40
Dames Point Middle	10,810	0.86	0.95	2.72	2.23	10.3	2.79
Dames Point Bottom	10,769	0.83	0.96	3.49	3.03	13.6	3.66
Acosta Top	12,160	0.93	0.99	-0.07	0.87	18.0	1.32
Acosta Middle	12,893	0.93	1.07	0.01	0.95	19.5	1.46
Acosta Bottom	12,436	0.93	1.11	0.00	1.05	21.8	1.63
Buckman Top	13,048	0.85	0.93	0.04	0.25	22.9	0.59
Buckman Middle	12,224	0.91	1.24	-0.14	0.33	30.9	0.69
Buckman Bottom	10,528	0.90	1.19	-0.08	0.43	32.8	0.94
Shands Top	13,473	0.90	0.71	0.07	0.06	13.9	0.08
Shands Middle	13,257	0.90	0.71	0.07	0.06	13.9	0.08
Shands Bottom	13,353	0.90	0.71	0.07	0.06	13.9	0.08
Dancy Point Top	10,693	0.82	0.79	0.04	0.05	11.3	0.05
Dancy Point Bottom	10,700	0.93	0.79	0.04	0.05	11.3	0.05

NRECS = Number of paired values of simulated and observed salinity

r^2 = Coefficient of determination

m = Slope of regression line

b = Intercept of regression line

RMSE = Root-mean-square error

AVRE = Average relative error (%)

AVAE = Average absolute error

Figure 6–69 through Figure 6–73 compare the observed and simulated hourly salinities for each depth at each continuous monitoring station during the calibration period. (Note the vertical axes scales change between figures) The model correctly captures the temporal variability of salinity at each station. In the marine area, at Dames Point, the model closely matches observed salinity for the top depth, but slightly overpredicts salinity for the bottom depth.

Seasonal salinity variability at the two downstream stations, Dames Point (Figure 6–69) and Acosta Bridge (Figure 6–70), is very large. For example, salinity at Acosta Bridge during March of 1998 was near 0 and then rose to between 15 and 20 during June. The model correctly simulates this large variation of seasonal salinity at these locations.

The model also correctly simulates the differing ranges of salinity between stations, including the frequent intrusion of seawater at Acosta Bridge, the infrequent intrusion of seawater at Buckman Bridge, and the complete absence of intrusion of seawater at Shands Bridge and Dancy Point. These results show that the model is successfully predicting the response of river salinity to seasonal variations in discharge and the dynamic mechanisms that result in upstream transport of ocean salt into the river.

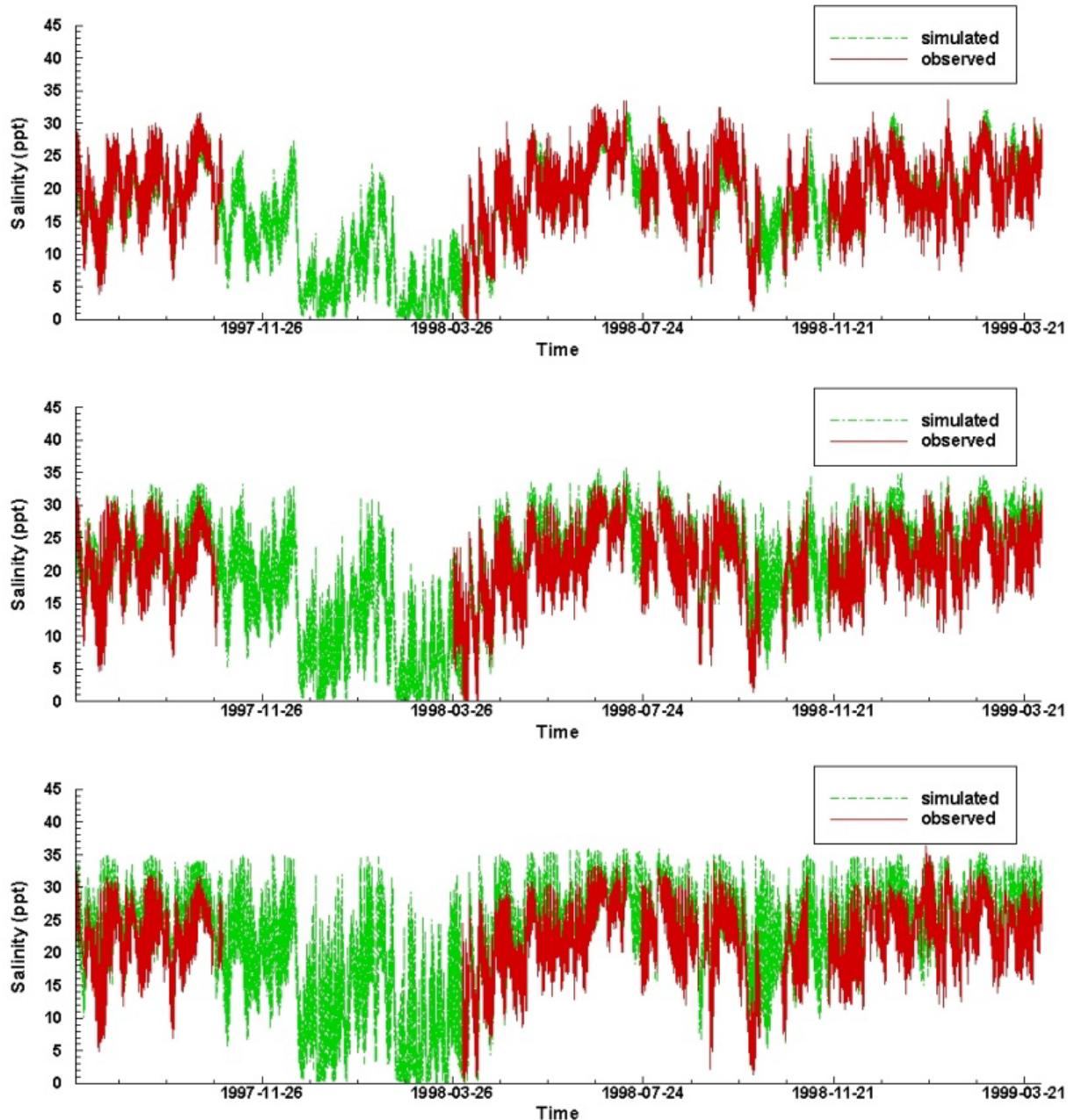


Figure 6–69. Salinity time series comparison at Dames Point station during the calibration period (top, middle, and bottom depths of observation).

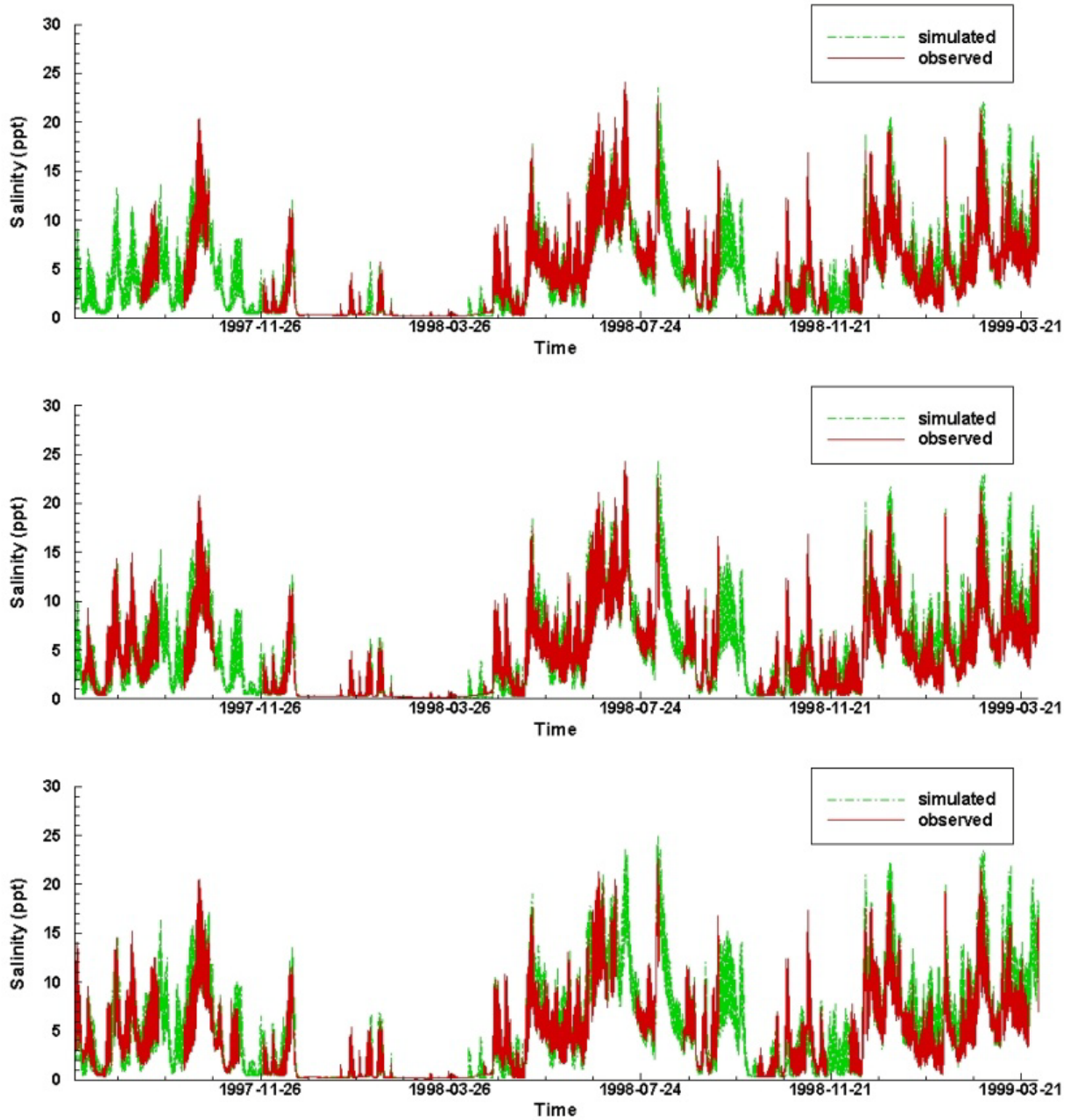


Figure 6–70. Salinity time series comparison at Acosta Bridge during the calibration period (top, middle, and bottom depths of observation).

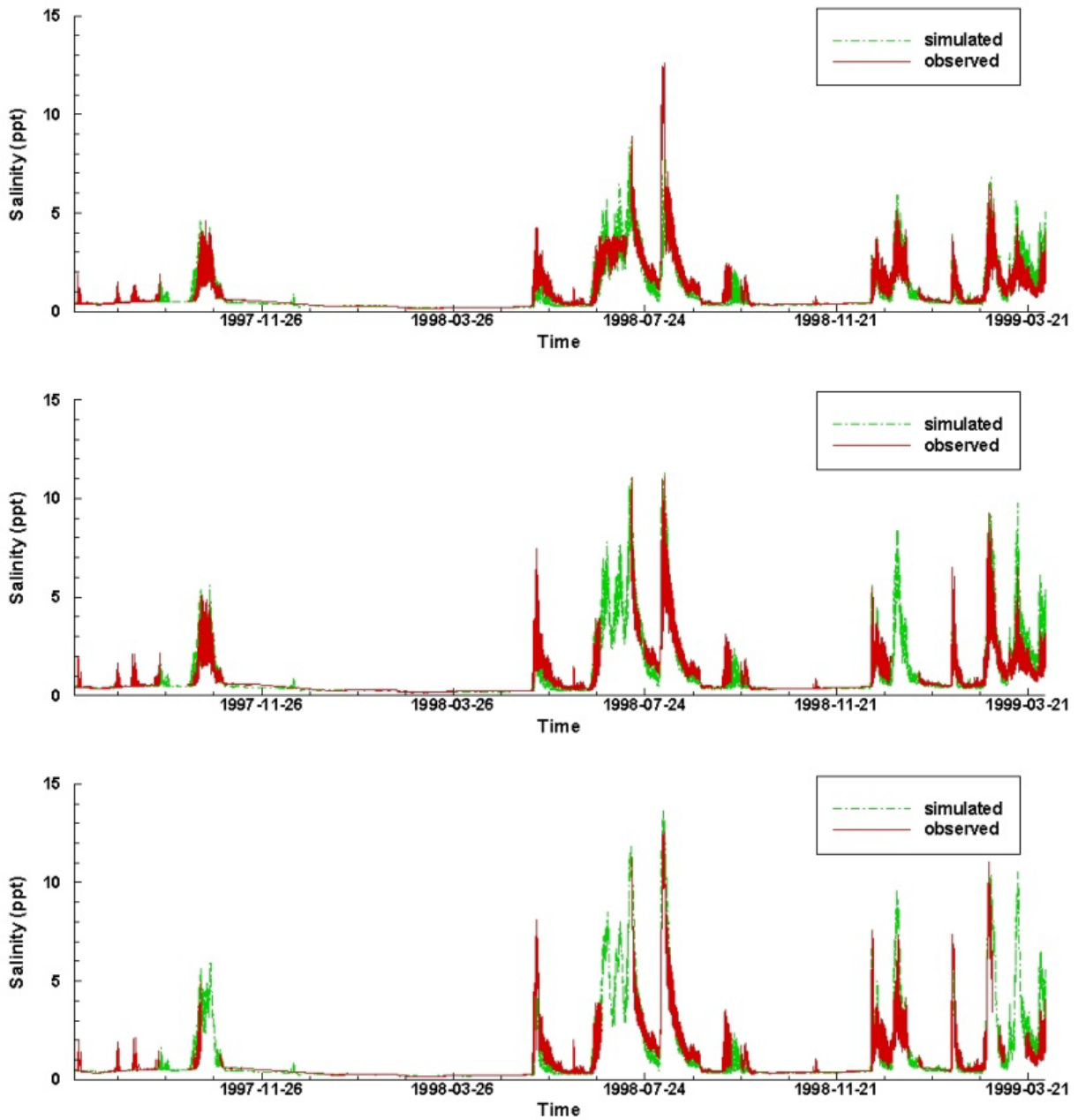


Figure 6–71. Salinity time series comparison at Buckman Bridge during the calibration period (top, middle, and bottom depths of observation).

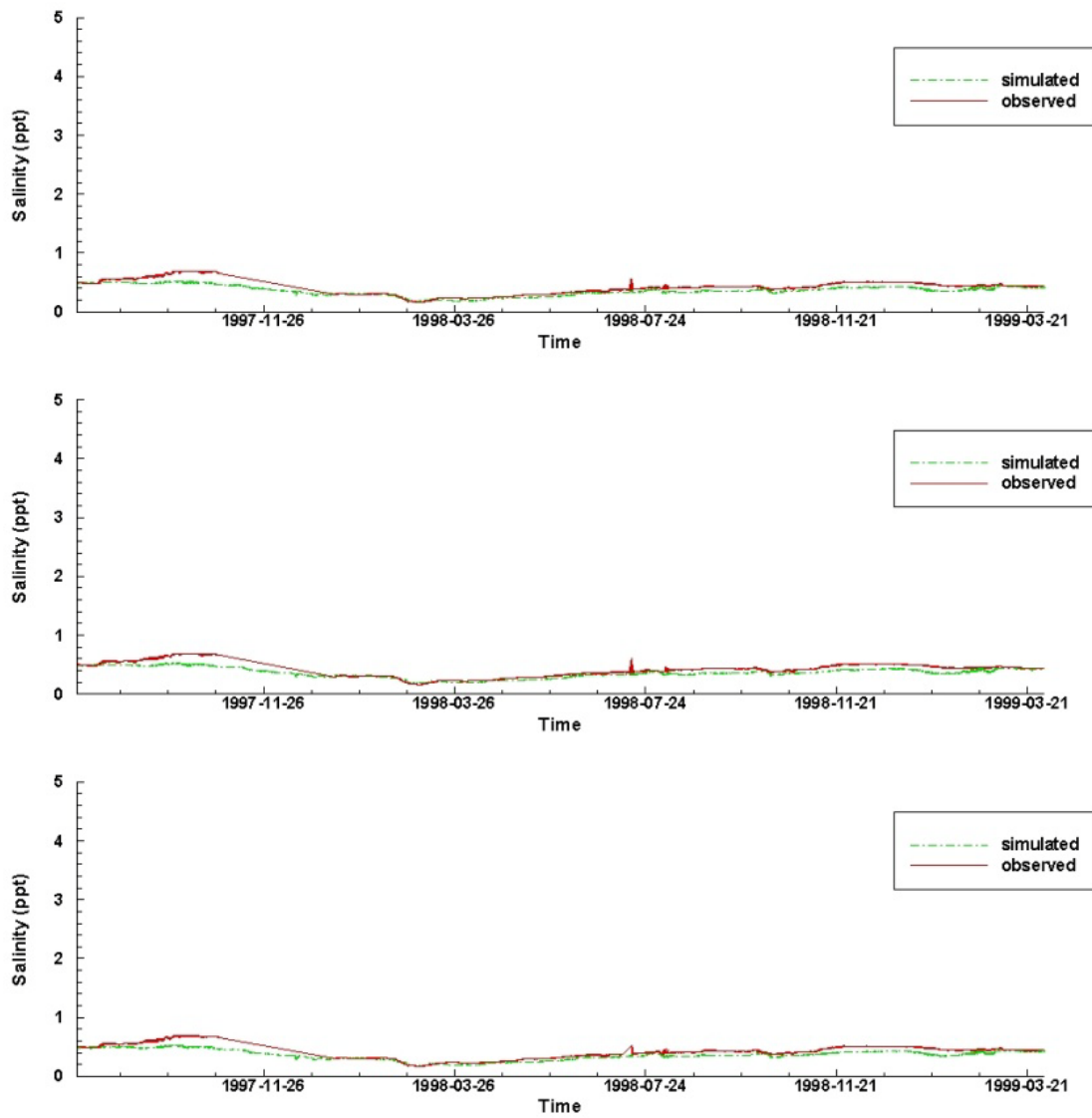


Figure 6–72. Salinity time series comparison at Shands Bridge during the calibration period (top, middle, and bottom depths of observation).

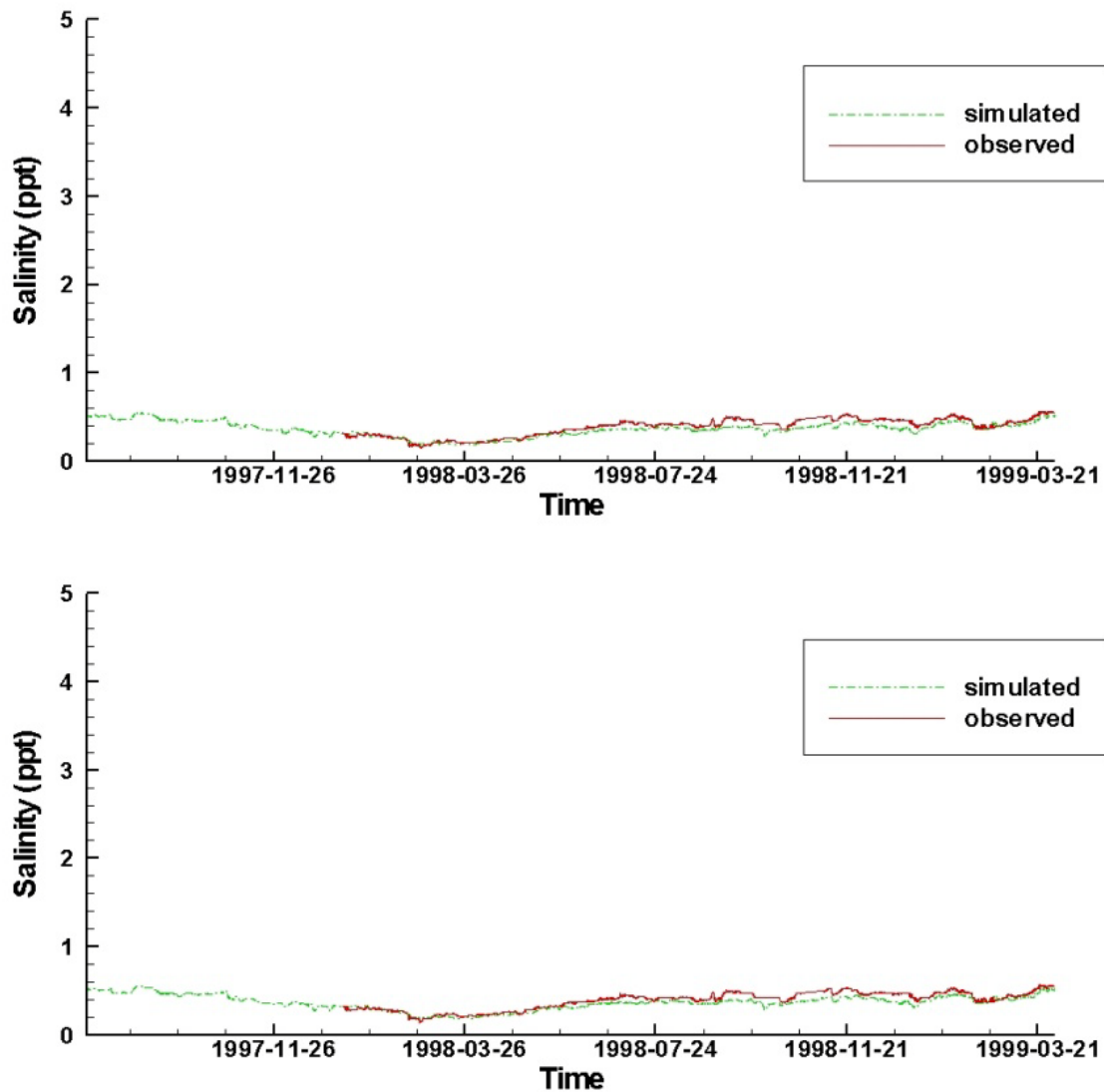


Figure 6-73. Salinity time series comparison at Dancy Point during the calibration period (top and bottom depths of observation).

6.7.2 FINAL CALIBRATION OF MIDDLE ST. JOHNS RIVER MODEL

Adjustment of Upstream Salinity Condition

After calibration of bottom roughness, the EFDC-MSJR hydrodynamic model underpredicted salinity during August to September 2001 (Figure 6-56) and salinity was shown to be largely insensitive to bottom roughness. We first assumed that the cause of this underprediction of salinity was the concurrent overprediction of discharge during this same period (see Figure 6-47), because overprediction of discharge would flush salt too quickly from the system. The model also underpredicted the peak in salinity during July 2001 (Figure 6-57) and this underprediction was thought to be caused by an underprediction of groundwater chloride flux upstream of Sanford. Both these hypotheses were incorrect, the first because during high discharge the upstream salinity boundary condition dominates the downstream response of

salinity, and the second because no reasonable diffuse groundwater discharge could explain the rapid rise of salinity in July for the given river discharge. The cause of the underprediction of salinity is instead largely attributable to the uncertainty of the salinity entering Lake Harney at the upstream model boundary.

The original upstream salinity boundary condition for discharge entering Lake Harney was developed from a salinity–discharge relationship. A new boundary condition, developed from observed data, was compared with the original boundary condition. The model run using the new boundary condition with the Low Roughness model is called the SR46H Observed Scenario.

Each salinity boundary condition requires an estimate of daily salinity at the SR 46 at Lake Harney boundary. The salinity boundary condition for the Low Roughness model differs from the SR46H Observed Scenario because it was developed from an empirical model of salinity as a function of discharge at this location. The new salinity boundary condition used linearly interpolated observations. This new salinity boundary condition based on salinity observations is also a model and subject to uncertainty, because the true daily variability between monthly observations is not known and is unlikely to exactly follow a linear path. Before the model testing (described below), we did not know which of these two models of daily salinity would be the most robust.

The SR46H Observed Scenario was run for the calibration period and the results for simulated salinity are compared with simulated salinity for the Low Roughness model and observed salinity at SR 46 at Lake Harney (Figure 6–74), station OW-SJR-1 (Figure 6–75), Sanford (Figure 6–76), and DeLand (Figure 6–77).

At SR 46 at Lake Harney, the SR46H Observed Scenario matches observed salinity exactly because salinity at this location is specified as the upstream model boundary condition. Again, the daily variability of salinity between salinity observations (green squares) is not known and cannot a priori be assumed to follow the linear paths of the SR46H Observed Scenario.

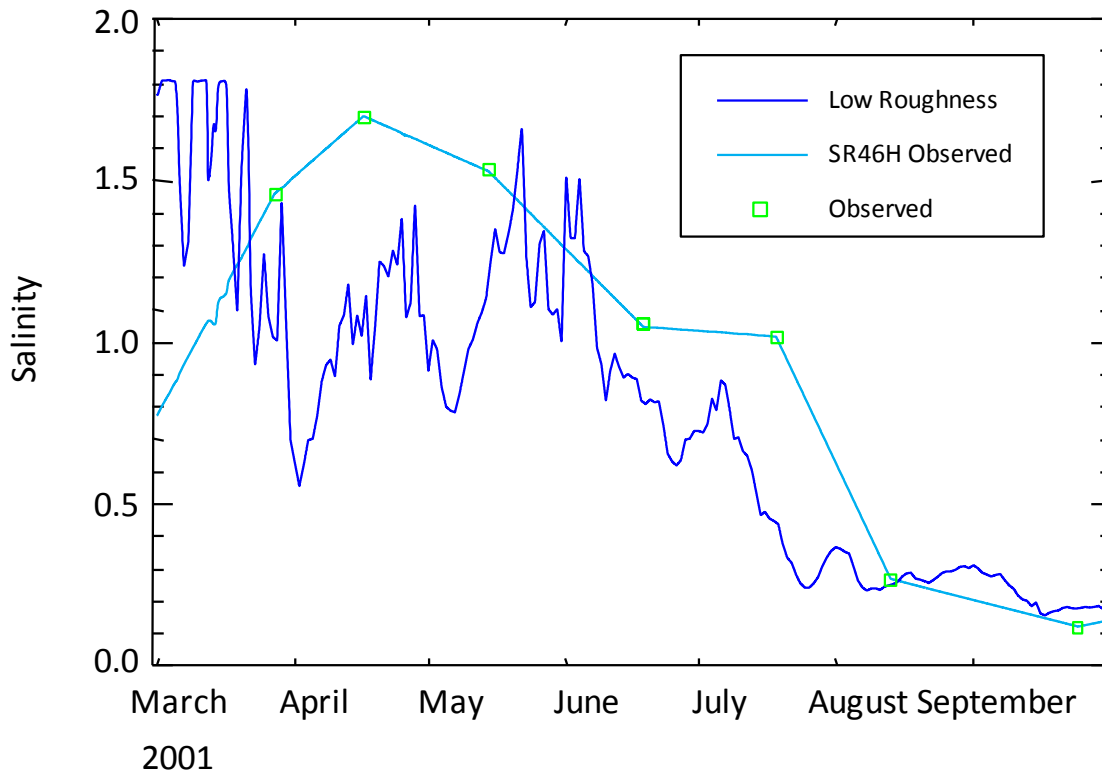


Figure 6–74. Simulated versus observed daily salinity above Lake Harney (SR 46 AT Lake Harney) over the calibration period. Simulated salinity compares the Low Roughness model and SR46H Observed Scenario.

At station OW-SJR-1, the Low Roughness model underestimates salinity during the dry period of May to June by nearly 0.5, but the SR46H Observed Scenario captures the rise in salinity during this period. This plot demonstrates the importance of the upstream salinity boundary at this location even under low flow conditions. Both models, however, now exhibit similar daily variability of salinity.

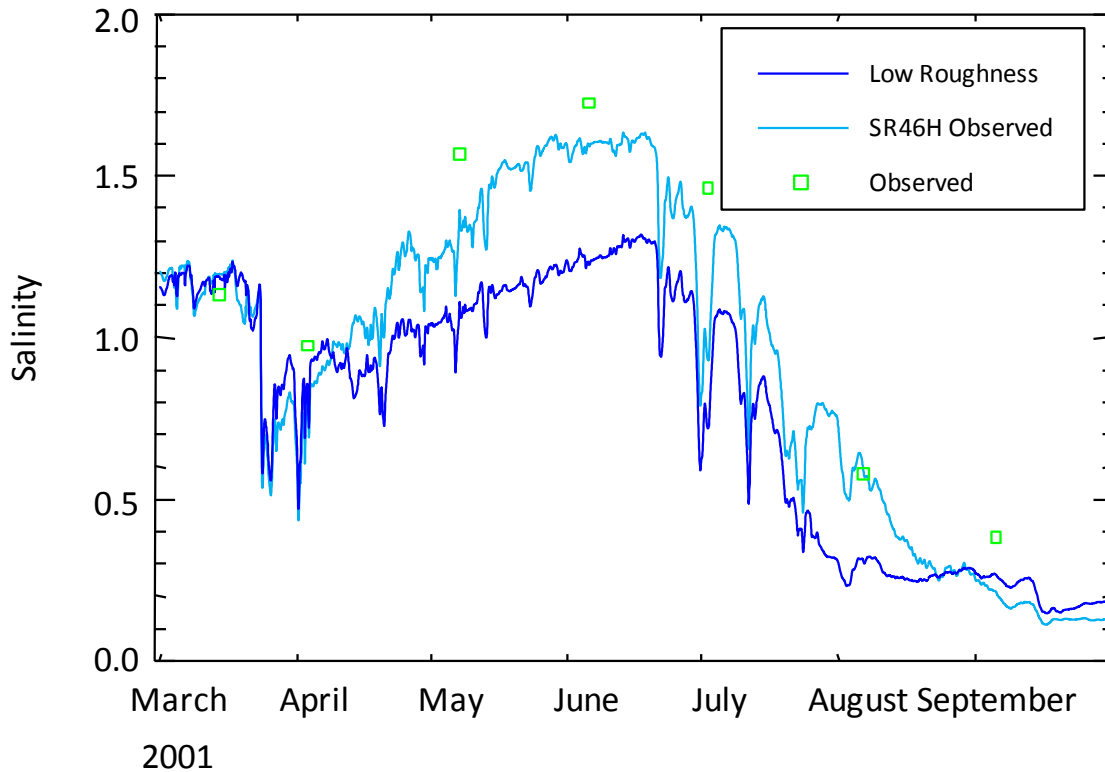


Figure 6–75. Simulated versus observed daily salinity upstream of Lake Monroe (station OW-SJR-1) over the calibration period. Simulated salinity compares the Low Roughness model and SR46H Observed Scenario.

At Sanford, the SR46H Observed Scenario overpredicts salinity in June, but the peak salinity of July is captured and the drop of salinity through August and September is greatly improved over the Low Roughness model.

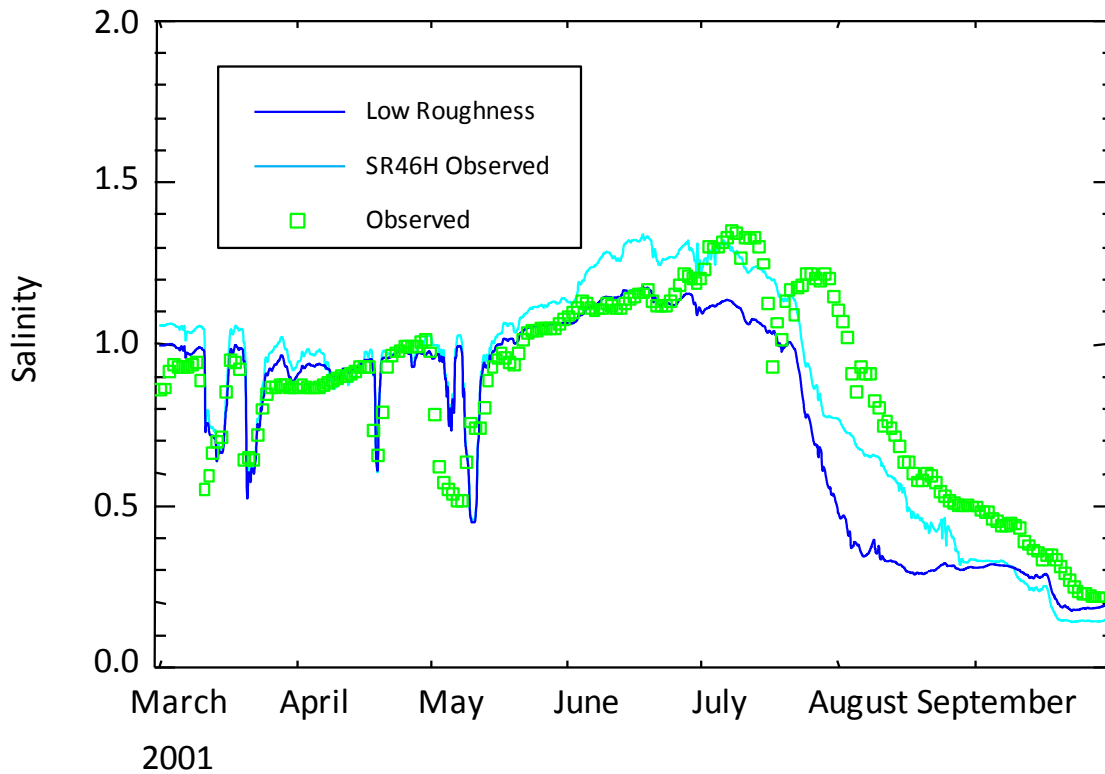


Figure 6–76. Simulated versus observed daily salinity at Sanford (US 17) over the calibration period. Simulated salinity compares the Low Roughness model and SR46H Observed Scenario.

At DeLand, both models produced similar and good matches with observed salinity from March through July, but the SR46H Observed Scenario again captures the drop of salinity through August and September much better than the Low Roughness model.

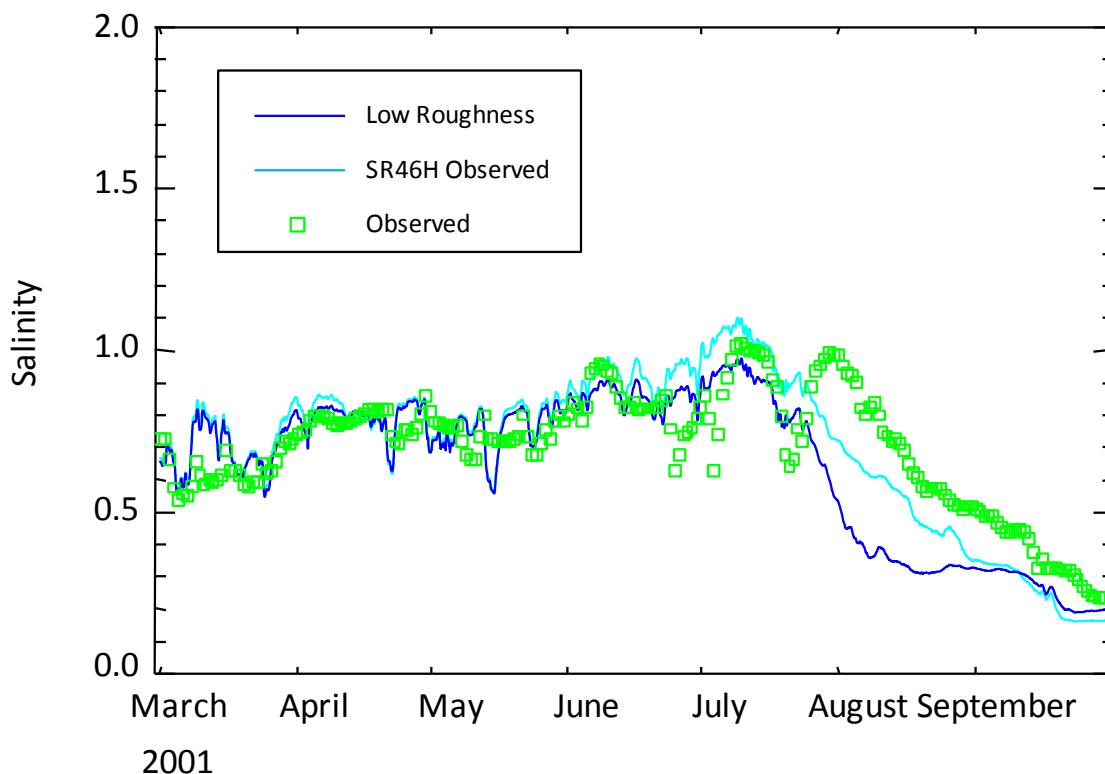


Figure 6–77. Simulated versus observed daily salinity at DeLand (SR 44) over the calibration period. Simulated salinity compares the Low Roughness model and SR46H Observed Scenario.

Comparative statistics between observed and simulated salinity show that the SR46H Observed Scenario is superior to the Low Roughness model at the SR 44, U.S.17, and OW-SJR-1 (Table 6–22). For the Low Roughness model, the Nash–Sutcliffe statistic was unsatisfactory at all stations, but for the SR46H Observed Scenario this statistic improves to satisfactory at SR 44 (DeLand), good at U.S.17 (Sanford), and very good at SJR-OW-1.

The use of observed salinity proved superior to a salinity–discharge relationship for modeling the upstream salinity boundary at SR 46 at Lake Harney. The SR46H Observed Scenario becomes the final calibration of the middle St. Johns River. Hereafter the EFDC model using observed salinity for the upstream boundary is again called simply the EFDC-MSJR hydrodynamic model.

Table 6–22. Statistical comparison of simulated and observed daily salinity for the Low Roughness model and SR46H Observed Scenario at three locations.

	SR 44		US 17		OW-SJR-1	
	Low Roughness Model	SR46H Observed Scenario	Low Roughness Model	SR46H Observed Scenario	Low Roughness Model	SR46H Observed Scenario
<i>NRECS</i>	214		214		7	
r^2	0.551	0.740	0.651	0.801	0.714	0.856
<i>m</i>	0.956	1.140	0.922	1.081	0.670	0.865
<i>NS</i>	0.163	0.522	0.461	0.703	0.285	0.751
<i>AVAE</i>	0.115	0.103	0.143	0.125	0.321	0.176
<i>AVRE (%)</i>	17.7	16.5	19.6	18.0	28.9	17.7
<i>RMSE</i>	0.164	0.123	0.214	0.159	0.396	0.234

NRECS = Number of paired values of simulated and observed salinity

r^2 = Coefficient of determination

m = Slope of linear regression line

NS = Nash–Sutcliffe statistic

RMSE = Root–mean–square error

AVRE = Average relative error (%)

AVAE = Average absolute error

Cumulative Density Function for Observed and Simulated Salinity

St. Johns River Main Stem

As an additional check on the salinity calibration of the EFDC-MSJR hydrodynamic model, cumulative density functions (CDFs) for observed and simulated salinity are presented below. The alteration of the upstream salinity boundary condition described in the previous section does not affect the simulation of water level and discharge, so that comparative statistics for water level (see Table 6–10) and discharge (see Table 6–11) are unchanged.

CDFs for salinity at U.S.17 (Sanford) and SR 44 (DeLand) (Figure 6–78) exhibit a mismatch between simulated and observed values for low salinities. Below the 25th percentile, simulated salinity is about 0.1 lower than observed. The model does correctly predict that salinity differences between these two stations collapse to 0 below this percentile. Similarly, the model correctly predicts the abrupt shift to a salinity gradient between the two stations of about 0.2 to 0.3 above the 25th percentile.

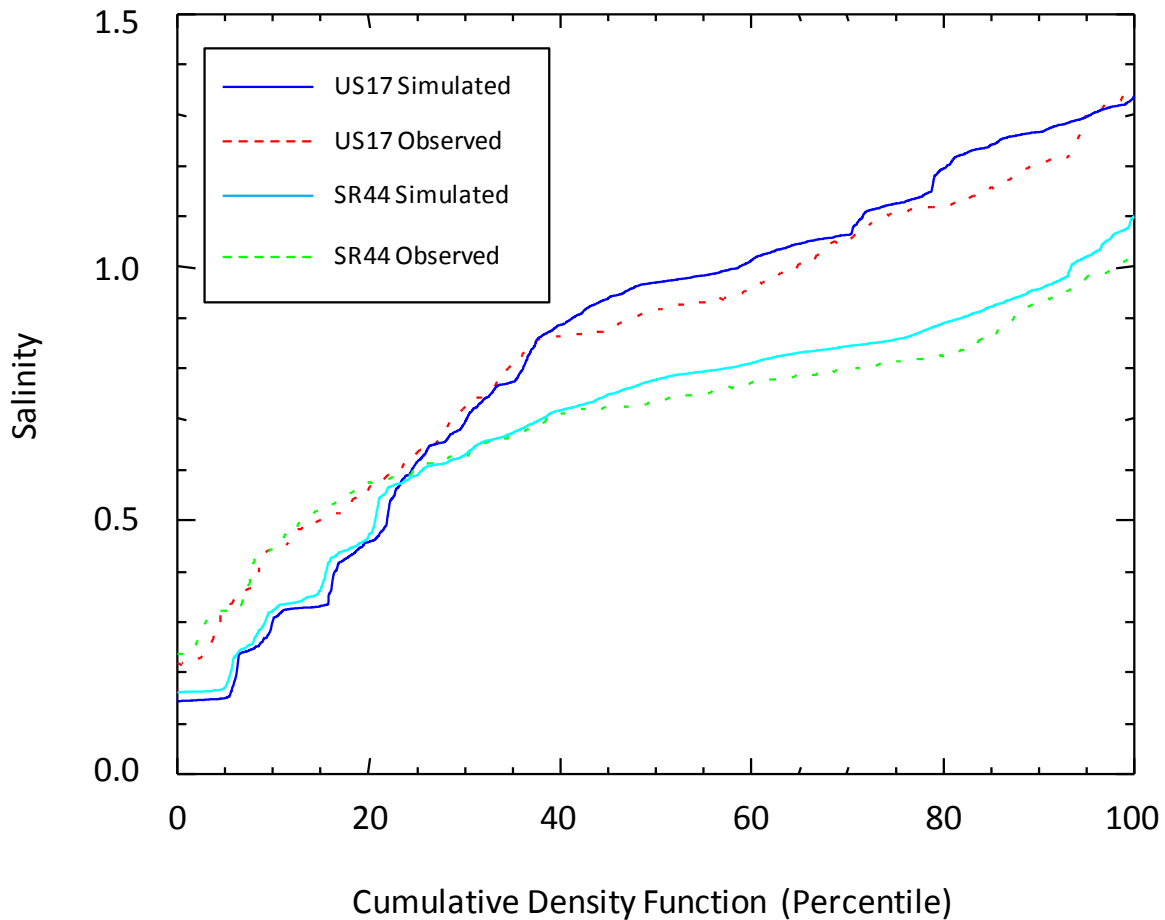


Figure 6–78. Cumulative density function comparing observed and simulated salinity at U.S.17 and DeLand for the calibration period, March to September 2001 using the EFDC-MSJR hydrodynamic model.

Lake Jesup and Lake Woodruff

The EFDC-MSJR hydrodynamic model correctly predicts the small, but persistent salinity gradient of about 0.2 to 0.3 across Lake Jesup (Figure 6–79). OW-2 is near the outlet of Lake Jesup and OW-6 is at the west end of the lake, opposite the mouth. This salinity gradient is caused in part by mixing of higher salinity river water through the lake outlet, and the correct simulation of this salinity gradient is evidence that the model correctly simulates circulation and mixing between the river and lake, at least at time scales relevant to maintenance of lake-scale salinity levels.

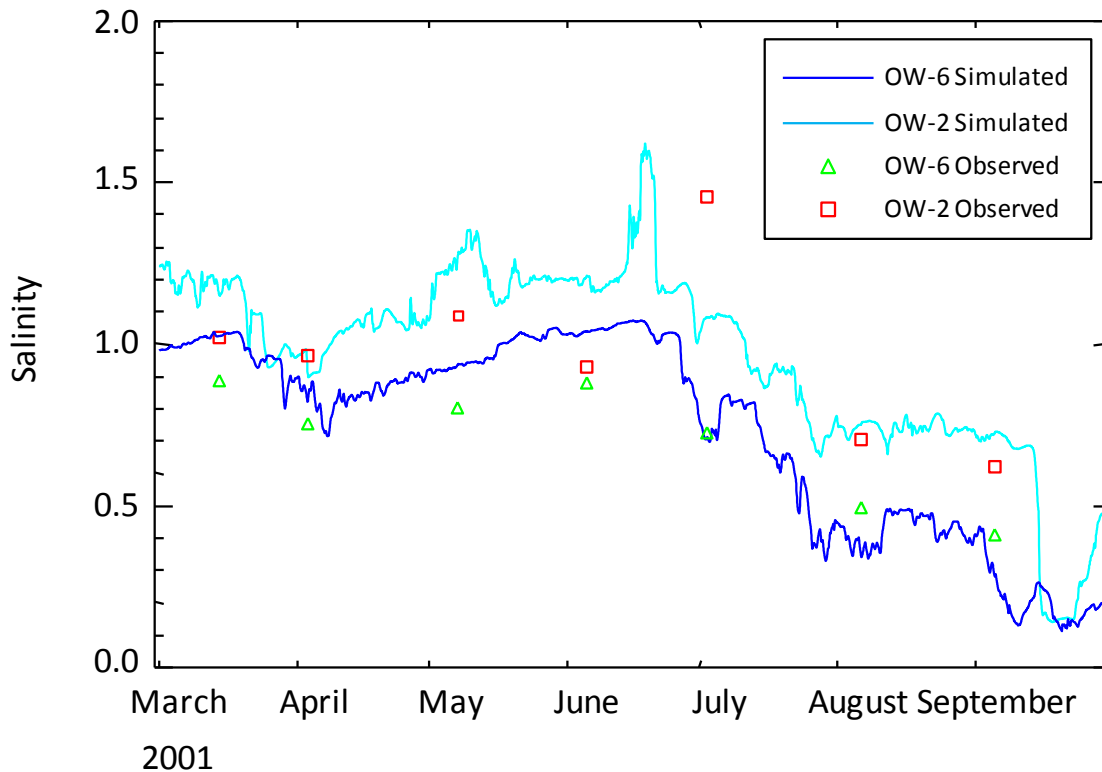


Figure 6–79. Simulated versus observed daily salinity near the outlet of Lake Jesup (station OW-2) and in the west end of the lake (station OW-6) over the calibration period using the EFDC-MSJR hydrodynamic model.

In Lake Woodruff, simulated salinity matches observed salinity nearly identically during the dry period of March to June (Figure 6–80). The observed salinity remained high, however, during the wet period of August and September, while simulated salinity declines similarly to the St. Johns River main stem near DeLand. The mismatch of salinity in Lake Woodruff during the wet period could indicate that the proportion of river discharge entering Lake Woodruff is overpredicted and flushing is too rapid. This question will be addressed again during model confirmation (see Section 7).

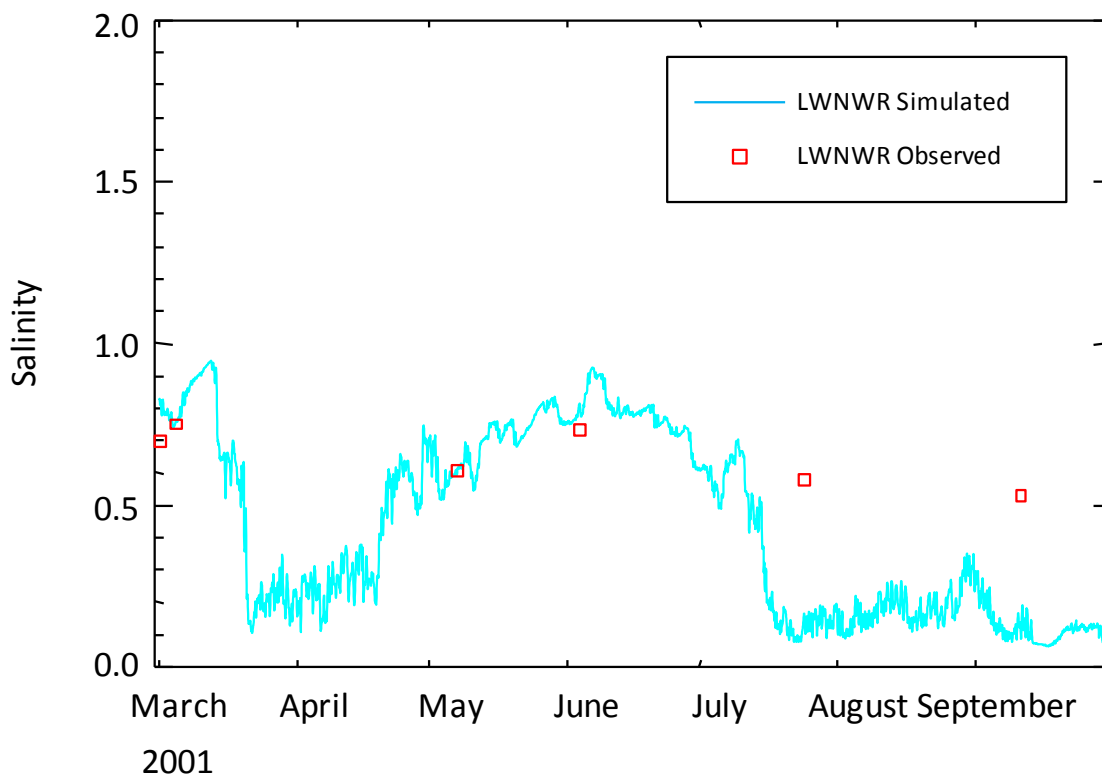


Figure 6-80. Simulated versus observed daily salinity in Lake Woodruff (station LWNWR) over the calibration period using the EFDC-MSJR hydrodynamic model.

6.8 SUMMARY

The EFDC-LSJR hydrodynamic model is calibrated by adjustment of bottom roughness to match observed tidal harmonics. Over most of the area, simulated M_2 amplitudes are within 10% of observed amplitudes and simulated and observed phases are generally within 5° . Not surprisingly, simulated hourly water level is highly correlated with observed values ($r^2 = 0.91$ to 0.97) because the variability of hourly water level is dominated by tidal motions in the lower St. Johns River. Simulated and observed hourly discharges are also highly correlated for the EFDC-LSJR hydrodynamic model for the same reason.

Daily averaged discharge in the lower St. Johns River exhibits both seasonal-scale patterns that result from hydrologic variability and synoptic scale patterns that result from low frequency ocean water level. Simulated and observed daily discharges are highly correlated ($r^2 = 0.81$ to 0.90) indicating that the model correctly captures water level variability caused by these important dynamic effects.

Importantly, the EFDC-LSJR hydrodynamic model captures the timing and intensity of intrusions of seawater. At Buckman Bridge, the *AVRE* between observed and simulated salinity is 23-33%. The percent errors are high, but *AVAE* for salinity is only 0.25-0.43.

The EFDC-LSJR hydrodynamic model is shown to be a good predictor of water level and discharge at tidal, daily, and seasonal time scales. The model also is a good predictor of salinity

and, in particular, is able to predict both the magnitude and duration of upstream intrusions of seawater into the broad, shallow portions of the normally freshwater tidal river.

The EFDC-MSJR hydrodynamic model was primarily calibrated by adjustment of bottom roughness to match observed surface slope–discharge relationships in several river segments. The good match of the model to surface slope–discharge relationships is reflected in the high correlation of simulated and observed daily water level ($r^2 = 0.974$ to 0.996) and very good Nash–Sutcliffe statistics (0.958 to 0.994).

Observed and simulated daily discharge compare well for middle St. Johns River mainstem locations. r^2 values are 0.73 to 0.96 and Nash–Sutcliffe statistics are very good (0.855 to 0.981). Simulation of daily discharge through the outlet to Lake Jesup is not as good, however. The daily discharge here is likely caused by the interactions of wind, remotely forced ocean setup, St. Johns River mainstem discharge, and local tributary discharge into the lake. Simulated and observed daily discharge has an r^2 of 0.433 and the Nash–Sutcliffe statistics are unsatisfactory (0.293). During certain periods simulated and observed hourly discharge match almost perfectly at this location, but at other times the comparisons are extremely poor. We suggest that the observed data are at times inconsistent with any reasonable volume budget of the lake.

Simulated and observed daily salinity match well for EFDC-MSJR hydrodynamic model with an $r^2 = 0.86$ to 0.90 and satisfactory to good Nash–Sutcliffe statistics (0.52 to 0.70). *RMS* errors are 0.12 to 0.16 .

Both the EFDC-LSJR and EFDC-MSJR hydrodynamic models are successfully calibrated to observed water level, discharge, velocity, and salinity. Both calibrated models use similar grid resolution and have similar ranges of bottom roughness. Model calibration shows that the models respond realistically to a wide variation of discharge conditions indicating that the models correctly simulate the hydrodynamic response of the river system to changes in river discharge over the calibration periods. Model confirmation is next shown to establish the robustness of each model for conditions different than the calibration periods.

7 MODEL CONFIRMATION

7.1 INTRODUCTION

Model confirmation uses the complete 10-yr model simulation period of 1996 to 2005. The confirmation period contains more extreme events than found in the calibration periods. In the middle St. Johns River, the confirmation period contains more extreme low flow events with durations less than about 30 days and more extreme high flow events with durations greater than 10 days. For the lower St. Johns River, the confirmation period contains more extreme intrusions of seawater than found in the calibration period. Salinity at Shands Bridge, for example, was unaffected by marine salinity during the calibration period, but experienced a 1-day salinity event of 8.8 during the confirmation period. More extreme intrusions of seawater are also found for 7- and 30-day durations.

To follow the goals of comparing calibration and confirmation, the confirmation period should be separate of the calibration period. Here the confirmation period is run as a continuous 10-yr

simulation for a period that includes the calibration period. For both models, the calibration periods are much shorter than the confirmation period and should not greatly skew the comparison of results because the greater fraction of the confirmation period is statistically independent of the calibration period. In addition, the focus for comparison between calibration and confirmation is on (a) the more extreme events found in the confirmation period, and (b) observations at locations not used for model calibration that are available within the longer confirmation period. This focus for comparison, then, is not diminished by examination of the complete 10-yr confirmation period of 1996 to 2005.

The goal of model confirmation is to demonstrate that the model is a robust and reliable tool for predicting hydrodynamic variables over a wide range of conditions so that the model can be used for model forecast of altered future conditions. This goal is achieved by examination of a 10-yr record that contains both extreme dry and wet periods over a wide range of durations.

7.2 CONFIRMATION OF THE LOWER ST. JOHNS RIVER MODEL

7.2.1 HOURLY WATER LEVEL

Comparative statistics for paired values of observed and simulated hourly water level over the confirmation period show the goodness-of-fit between simulated and observed total water level (Table 7-1). Correlation between paired values is high ($r^2 > 0.93$) at all stations. The squared correlation coefficients and *RMSE* statistics are nearly identical to the calibration statistics (Table 6-17).

Table 7-1. Comparative statistics for observed and simulated hourly water level during the confirmation period, 1996 to 2005.

Station	<i>NRECS</i>	r^2	<i>m</i>	<i>RMSE</i> (cm)
Bar Pilot Dock	87,649	0.98	0.96	7.8
Dames Point	43,327	0.96	0.98	8.5
Long Branch	47,433	0.97	0.99	6.0
Main Street Bridge	75,982	0.96	0.97	4.9
Buckman Bridge	79,640	0.96	1.00	4.1
Shands Bridge	76,745	0.95	1.00	4.2
Racy Point	34,580	0.94	0.96	5.1
Palatka	47,338	0.93	0.97	5.6
Buffalo Bluff	41,153	0.93	0.94	5.2
Welaka	79,609	0.95	0.95	4.7

NRECS = Number paired observed and simulated values

r^2 = Coefficient of determination

m = Slope of regression line

RMSE = Root-mean-square-error

Frequency distributions for both observed and simulated water level show that the model captured extreme water levels during the confirmation period (Table 7-2). Water level between the 10th and 90th percentile (80% of all values) provides a characteristic range of typical water level experienced at each station. Simulated results match low levels (10th percentile) within 2 cm and high levels (90th percentile) within 4 cm.

Table 7–2. Observed (Obs) and simulated (Sim) distribution of water level for all paired values during the confirmation period, 1996 to 2005. Water level in m NAVD88.

Station		Min	10 th Percentile	Median	90 th Percentile	Max
Bar Pilot Dock	Obs	-1.66	-0.85	-0.12	0.56	1.38
	Sim	-1.48	-0.83	-0.11	0.54	1.50
Dames Point	Obs	-1.19	-0.68	-0.10	0.43	1.14
	Sim	-1.11	-0.66	-0.11	0.44	1.34
Long Branch	Obs	-1.02	-0.50	-0.07	0.35	1.28
	Sim	-0.86	-0.49	-0.08	0.36	1.27
Main Street Bridge	Obs	-0.94	-0.43	-0.06	0.25	1.20
	Sim	-0.78	-0.42	-0.06	0.26	1.16
Buckman Bridge	Obs	-0.86	-0.27	-0.04	0.22	1.11
	Sim	-0.59	-0.28	-0.04	0.23	1.16
Shands Bridge	Obs	-0.58	-0.25	-0.03	0.24	1.01
	Sim	-0.52	-0.25	-0.03	0.24	1.07
Racy Point	Obs	-0.58	-0.26	-0.02	0.22	0.83
	Sim	-0.55	-0.28	-0.03	0.26	1.04
Palatka	Obs	-0.58	-0.29	-0.02	0.26	0.78
	Sim	-0.55	-0.30	-0.03	0.28	1.03
Buffalo Bluff	Obs	-0.51	-0.25	0.00	0.26	0.78
	Sim	-0.51	-0.26	-0.01	0.29	1.04
Welaka	Obs	-0.14	0.11	0.32	0.63	1.14
	Sim	-0.12	0.12	0.32	0.62	1.33

7.2.2 TIDAL DISCHARGE

The model matches tidal discharge well for all locations where ADCP discharges were measured over the confirmation period (Figure 7–1). Paired observed and simulated discharge for all times and locations of observed ADCP discharge (Table 3–10) are highly correlated ($r^2 = 0.97$).

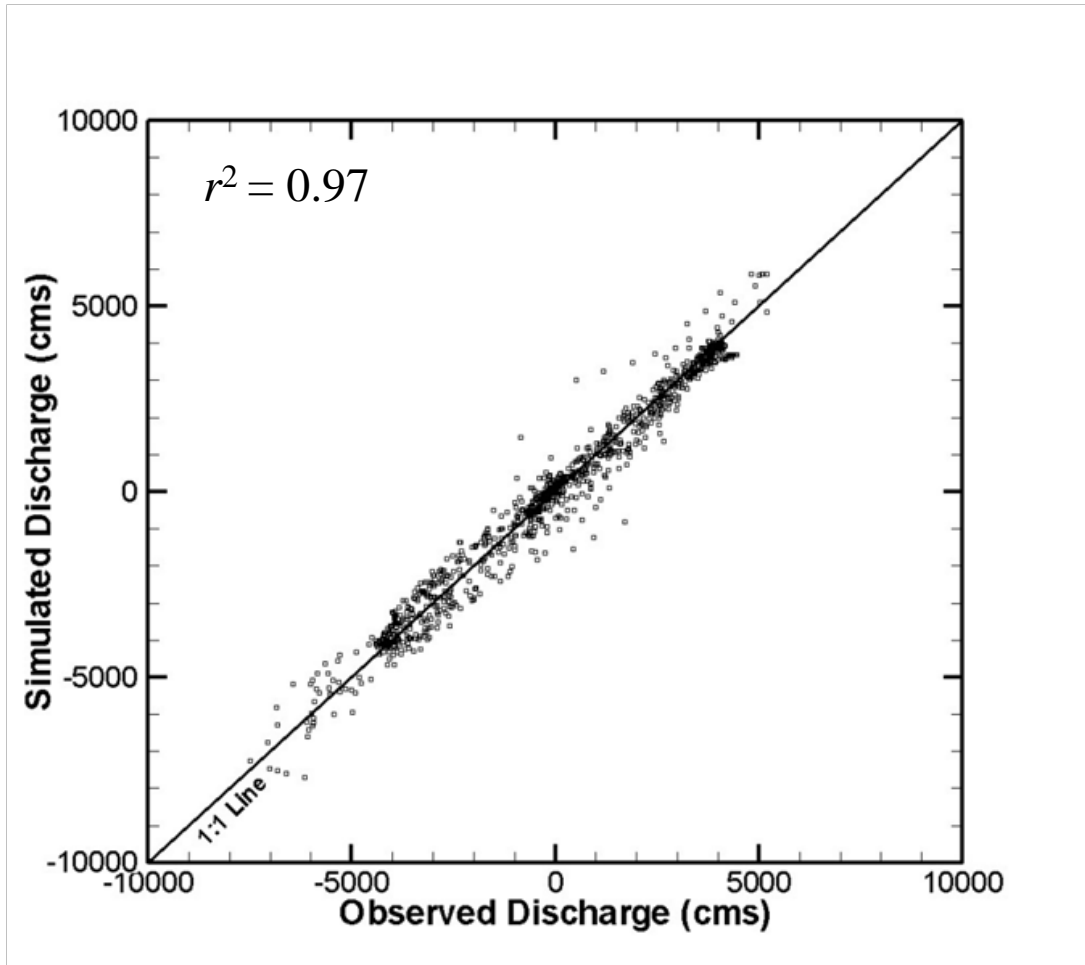


Figure 7-1. Point comparison of observed and simulated tidal discharge for all locations and times during the confirmation period, 1996 to 2005.

Tidal harmonic data for discharge over the confirmation period (Table 7-3) are essentially identical to the calibration period (Table 6-19).

Table 7-3. Comparison of observed (Obs) and simulated (Sim) tidal constituents for discharge at USGS continuous discharge stations during the confirmation period, 1996 to 2005. Tidal constituents are defined in Table 3-5.

Station		M ₂		N ₂		S ₂		O ₁		K ₁		M ₄	
		A	P	A	P	A	P	A	P	A	P	A	P
Main Street Bridge	Sim	4019	114	732	99	534	133	335	318	443	328	311	32
	Obs	4118	114	742	97	454	132	337	320	453	330	207	5
Buffalo Bluff	Sim	341	302	60	286	42	328	42	69	49	85	16	352
	Obs	273	287	48	270	32	321	30	61	37	76	15	350
Dunns Creek	Sim	83	273	14	256	10	298	7	57	9	73	15	328
	Obs	111	284	19	264	12	311	10	59	12	77	10	4

A = Amplitude in m³s⁻¹
P = Phase in degrees

Tidal Discharge near Mouth of Lake George

ADCP observations were made near the mouth of Lake George in 2002 for the specific goal of observing the relative portion of discharge on either side of Drayton Island (Figure 3-6). Because observed discharge at these locations was not available for the calibration period, these discharge measurements provide confirmation of the model's ability to simulate tidal discharge in areas not previously examined for the model calibration.

On 29 May 2002, simultaneous ADCP discharge measurements were made at Fruitland (Figure 7-2) and Georgetown (Figure 7-3). Discharge at Fruitland measures the total river discharge, while discharge at Georgetown measures the fraction of total river discharge through the eastern channel around Drayton Island. Discharge through the western channel around Drayton Island can then be estimated by difference.

Peak ebb and flood at Georgetown (Figure 7-3) are about half the magnitude of Fruitland (Figure 7-2) and the model correctly simulates this proportioning of discharge. The model also correctly captures the timing of the flood and ebb at Fruitland. Although the model slightly overestimates the peak flood discharge at Fruitland, it does correctly capture the stronger flood discharge as compared with ebb discharge that occurred on that day. At Georgetown, the model again matches the timing and strength of the observed tidal discharge.

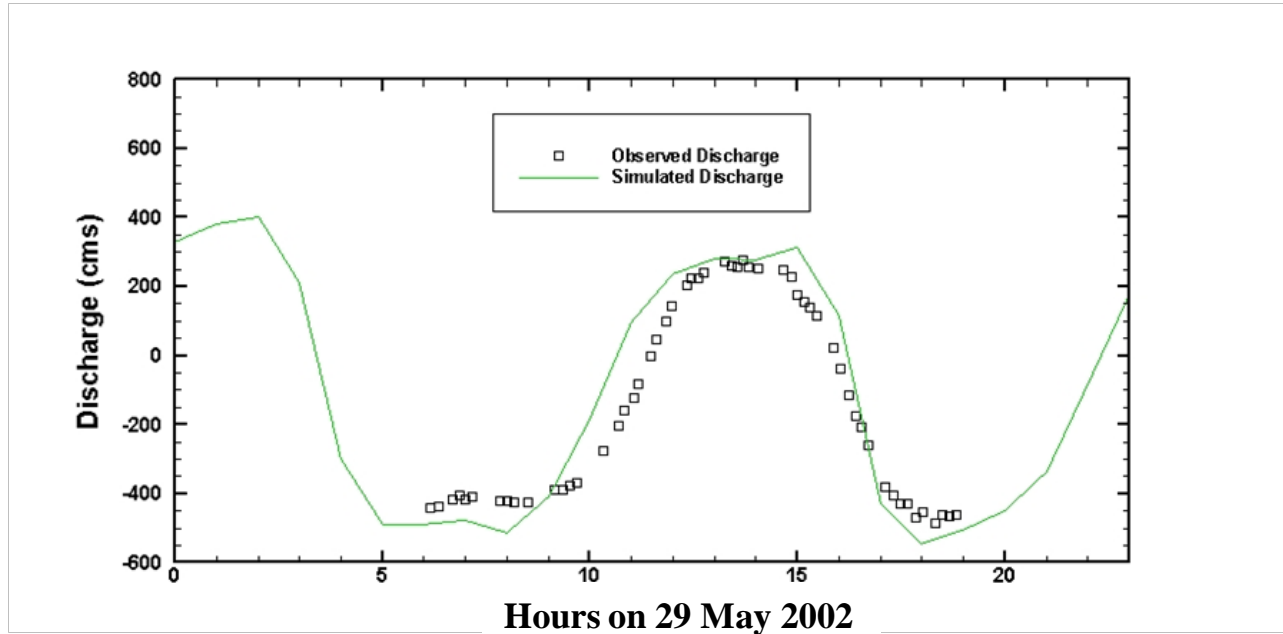


Figure 7-2. Comparison of observed and simulated tidal discharge at Fruitland on 29 May 2002.

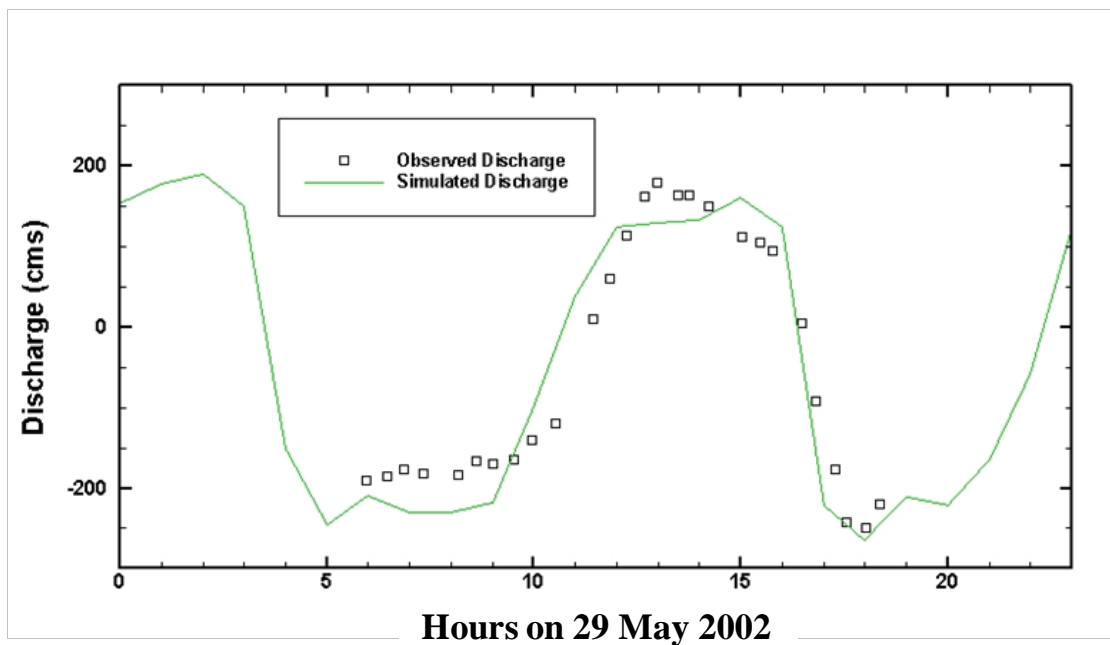


Figure 7-3. Comparison of observed and simulated tidal discharge at Georgetown on 29 May 2002.

Spatial Variability of Peak Tidal Discharge

The 10-yr confirmation period allows comparison of simulated tidal discharge with observed tidal discharge throughout the length of the lower St. Johns River. The ability of the model to capture the spatial variations of the strength of tidal discharge is illustrated by a comparison of

observed peak discharge at ebb tide with the distribution of simulated peak ebb discharge (Figure 7–4). Simulated peak ebb discharge by river kilometer was estimated from the daily maximum of tidal discharge over a 2-yr simulation period of 1996 and 1997, when the majority of ADCP measurements were made. The simulated time series of daily maximum discharge were sorted and ranked to determine the 90th, median, and 10th percentiles. The distribution of daily maximum discharge values defines the range of simulated peak ebb discharge throughout the lower St. Johns River and are plotted as solid lines in Figure 7–4. Maximum peak ebb discharge occurs at the mouth (as expected) but decreases near Marker 35 where the river channel bifurcates around Blount Island. Peak ebb discharge rises again upstream of Dames Point where the Blount Island Channel rejoins the St. Johns River main stem. Peak ebb discharge then decreases gradually to river km125 and then declines rapidly.

The comparison between simulated and observed peak ebb discharge shows that the model correctly simulates the spatial variability for peak ebb discharge described above.

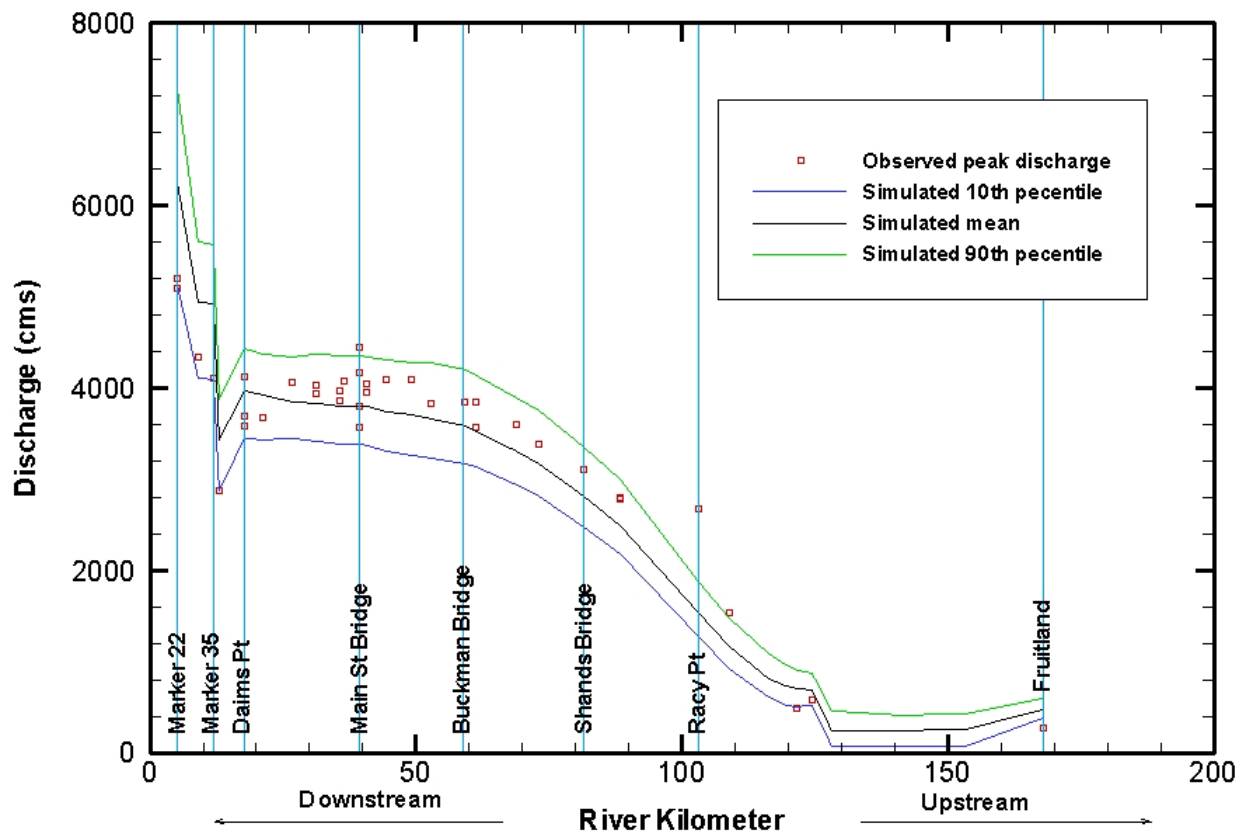


Figure 7–4. Simulated and observed peak ebb discharge by river kilometer over the confirmation period, 1996 to 2005.

Daily Discharge

Comparative statistics for observed and simulated daily averaged discharge are shown in Table 7–4 for each continuous discharge station. Comparative statistics for the confirmation period are nearly identical to statistics for the calibration period (Table 6–20).

Table 7-4. Comparison of observed and simulated daily discharge during the confirmation period, 1996 to 2005.

Station	<i>NRECS</i>	r^2	<i>m</i>	<i>b</i>	<i>AVAE</i>	<i>AVRE</i>	<i>RMSE</i>
Main Street Bridge	3161	0.90	0.80	21.2	100.5	26.7	141.5
Buffalo Bluff	3644	0.89	0.92	25.0	37.0	21.7	51.3
Dunns Creek	3575	0.80	0.65	5.6	14.5	44.6	20.0

NRECS = Number of paired values of simulated and observed salinity

r^2 = Coefficient of determination

m = Slope of linear regression line

b = Intercept of linear regression line

RMSE = Root-mean-square error ($\text{m}^3 \text{s}^{-1}$)

AVRE = Average relative error (%)

AVAE = Average absolute error ($\text{m}^3 \text{s}^{-1}$)

Plots of observed and simulated daily averaged discharge at the three sites are shown in Figure 7-5, Figure 7-6, and Figure 7-7. Each figure compares observed and simulated daily averaged discharge for both a dry year (2000) and a wet year (2005). The model correctly simulates both the seasonal and daily variability of discharge at each location, indicating the model captures discharge variability over a wide range of meteorological and hydrologic conditions.

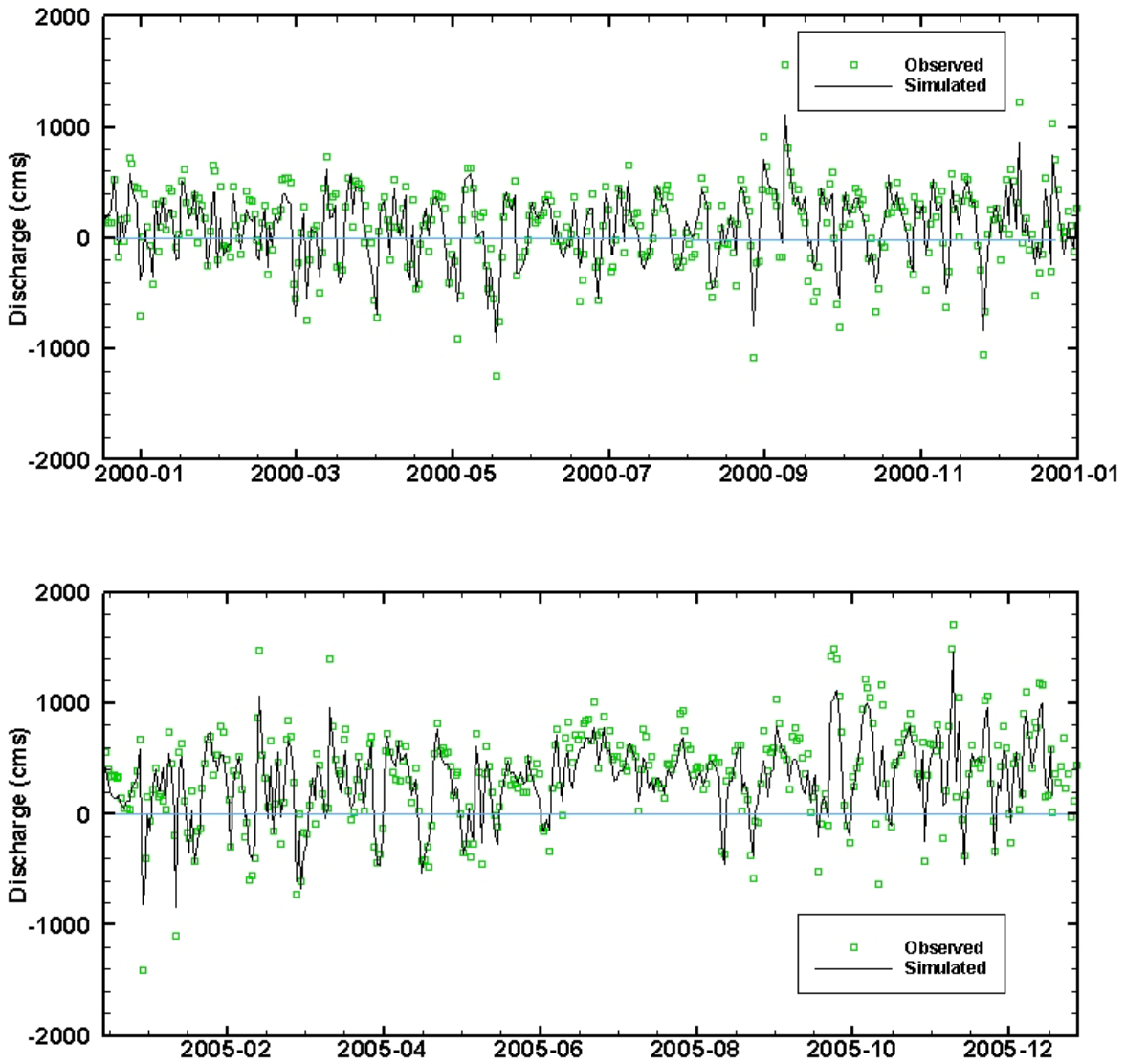


Figure 7-5. Simulated and observed daily averaged discharge at Main Street Bridge for a dry year (2000) and wet year (2005).

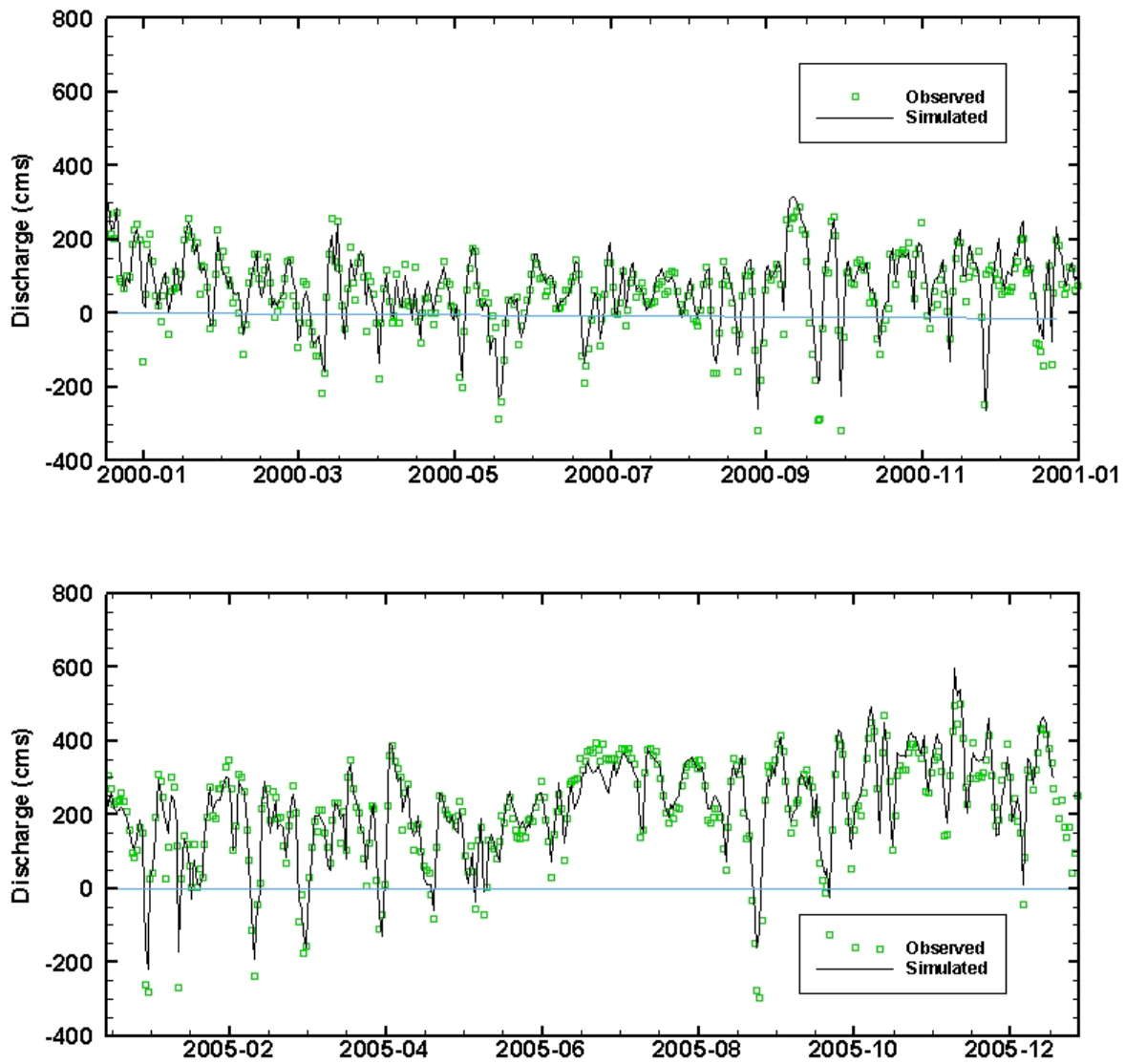


Figure 7–6. Simulated and observed daily averaged discharge at Buffalo Bluff for a dry year (2000) and wet year (2005).

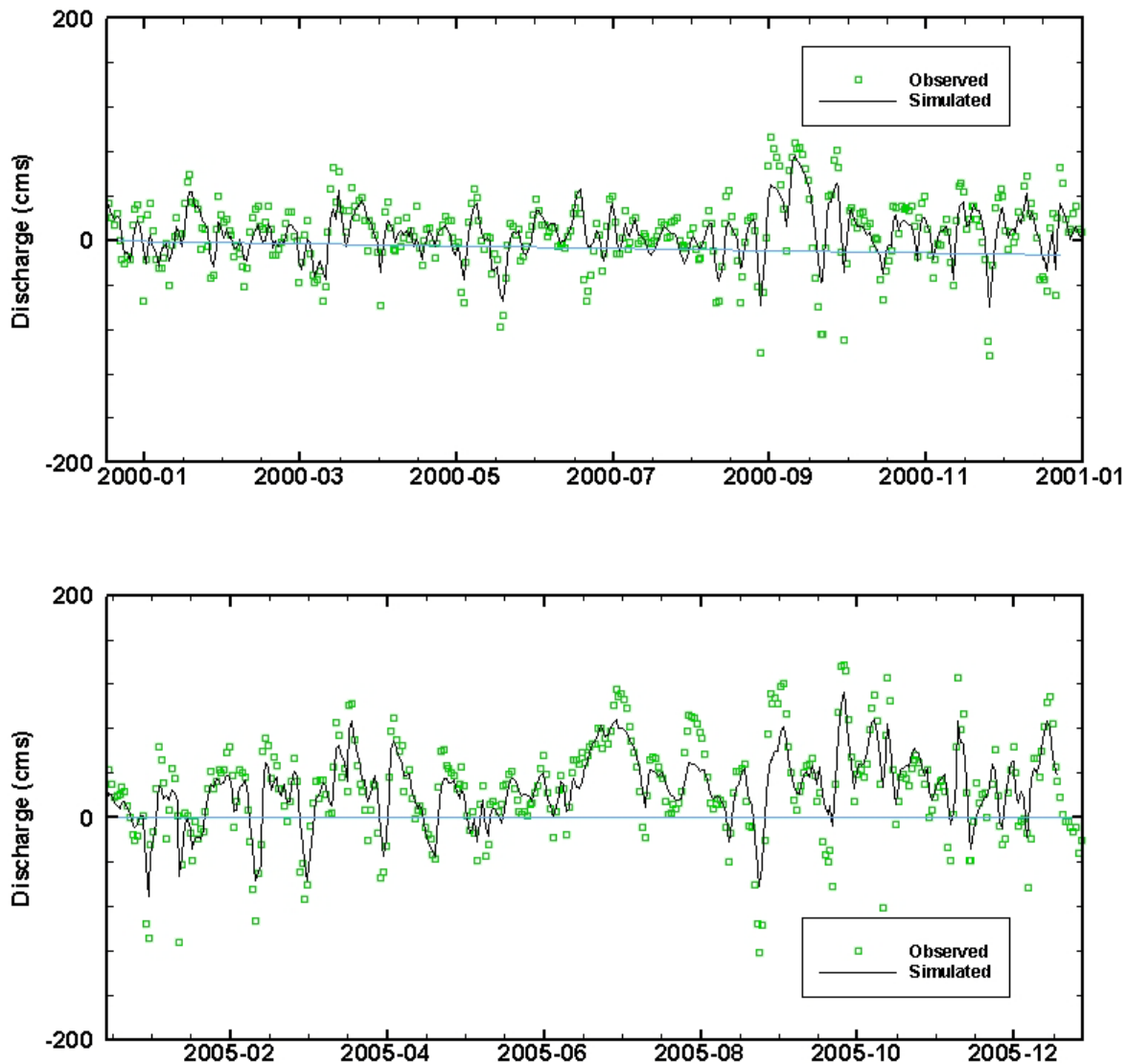


Figure 7-7. Simulated and observed daily averaged discharge at Dunns Creek for a dry year (2000) and wet year (2005).

7.2.3 SALINITY

Comparison with Synoptic Stations

Simulation over the model confirmation period (1996 to 2005) allows comparison of observed and simulated salinity at many more stations than were compared for model calibration (Table 7-5). Thirteen stations are used here for comparison of observed and simulated salinity over the confirmation period throughout the lower St. Johns River including Lake George (station LAG) and Crescent Lake (station GF33). These 13 stations are part of a synoptic water quality network, called the WQMN (Water Quality Monitoring Network), maintained by SJRWMD with monthly salinity observations.

Correlation between observed and simulated salinity are high at all stations, with r^2 ranging from 0.83 to 0.94. (For these stations, simulated vertically averaged salinity is compared to observed salinity regardless of measured depth.) The slopes and intercepts of the regression lines indicate no systematic bias in the model.

Table 7–5. Comparison of Observed and Simulated Salinity at Water Quality Monitoring Network (WQMN) Stations, 1996 to 2005.

Station	NRECS	r^2	m	b	AVAE	AVRE	RMSE
JAXSJR17	188	0.92	1.01	0.41	1.74	14.0	2.48
JAXSJR40	154	0.92	1.06	-0.28	0.83	20.6	1.44
MP72	128	0.94	1.05	0.03	0.33	20.7	0.69
DTL	255	0.93	0.85	0.06	0.40	19.6	0.72
SJRHBP	173	0.93	0.95	-0.08	0.28	21.6	0.56
SJSR16	122	0.91	0.88	0.00	0.11	16.9	0.30
SJWSIL	94	0.83	0.67	0.11	0.07	13.9	0.17
SRP	123	0.84	0.86	0.03	0.05	10.7	0.06
SJM37	107	0.86	0.87	0.03	0.04	8.9	0.05
FP42	71	0.88	0.85	0.04	0.04	9.4	0.05
BB22	137	0.84	0.90	0.02	0.04	9.8	0.05
GF33	67	0.89	0.86	0.06	0.04	15.2	0.05
LAG	58	0.91	0.91	0.03	0.04	8.0	0.05

NRECS = Number of paired values of simulated and observed salinity

r^2 = Coefficient of determination

m = Slope of linear regression line

b = Intercept of linear regression line

RMSE = Root-mean-square error

AVRE = Average relative error (%)

AVAE = Average absolute error

Observed and simulated salinity at WQMN station JAXSJR40 are compared in Figure 7–8 for the confirmation period. This station is located in the farthest downstream reach of the broad, shallow extent of the St. Johns River and is considered a mesohaline river segment. Simulated salinity is highly variable, ranging from near 0 to over 25. Salinity during the confirmation period is considerably higher than for the calibration period. Persistent high salinity occurred during the latter half of 1999 through 2002. Simulated salinity closely matches the higher salinity observed during this period. Simulated salinity matches the seasonal variability of observed

salinity closely throughout the confirmation period showing that the model is a good predictor of salinity at this location.

Simulated salinity at station JAXSJR40 is characterized by sharp, rapid spikes of salinity. These spikes are not as apparent for the observed data because of the monthly interval of the observations. Because the characteristic periods of salinity spikes (intrusions) are over several days, the monthly observations are aliased. During the first 6 months of 2001, for example, observed salinity at WQMN station JAXSJR40 remained below 10, while simulated salinity rose above 15 several times. The model and observed values compare well for this period, however. That is, the model predicts salinity below 10 for the dates and times of observation. This result indicates that the model provides better information than the observed data regarding maximum salinity and duration of salinity over this period.

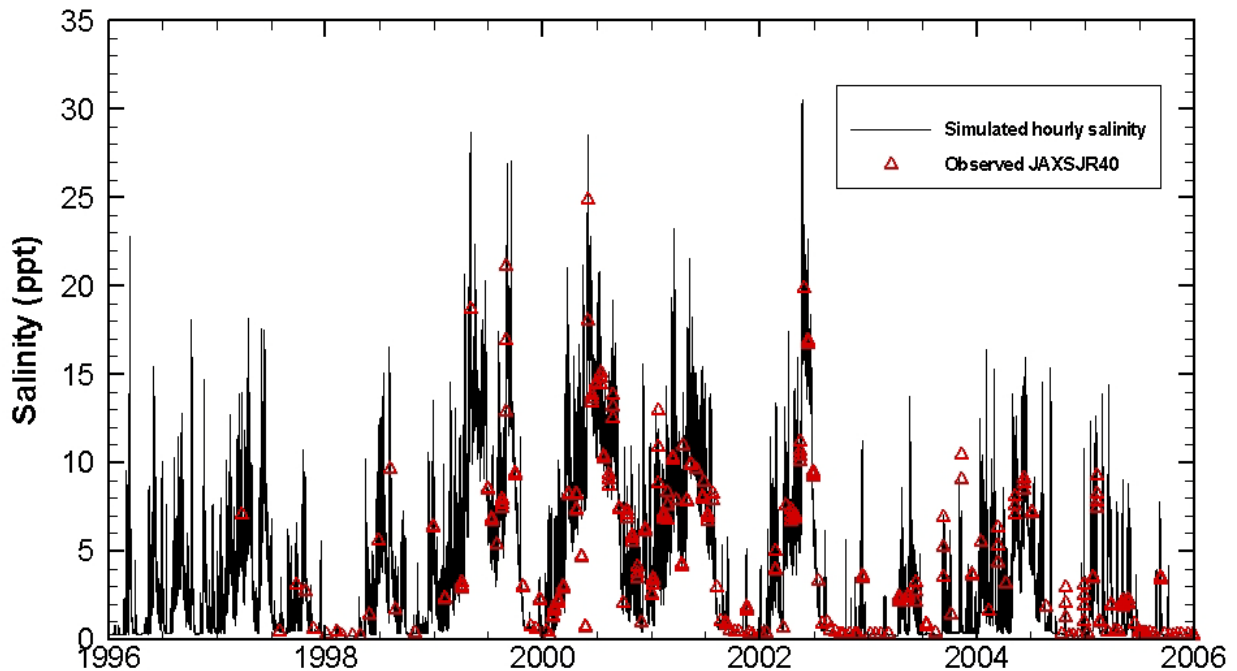


Figure 7–8. Simulated and observed salinity at station JAXSJR40 (Christopher Point), 1996 to 2005

Intrusion of Seawater

This study is particularly concerned with the intrusion of seawater into normally oligohaline and fresh river segments because of possible detriment to submersed aquatic vegetation. Marine salinity did not reach Shands Bridge during the calibration period, but reached this location several times during the confirmation period (Figure 7–9). The simulated salinity matches the intensity, timing, and duration of these upstream intrusions of seawater. These intrusions of seawater were, in part, a result of decreased river discharge during a drought period. The skill demonstrated by the model in predicting these intrusions of seawater shows that the model is also capable of predicting increased intrusion of seawater for discharge reductions caused by water withdrawals.

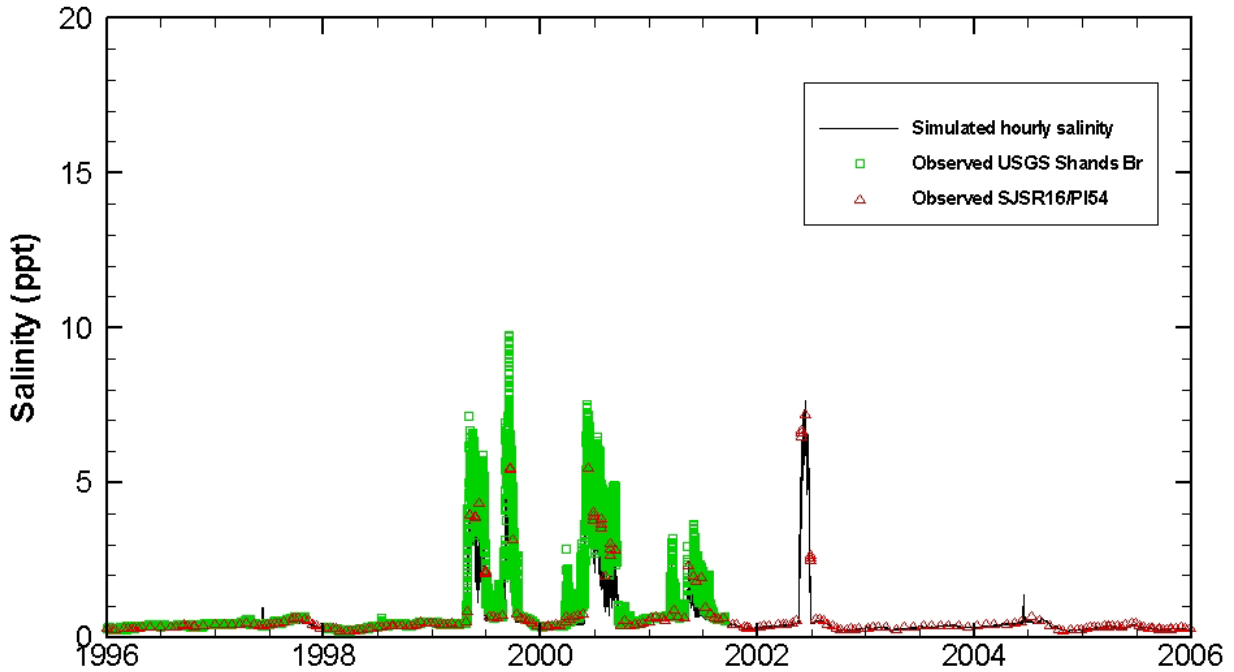


Figure 7–9. Simulated and observed salinity at Shands Bridge during the confirmation period, 1996 to 2005.

Hourly Salinity

Comparative statistics for paired simulated and observed hourly salinity at the USGS continuous salinity stations are shown in Table 7–6. Comparative statistics are nearly identical to the calibration period (Table 6–21).

Table 7–6. Comparison of observed and simulated hourly salinity at USGS continuous salinity stations during the confirmation period, 1996 to 2005.

Station	<i>NRECS</i>	r^2	<i>m</i>	<i>b</i>	<i>AVAE</i>	<i>AVRE</i>	<i>RMSE</i>
Dames Point Top	58325	0.84	0.93	0.23	2.36	11.1	3.09
Dames Point Middle	39870	0.82	0.87	4.21	2.33	10.0	3.04
Dames Point Bottom	54278	0.77	0.95	2.76	2.78	11.9	3.57
Acosta Top	56151	0.94	0.94	-0.16	1.21	16.8	1.73
Acosta Middle	59648	0.93	0.99	0.00	1.19	16.3	1.68
Acosta Bottom	59628	0.93	1.01	0.07	1.27	17.1	1.80
Buckman Top	55565	0.94	0.95	-0.13	0.51	18.2	0.85
Buckman Middle	52820	0.94	1.05	-0.15	0.61	20.6	1.03
Buckman Bottom	50796	0.92	1.03	-0.10	0.78	21.8	1.35
Shands Top	44065	0.91	0.65	0.08	0.24	27.0	0.53
Shands Middle	43256	0.90	0.68	0.06	0.24	26.7	0.54
Shands Bottom	39144	0.88	0.69	0.05	0.26	27.3	0.58
Dancy Point Top	58095	0.91	0.86	0.02	0.05	11.5	0.06
Dancy Point Bottom	57462	0.91	0.85	0.02	0.05	11.3	0.06

NRECS = Number of paired values of simulated and observed salinity
 r^2 = Coefficient of determination
m = Slope of linear regression line
b = Intercept of linear regression line
RMSE = Root-mean-square error
AVRE = Average relative error (%)
AVAE = Average absolute error

Longitudinal Variation of Salinity

The confirmation period allows for comparison of longitudinal variation of salinity between observed and simulated salinity. The longitudinal variation of salinity is characterized by the distribution of salinity during the confirmation period along the river main stem (Figure 7–10). The solid lines in the figure show the distribution of simulated salinity by river kilometer. The upper (green), middle (dark blue), and lower (red) lines represent the 90th percentile, median, and 10th percentile levels of the simulated salinity distributions. The vertical three point plots (cyan) show the distribution of observed salinity at selected WQMN and USGS stations. The vertical scale is logarithmic so that the range of low salinity values in the upper reaches of the river can be seen.

Salinity within the lower 20 km of the river generally ranges from 15 to 35. The river reach between 20 and 80 km (roughly Jacksonville upstream to Shands Bridge) is an area of both wide salinity fluctuation and declining peak salinity values. Upstream of Shands Bridge (SR 16) the river is considered fresh, although salinity still varies between 0.2 to 0.8 because of high chloride groundwater sources entering from Lake George and the middle St. Johns River. The model simulates the longitudinal variation of salinity throughout the river, showing that the calibrated model captures the dynamics of upstream transport of salinity in the lower portions of the river and the mixing and transport processes that redistribute salinity within the river.

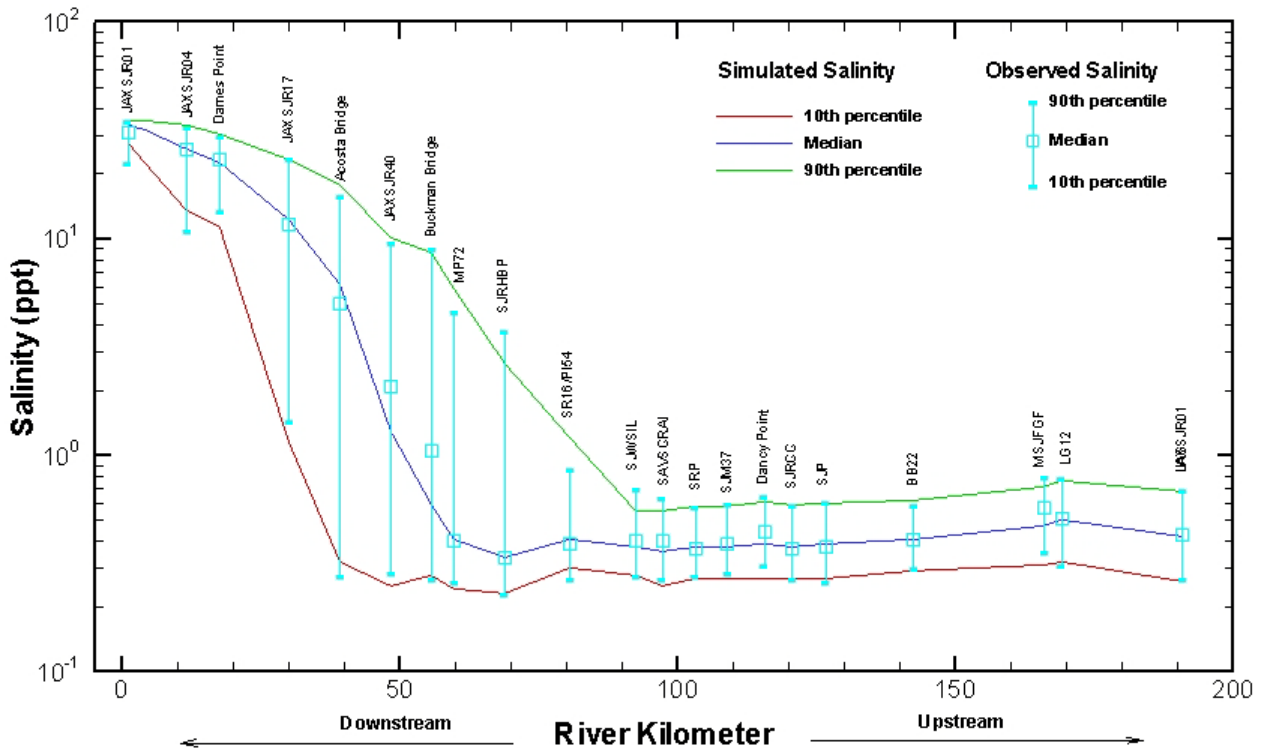


Figure 7–10. Longitudinal variation of salinity for observed and simulated salinity distributions in the lower St. Johns River during the confirmation period, 1996 to 2005.

Figure 7–11 compares the longitudinal variation of simulated and observed daily salinity range throughout the lower St. Johns River. Daily salinity range is defined as the difference between the highest and lowest salinity over a day. The distributions of observed daily salinity range are shown only for the five continuous USGS gauges where hourly salinity are available and daily range can be calculated.

Daily salinity range is greatest within the narrow navigational channel between Bar Pilot Dock and Acosta Bridge. The distribution of daily salinity range at Dames Point (5 to 15) is quite high given a median salinity of about 25. Daily salinity range declines gradually between Acosta and Buckman Bridge and then more rapidly between Buckman and Shands Bridge, where daily salinity range > 1 occurs only during relatively infrequent periods of intrusion of seawater. In the freshwater segment of the river, upstream of Shands Bridge, daily salinity range reduces to less than 0.1. Simulated daily salinity range compares closely with observed daily salinity range,

showing that the model is capable of predicting salinity dynamics in the river at hourly (tidal) time scales.

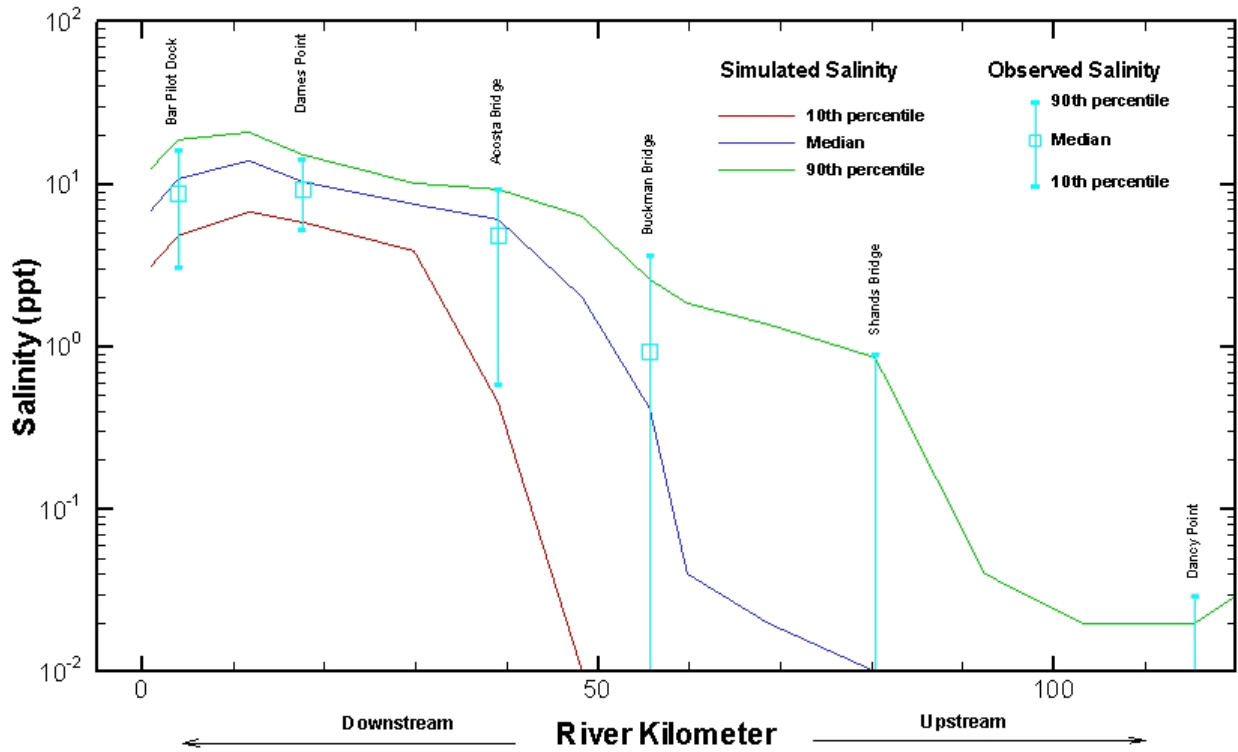


Figure 7–11. Longitudinal variation of daily salinity range for observed and simulated distributions of daily salinity range in the lower St. Johns River during the confirmation period, 1996 to 2005.

7.3 CONFIRMATION OF THE MIDDLE ST. JOHNS RIVER MODEL

7.3.1 DAILY WATER LEVEL

Comparative statistics for simulated and observed daily water level during the confirmation period are shown in Table 7–7 at five stations. Observations at four stations spanned the entire confirmation period, but observations at Oviedo are limited to the last 5.5 years of the confirmation period. Oviedo was not active during the model calibration period. Comparative statistics for the confirmation period are nearly identical to the calibration period (Table 6–10).

Table 7–7. Statistical comparison of simulated and observed daily water level during model confirmation period, 1996 to 2005.

Station	<i>NRECS</i>	r^2	<i>m</i>	<i>NS</i>	<i>AVAE</i>	<i>AVRE</i>	<i>RMSE</i>
DeLand	3572	0.984	0.973	0.984	0.028	15.9	0.040
Sanford	3653	0.968	1.050	0.961	0.058	19.1	0.092
Lake Jesup outlet	3415	0.974	0.958	0.974	0.059	19.6	0.081
Oviedo	1875	0.966	1.047	0.960	0.071	18.9	0.109
Lake Harney	3607	0.968	1.072	0.956	0.097	17.7	0.158

NRECS = Number of paired values of simulated and observed salinity

r^2 = Coefficient of determination

m = Slope of linear regression line

NS = Nash–Sutcliffe statistic

RMSE = Root-mean-square error

AVRE = Average relative error (%)

AVAE = Average absolute error

A comparison of observed and simulated time series of daily water level at DeLand show nearly perfect agreement over the entire confirmation period (Figure 7–12). The confirmation period contains periods of both lower and higher daily water levels than the calibration period (March to September 2001) and the model simulates these more extreme conditions well. Similarly good agreement between simulated and observed daily water levels are seen for Sanford (Figure 7–13) and the outlet of Lake Jesup (Figure 7–14).

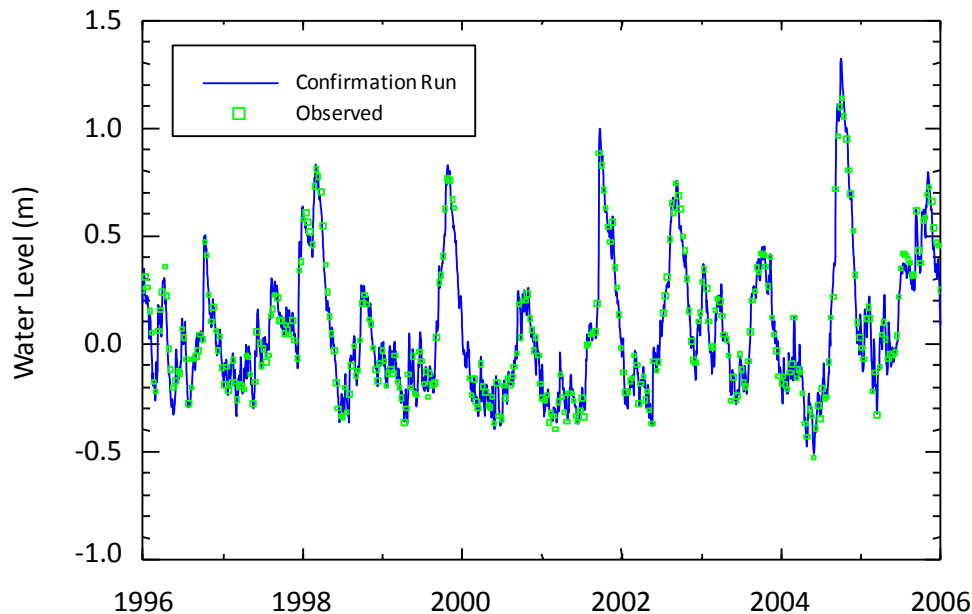


Figure 7–12. Simulated versus observed daily water level at DeLand (SR 44) over the model confirmation period, 1996 to 2005.

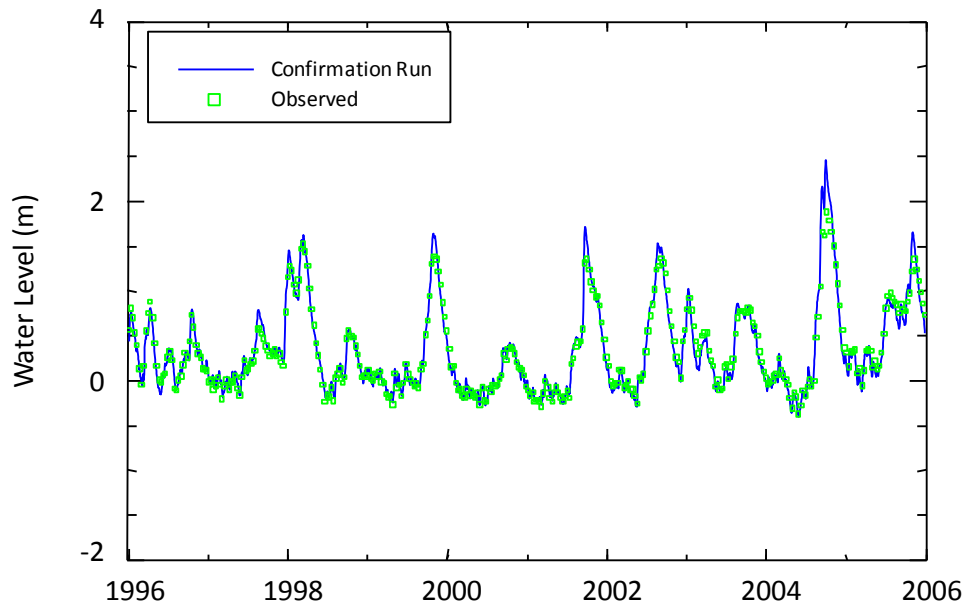


Figure 7–13. Simulated versus observed daily water level at Sanford (US 17) during the model confirmation period, 1996 to 2005.

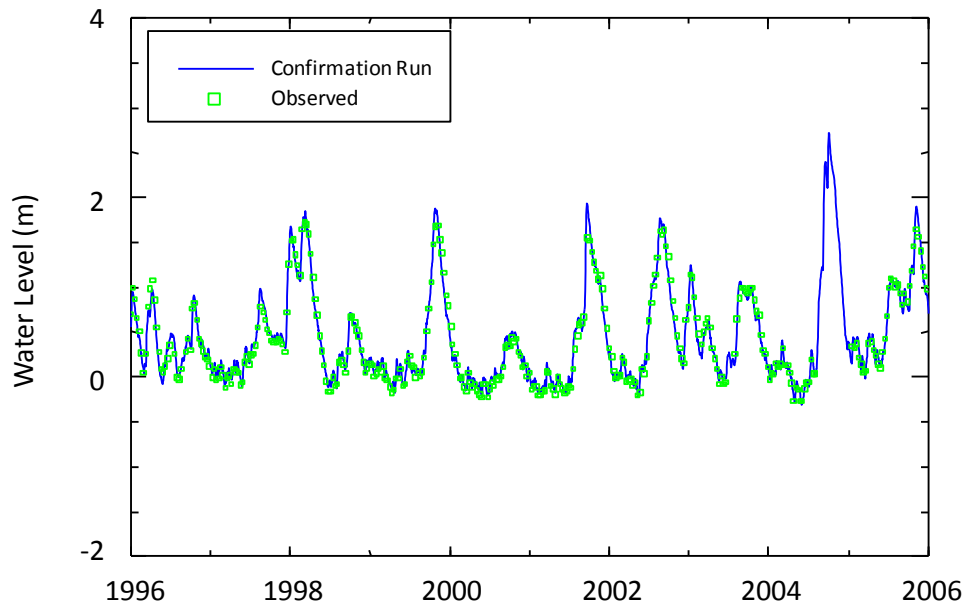


Figure 7–14. Simulated versus observed daily water level at Lake Jesup outlet (SR 46 at Lake Jesup) during the model confirmation period, 1996 to 2005.

Figure 7–15 and Figure 7–16 show that water levels in Lake Harney are overpredicted when observed water levels exceed about 2 m NAVD88. The overprediction of extreme high water levels is likely because the model does not contain adjacent floodplain storage, that is, the

EFDC-MSJR hydrodynamic model has no implementation of flooding and drying of adjacent wetlands by the river.

The overprediction by the model of high water levels in Lake Harney is not considered a detriment to the WSIS study because (a) high water level events of this magnitude are infrequent, and (b) the overprediction also leads to an overprediction of the change in water level caused by a water withdrawal which is a conservative assumption for assessing the effects of water withdrawals.

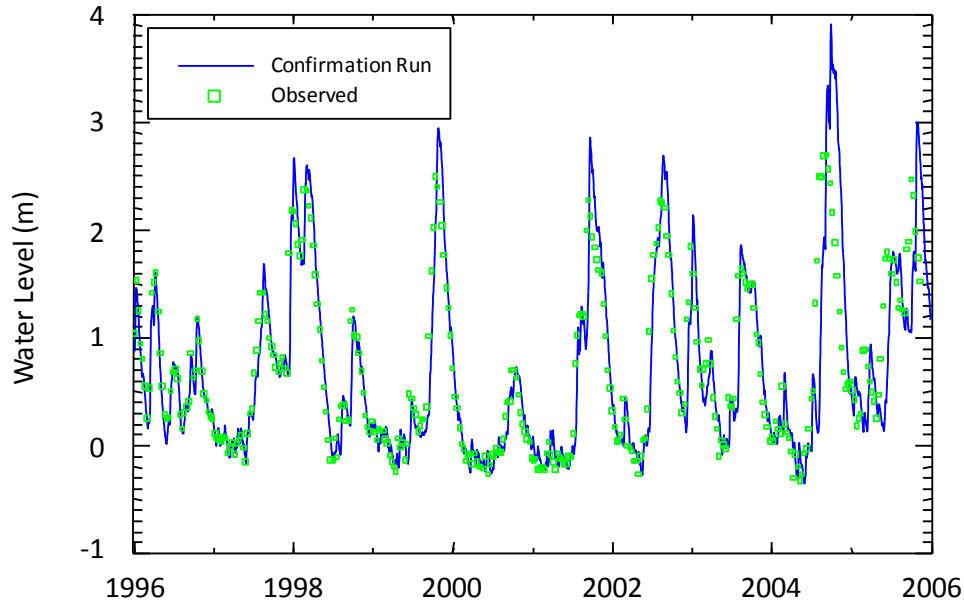


Figure 7–15. Simulated versus observed daily water level above Lake Harney (SR 46 at Lake Harney) during the model confirmation period, 1996 to 2005.

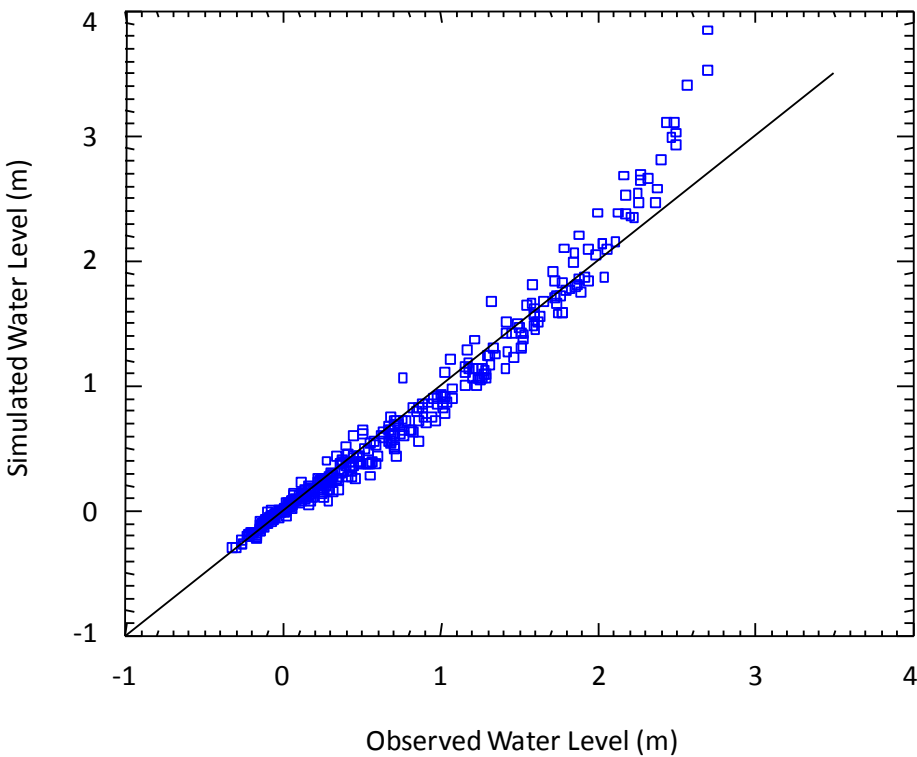


Figure 7–16. Scatter plot of paired values of observed and simulated daily water level above Lake Harney (SR 46 at Lake Harney) during the model confirmation period, 1996 to 2005.

7.3.2 DISCHARGE

Daily Discharge

Comparative statistics between observed and simulated daily discharge during the confirmation period are shown for five stations (Table 7–8). Station SR415 was not active during the calibration period and contains observations over only the last 11 months of 2005. Comparative statistics are similar to the calibration period (Table 6–11). Statistics are improved for the confirmation period compared to the calibration period at both Astor and Lake Jesup outlet. The Nash–Sutcliffe statistic at Astor improves from an unsatisfactory 0.367 to a very good 0.879. The Nash–Sutcliffe statistic at Lake Jesup outlet is unsatisfactory for both periods, but improves from 0.293 to 0.478 for the confirmation period.

Table 7–8. Statistical comparison of simulated and observed daily discharge during the model confirmation period, 1996 to 2005.

Station	<i>NRECS</i>	r^2	<i>m</i>	<i>NS</i>	<i>AVAE</i>	<i>AVRE</i>	<i>RMSE</i>
Astor	3,475	0.903	0.979	0.879	19.5	22.1	28.9
DeLand	3,653	0.958	1.010	0.948	12.5	17.5	17.5
Sanford	3,653	0.962	0.983	0.960	10.8	19.0	14.4
SR415	348	0.958	0.974	0.958	10.1	11.4	13.4
Lake Jesup outlet	3,491	0.555	0.705	0.478	4.1	70.4	6.1

NRECS = Number of paired values of simulated and observed salinity

r^2 = Coefficient of determination

m = Slope of linear regression line

NS = Nash–Sutcliffe statistic

RMSE = Root–mean–square error

AVRE = Average relative error (%)

AVAE = Average absolute error

The visual comparisons between simulated and observed daily discharge show that the model simulates the daily variability of discharge well. Comparisons are shown below for St. Johns River mainstem stations at Astor (Figure 7–17), DeLand (Figure 7–18), Sanford (Figure 7–19), and SR415 (Figure 7–20).

The visual comparison of observed and simulated daily discharge at Lake Jesup outlet (Figure 7–21) shows at least a reasonable match. A scatter plot of observed and simulated values shows that the poor comparative statistics are caused, in part, by a few observations of extremely low, negative discharge. We previously questioned these observed discharge values for the model calibration (Figure 7–22).

An additional cause of poor comparative statistics at Lake Jesup outlet is a mismatch of observed and simulated data because of phase errors. The simulated values could produce identical distributions as observed values, yet have large differences for the 1:1 pairing of simulated and observed values. Much of this phasing error could result from random uncertainty of boundary forces, particularly tributary discharge and wind.

Finally, the Nash–Sutcliffe statistic will produce low values when there are many values close to a mean value near zero. A mean value of discharge near zero is a particular feature of discharge at Lake Jesup outlet where the discharge oscillates in and out of the lake because of wind effects. The Nash–Sutcliffe statistic, then, may be a poor indicator of model performance for daily discharge at this particular location.

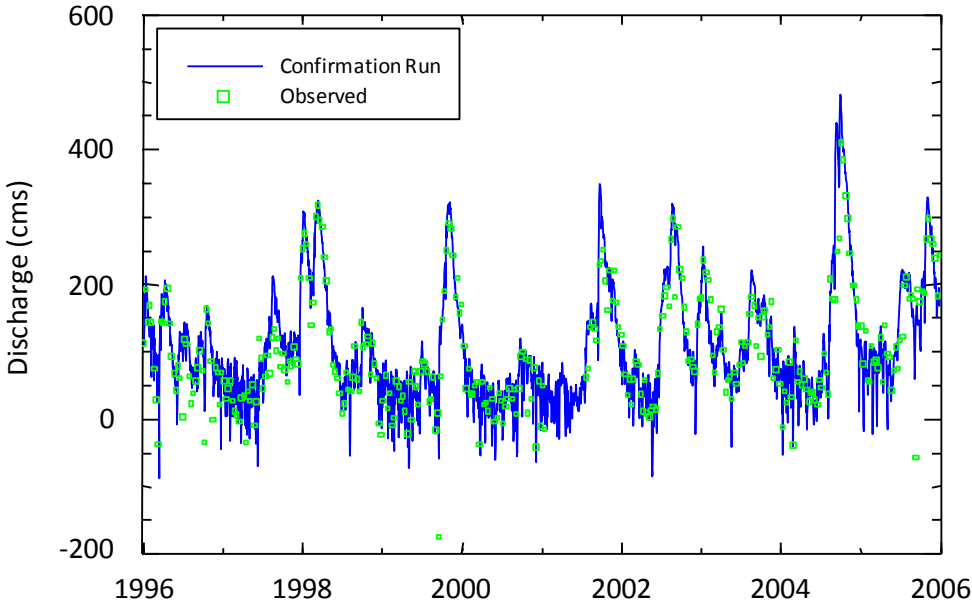


Figure 7–17. Simulated versus observed daily discharge at Astor (SR 40) during the model confirmation period, 1996 to 2005.

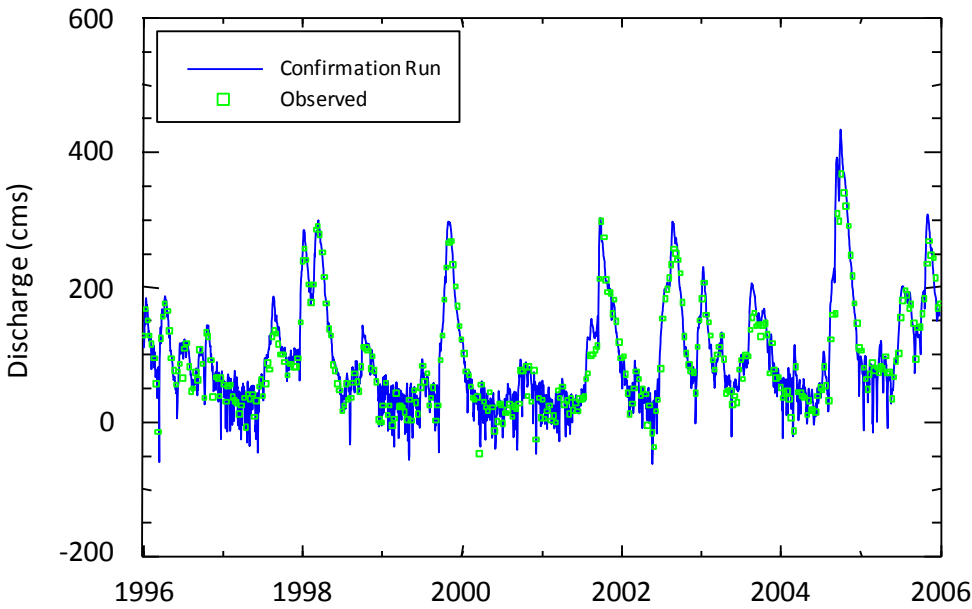


Figure 7–18. Simulated versus observed daily discharge at DeLand (SR 44) during the model confirmation period, 1996 to 2005.

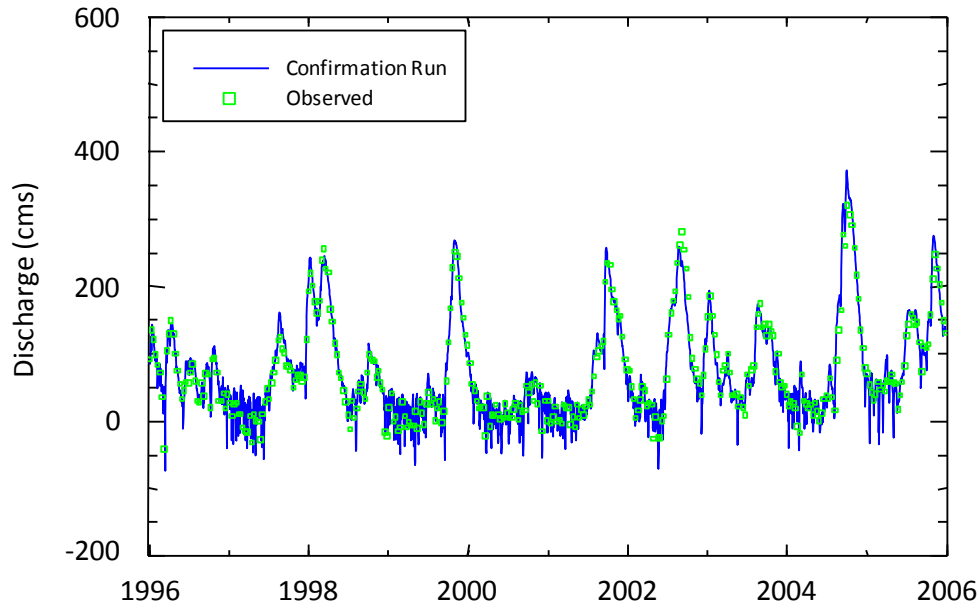


Figure 7–19. Simulated versus observed daily discharge at Sanford (US 17) during the model confirmation period, 1996 to 2005.

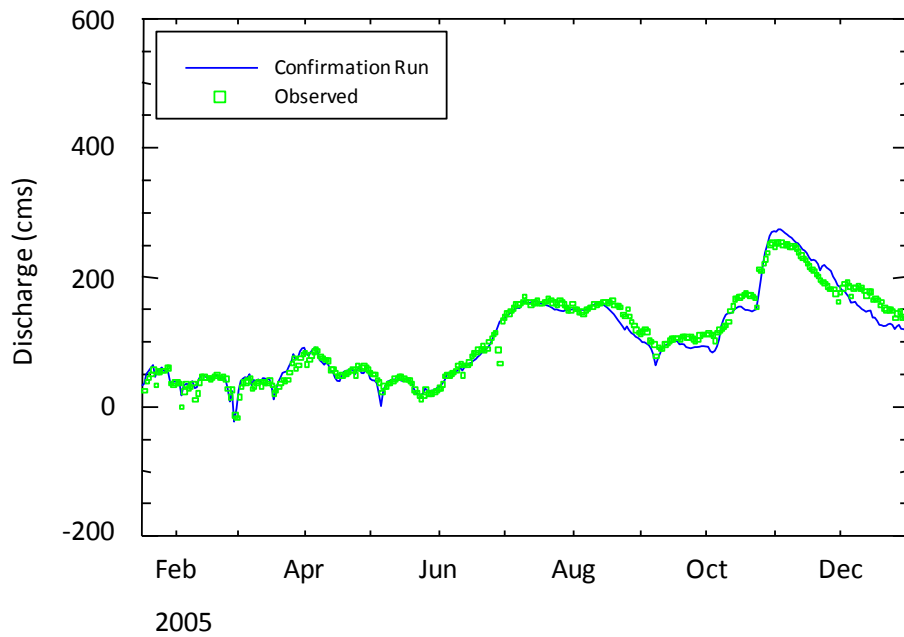


Figure 7–20. Simulated versus observed daily discharge at SR 415 over the period of gauge record (Feb. to Dec., 2005) contained within the model confirmation period.

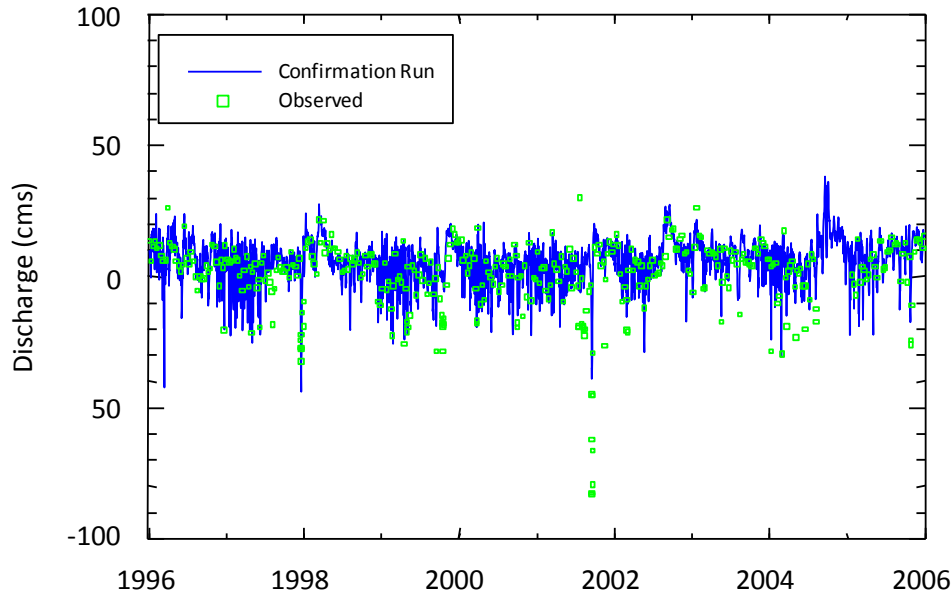


Figure 7–21. Simulated versus observed daily discharge at Lake Jesup outlet (SR 46 at Lake Jesup) during the model confirmation period, 1996 to 2005.

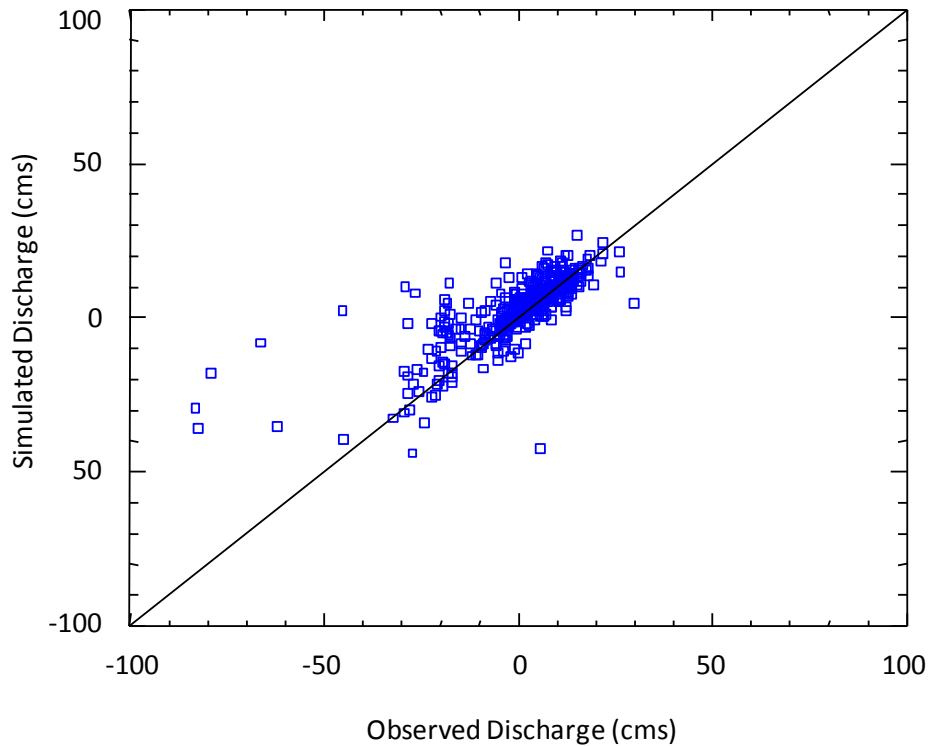


Figure 7–22. Scatter plot of paired values of observed and simulated daily discharge at Lake Jesup outlet (SR 46 at Lake Jesup) during the model confirmation period.

Monthly Discharge

Comparative statistics between observed and simulated monthly discharge are shown in Table 7–9. Simulated daily discharge compare well with observed values at St. Johns River mainstem locations. Nash–Sutcliffe statistics are very good (0.947 to 0.972) at these locations. However, comparative statistics were still poor at Lake Jesup outlet. As discussed previously the low discharge outliers in the observed record are partly responsible for the poor comparative statistics. For this reason the table lists two entries for Lake Jesup, the first containing all observations, and the second with the lowest four observations removed. Removing the four outliers from the observed record improves the comparative statistics. The Nash–Sutcliffe increases to a satisfactory 0.598. Many of the observed values are near 0 at this location, which also tends to distort the Nash–Sutcliffe and *AVRE* statistics.

Table 7–9. Statistical comparison of simulated and observed monthly discharge during the model confirmation period, 1996 to 2005.

Station	<i>NRECS</i>	r^2	<i>m</i>	<i>NS</i>	<i>AVAE</i>	<i>AVRE</i>	<i>RMSE</i>
Astor	113	0.947	1.041	0.916	14.6	15.4	21.5
DeLand	120	0.972	1.013	0.963	9.9	12.6	13.9
Sanford	120	0.974	0.973	0.972	8.8	18.5	11.6
SR415	11	0.974	0.977	0.972	7.9	7.3	10.3
Lake Jesup outlet-1	114	0.593	0.643	0.498	2.5	88.1	3.7
Lake Jesup outlet-2	110	0.689	0.811	0.598	2.1	46.1	2.9

NRECS = Number of paired values of simulated and observed salinity

r^2 = Coefficient of determination

m = Slope of linear regression line

NS = Nash–Sutcliffe statistic

RMSE = Root–mean–square error

AVRE = Average relative error (%)

AVAE = Average absolute error

Observed and simulated monthly discharge at DeLand (Figure 7–23) and Lake Jesup outlet (Figure 7–24) show that the model captures the general pattern of monthly discharge variability well.

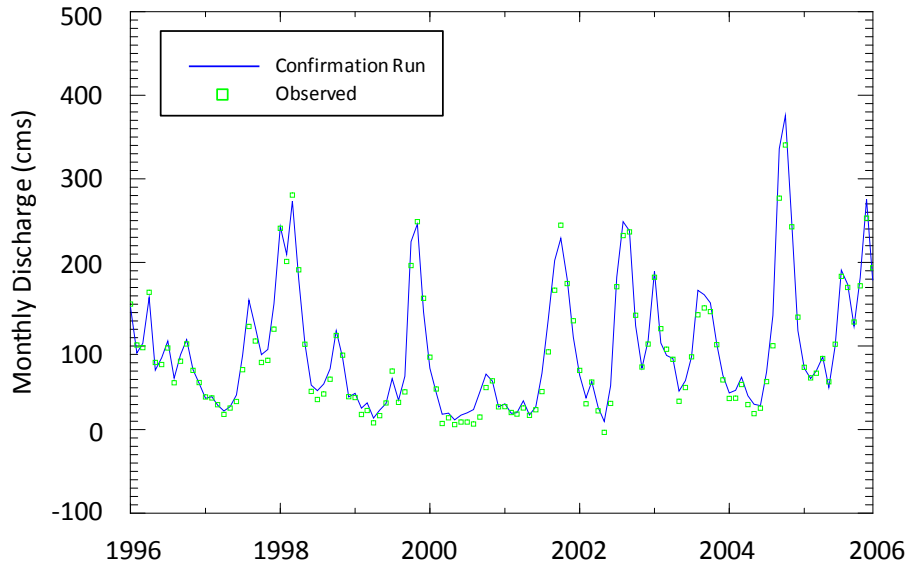


Figure 7–23. Simulated versus observed monthly discharge at DeLand (SR 44) during the model confirmation period, 1996 to 2005.

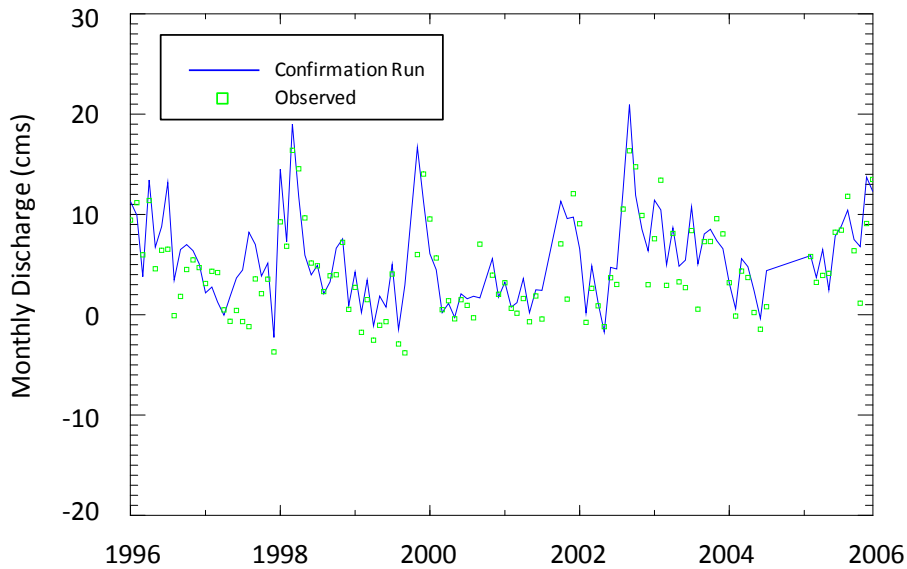


Figure 7–24. Simulated versus observed monthly discharge at Lake Jesup outlet (SR 46 at Lake Jesup) during the model confirmation period, 1996 to 2005.

Hourly Discharge

Comparative statistics for hourly discharge (Table 7–10) are similar to those for the calibration period (Table 6–13). As expected, comparative statistics remain poor for Lake Jesup outlet, although the Nash–Sutcliffe statistic improves from 0.094 to 0.280.

Table 7–10. Statistical comparison of simulated and observed hourly discharge during the model confirmation period, 1998 to 2001.

Station	<i>NRECS</i>	r^2	<i>m</i>	<i>NS</i>	<i>AVAE</i>	<i>AVRE</i>	<i>RMSE</i>
Astor	29604	0.887	0.925	0.877	22.6	34.0	31.9
DeLand	33112	0.947	0.949	0.942	14.3	26.4	19.8
Sanford	34594	0.956	0.959	0.955	12.1	30.5	15.6
Lake Jesup outlet	34901	0.329	0.443	0.280	7.3	118.8	11.0

NRECS = Number of paired values of simulated and observed salinity

r^2 = Coefficient of determination

m = Slope of linear regression line

NS = Nash–Sutcliffe statistic

RMSE = Root–mean–square error

AVRE = Average relative error (%)

AVAE = Average absolute error

The good agreement between observed and simulated hourly discharge for the St. Johns River mainstem locations is illustrated for May 1999 at DeLand (Figure 7–25).

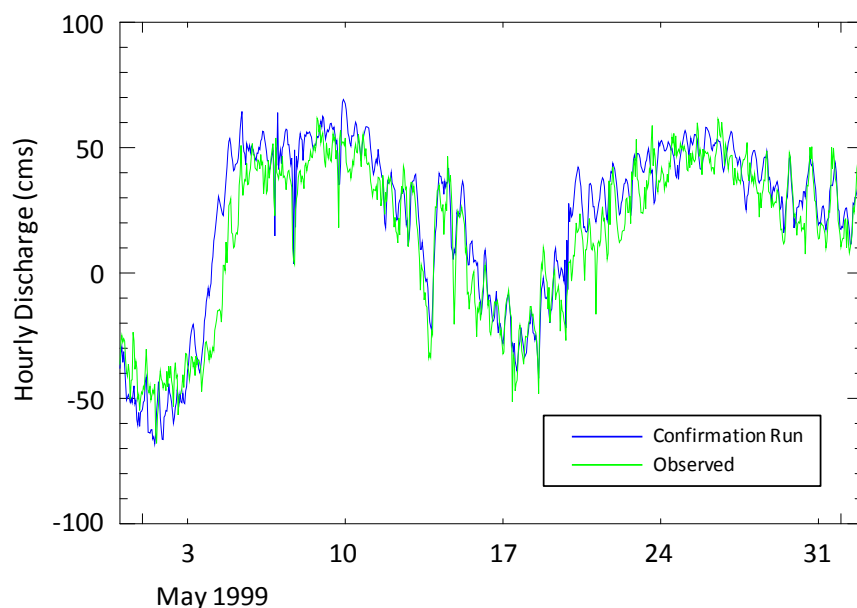


Figure 7–25. Simulated versus observed hourly discharge at DeLand (SR 44) during May 1999.

Figure 7–26 compares observed and simulated hourly discharge for the same 1-month period for Lake Jesup outlet.

A plot of simulated and observed hourly discharge at Lake Jesup outlet for May 1999 shows that the model does capture the larger seasonal patterns, but the observed hourly discharges show a generally larger range of variation than the simulated discharge.

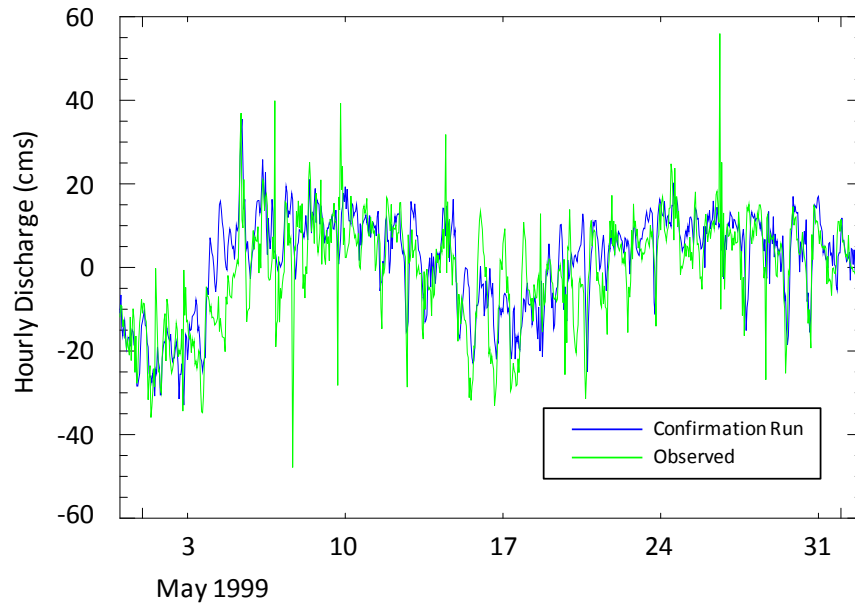


Figure 7–26. Simulated versus observed hourly discharge at Lake Jesup outlet (SR 46 at Lake Jesup) during May 1999.

Cumulative Density Functions (CDF) for observed and simulated hourly discharge at DeLand are quite similar in character (Figure 7–27). This match is expected given the good comparative statistics. The simulated CDF is slightly higher than the observed CDF over much of the distribution because the simulated discharge overestimates observed discharge by 6.7% over the 10-yr confirmation period.

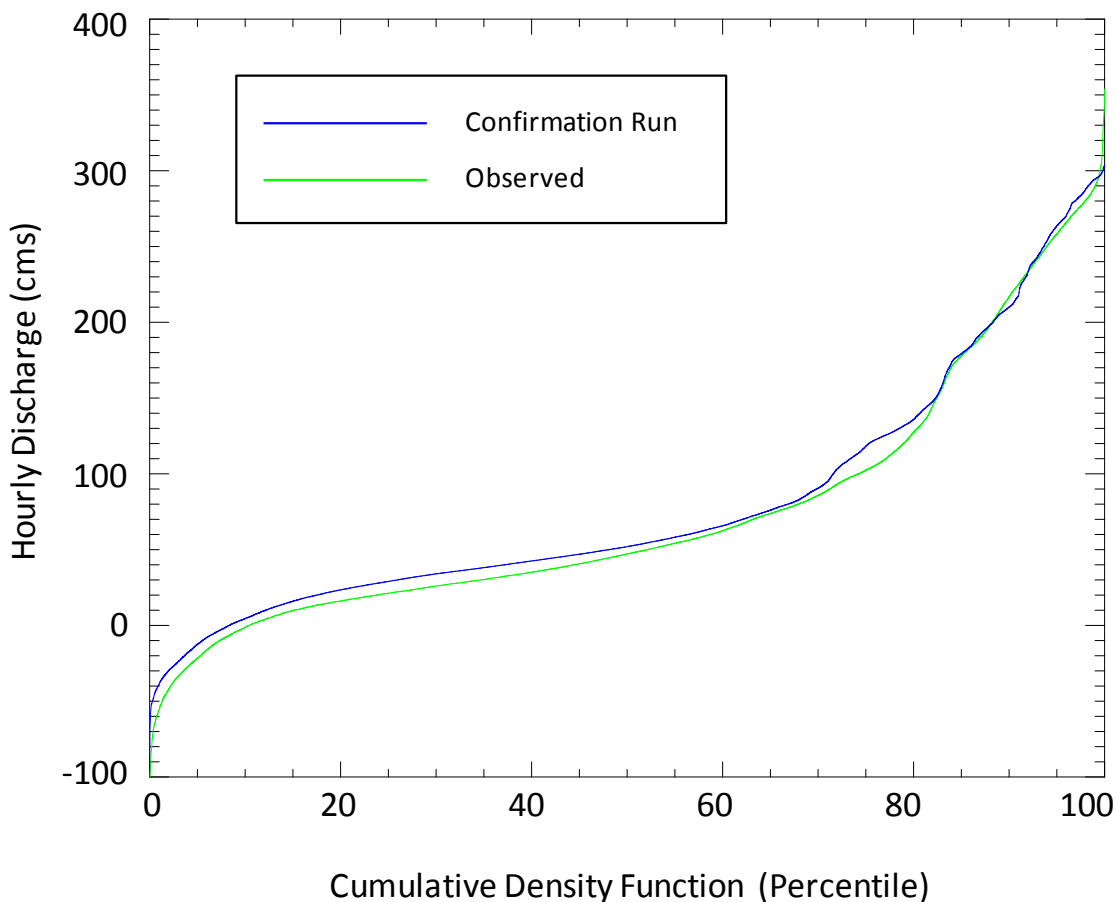


Figure 7–27. Cumulative density functions of observed and simulated hourly discharge at DeLand (SR 44) during the model confirmation period, 1996 to 2005.

The CDFs for observed and simulated hourly discharge at Lake Jesup outlet show that the distribution of simulated hourly discharge is nearly identical to observed discharge from the 30th to 90th percentiles of the distribution, nearly 60% of the time (Figure 7–28). As expected, the model overpredicts the lowest values and underpredicts the highest values, but the deviations are only large at the extreme tails of the distribution.

The reasonably good match of CDFs for hourly discharge at Lake Jesup outlet is some consolation to the poor comparative statistics. The CDFs suggest that the model is correctly simulating the overall physical behavior of oscillatory discharge at this location, even if the results must be viewed from a statistical perspective with the understanding that the model's ability to predict discharge on any given day is poor. This view is analogous to the ability of a climate model to correctly predict the distribution of air temperatures over a long period, but the inability of the same model to predict tomorrow's weather.

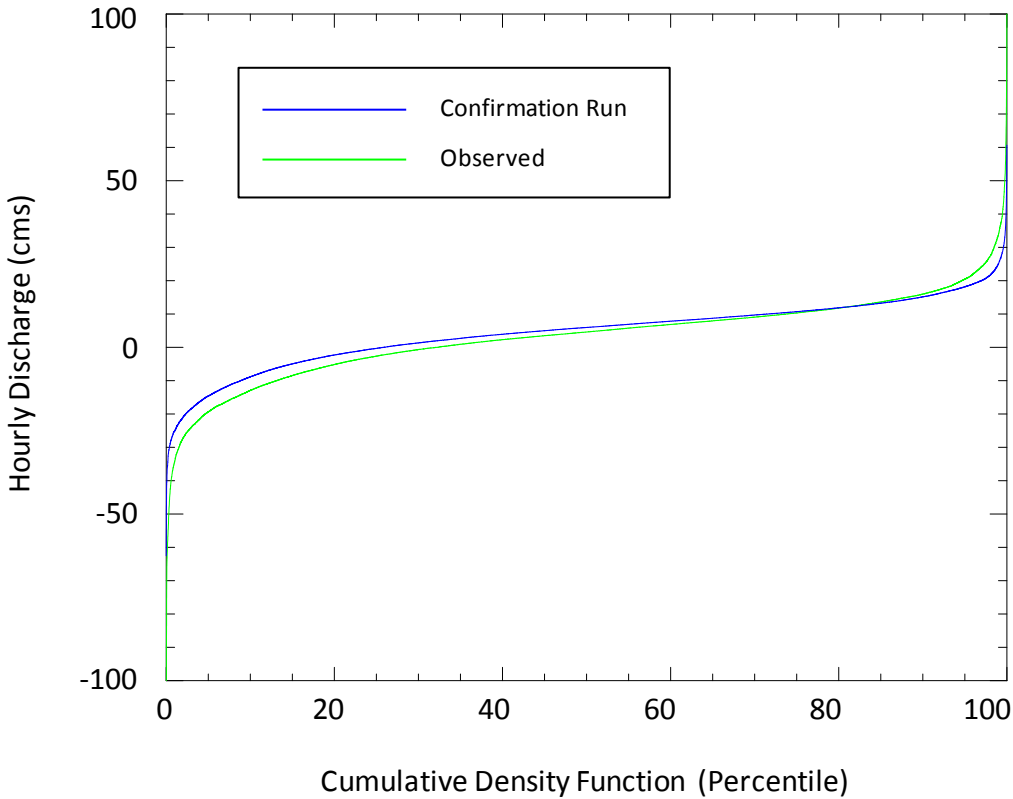


Figure 7–28. Cumulative density functions of observed and simulated hourly discharge at Lake Jesup outlet (SR 46 at Lake Jesup) during the model confirmation period, 1996 to 2005.

10-yr Mean Discharge

The 10-yr mean of observed and simulated discharge is shown in Table 7–11 for Astor, DeLand, and Sanford. Astor is located at the downstream model boundary so that mean discharge at this location is a measure of the cumulative water budget for the system. The model mean discharge was +10.5% greater than observed discharge at Astor—a reasonable error given all the possible uncertainties in the total water budget.

The percent error declines upstream and is +6.7% at DeLand and only 3.9% at Sanford. Standard deviations of observed and simulated discharge have nearly identical values indicating that the model realistically simulates the variability of daily discharge in the middle St. Johns River main stem.

Table 7–11. Mean and standard deviation of observed and simulated discharge at three locations during the confirmation period, 1996 to 2005. Mean and standard deviations in m^3s^{-1} .

Station	Mean Observed	Mean Simulated	Standard Deviation Observed	Standard Deviation Simulated	% Error of Means
Astor	101.0	111.6	74.5	79.7	+10.5
DeLand	90.5	96.6	72.7	74.7	+6.7
Sanford	72.0	74.8	69.1	68.1	+3.9

7.3.3 SALINITY

Continuous Salinity at DeLand and Sanford

The model calibration for salinity was primarily compared with two USGS stations located at DeLand and Sanford, which continuously measured daily salinity over a 2-yr period, from October 2000 through September 2002. The calibration period was contained within this period. Observed and simulated daily salinity for the entire 2-yr period of record are shown below for DeLand (Figure 7–29) and Sanford (Figure 7–30). Following the end of the calibration period in September 2001, the system exhibited a nearly linear rise in salinity to May 2002. The rate of rise in salinity during dry periods is in part determined by salt flux from groundwater, and the good match of observed and simulated salinity during this period is an indication that groundwater salt flux into the model is realistic.

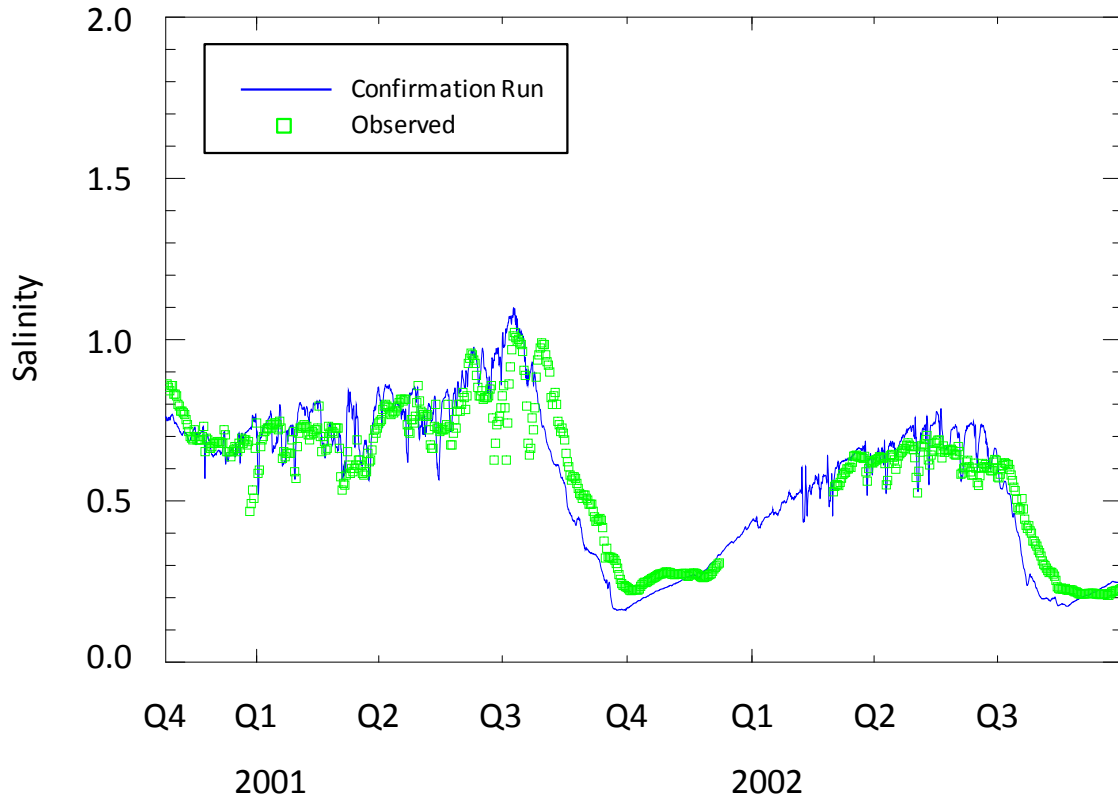


Figure 7–29. Simulated versus observed daily salinity at DeLand (SR 44) over the period of gauged record.

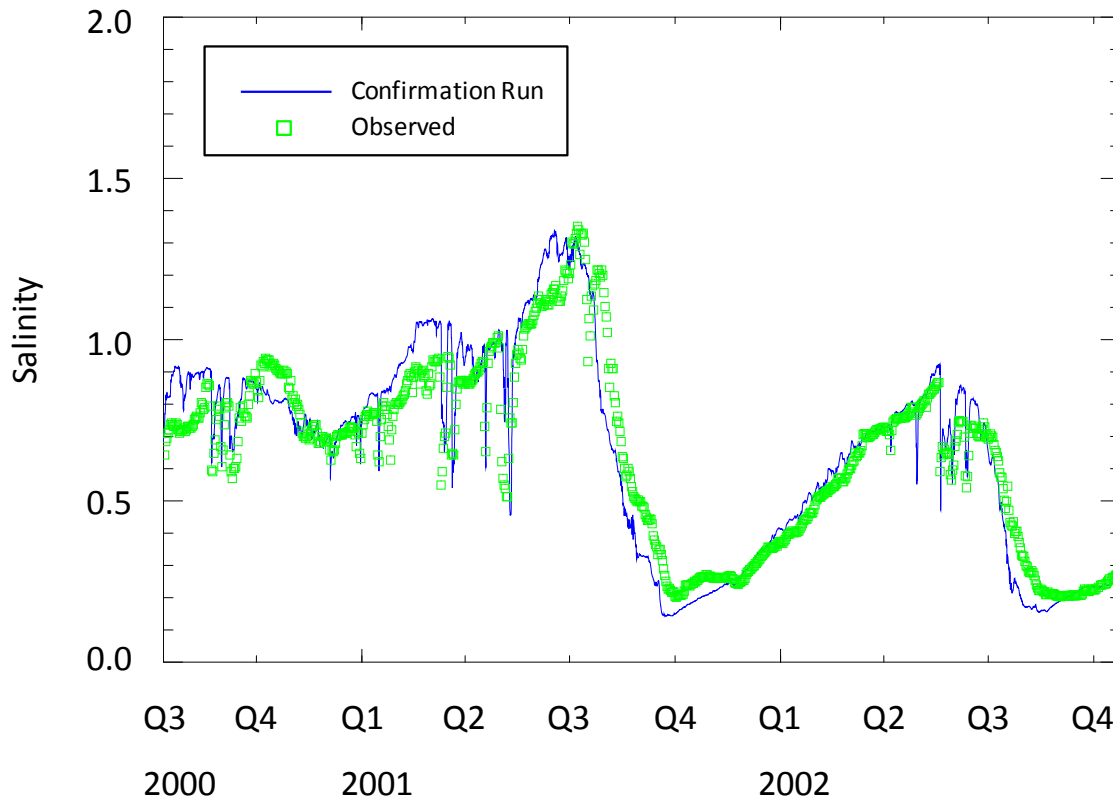


Figure 7–30. Simulated versus observed daily salinity at Sanford (U.S. 17) over the period of gauged record.

Synoptic Salinity

The model confirmation period allows comparison of simulated and observed salinity at stations that are part of a synoptic network maintained by SJRWMD. Comparative statistics for simulated and observed salinity are shown below at 14 salinity stations in the middle St. Johns River (Table 7–12). The Nash–Sutcliffe statistics for St. Johns River mainstem locations are all very good (0.817 to 0.939). In Lake Jesup (stations OW-2, OW-4, and OW-6) the Nash–Sutcliffe statistics are satisfactory (0.499 to 0.672) and correlation between observed and simulated salinity is good ($r^2 = 0.755$ to 0.823). Comparative statistics for salinity in Lake Woodruff (station LKWOOD) are extremely poor, with negative Nash–Sutcliffe statistics and $r^2 = 0.243$.

Table 7–12. Statistical comparison of simulated and observed salinity during the model confirmation period, 1996 to 2005.

Station	<i>NRECS</i>	r^2	<i>m</i>	<i>NS</i>	<i>AVAE</i>	<i>AVRE</i>	<i>RMSE</i>
SR40	229	0.880	1.015	0.855	0.05	11.1	0.07
LKWOOD	157	0.243	0.551	-0.293	0.13	54.6	0.17
SR44	726	0.876	1.072	0.832	0.07	14.3	0.09
SJR-DPP	40	0.891	0.958	0.866	0.04	10.5	0.06
US17	829	0.894	1.069	0.859	0.08	14.7	0.10
LMAC	84	0.931	1.143	0.877	0.07	17.1	0.08
SJR-415	41	0.945	1.060	0.932	0.04	12.4	0.06
OW-SJR-2	348	0.843	0.980	0.817	0.08	20.3	0.11
OW-SJR-1	259	0.870	0.919	0.849	0.08	23.2	0.12
OW-2	206	0.823	0.932	0.672	0.11	20.3	0.13
OW-4	245	0.755	1.020	0.658	0.076	24.6	0.10
OW-6	263	0.801	1.142	0.499	0.091	23.8	0.11
SJR-OLH	40	0.960	1.090	0.939	0.045	13.5	0.06
CLH	51	0.878	1.100	0.920	0.057	19.4	0.08

NRECS = Number of paired values of simulated and observed salinity

r^2 = Coefficient of determination

m = Slope of linear regression line

NS = Nash–Sutcliffe statistic

RMSE = Root–mean–square error

AVRE = Average relative error (%)

AVAE = Average absolute error

A scatter plot of paired simulated and observed salinity for all 14 synoptic salinity stations observations demonstrates that the model predicts salinity well over the entire temporal and spatial range of observed salinity (Figure 7–31). For the pooled data *AVRE* is 21%, and *RMSE* is within about 0.1. The mean for all the observed data is 0.46 with a standard deviation of 0.23, while the mean for the simulated values is 0.47 with a standard deviation of 0.25. The model has no measureable bias for global salinity, indicating that the modeled salt budget is accurate on average.

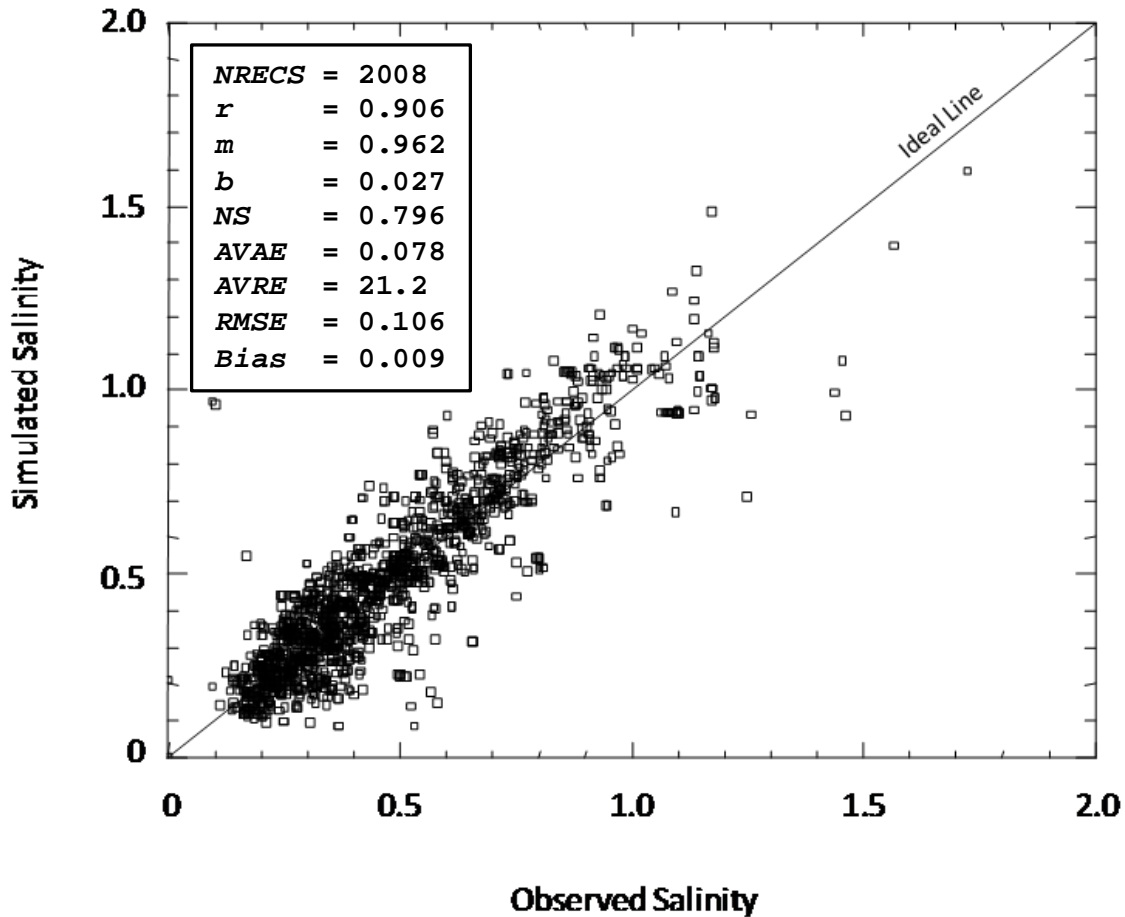


Figure 7–31. Scatter plot of paired values of observed and simulated daily discharge for all synoptic salinity stations during the model confirmation period, 1996 to 2005.

Time series Plots of Synoptic Salinity

For completeness, time series plots comparing observed and simulated salinity at each synoptic station are presented in Figure 7–32 through Figure 7–44. In general, these plots visually show the close match between simulated and observed salinity that was previously demonstrated by comparative statistics. The match of observed and simulated salinity in Lake Woodruff (Figure 7–33) appears better for the period 2002 to 2005 than for the period prior to 2002.

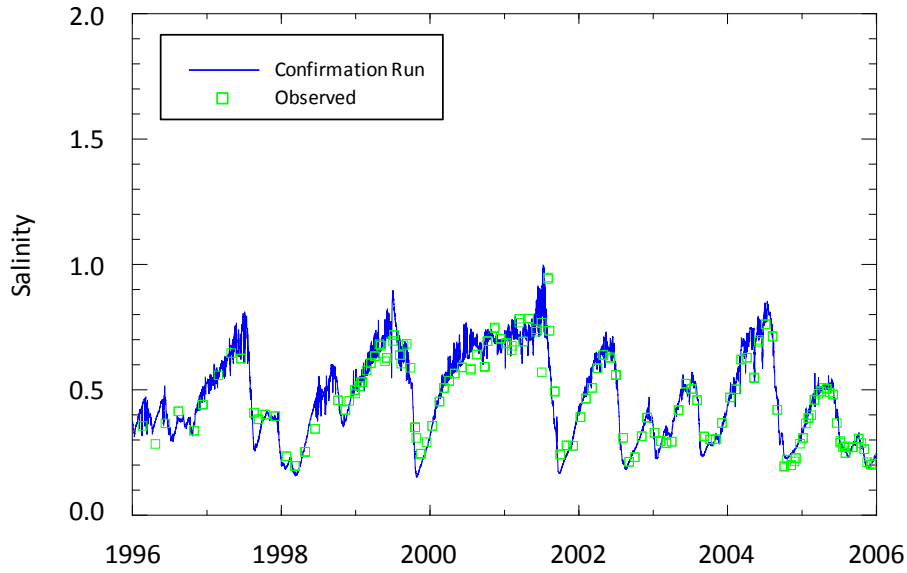


Figure 7–32. Simulated versus observed salinity at Astor (SR 40) during the model confirmation period, 1996 to 2005.

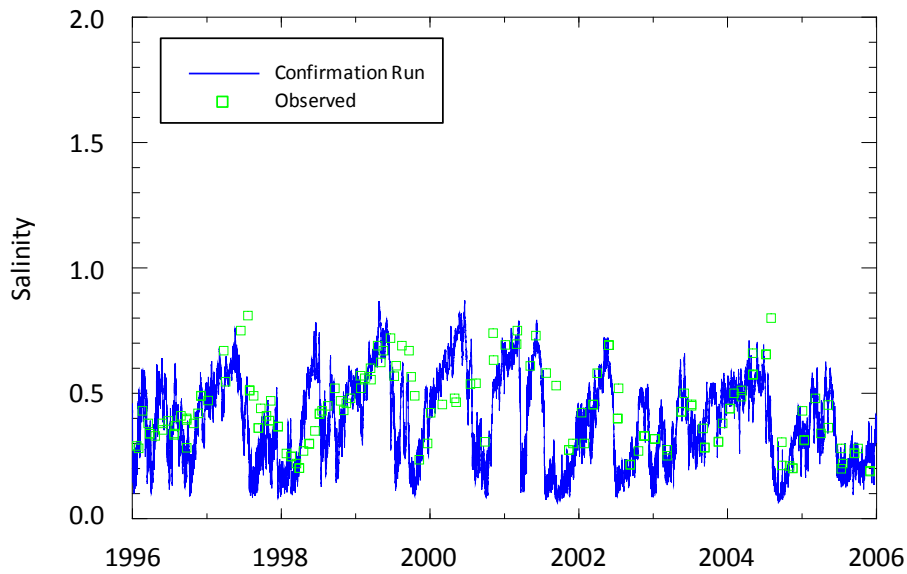


Figure 7–33. Simulated versus observed salinity in Lake Woodruff (station LKWNWR) during the model confirmation period, 1996 to 2005.

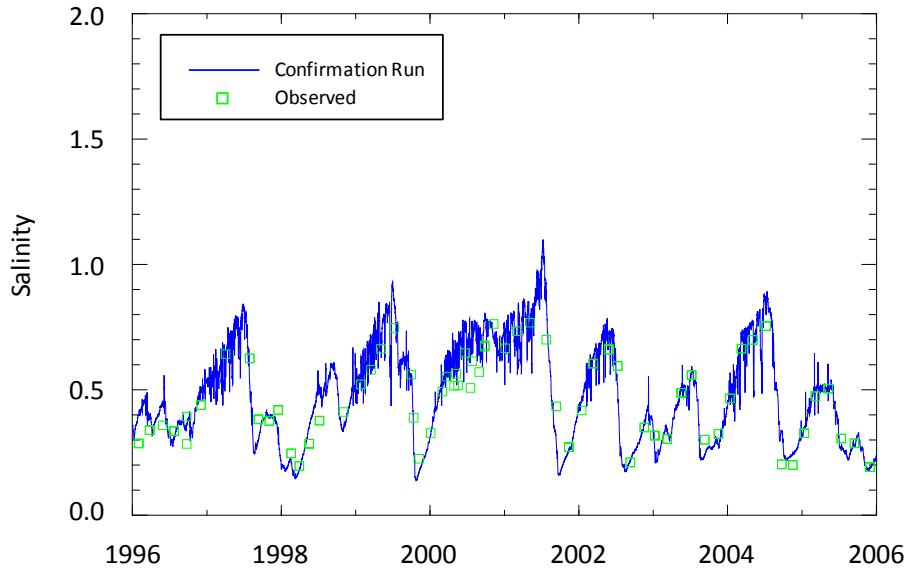


Figure 7–34. Simulated versus observed salinity at DeLand (SR 44) during the model confirmation period, 1996 to 2005.

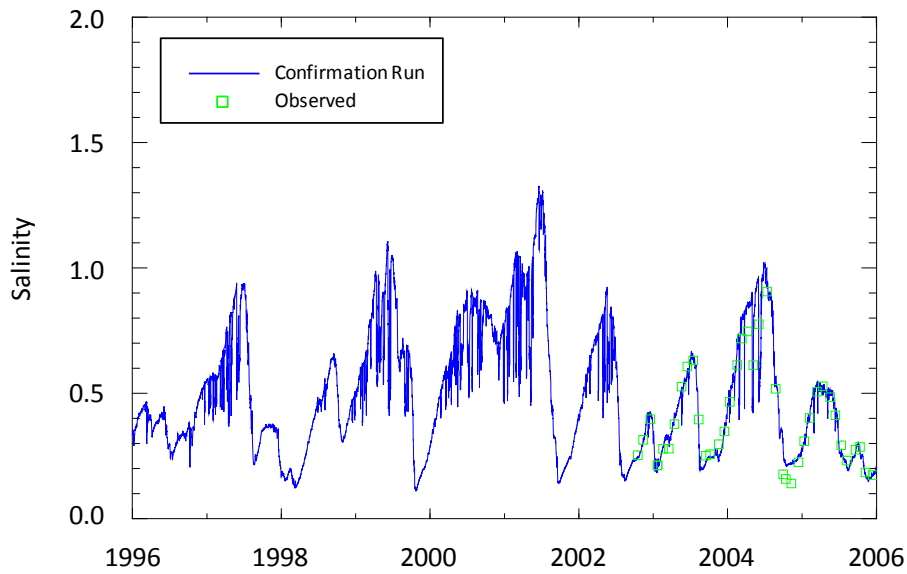


Figure 7–35. Simulated versus observed salinity at station SJR-DPP during the model confirmation period, 1996 to 2005.

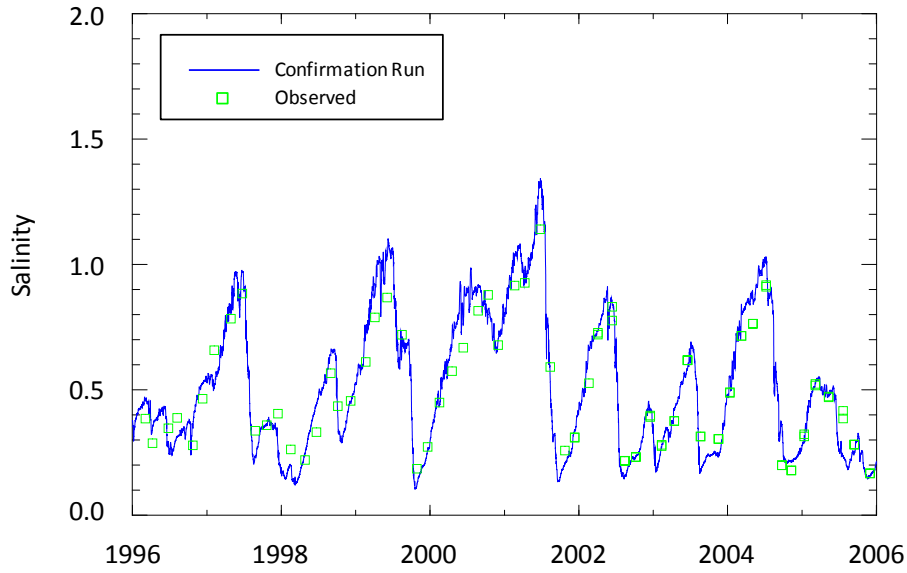


Figure 7–36. Simulated versus observed salinity in Lake Monroe (station LMAC) during the model confirmation period, 1996 to 2005.

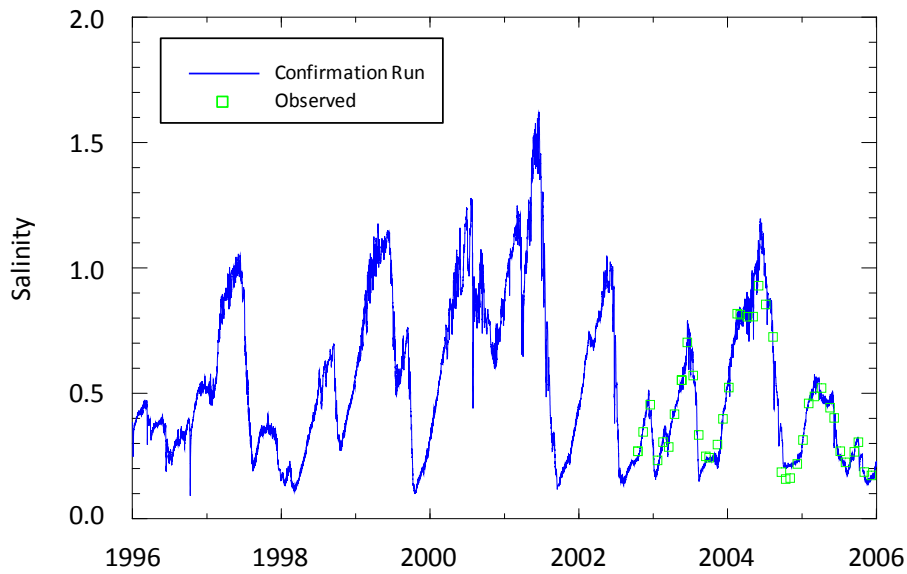


Figure 7–37. Simulated versus observed salinity at station SJR-415 (SR 415) during the model confirmation period, 1996 to 2005.

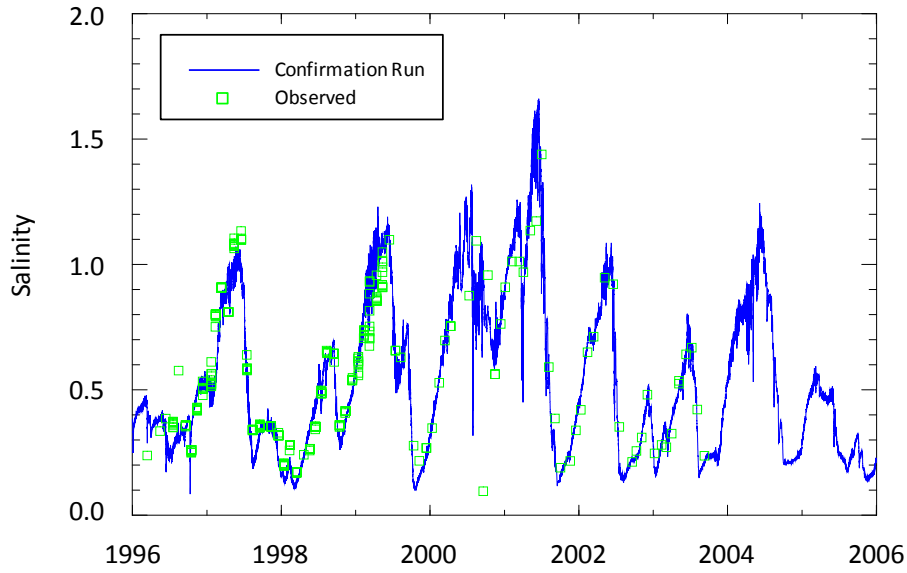


Figure 7–38. Simulated versus observed salinity at station OW-SJR-2 during the model confirmation period, 1996 to 2005.

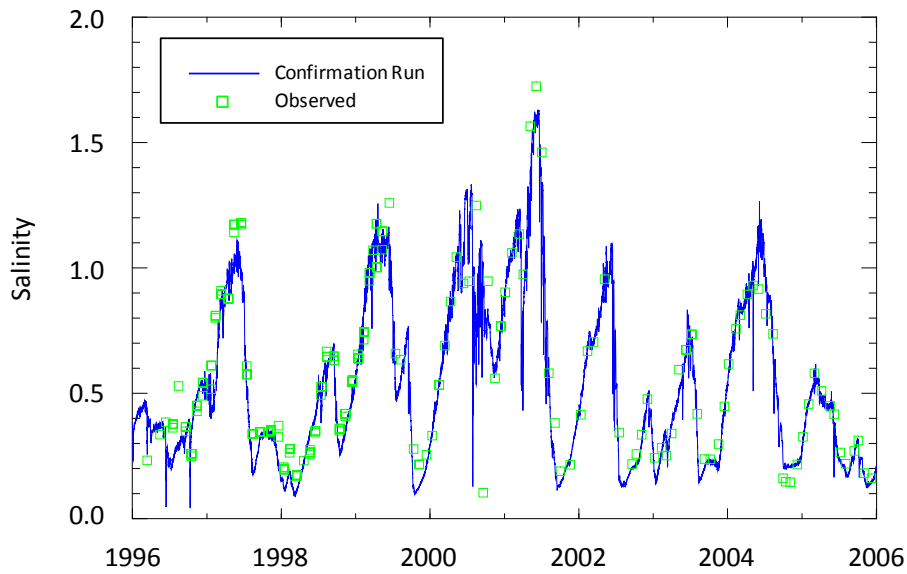


Figure 7–39. Simulated versus observed salinity at OW-SJR-1 during the model confirmation period, 1996 to 2005.

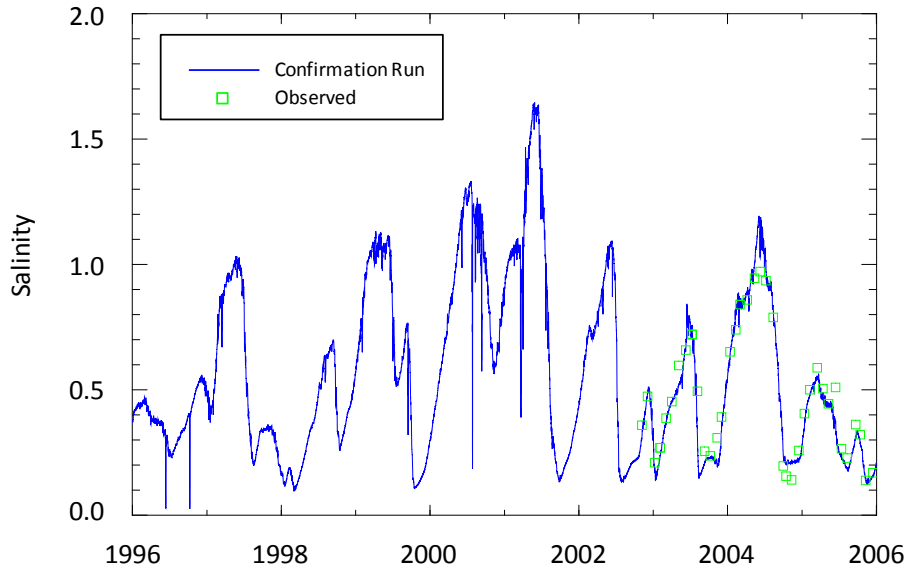


Figure 7–40. Simulated versus observed salinity at station SJR-OLH during the model confirmation period, 1996 to 2005.

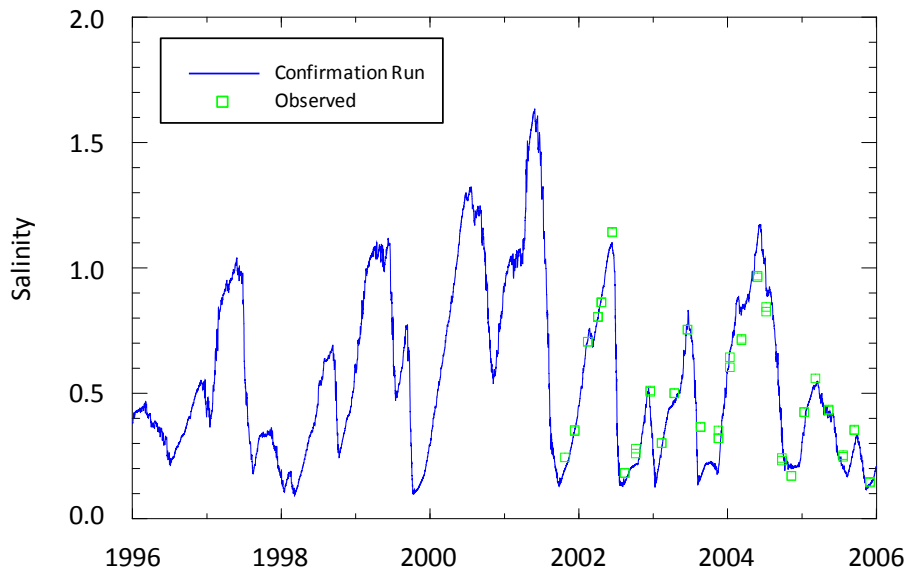


Figure 7–41. Simulated versus observed salinity in Lake Harney (station CLH) during the model confirmation period, 1996 to 2005.

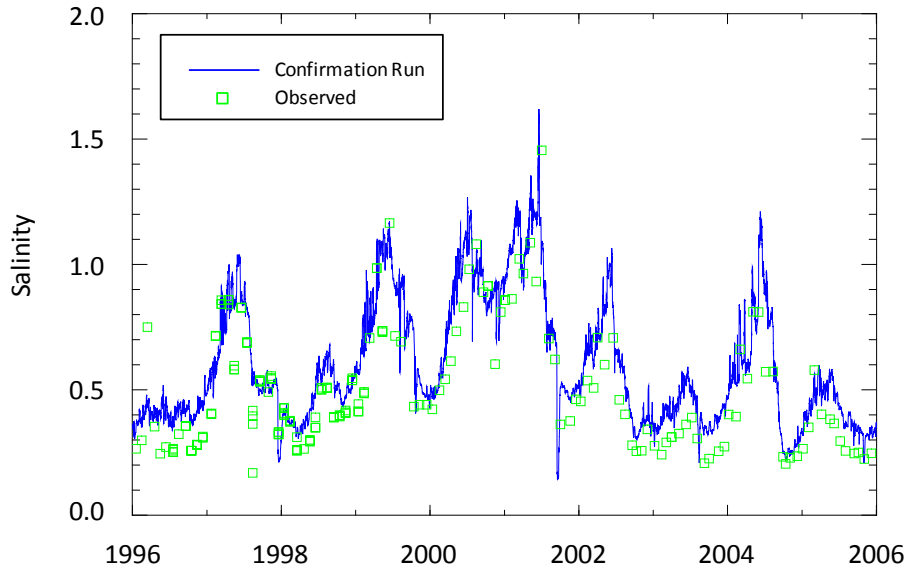


Figure 7–42. Simulated versus observed salinity in Lake Jesup (station OW-2) during the model confirmation period, 1996 to 2005.

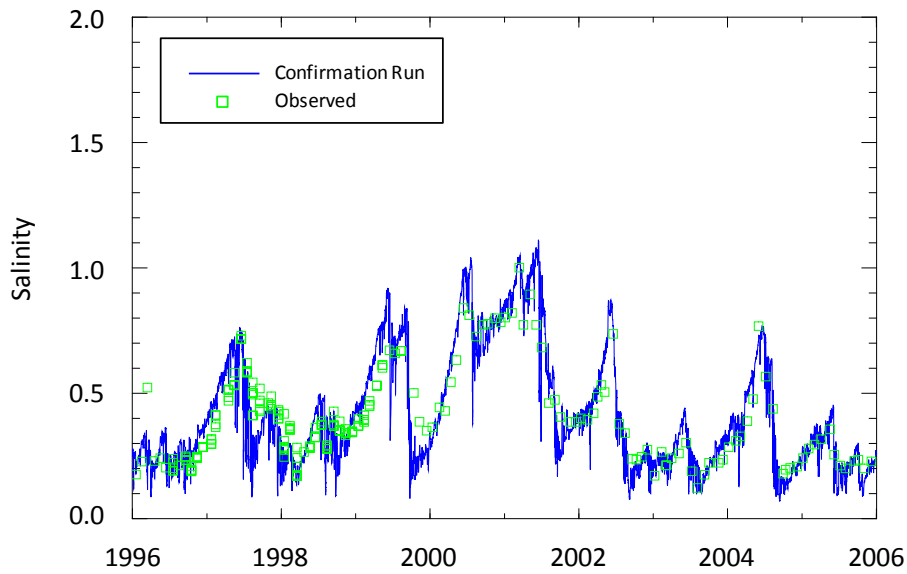


Figure 7–43. Simulated versus observed salinity in Lake Jesup (station OW-4) during the model confirmation period, 1996 to 2005.

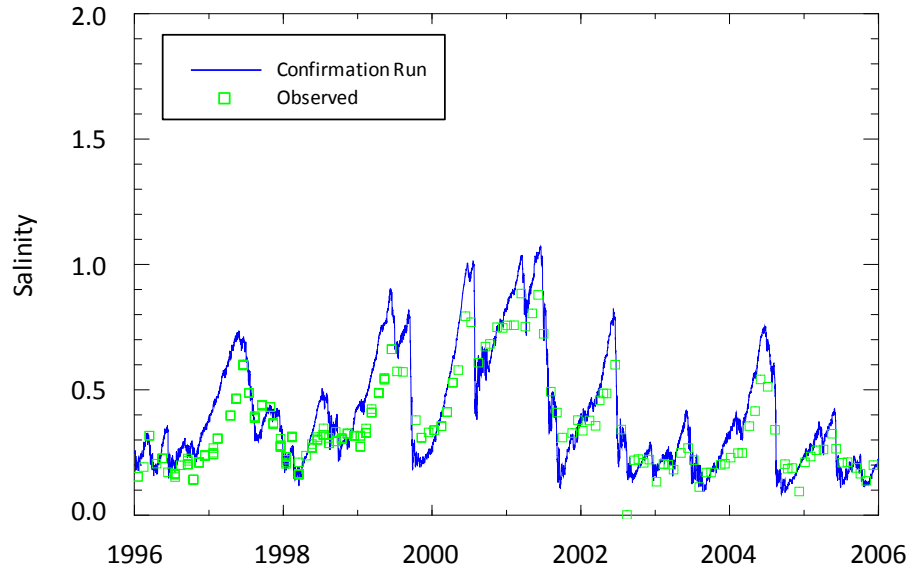


Figure 7–44. Simulated versus observed salinity in Lake Jesup (station OW-6) during the model confirmation period, 1996 to 2005.

Lake Woodruff Salinity and Tick Island Discharge

A possible cause for the poor match of simulated and observed salinity in Lake Woodruff is the simulation of the fraction of river flow entering the lake. The St. Johns River bifurcates between DeLand (SR 44) and Lake Woodruff (Figure 7–45.) Correct simulation of the fraction of discharge entering the lake through the east branch of the bifurcation is important for simulating flushing of the lake and salinity within the lake. Unfortunately, the only observed discharge data available for comparison with the model were collected outside the model confirmation period during the 2007 and 2008 water years. An indirect assessment of discharge entering the lake from the river was thus required.

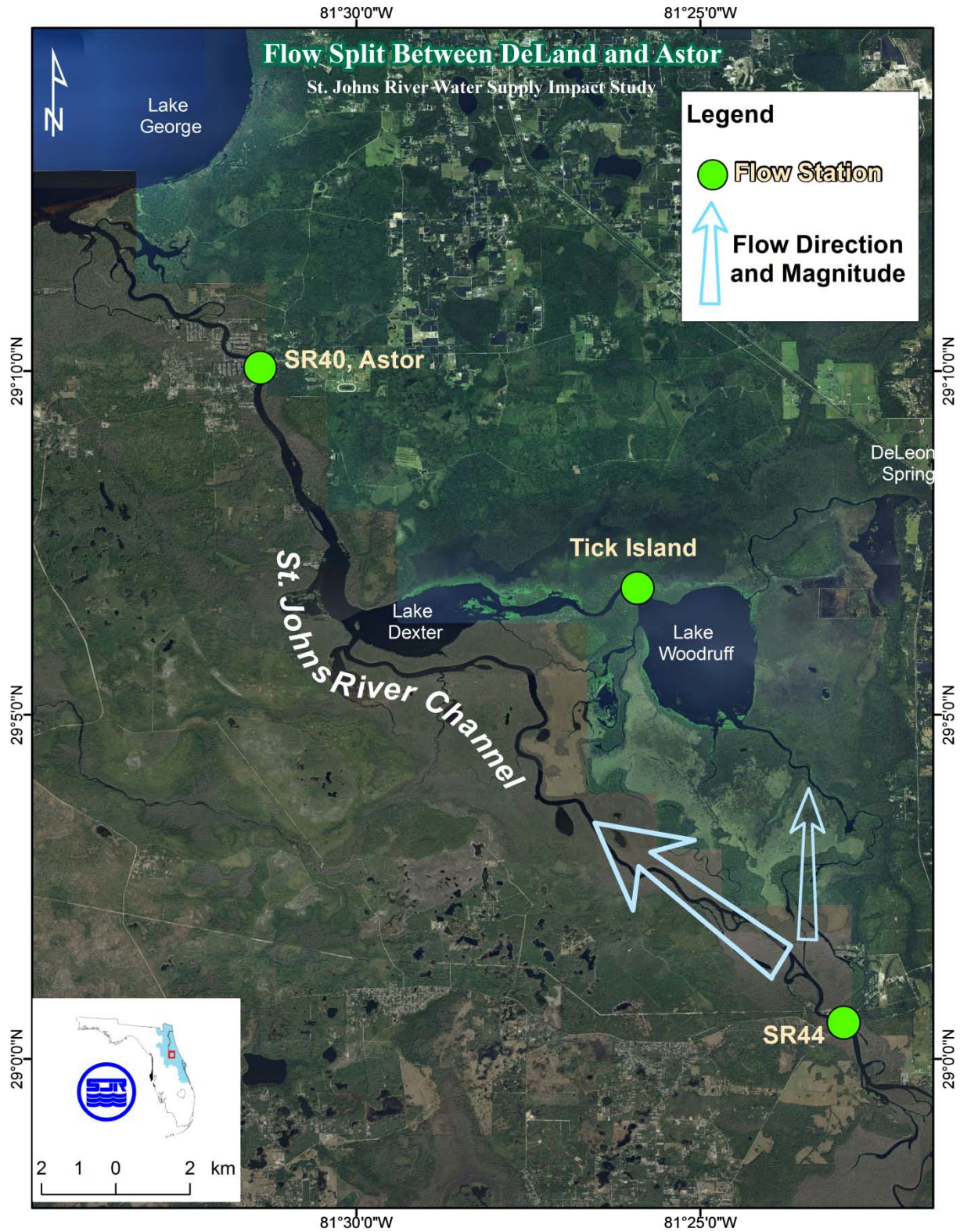


Figure 7–45. Map showing bifurcation of St. Johns River flow between DeLand (SR 44) and Lake Woodruff. A fraction of the flow passes through Lake Woodruff and exits at Tick Island.

SJRWMD contracted discharge measurements at Tick Island to measure discharge exiting Lake Woodruff for the WSIS (Figure 7–45). Because discharge exiting the lake at Tick Island is dependent on the fraction of discharge entering the lake, as part of the total water budget, correct simulation of the outflow at Tick Island would be evidence that the fractional split at the upstream bifurcation is reasonably modeled.

Observed daily discharge at DeLand and Tick Island have a strong positive correlation (Figure 7–46). The St. Johns River mainstem discharge at DeLand is considerably larger than the Tick Island discharge. During an extended dry period between October 2007 and July 2008, daily discharge at both locations exhibited reverse flow events.

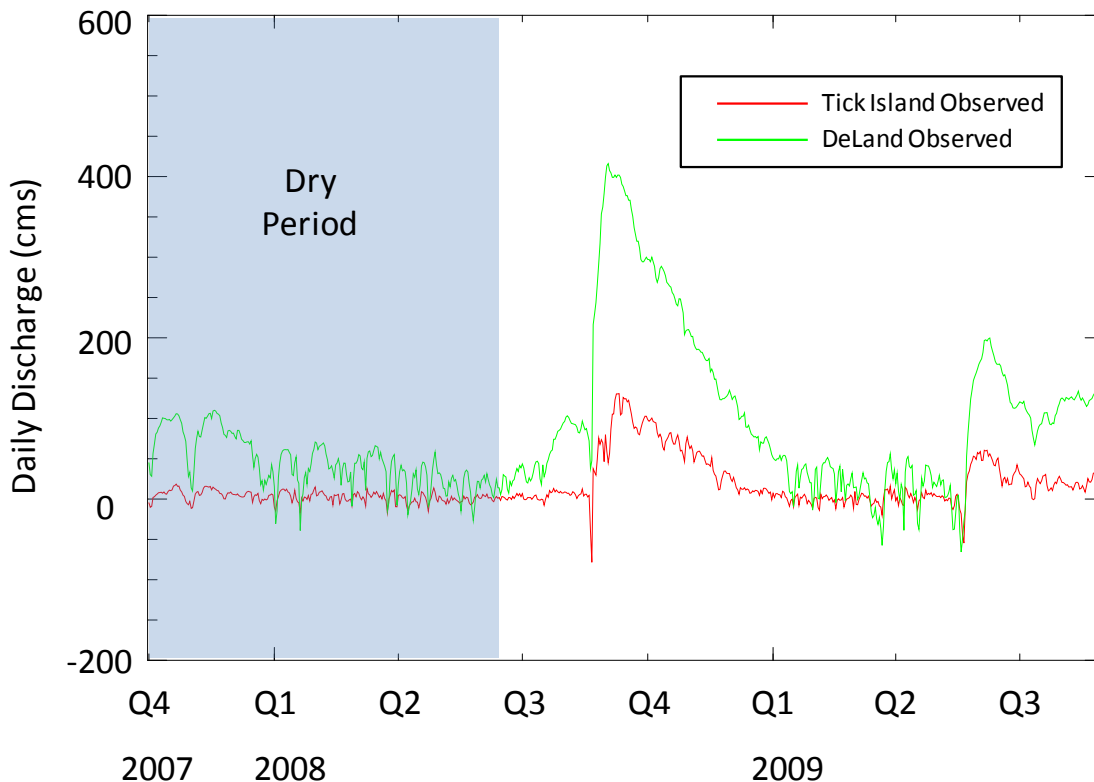


Figure 7–46. Comparison of observed daily discharge at DeLand and Tick Island for the 2008 and 2009 water years.

The ratio of Tick Island discharge to DeLand discharge ($R_{TD} = Q_{\text{Tick}}/Q_{\text{DeLand}}$) was calculated for each day over the 2-yr period. R_{TD} has a weak positive correlation with discharge, so was sorted by discharge intervals defined by percentile divisions for the distribution of Tick Island discharge. The mean of R_{TD} values was then assigned to each discharge interval (Table 7–13). Simulated discharge ratios were calculated for the 10-yr confirmation period.

Table 7–13. Ratio of Tick Island discharge to DeLand discharge (R_{TD}) for observed and simulated values sorted by percentiles of the observed distribution of Tick Island discharge.

Discharge Interval	R_{TD} Observed	R_{TD} Simulated
< 10th Percentile	-1.01	-0.47
10th Percentile to 1st Quartile	-0.04	0.05
1st Quartile to Median	0.05	0.15
Median to 2nd Quartile	0.12	0.16
2nd Quartile to 90th Percentile	0.23	0.17
> 90th Percentile	0.27	0.19

Observed and simulated discharge ratios are of the same order of magnitude. DeLand discharge would likely have the greatest influence on Lake Woodruff during high flow periods when the discharge at Tick Island is above the median discharge. Under these conditions observed R_{TD} ranges from 0.12 to 0.27 and simulated R_{TD} ranges from 0.16 to 0.19. These results indicate that the model may underpredict discharge through Lake Woodruff during high flows. But if this is so, then salinity in Lake Woodruff would be even more similar to salinity at DeLand, an effect counter to the observed salinity in Lake Woodruff. Simulation of salinity during the exact period of Tick Island discharge observations could help clarify this question, although additional salinity data may also be required. For now we take the results of Table 7–13 to indicate that the ratio of Tick Island discharge to DeLand discharge simulated by the model is reasonable and likely does not explain the mismatch of salinity in Lake Woodruff. No attempt was made to improve the model results for Lake Woodruff salinity because the mismatch is likely related to local dynamics within the lake that would require considerable additional study.

7.4 CONFIRMATION OF THE COMBINED ST. JOHNS RIVER MODEL

Development of the hydrodynamic models for the study area was done using separate models of the lower (EFDC-LSJR) and middle (EFDC-MSJR) St. Johns River. A single, combined model was used for WSIS scenarios for evaluating hydrodynamic effects of water withdrawals and other possible changes to the system. A single, combined model has the advantage of directly simulating cross-boundary effects between these two hydraulically connected systems.

The model grids, depths, bottom roughness parameters, and boundary conditions used for the combined model (EFDC-Combined hydrodynamic model) are identical to the individual EFDC-LSJR and EFDC-MSJR hydrodynamic models. Boundary conditions include ocean tide, rainfall, evaporation, wind, river discharge, groundwater discharge, and spring discharge.

Results using the EFDC-Combined hydrodynamic model are not expected to be identical to the individual models, but we do require that the EFDC-Combined hydrodynamic model be robustly similar throughout the model domain. The goal for confirmation of the EFDC-Combined hydrodynamic model is to show that combination of the individual models does not introduce

any spurious results and that any differences are noted and explained. Confirmation of the EFDC-Combined hydrodynamic model is done by comparison of the EFDC-Combined hydrodynamic model output with output from the individual models. Because the individual models are calibrated and confirmed in the previous sections, a demonstrated strong similarity between the EFDC-Combined hydrodynamic model and the individual EFDC-LSJR and EFDC-MSJR hydrodynamic models confirms the EFDC-Combined hydrodynamic model also.

7.4.1 WATER LEVEL

Simulated water level for the EFDC-Combined, EFDC-MSJR, and EFDC-LSJR hydrodynamic models are compared at 14 water level stations (Table 7–14). The models have a nearly perfect linear match in the lower St. Johns River where r^2 exceeds 0.98 and root-mean square differences (RMSD) are less than 2 cm. The intercept of the regression line and difference statistics for the middle St. Johns River are affected by an approximately 11.5 cm bias in mean water level at Astor. This bias results between the two models because the EFDC-MSJR hydrodynamic model uses observed water level at Astor for its downstream open boundary condition, and the observed mean water level at Astor is about 11.5 cm lower than the simulated mean water level from the EFDC-Combined hydrodynamic model. The effect of the offset of mean water level between the two models extends throughout the middle St. Johns River.

Table 7–14. Comparison of hourly water level between EFDC-MSJR, EFDC-LSJR, and EFDC-Combined hydrodynamic models during the confirmation period, 1996 to 2005.

Station	<i>NRECS</i>	r^2	<i>m</i>	<i>b</i> (cm)	<i>RMSE</i> (cm)	<i>AVRE</i> (cm)	<i>AVAE</i> (cm)
Bar Pilot Dock	87649	1.000	1.000	-0.487	0.627	0.478	0.505
Long Branch	87649	1.000	0.998	-0.837	1.077	0.829	0.871
Main Street Bridge	87649	1.000	0.995	-0.879	1.079	0.816	0.863
Buckman Bridge	87649	0.999	0.993	-0.836	1.113	0.844	0.898
Shands Bridge	87649	0.999	0.992	-0.804	1.121	0.821	0.891
Racy Point	87649	0.999	0.993	-0.803	1.167	0.822	0.912
Palatka	87649	0.998	0.992	-0.838	1.288	0.868	0.990
Buffalo Bluff	87649	0.988	0.988	-0.869	1.427	0.928	1.079
Welaka	87649	0.994	0.972	-0.912	1.954	1.147	1.428
Astor	87649	0.969	0.999	-11.436	12.139	11.453	11.463
Lake Woodruff	87649	0.974	1.000	-11.420	12.059	11.426	11.432
DeLand	87649	0.988	1.005	-11.482	11.853	11.425	11.361
Sanford	87649	0.997	1.006	-11.483	11.592	11.161	11.257
SR 46 at Lake Jesup	87649	0.998	1.006	-11.465	11.521	11.250	11.216
Osceola	87649	0.999	1.005	-11.355	11.252	11.033	11.033

NRECS = Number of paired values of simulated and observed salinity

r^2 = Coefficient of determination

m = Slope of linear regression line

b = Intercept of the linear regression line

RMSE = Root-mean-square error

AVRE = Average relative error (%)

AVAE = Average absolute error

The vertical offset between observed and simulated water level at Astor is confirmed by comparison of simulated water level using the EFDC-Combined hydrodynamic model with observed water level (Table 7–15). Simulated water level at Astor is highly correlated with observed water level ($r^2 = 0.985$) but with an 11.4 cm vertical offset in water level.

Table 7–15. Comparison of observed and simulated (EFDC-Combined hydrodynamic model) hourly water level at Astor during the confirmation period, 1996 to 2005.

Station	<i>NRECS</i>	r^2	<i>m</i>	<i>b</i>	<i>RMSE</i> (cm)	<i>AVRE</i> (cm)	<i>AVAE</i> (cm)
Astor	82002	0.985	0.994	-11.4	12.105	11.445	11.456

- NRECS* = Number of paired values of simulated and observed salinity
- r^2 = Coefficient of determination
- m* = Slope of linear regression line
- b* = Intercept of the linear regression line
- RMSE* = Root-mean-square error
- AVRE* = Average relative error (%)
- AVAE* = Average absolute error

As discussed in Section 3.1, the vertical leveling of the middle St. Johns River water level gauges deviate from a geoidal surface by up to ±15 cm. The mismatch of simulated and observed water level in the middle St. Johns River is a manifestation of this uncertainty in vertical levels. The distribution of water level throughout the model domain is shown in Figure 7–47 for the EFDC-MSJR and EFDC-LSJR hydrodynamic models (dashed line), EFDC-Combined hydrodynamic model (solid line), and observed data (square symbol with error bar) for the confirmation period. Simulated water level distributions are nearly identical for the EFDC-Combined hydrodynamic model and EFDC-LSJR hydrodynamic model from the river mouth to Welaka. Simulated water level distributions for the EFDC-Combined hydrodynamic model are shifted above distributions for the EFDC-MSJR hydrodynamic model between Astor and Osceola. Median water level simulated by the EFDC-Combined hydrodynamic model is within 1 cm of observed values throughout the model domain except at Astor and DeLand. The EFDC-Combined hydrodynamic model correctly simulates the median river slope of 50 cm over 295 km from Osceola to Bar Pilot Dock. The EFDC-Combined hydrodynamic model results indicate that the vertical datum at Astor and DeLand are physically inconsistent with locations both upstream and downstream. From this view, simulated water level using the EFDC-Combined hydrodynamic model provides more accurate surface water slopes than direct observations.

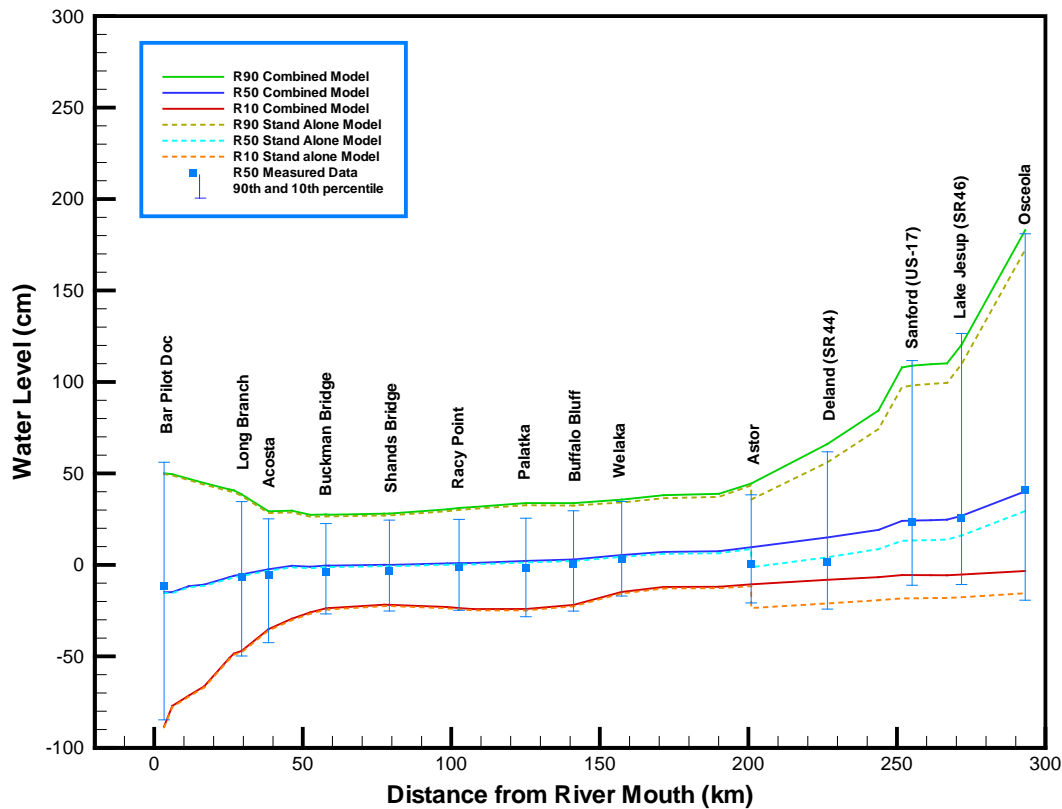


Figure 7–47. Longitudinal variation of the distribution of water levels for the EFDC-Combined, EFDC-MSJR, and EFDC-LSJR hydrodynamic models, and observations throughout the lower and middle St. Johns River during the confirmation period, 1996 to 2005.

7.4.2 DISCHARGE

Comparative statistics for hourly discharge between the EFDC-MSJR, EFDC-LSJR, and EFDC-Combined hydrodynamic models are shown in Table 7–16. The stand-alone and combined models have near perfect linear agreement at all stations. There is a 10 to 12 m^3s^{-1} bias for stations downstream of Astor that results from the overprediction of discharge at Astor for the EFDC-MSJR hydrodynamic model (Table 7–11). The EFDC-LSJR hydrodynamic model used observed Astor discharge as the upstream boundary condition, while the EFDC-Combined hydrodynamic model simulates discharge at this location. The 10.5% overprediction of discharge from the EFDC-MSJR hydrodynamic model is transferred to the entire lower St. Johns River area in the EFDC-Combined hydrodynamic model. This bias is seen in the intercept (b) of the linear regression line at Main Street Bridge and Buffalo Bluff.

Table 7–16. Comparison of hourly discharge between EFDC-MSJR, EFDC-LSJR, and EFDC-Combined hydrodynamic model during the confirmation period, 1996 to 2005. Units of *b*, *RMSE*, and *AVAE* are m^3s^{-1} .

Station	<i>NRECS</i>	r^2	<i>m</i>	<i>b</i>	<i>RMSE</i>	<i>AVRE</i> (%)	<i>AVAE</i>
Main Street Bridge	87649	1.00	1.00	-11.83	37.54	11.00	26.50
Buffalo Bluff	87649	0.99	1.00	-10.49	28.43	10.93	18.62
Astor (MSJR)	87649	0.95	0.97	2.96	20.33	0.03	13.68
DeLand	87649	0.99	0.99	0.57	6.92	0.00	4.58
Sanford	87649	0.99	0.99	0.46	6.44	0.01	4.10
SJR-415	87649	1.00	1.00	0.21	3.51	0.00	2.25
SR 46 at Lake Jesup	87649	0.95	0.98	0.13	2.35	0.00	1.47
Osceola	87649	1.00	1.00	0.06	1.18	0.00	0.73

- NRECS* = Number of paired values of simulated and observed salinity
- r^2 = Coefficient of determination
- m* = Slope of linear regression line
- b* = Intercept of the linear regression line
- RMSE* = Root-mean-square error
- AVRE* = Average relative error (%)
- AVAE* = Average absolute error

7.4.3 SALINITY

Comparative statistics for paired, vertically averaged hourly salinity between the stand-alone models and combined model are shown in Table 7–17. Correlation is high ($r^2 > 0.91$) for all locations except Shands Bridge ($r^2 = 0.68$). *RMSE* is highest in the estuarine portion of the river between Bar Pilot Dock and Shands Bridge. In these areas, the salinity for the EFDC-Combined hydrodynamic model is lower than the EFDC-LSJR hydrodynamic model. The increase in discharge entering the lower river through Astor is a possible reason for the decreased salinity of the EFDC-Combined hydrodynamic model.

The lower correlation at Shands Bridge compared to the other stations is due to its location in an area of the river near the farthest upstream extent of intrusions of seawater. The decreased salinity in the EFDC-Combined hydrodynamic model reduced the number of discrete salinity events at this location.

Table 7–17. Comparison of vertically averaged salinity between EFDC-MSJR, EFDC-LSJR, and EFDC-Combined hydrodynamic models during the confirmation period, 1996 to 2005.

Station	<i>NRECS</i>	r^2	<i>m</i>	<i>b</i>	<i>RMSE</i>	<i>AVRE</i>	<i>AVAE</i>
Bar Pilot Doc	87649	0.99	0.96	1.89	0.98	-0.81	0.83
Dames Point.	87649	0.99	0.97	1.75	1.35	-1.09	1.12
Acosta Bridge	87649	0.98	1.04	0.65	1.32	-0.91	0.94
Buckman Bridge	87649	0.96	1.24	0.26	1.18	-0.66	0.67
Shands Bridge	87649	0.68	2.96	-0.67	0.69	-0.17	0.19
BB-22 WQMN	87649	0.91	0.83	0.06	0.04	0.01	0.03
LAG-WQMN	87649	0.92	0.84	0.06	0.05	0.01	0.04
Astor	87649	0.99	0.97	0.01	0.02	0.01	0.01
DeLand	87649	0.98	0.99	0.01	0.03	0.01	0.01
Sanford	87649	0.99	1.00	-0.00	0.03	0.00	0.01
SJR-415	87649	1.00	1.00	-0.00	0.02	-0.00	0.01
SR 46 at Lake Jesup	87649	0.99	0.99	0.00	0.03	0.00	0.01
Osceola	87649	1.00	1.00	0.00	0.01	-0.00	0.00

NRECS = Number of paired values of simulated and observed salinity

r^2 = Coefficient of determination

m = Slope of linear regression line

b = Intercept of the linear regression line

RMSE = Root-mean-square error

AVRE = Average relative error (%)

AVAE = Average absolute error

The distribution of salinity over the confirmation period is compared for the EFDC-Combined hydrodynamic model, standalone models, and observation in Figure 7–48. EFDC-Combined hydrodynamic model exhibits a similar spatial pattern of salinity distribution as for the standalone models.

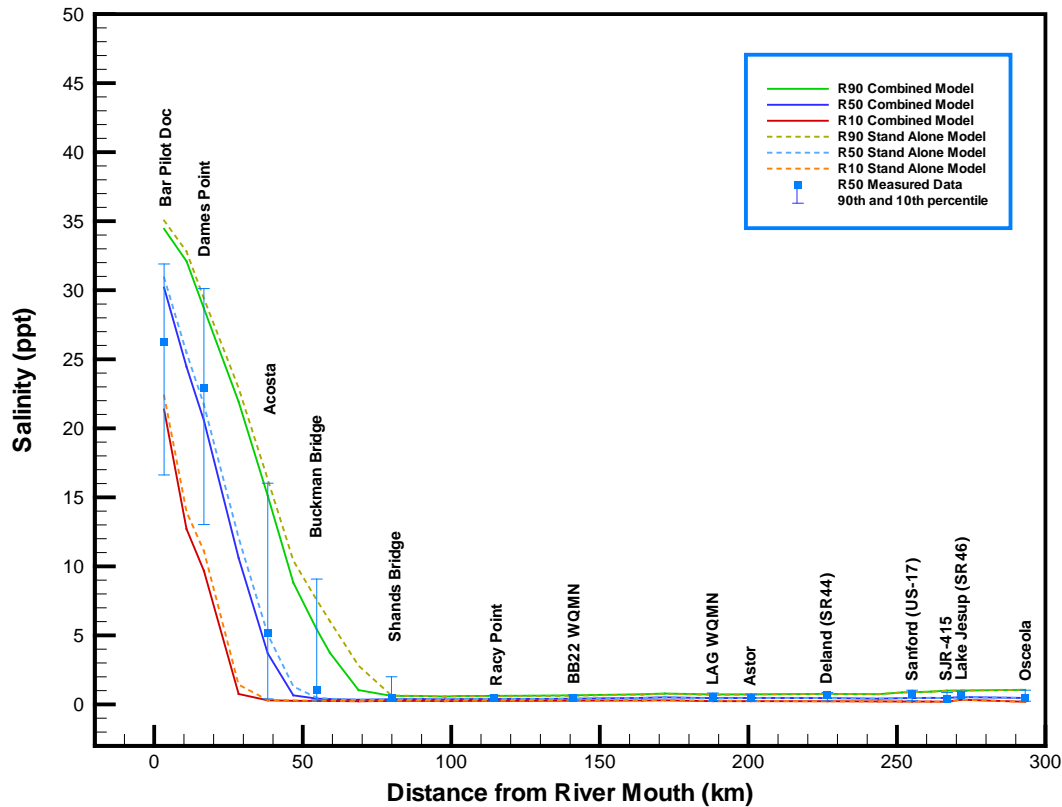


Figure 7-48. Longitudinal variation of distribution of salinity for the EFDC-Combined, EFDC-MSJR, and EFDC-LSJR hydrodynamic models, and observations throughout the lower and middle St. Johns River during the confirmation period, 1996 to 2005.

Summary

A combined model was created to facilitate the evaluation of hydrodynamic changes throughout the lower and middle St. Johns River due to water withdrawals. The combined model (EFDC-Combined hydrodynamic model) exhibits nearly identical variability of water level, discharge, and salinity as the stand-alone EFDC-LSJR and EFDC-MSJR hydrodynamic models. At nearly all locations and variables tested, the correlation between the EFDC-Combined hydrodynamic model output and stand-alone model output are very high.

Differences between the EFDC-Combined hydrodynamic model and stand-alone models are primarily a result of differences in the boundary conditions at Astor, the boundary between the stand-alone models. The EFDC-MSJR hydrodynamic model uses observed water level at Astor as a downstream open boundary condition. Application of the EFDC-Combined hydrodynamic model shows that the absolute level of the Astor gauge is likely biased low. Simulated water levels using the EFDC-Combined hydrodynamic model are thus about 11.5 cm higher than simulated water levels using the EFDC-MSJR hydrodynamic model. Astor is also the upstream flow boundary for the EFDC-LSJR hydrodynamic model, where observed discharges were used

as the upstream boundary condition. For the EFDC-Combined hydrodynamic model, the upstream flow boundary was moved to Lake Harney and flow at Astor was simulated. Simulated flow at Astor is, on average, about 10.5% higher than observed. Simulated discharge using the EFDC-Combined hydrodynamic model, then, is higher than for the stand-alone EFDC-LSJR hydrodynamic model. The higher discharge of the EFDC-Combined hydrodynamic model likely contributes to lower simulated salinity in the estuarine portion of the river for the EFDC-Combined hydrodynamic model compared to the EFDC-LSJR hydrodynamic model.

Despite the differences between the EFDC-Combined and stand-alone models, the underlying physics are unchanged. The differences between the models are readily explained as differences of boundary conditions and the model behavior is expected given the nature of these differences. The EFDC-Combined hydrodynamic model is regarded as equivalent to the stand-alone model, although with a perturbed system state. Relative differences calculated between scenarios using the EFDC-Combined hydrodynamic model should be equivalent to differences calculated using the stand-alone models. The system state for the WSIS scenarios will be perturbed further, because all model results shown here use observed tributary discharges, but all WSIS scenarios will use tributary discharge simulated by the HSPF hydrologic model. The use of simulated discharges allows for more accurate representation of hydrologic scenarios for testing land use alterations and structural changes to watersheds.

8 CONCLUSIONS

Quantification of the effects of water withdrawals on hydrodynamic variables is central to the goals of the WSIS. Evaluation of the effects of water withdrawals requires knowledge of how these withdrawals will affect water level, discharge, velocity, salinity, and discharge at many different locations and for a range of time scales. In addition, this evaluation needs to consider the interactions of water withdrawals with other future factors that will affect hydrodynamic variables, such as land use and structural changes within watersheds and sea level rise.

The EFDC hydrodynamic model application of the lower and middle St. Johns River, as developed for the WSIS, is the best available tool for assessing the effects of water withdrawals and other future hydrologic changes on river hydrodynamics. This model is demonstrated to provide robust simulations of hydrodynamic variables over a wide range of meteorological conditions that include winter and tropical storm events, periods of extended drought, and extreme wet periods. The ability of the model to dynamically simulate hydrodynamic variables over a wide range of conditions indicates that the model will correctly simulate perturbations to the system needed to test water withdrawal scenarios, both alone and in conjunction with other expected future conditions.

In the tidal portions of the St. Johns River, the model successfully captures tidal dynamics for water level, discharge, salinity, and salinity stratification. Importantly, the model correctly hindcasts the timing, strength, duration, and upstream extent of intrusions of seawater into the oligohaline and fresh segments of the river. The possible encroachment of salinity into normally oligohaline or fresh areas caused by flow reduction was an important question for several of the WSIS evaluations. The ability of the model to properly simulate intrusions of seawater results from its ability to integrate downstream freshwater transport, upstream tidal transport, estuarine circulation, and mass movements generated from low frequency ocean water level variability.

In the nontidal middle St. Johns River, the model correctly simulates daily variability of water levels, discharge, and salinity. Frictional resistance is calibrated using observed slope–discharge relationships. The ability of the model to correctly capture the slope–discharge relationships over a wide range of hydrologic conditions ensures that the model will accurately predict the reduction of river stage caused by water withdrawals in this area. Observed water level data are used to show that stage in the middle St. Johns River is dominated by low frequency ocean water level for periods when river discharge is below the median discharge. Below the median river discharge, then, river stage is independent of river discharge. This result partly justifies the use of a hydrodynamic model in the non-tidal middle St. Johns River. The model is shown to correctly propagate the low frequency ocean signal throughout the middle St. Johns River.

An additional important model skill for the WSIS is the ability of the model to simulate sea level rise. Because the model accounts for ocean effects throughout the lower 300 km of river, it implicitly accounts for sea level rise also. A long-term record of observed stage at DeLand shows that the rate of sea level rise in the middle St. Johns River is comparable (1 to 3 mm yr⁻¹) to sea level rise at the river mouth near Mayport. The WSIS is designed to assess hydrodynamic changes over a 35-yr period (1995 to 2030) for which sea level rise would minimally be 3.5 to 10.5 cm. This total rise is the same order of magnitude as expected stage reductions caused by water withdrawals (1 to 6 cm), illustrating the importance of considering sea level rise over the time frame established for the study.

Finally, the hydrodynamic model is a good predictor of salinity in the middle St. Johns River. This result shows that (a) salinity can reliably be used as a conservative tracer in the middle St. Johns River even though salinity levels are low (0.1 to 1.5), (b) the overall chloride budget of the middle St. Johns River, which depends greatly on groundwater inflows, is well-constrained, and (c) simulated water ages, a measure of flushing, are correct.

Although the EFDC hydrodynamic model of the St. Johns River meets the requirements of the WSIS, several model features need expansion, improvement, or additional testing for the future. This hydrodynamic model represents a considerable investment of SJRWMD resources and it will assuredly have continued application for other questions and studies in the future. As such, continued investment into model development will likely benefit future management of this important resource.

The addition of flooding and drying of adjacent flood plain areas in the middle St. Johns River would improve the model's prediction of flood stage in Lake Harney and could improve also the model's simulation of reverse flow events. The EFDC model code has the capability of simulating flooding and drying of tidal marshes and floodplain areas, but this feature was not used for the WSIS.

Additional tests are required to determine why the model could not simulate salinity variability in Lake Woodruff. The model correctly simulates the timing and spatial variation of salinity throughout the middle St. Johns River, except for Lake Woodruff. A first step towards examining this area is assessment of the channel geometry entering and exiting the lake. Examining the influence of the considerable amount of floating vegetative cover within the lake and side storage of the surrounding wooded swamps on lake hydrodynamics could also provide a better understanding of how Lake Woodruff interacts with the adjacent St. Johns River.

The model is now and will continue to be relied upon to simulate the salinity response in the estuarine portion of the river to a combination of factors: tide, storm surge, wind, discharge, sea level rise, and channel alterations. Although the model shows a realistic response to observed salinity at widely spaced locations, there is a paucity of data for confirming the model's dynamic simulation of salinity at tidal scales. Similarly, observations confirming the model's simulation of residual estuarine circulation are not presently available. Future data collection efforts should consider addressing this hole in our understanding of these important dynamic effects.

Finally, eight bridges cross the estuarine river over the lower 50 km of river. Six bridge crossings occur within a 7-km river reach near Jacksonville, between river km 33.5 and 39.6. This reach is also an area with large spatial and temporal variability of salinity. The constrictive effects of these bridges on flow, mixing, and salinity transport has not been studied, yet could be an important consideration for affecting the upstream transport of salt or salinity stratification.

BIBLIOGRAPHY

- Allen, R.G. *Evaluation of a Temperature Difference Method for Computing Grass Reference Evapotranspiration*. Rome: Food and Agricultural Organization of the United Nations, 1993.
- Alt, D., and H. Brooks. "Age of the Florida marine terraces." *The Journal of Geology*, 1965: Vol. 73 (2): 406-411.
- Apel, J. R. *Principles of Ocean Physics*. New York: Academic Press, 1987.
- APHA. *Standard Methods for the Examination of Water and Wastewater, 19th ed.* 1995.
- ASCE. "Criteria for Evaluation of Watershed Models." *J. Irrigation and Drainage Engineering*, 1993: Vol. 1993(3): 429-443.
- Atkinson, L. P. "Hydrography and Nutrients of the Southeastern U.S. Continental Shelf." In *Oceanography of the Southeastern U.S. Continental Shelf*, by L. P. Atkinson, D. W. Menzel and K. A. Bush, 77-92. Washington D.C.: American Geophysical Union, 1985.
- Bicknell, B. R., J. C. Imhoff, J. L. Kittle, A. S. Donigian, and R. C. Johanson. *Hydrologic Simulation Program - FORTRAN, User's Manual for Version 11*. Athens, GA: U.S. EPA, National Exposure Research Laboratory, 1997.
- Blanton, J. O., F. B. Schwing, A. H. Weber, L. J. Pietrafesa, and D. W. Hayes. "Wind stress climatology in the South Atlantic Bight." In *Oceanography of the Southeastern U.S. Continental Shelf*, by D. W. Menzel, K. A. Bush L. P. Atkinson, 10-21. Washington, D.C.: American Geophysical Union, 1985.
- Brown, D. W. *Water Resources of Brevard County, Florida. Report of Investigations No. 28*. Florida Geological Survey, 1962.
- Cera, Tim. *Tidal Analysis Program Python (TAPPY)*. 2010.
http://sourceforge.net/apps/mediawiki/tappy/index.php?title=Main_Page.
- Copeland, R. *Regional and Statewide Trends in Florida's Spring and Well Groundwater Quality (1991-2003)*. Florida Geological Survey Bulletin No. 69, 2009.
- Doherty, John. *PEST, Model-Independent Parameter Estimation, User Manual: 5th Edition*. Watermark Numerical Computing, 2004.
- EPA. *EFDC Page*. 2011. <http://www.epa.gov/athens/research/modeling/efdc.html> (accessed Feb. 7, 2011).
- FDEP. *Biological and Chemical Assessment of Water Quality in Tributaries of Lake Jesup, Seminole County, Florida*. FDEP, Central District Surface Water Assessment and Monitoring Section, 1997.
- Ferguson, G. E. *Springs of Florida*. Florida Geological Survey Bulletin No. 31, 1947.
- Fischer, H. B., E. J. List, R. C. Y. Koh, and N. H. Brooks. *Mixing in Inland and Coastal Waters*. New York: Academic Press, 1979.

- Flinchem, E. P., and D. A. Jay. "An introduction to wavelet transform analysis methods." *Estuarine and Coastal Shelf Science*, 2000: 51(2): 177-200.
- Hagen, S. C., and D. M. Parrish. "Mesh Requirements for Tidal Modeling in the Western North Atlantic." *J. Computational Fluid Dynamics*, 2004: Vol. 18(7): 585-595.
- Hamrick, J. M. *A three-dimensional environmental fluid dynamics code: Theoretical and computational aspects. Special Report 317*. Gloucester Point, VA: The College of William and Mary, Virginia Institute of Marine Sciences, 1992.
- Hargreaves, H. G., and R. G. Allen. "History of evaluation of Hargreaves Evaporation Equation." *J. of Irrigation and Drainage Engineering*, 2003: Vol. 129(1): 53-63.
- Hem, J. D. *Study and Interpretation of the Chemical Characteristics of Natural Waters. WSP 2254*. Washington, D.C.: USGS, 1992.
- Intra. "Statistical modeling of spring discharge at Rock and Wekiwa Springs in Orange County, Florida. Final Report. SJRWMD. Special Publication SJ2007-SP9." 2007a.
- Intra. "Statistical modeling of spring discharge at Ponce DeLeon, Green, and Gemini Springs in Volusia County, Florida. Final Report SJRWMD. Special Publication SJ2007-SP12." 2007b.
- Jensen, M. E., R. D. Burman, and R. G. Allen. *Evapotranspiration and Irrigation Water Requirements*. ASCE Manuals and Reports on Engineering Practice No. 70: 350 pp., 1990.
- Johnson, R. A. *Hydrogeology of the St. Johns River Water Management District. 82-SP2*. Palatka, FL: St. Johns River Water Management District, 1982.
- Kaufman, M. *The Chemical Type of Water in Florida Streams*. USGS Map Series., 1975.
- Kroening, S. E. *Streamflow and Water-Quality Characteristics at Selected Sites of the St. Johns River in Central Florida, 1933 to 2002*. Scientific Investigations Report 2004-5177, USGS, 2004.
- Lewis, E. L. "The practical salinity scale and its antecedents." *IEEE Journal of Ocean Engineering* OE 5, no. 1 (1980): 3-8.
- Lewis, E. L., and R. G. Perkin. "Salinity: Its definition and calculation." *J. Geophysical Res.*, 1978: Vol. 83 (C1): 466-478.
- Linsley, R. K. *Hydrology for Engineers*. 1982.
- Mangelsdorf, P. C. "Salinity measurements in estuaries." In *Estuaries*, by G.H. Lauff, 71-79. Washington D.C.: American Assoc. for the Advancement of Science, 1964.
- Martin, J. L., and S. C. McCutcheon. *Hydrodynamics and Transport for Water Quality Modeling*. Boca Raton, FL: CRC Press, Inc., 1999.
- Maucha, R. *Hydrochemische Methoden in der Limnologie*. Binnegewasser 12, 173 pp., 1932.
- Montgomery, D. *Introduction to Linear Regression Analysis, 4th ed*. New Jersey: Wiley and Sons, Inc., 2006.

- Moore, D. S., and G. P. McCabe. *Introduction to the Practice of Statistics*. New York: W.H. Freeman and Co., 1989.
- Morris, Frederick W. *Volume 3 of the Lower St. Johns River Reconnaissance: Hydrodynamics and Salinity of Surface Water*. Palatka, FL: St. Johns River Water Management District, 1995.
- Munch, D. *Saline Contamination of a Limestone Aquifer by Connate Intrusion in Agricultural Areas of St. Johns, Putnam, and Flagler Counties, Northeast Florida*. Palatka: Tech. Pub. SJ79-4, SJRWMD, 1979.
- Munson, B. R., D. F. Young, and T. H. Okiishi. *Fundamentals of Fluid Mechanics*. New York: John Wiley & Sons, 1990.
- NOAA. *Tides&Currents*. 08 02, 2010. <http://co-ops.nos.noaa.gov/> (accessed 08 12, 2010).
- Odum, H. T. "Factors controlling marine invasion into Florida fresh waters." *Bulletin Marine Science*, 1953: 3(2): 134-156.
- Oey, L., G. L. Mellor, and R. I. Hires. "A Three-Dimensional Simulation of the Hudson-Raritan Estuary. Part I: Description of the Model and Model Simulations." *J. Physical Oceanography*, 1985: Vol. 15: 1676-1692.
- Opdyke, N. D. "Origin of the epirogenic uplift of Pliocene-Pleistocene beach ridges in Florida and development of the Florida karst." *Geology*, 1984: Vol 12: 226-228.
- Pirkle, W. A. "The offset course of the St. Johns River, Florida." *Southeastern Geology*, 1971: Vol. 13: 39-59.
- Robison, C. P. *Middle St. Johns River Minimum Flows and Levels Hydrologic Methods Report*. Palatka, FL: Tech. Pub. SJ2004-2, SJRWMD, 2004.
- Sacks, L. A., and A. B. Tihansky. *Geochemical and Isotopic Composition of Groundwater, With Emphasis on Sources of Sulfate, in the Upper Floridan Aquifer and Intermediate Floridan Aquifer System, in Southwest Florida. WRI Report 96-4146*. Washington, D.C.: USGS, 1996.
- Sawyer, C. N., P. L. McCarthy, and G. F. Parkin. *Chemistry for Environmental Engineering*. New York: McGraw-Hill, Inc., 1994.
- Schureman, Paul. *Manual of Harmonic Analysis and Prediction of Tides*. Washington, D.C.: Special Publication No. 98, U.S. Department of Commerce, Government Printing Office, 1988.
- Scott, T. M. *The Geology of the Hawthorne Formation of Northeastern Florida. Report of Investigation No. 94*. Florida Bureau of Geology, 1983.
- Silberbauer, M. J., and J. M. King. "Geographical trends in the water chemistry of wetlands in the southwestern Cape Province, South Africa." *Southern African Journal of Aquatic Sciences.*, 1991: Vol. 17: 82-88.
- Slack, L. J., and J. C. Rosenau. *Water Quality of Florida Springs, Map Series No. 96*. Washington, D.C.: USGS, 1979.

- Spechler, R. M. *Saltwater Intrusion and Quality of Water in the Floridan Aquifer System, Northeast Florida*. Washington, D.C.: USGS Water-Resources Investigations Report 92-4174., 1994.
- Stewart, J. "Hydrodynamic and Circulation Study of Crescent Lake in the St. Johns River, Florida." *19th Biennial Conference of the Estuarine Research Federation*, 2008.
- Sturm, T. W. *Open Channel Hydraulics*. McGraw-Hill, 2001.
- Sucsy, P. V., and F. W. Morris. *Calibration of a Three-Dimensional Circulation and Mixing Model of the Lower St. Johns River*. Palatka, FL: St. Johns River Water Mgt. Dist., 2002.
- . "Salinity intrusion in the St. Johns River, Florida." Edited by M Spaulding. *Estuarine and Coastal Modeling, Proceedings of the Seventh International Conference*. Alexandria, VA: ASCE, 2001. 120-139.
- Thomann, R. V. "Verification of Water Quality Models." *J. Env. Eng. Div.*, 1982: Vol. 108(E5): 923-940.
- Thomas, G. B. *Calculus and Analytical Geometry*. Phillipines: Addison-Wesley Publishing Company, 1972.
- Tibbals, C. H. *Hydrology of the Florida Aquifer System in East-Central Florida. Professional Paper 1403E*. Washington, D.C.: U.S. Geological Survey, 1990.
- University of Florida IFAS Extension. August 24, 2010. <http://fawn.ifas.ufl.edu/>.
- USGS. *Water Resources Data, Florida Water Year 2004. Vol. 1A*. USGS Surface Water Data Report FL-0401A, 2004.
- Venice Symposium. "The Venice System for the classification of marine waters according to salinity." *Limnology and Oceanography*, 1958: Vol. 3(3); 346-347.
- Vincent, M., M. Luther, and M. Ross. "Analysis of the Tampa Bay Coastal Prediction System." *Estuarine and Coastal Modeling. Proceedings of the Seventh International Conference*. St. Petersburg, FL: ASCE, 2001. pp. 1023-1040.
- Visual Numerics. *PV - Wave 7.5 Reference Volumes 1 - 3*. Houston, Texas: Visual Numerics, Inc., 2001.
- Wetzel, R. G. *Limnology of Lakes and River Systems*. San Diego, CA: Academic Press, 2001.
- White, W. A. *The Geomorphology of the Florida Peninsula. Geological Bulletin No. 51*. Florida Bureau of Geology, 1970.
- Winkler, S. *Status and Trends in Water Quality at Selected Sites in the St. Johns River Water Management District*. Palatka: SJRWMD Tec. Pub. SJ2004-3, 2004.
- Wyrick, G. *The Groundwater Resources of Volusia County, Florida. Report of Investigations No. 22*. Tallahassee, FL: Florida Geological Survey, 1960.
- Zervas, C. *Sea Level Variations of the United States, 1854-1999*. NOAA Tech. Rept. (NOS COOPS 36), 2001.

Zilkoski D. B., J. H. Richards, and G. M. Young. "Result of the General Adjustment of the North American Vertical Datum of 1988." *Survey and Land Information Systems*, 1992: Vol. 52(3): 133-149.

